FACULTY OF ENGINEERING
AND ARCHITECTURE

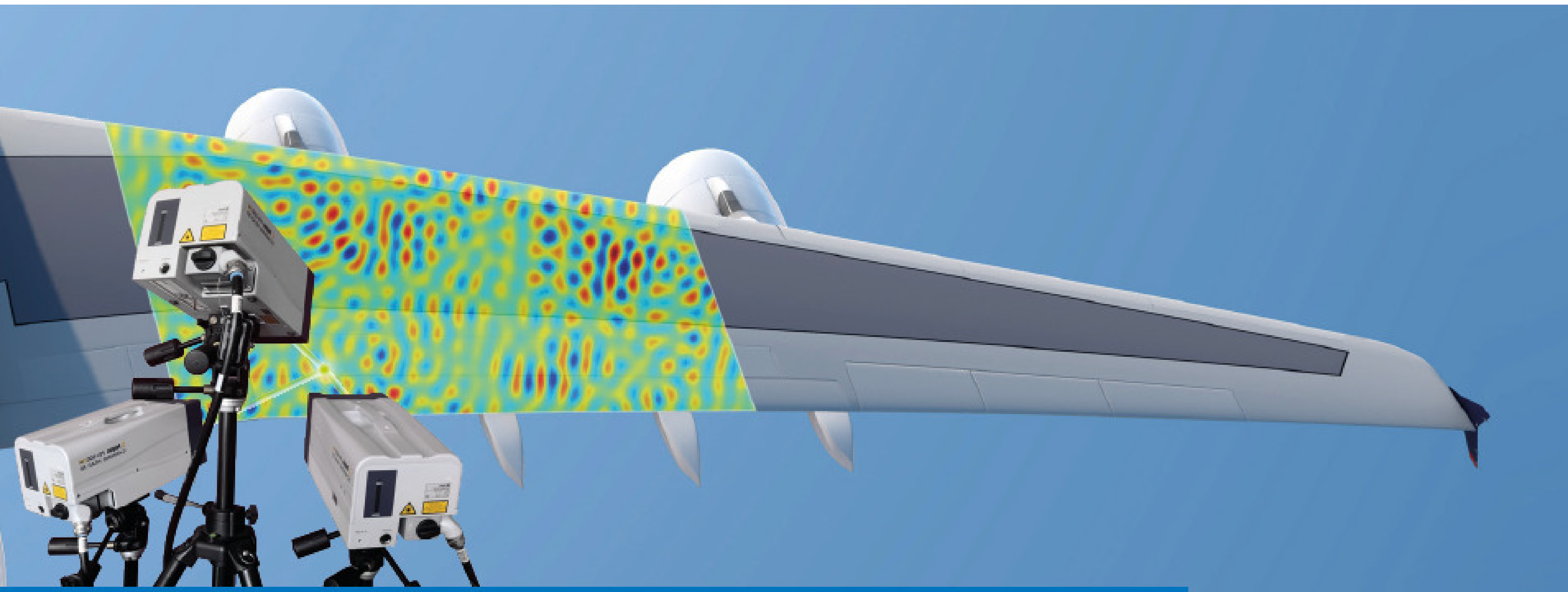

Full-Field Elastic Wave Imaging and Processing for Non-Destructive Inspection of Fiber-Reinforced Polymers

Joost Segers

Doctoral dissertation submitted to obtain the academic degree of
Doctor of Electromechanical Engineering

Supervisors
Prof. Mathias Kersemans, PhD - Saeid Hedayatrasa, PhD

Department of Materials, Textiles and Chemical Engineering
Faculty of Engineering and Architecture, Ghent University

December 2021

GHENT
UNIVERSITY

FACULTY OF ENGINEERING
AND ARCHITECTURE

Full-Field Elastic Wave Imaging and Processing for Non-Destructive Inspection of Fiber-Reinforced Polymers

Joost Segers

Doctoral dissertation submitted to obtain the academic degree of
Doctor of Electromechanical Engineering

Supervisors
Prof. Mathias Kersemans, PhD - Saeid Hedayatrasa, PhD

Department of Materials, Textiles and Chemical Engineering
Faculty of Engineering and Architecture, Ghent University

December 2021

GHENT
UNIVERSITY

ISBN 978-94-6355-550-0
NUR 971, 978
Wettelijk depot: D/2021/10.500/98

Members of the Examination Board

Chair

Prof. Filip De Turck, PhD, Ghent University

Other members entitled to vote

Prof. Paweł Kudela, PhD, Polish Academy of Sciences, Poland
Prof. Mia Loccufier, PhD, Ghent University
Prof. Łukasz Pieczonka, PhD, AGH University of Science and Technology, Poland
Prof. Koen Van Den Abeele, PhD, Katholieke Universiteit Leuven
Prof. Wim Van Paepegem, PhD, Ghent University

Supervisors

Prof. Mathias Kersemans, PhD, Ghent University
Saeid Hedayatrasa, PhD, Ghent University

Research Institute:

Ghent University
Faculty of Engineering and Architecture
Department of Materials, Textiles and Chemical Engineering
Technologiepark-Zwijnaarde 46
B-9052 Zwijnaarde
Belgium

Tel. +32 (0)9 331 04 59
Joost.Segers@ugent.be
Joost-Segers@hotmail.com

Research Funds:

This research is funded by The Research Foundation – Flanders (FWO-Vlaanderen, Fonds voor Wetenschappelijk Onderzoek in Vlaanderen, Grant no. 1148018N) and by the SBO project DETECT-IV (Grant no. 160455), which fits in the SIM research program MacroModelMat (M3) coordinated by Siemens (Siemens Digital Industries Software, Belgium) and funded by SIM (Strategic Initiative Materials in Flanders) and VLAIO (Flemish government agency Flanders Innovation & Entrepreneurship).

Acknowledgements

Performing a PhD study is an unexpected journey in the scientific world. It has been a learning adventure on the scientific level as well as on the personal level. The start of the study is intimidating because of the unfamiliar topic and big amount of work that must be handled. In the end, I managed to tackle it thanks to the help and support of several persons, to whom I wish to express my gratitude.

First, I want to thank Mathias Kersemans and Wim Van Paepegem for selecting this research topic and for giving me the chance to perform research on it. Thank you for triggering my interest in the world of NDT and composites and for guiding me through the PhD study. I also want to thank Mathias Kersemans for the excellent supervision and close collaboration during the last four years. I am grateful for the scientific freedom I received, for your immediate answers to all my questions and for the difficult but enjoyable discussions we had on various mathematical and physical problems. I could not have wished for a better supervisor. In addition to Mathias, the feedback of Wim and his extensive knowledge on the challenges related to composite components proved highly valuable.
In addition, I want to express gratitude to Saeid Hedayatrasa who helped supervising me through this PhD-journey. A big thanks for always being helpful, for giving detailed feedback on my work and for the enjoyable collaboration on vibrothermography and phononic crystals.

I also want to thank the following colleagues for their specific contributions to my PhD study. Gaétan, thank you for the good collaboration on finding the defects in the industrial components and for providing feedback on my ideas and papers. I also enjoyed the competition we had between your thermographic methods and my vibrometric approaches. A big thanks to Erik, the ultrasound and LabVIEW guru. Your ultrasonic NDT inspections are of excellent quality and improved the scientific value of this PhD work. Thank you, Ruben, for the support on the use of Matlab and Abaqus and for not getting angry when I used 100+ GB of RAM on the workstations. Ives, thank you for being my office mate and for the support, especially on the practical topics, that I received from you. Line, thank you for helping me with all the required administration. Technicians Luc and Pascal, thank you for making various parts and giving insights in solving technical problems.

Next to my colleagues and supervisors, the research could not have been performed without the financial support of FWO Flanders (grant 1148018N), SIM Flanders and VLAIO through the SBO project DETECT-IV (grant 160455) coordinated by Siemens (Siemens Digital Industries Software, Belgium). Also, indispensable were the test specimens we received from SABCA Limburg, Honda Japan, Engie Laborelec and Eddy Merckx bicycles. Also thanks to Emilio from Siemens for the good discussions and the collaboration on the SLDV noise study.

In addition, I would like to thank the jury members for reading and evaluating this dissertation.

The PhD-journey was not always easy. Thankfully, there were my colleagues who became good friends and provided excellent distraction in the stressful moments. I want to thank the colleagues listed above as well as all other members of the MMS and SMS research groups. The coffee breaks at 10h, the fun talks during lunch, the conference adventures and the get-togethers after the working hours made me really enjoy my years at the university.

Het laatste deel van mijn dankwoord wil ik graag richten aan mijn familie en vrienden. Ik ben blij dat ik dit moment met jullie allen kan delen. Dank u moeke en vake voor jullie onvoorwaardelijke steun en om er altijd voor mij te zijn. Ook bedankt aan mijn broers en hun partners: Dries en Ellen en nichtje Elise en Thijs en Tessa. Verder wil ik graag mijn vrienden bedanken bij wie ik de voorbije vier jaar mijn gedachten kon verzetten en me goed heb geamuseerd. Sommige onder jullie vroegen zich ongetwijfeld af wat ik naast koffie drinken nog deed aan de universiteit. Wel jullie hebben geluk, je kan het even bekijken in de volgende 16 hoofdstukken.
Als allerlaatste, maar tevens allerbelangrijkste, wil ik mijn allerliefste verloofde Marlies bedanken, die mij ongelofelijk veel heeft gesteund tijdens mijn doctoraat. Bedankt voor het begrip als ik niet goed gezind was omdat er een experiment niet goed was verlopen, om me steeds opnieuw te motiveren en om me te leren relativeren. Je bent een geweldige vriendin, je maakt me tot een betere persoon en ik ben benieuwd naar de volgende avonturen die we samen nog gaan beleven.

Table of Contents

PART 3: GUIDED WAVE BASED DAMAGE DETECTION

PART 4: DAMAGE DETECTION PERFORMANCE AND CONCLUSIONS

English Summary

Composite materials consist of two, or more, different material types, with the aim to exploit the beneficial properties of all. As an example, loose carbon fibers with high stiffness and strength are embedded in a low density polymer matrix, which distributes the mechanical stresses over the fibers, to form a carbon fiber reinforced polymer (CFRP) composite. The obtained CFRP material shows an excellent stiffness/strength-to-weight ratio and a good design flexibility which makes it highly suited for application in aerospace (and other) applications. A concern in the use of composites is that their typical layered material structure is susceptible to internal damage. While a small impact event (e.g. tool drop) on an aluminum wing tip will typically introduce no more than a small visible dent in the material, the same impact event on a CFRP wing tip may result in a multitude of internal damage features which, although invisible for the naked eye, can compromise the structural integrity of the wing. In addition to damage inflicted during the operation lifetime, internal defects may already be introduced during the manufacturing process. To assure the structural integrity and performance of composite components, a non-destructive testing (NDT) procedure is required that allows for accurate detection and evaluation of the internal damage (or defects).

During the last decades, multiple NDT methods were developed. Most often used in aerospace applications is the liquid-coupled ultrasonic C-scan. This NDT technique allows for accurate detection and evaluation of a large variety of damage features. However, there are some disadvantages to this technique. The ultrasonic method is relatively slow, may miss non-volumetric defects (e.g. closed cracks), requires a coupling agent (e.g. water) and is difficult to apply on strongly curved parts, at corners and on sandwich structures.

In this PhD study, a different NDT approach is investigated: Full-Field Elastic Wave Inspection. The elastic waves are guided by the surfaces of the thin-walled components, resulting in guided waves. Typical wave frequencies range from 10 to 300 kHz. The waves can travel a relatively long distance and follow the component's curvature. When a propagating elastic wave encounters a defect, a perturbation of the wave characteristic happens, e.g. change in amplitude, change in propagation direction, change in the frequency content, change in the local wavenumber, etc. As a result, the full-field monitoring of elastic waves provides a means to detect defects. This NDT approach seems promising for achieving faster inspection compared to the immersion ultrasonic inspection method. Also the coupling medium is not required, increasing the practicality of the NDT inspection. In addition, the properties of the elastic waves are related to the properties of the medium. As a result, elastic wave inspection should allow

for characterization of the defect's properties (e.g. the depth of the delamination).

The objective of this PhD thesis is to develop novel elastic wavefield manipulation strategies and damage map construction methods with the aim to accurately and efficiently detect and evaluate a wide range of damage features in industrial composite components. The thesis is built on theoretical derivations of the properties of linear and nonlinear elastic waves in combination with the development of novel signal processing strategies. These signal processing strategies are applied on experimental data. The experiments are performed using piezoelectric or laser excitation of the elastic waves in combination with full wavefield monitoring achieved by 3D scanning laser Doppler vibrometry. The dissertation consists of four major parts.

Part 1 of the dissertation starts with the theoretical framework of elastic wave dynamics. It is illustrated how wave equations are obtained by combing the theory of elasticity, i.e. the constitutive stress-strain relations, with Newton's second law of motion, i.e. the relation between acceleration and force (or stress). The wave equations reveal the existence of bulk waves travelling in solid materials. For thin-walled structures, such as the typical composite plates, stress free boundary conditions are imposed and the dispersion relations of the guided elastic waves are obtained. The dispersion relations provide the link between the material's stiffness properties, density and thickness and the guided waves' type (symmetric, anti-symmetric or shear horizontal), wavenumber and frequency. Important concepts, such as phase velocity, energy skew angle, slowness, standing waves and resonances are introduced.
When an elastic wave interacts with a defect, the frequency content of the wave may change as a result of non-classical nonlinearity. A phenomenological model of a clapping and a rubbing defect is used to understand the different nonlinear components that may appear in the frequency spectrum. This model shows that higher harmonics as well as modulation sidebands (in case of dual excitation) are generated at the defect.
In order to detect defects using (guided) elastic waves, high quality measurements of the full wavefield response of the test specimen are required. The full wavefield response is obtained by means of 3D infrared scanning laser Doppler vibrometry. The working principle of the experimental setup is discussed in detail. The typical processing of the measured velocity signals, which is often based on a range of integral transforms, is introduced.

In Part 2 of this dissertation, the local defect resonance (LDR) technique is studied in view of achieving reliable and efficient inspection of composites. After introduction of the concept of the LDR phenomenon, it is analytically illustrated that flexural waves (which are a simplified version of the fundamental anti-symmetric guided elastic wave) give rise to an out-of-plane local resonance (LDR_Z) at the defect at specific high frequencies (typically > 10 kHz). In a similar way, axial waves (which are a simplified version of the fundamental symmetric guided elastic wave) may trigger in-plane local defect resonances (LDR_{XY}) at even higher frequencies. Experimental evidence of LDR is obtained for a range of defects, including flat bottom holes, delaminations, barely visible impact damage, surface breaking cracks and skin-to-core disbonds.

A defect vibrating at its LDR frequency pops up in the operational deflection shape of the test specimen as a local increase in the vibrational amplitude. An algorithm is proposed to perform the search for LDR phenomena in an automated manner. The algorithm makes use of data compression to reduce the computational effort, and iterative thresholding procedures.

Finite element (FE) simulations have been set up for investigating the LDR behavior of defects in anisotropic multi-layered composite laminates that are too complex to investigate with a simplified analytical formulation. A parametric FE study surprisingly revealed that deep defects do not show LDR behavior at all, due to the limited reduction in rigidity imposed by these deep defects. However, a deep defect from one side, is a shallow defect from the other side. As a result, deep defects show LDR behavior at the invisible backside. Considering that the vibrational intensity under LDR is high, and as such could trigger a local nonlinear response, it was found that deep defects can be detected by searching for nonlinear vibrations. Hence, the monitoring of LDR-induced nonlinear vibrations proves highly promising for detection of shallow as well as deep defects. Apart from enhancing the nonlinear response of the defect, LDR may also induce heat generation at the defect due to viscoelastic and frictional processes. The contribution of LDR_Z and LDR_{XY} in vibration induced heating is investigated. Especially at LDR_{XY}, a pronounced increase in local heating is observed which makes the defect detectable using low power vibrothermographic inspection.

Part 3 presents the construction of guided wave damage maps by exploiting a range of defect-wave interactions. Each of the damage map construction strategies makes extensive use of wavefield manipulations in the frequency domain, the wavenumber domain, the frequency-wavenumber domain and/or the time-frequency domain. The various proposed wavefield manipulation procedures are meant to isolate a specific part of the vibrations in view of increasing the defect detectability. The constructed damage maps can be classified according to the wave characteristic which is being targeted: (i) linear vibrational energy, (ii) nonlinear vibrational energy, (iii) wavenumber and (iv) wave direction. The discussion of each damage map construction class starts with a review of the methods that are known in literature. Next, novel methods are proposed and it is illustrated how they outperform the traditional ones.

Mode-removed broadband weighted-root-mean-square energy calculation is proposed for damage map construction based on linear vibrational energy mapping. A robust damage map is obtained, with automated compensation of wave attenuation, which provides an exclusive view of the defects.

Nonlinear energy-based damage map construction is achieved through broadband bandpower calculation of the first modulation sideband. A novel time-frequency filtering procedure is proposed for extraction of the defect-induced nonlinear vibrations. The method allows for detection of shallow defects, but more important, also for detection of very deep defects.

A self-reference broadband local wavenumber estimation procedure is proposed for the construction of local thickness maps. This novel local wavenumber estimation procedure leads to an increase in robustness and an improved damage evaluation compared to the traditional methods.

At last, local wave-direction estimation of nonlinear waves is proposed for the localization of in-sight as well as out-of-sight defects. Again, this methods exploits the nonlinear source behavior of defects. Thus it can be used to find backside delaminations. Moreover, the out-of-sight defect detection capability proves successful for localizing hidden defects and for reduction of the inspection time.

In Part 4 of this dissertation, the novel developed damage map constructions methods are compared for damage detection in industrial CFRP components with typical damage features. At last future prospects are outlined.

Nederlandstalige Samenvatting

Composietmaterialen bestaan uit twee, of meer, verschillende materiaalsoorten, met het doel de gunstige eigenschappen van elke materiaalsoort te benutten. Zo worden losse koolstofvezels met hoge sterkte en stijfheid ingebed in een polymeermatrix met lage massadichtheid, die de mechanische spanningen over de vezels verdeelt, om zo een koolstofvezelversterkt polymeer te vormen. Het verkregen composietmateriaal heeft een uitstekende sterkte-gewicht verhouding, is bestand tegen corrosie en heeft een hoge ontwerp flexibiliteit, waardoor het zeer geschikt is voor toepassing in bijvoorbeeld lucht- en ruimtevaart. Een aandachtpunt in het gebruik van composietmaterialen is het feit dat hun typische gelaagde materiaalstructuur gevoelig is voor de vorming van interne schade. Terwijl een kleine impact (bv. hagel of gereedschap) op een aluminium vleugeltip meestal niet meer dan een kleine zichtbare deuk in het materiaal veroorzaakt, kan diezelfde inslag op een composiet vleugeltip resulteren in meerdere inwendige beschadigingen die, hoewel onzichtbaar voor het blote oog, de structurele integriteit van de vleugel in gevaar brengen. Om het onverwachts falen van de composietonderdelen te voorkomen, is een niet-destructieve testprocedure (NDT) noodzakelijk die de nauwkeurige detectie van de interne schade mogelijk maakt.

Gedurende de laatste decennia zijn verschillende NDT-methodes ontwikkeld. Het meest gebruikt in lucht- en ruimtevaart toepassingen is de onderwater ultrasone C-scan. Deze NDT-techniek maakt nauwkeurige detectie en evaluatie mogelijk van een grote verscheidenheid aan schadevormen. Er zijn echter ook enkele nadelen aan deze techniek. De methode is relatief traag, kan niet-volumineuze defecten missen (bv. gesloten scheuren), vereist een koppelingsmedium (bv. water) en is moeilijk toe te passen op sterk gebogen onderdelen, hoeken en sandwichstructuren.

In deze doctoraatsstudie wordt een alternatieve NDT-benadering onderzocht: *Elastische golfveld inspectie*. De elastische golven worden geleid door de oppervlakken van dunwandige structuren en vormen zo geleide golven. Typische golffrequenties variëren van 10 tot 300 kHz. De golven kunnen een relatief lange afstand afleggen en volgen de kromming van het onderdeel. Wanneer er zich een defect in het pad van de geleide elastische golven bevindt, veranderen de eigenschappen van de golven (b.v. verandering in amplitude, verandering in voortplantingsrichting, verandering in de frequentie-inhoud, verandering in het plaatselijke golfgetal, enz.). Bijgevolg maakt het opmeten van een golfveld het mogelijk om defecten op te sporen. Elastische golfveldinspectie lijkt veelbelovend voor het behalen van snellere inspectie tijden in vergelijking met de onderwater ultrasone inspectiemethode. Er is ook geen koppelingsmedium nodig. Bovendien zijn de eigenschappen van de elastische golven gerelateerd aan de eigenschappen van het medium. Als gevolg hiervan kan elastische golfveldinspectie ook de eigenschappen van het defect karakteriseren (bv. de grootte/diepte van het defect).

Het doel van deze doctoraatsthesis is het ontwikkelen van nieuwe strategieën voor golfveldmanipulatie en voor het bekomen van schadevisualizaties om efficiënt en accurate typische schadevormen in industriële composietonderdelen te detecteren en te evalueren. Het proefschrift is gebaseerd op de theoretische afleiding van de eigenschappen van lineaire en niet-lineaire elastische golven in combinatie met de ontwikkeling van nieuwe methodes voor signaalverwerking. De signaalverwerkingsmethodes worden toegepast op experimentele meetdata. De experimenten worden uitgevoerd met piëzo-elektrische of gepulste laser excitatie van de elastische golven in combinatie met de opmeting van het golfveld via 3D scanning laser Doppler vibrometry. Het proefschrift bestaat uit vier grote delen.

Deel 1 van het proefschrift begint met de theoretische bespreking van de elastische golfdynamica. Er wordt geïllustreerd hoe golfvergelijkingen worden verkregen door de elasticiteitstheorie, nl. de spanning-rek relaties, te combineren met de tweede wet van Newton, nl. de relatie tussen versnelling en kracht (of spanning). De golfvergelijkingen tonen het bestaan van bulkgolven die zich voortbewegen in vaste materialen. In dunwandige structuren, zoals typisch voor composietmaterialen, worden spanningsvrije randvoorwaarden opgelegd en worden zo dispersierelaties van geleide elastische golven verkregen. De dispersierelaties geven het verband tussen enerzijds de stijfheidseigenschappen, de dichtheid en de dikte van het materiaal, en anderzijds het type (symmetrisch, antisymmetrisch of horizontale-afschuif), het golfgetal en de golffrequentie van de geleide elastische golf. Belangrijke begrippen, zoals fasesnelheid, energiehoek, golftraagheid, staande golven en resonanties worden geïntroduceerd.
Wanneer een geleide elastische golf interageert met een defect, kan de frequentie-inhoud van de golf veranderen ten gevolge van niet-klassieke niet-lineariteit. Een fenomenologisch model van een klappend en een wrijvend defect wordt gebruikt voor het onderzoeken van de verschillende niet-lineaire componenten die verwacht worden in het frequentiespectrum van het defect. Hogere harmonische worden gevormd, evenals modulatie zijbanden (in geval van een dubbele excitatie).
Om defecten te detecteren met behulp van geleide elastische golfinspectie, zijn hoogkwalitatieve metingen vereist van de golfveldrespons van het proefstuk. De volledige golfveldrespons wordt opgemeten met behulp van 3D infrarood scanning laser Doppler vibrometry. Het werkingsprincipe van deze experimentele methode wordt in detail besproken. De signaalverwerking van de

verkregen snelheidssignalen is typisch gebaseerd op verschillende integraaltransformaties.

In deel 2 van het proefschrift, wordt de lokale defect resonantie (LDR) techniek bestudeerd met het oog op het efficiënt en betrouwbaar opsporen van schade in composieten. Na de introductie van het LDR fenomeen, wordt het analytisch aangetoond dat buiggolven (die een vereenvoudigde versie zijn van de fundamentele antisymmetrische geleide elastische golf) aanleiding geven tot een uit-het-vlak lokale defectresonantie (LDR_Z). Dit gebeurt enkele op specifieke hoge frequenties (typisch > 10 kHz). Op soortgelijke wijze kunnen axiale golven (d.w.z. een vereenvoudigde versie van de fundamentele symmetrische geleide elastische golf) aanleiding geven tot in-het-vlak lokale defectresonanties LDR_{XY}. LDR_{XY} vindt typisch plaats bij nog hogere frequenties. Experimenteel bewijs wordt gepresenteerd van LDR voor onder andere vlakke bodemgaten, delaminaties, nauwelijks zichtbare impact schade en oppervlaktescheurtjes.
Een trillend defect dat LDR vertoont komt naar voren in de trillingsvorm van het proefstuk als een lokale toename van de trillingsamplitude. Een algoritme wordt voorgesteld om de aanwezigheid van LDR op een geautomatiseerde manier te detecteren. Het algoritme maakt gebruik van datacompressie om de rekenintensiteit te verminderen en van een iterative threshold procedure.
Eindige elementen simulaties worden gebruikt om het LDR-gedrag te onderzoeken van defecten in anisotrope meerlaagse composietlaminaten (die te complex zijn om te onderzoeken met een vereenvoudigde analytische formulering). Een parametrische studie toonde verrassend aan dat diepe defecten helemaal geen LDR-gedrag vertonen, als gevolg van de beperkte vermindering in buigstijfheid bij deze diepe defecten. Echter, een diep defect van de ene kant, is een ondiep defect van de andere kant. Hierdoor vertonen diepe defecten LDR-gedrag aan de onzichtbare achterzijde. Aangezien de trillingsintensiteit onder LDR hoog is, en als zodanig een lokale niet-lineaire respons kan teweegbrengen, werd ontdekt dat diepe defecten kunnen worden gedetecteerd door te zoeken naar niet-lineaire trillingen. Het monitoren van de door LDR veroorzaakte niet-lineaire trillingen blijkt dus veelbelovend te zijn voor het opsporen van zowel ondiepe als diepe defecten. Naast het versterken van de niet-lineaire respons van het defect, kan LDR ook warmteontwikkeling in het defect veroorzaken als gevolg van lokale visco-elasticiteit en wrijvingsprocessen. De bijdrage van LDR_Z en LDR_{XY} aan de door trillingen veroorzaakte opwarming werd onderzocht. Vooral bij LDR_{XY} werd een duidelijke toename van de plaatselijke opwarming waargenomen, waardoor het defect detecteerbaar wordt met laag-vermogen vibrothermografische inspectie.

Deel 3 presenteert de constructie van geleide elastische golfschadevizualizaties door gebruik te maken van een reeks defect-golf interacties. Elk van de strategieën voor het samenstellen van schadevizualizaties maakt uitgebreid

gebruik van golfveldmanipulaties in het frequentie domein, het golfgetal domein, het frequentie-golfgetal domein en/of het tijd-frequentie domein. De verschillende voorgestelde golfveldmanipulatieprocedures hebben als hoofddoel een specifiek deel van de trillingen te isoleren om de detecteerbaarheid van defecten te verhogen. De opgestelde schadevizualizaties kunnen worden ingedeeld naargelang van het golfkenmerk waarop ze zijn gericht: (i) lineaire trillingsenergie, (ii) niet-lineaire trillingsenergie, (iii) golfgetal en (iv) golfrichting. De bespreking van elke klasse van schadevizualizatie begint met een overzicht van de in de literatuur bekende methodes. Vervolgens worden nieuwe methodes voorgesteld en wordt geïllustreerd hoe zij beter presteren dan de traditionele methodes.
Een breedbandige gewogen energieberekening voor de trillingen toegewezen aan abnormaliteiten wordt voorgesteld voor schadekaartconstructie op basis van de lineaire trillingsenergie. Een robuuste schadevizualizatie wordt verkregen, met automatische compensatie van golfverzwakking en die een exclusief beeld geeft van de defecten.
Een niet-lineaire energie-gebaseerde schadevizualizatie wordt bekomen door breedbandige bandpower berekening van de eerste modulatie zijband. Een nieuwe tijd-frequentie filter procedure wordt voorgesteld voor de extractie van de door het defect geïnduceerde niet-lineaire trillingen. De methode maakt de detectie van ondiepe defecten mogelijk, maar wat belangrijker is, ook van diepe defecten aan de achterzijde.
Een autonoom en breedbandig lokaal golfgetal schattingsprocedure wordt voorgesteld voor vizualizatie van de lokale materiaaldiktes. Deze nieuwe lokaal golfgetal schattingsprocedure leidt tot een grotere robuustheid en een betere schade-evaluatie in vergelijking met de traditionele methodes.
Tenslotte wordt de schatting van de lokale golf-richting van de niet-lineaire trillingen voorgesteld voor de lokalisatie van defecten. Ook deze methode maakt gebruik van het niet-lineaire brongedrag van defecten. De methode kan dus ook worden gebruikt om delaminaties, die zich aan de achterzijde bevinden, op te sporen. Bovendien blijkt de mogelijkheid tot detectie van defecten die zich buiten het gezichtsveld bevinden nuttig voor het lokaliseren van verborgen defecten en voor het verkorten van de inspectietijd.

Deel 4 van het proefschrift vergelijkt de performantie van de ontwikkelde methodes voor het opstellen van schadevizualizaties. Dit wordt gedaan op enkele industriële koolstofvezel versterkte kunststof onderdelen die veel voorkomende defecten bevatten. Tenslotte worden verschillende interessante toekomstperspectieven geschetst.

Abbreviations and Symbols

The following list summarizes the most commonly used abbreviations and symbols in this dissertation.

Abbreviations

BP	Bandpower
BVID	Barely Visible Impact Damage
CFRP	Carbon Fiber Reinforced Polymer
DBR	Defect-to-Background Ratio
DFT	Discrete Fourier Transform
DL	Digital Level
DTC	Defect induced Thermal Contrast
FBH	Flat Bottom Hole
FE	Finite Element
FFT	Fast Fourier Transform
FRF	Frequency Response Function
GFRP	Glass Fiber Reinforced Polymer
HH	Higher Harmonics
LDR	Local Defect Resonance
LDRxy	In-plane Local Defect Resonance
LDRz	Out-of-plane Local Defect Resonance
LVT	Lock-in Vibrothermography
LWDE	Local Wave-direction Estimation
LWE	Local Wavenumber Estimation
MS	Mode Shape
NEWS	Nonlinear Elastic Wave Spectroscopy
NWMS	Nonlinear Elastic Wave Modulation Spectroscopy
NL	Nonlinear
ODS	Operational Deflection Shapes
OMA	Operational Modal Analysis
PC	Principal Component
PCA	Principal Component Analysis
QSID	Quasi-Static Indentation Damage
SB	Sidebands
SH	Shear Horizontal
SLDV	Scanning Laser Doppler Vibrometer
SNR	Signal-to-Noise Ratio

SRB-LWE	Self-Reference Broadband Local Wavenumber Estimation
STD	Standard Deviation
STFT	Short-Time-Fourier-Transformation
SVT	Sweep Vibrothermography
WF	Weighting Factor
WRMS	Weighted-Root-Mean-Square

Symbols

σ	Stress [Pa]
F	Force [N]
u	Displacement [m]
E	Elastic modulus [Pa]
C	Elasticity tensor [Pa]
λ,μ	Lamé coefficients [Pa]
ν	Poisson's ratio [-]
ρ	Density [kg/m^3]
ω	Angular frequency [rad/s]
κ	Angular wavenumber [rad/m]
f	Frequency [1/s]
k	Wavenumber [1/m]
ϕ	Scalar field - Stokes-Helmholtz decomposition
$\bar{A}$	Vector field - Stokes-Helmholtz decomposition
V_L	Longitudinal (bulk) wave velocity [m/s]
V_S	Shear (or transversal) bulk wave velocity [m/s]
V_{ph}	Phase velocity [m/s]
V_{ph}^F	Phase velocity for Flexural waves [m/s]
V_{ph}^A	Phase velocity for Axial waves [m/s]
V_{SH_m}	Phase velocity of SH_m wave [m/s]
V_g	Group velocity [m/s]
V_e	Energy velocity [m/s]
V_F	Phase velocity: Flexural waves [m/s]
V_A	Phase velocity: Axial waves [m/s]
u_L	Displacement vector of longitudinal wave [m]
u_S	Displacement vector of shear wave [m]
U	Displacement amplitude [m]
φ	Wave-Propagation Direction [rad]
ψ	Skew angle [rad]
R	Coefficient of reflection [m/s]

V_X	Velocity in X direction [m/s]
V_Y	Velocity in Y direction [m/s]
V_Z	Velocity in Z direction [m/s]
h	Plate Thickness [m]
A	Area [m^2]
Ø, d	FBH Diameter [mm]
r	FBH Radius [mm]
KF	Wavenumber Filter
MF	Mode Filter
DF	Wave-Direction Filter
TFF	Time-Frequency Filter
BW	Bandwidth

Chapter 1 Introduction

Summary:

The chapter provides a general overview of the work performed during this PhD thesis. The background is outlined and the objectives are listed. The structure of the PhD thesis is explained, and each chapter is shortly introduced.

1. Background and Problem Statement

1.1. The Rise of Composite Materials

Over the last decades, the use of fiber reinforced plastics, or so-called composites, has increased significantly. Nowadays, composites are used in all kinds of industries: automotive, wind power, aerospace, maritime and others. Figure 1.1 (a) shows the increase in the demand of carbon fiber reinforced polymer (CFRP) from 2010 to 2023. In addition, Figure 1.1 (b) illustrates how more and more structural components of the Airbus aircrafts are manufactured from composite materials.

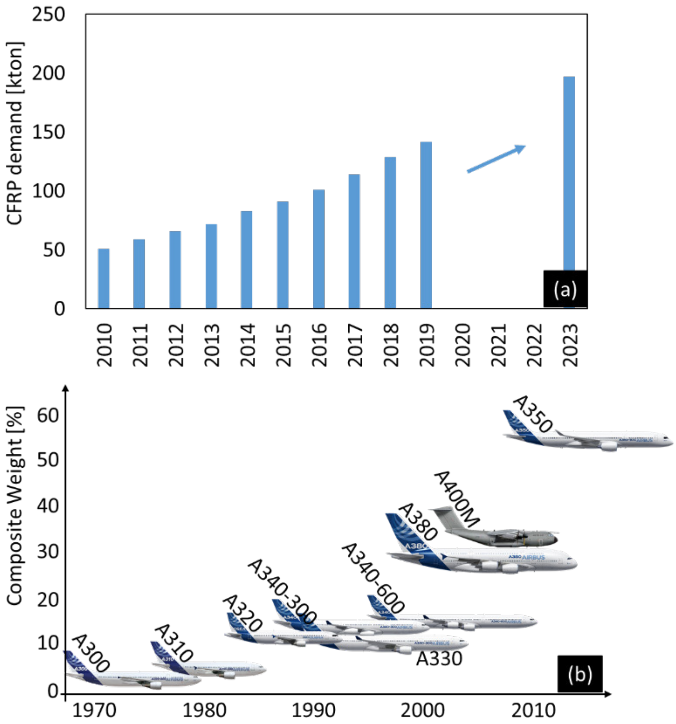

Figure 1.1: (a) Development of the global carbon fiber reinforced polymer demand (reproduced from [1]) and (b) Evolution of the relative composite weight in Airbus aircrafts (reproduced from [2]).

A composite is a material manufactured by combining two (or more) materials with the aim to exploit the best properties of both. For instance in civil engineering, reinforced concrete is a composite material in which the high compressive strength and corrosion resistance of concrete is combined with the high tensile strength of steel. In other industries, composites are typically manufactured using a polymer matrix in which reinforcing fibers are inserted.

The type, length, orientation and volume fraction of the reinforcing fibers are tuned to the application. As an example, in aerospace applications, where the weight, stiffness and strength of the materials is of utmost importance, long carbon fibers are dominantly used as the resulting CFRPs show high stiffness- and strength-to-weight ratios. The cheaper glass fiber reinforced polymers GFRP are often used for the blades of a wind mill.

Figure 1.2 (a) shows the typical structure of long fiber composite plies with ply angles 90°, 0° and -45°. A composite laminate is built-up of multiple individual plies. As an example, Figure 1.2 (b) shows a cross-ply laminate with layup $[(0/90)_2]_s$. The stiffness and strength of each ply is highest along the direction of the fibers. As a result, composite laminates are not isotropic. The ply angles, i.e. the so-called layup, is fine-tuned to match the expected loading conditions of the composite structure.

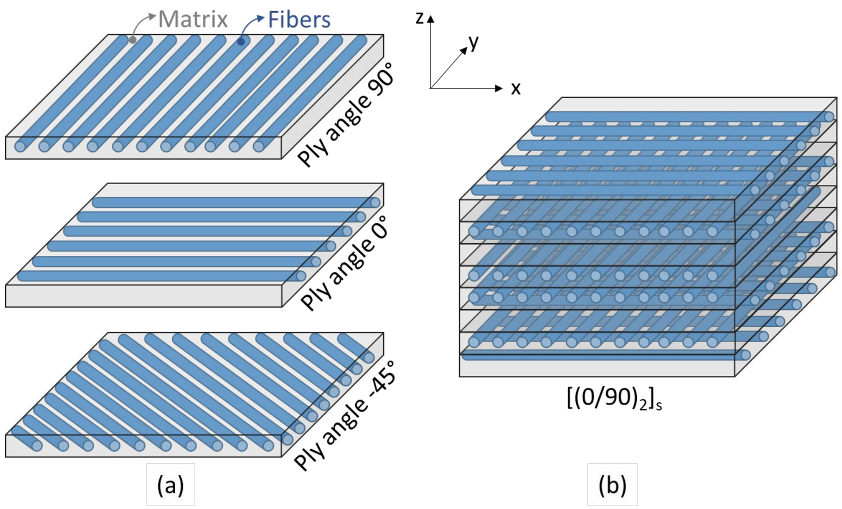

Figure 1.2: Typical structure of (a) individual composite plies and (b) a cross-ply composite laminate.

1.2. Composite Material Damage

Despite their numerous beneficial properties, such as the high stiffness- and strength-to-weight ratio, good corrosion resistance and excellent design flexibility, composites are susceptible to a range of damage features which may be caused by impact, fatigue, static overload, production errors, etc. The damage is often located internally in the material as a result of the composite's layered structure. Damage in composites can manifest itself in different forms leading to a variety of failure modes. Figure 1.3 gives an overview of the main defect types. Most often, composites fail by a combination of different modes and the failure is less sudden compared to metals [3].

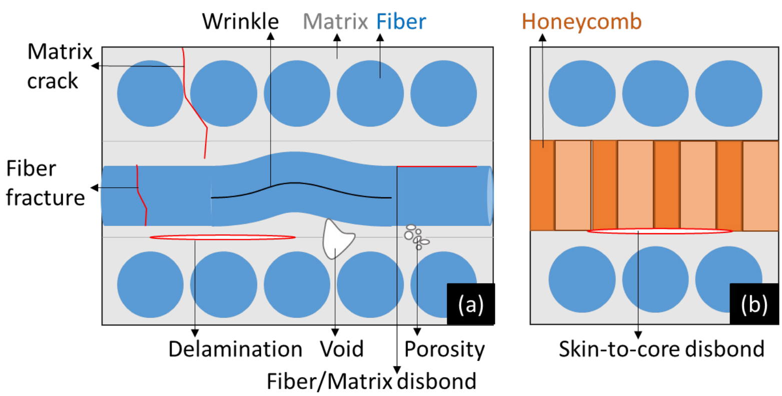

Figure 1.3: Typical defects encountered in (a) monolithic composite laminate and (b) composite sandwich panel.

A typical example of the combination of multiple damage features is the damage distribution caused by low velocity impact. Figure 1.4 shows the observed cluster of delaminations and cracks in a quasi-isotropic CFRP (with layup $[(45/0/-45/90)_3]_s$) subjected to a 5.3 J impact (according to the ASTM D7136 standard) [4]. Figure 1.4 (a) was obtained using in-house ultrasonic non-destructive C-scan inspection. Figure 1.4 (b) was obtained from post-mortem destructive microscopic inspection. Both figures reveal that the barely visible impact damage (BVID) is made up of multiple delaminations and matrix cracks that form a pine tree pattern through the laminate's thickness. Although the laminate has lost its ability to carry loads (especially compression and bending loads), the damage is hardly visible at the laminate's surface.

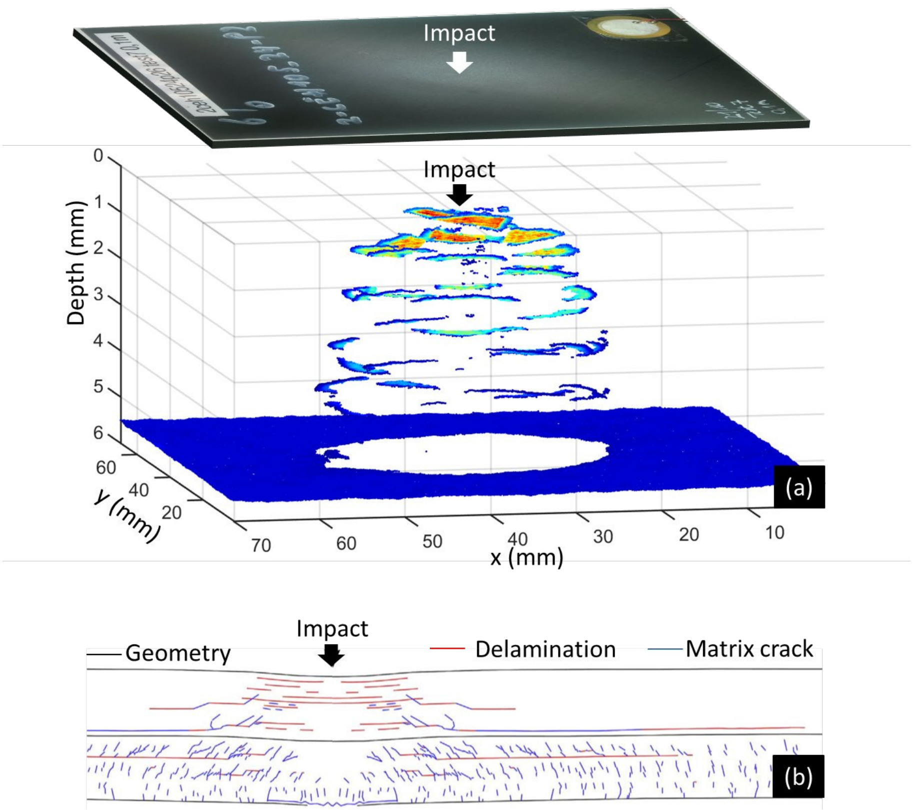

Figure 1.4: Barely visible impact damage in quasi-isotropic CFRP (a) 3D view obtained using ultrasonic C-scan inspection and (b) 2D side-view from destructive microscopic inspection with indication of delaminations and matrix cracks (Reproduced from [4]).

1.3. Non-Destructive Testing

As illustrated in the previous section, the damage resulting from impact or overload, or the defects resulting from production errors, are often invisible to the naked eye but may drastically compromise the overall strength of the composite structure. Unfortunately, dramatic accidents taught us that NDT is of utmost important when dealing with composite materials. As an example, on February 1st 2003 the space shuttle Columbia was destroyed upon re-entry into earth's atmosphere. The accident was attributed to a block of insulating foam that was badly bonded (i.e. internal production defect) to the fuel tank and that came off upon launch. The foam impacted the reinforced carbon-carbon (RCC) wing tips. Internal defects were likely already present in these RCC wing tips from previous flights. As a result, the impact damage was so severe that the heat shield function of the RCC was compromised, resulting in the catastrophic destruction of the aircraft during the re-entry. This failure costed the life of seven crew members. In order to avoid such accidents, NASA's Columbia accident investigation board prescribed the following [5]:

> "*Develop and implement a comprehensive inspection plan to determine the structural integrity of all Reinforced Carbon-Carbon system components. This inspection plan should take advantage of advanced non-destructive inspection technology*"

Or in other words: "Advanced NDT is required!"

Many different NDT techniques exist, including visual inspection, acoustic testing, ultrasonic testing, radiographic testing, electromagnetic testing and (vibro-)thermographic testing [6-8]. Table 1.1 gives on overview of the applicability of each method for detection of the damage features shown in Figure 1.3. Each of these techniques is briefly explained below together with their advantages and limitations. At the end, full-field elastic wave testing is briefly introduced.

Table 1.1: Applicability of conventional NDT methods (reproduced from [7]).

	Damage feature					
NDT Method	Porosity Voids	Delamination	Skin-to-core disbond	Cracks	Wrinkles	Surface damage
Visual inspection					✓	✔
Shearography	✓	✔	✔			
Acoustic testing		✓	✔			
Ultrasonic testing Pulse-echo	✔	✔		✓	✔	
Ultrasonic testing Through-Transmission	✔	✔	✓			
Radiographic testing	✔	✔		✔	✓	✔
Electromagnetic testing		✓		✓		
Thermography	✓	✔	✓			

1.3.1. Visual Inspection

Visual inspection is the most basic type of NDT techniques. It is very fast and low-cost which makes it the most regularly used NDT technique especially during in-service operations. To increase the detectability limit, a microscope or dye penetrant can be used. With dye penetrant testing, a fluorescent dye is applied to the component. The excess dye is removed and a developer is applied. The developer solution draws the fluorescent dye out of the cracks which makes them visible under UV light. The drawback of this visual testing technique is that for most materials only surface breaking defects can be detected. Only for translucent composites, internal damage may be visual.

A more advanced optical testing techniques is called *shearography* [9, 10] (or *speckle interferometry*). Shearography relies on the detection of local variations in stiffness (caused by e.g. cracks) by comparing the state of the surface before and after loading. The component can be loaded mechanically, thermally or vibrationally. The comparison of the surface is performed using optical interferometry which results in a shearographic *fringe pattern*. Surface and subsurface defects are revealed as distortions in this fringe pattern. It is a fast, non-contact full-field technique but it cannot be used to reliably evaluate the extent of internal damage. In addition, the detection of small and deep defects remains challenging.

1.3.2. Acoustic Testing

The most basic type of acoustic testing is called audible sonic testing. It involves tapping on the surface of the component and listening to the produced sound [11, 12]. A dull sound may indicate a damaged area. It is a very fast and low-cost technique but it requires an experienced operator and lacks the sensitivity for small and deep defect detection.

1.3.3. Ultrasonic Testing

Ultrasonic testing is one of the most often used methods for internal damage detection and evaluation in composite structures. High frequency sound waves, typically 1 MHz to 20 MHz [13-17], are transmitted in the material. Different ultrasonic testing configurations exist i.e. pulse-echo, through-transmission and phased array. Figure 1.5 gives an overview of these configurations.

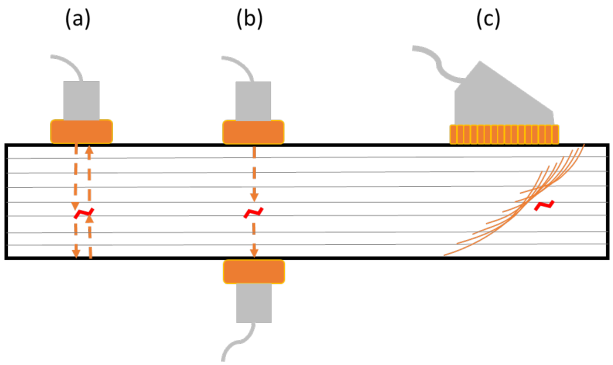

Figure 1.5: Ultrasonic testing configurations: (a) Pulse-echo (b) Trough-transmission and (c) Phased array.

For the pulse-echo technique (Figure 1.5 (a)), one ultrasonic transducer is used. The transmitted sound waves are reflected by the back wall of the component as well as by internal defects such as delaminations. These reflected waves are recorded by the same ultrasonic probe that excited the waves. Most frequently, the time-of-flight and amplitude of the reflected signal is analyzed. When a transmitter and a receiver are placed on opposite sides of the component, the technique is called through-transmission (Figure 1.5 (b)). The loss of signal is measured and related to the presence of damage. More advanced is the phased array technique [18, 19] (Figure 1.5 (c)). In this case, multiple transducers are used and they are grouped together. The ultrasonic wave emitted by the transducer group can be shaped, steered and focused by changing the phase delay between the transducers.

There exist three standard scan types referred to as A, B and C - scan. An A-scan is a single point measurement. The obtained information is the signal's magnitude in function of the time. When the transmitter and sensor units are translated along a straight line, a B-scan is made. Often the obtained information is visualized as a greyscale map of the amplitude through the thickness versus displacement of the transducer. C-scan images are obtained when translating the transmitter and sensor in two dimensions. A colormap is made with the time-of-flight values or amplitude over the scanned region. Figure 1.6 gives an overview of these scan types.

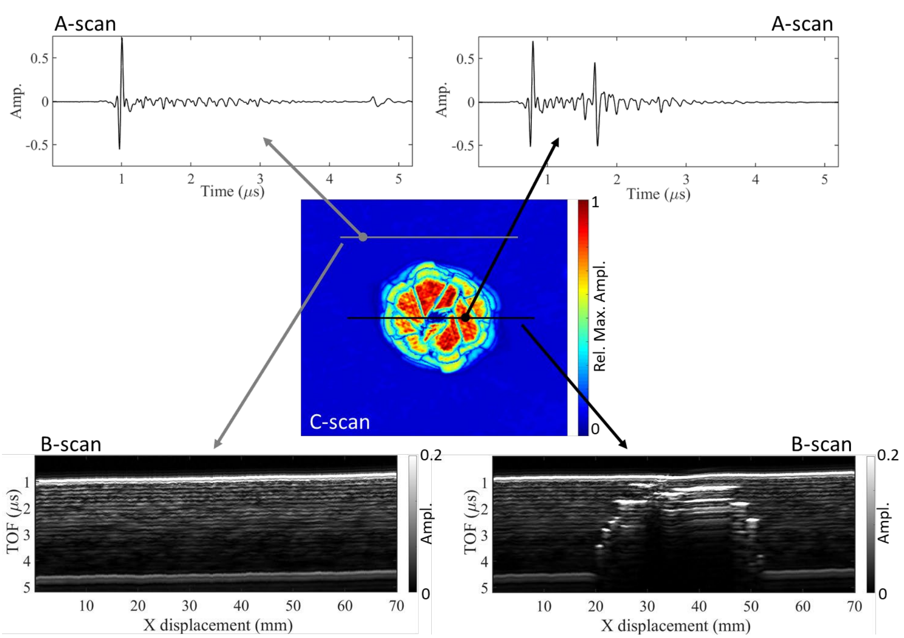

Figure 1.6: Ultrasonic scan types: A, B and C-scan of CFRP plate after low velocity impact.

The technique is routinely used in industry because it allows for accurate detection and evaluation of defects, even those that are small and located deep into the specimen. However, there are some limitations. Scanning a component can be a time consuming process comprising hours of labor and the necessity of a coupling agent imposes practical difficulties. In addition, inspection of strongly curved areas, such as corners, is extremely challenging.

1.3.4. Radiographic Testing

Radiographic testing uses λ or X electromagnetic radiation to scan trough the material. The radiation is attenuated by the material. The amount of attenuation depends on the type of material (incl. the potential damage) that the beam passes through. In a conventional setup, a film or detector is placed behind the radiated component. A two dimensional image is obtained where spots of increased or reduced intensity indicate defects.

Computed tomography (CT) takes this technique one step further [20-23]. The component is rotated and multiple 2D images are made. These images are combined using specialized software into an accurate three-dimensional model of the component. Figure 1.7 shows this method schematically. Next to the time consuming inspection, the equipment is big and expensive, and the spatial resolution is inversely proportional to the size of the inspected part. In addition, safety measures are required to contain the harmful radiation.

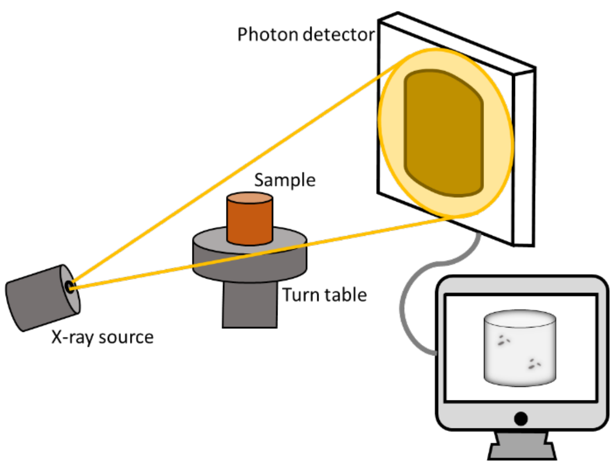

Figure 1.7: Schematic illustration of the X-ray computed tomographic setup.

1.3.5. Electromagnetic Testing

Electromagnetic testing involves the use of electricity and magnetism to detect and evaluate possible damage in conductive materials [24-26]. The test object is excited with electric current, magnetic fields, or both, and the electromagnetic response is investigated. Different methods exist such as eddy current testing and magnetic flux leakage. The main limitation of these techniques is the limited penetration depth (usually 5 mm [27]). In addition, it only works for conductive materials.

1.3.6. Thermography

Next to ultrasonic inspection, thermographic inspection is an often used NDT method for inspection of composite materials [28, 29]. Thermographic inspection approaches are based on the infrared radiation of the test specimen which is recorded with a sensitive thermographic camera. A distinction can be made between active [15, 30-33] and passive thermography [34]. Passive thermography takes advantage of the heat flow that is intrinsic to the sample, for instance the cooling down of a composite component after curing, or the warming up of an aircraft part after landing. In the active approach, the heat generation is stimulated by an external source. In general, thermographic techniques have been estimated to be up to 30 times quicker than immersion ultrasonic C-scanning.

One of the conventional active thermography methods is pulsed thermography [35, 36]. It involves the heating of the test object by a short pulse (milliseconds) of a xenon flash lamp. The transient thermal response is captured with the IR camera and analyzed. The idea is that an internal defect obstructs the heat flow inside the material which results in a faster temperature increase during heating and a slower temperature decrease during cooling. Figure 1.8 illustrates this method schematically.
Especially for composites, which have a relative low thermal diffusivity, the technique is limited to the detection of damage with aspect ratio (i.e. size/depth) bigger than one or two [37, 38].

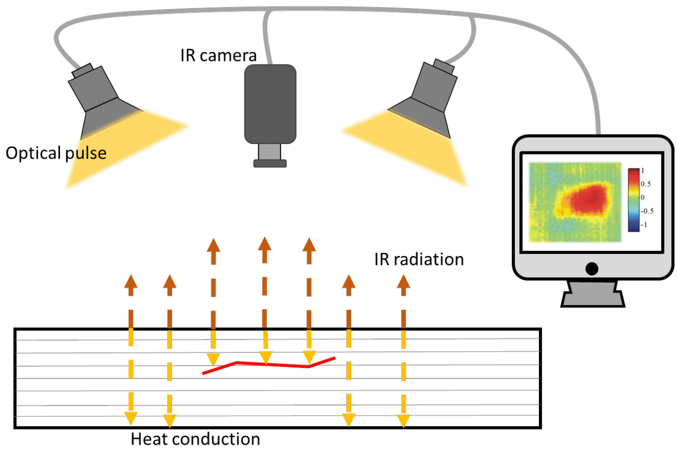

Figure 1.8: Setup and working principle of active infrared thermography.

The heat stimulant can also be induced by vibrations (instead of optical lamps), resulting in the vibro-thermography technique (also known as thermosonics, sonic thermography and ultrasonically stimulated thermography). The injected vibrations activate the defect interfaces, leading to localized heating through different dissipation mechanisms (e.g. rubbing friction and viscoelastic damping). Typically the vibrations are introduced by an ultrasonic horn using frequencies in the range of 1 to 100 kHz. The main disadvantage is the low reproducibility due to the complex nonlinear vibration pattern introduced by the ultrasonic horn. The horn excitation can also induce damage at the injection point. To overcome these problems, the ultrasonic horn can be replaced by piezoelectric transducers which introduce controlled low amplitude vibrations. Defects can still be detected by using the concept of local defect resonance and contact acoustic nonlinearity. More research has to be performed to this novel nonlinear ultrasonically stimulated thermography but it shows the ability to be a fast and sensitive NDT technique [39-42]. The LDR-based vibrothermographic inspection is discussed further in Chapter 9 of this PhD dissertation.

At this moment, active research is performed at our NDT lab towards (vibro-) thermographic inspection of composite materials. Advanced excitation [43-45] as well as post-processing techniques [41, 46-48] are applied to enhance the detection of deep defects, and to cope with the strong in-plane heat diffusion in composite materials.

1.3.7. Guided Elastic Wave Inspection

Guided elastic waves, or simply guided waves, are elastic waves that are guided by the surfaces of thin-walled components. The waves are generally excited by piezoelectric actuators or pulsed lasers and the resulting wavefield is monitored using piezoelectric sensors or a (scanning) laser Doppler vibrometer. Typical wave frequencies range from 10 to 300 kHz. The waves can travel a relatively long distance and follow the component's curvature. When a defect is located in the path of the guided waves, the properties of the waves change (e.g. change in amplitude, change in propagation direction, mode conversions, change in the frequency content, change in the local wavenumber, etc.). As a result, the monitoring of the guided waves allows to detect the defects [49].

The ability to travel great distances makes guided waves especially suited for inspection of the rather large CFRP composite components that are used in the aerospace industry. Guided wave NDT seems promising for achieving fast and accurate inspection. In addition, the properties of the guided waves are related to the properties of the medium. As a result, guided wave inspection should allow for characterization of the material properties and evaluation of the depth of the hidden defects in a baseline-free manner.

2. Objective

The promising properties of guided elastic waves for NDT of composites made them the subject of this PhD work. Yet, there are still important challenges to overcome before full-field guided elastic wave based inspection can challenge the classical water-coupled ultrasound scanning technique. Most important, the detection of small and deep damage in materials with unknown properties is very challenging, and requires the development of improved experimental methodologies and novel data analysis and processing tools.

In this PhD work, the physics behind linear and nonlinear elastic wave dynamics are reviewed. Based on these physics, and on the associated defect-wave interactions, novel wavefield manipulation and damage map construction methods are developed. The novel wave manipulation strategies and damage map construction methods are developed with the objective to prove the sensitivity and robustness of full-field (guided) elastic wave based inspection. After reading this PhD work, the reader should be convinced that full-field elastic wave testing has its place in future non-destructive inspection of composite components.

Note that it is not the objective to develop a NDT inspection system ready for implementation in an industrial environment. This PhD work rather shows the possibilities of full-field elastic wave inspection, thereby convincing ourselves and others (academic as well as industrial researchers) in further exploiting these findings in their NDT developments.

3. Thesis Outline

The thesis consists of four parts. Part 1 is dedicated to the theoretical investigation of linear and nonlinear elastic wave dynamics. In addition, the experimental approach for performing full-field elastic wave based inspection is outlined together with the required processing functions. In Part 2, the concept of local defect resonance (LDR) is investigated. LDR is used for damage detection using vibrational measurements as well as using thermographic measurements. Part 3 deals with inspection methods that are based on guided elastic waves and illustrates how defects can be efficiently found by analyzing different wave characteristics. At last, several of the most promising damage detection methods are compared in Part 4.

Part 1: Vibrations in Composite Components

Chapter 2 gives the theoretical framework for linear elastic wave dynamics in bulk solids and plates. Wave equations are derived by combining the theory of elasticity with Newton's second law of motion. Experimental results are shown to further investigate the properties of elastic waves in composite materials.

In Chapter 3, the nonlinear response of vibrating defects is investigated using phenomenological models. It is shown that higher harmonics and modulation sidebands can be formed due to clapping and rubbing effects of the defect's interfaces.

Sensitive full-field elastic wave based NDT is only possible when the associated experiments are of high quality. In Chapter 4, the employed experimental procedure is detailed, together with the basic signal processing steps.

Part 2: Local Defect Resonance based Damage Detection

Local defect resonance (LDR) makes use of high frequency vibrations to get a localized resonant activation of the defect. In Chapter 5, the concept of out-of-plane LDR is extended with in-plane LDR. Both LDR types are analytically investigated. In addition, finite element simulations are performed and experimental evidence of LDR is provided.

Chapter 6 presents an automated approach for defect detection by searching for LDR in the full wavefield response of the specimen. Various data compression methods are considered to speed up the automated LDR search.

The limitations of LDR for defect detection are discussed in Chapter 7. Both finite element simulations and experiments are performed. It is illustrated that shallow defects show a pronounced LDR behavior. As a result, they can be detected by searching for LDR in the operational deflection shapes of the test specimen. On the contrary, the limited rigidity reduction at deep defects results in the absence of LDR behavior. In order to detect these deep defects, weighted bandpower calculation is proposed.

In Chapter 8, the nonlinear response of deep delamination defects under sine excitation at the out-of-plane LDR frequency is investigated. It is experimentally observed that the deep delaminations behave as sources of nonlinear vibrational components, i.e. higher harmonics and modulation sidebands, making them detectable. Opportunities for out-of-sight damage detection and nonlinear resonant air-coupled emissions are discussed.

The vibration-induced local heating of defects is presented in Chapter 9. The significant contribution of in-plane LDR's in vibrational heating is demonstrated.

Part 3: Guided Wave Based Damage Detection

Wavefield manipulations are discussed in Chapter 10 in order to isolate waves with specific properties. As a result, these manipulations can be used to extract the defect-wave interactions from the full wavefield response. The wavefield manipulations make use of filters in the frequency domain, the wavenumber domain, the combined frequency-wavenumber domain or the combined frequency-time domain. The working principle of each filter is discussed and evidenced with experimental results.

The first damage map construction approach is based on the mapping of the linear vibration energy. These linear energy-based damage maps are presented in Chapter 11. Effective damage maps are obtained for broadband mode-removed weighted root mean square energy mapping.

In Chapter 12, a novel damage map construction method is proposed based on the mapping of the energy present in the nonlinear vibrational components. The damage map calculated for the modulation sidebands provides an exclusive imaging of the shallow as well as the deep defects.

The third damage map construction method is based on local wavenumber estimation (LWE) and is presented in Chapter 13. Traditional implementations of LWE are reviewed first. Next, a novel self-reference broadband LWE is proposed. It is shown that the novel LWE implementation allows for accurate estimation of the defect's depth in composite materials with unknown material properties.

In Chapter 14, a novel wavefield processing algorithm is proposed to localize sources of guided waves in full wavefield SLDV measurements. Using the proposed local wave-direction estimation LWDE method, nonlinear defects are detected as sources of nonlinear vibrational components. It is demonstrated that this technique provides the opportunity to localize out-of-sight and/or hidden defects.

Part 4: Damage Detection Performance and Conclusions

Chapter 15 presents a comparison of several damage map construction approaches that were proposed in Part 2 and in Part 3. The different methods are evaluated on multiple (aircraft) CFRP test specimens with variable damage types and sizes. The applicability, advantages and disadvantages of each of the proposed approaches are critically discussed.

Finally, Chapter 16 provides a summary of the conclusions made throughout the PhD work. In addition, interesting future research lines are presented.

A complete bibliographic list of the scientific output of the PhD thesis can be found at the very end of the dissertation.

References

1. Michael, S., *Composites Market Report 2019 - The global CF- und CC-Market 2019*. 2019, Carbon Composites e.V.
2. Gardiner, G. *SAMPE Europe highlights: Composites face challenges in next commercial airframes*. 2014.
3. Meo, M. and C. Mattei, *An overview of failure modes and inear elastic wave propagation damage detection methods in aircraft structures*, in *Universality of Nonclassical Nonlinearity*, P.P. Delsanto, Editor. 2007, Springer. p. 495-513.
4. Spronk, S.W.F., et al., *Comparing damage from low-velocity impact and quasi-static indentation in automotive carbon/epoxy and glass/polyamide-6 laminates.* Polymer Testing, 2018. **65**: p. 231-241.
5. Board, C.A.I., *Report of Columbia Accident Investigation Board*, NASA, Editor. 2003.
6. Gholizadeh, S., *A review of non-destructive testing methods of composite materials.* Procedia Structural Integrity, 2016. **1**: p. 050–057.
7. Bossi, R.H. and V. Giurgiutiu, *Nondestructive testing of damage in aerospace composites*, in *Polymer Composites in the Aerospace Industry*. 2015. p. 413-448.

8. Alhammad, M., L. Zanotti Fragonara, and N.P. Avdelidis, *Diagnosis of Composite Materials in Aircraft Applications–Brief Survey of Recent Literature.* Preprints, 2020(2020110216).
9. Hung, Y.Y., *Shearography for Non-destructive Evaluation of Composite Structures.* Optics and Lasers in Engineering 1996. **24**.
10. Hung, Y.Y., L.X. Yang, and Y.H. Huang, *Non-destructive evaluation (NDE) of composites: digital shearography*, in *Non-Destructive Evaluation (NDE) of Polymer Matrix Composites*. 2013. p. 84-115.
11. Cawley, P. and R.D. Adams. *An Automated Coin-Tap Technique For The Non-Destructive Testing Of Composite Structures*. in *Second International Conference on Testing, Evaluation and Quality Control of Composites*. 1987.
12. Hwang, J.S. and S.J. Kim. *Experimental Verification of Tapping Sound Analysis for the Inspection of Laminated Composite Structures*. in *Nondestructive Evaluation and Health Monitoring of Aerospace Materials and Civil Infrastructures*. 2002. San Diego, California, United States.
13. Imielińska, K., et al., *Air-coupled ultrasonic C-scan technique in impact response testing of carbon fibre and hybrid: glass, carbon and Kevlar/epoxy composites.* Journal of Materials Processing Technology, 2004. **157-158**: p. 513-522.
14. D'Orazioa, T., et al., *Automatic ultrasonic inspection for internal defect detection in composite materials.* NDT & E International, 2008. **41**.
15. Meola, C., et al., *Nondestructive evaluation of carbon fibre reinforced composites with infrared thermography and ultrasonics.* Composite Structures, 2015. **134**: p. 845-853.
16. Ibrahim, M.E., *Ultrasonic inspection of hybrid polymer matrix composites.* Composites Science and Technology, 2021. **208**.
17. Papa, I., V. Lopresto, and A. Langella, *Ultrasonic inspection of composites materials: Application to detect impact damage.* International Journal of Lightweight Materials and Manufacture, 2021. **4**(1): p. 37-42.
18. Taheri, H. and A.A. Hassen, *Nondestructive Ultrasonic Inspection of Composite Materials: A Comparative Advantage of Phased Array Ultrasonic.* Applied Sciences, 2019. **9**(8).
19. Li, C., et al., *Imaging composite material using ultrasonic arrays.* NDT & E International, 2013. **53**: p. 8-17.
20. Buffiere, J.Y., et al., *In Situ Experiments with X ray Tomography: an Attractive Tool for Experimental Mechanics.* Experimental Mechanics, 2010. **50**(3): p. 289-305.
21. Sket, F., et al., *Automatic quantification of matrix cracking and fiber rotation by X-ray computed tomography in shear-deformed carbon fiber-reinforced laminates.* Composites Science and Technology, 2014. **90**: p. 129-138.
22. Sisodia, S.M., et al., *High-resolution computed tomography in resin infused woven carbon fibre composites with voids.* Composites Science and Technology, 2016. **131**: p. 12-21.

23. Naresh, K., et al., *The use of X-ray computed tomography for design and process modeling of aerospace composites: A review.* Materials & Design, 2020. **190**.
24. Auld, B.A. and J.C. Moulder, *Review of Advances in Quantitative Eddy Current Nondestructive Evaluation.* Journal of Nondestructive Evaluation, 1999. **18**.
25. Chen, T., et al., *Feature extraction and selection for defect classification of pulsed eddy current NDT.* NDT & E International, 2008. **41**(6): p. 467-476.
26. Heuer, H., M.H. Schulze, and N. Meyendorf, *Non-destructive evaluation (NDE) of composites: eddy current techniques*, in *Non-Destructive Evaluation (NDE) of Polymer Matrix Composites*. 2013. p. 33-55.
27. Ginzburg, D., *Damage Propagation and Detection using Nonlinear Elastic Wave Spectroscopy in Aerospace Structures*, in *Department of Mechanical Engineering*. 2016, University of Bath.
28. Jorge Aldave, I., et al., *Review of thermal imaging systems in composite defect detection.* Infrared Physics & Technology, 2013. **61**: p. 167-175.
29. Shirazi, A. and V.M. Karbhari, *Non-destructive evaluation (NDE) of composites: application of thermography for defect detection in rehabilitated structures*, in *Non-Destructive Evaluation (NDE) of Polymer Matrix Composites*. 2013. p. 515-541.
30. Avdelidis, N.P., B.C. Hawtin, and D.P. Almond, *Transient thermography in the assessment of defects of aircraft composites.* NDT & E International, 2003. **36**(6): p. 433-439.
31. Chatterjee, K., et al., *A comparison of the pulsed, lock-in and frequency modulated thermography nondestructive evaluation techniques.* NDT & E International, 2011. **44**(7): p. 655-667.
32. Mayr, G., et al., *Active thermography as a quantitative method for non-destructive evaluation of porous carbon fiber reinforced polymers.* NDT & E International, 2011. **44**(7): p. 537-543.
33. Lizaranzu, M., et al., *Non-destructive testing of composite materials by means of active thermography-based tools.* Infrared Physics & Technology, 2015. **71**: p. 113-120.
34. Harizi, W., et al., *Mechanical damage assessment of Glass Fiber-Reinforced Polymer composites using passive infrared thermography.* Composites Part B: Engineering, 2014. **59**: p. 74-79.
35. Pawar, S.S. and K. Peters, *Through-the-thickness identification of impact damage in composite laminates through pulsed phase thermography.* Measurement Science and Technology, 2013. **24**(11).
36. Schmutzler, H., et al., *Degradation monitoring of impact damaged carbon fibre reinforced polymers under fatigue loading with pulse phase thermography.* Composites Part B: Engineering, 2014. **59**: p. 221-229.
37. Almond, D.P. and S.G. Pickering, *An analytical study of the pulsed thermography defect detection limit.* Journal of Applied Physics, 2012. **111**(9).

38. Oswald-Tranta, B., *Comparative study of thermal contrast and contrast in thermal signal derivatives in pulse thermography.* NDT & E International, 2017. **91**: p. 36-46.
39. Fierro, G.P.M., et al., *Imaging of Barely Visible Impact Damage on a Complex Composite Stiffened Panel Using a Nonlinear Ultrasound Stimulated Thermography Approach.* Journal of Nondestructive Evaluation, 2017. **36**(4).
40. Segers, J., et al., *In-plane local defect resonances for efficient vibrothermography of impacted carbon fiber-reinforced polymers (CFRP).* NDT & E International, 2019. **102**: p. 218-225.
41. Hedayatrasa, S., et al., *Vibrothermographic spectroscopy with thermal latency compensation for effective identification of local defect resonance frequencies of a CFRP with BVID.* NDT & E International, 2020. **109**.
42. Hedayatrasa, S., et al., *Vibro-Thermal Wave Radar: Application of Barker Coded Amplitude Modulation for Enhanced Low-Power Vibrothermographic Inspection of Composites.* Materials, 2021(Special Issue Mechanical Characterization of FRP Composite Materials).
43. Hedayatrasa, S., et al., *Performance of frequency and/or phase modulated excitation waveforms for optical infrared thermography of CFRPs through thermal wave radar: A simulation study.* Composite Structures, 2019. **225**.
44. Hedayatrasa, S., et al., *Novel discrete frequency-phase modulated excitation waveform for enhanced depth resolvability of thermal wave radar.* Mechanical Systems and Signal Processing, 2019. **132**: p. 512-522.
45. Hedayatrasa, S., et al., *On the application of an optimized Frequency-Phase Modulated waveform for enhanced infrared thermal wave radar imaging of composites.* Optics and Lasers in Engineering, 2021. **138**.
46. Poelman, G., et al., *An Experimental Study on the Defect Detectability of Time- and Frequency-Domain Analyses for Flash Thermography.* Applied Sciences, 2020. **10**(22).
47. Poelman, G., et al., *Multi-scale gapped smoothing algorithm for robust baseline-free damage detection in optical infrared thermography.* NDT & E International, 2020. **112**.
48. Poelman, G., et al., *Adaptive spectral band integration in flash thermography: Enhanced defect detectability and quantification in composites.* Composites Part B: Engineering, 2020. **202**.
49. Ostachowicz, W., M. Radzieński, and P. Kudela, *50th Anniversary Article: Comparison Studies of Full Wavefield Signal Processing for Crack Detection.* Strain, 2014. **50**(4): p. 275-291.

Part 1:

Vibrations in Composite Components

Chapter 2

Linear Elastic Wave Dynamics

Summary:

The theoretical framework for linear elastic wave dynamics in bulk solids and plates is outlined. This forms the foundation for all elastic wave-based NDT techniques. The framework is based on the theory of elasticity in combination with Newton's second law of motion. Wave equations are derived and important concepts, such as phase and group velocity, dispersion, slowness and resonance, are explained. In addition, experiments are performed to illustrate and visualize guided wave propagation in metallic and composite plates.

1. Introduction

In this chapter, the theoretical framework for linear elastic wave dynamics in bulk solids and plates is outlined. This framework forms the foundation for all ultrasonic NDT techniques.

The theoretical framework starts at the basis with the description of the theory of elasticity. The theory of elasticity handles the relation between stress and strain, or simply stated "how a material deforms when it is subjected to a static force". The difference between isotropic, orthotropic and anisotropic materials is explained.

When the force applied to the material is dynamic (instead of static), Newton's second law must be taken into account. The dynamic force results in dynamic stresses and strains, thus propagating elastic waves.
As a first step, it is assumed that the solid material, in which the waves propagate, is infinitely large. In this case, the resulting waves are called 'bulk waves'. Through a mathematical framework, the propagation characteristics of the bulk waves are derived. The effect of the material's symmetry class (isotropic or anisotropic) on the properties of these bulk waves is investigated.
Next, plate like structures are considered with limited thickness and infinitely large length and width dimensions. Imposing the boundary conditions on the wave equations results in mathematical expressions for the propagation of shear horizontal and Lamb waves in isotropic plates or, more general, guided waves in anisotropic plates, such as composites.
At last, the effect of having finite length and width dimensions on the propagating wave behavior is analyzed.
Next to the theoretical framework for linear elastic wave dynamics, experimental results are presented.

While this chapter contains all the necessary concepts required for understanding the remainder of this PhD work, it is far from a complete exposition on *linear elastic wave dynamics*. Those who are looking for more information on elastic wave dynamics are kindly referred to one of the extensive courses or books that are available [1-7].

2. Theory of Elasticity

2.1. Stress and Strain

In order to study the linear elastic wave dynamics, the theory of elasticity has to be considered first. The theory of elasticity handles the response of an elastic material when it is subjected to a force or pressure. In the case of a bar under tension (i.e. a one-dimensional problem), the stress σ [Pa = N/m^2], equals the tension force F [N] divided by the cross-sectional area of the rod A [m^2]:

$$\sigma = \frac{F}{A}.$$

In a three-dimensional case, the direction of the force with respect to the subjected area becomes important as the force can act in both the perpendicular and in the tangential direction. As a result, each face of a material can experience three stress components. These stress components are shown in Figure 2.1 for a three-dimensional body using a Cartesian coordinate system. Each stress component is given two indices where the first one '*i*' refers to the direction of the force vector and the second one '*j*' refers to the direction of the surface normal to the plane on which the force acts. All different stress components are grouped in the stress tensor $\bar{\bar{\sigma}}$:

$$\bar{\bar{\sigma}} = \begin{bmatrix} \sigma_{11} & \sigma_{12} & \sigma_{13} \\ \sigma_{21} & \sigma_{22} & \sigma_{23} \\ \sigma_{31} & \sigma_{32} & \sigma_{33} \end{bmatrix} = \begin{bmatrix} \sigma_{11} & \sigma_{12} & \sigma_{13} \\ \sigma_{12} & \sigma_{22} & \sigma_{23} \\ \sigma_{13} & \sigma_{23} & \sigma_{33} \end{bmatrix} \tag{2.1}$$

The condition of static equilibrium imposes the stress tensor to be symmetric, i.e. $\sigma_{ij} = \sigma_{ji}$, (see Eq. (2.1)). The diagonal elements are the normal stresses caused by a tensile or compression force perpendicular to the plane. The off-diagonal elements are the shear stresses caused by a force tangential to the plane.

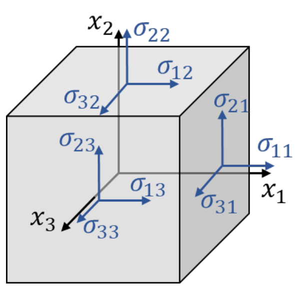

Figure 2.1: Definition of stress components for a three-dimensional body.

In a similar manner as for the stress tensor, a strain tensor $\bar{\bar{\varepsilon}}$ can be constructed for which the strain is defined as the amount of deformation in the direction of the applied force with respect to the initial length of the material. For the one-dimensional case of the bar under tension or compression, the (engineering) strain is found as $\varepsilon = \frac{\Delta l}{l_0}$, with Δl the change of the length of the bar and l_0 the initial bar length. Thus, the strain ε is a dimensionless quantity, often expressed as a percentage. In case of an infinitesimal small force, the expression of strain becomes $\varepsilon = \frac{du}{dx}$ with du the infinitesimal small displacement and dx the infinitesimal small bar length. Extending this example to three dimensions, the strain tensor is defined as:

$$\varepsilon_{ij} = \frac{1}{2}\left(\frac{\partial u_i}{\partial x_j} + \frac{\partial u_j}{\partial x_i}\right) \text{and } \bar{\bar{\varepsilon}} = \begin{bmatrix} \varepsilon_{11} & \varepsilon_{12} & \varepsilon_{13} \\ \varepsilon_{12} & \varepsilon_{22} & \varepsilon_{23} \\ \varepsilon_{13} & \varepsilon_{23} & \varepsilon_{33} \end{bmatrix} \tag{2.2}$$

Similar as the stress tensor, the strain tensor is symmetric. The diagonal and off-diagonal elements represent the normal strains and the shear strains, respectively. The displacement u_i takes place in the x_i-direction, with i = 1,2 or 3.

2.2. Stress – Strain Relation: Linear Elasticity

Let us consider again the case of a one-dimensional bar subjected to a tensile force. The engineering stress σ in the bar and the resulting engineering strain ε were already defined as: $\sigma = \frac{F}{A_0}$ and $\varepsilon = \frac{du}{dx} = \frac{\Delta l}{l_0}$. When the tensile force F is increased, the stress increases and so will the strain resulting in a typical engineering stress-strain curve as shown in Figure 2.2.

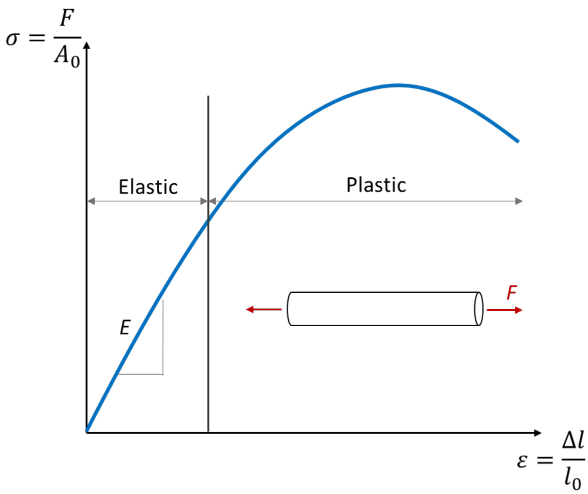

Figure 2.2: Typical engineering stress-strain curve for (1D) tension applied to a bar.

Two regimes can be identified from the stress-strain curve. When the stress and strain values are small, the deformation is elastic meaning that when the stress is reduced back to zero, the material will deform to its original shape. For high stress (and strain) values, the deformations become non-reversible and plasticity takes place. In the field of wave dynamics, including ultrasonic NDT techniques, the stresses and strains are most often very small ($\varepsilon < 10^{-6}$ [8]) and the material deformations are in good approximation fully linear elastic. Only in specific cases, a nonlinear elastic response has to be considered as will be explained in detail in Chapter 3.

In the linear elastic regime, the stress and strain relation in the one-dimensional bar can be written as:

$$\sigma = E\,\varepsilon$$

where E denotes the Elastic modulus (or Young's modulus) which is a material property often referred to as the material's stiffness. Extending this concept to three dimensions requires the shear stresses and shear strains to be included. The elasticity tensor, or C-tensor, $\bar{\bar{C}}$ is defined to capture the elastic response of the material:

$$\begin{aligned} &\bar{\bar{\sigma}} = \bar{\bar{C}}\,\bar{\bar{\varepsilon}} \\ &\sigma_{ij} = C_{ijkl}\,\varepsilon_{kl} \text{ with } i,j,k,l = 1,2,3 \end{aligned} \tag{2.3}$$

In this equation, and in the remainder of this chapter, Einstein's summation convention is used. This means that if an index appears twice in a single term, the term must be summed over all the possible values of that index.

The C-tensor is again a material property and has in its most general form 81 elements. Taking into account the natural symmetries ($\sigma_{ij} = \sigma_{ji}, \varepsilon_{ij} = \varepsilon_{ji}$ and $C_{ijkl} = C_{klij}$), the number of independent elements in the C-tensor is reduced from 81 to 21. As a result, the stress, strain and C-tensor can be written in a more comprehensible form (i.e. Voigt notation) by contraction of the indices ($11 \to 1, 22 \to 2, 33 \to 3, 23 = 32 \to 4, 13 = 31 \to 5, 12 = 21 \to 6$):

$$\begin{bmatrix} \sigma_1 \\ \sigma_2 \\ \sigma_3 \\ \sigma_4 \\ \sigma_5 \\ \sigma_6 \end{bmatrix} = \begin{bmatrix} C_{11} & C_{12} & C_{13} & C_{14} & C_{15} & C_{16} \\ & C_{22} & C_{23} & C_{24} & C_{25} & C_{26} \\ & & C_{33} & C_{34} & C_{35} & C_{36} \\ & & & C_{44} & C_{45} & C_{46} \\ & Symm & & & C_{55} & C_{56} \\ & & & & & C_{66} \end{bmatrix} \begin{bmatrix} \varepsilon_1 \\ \varepsilon_2 \\ \varepsilon_3 \\ 2\varepsilon_4 \\ 2\varepsilon_5 \\ 2\varepsilon_6 \end{bmatrix} \tag{2.4}$$

The use of this reduced notation has the additional benefit that the C-tensor can be transformed to a different coordinate system using only two rotation matrices [2].

2.2.1. Effect of Material Symmetry on C-tensor

Eq. (2.4) shows the 6x6 anisotropic C-tensor with 21 entries. A material is classified *anisotropic* if these 21 entries are independent from each other.

The large majorities of materials found in nature show symmetry along specific planes or axes, which thus reduces the number of independent elements in the C-tensor. As a result, by aligning the coordinate system with one of the symmetry planes and/or axes, multiple elements of the C-tensor become equal to zero.

A material is classified *orthotropic* when it has two orthogonal planes of symmetry. When the C-tensor is described along the material's symmetry axes, it is represented by only nine independent constants:

$$\bar{\bar{C}}^{orthotropic} = \begin{bmatrix} C_{11} & C_{12} & C_{13} & 0 & 0 & 0 \\ & C_{22} & C_{23} & 0 & 0 & 0 \\ & & C_{33} & 0 & 0 & 0 \\ & & & C_{44} & 0 & 0 \\ & Symm & & & C_{55} & 0 \\ & & & & & C_{66} \end{bmatrix}$$

Composite materials (such as CFRPs), which are manufactured by stacking multiple plies of long fibers that are orientated along specific directions, have typically two orthogonal planes of symmetry and are thus orthotropic.

The highest form of symmetry is obtained when there is an infinite number of planes of symmetry. As a result, the material's response is independent of its orientation and the C-tensor consists of only two independent constants. Materials who possess this highest symmetry class are called *isotropic* materials. The two remaining elastic constants are commonly chosen as the Lamé coefficients λ and μ and the C-tensor takes the form [6]:

$$\bar{\bar{C}}^{isotropic} = \begin{bmatrix} \lambda + 2\mu & \lambda & \lambda & 0 & 0 & 0 \\ & \lambda + 2\mu & \lambda & 0 & 0 & 0 \\ & & \lambda + 2\mu & 0 & 0 & 0 \\ & & & \mu & 0 & 0 \\ & Symm & & & \mu & 0 \\ & & & & & \mu \end{bmatrix} \tag{2.5}$$

Metallic materials, such as aluminum or steel, are mostly found in this isotropic material class.

2.2.2. Elastic Constants for Isotropic Materials

Next to the two Lamé coefficients λ and μ, there are other elastic constants that are often used in the case of isotropic materials because they are directly related to a measurement quantity:

- The elastic modulus or Young's modulus E was already defined at the start of this section. It represents the ratio between axial stress and axial strain for a 1D bar subjected to axial tension or compression. Hence, for isotropic materials: $E = \frac{\sigma_i}{\varepsilon_i} = \frac{\mu(3\lambda+2\mu)}{\lambda+\mu}$ $(i = 1,2,3)$.
- The Poisson's ratio ν is found as the ratio between the lateral contraction and the axial extension. Hence, for isotropic materials: $\nu = -\frac{\sigma_3}{\varepsilon_1} = -\frac{\sigma_2}{\varepsilon_1} = \frac{\lambda}{2(\lambda+\mu)}$.

Eliminating λ by combination of the above expressions for E and ν results in the well-known definition of the shear modulus for isotropic materials: $G = \mu = \frac{E}{2(1+\nu)}$. Table 2.1 summarizes the important relations between the elastic constants.

Table 2.1: Expressions for elastic constants in isotropic materials [6].

	$\boldsymbol{\lambda, \mu}$	$\boldsymbol{E, \nu}$	$\boldsymbol{E, \mu}$
$\boldsymbol{\lambda}$	λ	$\frac{E\nu}{(1+\nu)(1-2\nu)}$	$\frac{\mu(E-2\mu)}{3\mu-E}$
$\boldsymbol{\mu}$	μ	$\frac{E}{2(1+\nu)}$	μ
$\boldsymbol{E}$	$\frac{\mu(3\lambda+2\mu)}{\lambda+\mu}$	E	E
$\boldsymbol{\nu}$	$\frac{\lambda}{2(\lambda+\mu)}$	ν	$\frac{E}{2\mu}-1$

3. Bulk Waves in Solids

The theory of elasticity covers the static properties and thus the static response of a mechanical system. In that case, the resultant force acting on the body is zero. When the resulting force is nonzero, there will be a nonzero acceleration and Newton's second law of motion must be taken into account. Combining the equations of linear elasticity with Newton's second law results in the wave equation. The wave equations describe the propagation of elastic waves in solid media [2-4, 6, 7, 9].

3.1. One-Dimensional Wave Equation

Let us first consider a one-dimensional case, such as a rod of material subjected to an axial (i.e. longitudinal) dynamic load. The stress-strain relation of the rod element of length l, subjected to force F, is given by (see Section 2.2):

$$\sigma = \frac{F}{A} = E\varepsilon = E\frac{\partial u}{\partial x}$$

On the other hand, Newton's second law states:

$$\frac{\partial \sigma}{\partial x} = \rho \frac{\partial^2 u}{\partial t^2}$$

where ρ is the material's density. The one-dimensional wave equation is readily obtained from combining Newton's second law with the stress-strain relation:

$$\frac{\partial^2 u}{\partial x^2} = \frac{\rho}{E}\frac{\partial^2 u}{\partial t^2} \tag{2.6}$$

The solution of this differential equation for the displacement u is found as:

$$u(x,t) = A\exp\big(i(\omega t - \kappa x)\big) + B\exp\big(i(\omega t + \kappa x)\big) \tag{2.7}$$

where the coefficients A and B can be found by taking into account the boundary conditions. The first part corresponds to longitudinal waves travelling in the positive x-direction and the second part corresponds to longitudinal waves travelling in the negative x-direction. The expression of the longitudinal wave velocity $V_L \left[\frac{m}{s}\right]$ is obtained by substitution of Eq. (2.7) in Eq. (2.6):

$$V_L = \sqrt{\frac{E}{\rho}} = \frac{\omega}{\kappa} \tag{2.8}$$

with

$$\text{Angular frequency: } \omega \left[\frac{rad}{s}\right] = 2\pi f$$

$$\text{Angular wavenumber: } \kappa \left[\frac{rad}{m}\right] = 2\pi k$$

3.2. Three-Dimensional Wave Equation

Similar to the one-dimensional case, the wave equation in three dimensions is obtained by combination of the stress-strain relation and Newton's second law of motion. For an infinitesimal small volume element subjected to body forces g and surfaces forces T, Newton's second law of motion can be written as:

$$\int \rho \frac{\partial^2 u_i}{\partial t^2} dV = \oint T_i dS + \int g_i dV$$

where the index i indicates the direction of the displacement. The body forces g are neglected because the force caused by gravity is extremely small and there are no other external forces. The surface forces are rewritten in terms of the stresses and the surface integral is transformed to a volume integral (by means of the Gauss' theorem [6]):

$$\oint T_i dS = \int \frac{\partial \sigma_{ij}}{\partial x_j} dV$$

As a result, following three-dimensional equation is obtained:

$$\rho \frac{\partial^2 u_i}{\partial t^2} = \frac{\partial \sigma_{ij}}{\partial x_j} \tag{2.9}$$

3.2.1. Isotropic Materials

Eq. (2.9) can be solved for the displacements u_i in multiple ways. For isotropic materials, it is common practice to make use of the Stokes-Helmholtz decomposition [7]. In this case, the displacement field $\bar{u} = [u_1\ u_2\ u_3]$ is decomposed as:

$$\bar{u} = \bar{\nabla}\phi + \bar{\nabla} \times \bar{A} \tag{2.10}$$

where ϕ and $\bar{A} = [A_1\ A_2\ A_3]$ are a scalar and vector field, respectively and $\bar{\nabla}$ is the Nabla operator:

$$
\begin{aligned}
\bar{\nabla}\phi &= \begin{bmatrix} \frac{\partial \phi}{\partial x_1} & \frac{\partial \phi}{\partial x_2} & \frac{\partial \phi}{\partial x_3} \end{bmatrix} \\
\bar{\nabla} \times \bar{A} &= \begin{bmatrix} \frac{\partial A_3}{\partial x_2} - \frac{\partial A_2}{\partial x_3} & \frac{\partial A_1}{\partial x_3} - \frac{\partial A_3}{\partial x_1} & \frac{\partial A_2}{\partial x_1} - \frac{\partial A_1}{\partial x_2} \end{bmatrix} \\
\bar{\nabla}.\bar{u} &= \frac{\partial u_1}{\partial x_1} + \frac{\partial u_2}{\partial x_2} + \frac{\partial u_3}{\partial x_3}
\end{aligned}
\tag{2.11}
$$

In order to make use of this decomposition of $\bar{u}$, the stress-strain relation given by Eq. (2.3) and (2.5) is rewritten in the form:

$$\sigma_{ij} = \lambda\,\bar{\nabla}.\bar{u}\,\delta_{ij} + \mu\left(\frac{\partial u_j}{\partial x_i} + \frac{\partial u_i}{\partial x_j}\right) \tag{2.12}$$

where $\delta_{ij} = 1$ if $i = j$ and $\delta_{ij} = 0$ elsewhere. Inserting this expression for the stresses σ_{ij} in Eq. (2.9) gives:

$$(\lambda + 2\mu)\bar{\nabla}(\bar{\nabla}.\bar{u}) + \mu\bar{\nabla} \times \bar{\nabla} \times \bar{u} = \rho\frac{\partial^2 \bar{u}}{\partial t^2} \tag{2.13}$$

The obtained equation is known as the Navier's equation [4]. At last, Eq. (2.10) is inserted into the Navier's equation (Eq. (2.13)) and one obtains (after some vector calculus):

$$\bar{\nabla}\left((\lambda + 2\mu)\Delta\phi - \rho\frac{\partial^2 \phi}{\partial t^2}\right) + \bar{\nabla} \times \left(\mu\Delta\bar{A} - \rho\frac{\partial^2 \bar{A}}{\partial t^2}\right) = 0 \tag{2.14}$$

with Laplacian operator $\Delta = \bar{\nabla}.\bar{\nabla}$:

$$
\begin{aligned}
\Delta\phi &= \sum_{i=1}^{3} \frac{\partial^2 \phi}{\partial x_i^2} \\
\Delta\bar{A} &= [\Delta A_1 \;\; \Delta A_2 \;\; \Delta A_3]
\end{aligned}
\tag{2.15}
$$

In order for Eq. (2.14) to hold, both parts between the parentheses need to be zero. As a result, the equation is decoupled resulting in one expression for the scalar field ϕ and one for the vector field $\bar{A}$:

$$
\begin{cases}
(\lambda + 2\mu)\Delta\phi = \rho\frac{\partial^2 \phi}{\partial t^2} \\
\mu\Delta\bar{A} = \rho\frac{\partial^2 \bar{A}}{\partial t^2}
\end{cases}
\tag{2.16}
$$

Both equations are wave equations that can be solved using classical methods. Looking back at the C-tensor of isotropic materials (Eq. (2.5)), it is clear that the first equation can be associated to longitudinal waves and the second one to transversal or shear waves. As a result, we state that:

$$
\begin{cases}
\bar{u}_L = \bar{\nabla}\phi \\
\bar{u}_S = \bar{\nabla} \times \bar{A}
\end{cases}
\quad \text{with} \quad
\begin{aligned}
\bar{\nabla} \times \bar{u}_L &= 0 \\
\bar{\nabla}.\bar{u}_S &= 0
\end{aligned}
\tag{2.17}
$$

and obtain the wave equations for longitudinal and shear bulk waves:

$$\begin{cases} V_L^2 \Delta \bar{u}_L = \dfrac{\partial^2 \bar{u}_L}{\partial t^2} \\ V_S^2 \Delta \bar{u}_S = \dfrac{\partial^2 \bar{u}_S}{\partial t^2} \end{cases} \quad \text{with} \quad \begin{aligned} V_L &= \sqrt{\frac{\lambda + 2\mu}{\rho}} \\ V_S &= \sqrt{\frac{\mu}{\rho}} \end{aligned} \tag{2.18}$$

with V_L and V_S, the longitudinal and shear (or transversal) wave speeds, respectively.

The vector properties of $\bar{u}_L$ and $\bar{u}_S$ (Eq. (2.17)) confirm that (i) $\bar{u}_L$ corresponds to a longitudinal wave for which the displacement direction $\bar{u}_L$ coincides with the wave vector direction and (ii) $\bar{u}_S$ corresponds to a shear wave for which the displacement direction $\bar{u}_S$ is perpendicular to the wave vector direction. Because there are two directions perpendicular to the wave direction, there are two shear wave types. When the particle displacement is parallel to the reference plane's surface, the shear wave is named 'horizontal'. Whereas when the particle displacement is perpendicular to the reference plane's surface, the shear wave is named 'vertical'. Figure 2.3 shows the particle displacement direction $\vec{u}$ for the three wave types.

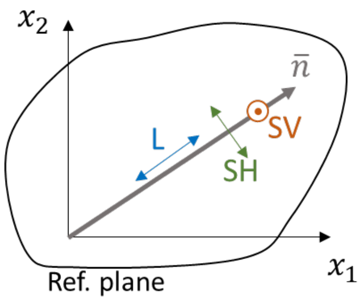

Figure 2.3: Polarization of longitudinal *L*, shear horizontal *SH*, and shear vertical *SV* bulk waves propagating in a solid in direction $\bar{n}$ [4].

3.2.2. Anisotropic Materials

For anisotropic materials, Eq. (2.12) is no longer valid and all the 21 C_{ij} components have to be taken into account. Inserting the general constitutive laws, Eq. (2.2) and (2.3), into Eq. (2.9) gives:

$$\rho \frac{\partial^2 u_i}{\partial t^2} = C_{ijkl} \frac{\partial \varepsilon_{kl}}{\partial x_j} = \frac{C_{ijkl}}{2} \left(\frac{\partial u_k}{\partial x_j \partial x_l} + \frac{\partial u_l}{\partial x_j \partial x_k} \right) \overset{\text{Sym}}{=} C_{ijkl} \frac{\partial u_l}{\partial x_j \partial x_k} \tag{2.19}$$

This equation is again a wave equation in the displacements u_i. Let us assume the harmonic solution:

$$u_i = U_i \exp\left(i\kappa\left(x_j n_j - V_{ph} t\right)\right)$$

with wave vector $\bar{\kappa} = \kappa\bar{n}$, phase velocity $V_{ph} = \omega/\kappa$, angular frequency $\omega = 2\pi f$, angular wavenumber $\kappa = 2\pi k$ and wave amplitude U_i. Note the analogy with the one-dimensional wave equation solution discussed in Section 3.1. The phase velocity is introduced here because each point on the wave front (which is defined as points of constant phase) has a different propagation velocity. Inserting the harmonic solution into Eq. (2.19) gives:

$$\left(C_{ijkl}n_j n_k - \rho V_{ph}^2 \delta_{il}\right)U_l = 0 \tag{2.20}$$

This equation is called the Christoffel equation [4]. It corresponds to an eigenvalue problem for the displacement amplitudes U_l. If the C-tensor C_{ijkl} and density ρ are known, Eq. (2.20) can be used to find the phase velocity V_{ph} along specific wave vector directions. Vice versa, if the phase velocity V_{ph} is derived from experimental data, the material properties C_{ijkl} and ρ can be calculated using Eq. (2.20).

Three possible solutions are obtained for the phase velocity. Thus, there are again three different bulk wave modes that can travel in the solid material. The bulk wave modes are named: *quasi-longitudinal*, *quasi-shear horizontal* and *quasi-shear vertical* in analogy with the bulk modes found in isotropic solids. For bulk waves travelling along a material's symmetry axes (e.g. in case of orthotropic materials), the modes are *pure*.

Figure 2.4 (a-b) shows the inverse of the obtained phase velocity values, along all propagation directions φ in the (x_1, x_3)-plane, for an isotropic aluminum alloy and for an orthotropic unidirectional CFRP material. The obtained curves are called *slowness* curves. They are derived by solving the Christoffel equation (Eq. (2.20)) using following material properties:

$$\begin{gathered}
\rho^{Al} = 2693\,\frac{\mathrm{kg}}{\mathrm{m}^3} \text{ and } \bar{\bar{C}}^{Al} = \begin{bmatrix} 108.9 & 56.4 & 56.4 & 0 & 0 & 0 \\ & 108.9 & 56.4 & 0 & 0 & 0 \\ & & 108.9 & 0 & 0 & 0 \\ & & & 26.2 & 0 & 0 \\ & Symm & & & 26.2 & 0 \\ & & & & & 26.2 \end{bmatrix} \mathrm{GPa} \\
\rho^{CFRP} = 1528\,\frac{\mathrm{kg}}{\mathrm{m}^3} \text{ and } \bar{\bar{C}}^{CFRP} = \begin{bmatrix} 122.7 & 6.3 & 6.3 & 0 & 0 & 0 \\ & 13.2 & 5.3 & 0 & 0 & 0 \\ & & 13.2 & 0 & 0 & 0 \\ & & & 3.3 & 0 & 0 \\ & Symm & & & 5.1 & 0 \\ & & & & & 5.2 \end{bmatrix} \mathrm{GPa}
\end{gathered} \tag{2.21}$$

For the isotropic material, the phase velocity is independent of the wave propagation direction φ and could also be derived using Eq. (2.18). For the orthotropic unidirectional CFRP material, the phase velocity is strongly dependent on the propagation direction φ and the phase velocity of the horizontal and vertical shear waves is different.

The slowness curves also provide a means to visualize the direction and velocity of the wave energy flow. In lossless materials, the energy velocity V_e equals the group velocity V_g, which is defined as [7]:

$$V_e \approx V_g = \nabla_{\vec{\kappa}}\omega = \frac{V_{ph}}{\cos\psi}$$

This indicates that the energy travels in the direction normal to the slowness curve. The angle between the direction of wave propagation φ and the direction of energy flow is the skew angle ψ. The wave propagation direction, energy flow direction and skew angle are indicated on the slowness curve of the CFRP material (see Figure 2.4 (c)). Note that for isotropic materials, the skew angle is always zero. Figure 2.5 shows the phase velocity, V_{ph}, the skew angle ψ and the group velocity V_g in function of the propagation direction φ for bulk waves travelling in the (x_1, x_3)-plane of the unidirectional CFRP material.

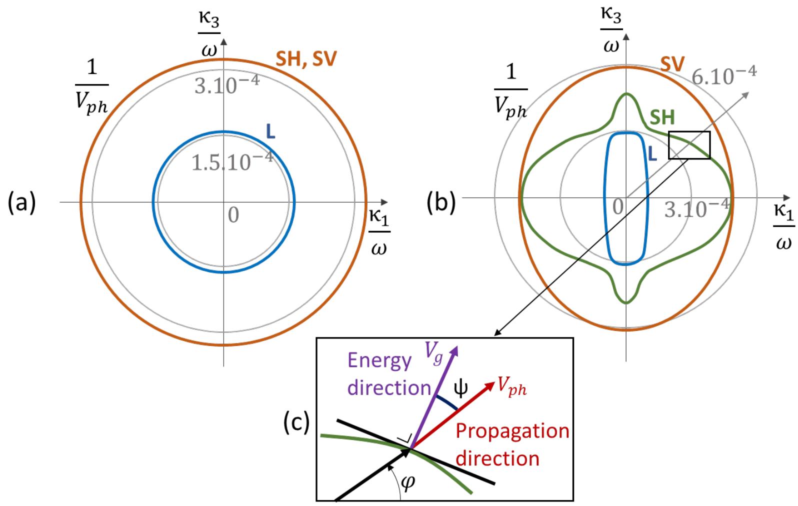

Figure 2.4: Slowness curves for (a) Isotropic aluminum and (b) Orthotropic unidirectional CFRP with (c) Definition of the propagation direction φ and skew angle ψ.

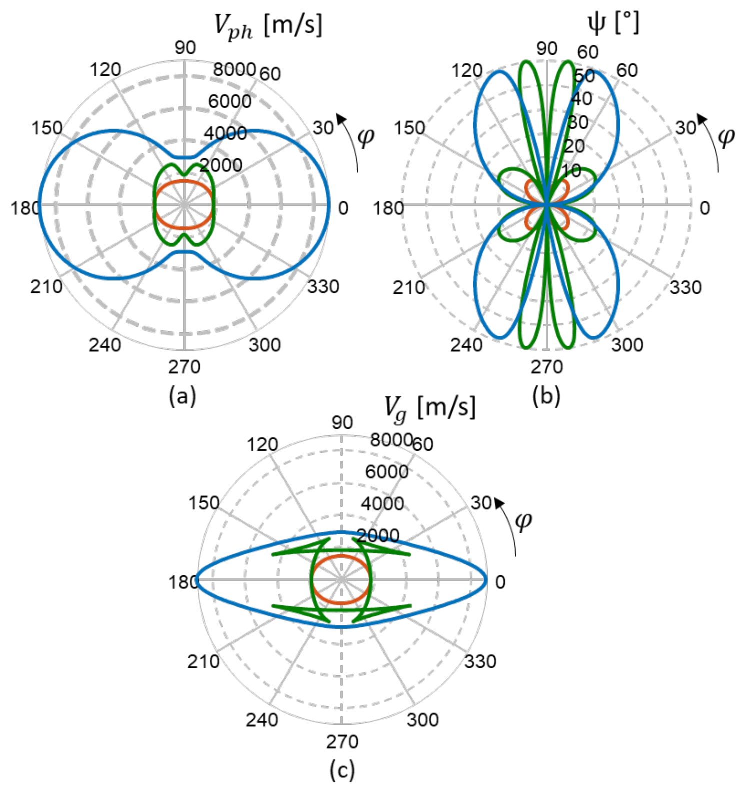

Figure 2.5: (a) Phase velocity V_{ph}, (b) Skew Angle ψ and (c) Group velocity V_g for bulk waves in orthotropic unidirectional CFRP in function of the propagation direction φ in the (x_1, x_3)-plane.

4. Guided Waves

Up to now, the mechanics of elastic waves travelling in infinitely large solids were studied. In this section, the wave propagation in a plate with a thickness smaller than a few times the wavelength of the propagating wave is investigated. These waves must fulfill the general 3D wave equation (Eq. (2.19)) as well as the traction-free boundary conditions at the plate's top and bottom surfaces. Because the waves are guided by the surfaces of the plate, they are referred to as *guided waves*. One of the most important properties of guided waves is that the propagation speed of guided waves is generally frequency-dependent, meaning that each frequency component of each mode moves with its own speed. This results in the dispersion (or the dispersive propagation) of guided waves in space and time. The coordinate system shown in Figure 2.6 is used throughout this section. The plate thickness is denoted h.

Solutions of the general wave equation, taking into account the plate's boundary conditions, are not easily obtained. Only in specific cases, the problem can be solved analytically. This is for instance the case for isotropic materials with traction-free boundaries. The resulting waves are named Lamb waves, after Sir Horace Lamb who was the first to describe and investigate these waves already in 1917 [1]. These waves in isotropic materials are discussed first. Next, the guided waves in anisotropic materials are considered. The important differences between guided waves in anisotropic materials and in isotropic materials are investigated. The mathematical derivations are based on the analysis found in [3, 4, 6, 9].

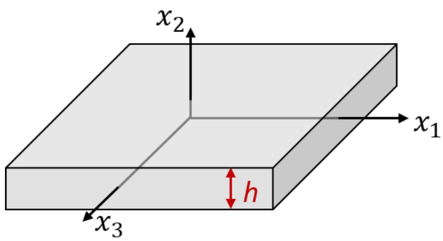

Figure 2.6: Coordinate system used in the theoretical framework of guided waves.

4.1. Guided Waves in Isotropic Materials

In isotropic materials, one can further distinguish between shear horizontal waves and Lamb waves.

4.1.1. Shear Horizontal Waves

Consider the isotropic plate aligned with the (x_1, x_3) plane and with thickness h (see Figure 2.6). In this case, the shear horizontal wave travelling in the x_1 direction has zero displacement in the x_1 and in the x_2 directions: $u_1 = u_2 = 0$ (see also Figure 2.3). As a result, and assuming that u_3 is independent of x_3 (i.e. infinitely large plate), the Navier equation for isotropic materials (Eq. (2.13)) becomes:

$$\mu\left(\frac{\partial^2 u_3}{\partial x_1^2} - \frac{\partial^2 u_3}{\partial x_2^2}\right) = \rho\frac{\partial^2 u_3}{\partial t^2}$$

The corresponding displacement field u_3 is found as:

$$u_3(x_1, x_2, t) = \big(A\sin(\beta x_2) + B\cos(\beta x_2)\big)\exp\big(i(\kappa x_1 - \omega t)\big)$$

$$\text{with } \beta = \sqrt{\frac{\omega^2}{V_S^2} - \kappa^2}$$

where $V_S = \sqrt{\frac{\mu}{\rho}}$ is the bulk shear wave velocity. Imposing the traction-free boundary conditions using Eq. (2.12) at $x_2 = \pm\frac{h}{2}$ leads to:

$$\begin{cases} \sigma_{32}\big|_{x_2=\frac{h}{2}} = 0 \\ \\ \sigma_{32}\big|_{x_2=-\frac{h}{2}} = 0 \end{cases} \rightarrow \begin{cases} \frac{\mu}{2}\beta\left(-A\cos\left(\beta\frac{h}{2}\right) + B\sin\left(\beta\frac{h}{2}\right)\right)\exp\big(i(\kappa x_1 - \omega t)\big) = 0 \\ \frac{\mu}{2}\beta\left(-A\cos\left(\beta\frac{h}{2}\right) - B\sin\left(\beta\frac{h}{2}\right)\right)\exp\big(i(\kappa x_1 - \omega t)\big) = 0 \end{cases}$$

In order to obtain non-trivial solutions for A and B, the determinant of the coefficient matrix must be equal to zero:

$$\begin{vmatrix} -\cos\left(\beta\frac{h}{2}\right) & \sin\left(\beta\frac{h}{2}\right) \\ -\cos\left(\beta\frac{h}{2}\right) & -\sin\left(\beta\frac{h}{2}\right) \end{vmatrix} = 0$$

Hence,

$$2\cos\left(\beta\frac{h}{2}\right)\sin\left(\beta\frac{h}{2}\right) = 0$$

$$\rightarrow \beta\frac{h}{2} = m\frac{\pi}{2} \text{ with } m = 0,1,2 \ldots$$

Using the definition of β, the phase velocity of the shear horizontal mode is finally obtained as:

$$V_{SH_m} = \frac{\omega}{\kappa} = \frac{V_S}{\sqrt{1 - \left(\frac{m\pi}{h}\right)^2\left(\frac{V_S}{\omega}\right)^2}} \tag{2.22}$$

Solutions of this dispersion equation are shown in Figure 2.7 for a 5 mm thick aluminum material with properties listed in Eq. (2.21).

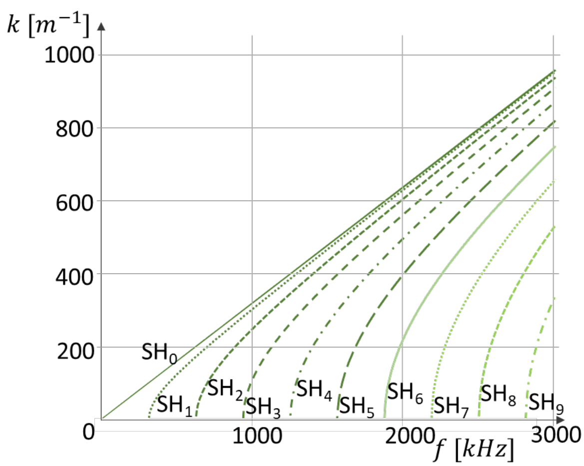

Figure 2.7: Dispersion curves for shear horizontal modes in 5 mm thick aluminum plate.

The fundamental mode, named SH_0 ($m = 0$), is non-dispersive because the phase velocity is equal to the phase velocity of the bulk shear wave: $V_{SH_0} = V_S$. This corresponds to a straight line in the wavenumber-frequency map (see Figure 2.7). The SH_0 displacement field equals:

$$u_3(x_1, x_2, t)|_{SH_0} = B \exp\left(i\omega\left(\frac{x_1}{V_S} - t\right)\right)$$

The displacement field is constant over the thickness of the plate. The mode is classified as symmetric because the displacement field is symmetric with respect to the center of the plate.

The higher order modes ($m > 0$) show a cut-off frequency. The phase velocity V_{SH_m} depends on the frequency making these higher order modes dispersive. The displacement field is given by:

$$u_3(x_1 x_2, t)|_{SH_m} = A \ \sin\left(\frac{m\pi x_2}{h}\right) \exp\left(i\omega\left(\frac{x_1}{V_{SH_m}} - t\right)\right) \quad \text{if } m \text{ odd}$$

$$u_3(x_1 x_2, t)|_{SH_m} = A \ \cos\left(\frac{m\pi x_2}{h}\right) \exp\left(i\omega\left(\frac{x_1}{V_{SH_m}} - t\right)\right) \quad \text{if } m \text{ even}$$

The modes for which m is odd are anti-symmetric and the modes for which m is even are symmetric.

4.1.2. Lamb Waves

The same coordinate system as was used in previous section (see Figure 2.6) is considered here for deriving the dispersion equations of Lamb waves. The plate (with thickness h) coincides with the (x_1, x_3) plane and the Lamb waves travel in the x_1 direction. The Lamb waves are a combination of longitudinal and shear vertical bulk waves. As a result, they have no displacement component in the x_3 direction (i.e. $u_3 = 0$).

Similar to Section 3.2.1, the displacement field is written as the sum of a scalar ϕ and a vector potential $\bar{A}$ (see Eq. (2.10)). Taking into account that $u_3 = 0$ and that u_1 and u_2 are independent of x_3 (i.e. infinitely large plate), the following expressions for the displacements are obtained (with $\bar{\mathrm{A}} = [0\ 0\ \mathrm{A}_3]$, because $u_3 = 0$):

$$\begin{cases} u_1 = \dfrac{\partial \phi}{\partial x_1} + \dfrac{\partial A_3}{\partial x_2} \\ u_2 = \dfrac{\partial \phi}{\partial x_2} - \dfrac{\partial A_3}{\partial x_1} \\ u_3 = 0 \end{cases} \tag{2.23}$$

Proposed solutions for ϕ and A_3 are:

$$\begin{cases} \phi(x_1, x_2, t) = \hat{\phi}(x_2) \exp\big(i(\kappa x_1 - \omega t)\big) \\ A_3(x_1, x_2, t) = \widehat{A_3}(x_2) \exp\big(i(\kappa x_1 - \omega t)\big) \end{cases} \tag{2.24}$$

Inserting these solutions into the decomposed wave equations (Eq. (2.16)) gives:

$$\begin{cases} \dfrac{d^2\hat{\phi}(x_2)}{dx_2^2} = \hat{\phi}(x_2)\left[\kappa^2 - \dfrac{\omega^2}{V_L^2}\right] \\ \dfrac{d^2\widehat{A_3}(x_2)}{dx_2^2} = \widehat{A_3}(x_2)\left[\kappa^2 - \dfrac{\omega^2}{V_S^2}\right] \end{cases}$$

Here, V_L and V_S are the phase velocities of the bulk longitudinal and bulk shear waves (see Eq. (2.18)), respectively. Both equations are ordinary differential equations with general solutions:

$$\begin{cases} \widehat{\Phi}(x_2) = A\exp(i\alpha_1 x_2) + B\exp(-i\alpha_1 x_2) \\ \widehat{A_3}(x_2) = C\exp(i\alpha_2 x_2) + D\exp(-i\alpha_2 x_2) \end{cases} \quad \text{with} \quad \begin{aligned} \alpha_1^2 &= \kappa^2 - \frac{\omega^2}{V_L^2} \\ \alpha_2^2 &= \kappa^2 - \frac{\omega^2}{V_S^2} \end{aligned}$$

In order to simplify the analysis, the problem can be decomposed into a symmetric and an asymmetric problem by choosing the general solutions as:

$$\begin{cases} \widehat{\Phi}(x_2) = E\sinh(\alpha_1 x_2) + F\cosh(\alpha_1 x_2) \\ \widehat{A_3}(x_2) = G\sinh(\alpha_2 x_2) + H\cosh(\alpha_2 x_2) \end{cases}$$

Inserting these general solutions in Eq. (2.24) and using (2.23) gives:

$$\begin{cases} u_1 = [i\kappa E\sinh(\alpha_1 x_2) + i\kappa F\cosh(\alpha_1 x_2) + G\alpha_2\cosh(\alpha_2 x_2) + H\alpha_2\sinh(\alpha_2 x_2)] \\ \qquad .\exp\big(i(\kappa x_1 - \omega t)\big) \\ u_2 = [\alpha_1 E\cosh(\alpha_1 x_2) + \alpha_1 F\sinh(\alpha_1 x_2) - \kappa i G\sinh(\alpha_2 x_2) - \kappa i H\cosh(\alpha_2 x_2)] \\ \qquad .\exp\big(i(\kappa x_1 - \omega t)\big) \\ u_3 = 0 \end{cases} \tag{2.25}$$

Next, the traction-free boundary conditions at the surface of the plate $x_2 = \pm\frac{h}{2}$ are imposed (using Eq. (2.12)):

$$\sigma_{22}|_{x_2=\frac{h}{2}} = 0 \rightarrow \begin{aligned} &\Big[\Big((\lambda+2\mu)\alpha_1^2 - \lambda\kappa^2\Big)E\sinh\left(\frac{\alpha_1 h}{2}\right) \\ &+\Big((\lambda+2\mu)\alpha_1^2 - \lambda\kappa^2\Big)F\cosh\left(\frac{\alpha_1 h}{2}\right) + (2\mu\kappa i\alpha_2)G\cosh\left(\frac{\alpha_2 h}{2}\right) \\ &+(2\mu\kappa i\alpha_2)H\sinh\left(\frac{\alpha_2 h}{2}\right)\Big]\exp\big(i(\kappa x_1 - \omega t)\big) = 0 \end{aligned} \tag{2.26}$$

$$\sigma_{22}|_{x_2=\frac{-h}{2}} = 0 \rightarrow \begin{aligned} &\Big[-\Big((\lambda+2\mu)\alpha_1^2 - \lambda\kappa^2\Big)E\sinh\left(\frac{\alpha_1 h}{2}\right) \\ &+\Big((\lambda+2\mu)\alpha_1^2 - \lambda\kappa^2\Big)F\cosh\left(\frac{\alpha_1 h}{2}\right) + (2\mu\kappa i\alpha_2)G\cosh\left(\frac{\alpha_2 h}{2}\right) \\ &-(2\mu\kappa i\alpha_2)H\sinh\left(\frac{\alpha_2 h}{2}\right)\Big]\exp\big(i(\kappa x_1 - \omega t)\big) = 0 \end{aligned} \tag{2.27}$$

$$\sigma_{12}\big|_{x_2=\frac{h}{2}}=0\rightarrow \begin{array}{l}\frac{\mu}{2}\Big[(2i\kappa\alpha_1)E\cosh\left(\frac{\alpha_1 h}{2}\right)\\ +(2i\kappa\alpha_1)F\sinh\left(\frac{\alpha_1 h}{2}\right)+(\kappa^2+\alpha_2^2)G\sinh\left(\frac{\alpha_2 h}{2}\right)\\ +(\kappa^2+\alpha_2^2)H\cosh\left(\frac{\alpha_2 h}{2}\right)\Big]\exp\big(i(\kappa x_1-\omega t)\big)=0\end{array} \tag{2.28}$$

$$\sigma_{12}\big|_{x_2=\frac{-h}{2}}=0\rightarrow \begin{array}{l}\frac{\mu}{2}\Big[(2i\kappa\alpha_1)E\cosh\left(\frac{\alpha_1 h}{2}\right)\\ -(2i\kappa\alpha_1)F\sinh\left(\frac{\alpha_1 h}{2}\right)-(\kappa^2+\alpha_2^2)G\sinh\left(\frac{\alpha_2 h}{2}\right)\\ +(\kappa^2+\alpha_2^2)H\cosh\left(\frac{\alpha_2 h}{2}\right)\Big]\exp\big(i(\kappa x_1-\omega t)\big)=0\end{array} \tag{2.29}$$

These four equations are simplified:

$$\begin{array}{l}\text{Eq. (2.26)+Eq. (2.27)}\rightarrow\\ \left((\lambda+2\mu)\alpha_1^2-\lambda\kappa^2\right)F\cosh\left(\frac{\alpha_1 h}{2}\right)+(2\mu\kappa i\alpha_2)G\cosh\left(\frac{\alpha_2 h}{2}\right)=0\\ \text{Eq. (2.28)-Eq. (2.29)}\rightarrow\\ (2i\kappa\alpha_1)F\sinh\left(\frac{\alpha_1 h}{2}\right)+(\kappa^2+\alpha_2^2)G\sinh\left(\frac{\alpha_2 h}{2}\right)=0\\ \text{Eq. (2.28)+Eq. (2.29)}\rightarrow\\ (2i\kappa\alpha_1)E\cosh\left(\frac{\alpha_1 h}{2}\right)+(\kappa^2+\alpha_2^2)H\cosh\left(\frac{\alpha_2 h}{2}\right)=0\\ \text{Eq. (2.26)-Eq. (2.27)}\rightarrow\\ \left((\lambda+2\mu)\alpha_1^2-\lambda\kappa^2\right)E\sinh\left(\frac{\alpha_1 h}{2}\right)+(2\mu\kappa i\alpha_2)H\sinh\left(\frac{\alpha_2 h}{2}\right)=0\end{array} \tag{2.30}$$

In order to obtain non-trivial solutions for the coefficients E, F, G and H, the determinants of the two coefficient matrices must be zero:

$$\begin{vmatrix}\left((\lambda+2\mu)\alpha_1^2-\lambda\kappa^2\right)\cosh\left(\frac{\alpha_1 h}{2}\right) & (2\mu\kappa i\alpha_2)\cosh\left(\frac{\alpha_2 h}{2}\right)\\ (2i\kappa\alpha_1)\sinh\left(\frac{\alpha_1 h}{2}\right) & (\kappa^2+\alpha_2^2)\sinh\left(\frac{\alpha_2 h}{2}\right)\end{vmatrix}=0$$

$$\begin{vmatrix}(2i\kappa\alpha_1)\cosh\left(\frac{\alpha_1 h}{2}\right) & (\kappa^2+\alpha_2^2)\cosh\left(\frac{\alpha_2 h}{2}\right)\\ \left((\lambda+2\mu)\alpha_1^2-\lambda\kappa^2\right)\sinh\left(\frac{\alpha_1 h}{2}\right) & (2\mu\kappa i\alpha_2)\sinh\left(\frac{\alpha_2 h}{2}\right)\end{vmatrix}=0$$

From the above, the two dispersion equations are finally obtained [4]:

$$\frac{\tanh\left(\frac{\alpha_1 h}{2}\right)}{\tanh\left(\frac{\alpha_2 h}{2}\right)}=\frac{(\alpha_2^2+\kappa^2)^2}{4\kappa^2\alpha_1\alpha_2} \tag{2.31}$$

$$\frac{\tanh\left(\frac{\alpha_2 h}{2}\right)}{\tanh\left(\frac{\alpha_1 h}{2}\right)}=\frac{(\alpha_2^2+\kappa^2)^2}{4\kappa^2\alpha_1\alpha_2} \tag{2.32}$$

In the case that $E = H = 0$, and $F \neq 0, G \neq 0$, dispersion equation (2.31) must be satisfied and the displacement field given by Eq. (2.25) becomes:

$$\begin{cases} u_1 = [i\kappa F\cosh(\alpha_1 x_2) + G\alpha_2\cosh(\alpha_2 x_2)]\exp\big(i(\kappa x_1 - \omega t)\big) \\ u_2 = [\alpha_1 F\sinh(\alpha_1 x_2) - \kappa i G\sinh(\alpha_2 x_2)]\exp\big(i(\kappa x_1 - \omega t)\big) \\ u_3 = 0 \end{cases} \tag{2.33}$$

The obtained displacement field is symmetric with respect to the mid-thickness plane ($x_2 = 0$) and the corresponding Lamb modes are classified: *symmetric* modes.

In the opposite case of $F = G = 0$, $E \neq 0$ and $H \neq 0$, dispersion equation (2.32) most hold and the displacement field equals:

$$\begin{cases} u_1 = [i\kappa E\sinh(\alpha_1 x_2) + H\alpha_2\sinh(\alpha_2 x_2)]\exp\big(i(\kappa x_1 - \omega t)\big) \\ u_2 = [\alpha_1 E\cosh(\alpha_1 x_2) - \kappa i H\cosh(\alpha_2 x_2)]\exp\big(i(\kappa x_1 - \omega t)\big) \\ u_3 = 0 \end{cases} \tag{2.34}$$

The displacement field is anti-symmetric with respect to the mid-thickness plane ($x_2 = 0$), and the modes are classified: *anti-symmetric* modes.

Figure 2.8 shows the dispersion curves corresponding to a h = 5 mm thick aluminum plate in a (f, k) coordinate system. At low frequencies, only the fundamental symmetric S_0 and the fundamental anti-symmetric A_0 Lamb mode can travel. The higher order modes have a cut-off frequency.

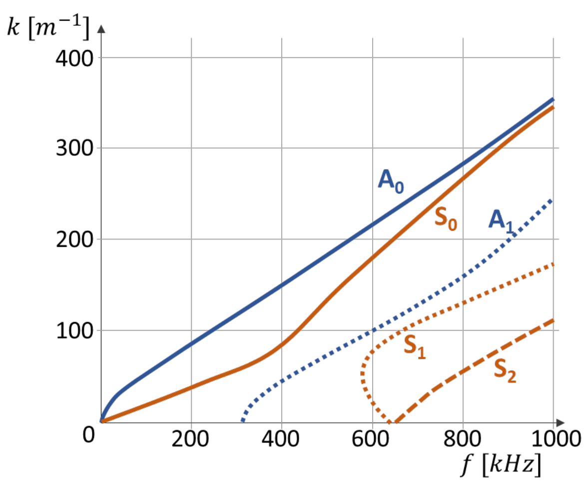

Figure 2.8: Dispersion curves for anti-symmetric A and symmetric S Lamb modes in 5 mm thick aluminum plate.

The (u_1, u_2) displacement fields corresponding to the first five Lamb modes are calculated using Eq. (2.33), (2.34) and (2.30) and plotted in Figure 2.9. Note again that the displacement field is anti-symmetric with respect to the mid-thickness of the plate for the anti-symmetric modes and vice-versa for the symmetric modes.

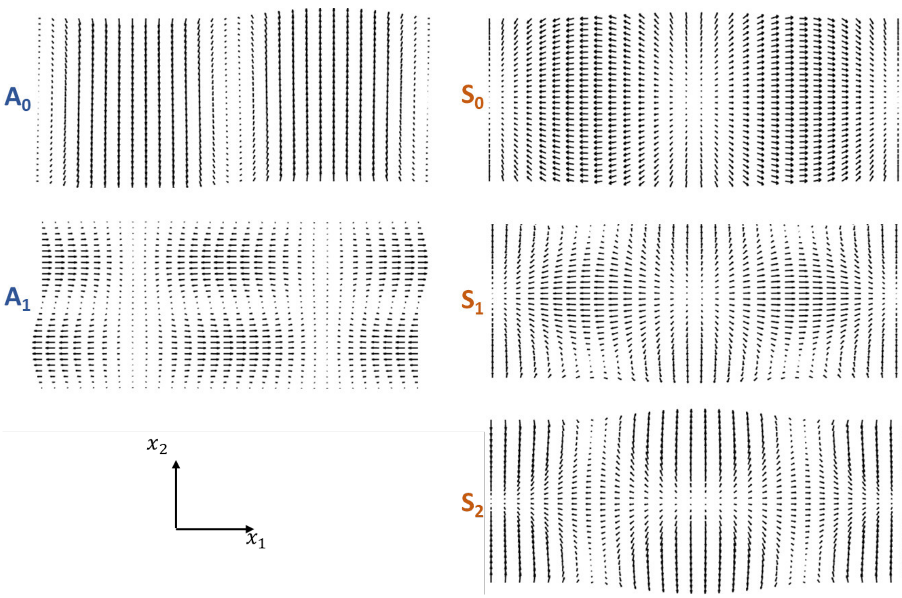

Figure 2.9: Displacement field calculated for the first five Lamb modes in a 5 mm thick aluminum plate.

4.2. Guided Waves in Composite Materials

In previous section, the foundations of guided wave propagation in single-layered free isotropic plates were outlined. Let us now investigate guided waves in composite materials. Composite materials are constructed by stacking multiple anisotropic (or orthotropic) thin layers together, following a predefined stacking sequence (see also Chapter 1). As a result, the analysis of guided waves in these composite materials must take into account (i) the anisotropic material properties and (ii) the multi-layered structure of the medium. Both characteristics make the analytical derivation of the dispersion equations and the displacement fields extremely challenging.

In order to deal with anisotropic material properties, we reflect back on the investigation of bulk waves in anisotropic materials (see Section 3.2.2). For layered materials, the Christoffel equations (Eq. (2.20)) must be constructed and solved for every individual material layer. Next, the boundary conditions are imposed. At the plate's top and bottom surfaces, the stress must be zero. At the layer interfaces, the displacement components (u_1, u_2, u_3) and the stress components normal to the layer interface $(\sigma_{12}, \sigma_{22}, \sigma_{23})$ must be continuous. It is common practice to assembly all these boundary conditions in one big matrix problem. This approach is called the *global matrix method* [4]. Alternatively, it is also possible to follow a *semi-analytical finite element SAFE* approach [3]. In that case, the material is discretized in the thickness direction using a one-dimensional finite element. The reader is referred to literature for an in-depth mathematical description of these approaches [3-5].

In the following, results are reported for CFRP laminates which were computed by means of a numerical approach based on the expansion of the displacement and stress fields onto a base of Legendre polynomials [10]. Figure 2.10 (a-b) shows the slowness curves at $f = 150$ kHz for the fundamental anti-symmetric A_0, symmetric S_0 and shear horizontal SH_0 guided waves in a 5.45 mm thick composite plate constructed out of 24 layers of unidirectional CFRP according to (i) a quasi-isotropic stacking sequence $[(45/0/\text{-}45/90)_3]_s$ and (ii) a cross-ply stacking sequence $[(0/90)_6]_s$, respectively. The corresponding dispersion curves are plotted for three specific propagation directions φ in Figure 2.10 (c-d). The materials properties of each of the unidirectional plies, which make up the composite laminate, were given in Eq. (2.21). These composite materials are frequently used throughout this PhD work. The results shown in Figure 2.10 are limited to the fundamental guided waves up to 300 kHz. This is because the NDT methods investigated in this dissertation make use of the guided waves in this part of the spectrum.

The slowness and dispersion curves for the quasi-isotropic CFRP (Figure 2.10 (a,c)) reveal that there is a minor effect of the propagation direction φ on the

characteristics of the A_0, S_0 and SH_0 waves. The slowness curves are quasi-circular indicating that the direction of the energy flow is almost equal to the direction of the wave propagation (i.e. skew angle $\psi \approx 0$). Likewise, the dispersion curves for different propagation directions are almost identical.
The situation is different when a cross-ply stacking sequence is considered (see Figure 2.10 (b,d)). The slowness curves at 150 kHz reveal that for the S_0 and SH_0 modes, the phase velocity depends heavily on the direction of wave propagation φ (i.e. skew angle $\psi \neq 0$). This is also seen by the shift of the dispersion curves for different values of φ. On the other hand, the characteristics of the A_0 mode remain almost independent of the wave propagation direction in this cross-ply CFRP plate.

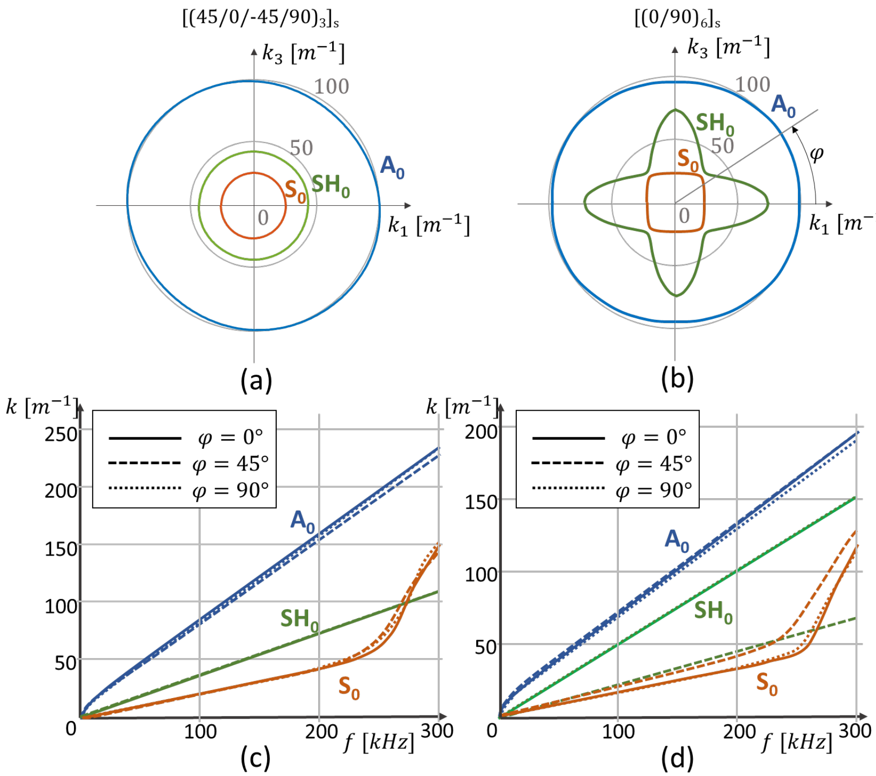

Figure 2.10: (a-b) Slowness curves at f = 150 kHz and (c-d) Dispersion curves along three propagation directions φ corresponding to the fundamental guided waves travelling in a 5.45 mm thick CFRP plate with (left) quasi-isotropic $[(45/0/-45/90)_3]_s$ and (right) cross-ply $[(0/90)_6]_s$ layup.

4.3. Experimental Demonstration of Guided Waves

The guided wave behavior is experimentally demonstrated for three different test specimens: (i) a 400x400x5 mm^3 (isotropic) aluminum plate (see Figure 2.11 (a)), (ii) a 330x330x5.45 mm^3 CFRP plate manufactured out of 24 layers of unidirectional carbon fiber prepreg using the quasi-isotropic stacking sequence $[(45/0/-45/90)_3]_s$ (see Figure 2.11 (b)) and (iii) a similar 330x330x5.45 mm^3 CFRP plate manufactured out of 24 layers of unidirectional carbon fiber prepreg now using the cross-ply stacking sequence $[(0/90)_6]_s$ (see Figure 2.11 (c)). Broadband vibrations are introduced through a small piezoelectric actuator attached to the center of each test specimen. The full wavefield velocity response of the entire plates is recorded with a 3D scanning laser Doppler vibrometer (SLDV). The obtained velocity response is denoted $V_X(x,y,t)$, $V_Y(x,y,t)$ and $V_Z(x,y,t)$ where the X and Y directions are the in-plane directions corresponding to (x_1, x_3) in previous sections, and the Z direction is the out-of-plane direction (along the x_2 axis). The directions of the three velocity components, and the coordinate system, are shown in Figure 2.11 (d). A detailed description of the experimental measurement procedure is provided in Chapter 4.

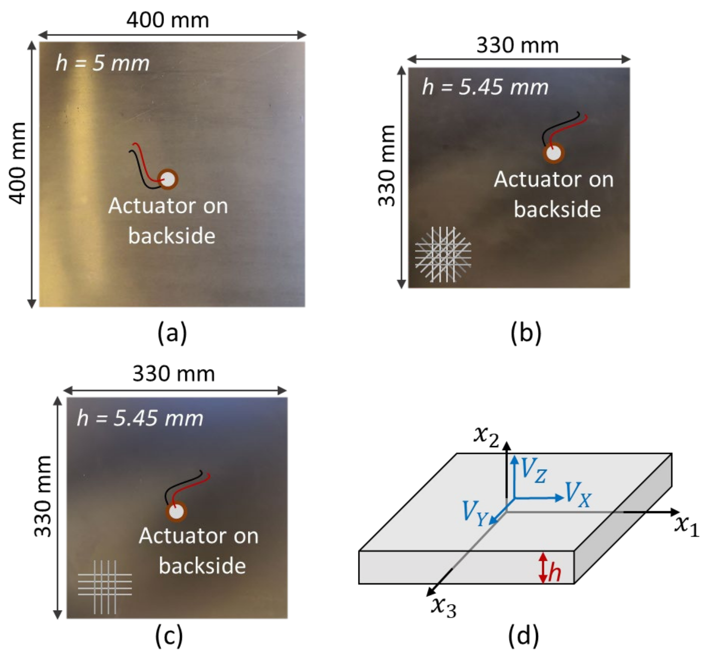

Figure 2.11: (a) Aluminum plate, (b) Quasi-isotropic CFRP plate $[(45/0/-45/90)_3]_s$ (b) Cross-Ply CFRP plate $[(0/90)_6]_s$ and (c) Coordinate system with direction of velocity components.

The piezoelectric actuator is supplied with a seven-cycle Hanning windowed sine signal with center frequency f_c = 150 kHz. For each test specimen, Figure 2.12 (a) and (c) show snapshots of the resulting V_Z and the V_X velocity response, respectively. The snapshots of the out-of-plane V_Z response (Figure 2.12 (a)) reveal propagating waves moving away from the excitation location. Two different mode types can be distinguished: a leading (fast) wave with large wavelength, i.e. the S_0 mode and a slow wave with short wavelength, i.e. the A_0 mode. The A_0 mode has a dominant out-of-plane velocity response. On the other hand, the S_0 mode shows a dominant in-plane velocity response. This is apparent when comparing the snapshots of V_Z (Figure 2.12 (a)) with the snapshots of V_X (Figure 2.12 (c)). This observation is in agreement with the displacement fields of the A_0 and S_0 mode shown earlier in Figure 2.9.

For the isotropic aluminum plate and for the quasi-isotropic CFRP plate, the wavefront of both the A_0 and the S_0 wave are (quasi-) circular (see Figure 2.12 (a1,c1,a2,c2)). For the orthotropic cross-ply CFRP plate, the wavefront of the A_0 mode is also quasi-circular. However, the wavefront of the S_0 mode is affected by the anisotropic material making it square shaped (see Figure 2.12 (a3,c3)).

To further investigate the behavior of the guided waves, the wavenumber maps at $f = f_c$ = 150 kHz are shown in Figure 2.12 (b) and (d). These maps were obtained through 3D fast Fourier transformation (see Chapter 4) of the out-of-plane V_Z and in-plane V_X velocity responses, respectively. In the V_Z wavenumber maps (Figure 2.12 (b)), the slowness curves corresponding to the A_0 and S_0 modes are revealed as lines of increased intensity. The experimentally obtained slowness curves are in good agreement with the theoretical ones shown earlier in Figure 2.10 (a-b). Note again that the S_0 mode is affected by the anisotropic material properties of the cross-ply CFRP plate (corresponding to the square S_0 wavefront). Also the wavenumber maps calculated for V_X (Figure 2.12 (c)) reveal the S_0 mode slowness curves. In addition, the slowness curve corresponding to the SH_0 mode can be distinguished in these maps. As already predicted by Figure 2.10 (a-b), the SH_0 mode is significantly affected by anisotropic material properties, resulting in the distorted slowness curve for the cross-ply CFRP.

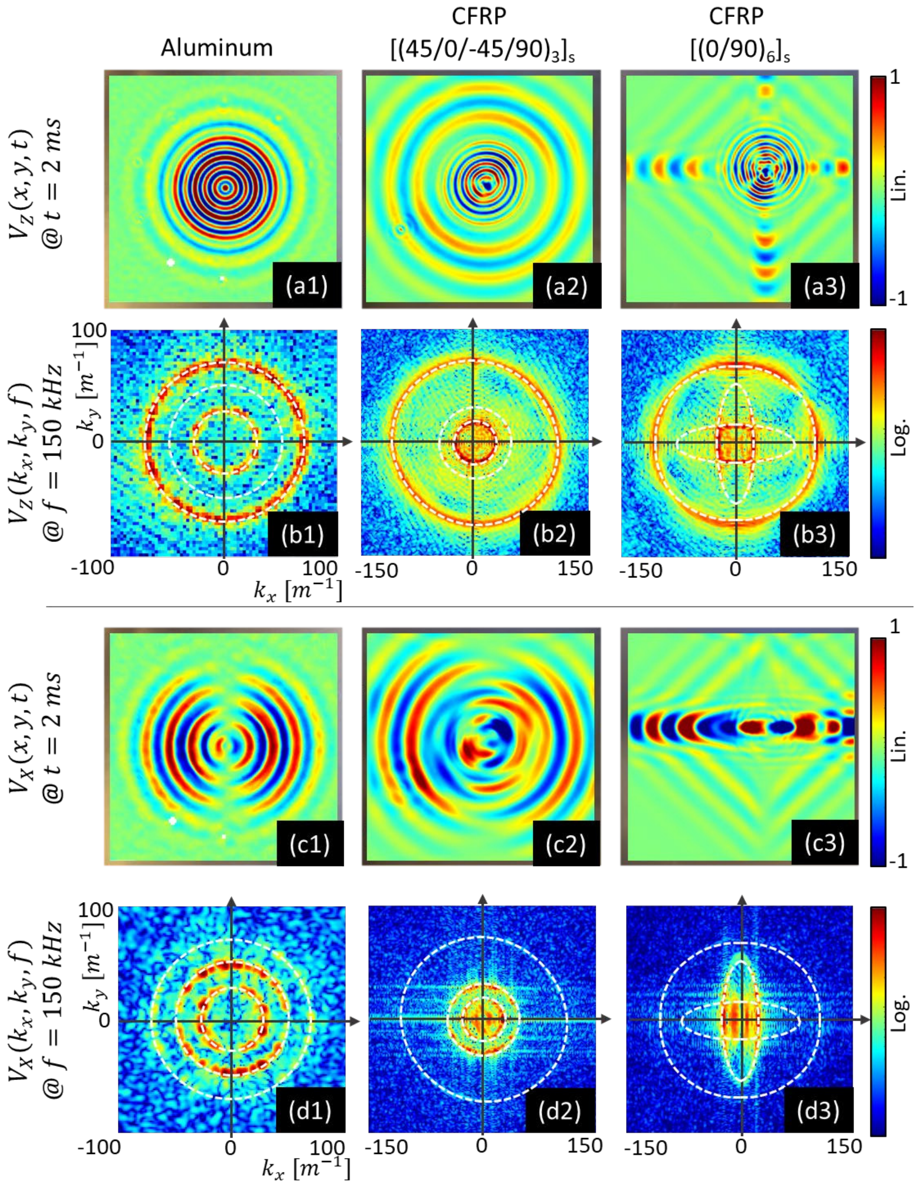

Figure 2.12: (a) Snapshots of V_Z response, (b) Wavenumber maps of V_Z, (c) Snapshots of V_X response, (d) Wavenumber maps of V_X. (1) Aluminum plate, (2) Quasi-isotropic CFRP plate and (3) Cross-ply CFRP plate.

5. Plate Resonances

5.1. Wave Reflections

5.1.1. Normal Incidence in Homogeneous Isotropic plates

Let us first consider what happens when a wave packet, which is travelling in the x_1 direction, meets the free edge of the plate. For an A_0 Lamb wave travelling towards the free edge of an homogeneous isotropic plate, the stress field can be derived from the relation between stress and displacement (Eq. (2.12)), taking into account the displacement solutions given by Eq. (2.34). As an example, Figure 2.13 shows the variation of the displacements and the associated stresses over the thickness for the A_0 mode at 150 kHz in a 5 mm thick aluminum plate. Important to note, but not shown in the figure, is that shear stress σ_{xz} lags 90° with respect to the tensile stress σ_{xx} [11]. At the plate's free edge, both stress components must be zero. This boundary condition can never be fulfilled when the incident A_0 wave would simply be reflected as a backward propagating A_0 wave of identical amplitude. This because of the 90° phase lag between σ_{xz} and σ_{xx}. As a result, other mode types must be formed at the edge.

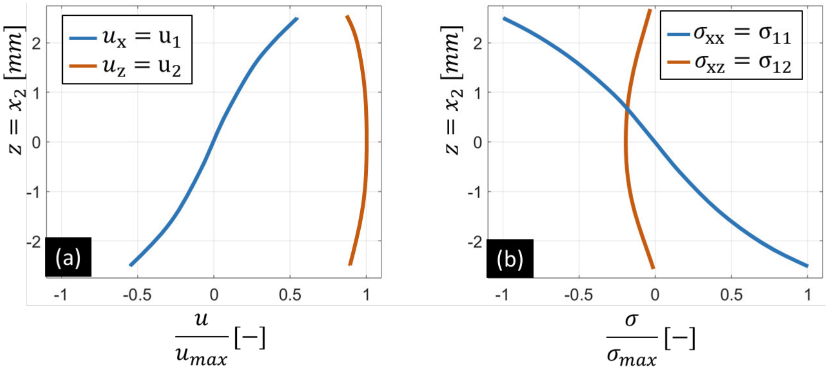

Figure 2.13: (a) Displacement and (b) Stress field over thickness for the A_0 Lamb mode in a 5 mm thick aluminum plate at 150 kHz.

Over the last decades, multiple researchers have investigated the reflection of a plane guided wave on an isotropic plate's free edge [11-16]. In the case of normal incidence, it was observed that:

- Anti-symmetric (symmetric) Lamb modes cannot be converted into symmetric (anti-symmetric) Lamb modes or shear horizontal modes. Likewise, shear horizontal modes cannot be converted into anti-symmetric or symmetric Lamb modes.
  This is a consequence of the symmetry of the problem with respect to the mid-thickness of the plate.

- While mode conversion to other symmetry classes is impossible, mode conversion takes place within the same symmetry class. For each formed mode, a reflection coefficient can be derived. In order to conserve the energy, the sum over all reflection coefficients must be one.
- The mode conversion behavior is strongly dependent on the frequency because of the cut-off frequencies associated with high order guided waves. As a result, an incident A_0 mode will be partially converted to an A_1 mode only if the frequency is bigger than the cut-off frequency of the A_1 mode. If the frequency is lower, an incident A_0 mode of unit amplitude is reflected as a linear combination of a backward propagating A_0 mode (of unit amplitude) and non-propagating modes.
- The existence of non-propagating modes is required to fulfill the stress-free boundary conditions. The non-propagating modes do not carry energy and are confined to about five plate thicknesses from the free edge [11]. They correspond to the imaginary and complex solutions of the dispersion equations (Eq. (2.22) and Eq. (2.31)).

5.1.2. Oblique Incidence and Non-Homogeneity

While most research is performed on the case of normal incidence of a plane wave on a free-edge, this situation rarely occurs in real structures. In general, the incident wave front is not a plane wave, and the propagation direction does not match the direction of the surface normal at the free edge. As a result, oblique incidence takes place. Santhanam et al. [16] showed that shear horizontal modes are formed in response to an oblique incident A or S Lamb mode. In the case of oblique incidence in anisotropic materials, Snell's law must be taken into account. Snell's law states that the projection of every reflected wave vector $\vec{k}_{ref}$ on the plane of the free edge must be equal to the projection of the incident wave vector $\vec{k}_{inc}$ on this plane.

Apart from the incident angle, also the non-homogeneity and potential anisotropy of the material changes the properties of the reflected waves considerably. Non-homogeneous material can be asymmetric with respect to the mid-thickness of the plate. As a result, symmetric (asymmetric) modes can be converted to asymmetric modes upon reflection. The conversion of a mode to the opposite symmetry class is also possible when the free edge of the plate is not perfectly square.

5.2. Standing Waves and Resonances

The concept of standing waves can be easily understood by considering again the free edge reflection of a plane Lamb wave at normal incidence [6]. Using the reflection coefficient R, the incident wave and reflected waves are written as:

$$\vec{u}_{inc}(x_1, x_2, x_3, t) = \bar{A}_{inc}(x_2)\exp\big(i(\omega t - \kappa x_1)\big)$$
$$\vec{u}_{ref}(x_1, x_2, x_3, t) = R\bar{A}_{inc}(x_2)\exp\big(i(\omega t + \kappa x_1)\big)$$

with $\bar{A}_{inc} = [A_{1,inc}(x_2)\ A_{2,inc}(x_2)\ 0]$ the incident wave amplitude. When there is no mode conversion, the coefficient of reflection equals 1, and the wave pattern is found as:

$$\vec{u}_{tot} = \vec{u}_{inc} + \vec{u}_{ref} = 2\bar{A}_{inc}(x_2)\ \cos(\kappa x_1)\ \exp\big(i(\omega t)\big)$$

As a result, a standing wave pattern is obtained. The standing waves form a static pattern of nodes ($\cos(\kappa x_1) = 0$) and anti-nodes ($\cos(\kappa x_1) = 1$). There is no transportation of energy by the standing waves. When there is mode conversion, the reflection coefficient becomes smaller $R < 1$ and the total wave pattern is the superposition of a standing wave and one or more propagating waves.

Now that we know that standing waves are formed due to the reflection of a plane wave at a free edge, let us consider a semi-infinite plate with free edges at $x_1 = \pm\frac{b}{2}$. Plane waves are continuously excited at the center of the plate ($x_1 = 0$) and are reflected by the free edges. Part of the excited waves travell in the positive x_1 direction and reflect at $x_1 = \frac{b}{2}$, resulting in a standing wave of the form:

$$2\vec{A}_{inc}(x_2)\ \cos\left(\kappa\left(x_1 - \frac{b}{2}\right)\right)\ \exp\big(i(\omega t)\big)$$

At the same time, the excited waves travelling to the left and reflecting at $x_1 = \frac{-b}{2}$ results in a standing wave of the form:

$$2\vec{A}_{inc}(x_2)\ \cos\left(\kappa\left(x_1 + \frac{b}{2}\right)\right)\ \exp\big(i(\omega t)\big)$$

Both standing wave patterns interfere with each other. Constructive interference is achieved when:

$$\kappa\left(x_1 + \frac{b}{2}\right) = \kappa\left(x_1 - \frac{b}{2}\right) + m2\pi \text{ with } m = 0,1,2 \ldots$$
$$\rightarrow \kappa b = m2\pi \text{ or } k = \frac{\kappa}{2\pi} = \frac{m}{b}$$

The resonance conditions of a free vibrating beam are obtained. Because there is no transportation of energy by the standing wave pattern, the amplitude of the standing wave grows over time as long as the input excitation force stays active. However, the maximum amplitude of the standing wave, or resonance, is limited by the material damping.

Back in the 18th century, the German scientist Ernst Chladni proposed a straightforward approach for visualization of resonance patterns in thin plates (e.g. thickness ≤ 1 mm) [17]. His experiment consisted of drawing a bow over the edge of a metal plate covered with fine grains of sand. The plate was bowed until one of its resonance frequencies was triggered. At that moment, the sand grains move away from positions of high amplitude and concentrate along the nodal lines where the surface vibrations are (almost) zero.
His experiment is reproduced here with a thin 200x200x0.5 mm^3 woven CFRP plate, covered in fine sea salt, and excited using a piezoelectric actuator bonded to the backside. Chladni (or resonance) patterns are successfully obtained at a multitude of frequencies. Figure 2.14 shows three examples. Note that the wavelength ($\lambda = 1/k$) becomes smaller when the excitation frequency is increased as predicted by the dispersion curves (e.g. see Figure 2.10 (c-d)).

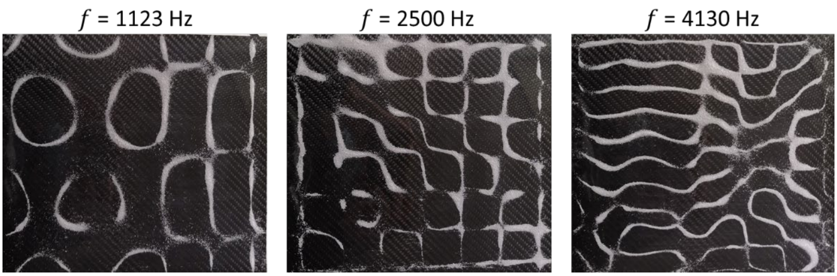

Figure 2.14: Resonance (or Chladni) patterns in a 0.5 mm thin CFRP panel revealed using sea salt.

Also with the SLDV, resonances can be revealed. Looking back at the experimental observation of guided waves in the three square plates of different materials (see Section 4.3), resonances are observed at maxima in the *frequency response function* FRF. The FRF is defined in the frequency domain as the ratio of the output amplitude over the input amplitude. For our specific case:

$$FRF_i(x, y, f) = \frac{V_i(x, y, f)}{U_{ref}(f)} \quad i = X, Y \text{ or } Z \qquad (2.35)$$

with $V_i(x, y, f)$ the Fourier transform of the velocity component measured at the point with coordinates (x, y) and $U_{ref}(f)$ the Fourier transform of the excitation voltage supplied to the piezoelectric actuator.
For the quasi-isotropic CFRP plate, Figure 2.15 shows the magnitude of FRF_Z averaged over all scan points. In the lower frequency range, pronounced maxima are observed. The operational deflection shapes (i.e. $|V_i(x, y, f)|$) reveal the standing waves patterns associated with these resonance peaks. For high frequencies, the material damping prevents the standing waves pattern from growing to a considerable amplitude. This results in a smoother FRF without pronounced resonance peaks.

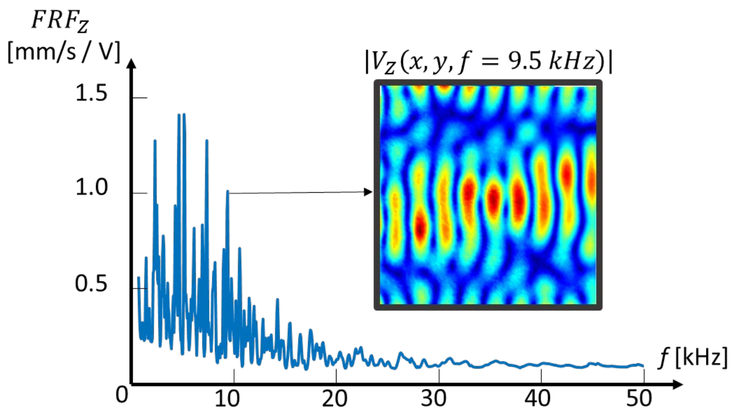

Figure 2.15: Frequency response function for the out-of-plane velocity response in quasi-isotropic CFRP plate and standing wave pattern at 9.5 kHz.

6. Conclusion

In this chapter, the concept of wave motion in solid materials was introduced. The theoretical investigation of linear elastic wave dynamics started with the theory of elasticity and the definition of the stress, strain, C-tensor and material symmetry classes. The linear elastic relations between stress, strain and displacements were given in their most general form.

Next, the derived relations between stress, strain and displacements were combined with Newton's second law of motion, resulting in wave equations for bulk waves propagating in infinitely large solid materials. Three types of bulk waves were differentiated: longitudinal, shear horizontal and shear vertical bulk waves. Slowness curves were calculated giving the phase velocity in function of propagation direction. In addition, the skew angle was defined as the angle between the direction of wave propagation and the direction of the energy flow.

Additional boundary conditions are imposed when dealing with thin plate like structures. Three classes of guided waves were found to propagate the plate: (i) shear horizontal waves, (ii) anti-symmetric (Lamb) waves and (iii) symmetric (Lamb) waves. The dispersion relations and slowness curves were derived for an isotropic aluminum plate, a quasi-isotropic CFRP laminate and a cross-ply CFRP laminate. Experimental measurements, using 3D scanning laser Doppler vibrometry, confirmed the theoretical predictions.

In the end, plates of finite spatial dimensions were considered. It was explained how edge reflections lead to standing wave patterns. These standing waves can further result in resonances. Resonance patterns were revealed using the scanning laser Doppler vibrometer as well as using Chladni's experiment.

References

1. Lamb, H., *On Waves in an Elastic Plate.* Proceedings of the Royal Society A, 1917. **93**: p. 114-128.
2. Landau, L.D. and E.M. Lifshitz, *Theory Of Elasticity*. Vol. 3. 1986: Elsevier.
3. Lammering, R., et al., *Lamb-Wave Based Structural Health Monitoring in Polymer Composites*. 2018: Springer.
4. Kundu, T., *Ultrasonic nondestructive evaluation : engineering and biological material characterization* 2004: CRC Press LLC.
5. Giurgiutiu, V., *Structural health monitoring with piezoelectric wafer active sensors*. Academic Press. 2008, USA: Elsevier Inc.
6. Cheeke, J.D.N., *Fundamentals and Applications of Ultrasonic Waves*. 2002: CRC Press.
7. Rose, J.L., *Ultrasonic Guided Waves in Solid Media*. 2014: Cambridge University Press.
8. Delsanto, P.P., *Universality of Nonclassical Nonlinearity*, ed. P.P. Delsanto. 2006: Springer.
9. Martens, A., *Visco-elastic material characterisation by means of the Ultrasonic Polar Scan*, in *Faculty of Science*. 2019, KU Leuven: Kortrijk(Belgium).
10. Bou Matar, O., et al., *Legendre and Laguerre polynomial approach for modeling of wave propagation in layered magneto-electro-elastic media.* The Journal of the Acoustical Society of America, 2013. **133**(3): p. 1415-24.
11. Lowe, M.J.S., *Reflection of the fundamental Lamb modes from the ends of plates*, in *AIP Conference Proceedings*. 2001. p. 89-96.
12. Morvan, B., et al., *Lamb wave reflection at the free edge of a plate.* The Journal of the Acoustical Society of America, 2003. **113**(3): p. 1417-25.
13. Maze, G., et al., *Separation of Lamb modes at a plate edge by using orthogonality relation.* Estonian Journal of Engineering, 2013. **19**(4).
14. Pagneux, V., *Revisiting the edge resonance for Lamb waves in a semi-infinite plate.* The Journal of the Acoustical Society of America, 2006. **120**(2): p. 649-656.
15. Kersemans, M., et al., *Leakage and Scattering of a Leaky Lamb Wave by a Structural Discontinuity: Acousto-Optics and FEM.* IEEE International Ultrasonics Symposium Proceedings, 2012: p. 735-738.
16. Santhanam, S. and R. Demirli, *Reflection of Lamb waves obliquely incident on the free edge of a plate.* Ultrasonics, 2013. **53**(1): p. 271-82.
17. Chladni, E., *Entdeckungen über die Theorie des Klanges*. 1787, Leipzig: Weidmanns Erben und Reich.

Chapter 3

Nonlinear Elastic Wave Dynamics

Summary:

Every material that is excited with vibrations will respond in a combined linear and nonlinear manner. This chapter focusses on the nonlinear part of the response which is inherently related to a frequency change of the input vibrations. A distinction is made between classical and non-classical nonlinearity. The latter is triggered by the presence of defects and results in nonlinear vibrational components that are of sufficient amplitude to detect with typical ultrasonic non-destructive testing equipment.
The different nonlinear components are investigated based on straightforward phenomenological models of clapping and rubbing defects.

1. Introduction

Most ultrasound-based material characterization and damage detection methods make use of the linear elastic wave dynamics. The component is excited with low power ultrasonic vibrations and the linear elastic response is observed. The presence of a defect can alter the linear elastic response in multiple ways: decrease or increase the local amplitude (e.g. see local defect resonance - Chapter 5), alter the local wavenumber or change the local wave-direction. These linear defect-wave interactions are exploited for damage map construction as explained in Chapter 11 and Chapter 13.

Apart from the linear material response, one can also exploit its nonlinear response. The nonlinear response is related to the change of the frequency content of the input excitation. Often a distinction is made between *classical* nonlinearity and *non-classical* nonlinearity. The former is related to homogeneous (i.e. damage-free) solids where the nonlinearity originates on the molecular level due to nonlinear atomic force relations [1]. On the other hand, the latter is attributed to discontinuities introduced by defects which result in clapping or rubbing at contact interfaces [2]. Both classes of nonlinearity are discussed in this chapter. Most attention is given to non-classical nonlinearity because this is the kind of nonlinearity that can be exploited for damage detection.

A nonlinear (defected) material can change the output frequency spectrum in multiple ways [3]. As an example, Figure 3.1 shows the frequency response function of an undamaged and a delaminated glass fiber reinforced polymer (GFRP) coupon excited with a 50 kHz sine signal [4]. The nonlinear response of the delaminated GFRP coupon is revealed by the higher harmonic components (at 100 kHz, 150 kHz and 200 kHz) in the frequency spectrum of Figure 3.1 (b).

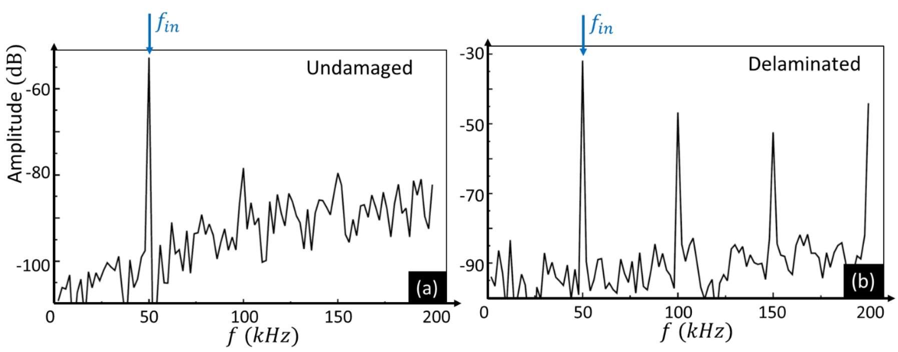

Figure 3.1: Frequency response functions of (a) undamaged and (b) delaminated GFRP (figure reproduced from reference [4]).

Apart from higher harmonics, other nonlinear artifacts may be present in the nonlinear response of the material, such as subharmonics [5], slow dynamics [6], hysteresis [7] or a resonance frequency shift [8]. As an example, Figure 3.2 shows the frequency response around the natural resonance frequency f_{res} observed in a damaged and undamaged concrete sample [8]. The sample is subjected to input vibrations of different amplitudes. The resonance frequency reduces for increasing excitation amplitudes. This is most pronounced for the damaged sample because the presence of the damage increases the nonlinearity of the material.

In this chapter, the focus is on the higher harmonics and wave mixing artifacts that are present in defected composite parts. These nonlinear artifacts are exploited later on in this PhD book for defect detection. The reader that is interested in other nonlinear artifacts, such as subharmonics and slow dynamics, is kindly referred to one of the many extensive works on nonlinear elastic wave dynamics: [3, 9-14].

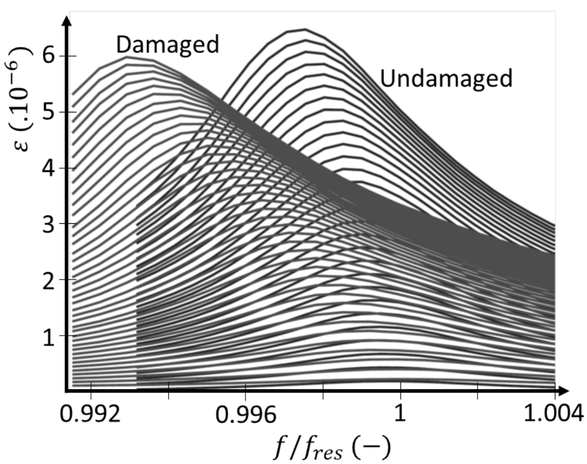

Figure 3.2: Frequency response close to the natural resonance frequency f_{res} for damaged and undamaged concrete at different levels of excitation amplitude (figure reproduced from reference [8]).

2. Classical Nonlinearity

The classical nonlinear elasticity theory considers homogeneous materials in which nonlinearity arises from physical interactions at the microscopic and mesoscopic scale [13]. This results in a deformation of the sinusoidal input wave to a saw-tooth profile containing higher harmonics of the input frequency [12, 15]. This type of nonlinearity is a material characteristic and can be clearly distinguished from the other type, i.e. non-classical nonlinearity, which is thoroughly discussed in the next section.

Mathematically, classical nonlinear elasticity is explained by accounting for the higher order terms in the stress-strain relation. The stress-strain relation $\sigma(\varepsilon)$ is expressed as:

$$\sigma(\varepsilon) = K_0\,(1 + \beta\varepsilon + \delta\varepsilon^2 + \cdots)\,\varepsilon$$

where K_0 is the linear material stiffness and β and δ denote the quadratic and cubic classical nonlinearity coefficients. The quadratic nonlinearity produces both odd and even higher harmonics ($2f_0$, $3f_0$, $4f_0$ ...) whereas the cubic nonlinearity produces only odd harmonics ($3f_0$, $5f_0$, $7f_0$ ...), with f_0 the input frequency [6].

The typical strain amplitude during an ultrasonic test is very small ($\varepsilon < 10^{-6}$ [9]). The strain ε_{xx} in a plate under bending is given by [16]:

$$\varepsilon_{xx}(x,y,t) = -z\,\frac{\partial^2 u_Z(x,y,t)}{\partial x^2}$$

with u_Z the out-of-plane displacement. The maximum amplitude of ε_{xx} is found as:

$$\varepsilon_{xx}^{max}(f) = \frac{A(f)\;h\;\pi\;k(f)^2}{f}$$

when assuming that the vibrations are associated with a plane wave out-of-plane velocity profile of the form: $V_Z(x,y,t) = A(f)\cos[2\pi k(f)x - 2\pi f t]$. As an example, the maximum strain attributed to the A_0 mode waves at frequency f = 150 kHz in the aluminum plate of thickness h = 5 mm, discussed in Chapter 2 Section 4.3, is equal to $1.03 \cdot 10^{-6}$ (with velocity amplitude A(150 kHz) = 2 mm/s and A_0 wavenumber k(150 kHz) = 70 m^{-1}). For aluminum, the quadratic nonlinearity parameter β is around 5 to 9 [17]. As a result, the classical nonlinear response is of extremely low amplitude. Generally only the second higher harmonic at $f = 2f_0$ can be detected using specialized measurement approaches [10, 18]. This classical nonlinearity theory can also not be used to explain specific nonlinear phenomena such as hysteresis and slow dynamics which are observed in damaged materials [19].

3. Non-Classical Nonlinearity

The nonlinear response of a material can also be caused by contact mechanisms such as the opening and closing of a dynamically loaded delamination or crack. These mechanisms trigger a number of nonlinear effects including but not limited to [6, 14]:

- Higher harmonic generation [11, 20]
- Subharmonic generation and DC response [5, 18]
- Wave modulation (or frequency mixing) [11, 21-23]
- Nonlinear damage resonance intermodulation [24]
- Hysteresis and end-point memory [25, 26]
- Amplitude dependent resonance frequency and resonance amplitude [2, 12, 27]

These effects can generally not be explained by the classical nonlinear elasticity theory. As a result, they are classified as *non-classical*. These non-classical nonlinear responses are detectable even at the small strains associated with ultrasonic experiments [28], opening opportunities for nonlinearity-based ultrasonic NDT methods.

No physical models exist to relate the nonlinear response to the physical damage characteristics (e.g. delamination depth or crack length) [8]. As a result, different phenomenological (and empirical) models were developed to describe the origin of these non-classical nonlinearities. In this section, various phenomenological models are described for *Contact Acoustic Nonlinearity* (CAN) [29-31]. The models explain the formation of (i) higher harmonics of the excitation frequency and (ii) modulation (or mixing) sidebands in the case of dual frequency excitation, at the contact interfaces of defects.

3.1. Contact Acoustic Nonlinearity - Clapping Contact

In order to model the contact acoustic nonlinearity arising from the (out-of-plane) opening and closing of a crack or delamination, a bi-linear stress-strain relation is assumed [6, 15, 30-32]. The stiffness is low when the contact interfaces are separated and the stiffness drastically increases to the damage-free material stiffness when the interfaces come into contact. This bi-linear stiffness behavior is schematically shown on Figure 3.3 (a). The associated stress-strain relation $\sigma(\varepsilon)$ relation is (see also [32]):

$$\begin{aligned}\sigma(\varepsilon) &= \begin{cases} K_r\varepsilon & \text{if } \varepsilon > -\varepsilon_0 \\ K_r\varepsilon_0 + K_0(\varepsilon + \varepsilon_0) & \text{if } \varepsilon < -\varepsilon_0 \end{cases} \\ &= K_r\left[1 - H(-\varepsilon - \varepsilon_0)\frac{K_r - K_0}{K_r}\frac{\varepsilon + \varepsilon_0}{\varepsilon}\right]\varepsilon \end{aligned} \tag{3.1}$$

in which K_r and K_0 are the stiffness when the contact is open (i.e tension) and closed, respectively. $H(\cdot)$ is the Heaviside function and ε_0 is the compressive strain at contact. In order to investigate the nonlinear response to an incoming wave (i.e. varying stress), the stress-strain relation $\sigma(\varepsilon)$ relation is expressed in terms of compliance instead of stiffness:

$$\varepsilon(\sigma) = C_r\left[1 - H(-\sigma - \sigma_0)\frac{C_r - C_0}{C_r}\frac{\sigma + \sigma_0}{\sigma}\right]\sigma$$

with $C_r = K_r^{-1}$ the compliance when there is no contact (i.e. tension), $C_0 = K_0^{-1}$ the compliance when there is contact (i.e. compression) and $\sigma_0 = K_r\varepsilon_0$. This bi-linear stiffness model thus represents a breathing crack and results in a mechanical diode effect. When the crack is closed ($\varepsilon < -\varepsilon_0$), it can be easily penetrated by an elastic wave, whereas when the crack is open ($\varepsilon > -\varepsilon_0$) penetration does not occur [6].

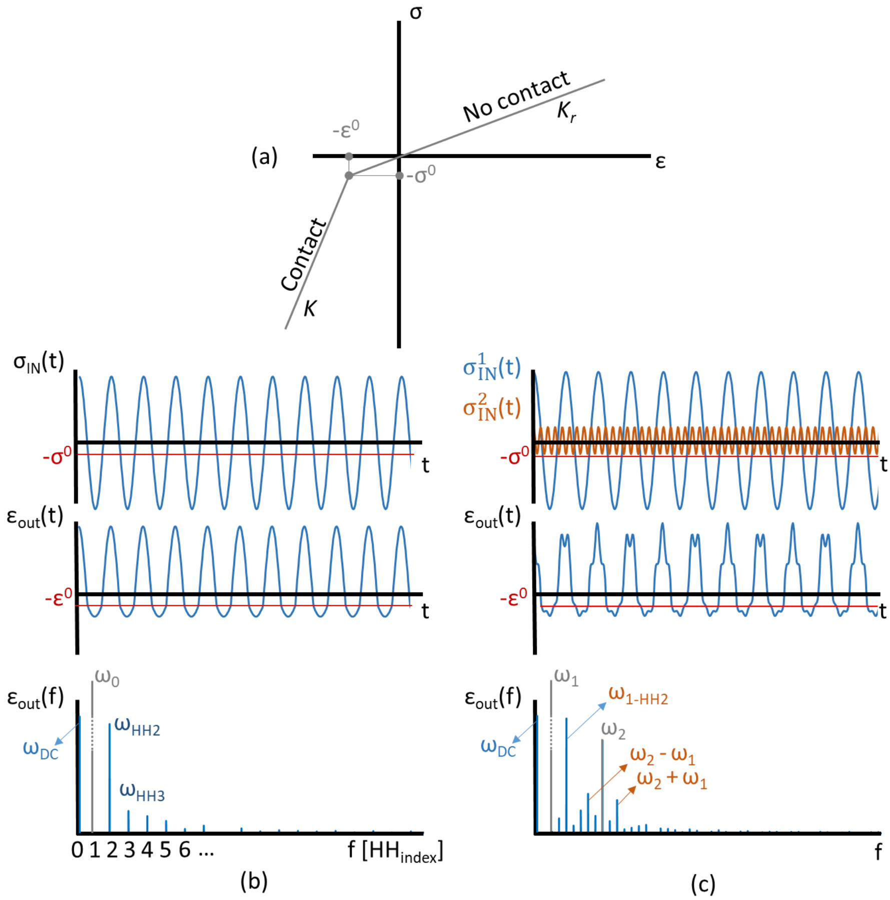

Figure 3.3: Bi-linear stiffness model for clapping defect (a) Stress-strain relation, (b) Response to sinusoidal input stress, (c) Response to dual sinusoidal input stress.

3.1.1. Higher Harmonic Generation: Odd and Even

In order to determine the frequency response spectrum of the nonlinear response, the strain response corresponding to a sinusoidal varying stress field $\sigma(t) = \sigma_a \cos(\omega t)$ is calculated. The stress field and strain response is shown in Figure 3.3 (b). It is observed that the defect results in a distorted output strain wave in case that the input wave amplitude is big enough to make the defect's interfaces come into contact ($\sigma_a > \sigma_0$). Both even and odd harmonics are present in the distorted wave's frequency spectrum (see Figure 3.3 (c)). The amplitude of the harmonics is *sinc* modulated. The observations are confirmed by the analytical expression for the higher harmonics amplitude (see also [30]):

$$\varepsilon_{HH}^{NL}(m\omega) = (C_0 - C_r)\,\sigma_a \frac{\tau}{T}\left[\mathrm{sinc}\left((m \pm 1)\frac{\tau}{T}\right) - 2\cos\left(\pi\frac{\tau}{T}\right)\mathrm{sinc}\left(m\frac{\tau}{T}\right)\right]$$

$$\text{with } \tau = \frac{T}{\pi}\mathrm{acos}\left(\frac{\sigma_0}{\sigma_a}\right), T = \frac{2\pi}{\omega} \text{ and } m = 2, 3, 4\ldots$$

It can be noted that both even and odd harmonics are generated but that the odd harmonics die out for $\sigma_a \gg \sigma_0$ as τ increases from $0 \to \frac{T}{2}$.

Experimental proof of the *sinc* modulated higher harmonic amplitude was provided by Krohn et al. [4]. They measured the response of a delaminated GFRP to a sine excitation with frequency 1 kHz. The output spectrum reveals the *sinc* modulated odd and even higher harmonics as shown in Figure 3.4. The investigation of nonlinear components in the frequency spectrum of a test specimen is called *nonlinear elastic wave spectroscopy* NEWS [12].

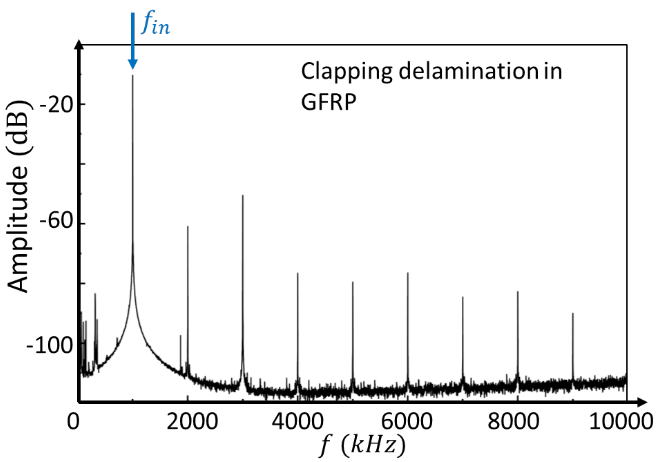

Figure 3.4: Response spectrum of a delaminated GFRP (figure reproduced from [4]).

3.1.2. Wave Modulation

Next to the modelling of higher harmonics, the bi-linear stiffness model can also be used to explain the phenomena of wave modulation or frequency mixing. These nonlinear responses are investigated during *nonlinear wave modulation spectroscopy* NWMS [11, 13].

Wave modulation requires the system to be excited with two elastic waves of different frequencies. In general, the low frequency wave is used to open and close the crack interface. As a result, the high frequency wave that passes through the crack will be modulated by the low frequency wave. The frequency response spectrum of this modulated signal contains higher harmonics of both input waves as well as modulation sidebands with frequencies $\omega_{SB_{k,l}} = k\omega_1 \pm l\omega_2$ (with k, l = 1,2,3...). This effect is schematically shown in Figure 3.3 (c). Note again that the amplitude of the sidebands is *sinc* modulated. An analytical expression of the amplitude of the sideband components around ω_2 can be obtained when assuming $\sigma_{a1} \gg \sigma_{a2}$ [33]:

$$\varepsilon^{NL}_{SB_{1,l}}(\omega_2 \pm l\omega_1) = (C_0 - C_r)\sigma_{a2}\frac{\tau}{T_1}\,\mathrm{sinc}\left(\frac{n\tau}{T_1}\right)\,[\cos(\omega_2 \pm l\omega_1) + \cos(\omega_2 \pm l\omega_1)]$$

$$\text{with } \tau = \frac{T_1}{\pi}\,\mathrm{acos}\left(\frac{\sigma_0}{\sigma_{a1}}\right) \text{ and } T_1 = \frac{2\pi}{\omega_1}$$

with σ_{a1}, σ_{a2} the stress amplitude of the excitation at ω_1 and ω_2, respectively, and $\sigma_{a1} > \sigma_0$. The modulation sidebands are of high interest for nonlinearity-based NDT because these nonlinear components are only generated at the damage and not by the measurement system. This is further explained and exploited in Chapter 12.

3.2. Contact Acoustic Nonlinearity - Rubbing Contact

Next to the clapping CAN mechanism outlined above, the effect of rubbing or friction between the adjacent sides of a contact has to be modelled and evaluated. The friction force is caused by the interaction between asperities (i.e. roughness peaks) for a crack driven by a shear wave (i.e. in-plane drive). The stress-strain relation $\sigma(\varepsilon)$ is expressed as (see also [34]) :

$$\begin{aligned}\sigma(\varepsilon) &= \begin{cases} K_r\varepsilon & \text{if } |\varepsilon| < \varepsilon_0 \\ K_r\varepsilon_0 + K_0(\varepsilon - \varepsilon_0) & \text{if } |\varepsilon| > \varepsilon_0 \end{cases} \\ &= K_r\left[1 - H(|\varepsilon| - \varepsilon_0)\frac{K_r - K_0}{K_r}\frac{|\varepsilon| - \varepsilon_0}{|\varepsilon|}\right]\varepsilon\end{aligned}$$

or

$$\varepsilon(\sigma) = C_r\left[1 - H(|\sigma| - \sigma_0)\frac{C_r - C_0}{C_r}\frac{|\sigma| - \sigma_0}{|\sigma|}\right]\sigma$$

This step-wise increase in stiffness is shown in Figure 3.5 (a). The equation is very similar to Eq. (3.1) with the important difference that the stiffness modulation due to friction is symmetrical.

3.2.1. Odd Higher Harmonic Generation and Wave Modulation

Making the analogy with Section 3.1, it is clear that the stiffness modulation by rubbing results in higher harmonics and modulation sidebands. In this case however, the stiffness modulation is symmetrical and as a result, only the odd higher harmonics are generated. The rubbing contact's time and frequency responses to a single and a dual sinusoidal stress field are shown in Figure 3.5 (b) and (c), respectively. The *sinc* modulated amplitudes of the odd harmonics are (see also [32]):

$$\varepsilon_{HH}^{NL}(m\omega) = 2(C_r - C_0)\,\sigma_a \frac{\tau}{T}\left[\mathrm{sinc}\left((m \pm 1)\frac{\tau}{T}\right)\right]$$

$$\text{with } \tau = \frac{T}{\pi}\mathrm{acos}\left(\frac{\sigma_0}{\sigma_a}\right),\ T = \frac{2\pi}{\omega} \text{ and } m=1, 3, 5\ldots$$

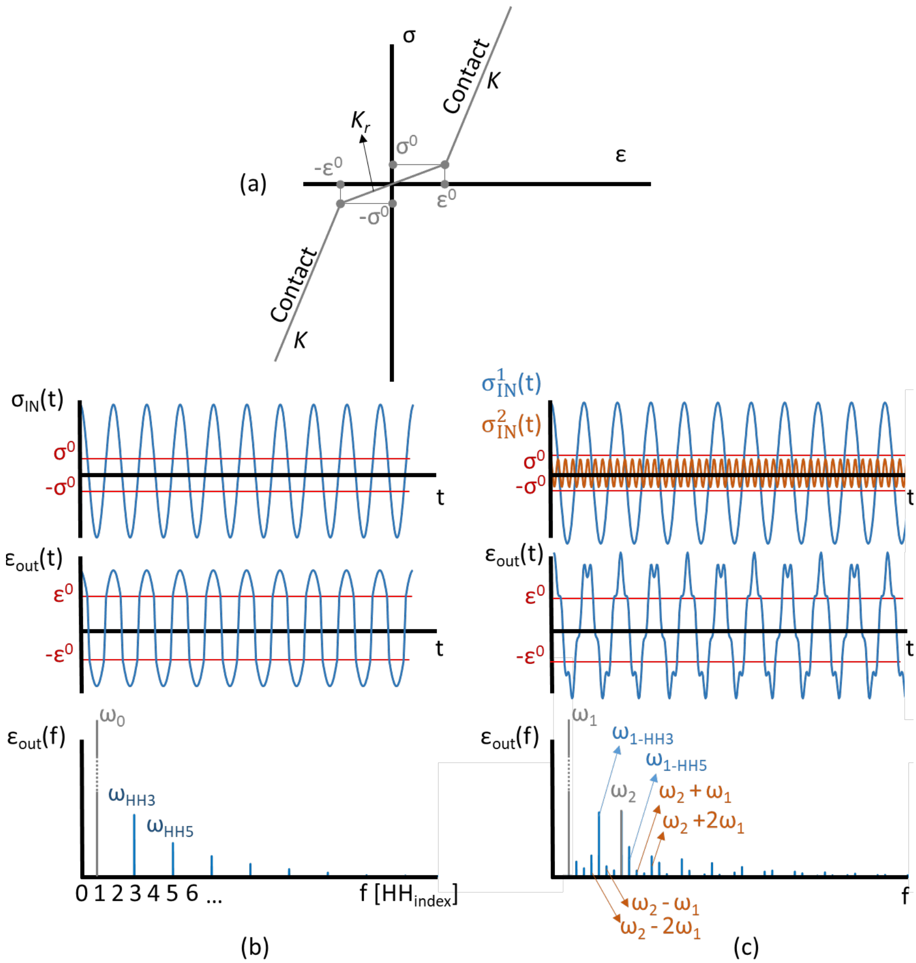

Figure 3.5: Step-wise stiffness model for rubbing defect (a) Stress-strain relation, (b) Response to sinusoidal input stress, (c) Response to dual sinusoidal input stress.

3.3. Nonlinear Equation of Motion – Resonance Fold-over

The phenomenological models discussed in previous sections show the origin of higher harmonic frequency components for clapping and rubbing cracks or delaminations. In order to explain other non-classical nonlinear effects, such as subharmonics, parametric resonances and the resonance frequency fold-over, more advanced models are required taking into account the inertia of the vibrating crack interfaces. These type of models are often referred to as nonlinear (or anharmonic) oscillators [9, 10, 14, 31, 35].

The vibrations of a one-dimensional nonlinear oscillator are governed by a nonlinear equation of motion [2]:

$$\frac{d^2x(t)}{dt^2} + 2\gamma\frac{dx(t)}{dt} + \omega_0^2x(t) = f(t) + f^{NL}(x(t))$$

where $x(t)$ represents the displacement, γ is the damping factor, $\omega_0 = 2\pi f_0$ is the natural resonance frequency of the oscillator, $f(t) = F_0\cos(\omega t)$ is the external harmonic driving force and $f^{NL}(t) = \alpha x^2(t) + \beta x^3(t) + \cdots$ is the nonlinear driving force caused by the nonlinear contact stiffness. Assuming a steady-state solution $x(t) = A(\omega)\cos(\omega t)$, the following expression is obtained for the amplitude of vibration [2]:

$$A(\omega) = \frac{F_0}{2\omega_0 m\sqrt{\left[(\omega-\omega_0) - \frac{3\beta A(\omega)^2}{8\omega_0}\right]^2 + \gamma^2}}$$

As a result, the nonlinear resonance frequency ω_0^{NL} is no longer equal to the natural frequency ω_0 but depends on the amplitude of vibration:

$$\omega_0^{NL} = \omega_0 + \frac{3\beta A(\omega)^2}{8\omega_0}$$

This results in the fold-over of the resonance peak as was observed in Figure 3.2. In addition, the perturbation method can be used to solve the nonlinear equation of motion for investigation of parametric resonances, higher harmonics and subharmonics [2].

Ciampa et al. [24] provided a two-dimensional nonlinear oscillator model by derivation of the nonlinear equation of motion for bending deflection of a symmetric composite plate. Their model showed that depending on the driving frequency conditions, a multitude of nonlinear frequency components are generated at the defect. These nonlinear vibrations are detectable also at locations away from the nonlinear defect. Apart from higher harmonics and subharmonics, they showed the existence of nonlinear damage resonance intermodulation NDRI. These NDRIs correspond to a frequency mixing between the defect's resonance frequency and the driving frequency.

4. Conclusion

All materials show some level of nonlinearity when subjected to vibrations. For damaged materials, the defects enhance the nonlinear response of the material considerably. This defect-induced nonlinearity is classified as *non-classical* nonlinearity. The associated nonlinear artifacts, such as higher harmonics and modulation frequencies, are of sufficient amplitude to be exploited for non-destructive testing.

Two straightforward phenomenological models prove valuable for investigation of the non-classical nonlinear response associated to a defect, such as a delamination in a composite plate. The first one is based on a bi-linear stress-strain relation and predicts the formation of odd and even higher harmonics of the input excitation frequency. In addition, the model predicts the formation of modulation sidebands when a dual sine excitation is used. This bi-linear stiffness model is representative for a crack or delamination that is opened and closed by the elastic waves. Next, the step-wise stiffness model is outlined to investigate the nonlinear response of rubbing defects. Again, it is shown that higher harmonics and modulation sidebands are formed. However, in this case only odd higher harmonics are generated. More advanced models, such as the anharmonic oscillator model with nonlinear equation of motion, prove valuable to study other nonlinear response artifacts such as the amplitude-dependent resonance frequency and the associated frequency fold-over phenomenon.

References

1. Zarembo, L.K. and V.A. Krasil'Nikov, *Nonlinear phenomena in the propagation of elastic waves in solids.* Soviet Physics Uspekhi, 1971. **13**.
2. Solodov, I., *Resonant Acoustic Nonlinearity of Defects for Highly-Efficient Nonlinear NDE.* Journal of Nondestructive Evaluation, 2014. **33**(2): p. 252-262.
3. Van Den Abeele, K., et al., *On the quasi-analytic treatment of hysteretic nonlinear response in elastic wave propagation.* Acoustical Society of America, 1996. **101**(4): p. 1885-1898.
4. Krohn, N., R. Stoessel, and G. Busse, *Acoustic non-linearity for defect selective imaging.* Ultrasonics, 2002. **40**(1): p. 633–637.
5. Kundu, T., et al., *Investigation of the threshold behavior of subharmonics for damage detection of a structure with a breathing crack*, in *Health Monitoring of Structural and Biological Systems 2010*. 2010.
6. Broda, D., et al., *Modelling of nonlinear crack–wave interactions for damage detection based on ultrasound-A review.* Journal of Sound and Vibration, 2014. **333**(4): p. 1097-1118.

7. Moussatov, A., V. Gusev, and B. Castagnede, *Self-induced hysteresis for nonlinear acoustic waves in cracked material.* Phys Rev Lett, 2003. **90**(12): p. 124301.
8. Johnson, P.A., *Nonequilibrium Nonlinear-Dynamics in Solids: State of the Art*, in *Universality of Nonclassical Nonlinearity*, P.P. Delsanto, Editor. 2006, Springer. p. 49-69.
9. Delsanto, P.P., *Universality of Nonclassical Nonlinearity*, ed. P.P. Delsanto. 2006: Springer.
10. Jhang, K.-Y., et al., *Measurement of Nonlinear Ultrasonic Characteristics*. Measurement Science and Technology, ed. M.G. Cain, et al. 2020: Springer.
11. Van Den Abeele, K., P.A. Johnson, and A. Sutin, *Nonlinear Elastic Wave Spectroscopy (NEWS) Techniques to Discern Material Damage, Part I: Nonlinear Wave Modulation Spectroscopy (NWMS).* Res Nondestr Eval 2000. **12**: p. 17–30.
12. Van Den Abeele, K., et al., *Nonlinear Elastic Wave Spectroscopy (NEWS) Techniques to Discern Material Damage, Part II: Single-Mode Nonlinear Resonance Acoustic Spectroscopy.* Res Nondestr Eval 2000. **12**: p. 31–42.
13. Pieczonka, L., et al., *Impact damage detection in light composite sandwich panels using piezo-based nonlinear vibro-acoustic modulations.* Smart Materials and Structures, 2014. **23**(10).
14. Jhang, K.Y., *Nonlinear Ultrasonic Techniques for Nondestructive Assessment of Micro Damage in Material: A Review.* International journal of Precision Engineering and Manufacturing 2009. **10**(1): p. 123-135.
15. Ginzburg, D., *Damage Propagation and Detection using Nonlinear Elastic Wave Spectroscopy in Aerospace Structures*, in *Department of Mechanical Engineering*. 2016, University of Bath.
16. Vuye, C., et al., *Optical measurement of the dynamic strain field of a fan blade using a 3D scanning vibrometer.* Optics and Lasers in Engineering, 2011. **49**(7): p. 988-997.
17. Li, P., et al. *Dependence Of Acoustic Nonlinearity Parameter On Second Phase Precipitates Of Aluminuh Alloys*. in *IEEE 1985 Ultrasonics Symposium*. 1985. San Francisco, CA, USA.
18. Solodov, I., *Resonant acoustic nonlinearity for defect-selective imaging and NDT*, in *AIP Conference Proceedings*. 2015.
19. Ostrovsky, L.A. and P.A. Johnson, *Dynamic nonlinear elasticity in geomaterials.* RIVISTA DEL NUOVO CIMENTO, 2001. **24**(7): p. 1-46.
20. Segers, J., et al., *Nonlinear Elastic Wave Energy Imaging for the Detection and Localization of In-Sight and Out-of-Sight Defects in Composites.* Applied Sciences, 2020. **10**(3924).
21. Pieczonka, L., et al., *Damage imaging in composites using nonlinear vibro-acoustic wave modulations.* Structural Control and Health Monitoring, 2017.
22. Mevissen, F. and M. Meo, *A Nonlinear Ultrasonic Modulation Method for Crack Detection in Turbine Blades.* Aerospace, 2020. **7**(6).

23. Segers, J., et al., *Broadband nonlinear elastic wave modulation spectroscopy for damage detection in composites.* Structural Health Monitoring, 2021.
24. Ciampa, F., G. Scarselli, and M. Meo, *On the generation of nonlinear damage resonance intermodulation for elastic wave spectroscopy.* The Journal of the Acoustical Society of America, 2017. **141**(4): p. 2364.
25. Solodov, I.Y. and B.A. Korshak, *Instability, chaos, and "memory" in acoustic-wave-crack interaction.* Phys Rev Lett, 2002. **88**(1): p. 014303.
26. Kober, J. and Z. Prevorovsky, *Theoretical investigation of nonlinear ultrasonic wave modulation spectroscopy at crack interface.* NDT and E International, 2014. **61**: p. 10-15.
27. Meo, M., U. Polimeno, and G. Zumpano, *Detecting Damage in Composite Material Using Nonlinear Elastic Wave Spectroscopy Methods.* Applied Composite Materials, 2008. **15**(3): p. 115-126.
28. Klepka, A., et al., *Nonlinear acoustics for fatigue crack detection – experimental investigations of vibro-acoustic wave modulations.* Structural Health Monitoring, 2011. **11**(2): p. 197-211.
29. Sarens, B., et al., *Investigation of Contact Acoustic Nonlinearity in Delaminations by Shearographic Imaging, Laser Doppler Vibrometric Scanning and Finite Difference Modeling.* IEEE Transactions on Ultrasonics, 2010. **57**(6): p. 1383-1395.
30. Solodov, I., N. Krohn, and G. Busse, *CAN: an example of nonclassical acoustic nonlinearity in solids.* Ultrasonics, 2002. **40**(1): p. 621–625.
31. Yamanaka, K., T. Mihara, and T. Tsuji, *Evaluation of Closed Cracks by Model Analysis of Subharmonic Ultrasound.* Japanese Journal of Applied Physics, 2004. **43**(5B): p. 3082-3087.
32. Pecorari, C. and I. Solodov, *Nonclassical nonlinear dynamics of solid surfaces in partial contact for NDE applications* in *Universality of Nonclassical Nonlinearity*, P.P. Delsanto, Editor. 2007, Springer. p. 309-326.
33. Solodov, I., *Nonlinear acoustic NDT: approaches, methods and applications*. 2007, Department of Non-Destructive Testing, Institute of Polymer Technology (IKT), University of Stuttgart, Stuttgart.
34. Solodov, I., N. Krohn, and G. Busse, *Nonlinear ultrasonic NDT for early defect recognition and imaging*. 2010, Institute of polymer technology, Department of nondestructive testing (ikt-zfp), University of Stuttgart.
35. Solodov, I., et al., *Nonlinear self-modulation and subharmonic acoustic spectroscopyfor damage detection and location.* Applied Physics Letters, 2004. **84**(26): p. 5386-5388.

Chapter 4

Experimental Protocol for Investigating Vibrations in Thin-Walled Structures

Summary:

Sensitive full-field elastic wave based NDT is only possible when the associated experiments are of sufficient high quality. In this chapter, the experimental protocol used throughout this PhD work is outlined. Piezoelectric actuators are used to excite the vibrations and a 3D scanning laser Doppler vibrometer is used for recoding of the full wavefield response. Typical signal processing, which often relies on integral transforms, is presented.

1. Introduction

In order to detect defects using full-field elastic wave analysis, the first step is to perform the experiment. Vibrations are excited into the test specimen and the resulting wavefield is recorded through sensor networks or specialized measurement systems. In order to achieve a high defect detection performance, it is of utmost importance that high quality measurement results are obtained. This imposes high demands on the equipment used for excitation and for sensing of the vibrations.

Multiple options are available for wave actuation as well as for wave visualization. The following requirements should be considered for the wave visualization system:

- High sensitivity over a large bandwidth:
  The frequency of the vibrations used for full-field elastic wave based NDT is typically in the 10 to 300 kHz range. The amplitude associated with the vibrations is low, especially for the nonlinear vibrational components (e.g. down to 10 μm/s, see Chapter 12 Figure 12.9). As a result, the measurement device must be highly sensitivity, and allow for high sampling frequencies.
- Non-invasive and user-friendly:
  Setup of the measurement device is preferably fast and easy. No damage can be afflicted to the inspected component. As a result, a non-contact measurement is preferred.
- Fast full wavefield measurement in case of single point excitation:
  The best NDT performance is achieved when the full wavefield response is obtained. When the vibrations are excited at one (or a discrete number of) fixed point(s), the measurement device must record the full wavefield response of the component. However, most measurement systems measure the response at one point at the time. In order to achieve a fast NDT technique, the switching from one measurement point to another must be as fast as possible.

Also for the excitation device, a number of requirements should be considered:

- Large bandwidth of excitation:
  The actuator must be able to excite waves of detectable amplitude in the desired broadband frequency range (e.g. 10 to 300 kHz).
- Non-invasive and user-friendly:
  Similar to the measurement device, the setup of the actuator must be easy and may not inflict damage to the component.

- Fast scanning excitation in case of single point measurement:
  When the vibrations are recorded at a single point of the component, an excitation system that can rapidly excite a large number of locations (one point at the time) is required.

Taking these requirements into account, a measurement protocol is proposed. Wave excitation is achieved using low power piezoelectric actuators. A 3D infrared scanning laser Doppler vibrometer (SLDV) is used for acquisition of the full wavefield response. The wave excitation strategy and the wave acquisition strategy are explained in Section 2 and Section 3, respectively. Typically vibrational signal processing is performed in the frequency or wavenumber domain. In Section 4, the required integral transformation algorithms are presented.

2. Piezoelectric Wave Excitation

2.1. Working Principle of Piezoelectric Transducers

As the name indicates ('piezo' is Greek for 'press'), a piezoelectric transducer possesses the piezoelectric effects that allows for energy conversion between mechanical and electrical energy. The transducer consists of a piezoelectric material on which electrodes are soldered. When the piezoelectric material is excited with an alternating voltage over the electrodes, an oscillatory mechanical force is produced. Vice versa, when the piezoelectric material is loaded by a dynamic force, the element produces an alternating voltage. Piezoelectric transducers are available in a large variety of shapes and sizes. The piezoelectric material is typically a ceramic material such as lead zirconate titanate (often referred to as PZT).

The piezoelectric transducers used for (guided) elastic wave generation (and sensing) are relatively thin round or rectangular discs of piezoelectric material. They are often referred to as piezoelectric wafer active transducers or sensors (PWAT, PWAS) [1]. Depending on the amount and the quality of the piezoelectric material, the price ranges from less than 1 euro up to ± 100 euro apiece. Figure 4.1 shows the different parts of a typical piezoelectric bending disc and gives a schematic illustration of the working principle for sensing and actuation of vibrations. When a voltage is applied to the electrodes, the piezoelectric element wants to change in diameter due to the transverse piezoelectric effect. This results in the bending of the element and the plate. Vice versa, the bending of the element (caused by the vibration of the substrate) induces a voltage over the electrodes.

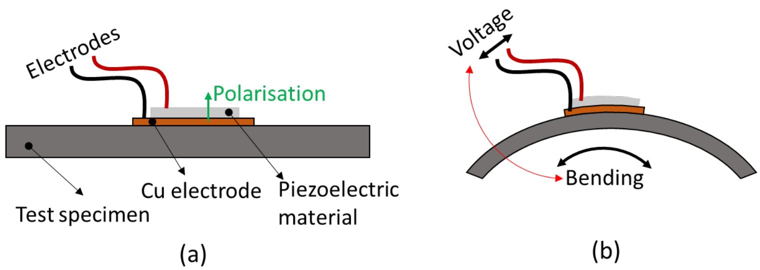

Figure 4.1: Bending disc piezoelectric transducer (a) Design and (b) Working principle.

In the last decades, multiple research groups studied the properties of piezoelectric transducers for generation (and sensing) of guided waves [1]. Advanced piezoelectric actuator designs and arrays are proposed for excitation of specific guided wave mode types or for focusing the excited waves at specific locations of the component. As an example, Kamal and Huan et al. [2, 3] developed transducer for efficient excitation of the non-dispersive SH_0 waves, Su et al. [4] used multiple piezoelectric actuators with specific phase delay for selective generation of anti-symmetric, symmetric and shear modes, and Fu et al. used a piezoelectric beamforming array to improve the performance of defect detection using the MUSIC algorithm [5].

In this PhD work, advanced data processing methods are developed for extracting specific guided wave modes out of the full wavefield SLDV measurements. These methods are discussed in Chapter 10. As a result, the excitation can be performed using simple and cheap piezoelectric bending discs. The bending discs excite all guided waves modes and the advanced data processing methods are used to transform the structure's multi-mode (and multi-frequency) response to the one needed for construction of the damage map. In order for this approach to be successful, the piezoelectric transducers used here must be able to repeatedly, and consistently, excite waves of detectable amplitude.

2.2. Comparison of Different Types of Piezoelectric Transducers

In the scope of a master thesis, performed by Tijs Vancoillie [6], the performance of eight different low power piezoelectric actuator was compared. An identical experiment is performed for each actuator. The actuator is attached to a 330x330x5.45 mm^3 quasi-isotropic CFRP plate and excited with a 40 ms broadband sine sweep voltage signal from 1 kHz up to 300 kHz. The test specimen is shown in Figure 4.2 together with the evaluated actuators. All but one actuators are bonded to the CFRP plate using phenyl salicylate (see inset in figure). This substance melts at 41.5 °C which allows for easy actuator bonding and removal. The Isi-Sys piezoshaker is attached with vacuum pressure, increasing its practicality.

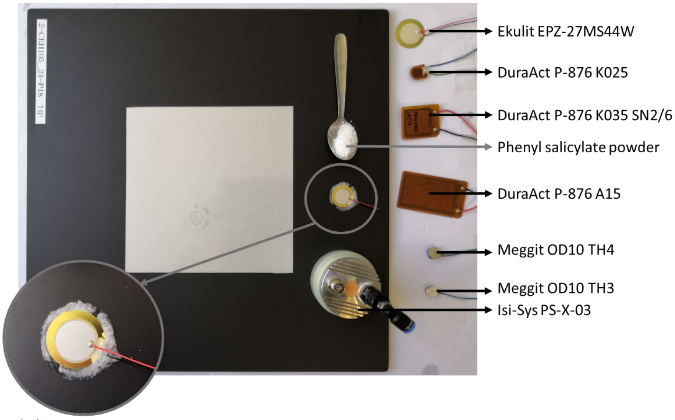

Figure 4.2: Performance comparison of different piezoelectric actuators: Test specimen and actuators.

The middle of the CFRP plate is covered with retroreflective tape. The 3D SLDV is used to measure both the in-plane and out-of-plane vibrations at ±750 scan points distributed over this reflective area. For each scan point, 25 000 time samples are taken using a sampling frequency of 625 kS/s. The average frequency response function FRF is calculated as:

$$FRF_i(f) = \frac{\sum_{(x,y)}\left|\tilde{V}_i(x,y,f)\right|}{N_{sp}\left|\tilde{U}(f)\right|}$$

with $\tilde{V}_i$ the FFT of the velocity response in the $i = X, Y, Z$ direction, $\tilde{U}$ the FFT of the sweep voltage signal supplied to the actuator and N_{sp} the number of scan points.

The voltages supplied to every actuator were selected as the maximum voltage for safe and consistent operation. Increasing the voltage beyond the selected value resulted in an excessive heating of the piezoelectric material, which leads to the melting of the bonding agent and potential degradation of the piezoelectric material. A parametric study towards the effect of the voltage amplitude on the excited vibrations can be found in [6].

The out-of-plane FRF_Z results are shown in Figure 4.3. The figure is split into two parts in order to improve its readability. In addition, a logarithmic scale for the FRF_Z-axis is used. For each actuator, the excitation voltage amplitude is indicated in the corresponding legend entry. As expected, the biggest actuator, i.e. the DuraAct P-876 A15, is most capable of generating the low frequency vibrations < 20 kHz. In the middle frequency regime (20 to 200 kHz), the Ekulit actuators prevail. At last, for generation of high frequency out-of-plane vibrations, the small DuraAct P-876 K025 is most effective. The Isi-Sys actuator and the Meggit discs show a very irregular response with high excitation only at specific frequencies. This is attributed to their design. These actuators are relatively thick and deform in the longitudinal direction. Their output response is high only in case that the excitation frequency matches one of its longitudinal resonance frequencies.

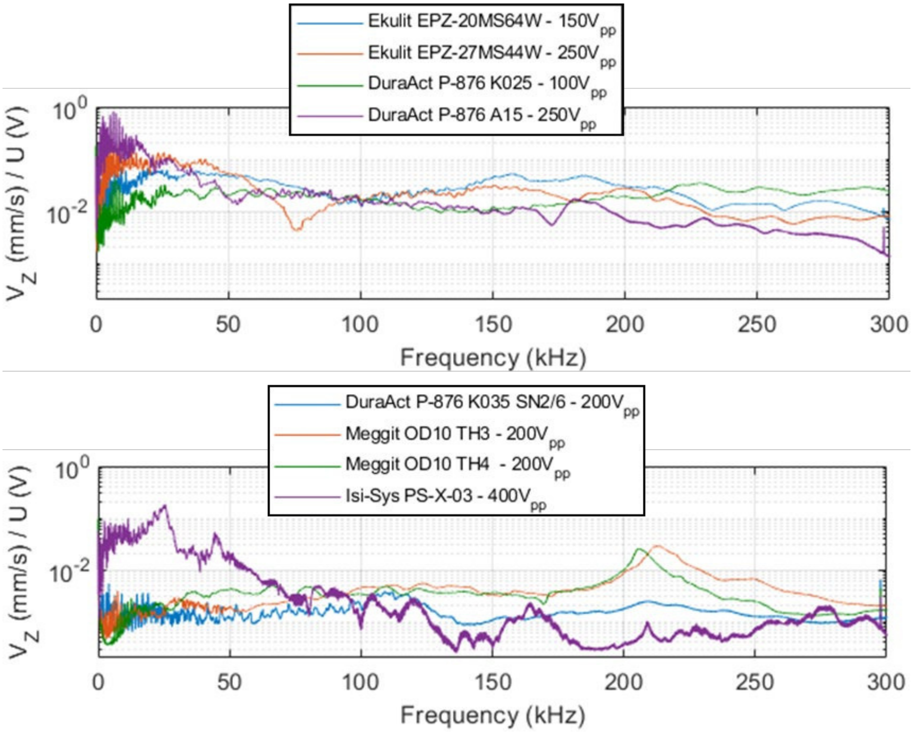

Figure 4.3: Average out-of-plane frequency response FRF_Z function of eight different piezoelectric actuators.

The in-plane FRF_Y results are shown in Figure 4.4. Similar conclusions can be drawn as for the FRF_Z results with the only difference that the big DuraAct P-876 A15 actuators shows the most effective in-plane vibration generation up to around 75 kHz (compared to 25 kHz for the out-of-plane vibrations).

Most of the elastic wave damage map construction methods developed in this PhD work require a broadband excitation of the test specimen. This requires a piezoelectric actuator with good excitation performance over the entire frequency range (10 to 300 kHz). As a result, the Ekulit actuators are chosen for wave actuation in the majority of experiment. This is because the FRF spectrum corresponding to this actuator is relatively flat and of sufficient amplitude (see Figure 4.3 and Figure 4.4).

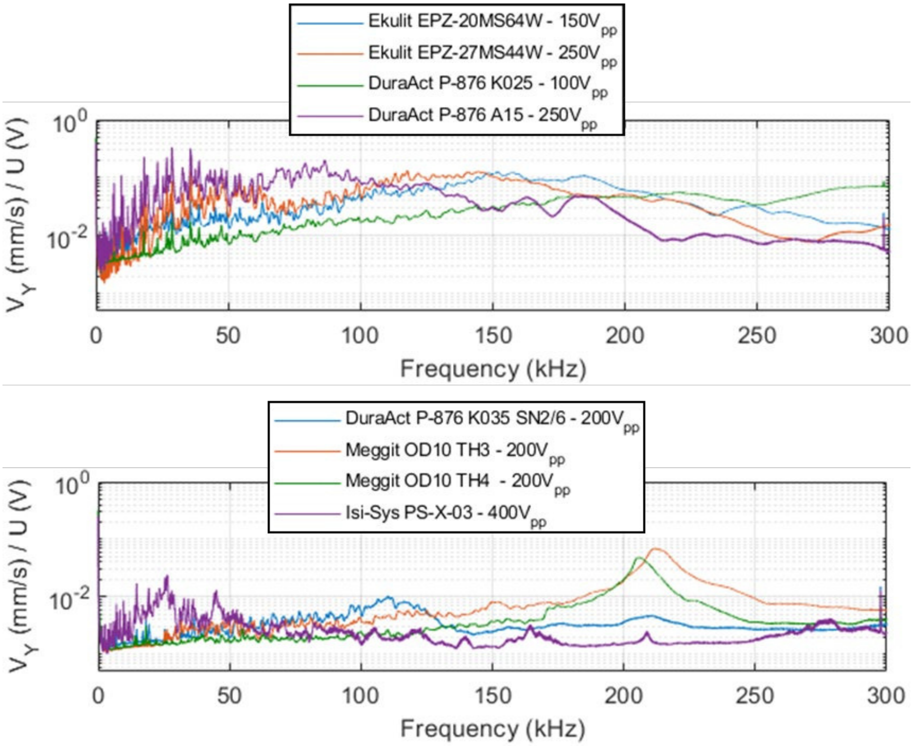

Figure 4.4: Average in-plane horizontal frequency response function FRF_Y of eight different piezoelectric actuators.

2.3. Power of the Piezoelectric Actuator

An experiment is designed in order to measure the power consumed by an Ekulit type EPZ-20MS64W piezoelectric actuator. The experimental setup is shown in Figure 4.5. The piezoelectric actuator is supplied with a sine sweep excitation voltage using a Falco WMA-300 high voltage amplifier. The sweep starts at 1 Hz and ends at 500 kHz. The amplitude is varied resulting in amplifier output voltage amplitudes of 12.5 V, 25 V, 50 V, 75 V, 100 V and 125 V. Three resistors are present with resistance of R_1 = 1 Ω, R_2 = 472 kΩ and R_3 = 462 Ω. These resistors allow to record the voltages V_1 and V_3 using an oscilloscope (with a maximum input voltage 10 V) over the total sweep duration. The voltage and current amplitudes at the piezoelectric actuator, and the consumed average power, are obtained as:

$$I_{PZT} = \frac{V_1}{R_1} \quad ; \quad V_{PZT} = \frac{V_3}{R_3}(R_2 + R_3) - V_1 \quad ; \quad P_{PZT} = \frac{V_{PZT}\, I_{PZT}}{2}$$

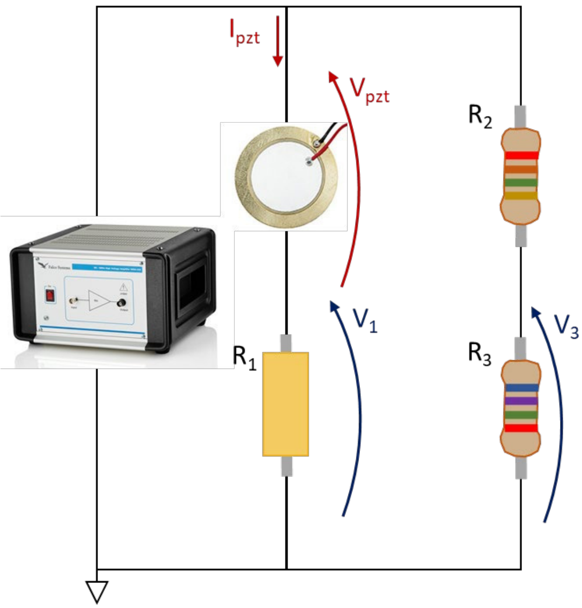

Figure 4.5: Setup for measurement of the power consumed by the piezoelectric actuator.

Figure 4.6 shows the voltage, current and power at the piezoelectric actuator in function of the sine sweep frequency and in function of the voltage amplitude supplied by the amplifier. The curves show the typical behavior of a piezoelectric actuator with equivalent circuit [7] shown in Figure 4.6 (d). The actuator behaves as a dominant capacitive load but has multiple electrical resonance frequencies at $f = 1/(2\pi\sqrt{L_{ai}C_{ai}})$. At these resonance frequencies, the actuator's impedance is low and the voltage and current drops. Figure 4.6 (a) and (b) reveal two of these resonances at around 150 and 475 kHz. The resonances are also visible in the power curves of Figure 4.6 (c). As expected, the power increases linearly with the excitation voltage that is supplied to the actuator. Overall, the power is low. For instance, the actuator consumes an average power of around 3.5 W when it is excited with an excitation voltage amplitude of 75 V (i.e. 150 V_{pp}).

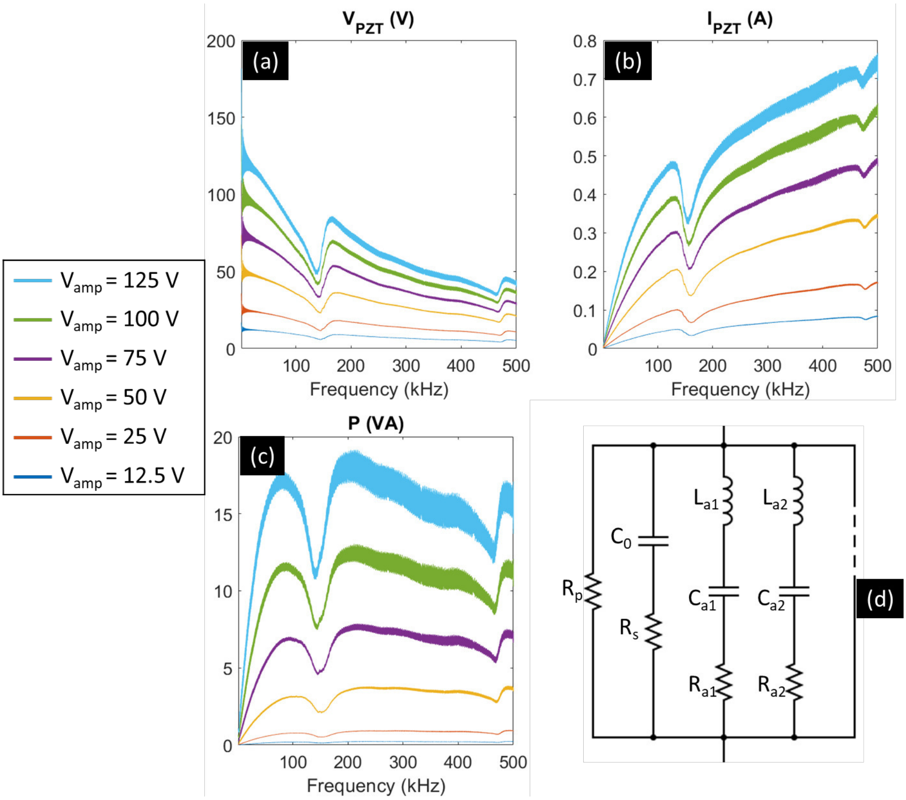

Figure 4.6: (a) Voltage amplitude, (b) Current amplitude and (c) Total power at the piezoelectric actuator (Ekulit EPZ-20MS64W) for different excitation voltage amplitudes with (d) Equivalent circuit of the actuator (Reproduced from [7]).

2.4. Other Options for High Frequency Wave Excitation

In case that it is impossible to bond a piezoelectric actuator to the test specimen, there are other solutions for high frequency wave excitation.

A first option is to use air-coupled ultrasonic actuators [8-11]. The air-coupled actuators may show satisfying frequency bandwidths but cannot reach the same amplitude levels as the bonded piezoelectric actuators.

A second option is to use a pulsed laser that fires extremely short (order of ns) laser pulses of relatively high energy (order of mJ). The pulse energy is partially absorbed by the surface of the test specimen. The generated heat induces a rapid expansion and contraction of the material, exciting ultrasonic waves. For NDT purposes, the energy density (i.e. pulse energy divided by laser spot size) must be limited in order not to ablate the surface. A more detailed description of the working principle of pulsed lasers for generation of ultrasonic waves is found in [12]. A proof-of-concept of laser excited ultrasonic waves is provided in Chapter 13.

3. Wave Acquisition with Scanning Laser Doppler Vibrometry

The 3D scanning laser Doppler vibrometer (SLDV) is a state-of-the-art measurement system that fulfills almost all requirements for ultrasonic vibrational measurements. It allows for relatively fast full wavefield quantitative measurements of the total (3D) velocity response. Moreover, the measurement is non-contact. On the other hand, there are some disadvantages related to the use of a 3D SLDV that have to be considered. First, a 3D SLDV system is highly expensive (> 100 k€). In addition, it takes some time and experience to perform the necessary alignment procedures. At last, depending on the surface finish of the test object, it may be necessary to perform averaging or to cover the surface with retroreflective tape (or spray) in order to achieve the desired signal-to-noise ratio (see further).

Laser Doppler vibrometry is a velocity measurement technique that finds its origin in the early 1960's, with the measurement of fluid velocity [13]. Nowadays, LDVs are used in a multitude of industrial and research application. Well-known LDV development and manufacturing companies are *Polytec*, *Optomet* and *Ometron*. The SLDV system used in this PhD thesis is a *PSV-500 3D Xtra* designed and manufactured by *Polytec*. The SLDV has infrared measurement lasers with wavelength λ = 1550 nm. The power of each laser is limited to 3.3 mW resulting in eye safe operation (laser class 2).

In this section, the working principle of the SLDV used in this PhD thesis is explained first. It is shown that the use of three laser heads allows to distinguish between in-plane vibrations (along the X and Y-direction) and out-of-plane vibrations (along the Z-direction). Next, a typical SLDV measurement is presented. At last, a parametric study is performed to evaluate the noise level of the SLDV measurement.

3.1. SLDV Working Principle

3.1.1. Working Principle: 1D LDV

A 1D LDV system consists of one laser head, a data acquisition system and a computer. The laser head emits a coherent and monochromatic light beam. The beam is focused at the location of the test specimen for which the vibrational velocity must be measured. The head is typically positioned perpendicular to the test specimen's surface. In the past, Helium-Neon lasers with a wavelength λ = 632.8 nm [13] were often used. In recent years, infrared lasers gained popularity because the reflection of infrared light from mat black objects, such as CFRP, is higher compared to the reflection of Helium-Neon lasers.

The measurement of the surface's velocity is based on the Doppler effect. If the position of the laser source is fixed and perpendicular to the object's surface, and if the observed surface is moving towards the laser source with out-of-plane velocity V_Z, the frequency of the laser light scattered by the surface equals:

$$f' = f \frac{c}{c - 2\,V_Z} \tag{4.1}$$

with f the frequency of the laser source (= c/λ) and c = 299 792 458 m/s the speed of light. Because $c \gg V_Z$, Eq. (4.1) can be simplified using the Taylor expansion to:

$$f' \approx f\left(1 + 2\,\frac{V_Z}{c}\right) \tag{4.2}$$

As a result, the out-of-plane velocity V_Z can be calculated if the frequency of the reflected laser light f' is known.

A direct demodulation of the measurement beam's frequency f' is impossible because the frequency of the laser light is too high [13]: $f = \frac{c}{\lambda} = 1.9\ 10^{14} Hz$. This problem is overcome through the use of an interferometer. There are two common types of interferometers used in SLDV systems: homodyne interferometers and heterodyne interferometers. For the sake of brevity, only the heterodyne interferometer is discussed, as this is the type present in most commercial LDV systems. Figure 4.7 shows the working principle of the heterodyne interferometer. First, the emitted laser light is split into a measurement beam and a reference beam. The measurement beam is passed through a Bragg cell, shifting the frequency from $f \to f + f_b$. The frequency shift f_b is typically 40 or 70 MHz [13, 14]. Next, the measurement beam is pointed at the test specimen where the light is scattered and the frequency is shifted due to the Doppler effect (see Eq. (4.2)). The scattered light is collected and recombined with the reference beam. The two beams interfere at the photodetector. The electric fields inflicted at the photodetector by the reference beam (E_r) and by the measurement beam (E_m) are:

$$\begin{aligned} E_r &= a_r \exp[j(2\pi f t - \varphi_r)] \\ E_m &= a_m \exp\left[j\left(2\pi(f + f_b)\left(1 + 2\frac{V_Z}{c}\right)t - \varphi_m\right)\right] \end{aligned} \tag{4.3}$$

The intensity observed by the photodetector (after interference) equals:

$$\begin{aligned} P_d &= (E_r + E_m)(E_r + E_m)^* \\ &= P_r + P_m + 2\sqrt{P_r P_m}\cos\left(2\pi f_b\left(1 + 2\frac{V_Z}{c}\right) - (\varphi_r - \varphi_m)\right) \end{aligned} \tag{4.4}$$

Where $P_r = E_r E_r^*$ and $P_m = E_m E_m^*$ are the power related to the reference and measurement beam, respectively and the symbol * refers to the complex conjugate. The intensity P_d has a beating frequency: $f_b\left(1 + 2\frac{V_Z}{c}\right)$. This beating frequency is low enough to demodulate, thus providing the out-of-plane surface velocity V_Z.

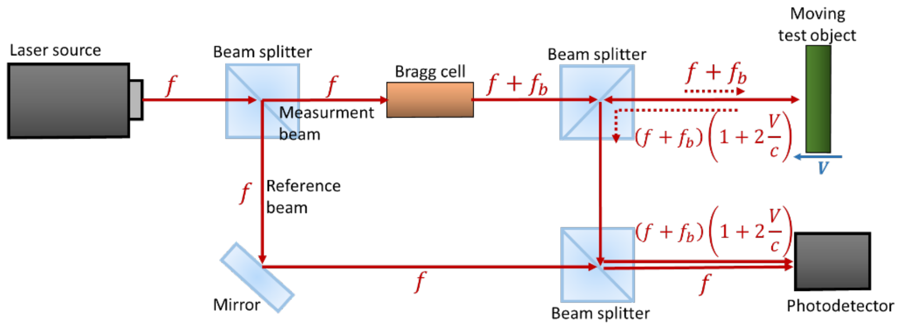

Figure 4.7: Working principle of the heterodyne interferometer.

3.1.2. Working Principle: 3D LDV

The velocity vector of a point in space has three components: $\vec{V} = [V_X \ \ V_Y \ \ V_Z]$. In previous section, it was explained how the out-of-plane component V_Z is measured with a 1D LDV system when the laser head is positioned perpendicular to the test specimen. In order to determine all three velocity components, three individual laser heads are required, each under a specific angle with respect to the test specimen's surface. The velocity vector $[V_X \ \ V_Y \ \ V_Z]$ can than be obtained from the velocities measured by the three laser heads through a coordinate transformation. The coordinate transformation requires that the position of each laser head with respect to the test object is known. This information is obtained from a 3D alignment procedure that is performed upon setup of the measurement.

The measurement of the in-plane vibrational components (V_X, V_Y) is only possible when sufficient light of the incident beam is reflected back to the laser head, even when the incident angle is large. It is therefore essential that the surface of the test object is retroreflective. Most everyday object (and also CFRP components) are retroreflective to some extent and allow for the measurement of the in-plane vibrational components without surface treatment. For mirror like objects, or to reduce the noise level of the measurement (see next section), the object's surface must be covered with a retroreflective tape or spray. Figure 4.8 (a,b) graphically illustrated the benefits of using retroreflective tape for measurements on mirror-like surfaces under large incident angles. Very small glass beads are dispersed in these tapes and acts as retroreflective mirrors (see Figure 4.8 (c)).

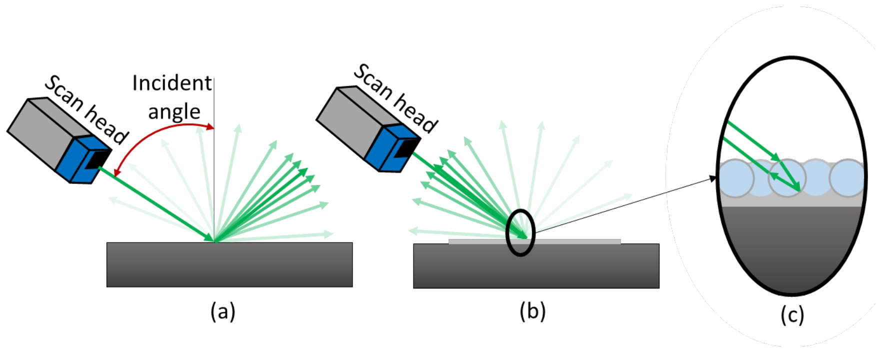

Figure 4.8: Reflection of laser beam under large incident angle: (a) Mirror-like surface, (b) Retroreflective tape and (c) Glass beads inside the retroreflective tape.

3.1.3. Working Principle: 3D SLDV

Transforming a single point LDV to a SLDV requires the addition of a XYZ scanner using galvanometers in each of the three laser scan heads. Upon setup of the experiment, an additional alignment procedure is required to teach each XYZ scanner the scan angles that are needed to reach specific points of the test specimen. A grid of scan point is defined for which the velocity is measured.

Elastic wave events happen fast. As a result, a single measurement at one scan point lasts typically no longer than a few tens of milliseconds. In order not to delay the measurement, the XYZ scanner must be able to switch angles extremely fast. The maximum scan speed of the PSV-500 3D Xtra is around 30 points/second.

3.2. Typical SLDV measurement

A typical SLDV measurement is performed on the 330x330x5.45 mm^3 plate manufactured out of 24 layers of unidirectional carbon fiber prepreg according to quasi-isotropic layup $[(45/0/\text{-}45/90)_3]_s$. Figure 4.9 shows the experimental setup. The test specimen is vertically positioned in front of the 3D SLDV using a vice. A piezoelectric actuator (Ekulit type EPZ-20MS64W) is attached to its backside (using phenyl salicylate) and supplied with a sine sweep excitation signal from 5 kHz up to 300 kHz with a peak-to-peak amplitude of 150 V_{pp}. The velocity response is recorded with the SLDV at 19437 scan points distributed over the test specimen using a sampling frequency of 625 kS/s and a number of time samples equal to 10 000. An experienced user performs the required alignment procedures in around 3 minutes. The measurement itself took around 20 minutes.

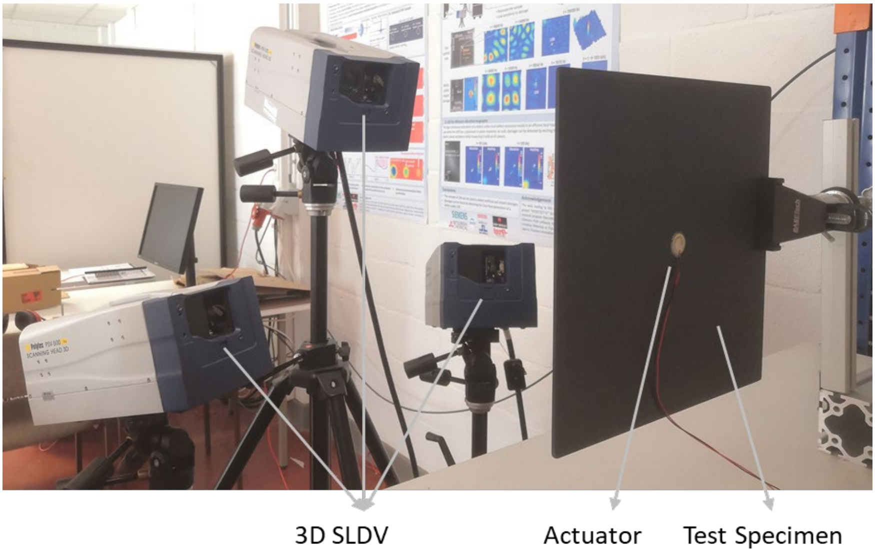

Figure 4.9: Test setup with test specimen suspended in front of a 3D scanning laser Doppler vibrometer.

Figure 4.10 shows the obtained experimental results. Three curves are obtained at every scan point, i.e. one curve for every component of the velocity vector $\vec{V} = [V_X \;\; V_Y \;\; V_Z]$. Figure 4.10 (a) shows the velocity at a random scan point in function of time. Figure 4.10 (b) shows the velocity, averaged over all scan points, in function of frequency. In addition, the full wavefield measurement allows to plot the operational deflection shape at specific frequencies. Three operational reflection shapes are shown in Figure 4.10 (c).

The out-of-plane velocity response V_Z has the highest amplitude in the low frequency regime (< 80 kHz). In this frequency regime, the piezoelectric actuator efficiently excites the A_0 mode which has a wavelength similar to the size of the actuator and which has a dominant out-of-plane surface vibration. In the higher frequency regime (> 80 kHz), the in-plane velocity components (V_X and V_Y) are best excited. At these frequencies, the wavelength of the S_0 mode, which has a dominant in-plane surface vibration, matches better with the actuator's size compared to the wavelength of the A_0 mode.

The local maxima in the frequency spectra correspond to plate resonances. These resonances are revealed by the operational deflection shapes presented in Figure 4.10 (c) (see also Section 5 of Chapter 2). Note again the difference in wavelength between in the out-of-plane A_0 mode resonances shown in Figure 4.10 (c.1-2) and the in-plane S_0 mode resonance shown in Figure 4.10 (c.3).

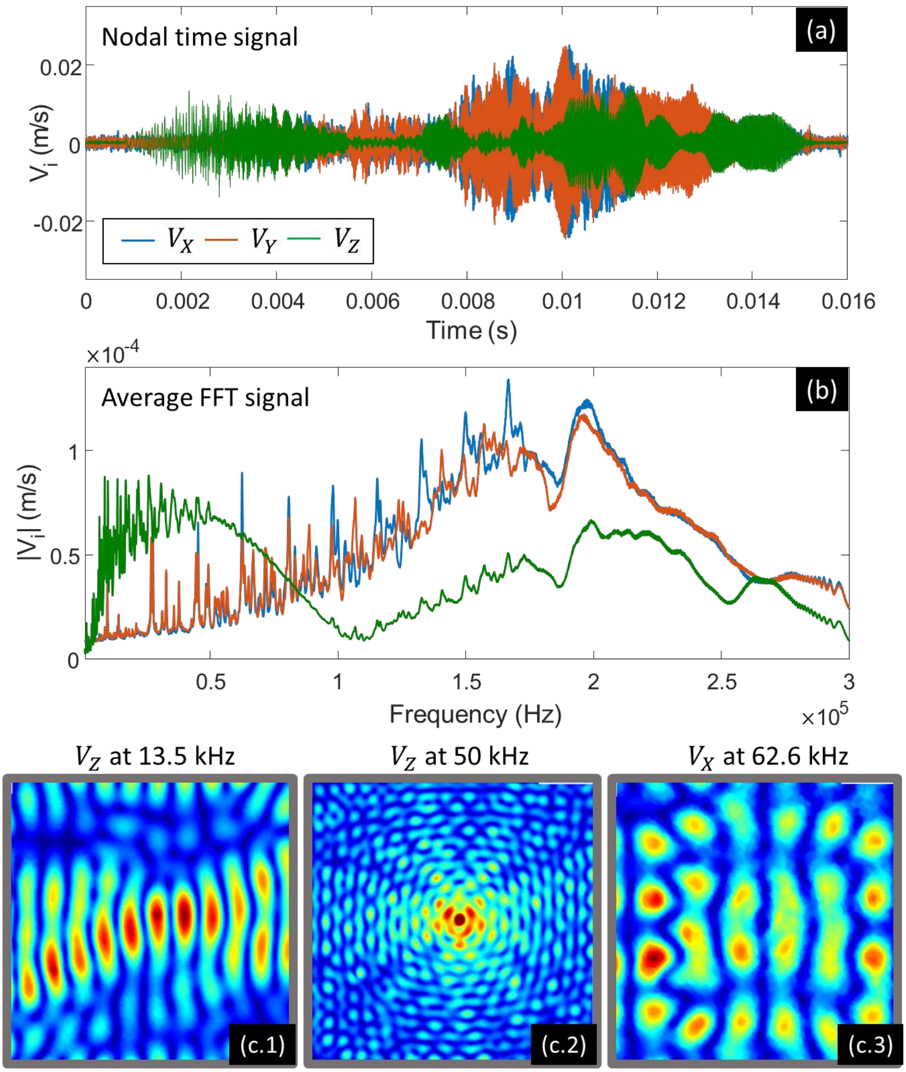

Figure 4.10: In-plane (V_X, V_Y) and out-of-plane (V_Z) velocity signals measured with the 3D SLDV: (a) in function of time at one scan point, (b) averaged over all scan points in function of frequency. (c) Three operational deflection shapes at indicated frequencies.

3.3. Parametric Evaluation of the Noise Level

A parametric evaluation of the noise level is performed for the PSV-500 3D Xtra system. The following parameters are varied:

- Configuration of the laser heads: equilateral triangle with (i) large incident angle of ±30° and (ii) small incident angle of ±10°.
- Surface condition of the test specimen: (i) Untreated (mat black) aerospace grade CFRP and (ii) Retroreflective tape type 680CRE-10 from 3M.
- Sampling frequency of the velocity decoder: 1 kS/s up to 12.5 MS/s.
- Number of averages: 0 up to 2000 averages.

The noise level is defined as the root mean square of the velocity signal measured when there is no vibrational excitation of the test specimen:

$$Noise\ Level = \sqrt{\frac{1}{N}\sum_{l=1}^{N} V_i(t_l)^2} \text{ with } i = X, Y \ or\ Z$$

Upon calculation of the noise level, a high pass filter with cutoff frequency 100 Hz is applied to remove the low frequency environmental vibrations and the associated rigid body vibrations of the object.

Figure 4.11 shows the measured noise level of each velocity component in function of the sampling frequency for laser incident angles 30° and 10°. The top row corresponds to the noise level measured on the untreated CFRP surface and the bottom row corresponds to the noise level on the retroreflective tape. Both the axis of the noise level and the axis of the sampling frequency are logarithmic scaled.

From Figure 4.11, it is observed that the sampling frequency has a significant effect on the noise level. Higher sampling frequency result in higher noise levels. As a result, it is advised to select the sampling frequency as low as possible, i.e. slightly above two times the maximum expected frequency of the vibrations (considering the Nyquist-Shannon sampling theorem).
The use of retroreflective tape improves the noise level of all velocity component, especially when high sampling frequencies are used. As an example, the noise level of V_Z for sampling frequency 1250 kS/s is reduced with a factor 17 and 6.5, when using 30° and 10° incident angles, respectively. As expected (see also Figure 4.8), the use of retroreflective tape is especially beneficial when the laser heads are positioned under large incident angles. At last, it is confirmed that the in-plane velocity components V_X and V_Y are most accurately determined using large incident angles. Vice versa, the out-of-plane velocity component V_Z shows the lowest noise level when using small incident angles.

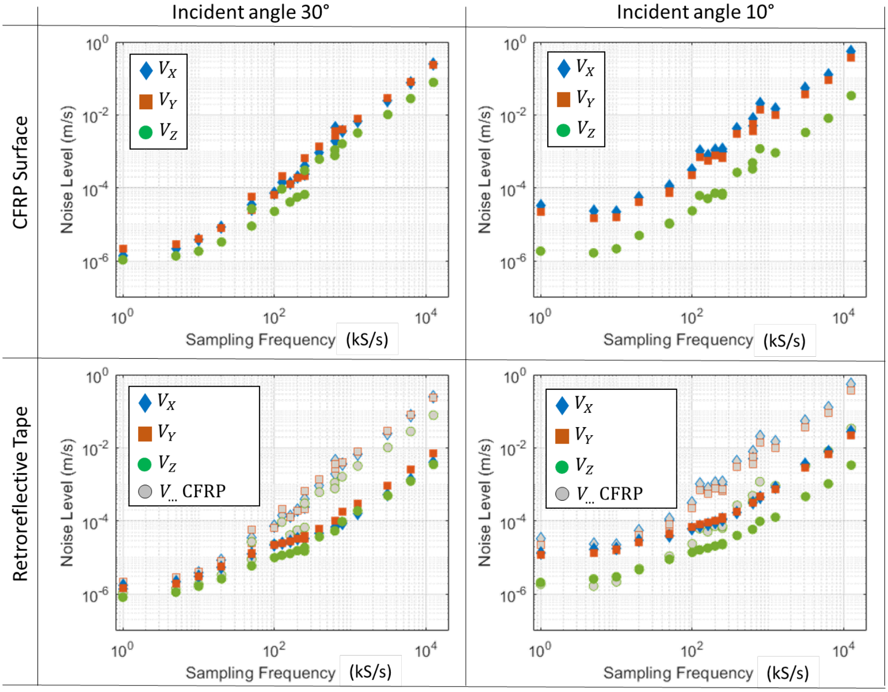

Figure 4.11: Noise level of velocity components measured on CFRP and on retroreflective tape in function of sampling frequency for 30° incident angle and 10° incident angle.

In order to gain more information on the noise level, the measured noise signals are transformed from the time domain to the frequency domain using the fast Fourier transformation. The obtained frequency spectra are plotted in Figure 4.12. The spectra shown in Figure 4.12 reveal that the noise level increases with frequency. This is especially observed for the spectra corresponding to noise measurements with high sampling frequencies on the untreated CFRP surface. The same observation was made by Hasheminejad et al. [15], who compared the noise level between a HeNe SLDV and a IR SLDV. Further, Figure 4.12 shows again that (i) in-plane vibrations are best measured using high incident angles, (ii) out-of-plane vibration is best measured using low incident angles and (iii) the use of retroreflective tape decreases the noise level considerably, especially when using high incident angles.

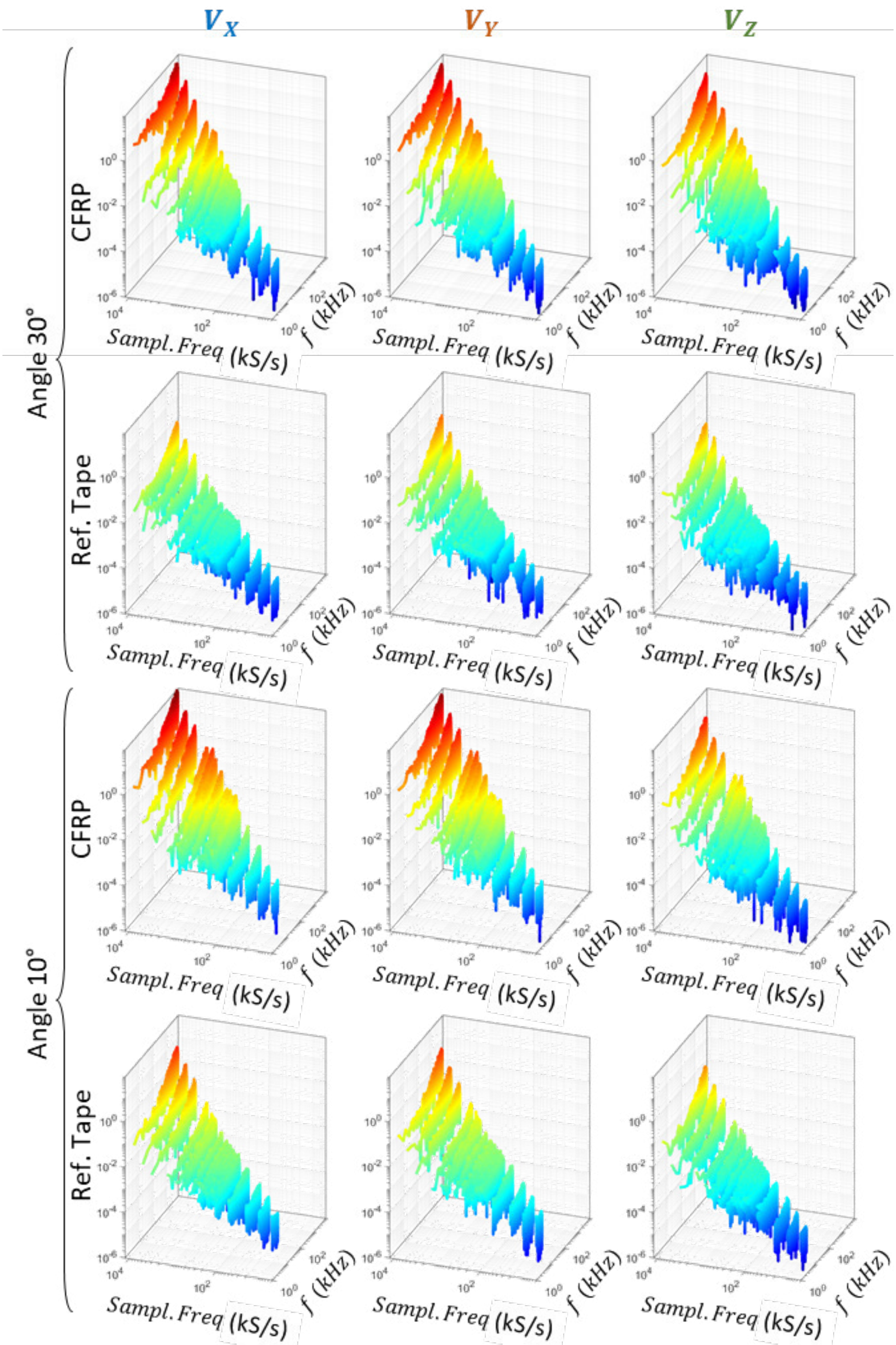

Figure 4.12: FFT of noise signal measured on CFRP and on retroreflective tape in function of sampling frequency for 30° and 10° incident angles.

Next to retroreflective tapes, signal averaging is a commonly used method to reduce the noise content of ultrasonic signals. At each scan point, the measurement is performed multiple times and the average is calculated and saved. Figure 4.13 shows the effect of averaging on the noise level corresponding to measurements on an untreated CFRP surface with 30° incident angles and a sampling frequency of 625 kS/s. The noise is reduced with a factor equal to the square root of the number of averages. This is expected, because it is well known that the variance of an averaged random variable equals the variance of the random variable divided by the number of averages. The dashed lines shown in Figure 4.13 correspond to the noise level of the same measurement performed without averages but with retroreflective tape. For the out-of-plane component (with incident angle 30° and sampling frequency 625 kS/s), the use of retroreflective tape is similar to the use of around 300 averages. For the in-plane components, the noise level corresponding to the measurement with retroreflective tape is not reached, even when using 2000 averages. Again, the big advantage of using retroreflective tape, especially for the measurement of the in-plane velocity components, is revealed.

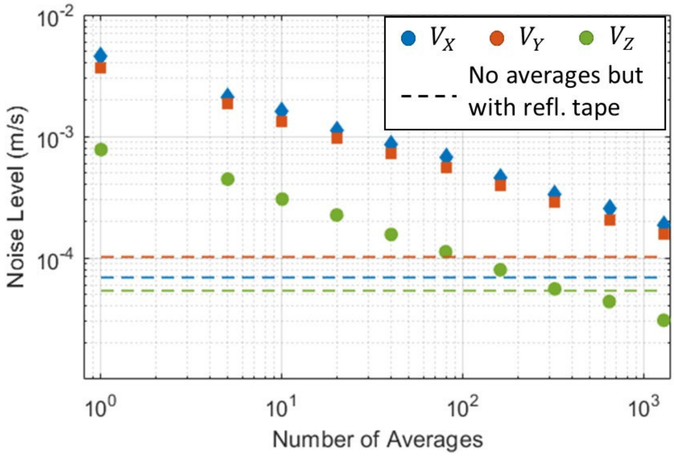

Figure 4.13: Noise level of velocity components for increasing number of averages at 625 kS/s sampling and 30° incident angles measured on untreated CFRP. Dashed line is the noise level without averages but with retroreflective tape.

A small amusing experiment is performed to get a better feeling for the magnitude of vibrational amplitude (and noise amplitude) considered here. The SLDV is pointed at the neck of a stressed-out researcher, more specific at the location of the carotid artery. The measured out-of-plane velocity signal is shown in Figure 4.14. The typical shape of a heartbeat, i.e. a big spike followed by a smaller pulse, is revealed. Although one would typically associate these heartbeat vibrations with very low amplitudes, they are easily detected by the sensitive SLDV.

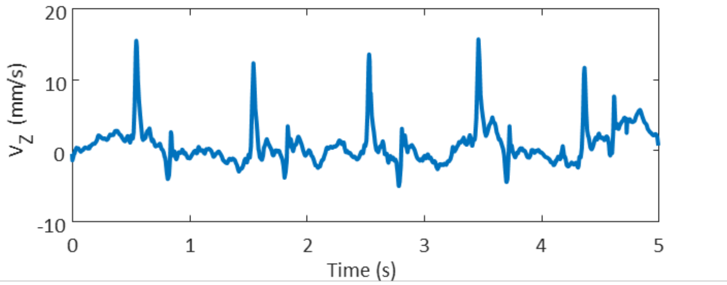

Figure 4.14: Heartbeat signal measured at the neck of a thermographic NDT expert using the SLDV.

4. Typical Signal Transformations

4.1. (Fast) Fourier Transform

Already two centuries ago, J.B. Fourier proved that a function (that is periodic in time) could always be presented as the sum of complex exponentials. The continuous Fourier transform of a function $g(t)$ is defined as:

$$\tilde{g}(f) = \int_{-\infty}^{\infty} g(t)\, e^{-i2\pi f t}\, dt$$

The inverse continuous Fourier transform is defined as:

$$g(t) = \int_{-\infty}^{\infty} \tilde{g}(f)\, e^{i2\pi f t} df$$

with f the frequency of the complex exponentials.

The time responses that is measured by the SLDV are discrete sequences with $\Delta t = 1/f_{sampling}$ the time between successive sampling points for a sampling frequency $f_{sampling}$, N the total number of samples and $\Delta f = \frac{f_{sampling}}{N}$ the obtained resolution in the frequency domain. As a result a discrete Fourier transform is defined as:

$$\tilde{g}(l\Delta f) = \frac{1}{N} \sum_{n=0}^{N-1} \left(g(n\Delta t) e^{-2\pi i \frac{ln}{N}} \right) \qquad (4.5)$$

The time and frequency indices are: n and l, respectively. The obtained result is called the spectrum of the function. The spectrum equals the complex amplitude of each complex exponential function (with frequency $l\Delta f$) that makes up the original function $g(n\Delta t)$:

$$g(n\Delta t) = \sum_{k=0}^{N-1} \left(\tilde{g}(l\Delta f) e^{2\pi i \frac{ln}{N}} \right) \qquad (4.6)$$

The latter is referred to as the inverse discrete Fourier transform.

Calculating the discrete Fourier transform according to Eq. (4.5) requires a total of $O(N^2)$ operations. Advanced algorithms were developed that require only $O(NlogN)$ operations. These are fast Fourier transformation FFT algorithms. Considering that N is most often in the thousands, the FFT algorithms lead to a significant reduction of the calculation time. Famous MIT mathematician Gilbert Strang described the FFT algorithm as: "The most important numerical algorithm in our lifetime".

The *fft* function in MATLAB© is extensively used in this PhD work. The function is based on the FFTW library [16]. Using the *fftshift* function, the zero-frequency component is shifted to the middle of the spectrum. The resulting frequency axis is found as:

$$f(l) = l\Delta f$$
$$\text{with } \begin{cases} l = -\dfrac{N-1}{2}, -\dfrac{N-3}{2}, \dots, 0, \dots, \dfrac{N-3}{2}, \dfrac{N-1}{2} & \text{if } N \text{ odd} \\ l = \dfrac{N}{2}, -\dfrac{N-2}{2}, -\dfrac{N-4}{2}, \dots, 0, \dots, \dfrac{N-4}{2}, \dfrac{N-2}{2} & \text{if } N \text{ even} \end{cases} \tag{4.7}$$

For real valued time responses, the negative part of the spectrum ($l < 0$) can be ignored as it does not provide any extra information. The maximum frequency for which useful information is found equal $f_{max} < \frac{f_{sampling}}{2}$ (Nyquist-Shannon's sampling theorem).

The velocity frequency spectra, obtained through FFT, were already presented in Figure 4.10 (b). The local maxima of the average spectra correspond to plate resonances as shown in Figure 4.10 (c).

4.2. 3D (Fast) Fourier Transform

Most often, (fast) Fourier transformations are performed on one-dimensional datasets, e.g. a piece of music. In this PhD work, each of the velocity datasets (V_X, V_Y and V_Z) obtained with the SLDV is three-dimensional. The dimensions are (i) the X-coordinate or horizontal position of the scan point, (ii) the Y-coordinate or vertical position of the scan point and (iii) the time instance. The discrete Fourier transformation can be applied simultaneously along all three dimensions:

$$\begin{aligned}&\tilde{V}(r\Delta k_x, s\Delta k_y, l\Delta f) \\ &= \frac{1}{N_x . N_y . N} \sum_{p=0}^{N_x-1} \left(\sum_{q=0}^{N_y-1} \left(\sum_{n=0}^{N-1} \left(V(p\,\Delta x, s\,\Delta y, n\,\Delta t) e^{-2\pi i \frac{l\,n}{N}} \right) e^{-2\pi i \frac{s\,q}{N_y}} \right) e^{-2\pi i \frac{r\,p}{N_x}} \right)\end{aligned} \tag{4.8}$$

with $\Delta k_x = \frac{1}{\Delta x}$ and $\Delta k_y = \frac{1}{\Delta y}$ the horizontal and vertical wavenumber resolution, Δx and Δy the horizontal and vertical distance between successive scan points and N_x and N_y the number of scan points along the horizontal and vertical directions. Similar to the 1D case, MATLAB is used to perform the multi-dimensions fast Fourier transformation using the built-in *fftn* function. Again, the *fftshift* function is used to shift the zero-frequency and zero-wavenumber components to the middle of the spectrum. The wavenumber axes $k_x(r\Delta k_x)$ and $k_y(s\Delta k_y)$ are found in an identical way as the frequency axis (see Eq. (4.7)) and Shannon's sampling theorem states: $k_x^{max} < \frac{1}{2\Delta x}$, $k_y^{max} < \frac{1}{2\Delta y}$.

The 3D FFT requires a 3D dataset with equidistance sampling along each dimension. This often requires an additional processing step where the spatially distributed SLDV measurement data is mapped upon the required equidistance grid of point. Alternatively, a more computational intensive non-uniform Fourier transform can be used [17, 18].

For the 3D Fourier transformation, the negative parts of the wavenumber spectra must be retained. The components for which $k_x < 0$ and $k_y < 0$, correspond to waves propagating from right to left, and waves propagating from top to bottom of the test specimen, respectively. Vice versa, positive wavenumber components are related to waves travelling from left to right and from bottom to top. This characteristic is exploited for localization of the sources of propagating waves, as will be shown in Chapter 8 Section 5.1 and in Chapter 14.

Here, the 3D FFT is again performed for the typical SLDV measurement discussed in Section 3.2. Figure 4.15 presents the resulting wavenumber-frequency maps for the in-plane horizontal velocity $\tilde{V}_X$, the in-plane vertical velocity $\tilde{V}_Y$ and the out-of-plane velocity $\tilde{V}_Z$, along $k_y = 0$ (i.e. waves travelling in the horizontal X direction). These wavenumber-frequency maps reveal the dispersion curves of the A_0, S_0, SH_0, A_1 and SH_1 modes as lines of increased intensity. In addition, plate resonances lead to an additional increase in local intensity as indicated on Figure 4.15 (a).

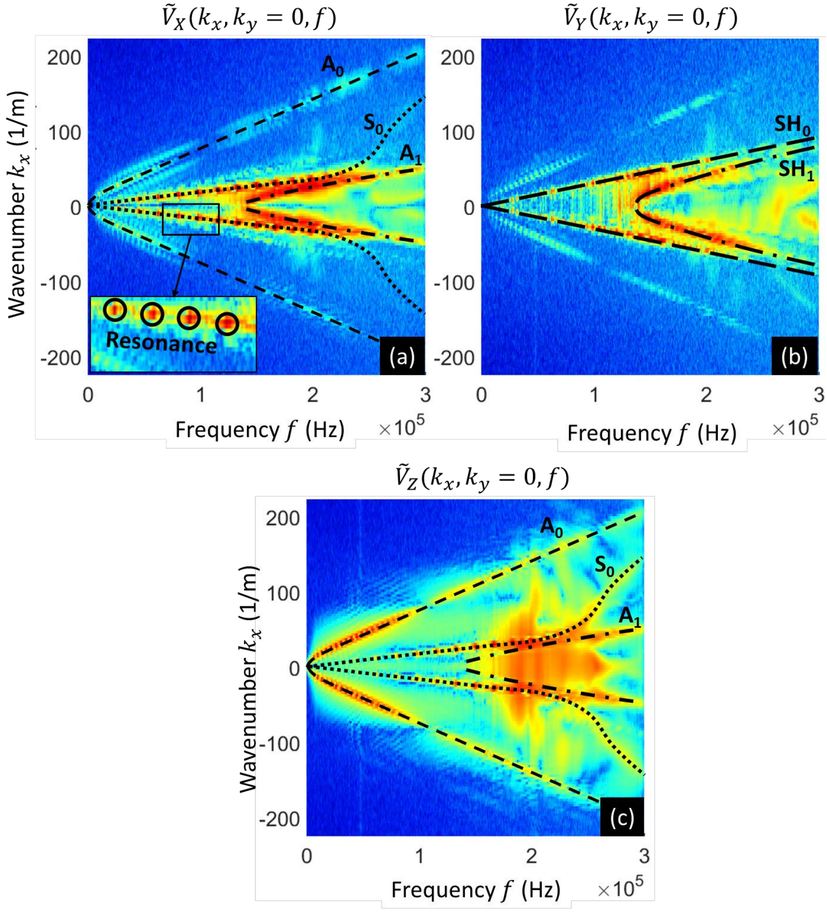

Figure 4.15: Wavenumber-frequency map along k_y = 0 for (a) In-plane horizontal $\tilde{V}_X$, (b) In-plane vertical $\tilde{V}_Y$ and (c) Out-of-plane $\tilde{V}_Z$ velocity component.

4.3. Short-Time-Fourier Transform

In some cases, it is desired to obtain the instantaneous frequency content of the signal in function of the signal length. Therefore, the short-time-Fourier-transformation STFT can be used. As the name indicates, the total signal is split up into multiple short time-divisions. The spectrum of each time-division is obtained through the Fourier transformation. The output of the STFT is a dataset with both a time and a frequency axis. This data representation is often referred to as the *spectrogram*.

The STFT of time sequence $g(n\Delta t)$ is calculated as:

$$\tilde{g}(lH\Delta t, k\Delta f) = \frac{1}{M}\sum_{m=1}^{M} g^l(m\Delta t)\ e^{-2\pi i\frac{mk}{M}}$$

$$\text{with } g^l(m\Delta t)\ =\ g((m+lH)\Delta t)\, w(m)$$

where L is the number of time-divisions and each time-division is represented by index $l = 1,2 \dots L$. M is the length of each time-division expressed in number of samples, while $m = 1,2 \dots M$ is the local time index within each time-division l. H is the hop size or distance between successive time-divisions, expressed in number of samples. The array $w(m)$ is a Hanning window that is multiplied with each time-division l to avoid spectral leakage (see Section 4.4). The output after the STFT is denoted as $\tilde{g}(lH\Delta t, k\Delta f)$ in which $k = 1,2 \dots K$ is the frequency index and $K = \frac{M}{2}$ (Nyquist–Shannon sampling theorem).

The STFT is performed in Matlab following the implementation proposed in reference [19]. As an example, Figure 4.16 (a) shows the obtained spectrogram of the out-of-plane velocity response, averaged over all scan points. The applied sine sweep excitation from 5 to 300 kHz results in a straight line of increased amplitude as indicated on the spectrogram.

The STFT was performed using a hop size H = 26, window length M = 256 and number of time divisions $L = 1 + \left\lfloor \frac{N-M}{H} \right\rfloor$ = 375 (with N = 10 000, total number of time samples).

Similar to IFFT, the inverse STFT (ISTFT) allows to transform the signal $\tilde{g}(lH\Delta t, k\Delta f)$ from the time-frequency domain back to the time domain:

$$g^l(m\Delta t) = \sum_{k=1}^{K} \tilde{g}(lH\Delta t, k\Delta f) \,.\, e^{2\pi i\frac{m\,k}{K}}$$

$$\rightarrow g(n\Delta t) = \frac{H}{E_{wv}}\sum_{l=1}^{L} g^l((n-lH)\Delta t)\, w(n-lH)\, v(n-lH)$$

The time-divisions g^l are shifted in time $(m = n - lH)$ and added in order to obtain the original signal $g(n\Delta t)$. $E_{wv} = \sum_{m=1}^{M} w(m)\, v(m)$ is the mutual energy in the analysis window w and the synthesis window v. The synthesis window v must be chosen carefully to fulfill the correct overlap-and-add (OLA) conditions [19]:

$$\sum_{l=1}^{L} w(n-lH)\, v(n-lH) = \text{constant} = \frac{E_{wv}}{H} \tag{4.9}$$

Here, a Hanning window is used for both w and v. The OLA requirement is met as shown in Figure 4.16 (b).

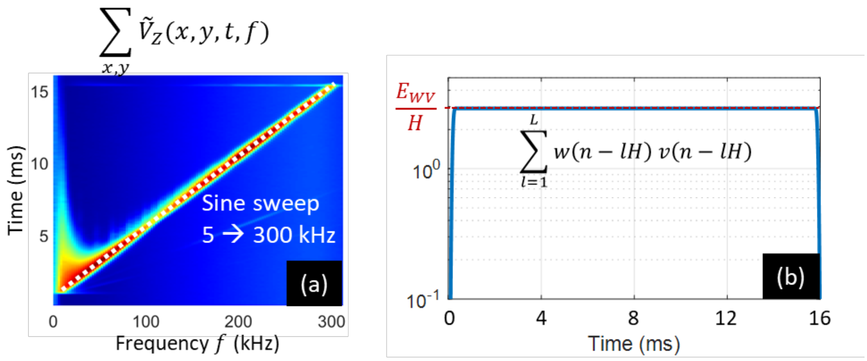

Figure 4.16: (a) STFT (i.e. spectrogram) of the out-of-plane sine sweep velocity response recorded by the SLDV and (b) Verification of the OLA requirement for ISTFT.

4.4. Leakage and Windowing

The discrete Fourier transform, and the associated FFT and STFT algorithms, assume that the signal is periodic in the observation window. If this is not the case, the energy at actual signal frequencies (or wavenumbers) is spread (or 'leaked') to nearby frequencies (or wavenumbers) causing a significant leakage error.

The leakage error must be avoided by making sure that the signal is periodic in the observation window. Along the time-axis, this periodicity can be achieved by a proper selection of the input excitation signal. For instance, a burst type excitation signal minimizes the leakage problem. A burst signal is derived from any standard excitation signal, such as a sweep, by truncating the first and the last part of the observation window with zeros. If the length of this truncation is long enough, the measured vibrations will be zero at the start and at the end (due to material damping) of the observation window. As a result, a periodic signal is obtained. Figure 4.17 (a) shows a typical burst sweep excitation signal used in this PhD work. The signal is zero over the first 5% and the last 5% of its length. The corresponding vibrational response is shown in Figure 4.17 (b). Indeed, the vibrations are able to die out before the measurement is ended and the measurement at the next scan point is started.

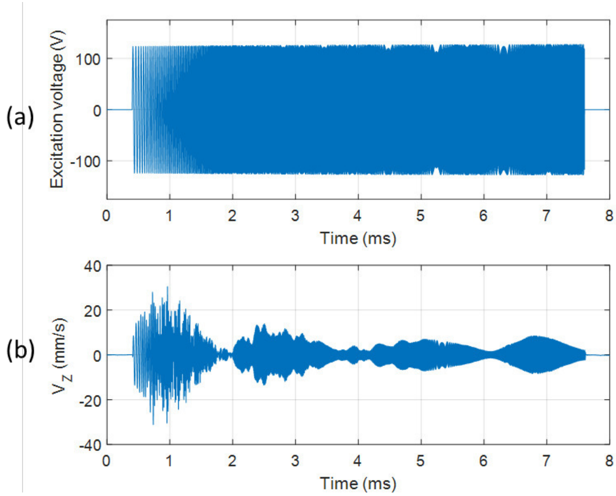

Figure 4.17: (a) Typical burst sweep excitation signal and (b) out-of-plane velocity response.

Along the spatial-axes (x,y), the leakage problem must be solved in a different way. Here, the finite spatial dimensions of the test specimen form a problem. It is practically impossible to add material to all free edges of the component to allow the propagating waves to die out. As a result, a software approach is required to force the velocity response to zero near the edges. Windows are constructed and multiplied with the dataset (before the FFT is performed). Typical windows are shown in Figure 4.18, i.e. a 1D Hanning, a 1D Tukey and a 2D (spatial) Tukey window. The Tukey window is also called a tapered-cosine window and has cosine factor 0.8. Multiplication of the window with the dataset (before the FFT is performed) forces the start and end points to zero, thereby reducing the leakage error.

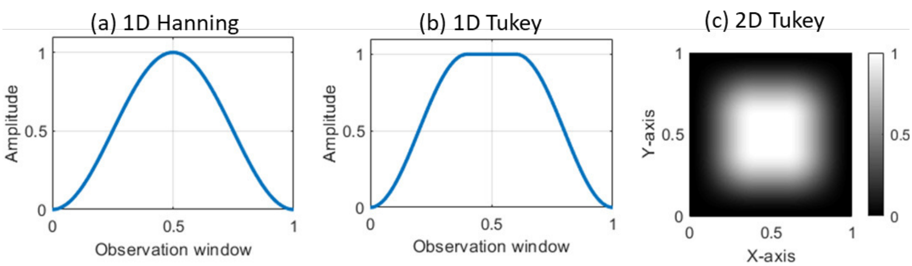

Figure 4.18: Reducing leakage using windows (a) 1D Hanning window, (b) 1D Tukey window with cosine factor 0.8 and (c) 2D Tukey window with cosine factor 0.8.

4.5. Zero padding

For a 1D time response, the frequency axis after FFT transform has a resolution equal to $\Delta f = \frac{f_s}{N}$. A straightforward way to increase the frequency resolution is to first truncate (or 'pad') the end of the signal with zeros. This zero-padding procedure artificially increases the number of samples N, resulting in the desired increase in frequency resolution after FFT calculation. Zero-padding can be equally performed along the spatial dimensions in order to increase the resolution of the k_x and k_y axes. Apart from increasing the frequency and wavenumber resolutions, zero-padding may be used to avoid wraparound errors [20].

5. Conclusion

The experimental protocol for generation and acquisition of guided elastic waves in thin-walled plates is presented.

First, the wave generation capability of piezoelectric actuators is explained. Piezoelectric actuators excite waves of relatively high amplitude and are cheap. The performance of different piezoelectric actuators is compared.

Next, it is illustrated how a scanning laser Doppler vibrometer is perfectly suited for acquisition of full wavefield responses. The total velocity tensor $[V_X, V_y, V_z]$ is obtained in a non-contact manner. Through a parametric study of the SLDV's measurement noise level, it is shown that the sampling frequency and laser's incident angles must be chosen with care. In addition, noise reduction using retroreflective tapes and averages is illustrated.

Analyzing vibrational responses often happens in the frequency and wavenumber domain. As a result, the discrete Fourier transform, and associated FFT and STFT algorithms, are extensively used in this PhD work.

References

1. Mei, H., et al., *Recent Advances in Piezoelectric Wafer Active Sensors for Structural Health Monitoring Applications.* Sensors (Basel, Switzerland), 2019. **19**(2).
2. Kamal, A. and V. Giurgiutiu, *Shear horizontal wave excitation and reception with shear horizontal piezoelectric wafer active sensor (SH-PWAS).* Smart Materials and Structures, 2014. **23**(8).
3. Huan, Q., M. Chen, and F. Li, *A practical omni-directional SH wave transducer for structural health monitoring based on two thickness-poled piezoelectric half-rings.* Ultrasonics, 2019. **94**: p. 342-349.

4. Su, Z. and L. Ye, *Selective generation of Lamb wave modes and their propagation characteristics in defective composite laminates.* Materials: Design and Applications, 2003. **218**.
5. Fu, T., et al., *Sector Piezoelectric Sensor Array Transmitter Beamforming MUSIC Algorithm Based Structure Damage Imaging Method.* Sensors (Basel, Switzerland), 2020. **20**(5).
6. Vancoillie, T., *Investigation on Local Defect Resonance in Delaminated Composites: Optimized Excitation and Controlled Defect Introduction*, in *Faculty of Engineering and Architecture*. 2020, Ghent Univeristy: Ghent.
7. Guan, M.J. and W.H. Liao, *On the Equivalent Circuit Models of Piezoelectric Ceramics.* Ferroelectrics, 2009. **386**(1): p. 77-87.
8. Castaings, M. and P. Cawley, *The generation, propagation, and detection of Lamb waves in plates using air-coupled ultrasonic transducers.* J. Acoust. Soc. Am. , 1996. **100**: p. 3070-3077.
9. Neuenschwander, J., R. Furrer, and A. Roemmeler, *Application of air-coupled ultrasonics for the characterization of polymer and polymer-matrix composite samples.* Polymer Testing, 2016. **56**: p. 379-386.
10. Solodov, I., A. Dillenz, and M. Kreutzbruck, *A new mode of acoustic NDT via resonant air-coupled emission.* Journal of Applied Physics, 2017. **121**(24).
11. Jurek, M., et al., *Non-contact excitation and focusing of guided waves in CFRP composite plate by air-coupled transducers for application in damage detection.* Procedia Structural Integrity, 2018. **13**: p. 2089-2094.
12. Davies, S.J., et al., *Laser-generated ultrasound: its properties, mechanisms and multifarious applications.* Journal of Physics D: Applied Physics, 1993. **26**(3): p. 329-348.
13. Prislan, R., *Laser Doppler vibrometry and modal testing*, in *Faculty of mathematics and physics*. **2008**, University of Ljubljana: Ljubljana,.
14. Johansmann, M., G. Siegmund, and M. Pineda, *Targeting the Limits of Laser Doppler Vibrometry.* Polytec, 2005.
15. Hasheminejad, N., et al., *A Comparative Study of Laser Doppler Vibrometers for Vibration Measurements on Pavement Materials.* Infrastructures, 2018. **3**(4).
16. Frigo, M. and S.G. Johnson. *FFTW: an adaptive software architecture for the FFT.* in *IEEE International Conference on Acoustics, Speech and Signal Processing, ICASSP '98* 1998. Seattle USA: IEEE.
17. Greengard, L. and J.-Y. Lee, *Accelerating the Nonuniform Fast Fourier Transform.* SIAM Review, 2004. **46**(3): p. 443-454.
18. Spytek, J., et al., *Multi-resolution non-contact damage detection in complex-shaped composite laminates using ultrasound.* NDT & E International, 2020. **116**.
19. Zhivomirov, H., *On the Development of STFT-analysis and ISTFT-synthesis Routines and their Practical Implementation.* TEM, 2019. **8**(1): p. 56-64.
20. Gopalakrishnan, S., M. Ruzzene, and S. Hanagud, *Computational Techniques for Structural Health Monitoring*. Series in Reliability Engineering. 2011: Springer.

Part 2:

Local Defect Resonance Based Damage Detection

Chapter 5

Local Defect Resonance for Different Damage Types

Summary:

Local defect resonance (LDR) makes use of high frequency vibrations to get a localized resonant activation of the defect. A distinction can be made between out-of-plane LDR and in-plane LDR. First, an analytical framework is established which allows to estimate the LDR frequencies for simple defects in isotropic materials. The framework assumes flexural and axial wave behavior for the out-of-plane and the in-plane LDRs, respectively. Next, it is shown how linear finite element simulations can be used for LDR prediction when dealing with more complex materials or defects. In addition, experiments are performed for various samples and damage features. In-plane and out-of-plane LDRs are manually identified in the full wavefield response of the test specimens.

Section 4 of this chapter is in close correspondence with journal publication:

[1] Segers, J., Kersemans, M., Hedayatrasa, S., Calderon, J., and Van Paepegem, W. *Towards in-plane local defect resonance for non-destructive testing of polymers and composites.* NDT & E International, 2018 **98**.

1. Introduction

In Chapter 2, the guided elastic waves in thin-walled structures were investigated and the dispersion equations for the shear horizontal, anti-symmetric and symmetric modes were derived. It was shown that these guided elastic waves reflect at the structure's free edges which resulted in the formation of standing waves and resonances (See Chapter 2 Section 5.2). Wave reflections also take place when a propagating wave meets a defect [2]. As a result, standing waves and resonances may form at the location of the defect. This phenomenon is referred to as local defect resonance LDR.

Local defect resonance was already described by Tenek et al. in 1993 [3]. They observed LDR at a delamination in a CFRP laminate and indicated that the LDR phenomenon shows great potential for use in NDT. Later on, other research groups encountered LDR. For instance, Jenal et al. [4] observed LDR in a delaminated CFRP using a SLDV. Also Sarens et al. [5] noted that, at specific excitation frequencies, resonance patterns form at the location of a delamination. They used a shearographic inspection system and indicated that the LDR phenomenon may lead to efficient generation of nonlinear components through contact acoustic nonlinearity at the defect.

In 2011, Solodov et al. [6] introduced the name 'local defect resonance'. Solodov showed (using SLDV measurements) that LDR could be observed at a delamination and confirmed that the LDR increases the generation of nonlinear higher harmonics. In addition, Solodov illustrated that heat is generated at a delamination defect under LDR conditions, which makes it visible using a sensitive thermographic camera. In subsequent years, Solodov published a large variety of papers on LDR. Part of the papers were focused on the analysis of LDR in the linear regime, including analytical derivations of the LDR frequency for simplified defects [7, 8]. Other paper focused on the defect nonlinearity and local heating, which was significantly enhanced by LDR [9, 10].

Nowadays, LDR is a hot topic and it is being investigated by multiple research groups. Fierro and Dionysopoulos et al. [11-14] exploited the concept of LDR for defect detection based on nonlinear vibrations and generated heat. Hetller et al. [15] developed a method for automated detection and sizing of a FBH and a delamination under LDR conditions. Pieczonka and Klepka et al. [16, 17] showed that the LDR at a barely visible impact damage (BVID) enhances nonlinear wave modulation. Derusova et al. [18] provided additional experimental proof of LDR at BVID. They showed that resonant air-coupled emissions appear around a defect under LDR, which was also observed by Solodov [19]. Roy et al. [20] illustrated that bicoherence analysis allows to identify LDR frequencies in the output spectrum of a defected component.

The traditional concept of LDR handles the out-of-plane vibrational response of the thin-walled structures. However, in this chapter it is illustrated that similar local resonances appear for the in-plane velocity, resulting in the concept of in-plane LDR [1].

During this PhD work, extensive research is performed towards the concept of LDR and the use of it for NDT of composite components [1, 21-24]. This part (i.e. Part 2) of the PhD dissertation describes the resulting interesting findings and developments.

To start, the concept of LDR is illustrated with an experiment. The broadband vibrational response is obtained for a 330x330x5.45 mm^3 plate manufactured out of 24 layers of unidirectional carbon fiber prepreg according to quasi-isotropic stacking sequence $[(45/0/-45/90)_3]_s$. An artificial defect is introduced in the plate in the form of a flat bottom hole FBH. The FBH has a diameter of 15 mm and a remaining material thickness of 1.5 mm. The broadband vibrations (i.e. sweep from 1 to 100 kHz) are excited with a piezoelectric actuator attached at the center of the plate. The SLDV measures the full wavefield response of the plate from the side where the FBH defect is not visible. The test specimen is shown in Figure 5.1 (a).
Figure 5.1 (b) shows the resulting frequency response function FRF of the out-of-plane velocity component V_Z at the location of the FBH defect (i.e. orange curve) together with the average FRF of the total wavefield (i.e. blue curve). In the lower frequency regime, pronounced local maxima are observed in the average FRF. Figure 5.1 (c-d) show the out-of-plane velocity amplitude at two local maxima (i.e. 10 kHz and 26 kHz). In both cases, a resonance of the plate is observed. For higher frequencies, the plate resonances are tempered by the increased damping of the waves and the average FRF smoothens. On the other hand, the local FRF at the FBH defect still shows multiple resonance peaks in the higher frequency range. For example, Figure 5.1 (e) shows the out-of-plane velocity amplitude at 40 kHz, in which the out-of-plane LDR is clearly observed.

In this Chapter, we take a closer look at the concept of LDR. First, an analytical framework is developed based on flexural and axial waves. The flexural waves give rise to out-of-plane LDRs, such as the LDR of the FBH in Figure 5.1 (e). The axial waves trigger in-plane LDRs. Hereafter, the out-of-plane and in-plane LDRs are referred to as LDR_Z and LDR_{XY}. Next, it is illustrated how numerical finite element methods allow for accurate investigation of LDR behavior in more complex cases (e.g. multi-layered anisotropic composites). At last, the LDR_Z and LDR_{XY} is experimentally investigated for typical damage types in CFRP components.

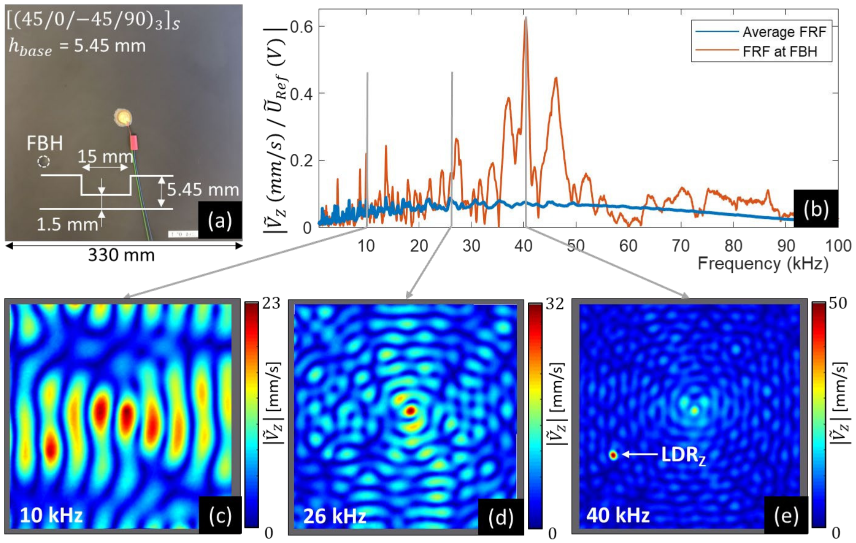

Figure 5.1: Out-of-plane LDR behavior of a flat bottom hole in a CFRP plate (a) Backside of test Specimen, (b) Frequency response function at defect and averaged over the total plate, (c-e) Out-of-plane velocity amplitude at 10 kHz, 26 kHz and 40 kHz.

2. Analytical Prediction of LDR Frequency

The analytical (closed-form) description of the LDR phenomenon is impossible without making stringent assumptions. Therefore, two specific cases are considered here: (i) Flexural waves in isotropic plates according to Love-Kirchhoff theory for the description of LDR$_Z$ and (ii) Axial waves in isotropic plates without out-of-plane displacement for the description of LDR$_{XY}$. In both cases, plane stress conditions are assumed for the thin-walled plates. The consecutive equations for plane stress ($\sigma_{22} = 0$) in isotropic materials are [25]:

$$\begin{cases} \sigma_{11} = \dfrac{E}{1-\nu^2}(\varepsilon_{11} + \nu\varepsilon_{33}) \\ \sigma_{33} = \dfrac{E}{1-\nu^2}(\varepsilon_{33} + \nu\varepsilon_{11}) \\ \sigma_{13} = \dfrac{E}{1+\nu}\varepsilon_{13} \end{cases} \tag{5.1}$$

The coordinate system is shown in Figure 5.2. The following relations hold between this x_1, x_2, x_3 coordinate system and the x, y, z coordinate system that is used for representation of the velocity vector $[V_x, V_y, V_z]$:

$$x_1 \leftrightarrow x,\ x_2 \leftrightarrow z,\ x_3 \leftrightarrow y.$$

2.1. Flexural Waves in Isotropic Materials

Flexural waves comply with the Love-Kirchhoff theory of plate bending which assumes that a straight line normal to the mid-surface axis remains straight after the bending of the plate. The corresponding components of the displacement field, at any position x_2 in the plate's thickness, are given by [25]:

$$\begin{cases} u_1 = -x_2 \dfrac{\partial w}{\partial x_1} \\ u_2 = w \\ u_3 = -x_2 \dfrac{\partial w}{\partial x_3} \end{cases} \tag{5.2}$$

Figure 5.2 shows a schematic illustration of the plate under bending with indication of the out-of-plane displacement w, shear forces V and bending moments M. The resulting relevant strains are:

$$\begin{cases} \varepsilon_{11} = -x_2 \dfrac{\partial w^2}{\partial x_1^2} \\ \varepsilon_{33} = -x_2 \dfrac{\partial w^2}{\partial x_3^2} \\ \varepsilon_{13} = -x_2 \dfrac{\partial w^2}{\partial x_1 \partial x_3} \end{cases} \tag{5.3}$$

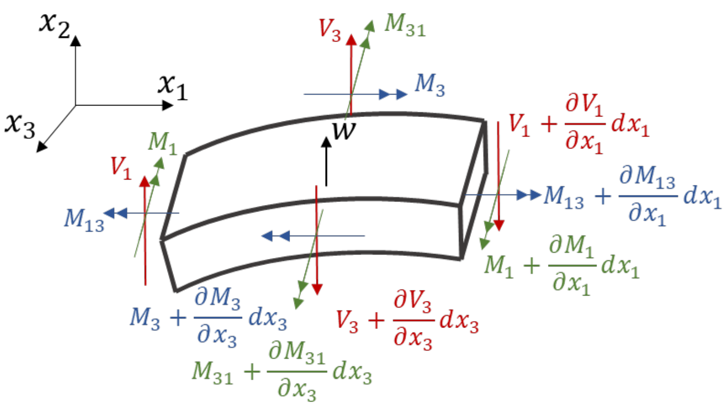

Figure 5.2: Plate element with shear forces and bending moments of interest for flexural wave vibration (reproduced from [25]).

Using Eq. (5.1), the stresses of interest are found as:

$$\begin{cases} \sigma_{11} = -x_2 \dfrac{E}{1-\nu^2}\left(\dfrac{\partial w^2}{\partial x_1^2} + \nu \dfrac{\partial w^2}{\partial x_3^2}\right) \\ \sigma_{33} = -x_2 \dfrac{E}{1-\nu^2}\left(\dfrac{\partial w^2}{\partial x_3^2} + \nu \dfrac{\partial w^2}{\partial x_1^2}\right) \\ \sigma_{13} = -x_2 \dfrac{E}{1+\nu} \dfrac{\partial^2 w}{\partial x_1 \partial x_3} \end{cases} \tag{5.4}$$

The stresses vary linearly over the plate's thickness h. The moments per unit width (see Figure 5.2) are found as:

$$\begin{cases} M_1 = \displaystyle\int_{-\frac{h}{2}}^{\frac{h}{2}} \sigma_{11}\, x_2\, dx_2 = -D_{flex}\left(\dfrac{\partial^2 w}{\partial x_1^2} + \nu \dfrac{\partial^2 w}{\partial x_3^2}\right) \\ M_3 = \displaystyle\int_{-\frac{h}{2}}^{\frac{h}{2}} \sigma_{33}\, x_2\, dx_2 = -D_{flex}\left(\nu \dfrac{\partial^2 w}{\partial x_1^2} + \dfrac{\partial^2 w}{\partial x_3^2}\right) \\ M_{13} = -M_{31} = -\displaystyle\int_{-\frac{h}{2}}^{\frac{h}{2}} \sigma_{13}\, x_2\, dx_2 = (1-\nu) D_{flex} \dfrac{\partial^2 w}{\partial x_1 \partial x_3} \end{cases} \tag{5.5}$$

with D_{flex} the flexural rigidity:

$$D_{flex} = \frac{E\, h^3}{12(1-\nu^2)} \tag{5.6}$$

Summing all the shear forces V and bending moments M indicated on Figure 5.2 gives:

$$\begin{cases} \dfrac{\partial V_1}{\partial x_1} + \dfrac{\partial V_3}{\partial x_3} = \rho h \dfrac{\partial^2 w}{\partial t^2} \\ \dfrac{\partial M_1}{\partial x_1} + \dfrac{\partial M_{31}}{\partial x_3} - V_1 = 0 \\ \dfrac{\partial M_{13}}{\partial x_1} - \dfrac{\partial M_3}{\partial x_3} + V_3 = 0 \end{cases} \tag{5.7}$$

The wave equation for flexural waves is obtained by combination of Eq. (5.5) and (5.7):

$$D_{flex}\left(\frac{\partial^4 w}{\partial x_1^4} + 2\frac{\partial^4 w}{\partial x_1^2 \partial x_3^2} + \frac{\partial^4 w}{\partial x_3^4}\right) + \rho h \frac{\partial^2 w}{\partial t^2} = 0 \tag{5.8}$$

In order to obtain a closed form solution of Eq. (5.8), it is further assumed that the flexural waves are straight-crested with the x_3-axis along the wave crest:

$$\begin{gathered} w(x_1, x_3, t) \rightarrow w(x_1, t) \\ \text{and } \frac{\partial w}{\partial x_3} = 0 \end{gathered} \tag{5.9}$$

As a result, the wave equation (Eq. (5.8)) reduces to:

$$\frac{\partial w(x_1, x_3)}{\partial x_1} \tag{5.10}$$

This wave equation has general solution [25]:

$$\begin{aligned} w(x_1, t) = \mathrm{A}\exp\big(i(\kappa x_1 + \omega t)\big) + \mathrm{B}\exp\big(-i(\kappa x_1 - \omega t)\big) \\ + \mathrm{C}\exp(\kappa x_1 + i\omega t) + \mathrm{D}\exp(-\kappa x_1 + i\omega t) \end{aligned} \tag{5.11}$$

The flexural wave's phase velocity V_{ph}^F is found by substitution of Eq. (5.11) into Eq. (5.10):

$$\begin{aligned} V_{ph}^F = \frac{\omega}{\kappa} = \left(\frac{D_{flex}}{\rho h}\right)^{\frac{1}{4}} \omega^{\frac{1}{2}} \\ = \left(\frac{Eh^2}{12\rho(1-\nu^2)}\right)^{1/4} \omega^{1/2} \end{aligned} \tag{5.12}$$

The flexural wave is dispersive as the phase velocity depends on the frequency.

2.2. Flexural or Out-of-plane LDRz Frequency

In order to find the out-of-plane LDRz frequency of a rectangular defect, it is assumed that the defect behaves as a clamped plate with length a, width b and thickness h. The corresponding boundary conditions are:

$$w = 0 \text{ at } \begin{cases} x_1 = 0 \\ x_1 = a \\ x_3 = 0 \\ x_3 = b \end{cases} \tag{5.13}$$

These boundary conditions are satisfied for all harmonic functions with nodes at the boundaries:

$$w_{mn} = A_{mn} \sin\left(\frac{m\pi x_1}{a}\right) \sin\left(\frac{n\pi x_3}{b}\right) \exp(i\omega t) \text{ with } \begin{matrix} m = 1, 2, \dots \\ n = 1, 2, \dots \end{matrix}$$

Substitution of w_{mn} into the wave equation (5.8) gives:

$$D_{flex}\left[\left(\frac{m\pi}{a}\right)^4 + 2\left(\frac{m\pi}{a}\right)^2\left(\frac{n\pi}{b}\right)^2 + \left(\frac{n\pi}{b}\right)^4\right] w_{mn} - \rho h \omega^2 w_{mn} = 0$$

From the above, the out-of-plane local defect resonance frequency f_{LDR_Z} is obtained:

$$\begin{aligned} f_{LDR_Z} = \frac{\omega}{2\pi} = \frac{1}{2\pi}\left[\left(\frac{m\pi}{a}\right)^2 + \left(\frac{n\pi}{b}\right)^2\right]\sqrt{\frac{D_{flex}}{\rho h}} \\ = \frac{h}{2\pi}\left[\left(\frac{m\pi}{a}\right)^2 + \left(\frac{n\pi}{b}\right)^2\right]\sqrt{\frac{E}{12\rho(1-\nu^2)}} \end{aligned} \tag{5.14}$$

In a similar way, the LDRz frequency of a circular defect with radius r and depth h can be found as [8]:

$$f_{LDR_Z} = \sqrt{\frac{5}{3}}\frac{4h}{\pi r^2}\sqrt{\frac{E}{12\rho(1-\nu^2)}} \tag{5.15}$$

These formulas indicate that the LDRz frequency:

- Scales linearly with the defect's depth $\sim h$
- Scales proportionally to the inverse of the lateral size squared: $\sim \frac{1}{r^2}$ or $\sim \frac{1}{a^2+b^2}$
- Depends on a material property factor: $\sqrt{\frac{E}{\rho(1-\nu^2)}}$

As an example, the fundamental ($m = n$ =1) LDRz frequency of a square 15 mm FBH with thickness 1 mm in an aluminum plate is estimated at 22 kHz.

2.3. Axial Waves in Isotropic Materials

Next to the bending motion of the plate, the plate can also deform in the axial or in-plane direction [25]. In this case, it is assumed that there is zero deformation in the thickness direction. As a result, the displacement field for axial waves corresponds to:

$$\begin{cases} u_1 = u \\ u_2 = 0 \\ u_3 = v \end{cases}$$

Figure 5.3 gives a schematic illustration of a plate element under axial deformation with indication of the in-plane displacements u and v, shear and normal forces N.

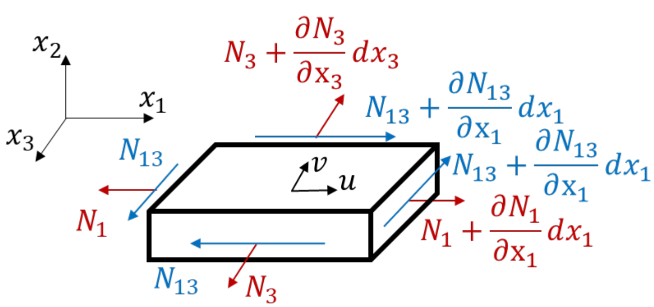

Figure 5.3: Plate element with shear and normal forces of interest for axial wave vibration (reproduced from [25]).

The stress and strain components of interest are found as:

$$\begin{cases} \varepsilon_{11} = \dfrac{\partial u}{\partial \mathrm{x}_1} \\ \varepsilon_{33} = \dfrac{\partial v}{\partial \mathrm{x}_3} \\ \varepsilon_{13} = \dfrac{1}{2}\left(\dfrac{\partial u}{\partial \mathrm{x}_3} + \dfrac{\partial v}{\partial \mathrm{x}_1}\right) \end{cases} \quad \& \quad \begin{cases} \sigma_{11} = \dfrac{E}{1-\nu^2}\left(\dfrac{\partial u}{\partial \mathrm{x}_1} + \nu \dfrac{\partial v}{\partial \mathrm{x}_3}\right) \\ \sigma_{33} = \dfrac{E}{1-\nu^2}\left(\dfrac{\partial v}{\partial \mathrm{x}_3} + \nu \dfrac{\partial u}{\partial \mathrm{x}_1}\right) \\ \sigma_{13} = \dfrac{E}{2(1+\nu)}\left(\dfrac{\partial u}{\partial \mathrm{x}_3} + \dfrac{\partial v}{\partial \mathrm{x}_1}\right) \end{cases}$$

The corresponding normal and shear forces are:

$$\begin{cases} N_1 = \displaystyle\int_{-\frac{h}{2}}^{\frac{h}{2}} \sigma_{11}\, dx_2 = \dfrac{Eh}{1-\nu^2}\left(\dfrac{\partial u}{\partial \mathrm{x}_1} + \nu \dfrac{\partial v}{\partial \mathrm{x}_3}\right) \\ N_3 = \displaystyle\int_{-\frac{h}{2}}^{\frac{h}{2}} \sigma_{33}\, dx_2 = \dfrac{Eh}{1-\nu^2}\left(\dfrac{\partial v}{\partial \mathrm{x}_3} + \nu \dfrac{\partial u}{\partial \mathrm{x}_1}\right) \\ N_{13} = \displaystyle\int_{-\frac{h}{2}}^{\frac{h}{2}} \sigma_{13}\, dx_2 = \dfrac{Eh}{2(1+\nu)}\left(\dfrac{\partial u}{\partial \mathrm{x}_3} + \dfrac{\partial v}{\partial \mathrm{x}_1}\right) \end{cases} \tag{5.16}$$

Making the analogy with flexural waves, an axial rigidity is defined as:

$$D_{axial} = \frac{Eh}{1-\nu^2} \tag{5.17}$$

Newton's second law states:

$$\begin{cases} \dfrac{\partial N_1}{\partial x_1} + \dfrac{\partial N_{13}}{\partial x_3} = \rho h \dfrac{\partial^2 u}{\partial t^2} \\ \dfrac{\partial N_3}{\partial x_3} + \dfrac{\partial N_{13}}{\partial x_1} = \rho h \dfrac{\partial^2 v}{\partial t^2} \end{cases} \tag{5.18}$$

Substitution of the Eq. (5.16) into Eq. (5.18) results in a coupled second-order partial differential equation in the displacements u and v. Finding a solution for this problem is cumbersome. In order to facilitate the mathematical problem, straight-crested axial waves are considered with $v = 0$. In this case, all terms containing v (and its differentials) and N_{13} can be removed from previous equations. As a result, the wave equation for straight crested axial waves is readily obtained as:

$$D_{axial} \frac{\partial^2 u}{\partial x_1^2} = \rho h \frac{\partial^2 u}{\partial t^2} \tag{5.19}$$

The phase velocity V_{ph}^A of this non-dispersive straight crested axial wave is found by substitution of the general solution $u(x_1, t) = A\exp\big(i(\omega t - \kappa x_1)\big) + B\exp\big(i(\omega t + \kappa x_1)\big)$ into Eq. (5.19):

$$\begin{aligned} V_{ph}^A = \frac{\omega}{\kappa} &= \left(\frac{D_{axial}}{\rho h}\right)^{\frac{1}{2}} \\ &= \sqrt{\frac{E}{\rho(1-\nu^2)}} \end{aligned} \tag{5.20}$$

2.4. Axial or In-plane LDRXY Frequency

Again, the defect is represented by a clamped rectangular plate with length a and height h. Note that the width dimension b is omitted here because the axial waves are assumed to be straight-crested and traveling in the defect's length direction. The boundary conditions equate to:

$$u = 0 \quad \text{at} \quad \begin{cases} x_1 = 0 \\ x_1 = a \end{cases} \tag{5.21}$$

These conditions are satisfied when the displacement field equals:

$$u_m = A_m \sin\left(\frac{m\pi x_1}{a}\right) \exp(i\omega t) \text{ with } m = 1,2,\ldots$$

Inserting this trial solution into wave equation (5.19) gives:

$$D_{axial}\left(\frac{m\pi}{a}\right)^2 u_{mn} = \rho h \omega^2 u_m$$

The corresponding condition for in-plane (axial) LDRXY is obtained as:

$$\begin{aligned} f_{LDR_{XY}} &= \frac{1}{2}\left(\frac{m}{a}\right)\sqrt{\frac{D_{axial}}{\rho h}} \\ &= \frac{1}{2}\left(\frac{m}{a}\right)\sqrt{\frac{E}{\rho(1-\nu^2)}} \end{aligned} \tag{5.22}$$

The LDRXY frequency:

- Is invariant of the defect's depth h
- Scales proportionally to the inverse of the defect's lateral size: $\sim\frac{1}{a}$
- Depends on the material property factor: $\sqrt{\frac{E}{\rho(1-\nu^2)}}$

As an example, the fundamental (m=1) LDRXY frequency of an a = 15 mm wide notch in an aluminum plate is estimated at 181 kHz. This LDRXY frequency is significantly higher compared to the corresponding LDRZ (see Section 2.2).

2.5. Validity of the Axial and Flexural Wave Assumptions

First, the assumptions made in the derivation of the dispersion equations for flexural and axial waves are considered. The dispersion curves of both the flexural and the axial waves (Eq. (5.12) and (5.20)) are plotted on Figure 5.4 for an aluminum plate with ρ = 2693 kg/m^3, E = 70 GPa and ν = 0.34. Note that also the Lamb mode dispersion curves are indicated.

At low frequency-thickness ($f.h$ < 250 kHz.mm), the dispersion curve of the flexural wave follows the dispersion curve of the A_0 Lamb mode. A similar correspondence is found between the axial wave and the S_0 Lamb wave, however in this case up to around 1000 kHz.mm. Looking back at the displacement fields of the A_0 and the S_0 Lamb modes, as shown in Chapter 2 Figure 2.9, it is evident that the A_0 and the S_0 Lamb modes correspond to flexural and axial waves (in the low frequency-thickness regime). It was also observed before that the A_0 mode shows a dominant out-of-plane bending (or flexural) motion while the S_0 mode shows a dominant in-plane longitudinal (or axial) motion. This observation indicates that the assumptions made in the derivation of the flexural and axial wave equations are only valid at low frequency-thickness. As a result, the obtained formulas for the LDR_Z and LDR_{XY} frequencies should not be trusted blindly at higher frequency-thickness.

In addition, it is important to elaborate on the defect's boundary conditions. The defect was assumed to be clamped along all the edges (see Eq. (5.13) and (5.21)). For thin defects in a thick plate, the assumption makes sense. On the contrary, for relatively thick defects, the clamping effect of the boundary reduces. This results in an overestimation of the LDR frequency for thick defect. Solodov et al. specified that the use of the clamped boundary condition is permitted for defects with thicknesses smaller than one-tenth of the base material's thickness [7].

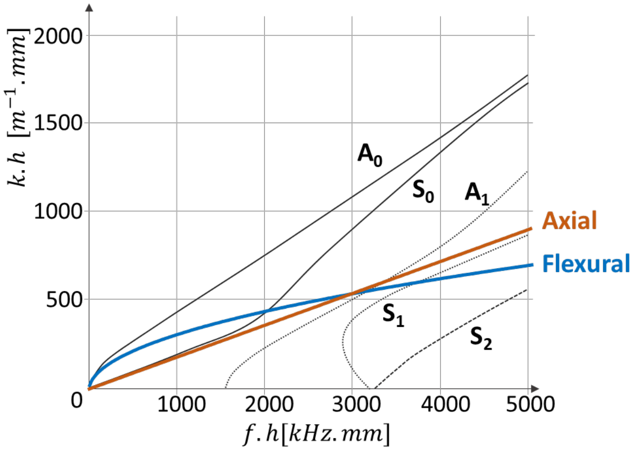

Figure 5.4: Dispersion behavior of axial, flexural and lamb waves in aluminum plate.

3. Finite Element Simulation of LDR

The derived analytical solutions are valuable especially because they provide information on how a certain parameter influences the LDR_Z and LDR_{XY} frequencies. However, the solutions are only valid when all assumptions are satisfied. Moreover, solutions are limited to simple cases of circular, rectangular or elliptical [8] defects in flat isotropic coupons. Finite element methods provide a means for accurate estimation of LDR in more complex structures and for thick defects that do not satisfy the assumptions made in the analytical framework.

A finite element simulation for LDR frequency identification is performed in Abaqus/CAE 2020. The simulation process comprises six big steps (see Figure 5.5):

1. Generate the test coupon:
   Draw the geometry of the test specimen. Here, a 150x200x5.45 mm³ rectangular plate is modelled. Only half of the plate is drawn because symmetric boundary conditions are imposed (see next step). The plate is a model for the test specimen discussed in the introduction. As a result, it consists of 24 layers of CFRP according to stacking sequence $[(45/0/-45/90)_3]_S$. Each unidirectional ply has density ρ, and a stiffness tensor $\bar{\bar{C}}$:

$$\rho = 1528 \frac{kg}{m^3}$$

$$\bar{\bar{C}} = \begin{bmatrix} 122.7 & 6.28 & 6.28 & 0 & 0 & 0 \\ & 13.2 & 6.28 & 0 & 0 & 0 \\ & & 13.2 & 0 & 0 & 0 \\ & & & 3.3 & 0 & 0 \\ & Symm & & & 5.1 & 0 \\ & & & & & 5.2 \end{bmatrix} \text{GPa}$$

   The FBH with diameter 15 mm and remaining material thickness 1.5 mm is accounted for by locally removing 17 plies (see inset on figure).

2. Applying the loads:
   The test specimen is allowed to vibrate freely, and thus, there are no external forces. Symmetric boundary condition are imposed on the symmetry plane. The use of symmetric boundary conditions, and modelling only half of the component, results in a significant reduction of the computational effort. However, the use of this symmetry condition obstructs the in-plane vertical vibration (V_Y) at the symmetry plane. As a result, it is advised not to use this symmetry condition when the simulation result is used for accurate investigation of in-plane LDRs.

3. Meshing the model:
   The main idea behind all finite element simulations is that a 'complex' structure is converted into a large number of 'simple' elements. The elements can take many forms. In this specific case, 8-node quadrilateral continuum shell elements, with linear shape functions, are used (type SC8R). One layer of elements is used for each ply of the CFRP material. As a result, the element's C-tensor is found by rotating the CFRP material's C-tensor according to the stacking angle of the ply where the element is located. In each element, the relation between nodal stresses and strains is simple and well defined. For this model, a mesh size of 1 mm is used in the plate's width and length directions, resulting in a total number of mesh elements of around 370,000.
   These discrete elements must be small enough to represent the continuous structure accurately. When modelling vibrations, it is advised to use at least 6 elements per wavelength at the highest frequency of interest [26]. For this 5.45 mm thick CFRP material, the wavelength of the A_0 mode at 100 kHz is estimated to be around 13 mm. As a result, there are 13 elements per wavelength which is more than sufficient for accurate simulation of these waves. This was confirmed by a mesh convergence study.

4. Construction of the global mass and stiffness matrix:
   The element's mass and stiffness matrices are grouped together in one global mass matrix M^{MN} and one global stiffness matrix K^{MN} based on the connectivity between the elements' nodes ($M \leftrightarrow N$).

5. Solving the problem:
   The structure's resonances frequencies $\omega = 2\pi f$ and corresponding nodal displacements φ^N are found as the eigenvalues and eigenvectors of the eigenvalue problem:
   $$(-\omega^2 M^{MN} + K^{MN})\varphi^N = 0$$
   The eigenvalue problem is solved in a computational efficient manner using the Lanczos algorithm [27].

6. Analyzing the results:
   All resonance frequencies and corresponding mode shapes are obtained up to a frequency of 100 kHz. The LDR_Z of the FBH defect is manually identified at 39.6 kHz (see Figure 5.5). The frequency is close to the experimentally observed LDR_Z at 40 kHz (see Figure 5.1).

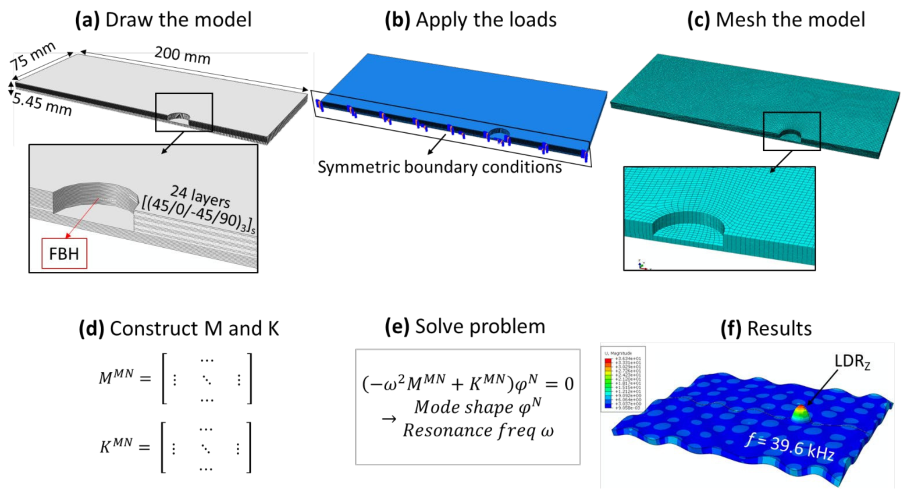

Figure 5.5: Schematic overview of the finite element simulation procedure for LDR identification in a quasi-isotropic CFRP plate.

As a second example, the LDR_Z and LDR_{XY} behavior is determined for a delaminated CFRP plate with cross-ply stacking sequence $[(0/90)_6]_s$. Three different finite element simulations are performed with a Ø 40 mm delamination defect at a depth of 0.675 mm (3 layers), 1.3 mm (6 layers) and 2.3 mm (10 layers). The delaminations are modelled using duplicated overlapping nodes (i.e. a seam crack with no interfacial interactions) in between the two element layers. The manually identified fundamental LDR_Z's and LDR_{XY}'s are shown in Figure 5.6 (a-c) and (d-f), respectively.

The LDR_Z's are triggered at relatively low frequencies. The amplitude of the out-of-plane velocity component is shown in Figure 5.6 (a-c). As analytically predicted, the LDR_Z frequency scales linearly with the depth of the delamination: $\frac{4}{0.675} \approx \frac{7}{1.3} \approx \frac{12}{2.3}$. The LDR_{XY}'s are triggered at significantly higher frequencies. The amplitude of the in-plane velocity component is shown in Figure 5.6 (d-e). The highest LDR_{XY} frequency, i.e. 81 kHz, is observed for the most shallow delamination (i.e. depth of 0.675 mm). The LDR_{XY} frequency decreases slightly to 74 kHz and further to 70 kHz for the delaminations at a depth of 1.3 mm and 2.3 mm. According to the analytical prediction, the LDR_{XY} frequency should be invariant of the delamination's depth. However, the analytical prediction assumed fully clamped boundary conditions at the defect. The thicker the defect, i.e. the deeper the delamination, the more that these clamped boundary conditions should be tempered.

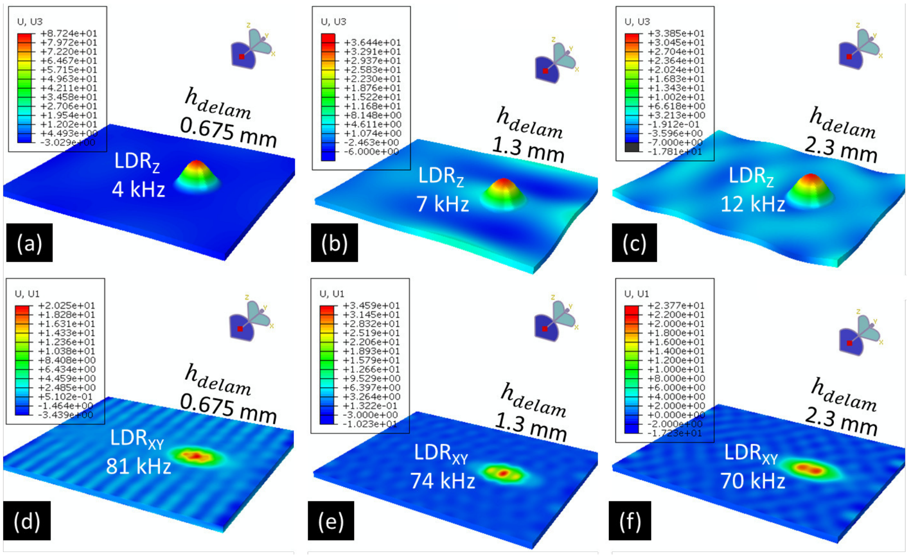

Figure 5.6: (a-c) Out-of-plane LDR_Z mode shape and (d-e) In-plane LDR_{XY} mode shape of a delaminated cross-ply CFRP plate. Delamination diameter 40 mm and depth (a,d) 0.675 mm, (b,e) 1.3 mm and (e,f) 2.3 mm.

4. Experimental Observation of LDR

In this section, five different test specimens are experimentally investigated for out-of-plane and in-plane LDR. The aim is to give an experimental proof-of-concept of LDR for different types of damage. In the next two chapters, a more in-depth investigation is performed towards (i) the automated detection of the LDRs (see Chapter 6) and (ii) the effect of the size and the depth of the defect on the LDR behavior (see Chapter 7).

4.1. Material and Methods

Five different test specimens are inspected for LDR (see Figure 5.7). The first test specimen is a 330x330x5.45 mm^3 CFRP plate with quasi-isotropic lay-up $[(45/0/\text{-}45/90)_3]_s$. Twelve FBH defects are milled into the backside to represent defects. The diameter Ø and the ratio of the remaining material thickness h over the thickness of the plate h_{base} are listed in Figure 5.7 (a).

The second test specimen (see Figure 5.7 (b)) is a 350x350x3 mm^3 (resin-transfer-molded) CFRP plate with cross-ply lay-up $[(0/90)_3]_s$. A total of 12 inserts were introduced in between the layers during the lay-up process. Each insert consists of two layers of 25 μm thin brass foil encapsulated in flash breaker tape. This type of insert is found to accurately model the vibrational behavior of a delamination [28].

The third specimen is a 400x400x5 mm^3 cracked laminated glass panel where the crack of interest starts at the vertical edge and ends at the closest horizontal edge (see Figure 5.7 (c)). The crack only runs in the top glass panel (see inset on the figure), and thus is representative for a surface breaking crack. The measurement area of the transparent glass panel is covered with retroreflective tape.

The fourth specimen is a 150x100x5.5 mm^3 CFRP coupon manufactured from unidirectional carbon fiber layers with layup $[(0/90)_6]_s$ (see Figure 5.7 (d)). A 7.7 kg weight is dropped on the CFRP plate from a height of 0.1 m according to the ASTM D7136 standard. This results in an impact energy of 6.3 J, which introduces barely visible impact damage (BVID). The inset on the figure shows the hair-like surface breaking crack in the middle of the BVID orientated along the X direction.

The fifth and last test specimen is a 250x230x12 mm^3 sandwich plate (see Figure 5.7 (e)). The top and bottom skin plates are 1 mm thick CFRP consisting of 3 layers of twill woven fabric [22 twill - ±45 biax - 22 twill]. The core material is an aluminum honeycomb with core thickness 10 mm, cell size 6.4 mm and cell wall thickness 0.07 mm. The skin plates are bonded to the core using prepreg epoxy sheets. Two defects are present in this sandwich plate. The first defect is a small area of BVID introduced by hammer hitting the top skin panel. This BVID was introduced before the sandwich structure was assembled. The second defect is a disbond between the top skin plate and the core. The disbond is introduced by making a 30x30mm^2 cutout in the epoxy sheet (before the sandwich structure was assembled).

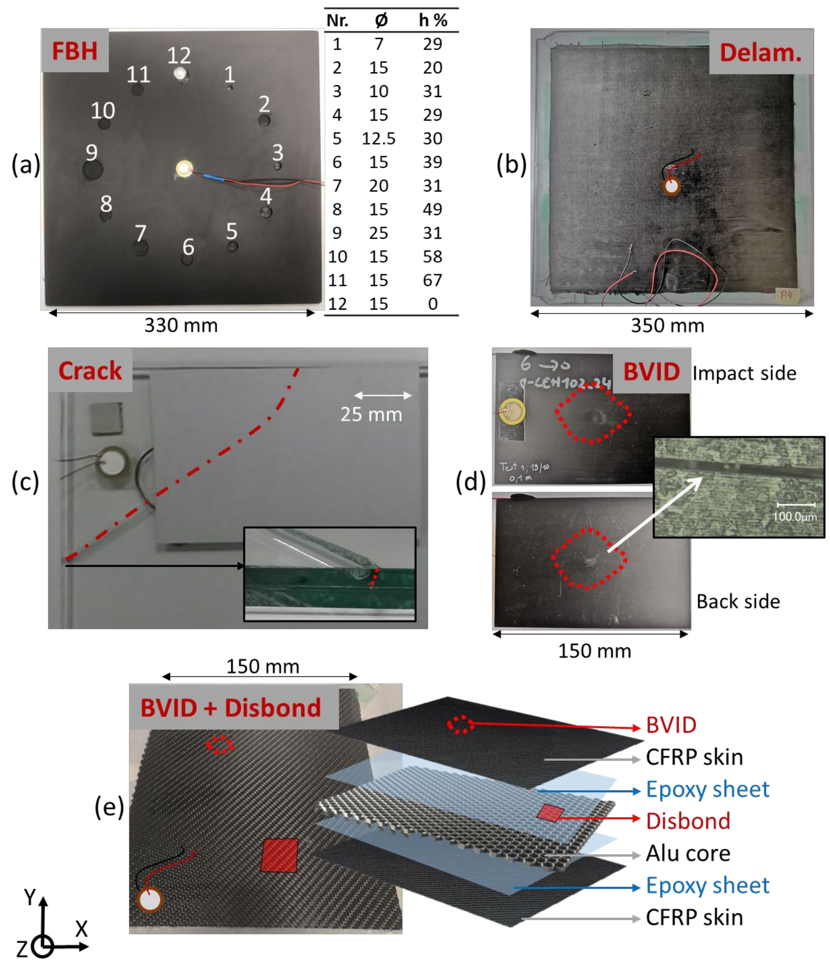

Nr.	Ø	h %
1	7	29
2	15	20
3	10	31
4	15	29
5	12.5	30
6	15	39
7	20	31
8	15	49
9	25	31
10	15	58
11	15	67
12	15	0

Figure 5.7: Defected test samples. (a) Quasi-isotropic CFRP plate with FBHs, (b) Cross-ply CFRP plate with artificial delaminations, (c) Laminated glass panel with crack in top layer, (d) Cross-ply CFRP coupon with BVID and (e) CFRP-Al sandwich panel with BVID and disbond.

All test specimens are excited using low power piezoelectric bending discs (type EPZ-20MS64W from Ekulit). The actuators are visible in Figure 5.7. A broadband sine sweep is used as excitation signal. A Falco System WMA-300 amplifier is employed to increase the energy input, resulting into a peak-to-peak voltage between 50 and 100 V_{pp}.
The in-plane and out-of-plane vibrational response is obtained with the 3D SLDV (Polytec PSV-500-3D Xtra). The out-of-plane component is indicated as V_Z. The two in-plane components in the left-to-right and bottom-to-top direction are indicated as V_X and V_Y, respectively. For all measurements, a uniform scan point

spacing of 2 mm is used. The measured velocity responses are transformed from the time domain to the frequency domain using FFT:

$$V_i(x,y,t) \xrightarrow{FFT} \tilde{V}_i(x,y,f) \text{ with } i = X, Y \text{ or } Z$$

The LDR_Z and LDR_{XY} are manually identified in the broadband frequency responses of the $\tilde{V}_Z$ and $\tilde{V}_X, \tilde{V}_Y$ components, respectively.

4.2. Observation of LDR for Various Defect Types

4.2.1. Flat Bottom Hole Defects

A selection of the observed LDRs at the FBHs is presented in Figure 5.8. LDR_Z is observed in the frequency range 20 to 105 kHz. As an example, the LDR_Z of a FBH with diameter Ø = 15 mm and remaining material thickness h =1.1 mm and of a FBH with Ø = 20 mm and h = 1.7 mm are visible in the out-of-plane velocity map at 30 kHz (see Figure 5.8 (a)). At higher frequencies, the smaller FBHs show their LDR_Z. For instance, the LDR_Z of a Ø = 12.5 mm, h = 1.6 mm FBH is triggered at 55 kHz and the LDR_Z of a Ø = 7 mm, h = 1.6 mm FBH is triggered at 102 kHz (see Figure 5.8 (b) and (c), respectively). In addition, a 3^{th} order LDR_Z of a Ø = 25 mm, h = 1.6 mm FBH is observed in Figure 5.8 (b). The effect of the FBH defect's diameter and thickness on the LDR_Z frequency is in correspondence with the analytical predictions made in Section 2.2.

LDR_{XY} is observed in the frequency range > 95 kHz. Two examples are shown in Figure 5.8 (d,e). Note that in this case, the amplitude of the total in-plane velocity $\sqrt{\tilde{V}_X^2 + \tilde{V}_Y^2}$ is plotted. The LDR_{XY} of the Ø = 25 mm, h = 1.6 mm FBH is observed at 97 kHz (see Figure 5.8 (d)). At 135 kHz, two FBHs of Ø 15 mm and h = 1.1 mm and h = 1.6 mm show their fundamental LDR_{XY}. These experimental observations confirm the analytical predictions made in Section 2.4. The LDR_{XY} frequencies are independent of the defect's depth and they are significantly higher compared to the out-of-plane LDR frequencies.

Only a selection of the observed LDRs is shown here. However, no apparent LDR_{XY} or LDR_Z behavior is found for the two relatively thick FBH defects (h > 50 %).

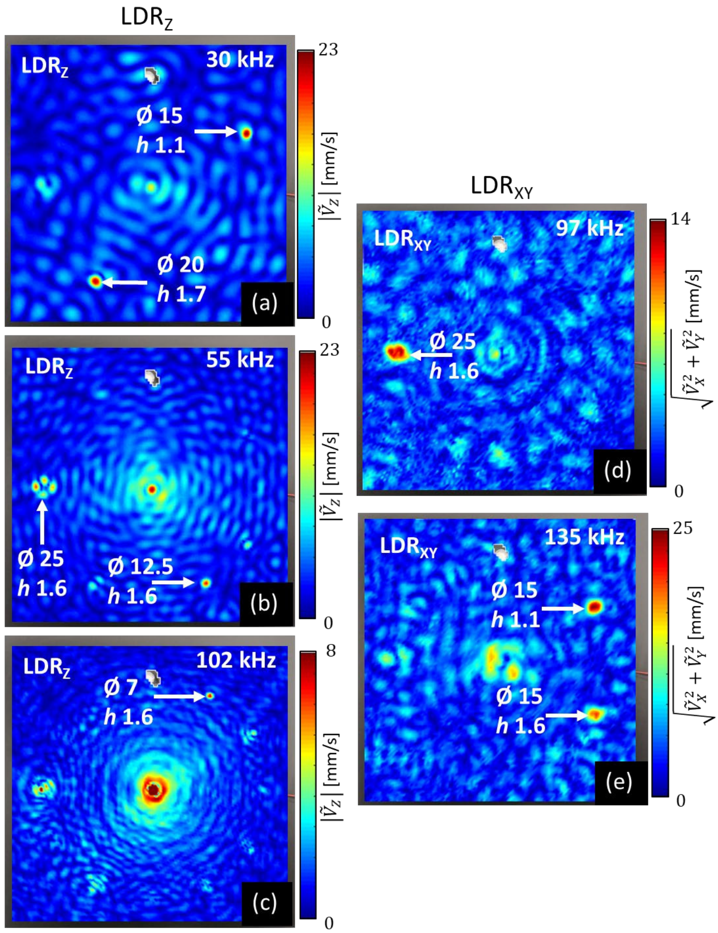

Figure 5.8: LDR of flat bottom holes in quasi-isotropic CFRP plate (a-c) Out-of-plane LDR_Z, (d-e) In-plane LDR_{XY}.

4.2.2. Artificial Delaminations

Figure 5.9 shows a selection of the observed LDRs in the cross-ply CFRP plate with artificial delaminations. The first LDR_Z is triggered at 6.7 kHz (see Figure 5.9 (a)). The delamination corresponding to this LDR_Z has size 20x20 mm^2 and is located in between layer 1 and layer 2 (i.e. shallow). The out-of-plane velocity map at 16 kHz reveals the LDR_Z of a 15x15 mm^2 delamination located in between layer 3 and layer 4 (see Figure 5.9 (b)). A higher order LDR_Z of this delamination is seen in the V_Z map at 39 kHz (see Figure 5.9 (c)). The LDR_{XY}'s pop up in the in-plane velocity amplitude maps. As an example, the LDR_{XY} of a 15x15 mm^2 delamination located in between layer 4 and layer 5 is triggered at 128 kHz (see Figure 5.9 (d)).

Note again that only a selection of the observed LDRs was discussed here and that there are imprints of (high order) LDRs visible at multiple locations in the velocity maps.

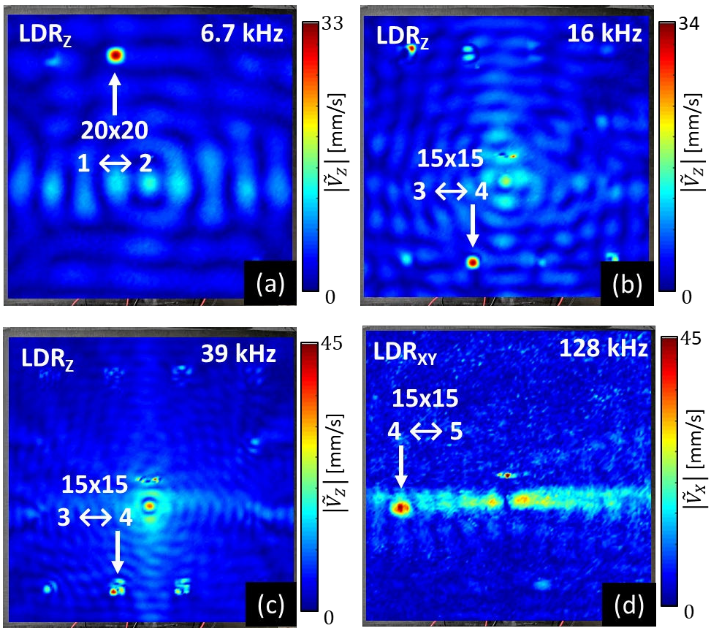

Figure 5.9: LDR of artificial delaminations in cross-ply CFRP plate (a-c) Out-of-plane LDR$_Z$, (d) In-plane LDR$_{XY}$.

4.2.3. Laminated Glass Panel with Surface Breaking Crack

The detectability of surface breaking cracks using in-plane and out-of-plane LDR is investigated by measuring the broadband vibrational response near the tip of the crack running in the top glass panel.

No LDR$_Z$ response could be identified in the considered broadband (0 to 80 kHz) frequency range. On the other hand, a clear LDR$_{XY}$ of the crack tip is found at 52 kHz. The magnitudes of the in-plane $\tilde{V}_Y$ and out-of-plane $\tilde{V}_Z$ components of the velocity response at f_{LDR_Z} = 52 kHz are shown in Figure 5.10 (a) and (b), respectively. In contrast to the out-of-plane component, the in-plane component clearly reveals the position of the crack tip.

The absence of a LDR$_Z$ is attributed to the lack of an in-plane defect interface. After all, an in-plane defect interface results in a reduced out-of-plane bending stiffness (or flexural rigidity) leading to the LDR_Z behavior. On the other hand, a clear LDR_{XY} is found due to the reduced in-plane stiffness caused by the cracks' out-of-plane interface. These results thus indicate that LDR_Z is most sensitive to defects with an in-plane defect interface (e.g. FBHs and delaminations) whereas LDR_{XY} is most sensitive to defects with an out-of-plane defect interface (e.g. surface breaking cracks).

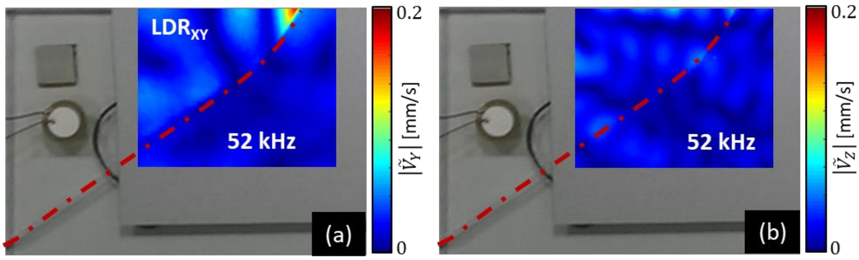

Figure 5.10: In-plane LDR_{XY} of a surface breaking crack running in a laminated glass plate at 52 kHz: (a) Amplitude of in-plane velocity $\tilde{V}_Y$ and (b) Amplitude of out-of-plane velocity $\tilde{V}_Z$.

4.2.4. Barely Visible Impact Damage

Low velocity impact damage in a composite plate manifests itself typically as a complex pattern of delaminations and matrix cracks [29]. The damage is distributed in the area near the impact zone and cannot be considered as a single idealized defect, which obviously complicates the LDR analysis. Indeed, this distributed damage shows LDR behavior over a wider frequency range, with different parts of the damage region resonating together or individually.

Figure 5.11 (a,b) shows the $\tilde{V}_Z$-data for the impact side and the backside of the impacted CFRP plate at f_{LDR_Z} of 25.9 kHz and at 15.8 kHz, respectively. The presence of internal damage is clearly identified. Figure 5.11 (c,d) shows the $\tilde{V}_Y$-data at the same LDR_Z frequencies. The V_Y-data of the backside (Figure 5.11 (d)) shows the opening and closing of a hair-like surface crack running through the center of the damaged area (see inset on Figure 5.7 (d)). The measurement of the in-plane vibrations at the f_{LDR_Z} thus yields an improved defect assessment.

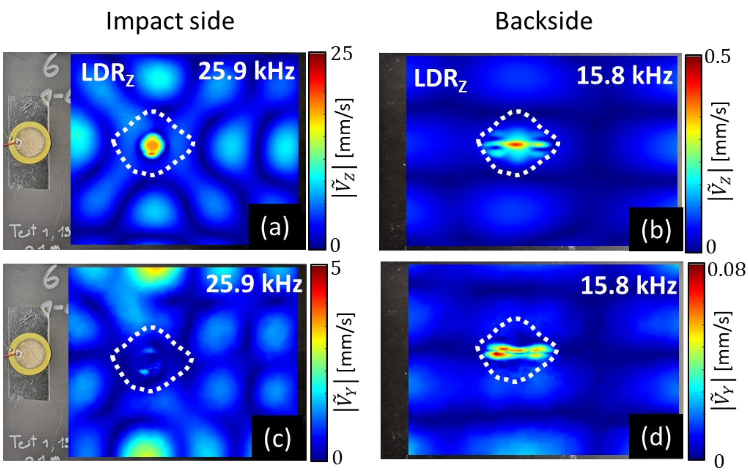

Figure 5.11: Out-of-plane LDRz of BVID in cross-ply CFRP coupon seen from (left) Impact side and (right) Backside. (a,b) Amplitude of out-of-plane velocity $\tilde{V}_Z$ and (c,d) Amplitude of in-plane velocity $\tilde{V}_Y$.

At higher frequencies, multiple LDRXY's are triggered. Due to the asymmetrical damage geometry and the anisotropy of the CFRP material, the vibrations at these LDRXY modes are predominantly along the X-axis, or predominantly along the Y-axis. Figure 5.12 shows four LDRXY modes observed at the backside of the impacted plate. Different zones of the BVID, which are isolated by the horizontal hair-like crack, resonate at different frequencies.
The top region of the defect has a $f_{LDR_{XY}}$ at 65.7 kHz, while the bottom region of the defect has its $f_{LDR_{XY}}$ at 99.8 kHz. The different frequency is related to the fact that top and bottom part of the damaged zone are not identical to each other. Figure 5.12 (c) further shows a higher order LDRXY mode of the top part of the damaged area. The same can be done for the lower region, but the associated frequency was at the limit of our considered excitation bandwidth. Note again the increase in $f_{LDR_{XY}}$ compared to f_{LDR_Z}.
At even higher frequencies (> 150 kHz), LDRXY is found with dominant vibration velocity along the X-axis (see Figure 5.12 (d)). This further increase in frequency is linked to the specific orientation of the hair-like surface crack, which induces higher in-plane stiffness of the damaged area in X-direction compared to in-plane stiffness in Y-direction. Hence, it is clear that from the combined analysis of the LDRXY and LDRz frequencies and corresponding operational deflection shapes, further insight on the internal structure of this complex defect can be obtained.

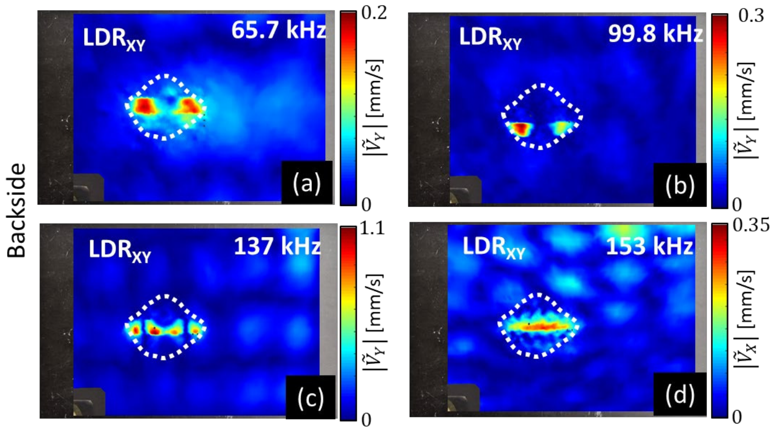

Figure 5.12: In-plane LDR$_{XY}$ of backside of BVID in cross-ply CFRP coupon: (a,c) Amplitude of vertical in-plane velocity $\tilde{V}_Y$ and (d) Amplitude of horizontal in-plane velocity $\tilde{V}_X$.

4.2.5. Skin-Core Disbond and BVID in Sandwich Plate

The last test specimen is the sandwich plate with thin CFRP skins and an aluminum honeycomb core. Already at 4.6 kHz, the disbond resonates in the out-of-plane direction (see Figure 5.13 (a)). At 10 kHz, a second order LDR$_Z$ is observed (see Figure 5.13 (b)). The LDR$_Z$ frequency of the disbond is relatively low because of its large size, i.e. 30x30 mm^2, and because of the limited thickness of the skin plate, i.e. 1 mm. At 29 kHz, LDR$_Z$ is observed at the location of the BVID (see Figure 5.13 (c)). Further, at 146 kHz a vertical LDR$_{XY}$ is triggered at the small BVID (see Figure 5.13 (d)).

The disbond between skin and core material results in a significant reduction of the out-of-plane flexural rigidity but a limited reduction of the in-plane axial rigidity. This is because the aluminum honeycomb core has almost zero stiffness in the in-plane directions. As a result, the disbond exhibits clear LDR$_Z$'s (at rather low frequencies) but it does not show LDR$_{XY}$ behavior.

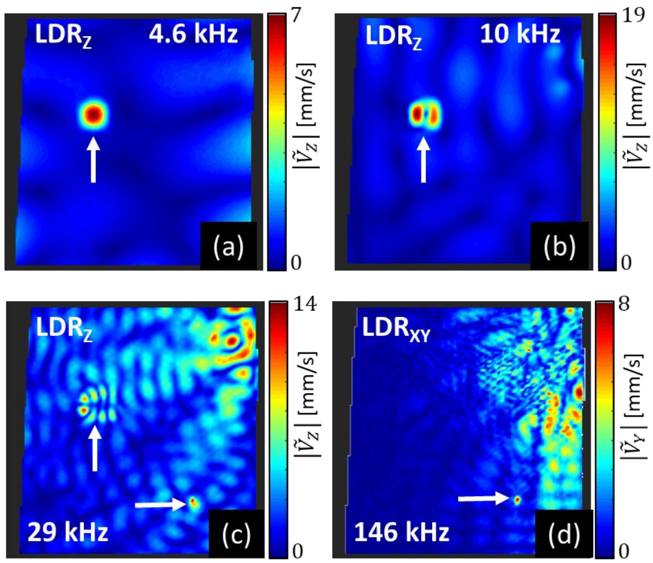

Figure 5.13: LDR_Z and LDR_{XY} in a defected CFRP-Al sandwich plate: (a,b) LDR_Z at disbond, (c) LDR_Z at disbond and at BVID and (d) LDR_{XY} at BVID.

5. Conclusion

The concept of local defect resonance LDR is investigated in an analytical, numerical (i.e. finite element simulation) and experimental manner. The traditional LDR, with dominant displacements in the out-of-plane direction, is extended with the concept of in-plane LDR.

The analytical investigation is based on flexural and axial waves. The dispersion curves of flexural and axial waves are derived and it is illustrated that these waves are a simplified form of the A_0 and S_0 lamb waves, respectively. The defect is represented as a clamped isotropic plate of specific thickness and size. The corresponding out-of-plane and in-plane LDR frequencies are derived by combining the derived flexural and axial wave equations with the assumed clamped boundary conditions. The out-of-plane LDR frequency (f_{LDR_Z}) scales with h/a^2, where h is the local material thickness at the defect and a is the defect's size. The in-plane resonance frequency ($f_{LDR_{XY}}$) scales with $1/a$, and is not affected by the thickness or depth of the defect. The $f_{LDR_{XY}}$'s are typically considerably higher than the f_{LDR_Z}'s.

Finite element simulation proves valuable for accurate identification of LDR behavior, especially for those cases for which the assumptions made in the analytical derivation are not valid. Simulations are performed for a delaminated cross-ply CFRP plate. The results confirm the analytical predicted relation between the defect depth and the LDR frequency.

At last, five different test specimens are experimentally investigated for LDR behavior. Each test specimen has a specific type of damage: flat bottom hole, artificial delamination, surface breaking crack, barely visible impact damage and disbond. Pronounced out-of-plane LDR's are observed at all defects with in-plane interfaces, such as flat bottom holes, delaminations, BVID and disbonds. On the other hand, defects with dominant out-of-plane defect interfaces, such as a surface breaking crack, show a high sensitivity to in-plane LDR.

The observed high amplitude of vibration under LDR conditions is promising for defect detection because:

- The defect can be found by searching for high amplitude spots in the velocity amplitude maps. In Chapter 6, an automated defect detection procedure is proposed based on this observation.
- As explained in Chapter 3, the high amplitude of vibration may trigger a non-classical nonlinear response at the defect. This will be further investigated in Chapter 8.
- In addition, the high vibrational amplitude and potential clapping and/or rubbing of defect interfaces results in vibrational heating at the defect. This is studied in Chapter 9.

However, one has to stay critical. Looking back at the defects for which the LDRs were observed, they are all located relatively close to the surface of the test specimens. In Chapter 7, a parametric study is performed towards the sensitivity of LDR for detection of shallow but also deep damage.

References

1. Segers, J., et al., *Towards in-plane local defect resonance for non-destructive testing of polymers and composites.* NDT & E International, 2018. **98**: p. 130-133.
2. Glushkov, E., et al., *Wave energy trapping and localization in a plate with a delamination.* Smart Materials and Structures, 2012. **21**(12).
3. Tenek, L.H., E.G. Henneke, and M.D. Gunzburger, *Vibration of delaminated composite plates and some applications to non-destructive testing.* Composite Structures, 1993. **23**: p. 253-262.
4. Jenal, B., et al., *Structural Damage Detection Using Laser Vibrometers*, in *NDT in Aerospace* 2010.
5. Sarens, B., et al., *Investigation of Contact Acoustic Nonlinearity in Delaminations by Shearographic Imaging, Laser Doppler Vibrometric*

Scanning and Finite Difference Modeling. IEEE Transactions on Ultrasonics, 2010. **57**(6): p. 1383-1395.

6. Solodov, I., et al., *A local defect resonance to enhance acoustic wave-defect interaction in ultrasonic nondestructive evaluation.* Applied Physics Letters, 2011. **99**(21).
7. Solodov, I., J. Bai, and G. Busse, *Resonant ultrasound spectroscopy of defects: Case study of flat-bottomed holes.* Journal of Applied Physics, 2013. **113**(22).
8. Solodov, I., M. Rahammer, and M. Kreutzbruck, *Analytical evaluation of resonance frequencies for planar defects: Effect of a defect shape.* NDT & E International, 2019. **102**: p. 274-280.
9. Solodov, I., *Resonant Acoustic Nonlinearity of Defects for Highly-Efficient Nonlinear NDE.* Journal of Nondestructive Evaluation, 2014. **33**(2): p. 252-262.
10. Solodov, I., D. Derusova, and M. Rahammer, *Thermosonic Chladni figures for defect-selective imaging.* Ultrasonics, 2015. **60**: p. 1-5.
11. Fierro, G.P.M., et al., *Nonlinear ultrasonic stimulated thermography for damage assessment in isotropic fatigued structures.* Journal of Sound and Vibration, 2017. **404**: p. 102-115.
12. Fierro, G.P.M., et al., *Imaging of Barely Visible Impact Damage on a Complex Composite Stiffened Panel Using a Nonlinear Ultrasound Stimulated Thermography Approach.* Journal of Nondestructive Evaluation, 2017. **36**(4).
13. Fierro, G.P.M. and M. Meo, *A combined linear and nonlinear ultrasound time-domain approach for impact damage detection in composite structures using a constructive nonlinear array technique.* Ultrasonics, 2018. **93**: p. 43-62.
14. Dionysopoulos, D., et al., *Imaging of barely visible impact damage on a composite panel using nonlinear wave modulation thermography.* NDT & E International, 2018. **95**: p. 9-16.
15. Hettler, J., et al., *Detection and Characterization of Local Defect Resonances Arising from Delaminations and Flat Bottom Holes.* Journal of Nondestructive Evaluation, 2017. **36**(1).
16. Pieczonka, L., et al., *Damage imaging in composites using nonlinear vibro-acoustic wave modulations.* Structural Control and Health Monitoring, 2017.
17. Klepka, A., et al., *Impact damage detection in laminated composites by non-linear vibro-acoustic wave modulations.* Composites Part B: Engineering, 2014. **65**: p. 99-108.
18. Derusova, D., et al., *Ultrasonic spectroscopic analysis of impact damage in composites by using laser vibrometry.* Composite Structures, 2019. **211**: p. 221-228.
19. Solodov, I. and M. Kreutzbruck, *Single-sided access remote imaging via resonant airborne activation of damage.* NDT & E International, 2019. **107**.

20. Roy, S., T. Bose, and K. Debnath, *Detection of local defect resonance frequencies using bicoherence analysis.* Journal of Sound and Vibration, 2019. **443**: p. 703-716.
21. Segers, J., et al., *In-plane local defect resonances for efficient vibrothermography of impacted carbon fiber-reinforced polymers (CFRP).* NDT & E International, 2019. **102**: p. 218-225.
22. Segers, J., et al., *Efficient automated extraction of local defect resonance parameters in fiber reinforced polymers using data compression and iterative amplitude thresholding.* Journal of Sound and Vibration, 2019. **463**.
23. Segers, J., et al., *Probing the limits of full-field linear Local Defect Resonance identification for deep defect detection.* Ultrasonics, 2020. **105**.
24. Segers, J., et al., *Backside delamination detection in composites through local defect resonance induced nonlinear source behaviour.* Journal of Sound and Vibration, 2020. **479**.
25. Giurgiutiu, V., *Structural health monitoring with piezoelectric wafer active sensors*. Academic Press. 2008, USA: Elsevier Inc.
26. Langer, P., et al., *More Than Six Elements Per Wavelength: The Practical Use of Structural Finite Element Models and Their Accuracy in Comparison with Experimental Results.* Journal of Computational Acoustics, 2017. **25**(04).
27. Lanczos, C., *An iteration method for the solution of the eigenvalue problem of linear differential and integral operators.* Journal of Research of the National Bureau of Standards, 1950. **45**: p. 255-282.
28. Vancoillie, T., *Investigation on Local Defect Resonance in Delaminated Composites: Optimized Excitation and Controlled Defect Introduction*, in *Faculty of Engineering and Architecture*. 2020, Ghent Univeristy: Ghent.
29. Spronk, S.W.F., et al., *Comparing damage from low-velocity impact and quasi-static indentation in automotive carbon/epoxy and glass/polyamide-6 laminates.* Polymer Testing, 2018. **65**: p. 231-241.

Chapter 6

Automated Detection of Local Defect Resonances

Summary:

A defect resonates when the frequency of excitation matches one of the defect's local defect resonance (LDR) frequencies. The defect can then be localized as an area of increased vibrational amplitude in the full wavefield velocity map. However, one of the major difficulties for applying this LDR concept for NDT, is the proper identification of the required LDR frequency, and the subsequent LDR localization.
In this chapter, post-processing methods are introduced in view of automated extraction of LDR parameters, i.e. LDR frequency and LDR location. In order to reduce the computational effort for large datasets (> 1 GB), various data compression methods have been considered: bandpower calculation (BP), principal component analysis (PCA) and operational modal analysis (OMA). The LDR parameter extraction from the (compressed) data is based on an iterative procedure to adaptively threshold the vibrational amplitudes. The automated LDR parameter extraction procedure is demonstrated on different CFRPs with various defect types: flat bottom holes, inserts and low velocity impact damage.

The chapter is in close correspondence with journal publication:
[1] Segers, J., Hedayatrasa, S., Verboven, E., Poelman, G., Van Paepegem, W. and Kersemans, M. *Efficient automated extraction of local defect resonance parameters in fiber reinforced polymers using data compression and iterative amplitude thresholding.* Journal of Sound and Vibration, 2019. **463**.

1. Introduction and Problem Statement

LDR-based damage detection requires the identification of the damage's LDR frequency. The LDR frequency is function of both material- and defect parameters. This is exactly one of the big challenges with LDR: How to find the LDR frequency for a test sample with unknown material and defect parameters? To demonstrate the difficulty in finding the LDR frequency, the broadband velocity response is measured for a 330x330x5.45 mm^3 cross-ply CFRP plate with a barely visible impact damage (BVID) (see Figure 6.1 (a)). Figure 6.1 (b) displays the average frequency response function (FRF) of the out-of-plane velocity V_Z (i.e. blue curve). There is not a single indication of a LDR phenomenon in this average FRF. By careful manual inspection of the V_Z amplitude maps for all frequencies, a clear LDR$_Z$ behavior of the BVID is discovered at 19 kHz (see Figure 6.1 (c)). This velocity map then provides the location of the defect. Subsequent selection of a measurement point within this BVID yields the nodal FRF displayed in orange in Figure 6.1 (b). Although there are several clear peaks observed, it is still challenging to distinguish between global mode shapes and LDR$_Z$ behavior.

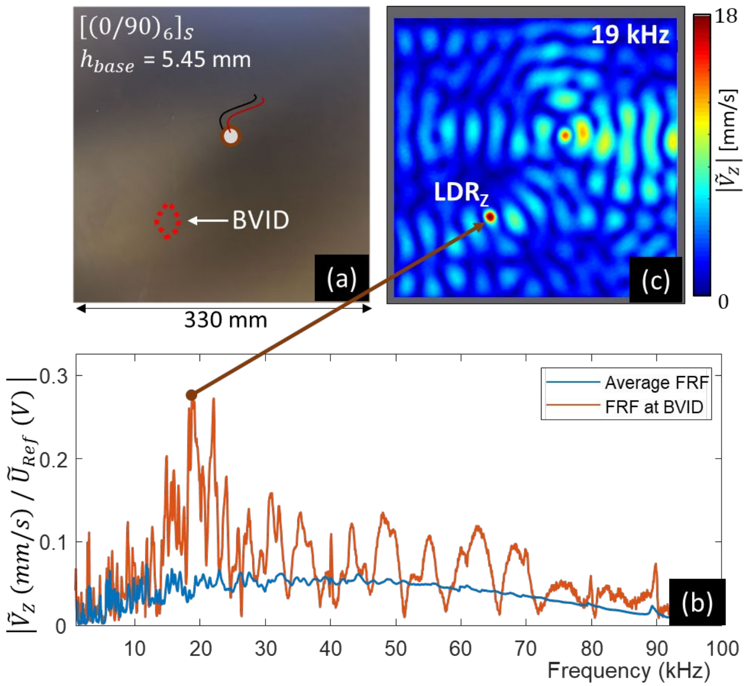

Figure 6.1: (a) Cross-ply CFRP plate with BVID, (b) Average frequency response function and frequency response function at the BVID and (c) Out-of-plane velocity amplitude at LDR$_Z$ frequency of 19 kHz.

The manual LDR identification approach is labor intensive, time consuming and operator dependent. As a result, it prevents the further use of LDR as an effective NDT technique. Recently, several studies showed that the LDR frequency can be identified by detection of nonlinear effects (e.g. higher harmonics and sidebands) in the frequency spectrum [2-4] and using bicoherence analysis [5]. However, these techniques require sufficient excitation power to provoke the (clapping and rubbing) nonlinearity at LDR and a high sensitivity measurement device to detect them (for instance using retroreflective tape). In addition, this nonlinear approach is obviously not well suited for defects that show limited nonlinear interaction (e.g. FBHs).

In this chapter, an algorithm is proposed to extract LDR parameters (i.e. LDR frequency and LDR location) in full wavefield broadband vibrational measurement data obtained using low-power piezoelectric actuation and SLDV sensing. The algorithm is based on an iterative thresholding procedure of the (linear) velocity amplitude maps. The workflow is first demonstrated for the out-of-plane velocity response of a CFRP test specimen with a single circular flat bottom hole (FBH). Second, the ability to find multiple defects in a single coupon is investigated using a test specimen with four FBHs of different depth and diameter. Third, the performance of the implemented algorithm is evaluated for artificial delaminations (i.e. inserts) in CFRP. Finally, a demonstration is given on a CFRP with barely visible impact damage (BVID). In order to improve the computational efficiency, several data compression techniques are evaluated: bandpower (BP) calculation, principal component analysis (PCA) and operational modal analysis (OMA).

The chapter is structured as follows. First, the experiment and the test specimens are described (Section 2). Next, the automated LDR procedure is explained (Section 3). This explanation is substantiated with out-of-plane velocity measurement results of the CFRP plate with a single FBH. Section 4 discusses the obtained results of the automated LDR_Z parameter extraction procedure for the different test samples. A final proof-of-concept of automated LDR_Z and LDR_{XY} detection is performed for the test specimen with BVID shown in Figure 6.1 (Section 5). In the end, the conclusions are summarized.

2. Experiment: Material and Method

Four CFRP coupons (autoclave curing cycle) with three distinct defect types are considered (see Figure 6.2).

The first test specimen (Figure 6.2 (a)) is a 330x330x5.45 mm^3 CFRP plate manufactured from unidirectional laminae according to quasi-isotropic layup $[(45/0/-45/90)_3]_s$. Artificial damage is introduced as a FBH of diameter 15 mm and remaining material thickness 1.5 mm. This sample is indicated as $\mathrm{CFRP}_{\mathrm{FBH,1}}^{\mathrm{Plate}}$.

The second specimen ($\mathrm{CFRP}_{\mathrm{FBH,4}}^{\mathrm{Coupon}}$ in Figure 6.2 (b)) is a 100x135x5.45 mm^3 CFRP coupon also manufactured from unidirectional laminae according to quasi-isotropic layup $[(45/0/-45/90)_3]_s$. The coupon contains four different FBHs. The diameter Ø and remaining material thickness *h* are indicated in the figure.

The third specimen ($\mathrm{CFRP}_{\mathrm{Inserts,5}}^{\mathrm{Coupon}}$ in Figure 6.2 (c)) is a 150×150×2.6 mm^3 CFRP coupon manufactured from unidirectional laminae according to layup $[(0/90)_2/0]_s$. Five ethylene tetrafluoroethylene ETFE polymer inserts are introduced in between the laminae during the layup process. The thin ETFE foil is folded over itself to create square 20×20×0.06 mm^3 pockets. The low stick polymer type and pocket like design of the inserts aim to create defects that behave as delaminations.

The fourth and last test specimen ($\mathrm{CFRP}_{\mathrm{BVID}}^{\mathrm{Coupon}}$ in Figure 6.2 (d-e)) is a 100x150x5.45 mm^3 CFRP coupon manufactured from unidirectional laminae according to cross-ply layup $[(0/90)_6]_s$. The specimen has been impacted with a 7.72 kg drop-weight with 16 mm impactor-tip according to the ASTM D7136 standard. The measured impact energy is 6.3 J, and this impact introduced BVID. Due to the complexity of the BVID [6], this sample is inspected from both the impacted (front) and the backside. As a benchmark, the ultrasonic C-scan results in reflection mode (5 MHz focused ultrasound with dynamic time gating) of both the impact side and backside are shown in Figure 6.2 (d) and (e), respectively.

All samples are suspended using rubber bands and excited with low power piezoelectric actuators (type EPZ-20MS64W from Ekulit) bonded to the surface (see Figure 6.2). A linear sine sweep signal from 1 kHz to 100 kHz is used as excitation signal. The voltage of excitation is amplified 50 times by the Falco System WMA-300 amplifier to increase the input energy. The in-plane and out-of-plane vibrational response is obtained using the 3D SLDV. Table 6.1 summarizes the measurement settings used for the different specimens.

The out-of-plane velocity component V_Z is predominantly used in this chapter for automated identification of the LDR_Z's. At the end (i.e. in Section 5), it is illustrated that the in-plane velocity components V_X, V_Y are useful as well, for automated identification of LDR_{XY}'s in the test specimen shown in Figure 6.1 (a).

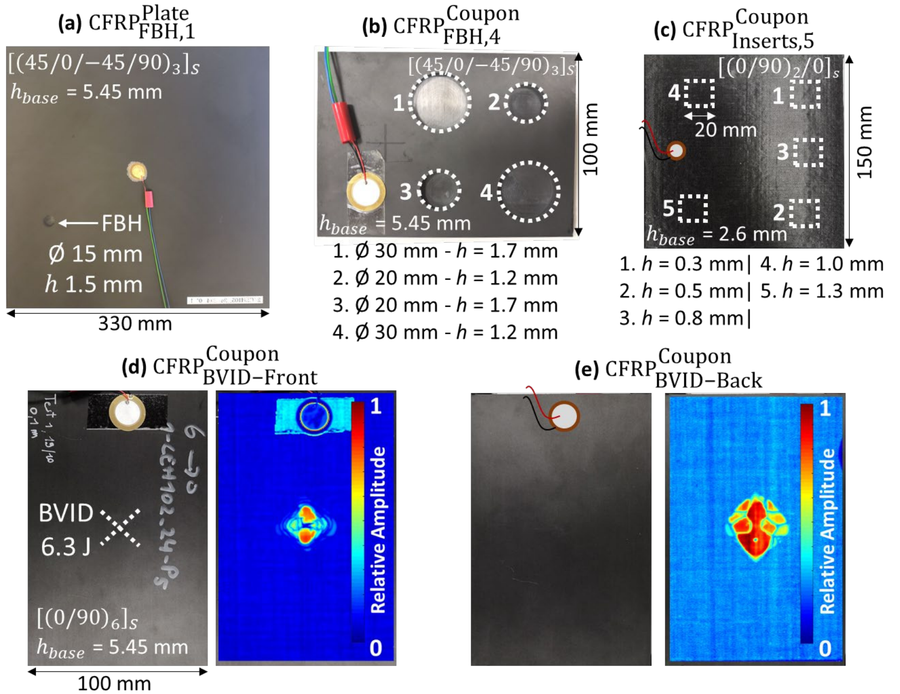

Figure 6.2: Tested CFRP samples (a) Quasi-isotropic plate with one FBH defect, (b) Quasi-isotropic coupon with four FBH defects, (c) Cross-ply coupon with five artificial delaminations (i.e. inserts), (d,e) Front and backside of cross-ply coupon with BVID, including ultrasonic C-scan amplitude maps.

Table 6.1: Experimental excitation and measurement settings.

	$CFRP^{Plate}_{FBH,1}$	$CFRP^{Coupon}_{FBH,4}$	$CFRP^{Coupon}_{Inserts,5}$	$CFRP^{Coupon}_{BVID}$	
				Impact side	**Backside**
# Scan points	19437	4420	9405	7763	8103
Scan point spacing (mm)	2.2	1.60	1.50	1.30	1.30
# Time samples	10000	5000	5000	10000	10000
Sampling frequency (kS/s)	625	250	250	250	250
V_{pp} (V)	150	150	150	200	200

3. Automated LDR Detection Procedure

An overview of the different steps of the automated LDR extraction procedure is shown in Figure 6.3. As indicated on the figure, the algorithm consists of two major blocks namely, *data conditioning* and *LDR extraction*. These steps are discussed in detail in the next two sections. Note that the algorithm equally works in both time and frequency domain. For brevity however, the results obtained in the time domain are not discussed.

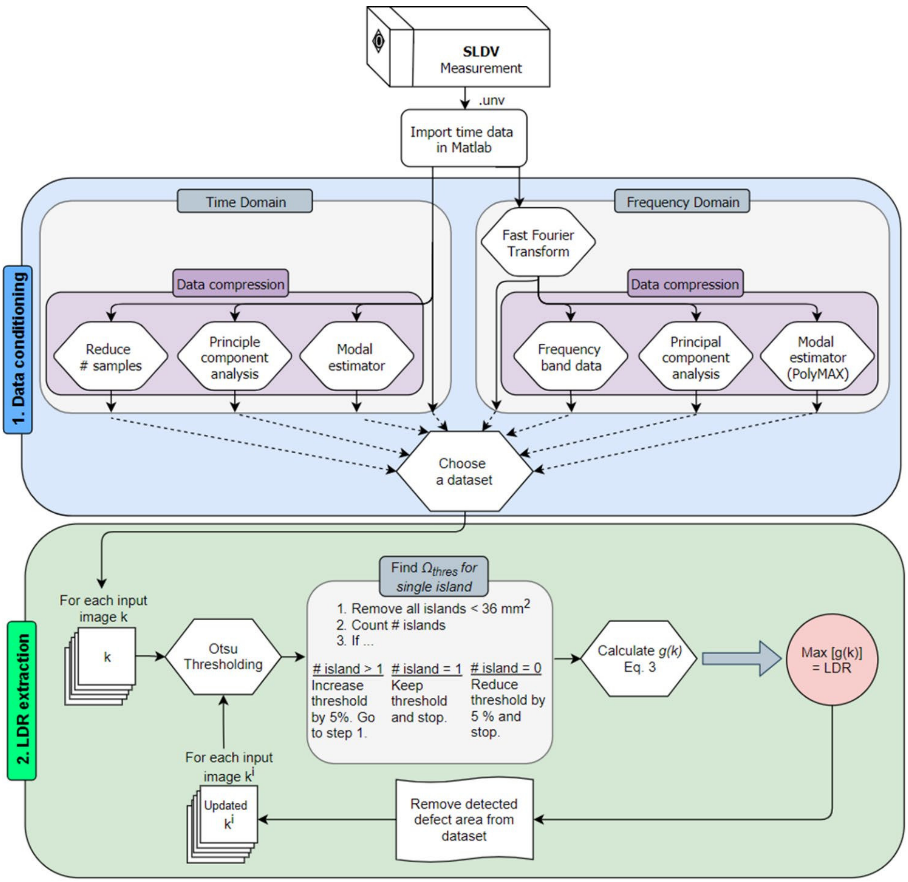

Figure 6.3: Graphical overview of the different steps in the automated LDR parameter extraction procedure.

3.1. Data Conditioning

The SLDV measurement data is imported into Matlab for further processing. The original size of the data can be up to a few GB's for our experiments. This temporal data is transformed to the frequency domain by FFT. Only the FFT lines within the bandwidth of investigation (i.e. 1 to 100 kHz) are kept, resulting in 1600 FFT lines for $\mathrm{CFRP}_{\mathrm{FBH},1}^{\mathrm{Plate}}$, 2000 FFT lines for $\mathrm{CFRP}_{\mathrm{Inserts},5}^{\mathrm{Coupon}}$ and $\mathrm{CFRP}_{\mathrm{FBH},4}^{\mathrm{Coupon}}$, and 4000 FFT lines for $\mathrm{CFRP}_{\mathrm{BVID}}^{\mathrm{Coupon}}$.

Three different data compression methods are implemented. These methods aim to reduce the size of the input data and thereby speed up the subsequent LDR extraction step. The investigated methods are: bandpower calculation, principal component analysis and operational modal analysis. Each of them is discussed separately in the next three sections. We illustrate the various approaches on the measurement results of $\mathrm{CFRP}_{\mathrm{FBH},1}^{\mathrm{Plate}}$.

3.1.1. Bandpower Calculation

The out-of-plane bandpower (BP) of a measurement point at location *(x,y)* is defined as:

$$BP_{FRF_Z}(x,y,f_1,f_2) = \frac{\Delta f}{f_2 - f_1} \sum_{f=f_1}^{f_2} \left(\frac{|\tilde{V}_z(x,y,f)\,|}{|\widetilde{U}_{Excitation}(f)\,|} \right)^2 \qquad (6.1)$$

where $\tilde{V}_z(\mathrm{x},\mathrm{y},f)$ and $\widetilde{U}_{Excitation}(f)$ represent respectively the out-of-plane velocity amplitude and the voltage amplitude of the excitation signal supplied to the piezoelectric actuator at the specified frequency *f*. Δf is the frequency resolution. The frequency limits f_1, f_2 must lie within the frequency band of excitation (i.e. 1 to 100 kHz). Thus the BP gives the vibrational energy averaged over a frequency band with bandwidth $BW = f_2 - f_1$. In order to compare the BP maps with operational deflection shapes, the square root of BP is taken and the result is referred to as $\sqrt{\mathrm{BP}}$.

As an example, Figure 6.4 shows the 10 bandpower images with BW = 10 kHz for $\mathrm{CFRP}_{\mathrm{FBH},1}^{\mathrm{Plate}}$. In all images, the center of the plate shows the highest intensity. This is the location where the vibrations are excited. Because the vibrational amplitude at $\mathrm{LDR_Z}$ is relatively high for this sample, the defect is visible in the bandpower image 30 to 40 kHz and 40 to 50 kHz (see insets). Different colorscale limits are used for the inset in order to reveal the intensity increase at the defect. The second order $\mathrm{LDR_Z}$ behavior is recognizable in the image for 70 to 80 kHz (see inset on figure).

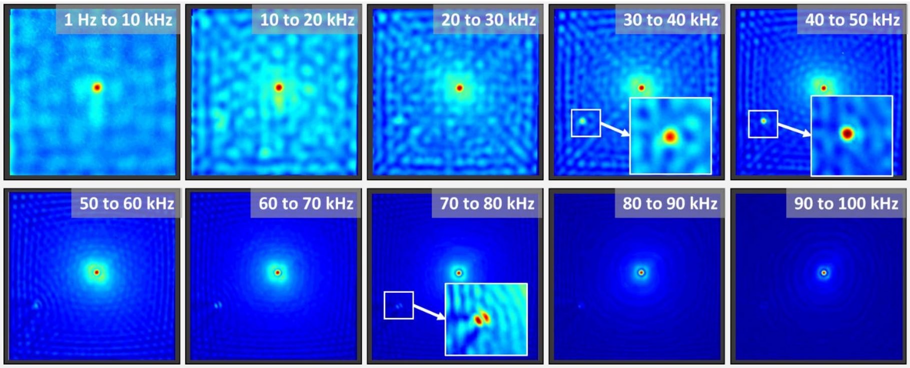

Figure 6.4: Square root of bandpower ($\sqrt{\mathrm{BP}}$) with bandwidth BW = 10 kHz for out-of-plane velocity V_Z in $\mathrm{CFRP}_{\mathrm{FBH},1}^{\mathrm{Plate}}$.

While the data compression is evident, there are two important drawbacks. First, the LDR behavior is less distinct. This is clear when comparing the operational deflection shape at $\mathrm{LDR_Z}$ (see inset on Figure 6.8 (a)) with the $\sqrt{\mathrm{BP}}$ image containing the $\mathrm{LDR_Z}$ frequency (see Figure 6.4: 40 to 50 kHz). This makes the automated LDR detection more challenging. Second, the LDR frequency estimation accuracy is reduced to the bandwidth of BP calculation. If the LDR frequency needs to be known precisely, an additional post-process step is required to identify the precise LDR frequency out of all FFT images in the bandwidth of the BP set.

In order to investigate the effect of data compression using BP calculation on the LDR detectability, a signal-to-noise ratio is introduced as:

$$SNR(\mathrm{f}_1, f_2) = 20\log\left[\frac{\frac{1}{n_{defect}}\sum_{(x_i,y_i)\in\Omega_{defect}}\sqrt{BP(x_i,y_i,f_1,f_2)} - \frac{1}{n_{sound}}\sum_{(x_i,y_i)\notin\Omega_{defect}}\sqrt{BP(x_i,y_i,f_1,f_2)}}{\sigma_{(x_i,y_i)\notin\Omega_{defect}}}\right]$$

where n_{defect} and n_{sound} are the number of data points in- and outside the damaged area (Ω_{defect}), respectively. $\sigma_{(x_i,y_i)\notin\Omega_{defect}}$ represents the standard deviation of $\sqrt{BP(x_i,y_i,f_1,f_2)}$ for the points outside Ω_{defect}. The damaged area Ω_{defect} equals the circular FBH area. Figure 6.5 shows the SNR and automated $\mathrm{LDR_Z}$ frequency prediction for an increasing bandwidth of BP. As indicated by the figure, the SNR and $\mathrm{LDR_Z}$ frequency accuracy starts decreasing when the bandwidth is larger than 1 kHz and the accuracy drops significantly for bandwidths above 5 kHz.

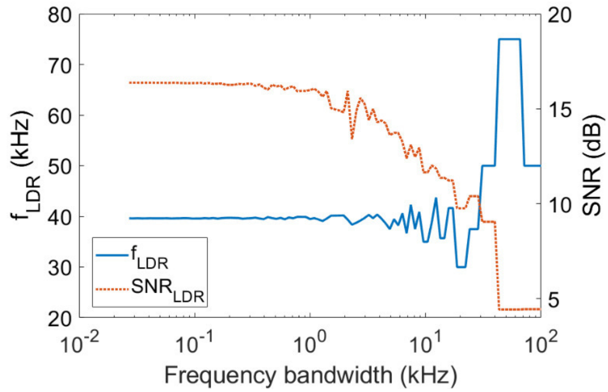

Figure 6.5: LDRz frequency prediction and SNR at LDRz for bandpower compression with increasing frequency bandwidth.

3.1.2. Principal Component Analysis

Principal component analysis (PCA) is a multivariate technique that aims to reduce the dimensionality of a large dataset. This is achieved by transforming the original dataset to a new basis of uncorrelated variables, i.e. principal components (PCs). The PCs are ordered such that the first few explain most of the variance present in the original large dataset. Hence, PCA is useful to compress the large number of FFT images into a limited number of PCs. As such, it is expected that the LDR phenomenon at the defect's location is captured in one or more PCs.

PCA is performed by singular value decomposition of the covariance matrix of all FFT lines between 1 and 100 kHz [7, 8]. Starting from the first PC, subsequent PCs are calculated until 99% of the variance present in original dataset is captured by the PCs. This results in the compression of the 1600 FFT lines into 101 PCs, i.e. a compression ratio of 15.8, for $\mathrm{CFRP}_{\mathrm{FBH,1}}^{\mathrm{Plate}}$.

Figure 6.6 shows the first 10 PCs (for the out-of-plane velocity V_Z) together with the explained variance for each of them. Two important vibration characteristics are captured. First, the PCs contain concentric rings around the excitation location. This feature can be used to localize the excitation location. Secondly, the LDRz behavior of the defect is clearly visible in PCs 4, 5 and 8 (see insets on figures). Although the data compression ratio is excellent, there are drawbacks to this method. First, it is unpredictable whether the LDR phenomenon will be captured as a single PC or that it will be mixed with other vibrational characteristics (which is the case here). As a result, there is a possibility that the LDR extraction is unsuccessful. Second, if a LDR is identified correctly in one of the PCs, an additional processing step is required to determine the corresponding LDR frequency. However, this can be easily done be analyzing the peaks in the FRF of a nodal point inside the identified LDR area. An example of this additional processing step is given in Section 4.2.

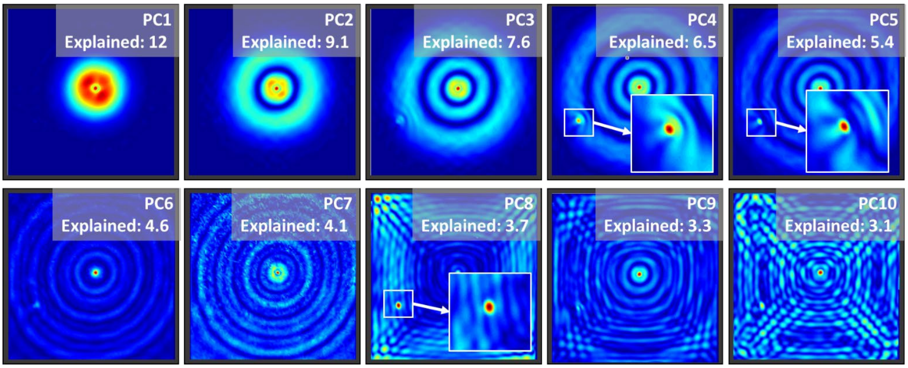

Figure 6.6: Principal components 1 to 10 (with explained variance [%]) for V_Z in $\mathrm{CFRP}^{\mathrm{Plate}}_{\mathrm{FBH,1}}$.

3.1.3. Operational Modal Analysis

The linear steady-state response of a structure subjected to a dynamic force can be described as a linear combination of orthogonal mode shapes. These mode shapes and corresponding resonance frequencies can be extracted from the full wavefield broadband vibration measurements using an operational modal analysis (OMA) algorithm. By definition, the LDR phenomenon comprises a resonance and should therefore correspond to one of these mode shapes.

Multiple modal parameter estimators exist, operating in either time or frequency domain. In this study, the *PolyMAX parameter estimation* [9] method within *Simcenter Testlab* software is used to identify the structure's resonances using all frequency response functions (FRFs) for the out-of-plane velocity component. The main idea is that several runs of the mode identification procedure are executed, by using models of increasing number of expected modes (i.e. increasing model order). Each time, the detected resonances are indicated with a symbol in the stabilization diagram (see example in Figure 6.7). This diagram also contains the average FRF. Physical modes always appear with nearly identical frequency, damping and eigenvector, independent of the assumed number of modes. Four different symbols are used to indicate the stability of a mode with respect to the increasing model order, namely '*f*: stable frequency', '*d*: stable frequency and damping', '*v*: stable frequency and eigenvector' and '*s*: all criteria stable'. The default stability criteria of the *PolyMAX* OMA software are used: 1% for frequency, 5% for damping and 2% for eigenvector.

Because there are a large amount of resonances expected within the measurement bandwidth (100 kHz), each dataset is split into 10 bands (1 to 10 kHz, 10 to 20 kHz, … and 90 to 100 kHz) on which the *PolyMAX* algorithm is executed separately. For each of the frequency bands, the mode identification procedure is ran up to a model order of 128. Only the mode shapes corresponding to the estimated stable modes are calculated and saved to use later in the automated detection procedure (see Section 3.2). For illustration, Figure 6.7 shows the stabilization diagram with two mode shapes. As can be seen on the figure, stable modes are detected at all local maxima in the average FRF. If this would not be the case, the mode stability criteria need optimization which can be done using advanced automated algorithms as illustrated in Ref. [10].

For all experiments discussed in this study, the PolyMAX algorithm with default stability criteria and maximum model order succeeded in identifying the LDR phenomena as stable modes. The main drawback behind this data compression method is the need for the advanced OMA software.

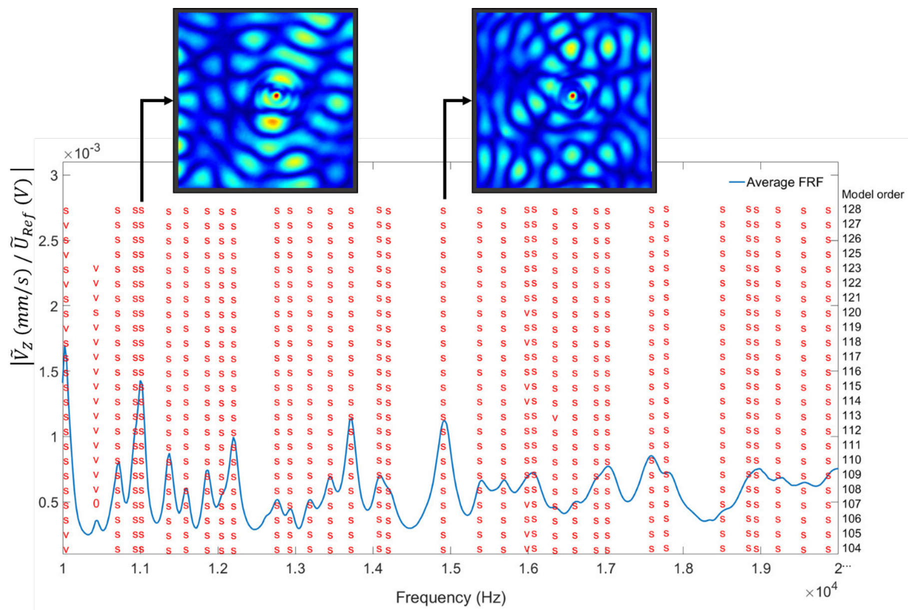

Figure 6.7: *Polymax* stabilization diagram from 10 kHz to 20 kHz with two mode shapes for V_Z in $\mathrm{CFRP}_{\mathrm{FBH},1}^{\mathrm{Plate}}$. The ‘s’ indicates a stable mode. (Diagram reproduced from *Simcenter Testlab*.)

3.1.4. Data Compression Performance

Table 6.2 gives an overview of the performance of the different data compression methods for $\mathrm{CFRP}_{\mathrm{FBH},1}^{\mathrm{Plate}}$ with an original data size of 1.65 GB. In the table, the compressed data sizes are listed, together with the calculation times needed to obtain them. All data has been processed with an i7-7820HQ 2.90 GHz processor, and 16 GB RAM. All three data compression methods reduce the 243 MB of FFT data considerably within a limited time span. This results in a reduced calculation time for the subsequent LDR extraction step (see Section 3.2). In case of multiple defects, this LDR extraction step has to be repeated multiple times (see for instance Section 4.2) which necessitates the proposed data compression.

Table 6.2: Data sizes and calculation times for different data compression methods and $\mathrm{LDR_Z}$ extraction when applied to $\mathrm{CFRP}_{\mathrm{FBH},1}^{\mathrm{Plate}}$ measurement results.

Processing step	Data size (MB)	Time for compression (s)	Time for LDR extraction (s)
Raw time data	1650	1520*	\
FFT	243	9.9	19.2
BP BW = 1 kHz	15.1	2.1	1.2
BP BW = 10 kHz	1.5	1.4	0.13
PCA	15.2	18.9	1.1
OMA	21.4	225	1.5

*Time for the SLDV measurement.

Table 6.3 summarizes the advantages and disadvantages of the three data compression methods. The BP calculation is fast and results in a large data compression (if a relatively large bandwidth is used e.g. >1 kHz). However, for increasing bandwidths, the LDR phenomenon becomes less distinct (SNR decreases) which reduces the detectability. Moreover, the LDR frequency accuracy is limited by the BP bandwidth. PCA calculation takes longer due to the singular value decomposition problem. The LDR detectability is somewhat unpredictable because it is not always the case that the LDR is captured nicely in a single PC. Moreover, all frequency information is lost which necessitates an additional process step to determine the LDR frequency. At last, operational modal analysis (*PolyMAX*) requires a separate OMA algorithm and shows a relatively long calculation time. On the other hand, it shows good performance with respect to the LDR detectability and frequency extraction.

Table 6.3: Pro's and con's for the data compression methods.

Method	Compression time	Compression ratio	LDR detectability	LDR frequency
FFT	\	\	+	+
BP 1 kHz	+	+	+	+
BP 10 kHz	+	++	-	-
PCA	-	+	--	--
OMA	-	+	++	++

3.2. LDR Detection Algorithm

The automated LDR detection algorithm is graphically shown in the lower part of Figure 6.3. The algorithm searches for LDR characteristics inside a given set of input images. These input images can be the total set of computed FFT images or a compressed dataset (BP, PCA or OMA).

First, an iterative thresholding procedure is executed for each input image k. Otsu's method is used to determine the initial threshold. Otsu thresholding is a statistical operation performed on the histogram of the image which maximizes the between-class variance [11]. Our experience on a large set of test data has shown that the resulting initial threshold area ($\Omega_{thres}(k)$) is often too large and that it is strongly dependent on the global size of the sample. As a result, the threshold is increased iteratively with 5 % until $\Omega_{thres}(k)$ comprises only 1 single zone or island. Because possible SLDV measurement errors typically result in a very localized (typically 1 scan point) increase in the value for the velocity amplitude, care has to be taken to not identify these measurement errors as LDR behavior. To overcome this problem, a defect size tolerance limit is introduced and thresholded islands with size smaller than this limit are removed from $\Omega_{thres}(k)$ before the number of islands in $\Omega_{thres}(k)$ is determined. The tolerance limit is set to 36 mm^2 which corresponds to the defect tolerance limit in certain aerospace applications. In the unlikely event that an image contains two or more perfectly identical LDR lobes, the threshold will be increased until the identical LDR islands become smaller than 36 mm^2 and are simultaneously removed. This would result in an empty $\Omega_{thres}(k)$. If this happens, the final threshold is reduced with 5 %, back to its former value, before calculation of the contrast curve. In this special case, $\Omega_{thres}(k)$ contains multiple islands corresponding to the identical LDR lobes.

Once the threshold value is found and the corresponding $\Omega_{thres}(k)$ is determined, a contrast function $g(k)$ is calculated according to:

$$g(k) = \frac{\underset{(x_i,y_i)\in\Omega_{thres}(k)}{\text{Mean}} |A(x_i,y_i,k)|}{\underset{(x_i,y_i)\notin\Omega_{thres}(k)}{\text{Mean}} |A(x_i,y_i,k)|} \quad \text{for} \quad k = 1 \rightarrow \#\ \text{input images}$$

$$\text{with} \quad A(x_i,y_i,k) = \begin{cases} V_z(x_i,y_i,k) & \text{for FFT data} \\ \sqrt{BP(x_i,y_i,(k-1).BW,k.BW)} & \text{for BP data} \\ PC(x_i,y_i,k) & \text{for PCA data} \\ MS(x_i,y_i,k) & \text{for OMA data} \end{cases}$$

Depending on the type of data used, $g(k)$ is calculated using: Out-of-plane velocity amplitude V_Z, Bandpower intensity $\sqrt{BP}$, Principal components PC or Mode shapes MS. As LDR behavior is characterized by a local increase in vibrational amplitude, the contrast function $g(k)$ reaches a maximum for the image k that contains the LDR.

In case multiple defects are expected, the thresholding procedure and consecutive contrast function calculation is performed again for the updated dataset of images k^i. This updated dataset is obtained by cropping out all former detected LDR areas from each image in the original dataset. A more detailed description of this cropping process is provided in Section 4.2, substantiated with results for $\text{CFRP}^{\text{Coupon}}_{\text{FBH,4}}$.

The next section illustrates the performance of the proposed algorithm for automated detection of LDR_Z the various test cases.

4. Automated LDR_Z Detection Results

4.1. CFRP Plate with a Single FBH

The automated LDR parameter extraction algorithm outlined above is executed for the out-of-plane velocity response of the CFRP plate with a single FBH ($\text{CFRP}^{\text{Plate}}_{\text{FBH,1}}$). Results are shown for the total FFT dataset as well as for all three compressed datasets i.e. BP set with BW = 1 kHz, PCA set and OMA set. The excitation location is cropped out of all the input images because it shows characteristics similar to a LDR. In the case that excitation location would be unknown, the described procedure can easily be used to locate also the excitation location. After cropping out the found excitation location, the procedure can be used for the detection of LDRs.

For each of the four (compressed) datasets, the contrast function is calculated as explained in Section 3.2 and the images associated to the maximum of the contrast functions are shown in Figure 6.8. As an illustration, Figure 6.8 (a)

displays the contrast curve for the case that all FFT images are used as input. The procedure was successful in detecting the LDRz frequency and the corresponding defect location (see red squares) in all cases expect for the PCA set.
For the BP set, the LDRz is found in band 40 to 41 kHz, which includes the LDRz frequencies identified using FFT and OMA sets. At these high frequencies, the damping is relatively high resulting in a small change in ODS over the band 40 to 41 kHz. As a result, the $\sqrt{BP}$ intensity image at LDRz is very similar to the FFT image and OMA image. In the PCA set, PC 1 shows a very high intensity ring surrounding the excitation location, in a low intensity background. The algorithm erroneously identified this high intensity ring as an LDRz.

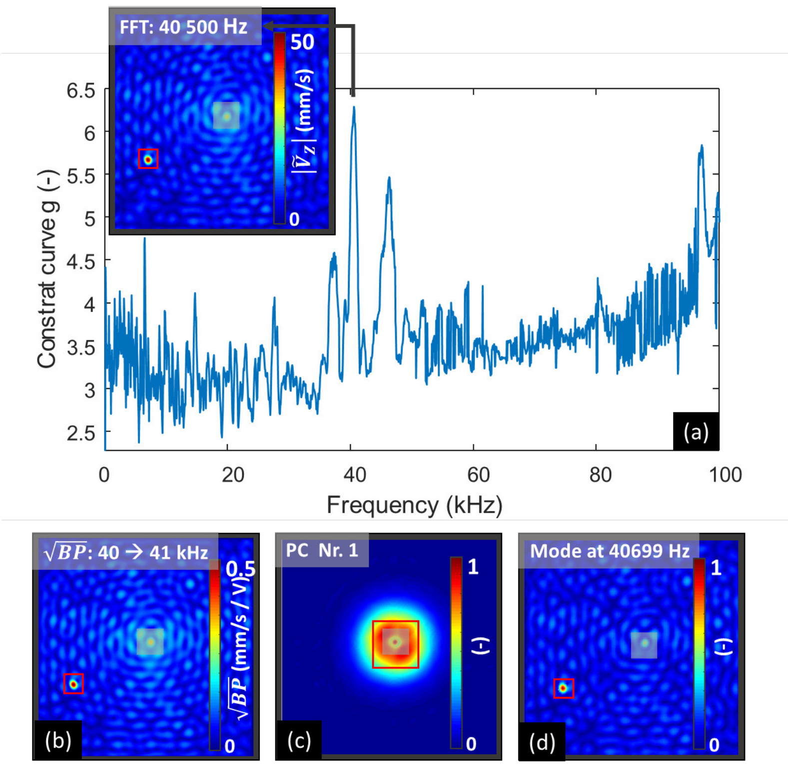

Figure 6.8: Automated LDRz detection results for V_Z in $\text{CFRP}_{\text{FBH},1}^{\text{Plate}}$ (a) Contrast curve and LDRz identified in FFT frames, (b) Bandpower images, (c) Principal components and (d) Mode shapes.

4.2. CFRP Coupon with Four FBHs

In the case of the CFRP coupon with four FBHs ($\mathrm{CFRP}_{\mathrm{FBH,4}}^{\mathrm{Coupon}}$), we are searching for multiple LDRs in the same dataset. Figure 6.9 illustrates the method to detect multiple LDRz's. The LDR extraction procedure is executed resulting in the first LDRz and defect localization (Ω_{thres}, see white area in Figure 6.9 (a)). In order not to detect the same defect in a successive execution of the algorithm, a sufficiently large area around the defect's location is cropped out of all input images. At this moment, the cropped area equals a tight rectangle around Ω_{thres} enlarged by 5 mm on each side, as illustrated respectively by the yellow and red rectangles in Figure 6.9 (b). After cropping out the detected LDR, the new dataset k^i (with i the iteration) is fed back to the Otsu thresholding step in order to find other LDR phenomena.

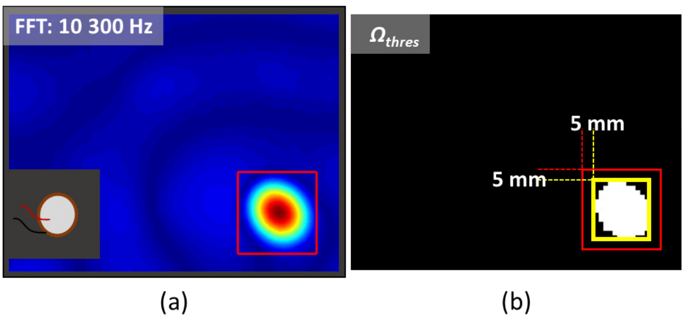

Figure 6.9: Cropping procedure for multiple LDR detection, illustrated for the first LDRz detected in the FFT set at 10.3 kHz for $\mathrm{CFRP}_{\mathrm{FBH,4}}^{\mathrm{Coupon}}$.

The results of the total LDRz extraction procedure with intermediate removal of the identified LDRz regions are shown as columns in Figure 6.10. Each row corresponds to a different set of input images i.e. all FFT lines, $\sqrt{BP}$ with BW = 1 kHz, PC's and OMA stable modes. The cropped out areas are marked with gray rectangles. In all cases, all four FBHs are localized by detecting their LDRz behavior. However, only for the FFT lines, all 4 fundamental LDRz phenomena are immediately extracted correctly. For the other cases, several higher-order LDRz's are found. Hence, an additional step is implemented in which a nodal FRF within the detected LDRz location is evaluated in order to identify the fundamental LDRz. This is explicitly illustrated in Figure 6.10 for Run 1 - OMA (which originally detected the 2nd order LDRz).

Note that the results for the FFT set are generally similar to the results for BP and OMA sets. For the BP set, this is again explained by the small alteration of the operational deflection shapes over a 1 kHz frequency band at these high (> 10 kHz) frequencies. This observation justifies the proposed use of BP calculation for data compression. The OMA algorithm is successful in detecting the LDR$_Z$'s as stable modes where the corresponding mode shapes are highly similar to the operational deflection shapes in the FFT set. For the PCA set, PC's 1 and 2 correspond to the LDR$_Z$ of a FBH whereas the other PC's contain a mixture of LDR$_Z$ behavior and other vibrational characteristics.

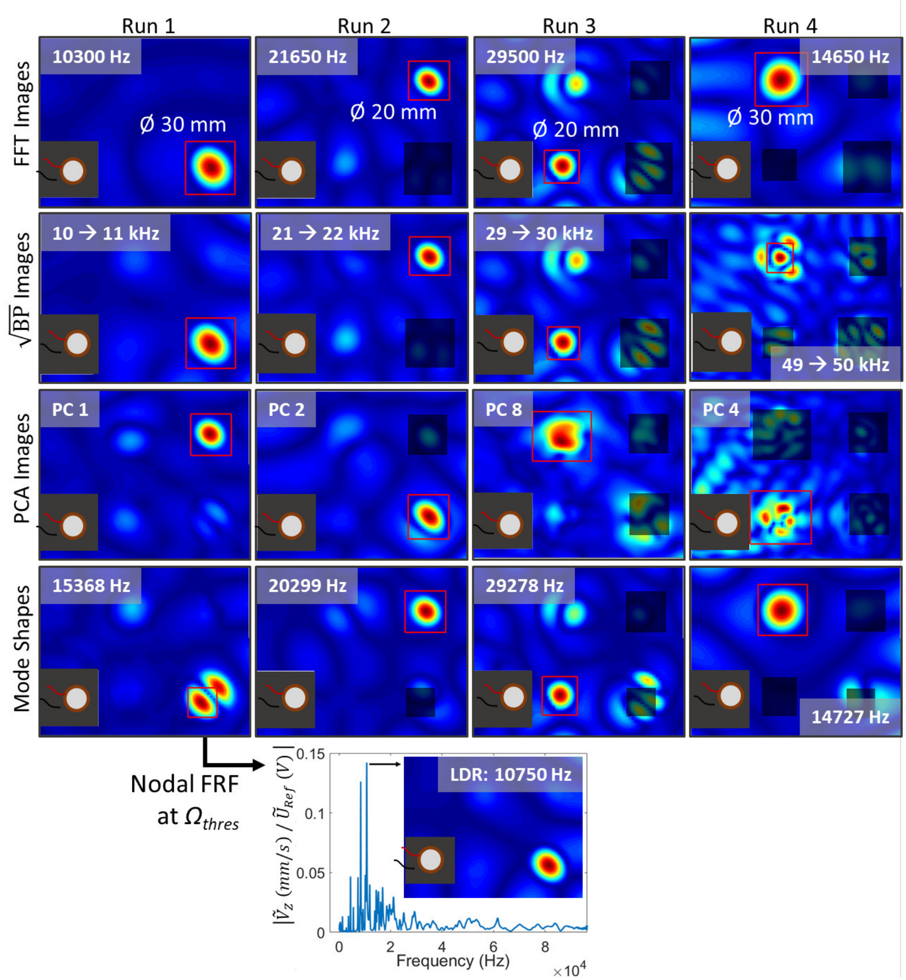

Figure 6.10: Automated LDR$_Z$ detection results for V_Z in $\text{CFRP}^{\text{Coupon}}_{\text{FBH},4}$ with illustration of the additional process step for fundamental LDR frequency identification.

4.3. CFRP Coupon with Five Inserts

The 3rd test specimen ($CFRP^{Coupon}_{Inserts,5}$) contains five artificial delaminations and therefore the automated LDR_Z detection procedure is again executed multiple times. After each iteration, the region identified as LDR_Z is cropped out of the original dataset, and the novel dataset is fed back to the LDR_Z detection procedure.

The obtained results are shown in Figure 6.11, where the red squares indicate the LDR_Z's detected by the algorithm and the dark squares represent previously found LDR_Z's that were cropped out from the original dataset. For the full set of FFT images, LDR_Z has been identified at four delaminations. After running the automated LDR_Z extraction procedure for the 5th time, it is seen that it has pin-pointed a resonance mode which is not linked to any of the inserts, and thus gives a false indication. Running the algorithm a 6th time, finally yields the LDR_Z detection of the deepest insert (not shown in figure). For the three compressed datasets, all five inserts are correctly localized.

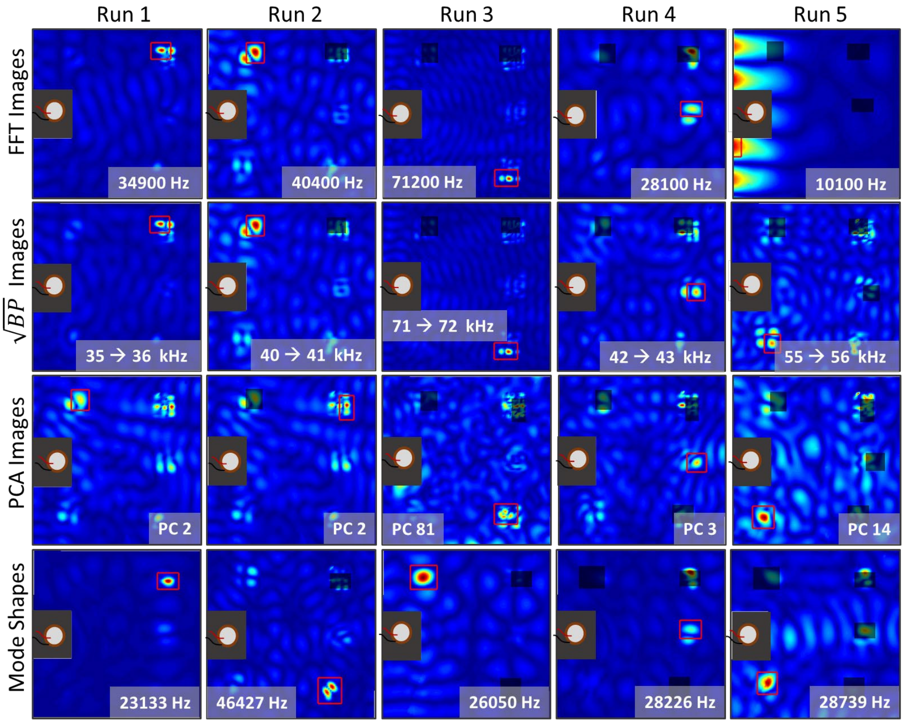

Figure 6.11: Automated LDR_Z detection results for V_Z in $CFRP^{Coupon}_{Inserts,5}$. See Figure 6.2 (c) for insert's depth.

Additional information about the defect's structure can be derived from the BP calculated over the entire bandwidth of the excitation signal (see Figure 6.12). The BP shows that there is an increased vibrational energy at the locations of the inserts but not over the entire insert's area. This indicates that the surfaces are not nicely separated and that the square inserts are not representative for delaminations with a square geometry, but rather correspond to delaminations with a complex geometry. As a result, most inserts do not show the expected fundamental LDR_Z behavior but show more complex LDR_Z behavior at a multitude of frequencies. This is visible in Figure 6.11 where only one fundamental LDR_Z is detected (See Mode Shapes – Run 3). Overall, our algorithm is able to pinpoint the defect locations quite well, even for this case of multiple complex defect features that each possess a multitude of LDR_Z phenomena. In Chapter 7 and Chapter 11, it is illustrated that the broadband BP maps can be used as a damage maps on their own.

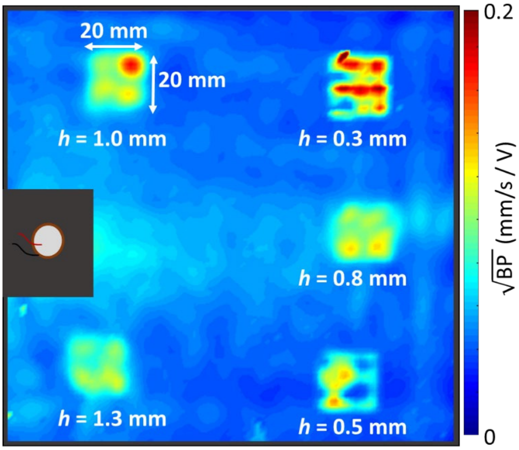

Figure 6.12: Square root of bandpower 1 kHz → 100 kHz calculated using Eq. (6.1) for $\mathrm{CFRP}^{\mathrm{Coupon}}_{\mathrm{Inserts,5}}$.

4.4. CFRP Coupon with Impact Damage

The fourth sample ($\mathrm{CFRP}_{\mathrm{BVID}}^{\mathrm{Coupon}}$) to test the automated $\mathrm{LDR_Z}$ parameter extraction procedure is a cross-ply CFRP coupon which has been impacted at 6.3 J, resulting in BVID. BVID is a very complex damage, consisting of matrix cracks as well as multiple delaminations (see the reflection C-scan data displayed in Figure 6.2 (d)). The damage is distributed in the area near the impact zone and cannot be considered as a single idealized defect, which obviously complicates the LDR analysis. The test sample is inspected from both the impact- and the backside. Within the large measurement bandwidth of 100 kHz, multiple small regions within the global damaged area show $\mathrm{LDR_Z}$ behavior at different frequencies. Calculating the BP over the entire measurement bandwidth (1 to 100 kHz) summarizes the vibrational energy and captures all these small individual $\mathrm{LDR_Z}$'s (see Figure 6.13). This allows for damage localization without the need of extensive post-processing.

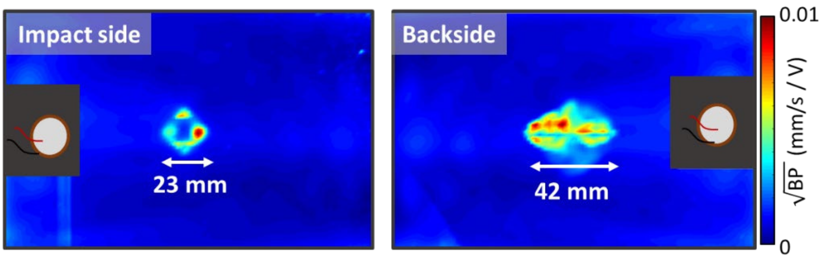

Figure 6.13: Square root of BP 1 kHz → 100 kHz calculated using Eq. (6.1) for V_Z in $\mathrm{CFRP}_{\mathrm{BVID}}^{\mathrm{Coupon}}$.

Nevertheless, the proposed automated LDR detection procedure can be used to gain additional information on the defect. The LDR information can then be used for nonlinear and/or vibrothermographic studies of the BVID as explained in Chapter 8 and Chapter 9, respectively. The results of the automated $\mathrm{LDR_Z}$ parameter extraction are shown in Figure 6.14 and Figure 6.15. Figure 6.14 shows the contrast curve calculated for all FFT lines for the backside of the sample, together with the operational deflection shapes corresponding to the four highest local maxima. All these four local maxima correctly relate to $\mathrm{LDR_Z}$ behavior inside the complex damage distribution. Figure 6.15 summarizes the $\mathrm{LDR_Z}$'s detected using the automated procedure for the measurements of both sides of the sample and all four proposed datasets. For all cases, $\mathrm{LDR_Z}$ behavior of part of the distributed BVID damage is successfully detected. It is clear that for this type of distributed damage, the classification of the order of $\mathrm{LDR_Z}$ is ambiguous.

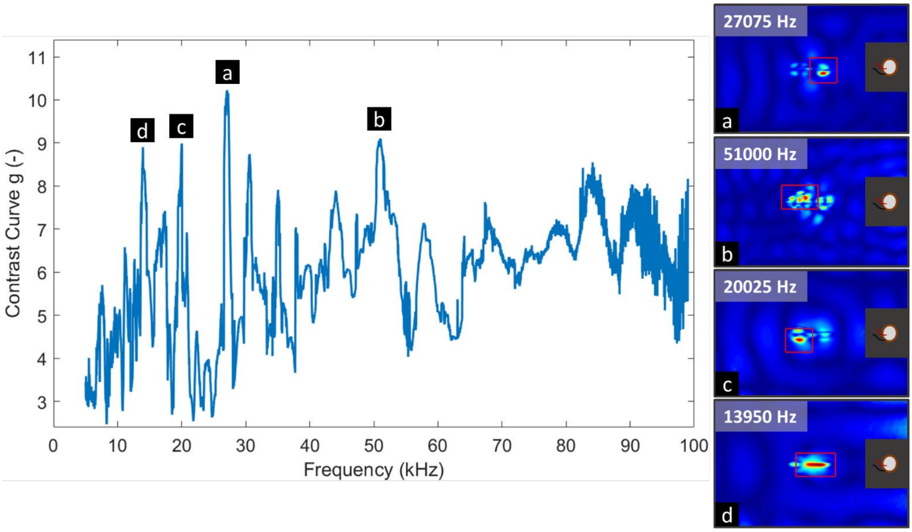

Figure 6.14: Contrast curve for FFT data and operational deflection shape corresponding to four local maxima for V_Z in $\mathrm{CFRP}_{\mathrm{BVID\text{-}Back}}^{\mathrm{Coupon}}$.

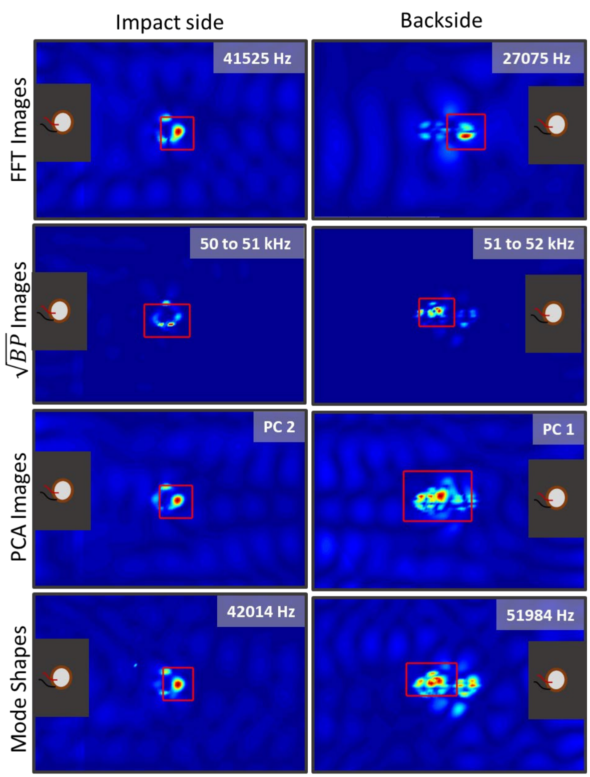

Figure 6.15: Automated LDRz detection results for $\mathrm{CFRP}_{\mathrm{BVID}}^{\mathrm{Coupon}}$ inspected from the impact and backside.

5. LDR$_Z$ and LDR$_{XY}$ Detection at Impact Damage

As a final test of the proposed automated LDR detection algorithm, the algorithm is operated on the measurement results of the rather large CFRP panel with BVID that was shown in Figure 6.1. The plate is excited with a broadband chirp from 1 to 100 kHz and the vibrational response at the backside of the component is recorded with the 3D SLDV. Figure 6.1 already showed a LDR$_Z$ behavior of the BVID visible at the impact side.

The automated search for LDR is performed in the bandpower images with a bandwidth of 1 kHz. This data compression strategy showed the best performance (see Section 3.1.4). All three velocity components (V_X, V_Y and V_Z) are considered. As a result, the bandpower is calculated according to Eq. (6.1) where the velocity component equals V_X, V_Y and V_Z for detection of in-plane horizontal, in-plane vertical and out-of-plane LDRs respectively.

Figure 6.16 (a-b), (c-d) and (e-f) shows the detected in-plane horizontal, in-plane vertical and out-of-plane LDRs, respectively. For each case, two runs of the algorithm were performed. Correct LDRs are identified for all velocity directions and for both runs. As a result, the automated LDR detection algorithm proves successful for BVID detection and localization. The compression of the data using bandpower calculation resulted in an efficient LDR search where each run took only ± 1 second to perform.

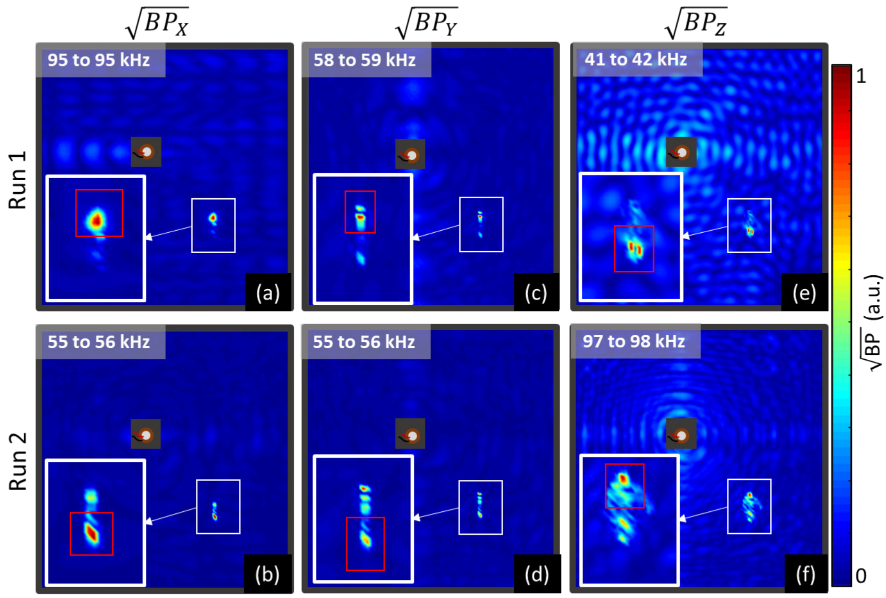

Figure 6.16: Automated in-plane horizontal (a-b), in-plane vertical (c-d) and out-of-plane (e-f) LDR detection for a BVID in cross-ply CFRP plate using bandpower data compression.

6. Conclusion

This study addresses one of the major obstacles encountered for using the concept of LDR for NDT, namely how to identify the LDR frequency and subsequent defect location from a broadband measurement result. To this purpose, an automated LDR parameters extraction procedure (LDR frequency and corresponding defect location) is proposed.

The automated LDR identification procedure is operated on the full wavefield velocity response data of a specimen subjected to a low power broadband excitation at a single position. The procedure is applied on vibrational data in the frequency domain (but it can be equally applied to time domain data). Data compression techniques, namely bandpower calculation, principal component analysis and operational modal analysis, are implemented in order to reduce the computational effort. The automated LDR parameter extraction procedure is further based on an iterative thresholding procedure to search for a single high amplitude island on each image of the dataset followed by the calculation of a contrast function where the maximum in this function pinpoints the LDR.

The proposed algorithm is tested on the experimental data of different test specimens. The algorithm shows good performance in localizing all defects and deriving LDR frequency information. For complex defects, e.g. BVID, a multitude of small LDRs are observed inside the damage distribution rather than one fundamental LDR. In this case, bandpower calculation over a large bandwidth is used to captures all these small individual LDRs and show the extent of the damage.

References

1. Segers, J., et al., *Efficient automated extraction of local defect resonance parameters in fiber reinforced polymers using data compression and iterative amplitude thresholding.* Journal of Sound and Vibration, 2019. **463**.
2. Fierro, G.P.M. and M. Meo, *Nonlinear elastic imaging of barely visible impact damage in composite structures using a constructive nonlinear array sweep technique.* Ultrasonics, 2018. **90**: p. 125-143.
3. Fierro, G.P.M., et al., *Imaging of Barely Visible Impact Damage on a Complex Composite Stiffened Panel Using a Nonlinear Ultrasound Stimulated Thermography Approach.* Journal of Nondestructive Evaluation, 2017. **36**(4).
4. Ginzburg, D., et al., *SHM of single lap adhesive joints using subharmonic frequencies.* Smart Materials and Structures, 2017. **26**(10).

5. Roy, S., T. Bose, and K. Debnath, *Detection of local defect resonance frequencies using bicoherence analysis.* Journal of Sound and Vibration, 2019. **443**: p. 703-716.
6. Spronk, S.W.F., et al., *Comparing damage from low-velocity impact and quasi-static indentation in automotive carbon/epoxy and glass/polyamide-6 laminates.* Polymer Testing, 2018. **65**: p. 231-241.
7. Abdi, H. and L.J. Williams, *Principal component analysis.* Wiley Interdisciplinary Reviews: Computational Statistics, 2010. **2**(4): p. 433-459.
8. Jolliffe, I.T., *Principal Component Analysis*. 2 ed. 2002: Springer.
9. Peeters, B., et al., *The PolyMAX Frequency-Domain Method: A New Standard for Modal Parameter Estimation?* Shock and Vibration, 2004. **11**(3-4): p. 395-409.
10. Reynders, E., J. Houbrechts, and G. De Roeck, *Fully automated (operational) modal analysis.* Mechanical Systems and Signal Processing, 2012. **29**: p. 228-250.
11. Otsu, N., *A Threshold Selection Method from Gray-Level Histograms.* IEEE Transactions on Systems, Man, and Cybernetics, 1979. **9**(1): p. 62-66.

Chapter 7

Probing the Limits of Local Defect Resonance

Summary:

The opportunities and limitations of (linear) LDR identification for NDT are investigated in a parametric way. Both finite element simulations and experiments (using SLDV) are performed for aluminum and CFRP coupons with flat bottom holes and delaminations ranging in both depth and diameter. The LDR frequencies as well as the associated defect-to-background ratios are parametrically evaluated.
For shallow defects, a clear LDR is observed caused by the strong local flexural and axial rigidity reduction at the defect. On the contrary, deep defects are associated with a limited flexural and axial rigidity decrease that results in the absence of LDR behavior.
The local flexural rigidity reduction at deep damage is further exploited using a weighted bandpower calculation. It is shown that using this technique, deep defects can be detected for which no LDR behavior was observed.

The chapter is in close correspondence with journal publication:

[1] Segers, J., Hedayatrasa, S., Poelman, G., Van Paepegem, W. and Kersemans, M. *Probing the limits of full-field linear Local Defect Resonance identification for deep defect detection.* Ultrasonics, 2020. **105**

1. Introduction

In the previous two chapters, the (automated) identification of out-of-plane and in-plane local defect resonances (LDR_Z and LDR_{XY}, respectively) in operational deflection shapes (ODS) has shown to be successful for detection of flat bottom holes (FBH), artificial delaminations, disbonds and barely visible impact damage (BVID) in composite materials. LDR-based defect detection is further illustrated by other researchers. As an example, detection of BVID based on LDR_Z is illustrated in [2-4] and the detection of inserts (or artificial delaminations) is shown in [3, 5-7].

Despite these promising experimental results, a critical remark has to be made concerning the depth of the investigated defects. All successfully detected defects (described in previous two chapters and in literature) should be considered 'shallow defects', as they are all located at depths less than half the thickness of the damage-free base material. Considering that the existence of LDR is linked to the difference in rigidity between the defect and the surrounding sound material, it may be expected that the LDR-based detection of a deep defect (that corresponds to a limited local rigidity reduction in the top surface) can be challenging.

In this chapter, the opportunities and limitations of linear LDR-based defect detection are investigated through a parametric study. The focus is in LDR_Z as this is the type of LDR that is most easily used for detection of delamination like defects in CFRPs. Aluminum and CFRP coupons with FBHs are evaluated by finite element (FE) simulation and experimentally. Moreover, the LDR_Z behavior of FBHs is compared with the LDR_Z behavior of delaminations by FE simulation. The analytically predicted LDR_Z frequency is also included as a benchmark and its validity range is highlighted. The defects' diameter d and local material thickness h_{defect} are varied in order to investigate the influence of defect size and depth on the LDR_Z behavior. A relative thickness h [%] is defined as the ratio of defect thickness (h_{defect}) over the base material thickness (h_{base}): $h = 100 * \frac{h_{defect}}{h_{base}}$ (see Figure 7.1). Thus, small h values (h < 50 %) correspond to shallow defects (i.e. small h_{defect}) while high h values (h > 50 %) correspond to deep defects (i.e. high h_{defect}). A short discussion of the LDR_{XY}'s observed in the experimental results of the aluminum coupons with FBHs is provided to investigate the similarities and differences between LDR_{XY} and LDR_Z.

The first section describes the setup of the FE simulations and the experimental approach that are used to study the LDR behavior of the FBHs and the delaminations. Next, for both materials, the obtained LDR_Z frequencies as well as the associated defect-to-background ratios are parametrically evaluated in function of the defect's depth and size. A discussion of the LDR_{XY} behavior observed at the FBHs in the aluminum coupons is included. Apart from the LDR-based defect identification, an approach is presented for defect detection using (weighted) bandpower calculation. Finally, the conclusions are summarized.

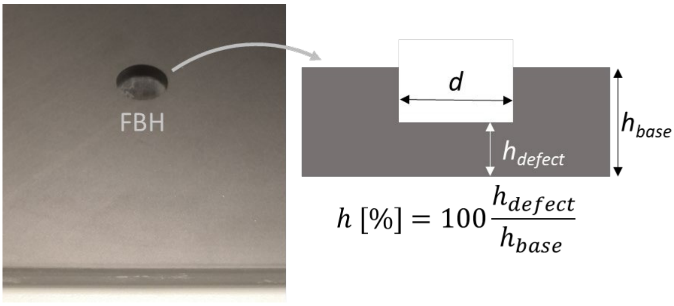

Figure 7.1: Flat bottom hole (FBH) defect with definition of base material thickness h_{base}, defect thickness h_{defect} and relative thickness h.

2. Materials and Methods

2.1. Finite Element Simulation

In order to investigate the LDR behavior for a range of defect parameters, an implicit FE simulation model is developed (in Abaqus/CAE 2020). The idea behind FE simulations for investigation of LDRs, and the different steps of the simulation, was already outlined in Chapter 5 Section 3. The model parameters are schematically shown in Figure 7.2. The model consists of a flat 200 mm by 150 mm coupon with one defect of diameter d and local thickness h_{defect}. In accordance with the experimental samples, the base material thicknesses h_{base} are 5 mm and 5.45 mm for the aluminum and for the CFRP coupon, respectively. Also, the material properties used in the simulations (see Figure 7.2 (b-c)) are identical to these of the experimental test specimens. Each of the 24 laminae of the quasi-isotropic $[(45/0/-45/90)_3]_s$ CFRP coupon is modelled as one element layer with the material's C-tensor given in Figure 7.2 (c) and with local orientation according to the ply angle.

To reduce the calculation time, the bottom halve of the model is disregarded and symmetric boundary conditions are imposed on the horizontal symmetry line. The use of this symmetry condition obstructs the in-plane vertical vibration (V_Y) at the symmetry plane. As a result, it is advised not to use this symmetry condition when the simulation result is used for the investigation of in-plane LDRs. The remaining top part of the coupon is modelled using a uniform mesh of linear eight node continuous shell elements (type SC8R). In the thickness direction, the model is divided into 24 element layers. In case of a FBH defect, a specific amount of the layers is eliminated at the location of the defect. In the specific case of a delamination, the defect is modelled using duplicated overlapping nodes (i.e. a seam crack with no interfacial interactions) in between two element layers. The parametric space of the investigated defects is listed in Table 7.1. The thickness of the defects is changed in steps of 2 elements layers resulting in a Δh = 2/24 = 8.3 %.

The natural frequencies and corresponding mode shapes of the system are calculated using the Lanczos solver [8] up to a maximum frequency of 150 kHz. Based on a mesh-convergence study, a mesh size of 1 mm is used in the in-plane directions that corresponds to 17 and 10 elements per wavelength at the highest frequency of interest for the aluminum and CFRP coupon, respectively. This is in agreement with the rule-of-thumb that states that more than six elements per wavelength should be used for simulation of guided elastic waves [9]. The total model contains around 370.000 mesh elements. No artificial noise was added to the computed mode shapes. Instead, the results and conclusions obtained using the numerical data are validated with experimental measurements.

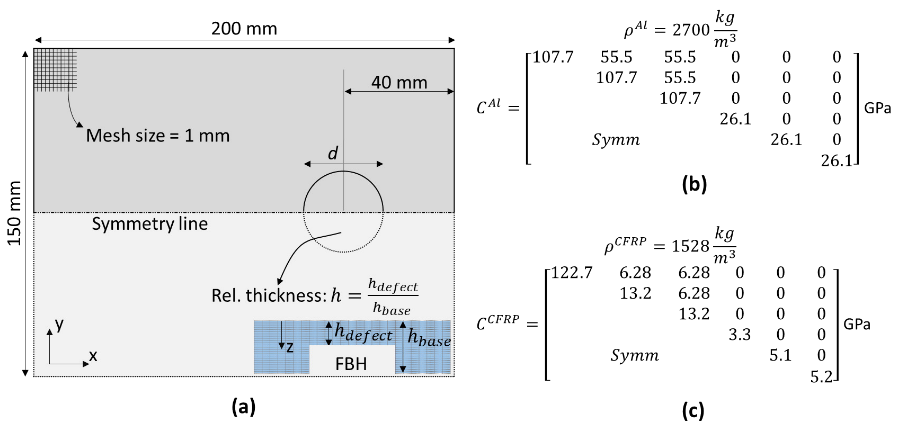

Figure 7.2: (a) Schematic view of the FE simulation model and (b-c) Material properties of the aluminum alloy [10] and CFRP lamina [11], respectively.

Table 7.1: Defect characteristics modelled in the FE simulation.

Material	Defect type	*d* (mm)	*h* (%)
Aluminum	FBH	10, 15, 20, 25, 35	8.3, … (Δh = 8.3) … , 92
CFRP	FBH	10, 12.5, 15, 20, 25, 30	8.3, … (Δh = 8.3) … , 92
$[(45/0/\text{-}45/90)]_{3S}$	Delamination	15	8.3, … (Δh = 8.3) … , 92

2.2. SLDV Experiment

To assist and validate the FE simulations, several full wavefield experimental measurements are performed. The broadband vibration response of four flat square plates with multiple FBHs is measured using the 3D SLDV. Figure 7.3 shows the backside of one of the three aluminum coupons and the backside of the CFRP coupon. The material properties are given in Figure 7.2 (b-c). The CFRP plate is manufactured (autoclave) out of 24 unidirectional (UD) carbon fiber laminae according to the quasi-isotropic layup $[(45/0/-45/90)_3]_s$. The FBH defects are visible from the backside and the diameters *d* and relative thicknesses *h* are listed (see also Figure 7.1). For each aluminum plate, the FBHs have a fixed diameter but range in thickness. The CFRP plate contains FBHs that range in both diameter and thickness. As listed in Figure 7.3, the plates contain in total four through holes (i.e. h = 0 %) that were introduced by accident.

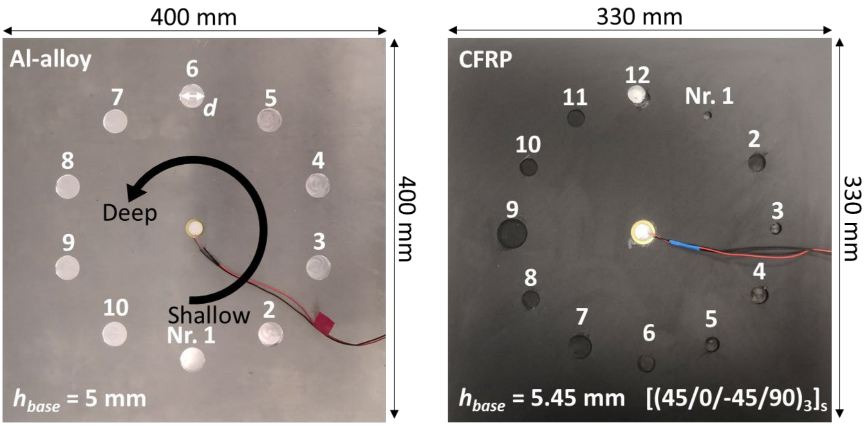

		Nr.	1	2	3	4	5	6	7	8	9	10
Al-alloy	Plate 1	*d* (mm)	15	15	15	15	15	15	15	15	15	15
		h (%)	0	0	12	29	39	49	59	70	76	83
	Plate 2	*d* (mm)	25	25	25	25	25	25	25	25	25	25
		h (%)	0	6	18	27	38	54	59	66	78	87
	Plate 3	*d* (mm)	35	35	35	35	35	35	35	35	35	35
		h (%)	9	13	20	30	43	57	64	71	83	93

	Nr.	1	2	3	4	5	6	7	8	9	10	11	12
CFRP	*d* (mm)	7	15	10	15	12.5	15	20	15	25	15	15	15
	h (%)	29	20	31	29	30	39	31	49	31	58	67	0

Figure 7.3: Backside of the aluminum and CFRP test specimens with FBHs ranging in relative thickness *h* and diameter *d*.

All coupons are excited using a low power piezoelectric bending disc (type EPZ-20MS64W from Ekulit) bonded to the backside with phenyl salicylate (see Figure 7.3). The actuator is supplied with a sine sweep signal. The sweep frequency starts at 1 kHz and ends at 100 kHz for the aluminum plates and at 150 kHz for the CFRP plate. The voltage of excitation is amplified 50 times to 150 V_{pp} (by the Falco System WMA-300 voltage amplifier) to increase the input energy. The in-plane and out-of-plane vibrational response of the flat frontside is measured with the 3D SLDV. A uniform scan point spacing of 1.5 mm is used. For each scan point, 10000 time samples are recorded with a sampling rate of 250 kS/s (i.e. signal length of 40 ms) and 512 kS/s (i.e. signal length of 20 ms) for the aluminum plates and for the CRFP plate, respectively. FFT is performed to obtain the ODS at each frequency bin:

$$V_i(x,y,t) \xrightarrow{FFT} \tilde{V}_i(x,y,f) \text{ with } i = X, Y \text{ or } Z$$

2.3. Identification of LDR Frequency

In order to identify the specific mode shape or ODS corresponding to the LDR of the defect, the defect-to-background ratio DBR is calculated as:

$$\begin{gathered} DBR_Z(f) = \frac{n_{healthy}}{n_{defect}} \frac{\sum_{(x,y)\in\Omega_{defect}} \left|\tilde{V}_Z(x,y,f)\right|}{\sum_{(x,y)\notin\Omega_{defect}} \left|\tilde{V}_Z(x,y,f)\right|} \\ DBR_{XY}(f) = \frac{n_{healthy}}{n_{defect}} \frac{\sum_{(x,y)\in\Omega_{defect}} \sqrt{\left|\tilde{V}_X(x,y,f)\right|^2 + \left|\tilde{V}_Y(x,y,f)\right|^2}}{\sum_{(x,y)\notin\Omega_{defect}} \sqrt{\left|\tilde{V}_X(x,y,f)\right|^2 + \left|\tilde{V}_Y(x,y,f)\right|^2}} \end{gathered} \tag{7.1}$$

where Ω_{defect} is the known defected area that contains n_{defect} measurement points and the surrounding healthy area contains $n_{healthy}$ measurement points. $\left|\tilde{V}_i(x,y,f)\right|$ is the magnitude of in-plane horizontal ($i = X$), in-plane vertical ($i = Y$) or out-of-plane ($i = Z$) velocity at the point with location (x, y) for the mode shape or ODS corresponding to frequency f. Thus for each mode shape or ODS, the DBR_Z and DBR_{XY} equals the average amplitude of vibration at the defect's location compared to the average amplitude of vibration at the remainder of the coupon in the out-of-plane and in the in-plane directions, respectively. As a result, a local maximum in the $DBR_Z(f)$ curve is related to a LDR_Z and a local maximum in the $DBR_{XY}(f)$ curve corresponds to a LDR_{XY}. This LDR identification (for known defect locations) procedure is further illustrated in Section 3.

Next to the numerical and experimental identification of the LDR frequency, an analytical prediction can be made (see Chapter 5 Section 2 or [12, 13]):

$$f_{LDR_Z} = \sqrt{\frac{5}{3}} \frac{16\ h_{defect}}{\pi d^2} \sqrt{\frac{E}{12\rho(1-\nu^2)}} \tag{7.2}$$

$$f_{LDR_{XY}} = \frac{1}{2a} \sqrt{\frac{E}{\rho(1-\nu^2)}} \tag{7.3}$$

where a is the width of the defect for which the in-plane LDR_{XY} is triggered.

According to Eq. (7.2) and as discussed in Chapter 5, it is predicted that f_{LDR_Z} linearly depends on the ratio of defect thickness over defect size squared: $\frac{h_{defect}}{d^2}$. This analytical prediction is based on flexural waves and assumed clamped boundary and thin plate conditions for the resonating defect. These assumptions limit the validity of Eq. (7.2) to shallow and large defects (see Chapter 5 Section 2.5): $f.h_{defect} <$ 250 kHz.mm and $\frac{d}{h_{defect}} > 7$ to 10 [13].

On the other hand, according to Eq. (7.3), $f_{LDR_{XY}}$ linearly depends on the inverse of defect size: $\frac{1}{d}$, and is independent of the defect's thickness h_{defect}. This time the prediction is based on axial waves and again assumed clamped boundary and thin-plate conditions, which limits the applicability of Eq. (7.3) to $f.h_{defect} <$ 1000 kHz.mm (see Chapter 5 Section 2.5).

3. LDR$_Z$ of FBHs in Aluminum Plate

For each FBH defect, the out-of-plane vibrational response in frequency domain is analyzed and the LDR$_Z$ frequency (f_{LDR_Z}) is identified. As an example, the experimental identification of f_{LDR_Z} using $DBR_Z(f)$ calculation is illustrated for the FBHs of h = 18, 27 and 59 % and d = 25 mm in the aluminum coupon (see Figure 7.4). For the shallow defect, i.e. FBH with h = 18 %, the $DBR_Z(f)$ curve shows a clear maximum at the fundamental LDR$_Z$ frequency (14 kHz) of the defect (see ODS in Figure 7.4 (a)). Other local maxima correspond to higher order LDR$_Z$ modes (see ODS in Figure 7.4 (b,c)). Note that the ODS at 45 kHz (Figure 7.4 (c)) by coincidence also shows the higher order LDR$_Z$ of another shallow FBH. For the FBH of h = 27 %, a similar observation can be made but with a clear reduction in maximum DBR_Z amplitude. The corresponding ODSs are presented in Figure 7.4 (d,e). For the deep defect at h = 59 %, the DBR_Z curve does not show a clear peak anymore and thus no LDR$_Z$ behavior could be identified (see also inset of Figure 7.4). In this case, the ODS at maximum DBR_Z corresponds rather to a global plate resonance at 8 kHz with an anti-node coinciding with the location of the defect (see Figure 7.4 (f)).

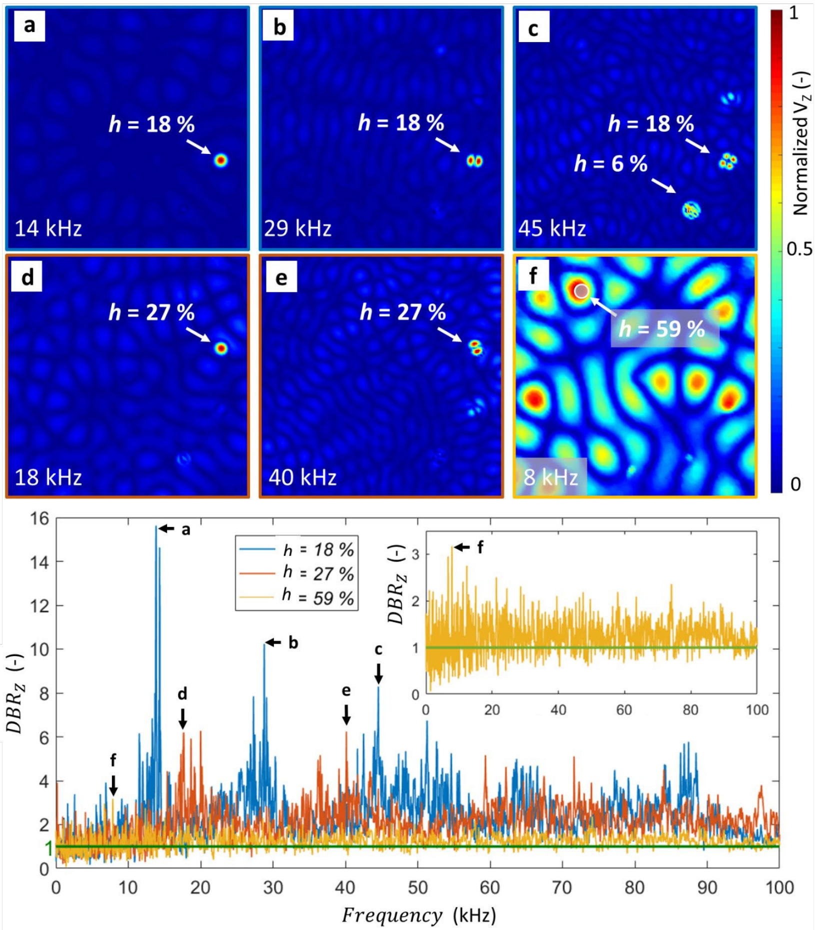

Figure 7.4: Experimentally obtained defect-to-background ratio for the out-of-plane velocity component in function of frequency at three FBHs in the aluminum plate (d = 25 mm, h = 18, 27 and 59 %). Several out-of-plane velocity amplitude maps at local maxima in the DBR_Z curve are added.

In an identical way, the f_{LDR_Z} is identified for all numerical and experimental investigated defects. The results are grouped in Figure 7.5. Each defect has a specific diameter d and relative thickness h. The data for defects of the same diameter are given the same color (see legend) whereas the h values are shown on the x-axis. Filled markers refer to simulations whereas the empty markers correspond to experimental results. Figure 7.5 (a) and (b) both show f_{LDR_Z} in function of the defect's relative thickness whereas the DBR_Z value corresponding to f_{LDR_Z} is shown in Figure 7.5 (c) and (d). The results are separated into small and large diameter defects to improve the readability of the figures. For the FBHs with d = 10, 15 and 20 mm (orange, yellow and purple color, respectively), the analytical prediction of f_{LDR_Z} using Eq. (7.2) is included. In addition, four mode shapes are included for the simulated defects with d = 15 mm and the corresponding data points are indicated on Figure 7.5 (a) and (c). In a similar way, the ODSs discussed in Figure 7.4 are marked on Figure 7.5 (b) and (d) (i.e. 4.a, 4.d and 4.f).

For the aluminum plate with FBH size 15 mm, an additional measurement is performed up to 300 kHz to validate that all LDR_Z frequencies are indeed below 100 kHz. A difference in LDR_Z behavior is observed between shallow and deep defects. The results are discussed separately for both defect types in the next two sections.

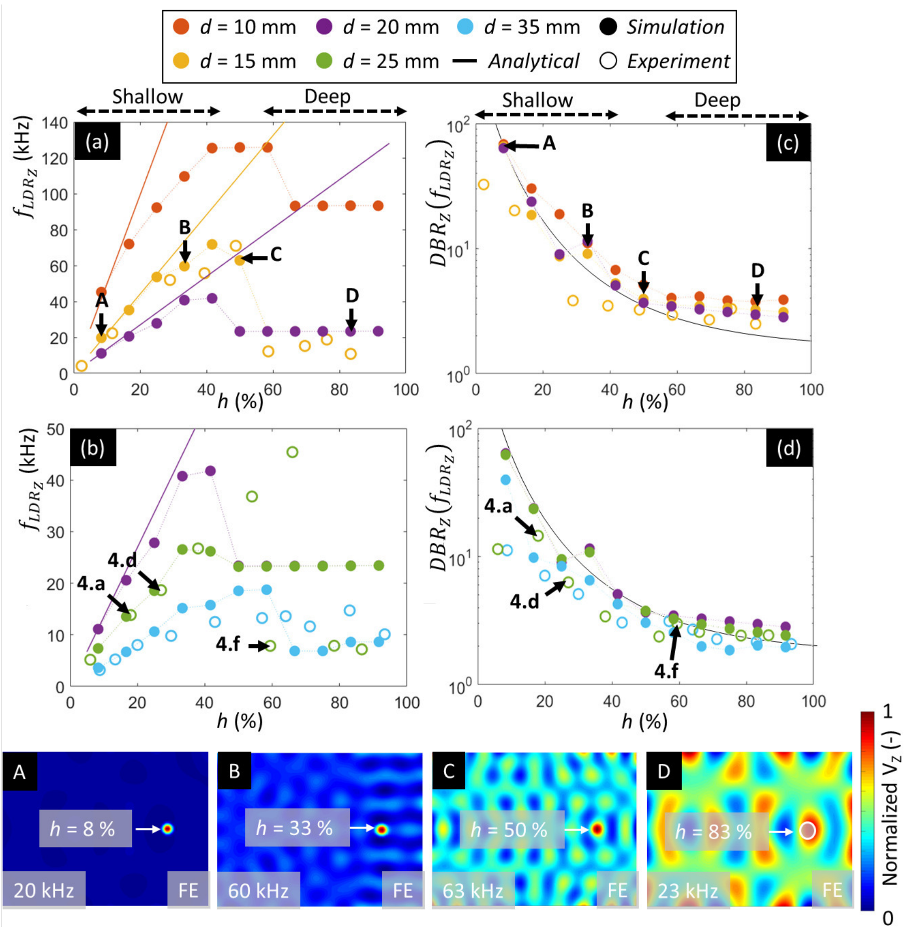

Figure 7.5: (a,b) LDR_Z frequency and (c,d) corresponding defect-to-background ratio for FBHs in aluminum plate. The numerically computed LDR_Z mode shape is provided for the FBHs with d = 15 mm and h = 8, 33, 50 and 83 % (A-D). The markers of the modes shapes shown in Figure 7.4 are indicated with 4.a, 4.b and 4.c.

3.1. Shallow Defects: h < 50 %

The shallow defects (h < 50 %), show a clear local maximum in the $DBR_Z(f)$ curve related to LDRZ behavior. This strong LDRZ is presented in Figure 7.5 (A) for a FBH with d = 15 mm (yellow color) and h = 8 %. The LDRZ is triggered at 20 kHz. From this mode shape, the defect can be easily identified due to the high DBR_Z value of 68 (see Figure 7.5 (c)). When the relative thickness of the defect increases, the LDRZ behavior gets tempered and the related DBR_Z decreases (see Figure 7.5 (c,d)). Mode shape (B) corresponds to a LDRZ (at 60 kHz) for the FBH of d = 15 mm (yellow color) and h = 33 %. The defect is still detectable but the decrease in DBR_Z is evident when comparing mode shapes (A) and (B). The DBR_Z decreases with the third power of the defect's thickness h (see black line on Figure 7.5 (c,d)). This comes as no surprise knowing that the flexural rigidity, as deducted in Chapter 5 Eq. (5.6), is dependent on h^3.

For these shallow defects, a good correspondence is found between the f_{LDR_Z} deducted from FE simulation (filled symbols) and experiments (open symbols). On Figure 7.5 (b) and (d), the fundamental LDRZ frequencies, for which the ODSs were discussed in Figure 7.4, are indicated. The frequencies match with the numerical predictions and the mode shapes show the strong LDRZ behavior. Also the analytical estimation (straight lines on Figure 7.5 (a,b)) is in accordance with the results showing the linear dependency of f_{LDR_Z} with h. For defects with small d/h_{defect} ratio, the assumptions of the analytical prediction are not valid resulting in an overestimation of f_{LDR_Z}. This explains the mismatch between the analytical predicted and numerically obtained f_{LDR_Z} for FBH's of diameter d = 10 mm and h > 18 %.

To further investigate the validity of Eq. (7.2), the f_{LDR_Z} results are plotted in function of the defect diameter for defects of h = 8 % and h = 33 % (see Figure 7.6). Again, a good correspondence is found between the analytical prediction and the FE simulations except for the defects with relative thickness h = 33 % and d < 20 mm. For these defects, the thin plate, clamped boundary assumptions are not valid and f_{LDR_Z} is overestimated. In addition, this figure confirms the quadratic reduction of f_{LDR_Z} with increasing defect diameter.

In a practical case of NDT using the concept of LDR, the shallow defect's LDRZ behavior can be detected from the broadband V_Z response either manually or automated (see Chapter 6 or [14]) by exploiting the characteristic high DBR_Z. The size of the defect can be estimated from its ODS at the identified LDRZ frequency. With known material parameters (i.e. stiffness tensor and density), the defect depth can then be derived from an iterative FE procedure or approximated using Eq. (7.2).

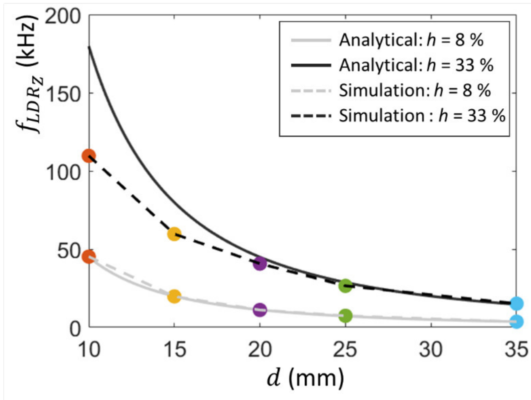

Figure 7.6: Numerically computed and analytically predicted f_{LDR_Z} in function of defect's diameter for shallow defects with relative thickness h = 8 and 33 %.

3.2. Deep Defects: h > 50 %

For the deep defects (h > 50 %), the $DBR_Z(f)$ curve does not show a pronounced maximum (see also inset of Figure 7.4) that indicates the absence of LDRz behavior. This observation is further illustrated by evaluating the mode shapes at maximum DBR_Z for FBHs of d = 15 mm (yellow color Figure 7.5 (a)) at depth h = 50 and h = 83 % (see Figure 7.5, mode shapes (C) and (D)). The FBH with h = 50 % shows an increased vibrational amplitude at f_{LDR_Z} = 63 kHz with corresponding DBR_Z = 4. This f_{LDR_Z} is significantly lower than analytically predicted. From observing mode shape (C), the significant vibrational activity of the sound area of the coupon is visible. For the FBH with h = 83 %, the maximum DBR_Z decreases to 3 for the corresponding mode shape (D) at 23 kHz. It is clear that this mode shape is not showing LDRz but rather a global plate resonance with an anti-node at the defect's location.

For all simulations, the defects are located at the same position. As a result, in the case of deep defects, it is often the same global resonance that is identified by the maximum DBR_Z. This explains the convergence of f_{LDR_Z} for deep defects to a specific global resonance frequency, for instance 23 kHz in the case of the sample with FBH of diameter 15 and 20 mm (yellow and purple curve in Figure 7.5 (a)). A similar observation can be made for the experimental results of deep defects. The frequency of maximum DBR_Z is again related to a global resonance frequency with an anti-node at the defect's location. This f_{LDR_Z} thus depends largely on the global plate parameters and only limitedly on the defect's parameters. Considering that the global plate dimensions are different in the FE simulation and experiment, it is normal that there is a bad correspondence between f_{LDR_Z} derived from simulation and from experiment.

The limited DBR_Z value makes the detection of these deep defects by ODS investigation impossible. As such, other methods are required to detect these deep defects.

4. LDR$_{XY}$ of FBHs in Aluminum Plate

The LDR$_{XY}$ frequencies and corresponding defect-to-background ratios are identified for the experimental results of the aluminum plate with FBHs of diameter 35 mm. For all FBHs, the $f_{LDR_{XY}}$ is identified between 80 and 90 kHz (see Figure 7.7 (a)). This is slightly above the $f_{LDR_{XY}}$ predicted using Eq. (7.3) which equals 77.3 kHz. Note again that Eq. (7.3) was derived using the assumptions of straight-crested axial waves and infinitely long notch like defects with spatial width a. The $f_{LDR_{XY}}$ value of 77.3 kHz is obtained by approximating the FBH with diameter d as such an infinitely long notch with width $a = d$. This approximation could explain the observed underestimation of $f_{LDR_{XY}}$.

The in-plane velocity amplitude maps at three LDR$_{XY}$'s are shown in Figure 7.7 (A-C). At 80 kHz, the LDR$_{XY}$ of the most shallow FBH is triggered. This LDR$_{XY}$ corresponds to a DBR_{XY} of 7.4 (see Figure 7.7 (b)). The DBR_{XY} decreases for increasing FBH material thicknesses. As an example, the DBR_{XY} for the FBH of h = 57 % is only 2.3 which makes the defect hardly distinguishable in the ODS (see Figure 7.7 (c)). Based on the expression of axial rigidity (see Eq. (5.17)), a linear decrease of DBR_{XY} for increasing defect thicknesses h is predicted. As seen on Figure 7.7 (b), the experimental observed decrease of DBR_{XY} is (approximately) in agreement with this prediction.

Similar as for LDR$_Z$, it is concluded that deep defects cannot be detected by searching for LDR$_{XY}$ behavior. Moreover, the DBR_{XY}'s are low compared to the DBR_Z's, which is related to h^3-dependecy of the flexural rigidity compared to the h-dependecy of the axial rigidity (see Eq. (5.6) and (5.17)). As a result, the remainder of this chapter focusses exclusively on LDR$_Z$.

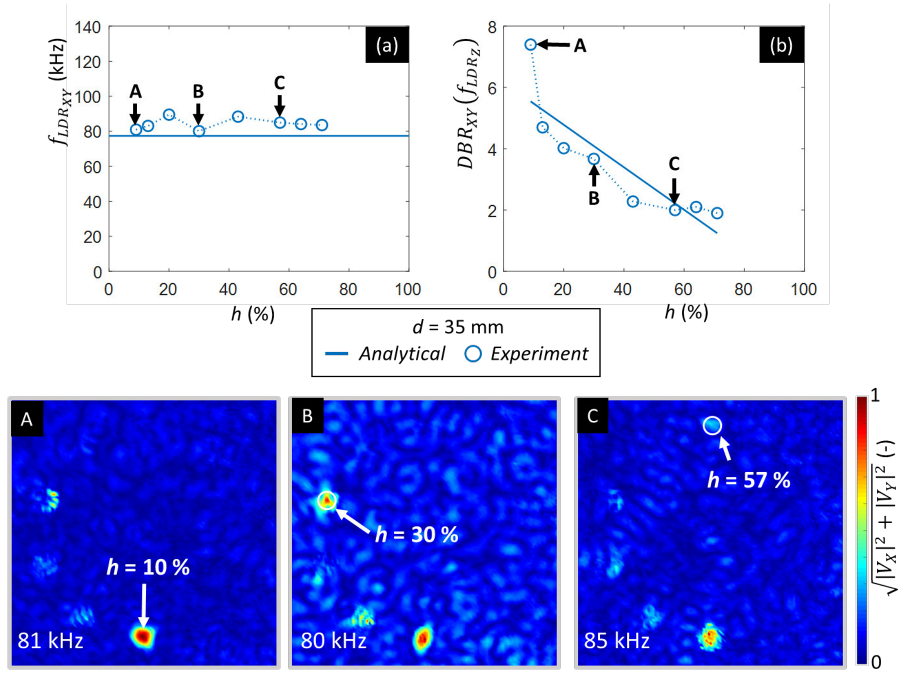

Figure 7.7: (a) LDR$_{XY}$ frequency and (b) corresponding defect-to-background ratio for FBHs in aluminum plate with diameter d = 35 mm. Experimental in-plane ODSs at LDR$_{XY}$ for the FBHs with (A) h = 10, (B) h = 30 and (C) h = 57 %.

5. LDR$_Z$ of FBHs and Delaminations in CFRP Plate

To verify if the observations made in Section 3 are valid for more complex materials, a similar investigation to the LDR$_Z$ behavior of FBHs is performed for the CFRP material. In composite materials, FBHs are popular for benchmarking NDT methods because a FBH mimics a delamination with size and depth controlled through the high speed milling process. In order to validate the similarity in vibrational response between FBHs and delaminations, FE simulations of delaminations are also included and discussed in a separate section. The defects' parameters, namely: type, diameter d and relative thickness h, were listed in Table 7.1 (FE simulation) and Figure 7.3 (Experiments).

5.1. LDR_Z of FBHs in CFRP Plate

The LDR_Z results for the FBH defects are shown in Figure 7.8. For the FBHs, experiments as well as simulations are performed indicated by the empty and filled markers, respectively. As was the case for the FBHs in aluminum (see Figure 7.5), two specific regions can be distinguished.

The first region corresponds to the shallow defects (h < 50 %). The relatively thin FBHs show a clear LDR_Z behavior. The LDR_Z frequency increases linearly with the defect's thickness h for defects with relatively low h_{defect}/d ratio, in accordance with the analytical prediction (Eq. (7.2)), and somewhat less than linearly for defects with higher h_{defect}/d ratio (see Figure 7.8 (a,b)). The FE results match well with the experimental observations. Figure 7.8 (A), (B) and (C) show the ODS at f_{LDR_Z} for three shallow FBHs of d = 15 mm (purple color). The resonant behavior of the defect is visible in each ODS. The ODSs also illustrate the decrease in DBR_Z with increasing relative thickness. As can be seen in Figure 7.8 (c), the DBR_Z value is lower for the experimental results compared to the simulations. Firstly, there is the effect of damping which is not present in the computed mode shapes. This results in a zone of relatively high amplitude around the excitation location (see ODS (B) and (C)) that decreases the DBR_Z at LDR_Z. Secondly, the ODS at f_{LDR_Z} is influenced by plate resonances with frequencies close to f_{LDR_Z}. This also results in an increase of the amplitude at the sound region and a reduction of DBR_Z. At last, the measurement noise reduces the DBR_Z slightly. This reduction in maximum DBR_Z can further complicate the LDR identification in practical NDT applications.

The second region corresponds to the deep defects (h > 50 %) for which no LDR_Z behavior could be detected. In this case, the maximum in the $DBR_Z(f)$ curve is low and related to a global resonance of the plate with an anti-node at the location of the defect. In case of the simulation data with fixed defect location, this results in the convergence of f_{LDR_Z} to a specific global resonance. The absence of LDR_Z is further illustrated using the experimentally measured ODS at maximum DBR_Z (i.e. f = 18 kHz) for the FBH of d = 15 mm and h = 58 % (see Figure 7.8 (D)). Note that this ODS, by coincidence, shows LDR_Z at the shallow FBH of d = 25 mm and h = 31 %.

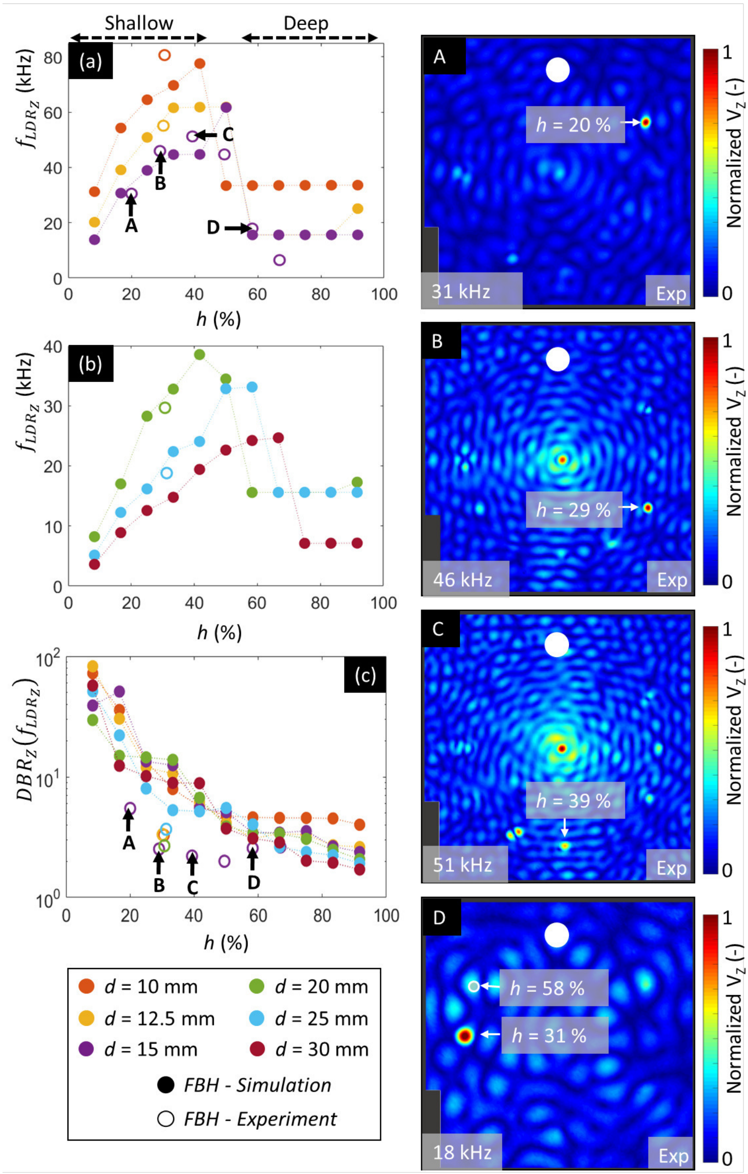

Figure 7.8: LDRz frequency and corresponding defect-to-background ratio (DBR_Z) for FBHs in CFRP plate. The experimentally observed ODS (after normalization) is provided for FBHs with d = 15 mm and h = 20, 29, 39 and 58 %.

5.2. LDRz of Delaminations in CFRP plate

Figure 7.9 shows the comparison of the numerically computed LDRz frequency for FBHs and for delaminations with diameter d = 15 mm. Cross-sectional views of three mode shapes of each defect type are included. The results for the shallow defects (h < 50 %) indicate the similarity between shallow delaminations and shallow FBHs in both the LDRz frequency as well as their mode shape (see Figure 7.9 (A) and (B)).

In contrast, the correspondence between FBHs and delaminations diminishes for deep defects. For the FBHs, the convergence of f_{LDR_Z} to a global resonance frequency is clear (see Figure 7.9 (C)). In the case of a deep delamination, the frequency of maximum DBR_Z of the thick top part of the delamination coincides with the f_{LDR_Z} of the corresponding thin bottom part of the delamination at the backside as deducted from delamination mode shape (B) and (C). This phenomenon is caused by the interaction between the two sides of the delamination and results in the symmetry of the f_{LDR_Z} curve around h = 50 %. Only the deepest delamination is an exception to this. However, the maximum DBR_Z value is still very low for these deep delaminations. As such, the observed phenomenon does not help in detecting them.

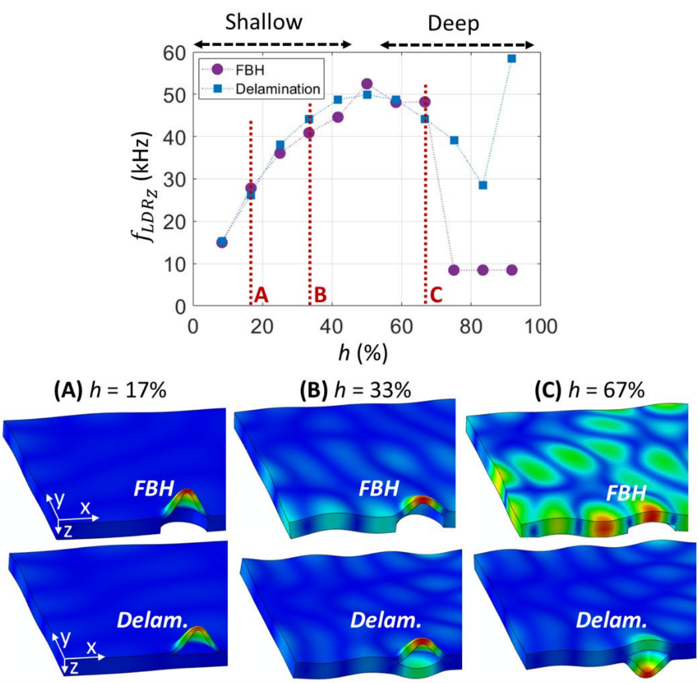

Figure 7.9: Numerically computed LDRz frequency for FBHs and delamination of d = 15 mm in CFRP plate with corresponding profile cuts for three mode shapes of each defect type.

Looking back at Section 3, it is clear that the LDRz behavior of the defects in the CFRP coupon is similar to the LDRz behavior of the defects in the aluminum coupon. Again, it is concluded that shallow defects show a pronounced LDRz behavior which allows for shallow defect detection using LDRz identification in the broadband frequency response of the structure. On the contrary, deep defects do not show LDRz behavior. An attempt can be made to exploit the non-linear response of deep defects (see Chapter 8). Alternatively, energy- or wavenumber-based approaches can be used. A simple energy-based method is presented in the next section. More advanced methods, which show an improved sensitivity, are investigated in Part 3 of the PhD thesis.

6. Bandpower Calculation for Deep Defect Detection

The parametric evaluation of LDR for FBHs in aluminum (Sections 3-4) and in CFRP (Section 5) plates revealed that the detection of deep defects by searching for LDRs in the ODSs is not possible. Indeed, the phenomenon of local defect resonance does not appear if the rigidity contrast between defect and sound area is not sufficient. Nevertheless, deep defects are still related to a small local reduction in rigidity which should lead to a slightly higher vibrational activity compared to the surrounding sound material. This is especially the case for the flexural rigidity and corresponding out-of-plane velocity component.

The increased out-of-plane vibrational activity is also deducted from Figure 7.4 in which $DBR_Z(f) > 1$ for the large majority of the frequency bins. In order to make this more visible, these three $DBR_Z(f)$ curves are repeated in Figure 7.10 together with the same curves after applying a Savitzky-Golay smoothing filter. The area below the filtered $DBR_Z(f)$ curves, for which $DBR_Z(f) > 1$, is shaded. This area is a measure for the elevated vibrational activity of the defect compared to the sound material. The elevated activity is very pronounced for shallow damage, especially at the LDRz modes (see large shaded area for defect h = 18 %). However, also for deeper defects, which do not show LDRz behavior, this elevated activity is observed (see shaded area for defect h = 59 %). This characteristic is exploited for defect detection using a weighted bandpower (WBP) calculation which is defined as:

$$WBP_Z(x,y,f_1,f_2) = \frac{\Delta f}{f_2 - f_1} \sum_{f=f_1}^{f_2} \frac{\left|\tilde{V}_z(x,y,f)\right|^2}{\left|\tilde{U}_{Excitation}(f)\right|^2 \; WD(r,f)} \qquad (7.4)$$

with $\tilde{U}_{Excitation}$ the excitation signal's amplitude for frequency f and Δf the frequency resolution. $WD(r,f)$ is the frequency specific weighting function. The frequency limits f_1 and f_2 must lie within the frequency bandwidth of the excitation signal. The weighting functions WD are introduced to compensate for the damping of the elastic waves. For each frequency bin f, this weighting function is obtained by curve fitting a second order exponential decay function to the scatter plot of $\left|\tilde{V}_z(x,y,f)\right|^2$ in function of the distance to the excitation position $r = \sqrt{(x - x_{PZT})^2 + (y - y_{PZT})^2}$. This procedure for calculation of $WD(r,f)$ is further discussed in Section 6.2. As such, the WBP_Z represents the (weighted) energy of out-of-plane vibration over the frequency band of interest.

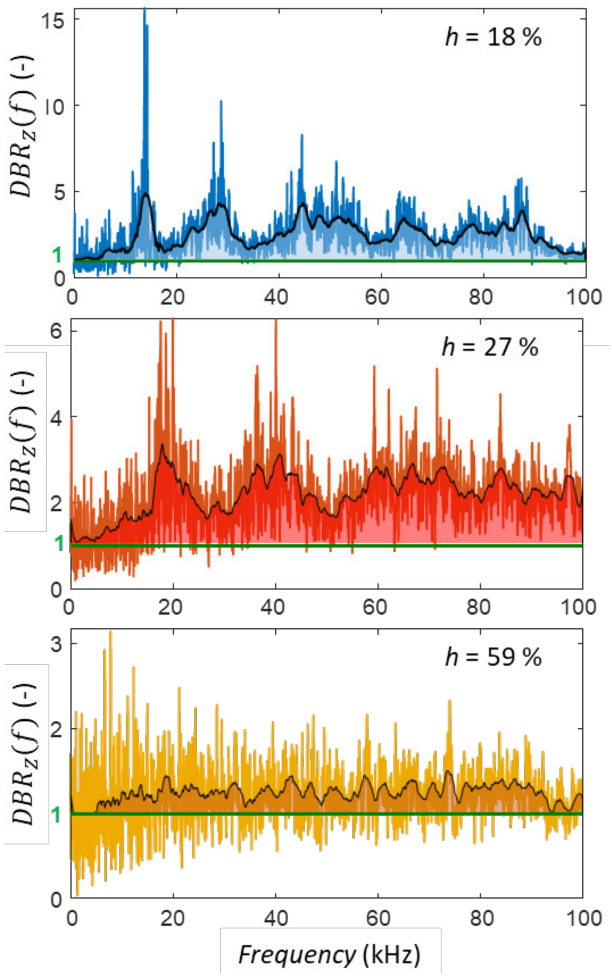

Figure 7.10: Experimentally obtained DBR_Z in function of frequency for three FBHs in the aluminum plate (d = 25 mm, h = 18, 27 and 59 %). Indication of area under Savitzky-Golay filtered DBR_Z curve (black line) for which $DBR_Z > 1$.

6.1. Bandpower for Aluminum Plate

For the three aluminum plates (with defects of d = 15, 25 and 35 mm), the bandpower (BP_Z) map is calculated over the total excitation bandwidth (f_1 = 1 kHz, f_2 = 100 kHz). For now, the weighting functions are not used: $WD(r, f) = 1$. The low material damping of aluminum allows for omitting the weighting function calculation step. For each plate, the calculation time is around 5s when performed on a Dell Latitude with Intel core i7-7820 HQ CPU @2.90 MHz and 32 GB RAM memory. The results are normalized and median filtered (with mask [3x3]) to remove erroneous measurement points. Figure 7.11 presents the obtained BP_Z maps in logarithmic colorscale.

The relative thickness of each FBH determines the local flexural rigidity reduction which in turn determines the increase in vibrational activity. This is seen in Figure 7.11, where an elevated BP_Z is observed especially at the most shallow defects. Although the BP_Z decreases for deep defects, all FBHs up to h = 90% are visually distinguishable in the BP_Z maps. Thus despite the absence of prominent LDR_Z behavior, deep defect can be detected by taking advantage of the small increase in vibrational activity summed over a large amount of frequencies.

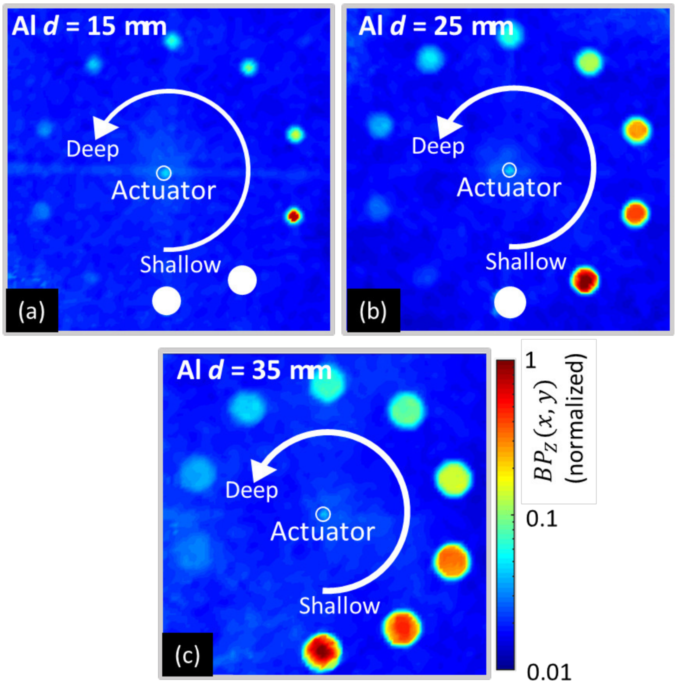

Figure 7.11: Out-of-plane bandpower (1 → 100 kHz, WD = 1) for aluminum plates with FBHs of d = 15 mm (a), d = 25 mm (b) and d = 35 mm (c).

In a successive step, these bandpower images can be used for automated defect identification sizing. As an example, Figure 7.12 shows the identification and sizing of the FBHs in the aluminum plate with FBHs of diameter 25 mm. The black and white image is obtained after thresholding the bandpower frame with a threshold equal to 0.05. The actual defect's size is indicated with red circles. The shallow defects are overestimated in size whereas the deep defects are underestimated. The deepest FBH is not detected using this 0.05 threshold value. In order to solve this, more advanced adaptive thresholding is required, taking into account the desired probability of detection. If multiple identical samples are available, a self-learning approach could be used.

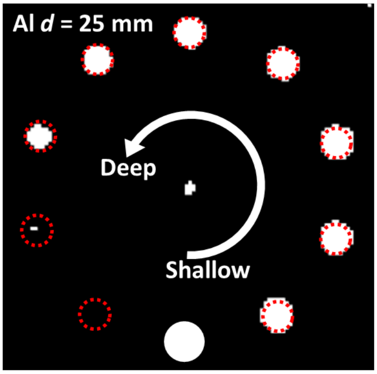

h (%)	d_{est} (mm)
6	30
18	29
27	30
38	28
54	27
59	26
66	21
78	5
87	-

Figure 7.12: Defect sizing in out-of-plane bandpower image for aluminum with FBHs of diameter 25 mm using 5 % threshold. Actual defect size is indicated with red circles.

6.2. Weighted Bandpower for CFRP Plate

The same procedure is performed to calculate the BP_Z map for the CFRP plate with FBHs (see Figure 7.13 (a)). An elevated BP_Z is observed around the excitation location. This is caused by (i) the relatively high material damping of CFRP compared to aluminum, (ii) the increased maximum frequency (i.e. 150 kHz instead of 100 kHz) and (iii) the shorter sweep length (i.e. 20 ms compared to 40 ms). This increase in BP_Z around the excitation location partially obscures the effect of the defects, especially if defects would be located close to the excitation source.

In order to compensate for the damping, the frequency specific weighting functions $WD(r, f)$ are determined. Figure 7.13 (b) shows the scatter plot of the square of out-of-plane velocity amplitude (i.e. $\left|\tilde{V}_z(x, y, f)\right|^2$) at f = 65 kHz in function of the distance to the actuator r. $WD(r, f = 65\ kHz)$ corresponds to the second order exponential decay curve fitted to this scatter plot. The resulting

WBP_Z is shown in Figure 7.13 (c). The use of the weighting function increases the calculation time to around 1 minute. The use of the weighting functions leads to a visible impression of all defects, including those for which no LDR_Z behavior could be detected. Apart from the increased vibrational response at the defects and the effect of damping, other elastic wave artifacts are captured in the WBP_Z map. As an example, the diagonals show an increased WBP_Z due to the local constructive interference of travelling elastic waves reflected from the plate's boundaries. Also around the FBHs, the WBP_Z is influenced due to wave reflection, attenuation and interference effects.

An important drawback of this WBP_Z calculation for defect detection is that the weighting method assumes a directional-independent wave attenuation. This is only valid for (quasi-)isotropic plates with uniform thickness and fully damped edged. In order to overcome these limitation, more advanced wave attenuation compensation strategies are required as will be discussed in Chapter 11.

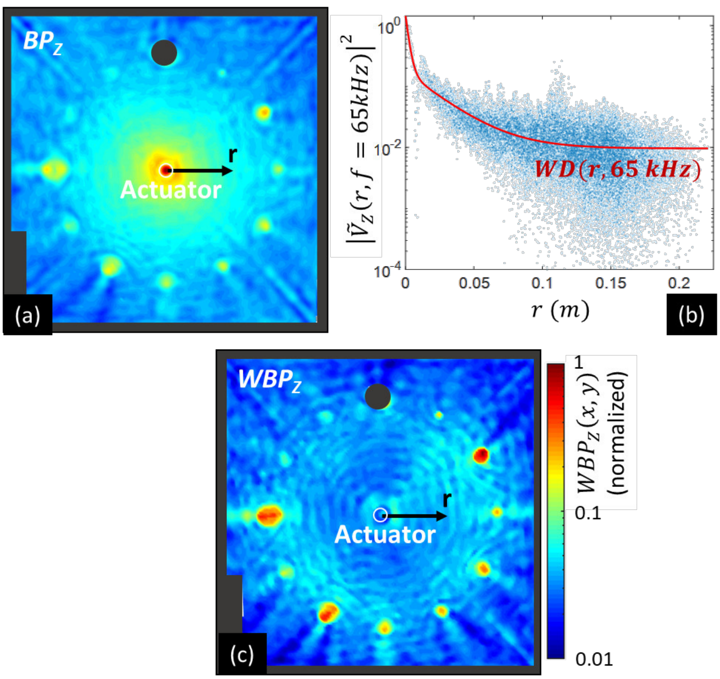

Figure 7.13: (a) Out-of-plane bandpower map (1 → 150 kHz), (b) Square of $|\tilde{V}_Z|$ at 65 kHz in function of distance to excitation location (i.e. radius r) and (c) Weighted bandpower map (1 → 150 kHz) for CFRP plate with FBHs.

7. Conclusions

The LDR behavior of FBHs is parametrically evaluated for aluminum and CFRP material. Finite element modal analysis as well as experiments using contact excitation and scanning laser Doppler vibrometry are performed. For each FBH of specific diameter and thickness, the defect-to-background ratio (DBR) is calculated for all modes shapes (FE simulation) and operational deflection shapes (experiment). Local maxima in the DBR curves are determined and investigated for LDR behavior.

For the shallow defects, i.e. FBHs with relative thickness smaller than 50 %, clear out-of-plane LDR_Z behavior at a frequency proportional to the ratio of defect's thickness over squared diameter is detected. A good correspondence between experiments and simulations is found. Additionally, it is shown that a shallow FBH is representative for a shallow delamination in layered composite materials when investigating the LDR_Z behavior. The shallow FBHs in the aluminum plate also show in-plane LDR_{XY} behavior at frequencies proportional to the inverse of the defect's size, and independent of the defect's thickness. However, the contrast at the defect under LDR_{XY} conditions is relatively small due to the limited reduction in axial rigidity.
It is concluded that such shallow defects can be detected by searching for LDR behavior in the broadband frequency response of the test specimens.

For the deep defects, i.e. relative thickness higher than 50 %, no LDR behavior corresponding to a high DBR is present. As a result, using the classical linear LDR identification techniques for detection of deep defects is impossible.

While the limited local stiffness reduction of deep defects does not result in LDR, it does slightly increase the vibrational activity at the defected area. This observation is exploited using a weighted band power calculation in which the small increase in local vibrational activity is summed over a large amount of excitation frequencies. Based on the experiments, it is shown that this simple approach allows for the detection of deep defects up to 90 % of the test specimen's depth.

References

1. Segers, J., et al., *Probing the limits of full-field linear Local Defect Resonance identification for deep defect detection.* Ultrasonics, 2020. **105**.
2. Derusova, D., et al., *Ultrasonic spectroscopic analysis of impact damage in composites by using laser vibrometry.* Composite Structures, 2019. **211**: p. 221-228.

3. Solodov, I. and M. Kreutzbruck, *Single-sided access remote imaging via resonant airborne activation of damage.* NDT & E International, 2019. **107**.
4. Girolamo, D., H.Y. Chang, and F.G. Yuan, *Impact damage visualization in a honeycomb composite panel through laser inspection using zero-lag cross-correlation imaging condition.* Ultrasonics, 2018. **87**: p. 152-165.
5. Sarens, B., et al., *Investigation of Contact Acoustic Nonlinearity in Delaminations by Shearographic Imaging, Laser Doppler Vibrometric Scanning and Finite Difference Modeling.* IEEE Transactions on Ultrasonics, 2010. **57**(6): p. 1383-1395.
6. Hettler, J., et al., *Detection and Characterization of Local Defect Resonances Arising from Delaminations and Flat Bottom Holes.* Journal of Nondestructive Evaluation, 2017. **36**(1).
7. Lamboul, B. and D. Osmont, *Delamination detection in foam core composite structures using transient flexural wavefields.* Journal of Sound and Vibration, 2016. **366**: p. 190-198.
8. Lanczos, C., *An iteration method for the solution of the eigenvalue problem of linear differential and integral operators.* Journal of Research of the National Bureau of Standards, 1950. **45**: p. 255-282.
9. Langer, P., et al., *More Than Six Elements Per Wavelength: The Practical Use of Structural Finite Element Models and Their Accuracy in Comparison with Experimental Results.* Journal of Computational Acoustics, 2017. **25**(04).
10. Stockist, A.-F.a.N.-F.M. *Aluminium Alloys - Aluminium 6082 Properties, Fabrication and Applications*. 2005; Available from: https://www.azom.com/article.aspx?ArticleID=2813.
11. Martens, A., et al., *Characterization of the orthotropic viscoelastic tensor of composites using the Ultrasonic Polar Scan.* Composite Structures, 2019. **230**.
12. Solodov, I., J. Bai, and G. Busse, *Resonant ultrasound spectroscopy of defects: Case study of flat-bottomed holes.* Journal of Applied Physics, 2013. **113**(22).
13. Solodov, I., M. Rahammer, and M. Kreutzbruck, *Analytical evaluation of resonance frequencies for planar defects: Effect of a defect shape.* NDT & E International, 2019. **102**: p. 274-280.
14. Segers, J., et al., *Efficient automated extraction of local defect resonance parameters in fiber reinforced polymers using data compression and iterative amplitude thresholding.* Journal of Sound and Vibration, 2019. **463**.

Chapter 8

Local Defect Resonance Induced Nonlinearity

Summary:

Shallow damage can be detected by searching for local defect resonance (LDR) behavior in the fundamental vibrational response. However, this is not possible for defects that are located deeper than half the thickness of the coupon due to the limited rigidity difference between the defect and the sound material.
In this study, it is shown that delaminations under harmonic excitation at the out-of-plane LDR frequency behave as sources of nonlinear higher harmonic components. Next to the higher harmonics, modulations sidebands are observed in the spectrum when a dual harmonic excitation is used. These nonlinear components are detectable when examining the delaminated component from the side where the delamination is close to the surface. In addition, the nonlinear components are detectable when examining the delaminated component from the other side, i.e. the side where the delamination is very deep. As such, monitoring of these nonlinear components allows for the detection of backside delaminations which cannot be found using traditional linear LDR techniques. Opportunities for out-of-sight damage detection and nonlinear resonant air-coupled emissions are discussed.

Sections 2 and 3 are in close correspondence with journal publication:

[1] Segers, J., Hedayatrasa, S., Poelman, G., Van Paepegem, W. and Kersemans, M. *Backside delamination detection in composites through local defect resonance induced nonlinear source behaviour.* Journal of Sound and Vibration, 2020. **479**

1. Introduction

This chapter builds further on the concept of local defect resonance (LDR) that was thoroughly discussed in the last three chapters. The parametric study of Chapter 7 indicated that NDT based on searching for high amplitude LDRs in the (linear) frequency response of the test specimen can be used to detect defects up to a depth of ±50% (relative to full thickness of the sample) [2].

Several studies proposed enhanced defect detection using nonlinear defect imaging, exploiting the relatively high vibrational activity of the defect under LDR frequency excitation [3-7]. As explained in Chapter 3, the high vibrational activity at the defect can trigger a nonlinear vibrational response caused by multiple mechanisms: contact, friction, viscoelastic damping, etc. [7-10]. Which of these mechanisms is dominant depends on the properties of the defect as well as the characteristics of the vibration field (e.g. dominant in-plane versus out-of-plane) [10, 11]. However, deep defect detection in monolithic composite components based on LDR induced nonlinearity was not yet demonstrated.

In this chapter, the nonlinear response of a delamination in a CFRP component is further investigated. It is demonstrated that delaminations behave as sources of higher harmonics when the excitation frequency matches the LDR frequency. In addition, when a second sine excitation is added, the frequencies are mixed at the defect and modulation sidebands are formed. It is numerically and experimentally proven that the defect's nonlinear source behavior is visible from both sides of the component. This allows for the detection of shallow delaminations, and more importantly, it allows for the detection of deep, backside, delaminations. At last, two important consequences of the findings are discussed: (i) the possibility to detect out-of-sight damage and (ii) the resonant air-coupled emission of the nonlinear components.

2. Higher Harmonic Generation - Simulation

As a proof of concept, an explicit finite element simulation (Abaqus/CAE 2020) is performed for a 180x165x2 mm^3 CFRP coupon, with layup $[(0/90)_2]_s$, using 115.736 linear hexahedral elements. Orthotropic material properties are used in accordance with the material properties of the experimentally investigated coupon (see Figure 7.2 (c) in Chapter 7). A delamination defect of 20x20 mm^2 is modeled as a 2 µm gap between the first and the second ply, and both normal (hard contact) and tangential (friction) interactions are prescribed. This defect model allows for contact acoustic nonlinearity (see also Chapter 3) at the gap closures when the defect is resonated. A harmonic force excitation of 50 kPa amplitude and duration 2 ms is applied at the lower left corner over a circular area (diameter 20 mm). The excitation frequency is set to 28 kHz which corresponds to an out-of-plane LDR (LDR_Z) frequency of the modelled delamination.

The out-of-plane vibrational surface response of both sides of the sample is transformed to, and analyzed in, the frequency domain:

$$V_Z(x,y,t) \xrightarrow{FFT} \tilde{V}_Z(x,y,f)$$

At the excitation frequency of 28 kHz, the LDR_Z behavior of the defect is clearly visible in the out-of-plane velocity response of the Shallow Side (see Figure 8.1 (a)). From the Deep Side however, no indication of the defect is observed due to the limited flexural rigidity mismatch between sound material and the thick side of the delamination (Figure 8.1 (b)).

At the second and third higher harmonic (HH) frequencies with f_{HH_2} = 2 x 28 kHz and f_{HH_3} = 3 x 28 kHz, respectively, the delamination shows a relatively high amplitude of vibration. While this high amplitude of vibration is especially visible from the Shallow Side (Figure 8.1 (c,e)), it is clear that the higher harmonic components are also observed from the Deep Side (Figure 8.1 (d,f)).

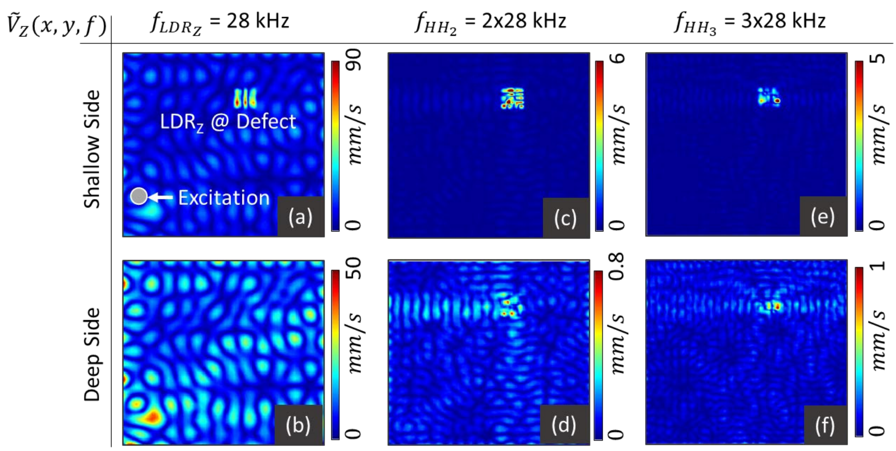

Figure 8.1: Out-of-plane velocity ($\tilde{V}_Z$) amplitude at (a-b) excitation frequency and at (c-d) second and (e-f) third higher harmonic frequency (f_{HH_2}, f_{HH_3}) for sine excitation at f_{LDR_Z}. (Top row) Shallow side, (Bottom row) Deep side – Simulation results.

3. Higher Harmonic Generation – Experiment

Furthermore, experimental verification is performed using an eight-ply 290x140x2.2 mm^3 CFRP coupon with layup $[(0/90)_2]_s$ (see Figure 8.2 (a)). Similar to the finite element model, a 20x20 mm^2 delamination is present between the first and second ply. The delamination is made by inserting two layers of 25 µm thick brass foil, sealed with flask break tape, between the first and second ply. Vibrations are introduced using two low power piezoelectric actuators (Ekulit EPZ-20MS64W) bonded to the Deep Side surface using phenyl salicylate. The Falco systems WMA-300 voltage amplifier is used to increase the voltage supplied to the actuators. The full wavefield surface vibrations are obtained with the 3D SLDV. Only the out-of-plane velocity component V_Z is considered here. The vibrations are measured from both the Shallow Side as well as the Deep Side. The surfaces of the coupon is covered with retroreflective tape to increase the signal-to-noise ratio of the acquired signals (see also Chapter 4 Section 3.3).

As a first step, the LDR_Z behavior of the delamination is investigated. To this end, both actuators are supplied with a 50 V_{pp} sweep signal from 1 to 100 kHz and the measured velocity response is analyzed for both sides of the coupon. As also done in Chapter 7, a defect-to-background ratio (DBR) is calculated as:

$$DBR_Z(f) = \frac{n_{healthy}}{n_{defect}} \frac{\sum_{(x,y)\in\Omega_{defect}} \left|\tilde{V}_Z(x,y,f)\right|}{\sum_{(x,y)\notin\Omega_{defect}} \left|\tilde{V}_Z(x,y,f)\right|} \tag{8.1}$$

where Ω_{defect} is the defected area which contains n_{defect} measurement points and the surrounding healthy area contains n_{healthy} measurement points. $\left|\tilde{V}_Z(x,y,f)\right|$ is the magnitude of out-of-plane velocity of the scan point at location (x,y) for the operational deflection shape (ODS) at frequency f. As a result, a local maximum in the $DBR_Z(f)$ curve is related to an LDR_Z. The $DBR_Z(f)$ curve, together with the average velocity amplitude at the location of the delamination, is shown in Figure 8.2 (b) and (c) for the Shallow and Deep Side of the delamination, respectively. From the Shallow Side, a clear LDR_Z behavior is observed at 27 kHz as shown by the ODS (Figure 8.2 (a)). However, from the Deep Side of the sample, no LDR_Z behavior is present due to the limited rigidity mismatch between the sound material (8 plies) and the thick part of the delamination (7 plies). Thus, the exploration of the nonlinear defect response is necessary in order to detect the deep delamination.

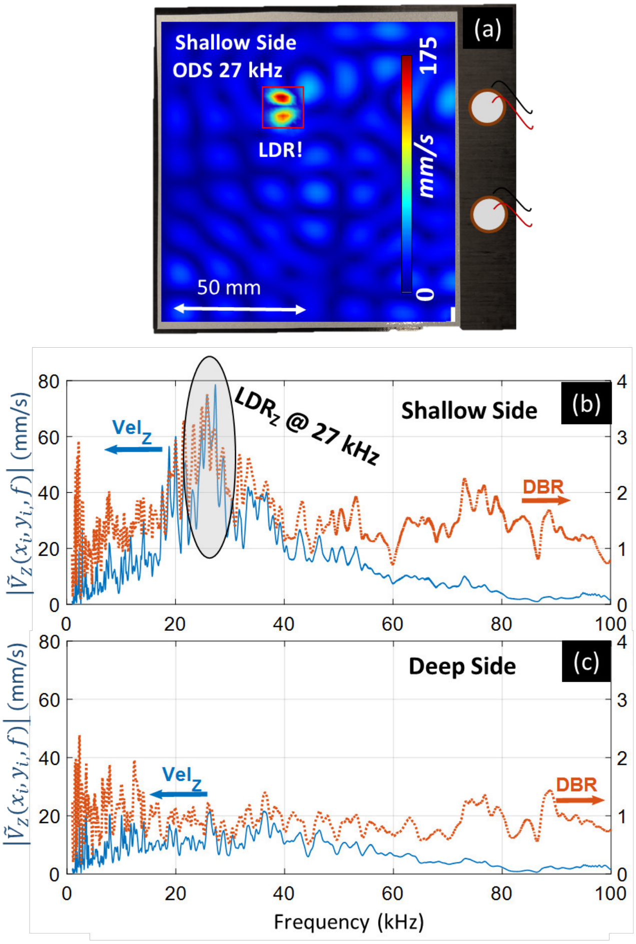

Figure 8.2: (a) Test specimen as seen from the side where the delamination is close to the surface (i.e. Shallow Side) with out-of-plane velocity amplitude at the LDR_Z frequency of 27 kHz. Defect-to-background ratio DBR_Z and out of-plane velocity amplitude V_Z at delamination as measured from (b) Shallow Side and (c) Deep Side.

In the next step, only the top actuator is used and supplied with a harmonic excitation signal with frequency equal to the above identified f_{LDR_Z} of 27 kHz and voltage 150 V_{pp}. The resulting spectrum of the out-of-plane velocity component at the defect is shown in Figure 8.3 (a). The spectrum reveals the presence of higher harmonics (HH_i with $f_{HH_i} = i * f_{Actuator}$) at the Shallow Side of the delamination as well as at the Deep Side. The ODSs corresponding to the excitation frequency ($f_{Actuator} = f_{LDR_Z}$) and to the 2nd and 3th higher harmonics are shown in Figure 8.3 (b-g).

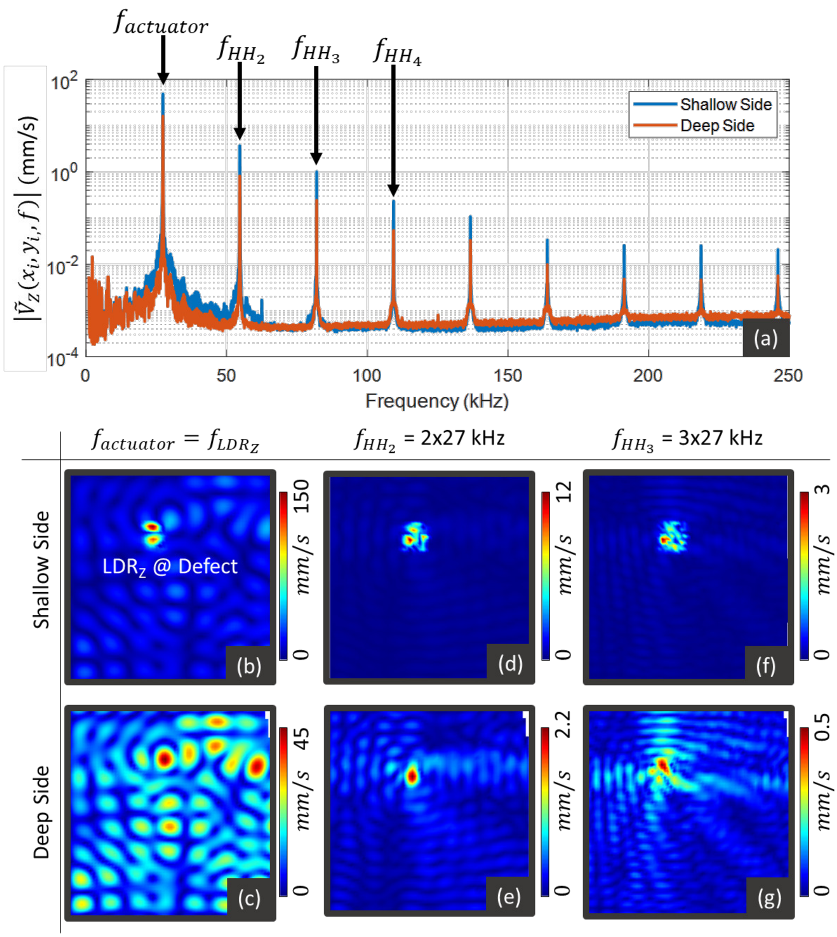

Figure 8.3: (a) Out-of-plane velocity spectrum at the defect and operational deflection shapes at (b-c) excitation frequency and at (d-e) second and (f-g) third higher harmonic frequency (f_{HH_2}, f_{HH_3}) for sine excitation at f_{LDR_Z}. (Top row) Shallow side, (Bottom row) Deep side - Experimental observations.

This experimental observation is highly similar to the numerical observation (see Figure 8.1). The ODS at f_{LDR_Z} displays the LDR_Z behavior at the Shallow Side of the delamination, while there is no indication of the delamination from the Deep Side. The ODS corresponding to the HH frequencies on the other hand show a local high amplitude at the defect and, more importantly, the defect behaves as a source, radiating these harmonics to the surrounding sound material. This source behavior is most pronounced at the Shallow Side but is also clearly visible from the Deep Side.

To further prove that the HH components are present due to the defect nonlinearity, and not as a result of potential source nonlinearity, the specimen is excited using a sine frequency at f = 54 kHz. The obtained ODSs (Figure 8.4 (a,b)) are compared with the ODSs corresponding to the HH_2 component (for sine excitation at f = 27 kHz) found earlier (Figure 8.4 (c,d)). The large mismatch between these velocity amplitude maps indicate that the HH_2 vibrations are indeed dominantly formed at the defect and are not the result of source nonlinearity.

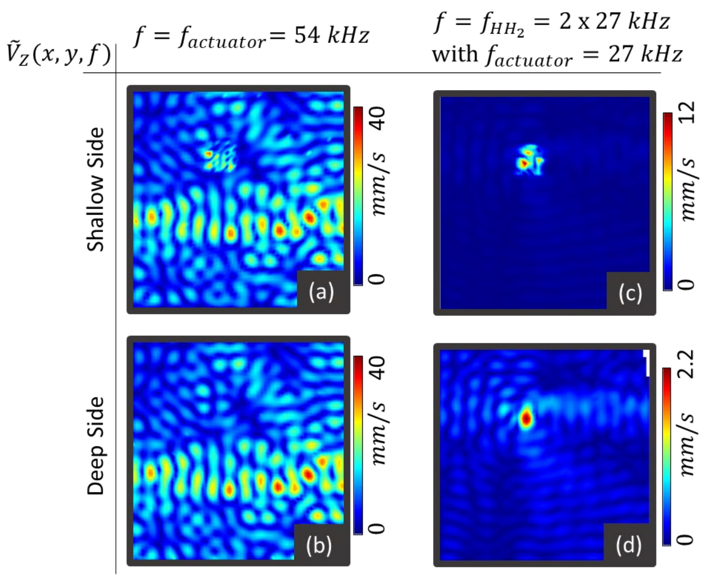

Figure 8.4: Out-of-plane velocity amplitude at 54 kHz when excited using (a,b) 54 kHz sine, versus, (c,d) 27 kHz sine (see Figure 8.3 (c,d)).

4. Sideband Component Generation – Experiment

A second experiment is performed using a dual harmonic excitation. The top actuator is again supplied with the 27 kHz sine signal of amplitude 150 V_{pp} (i.e. identical to the excitation signal used in the previous section), and the second (lower) actuator is supplied with a sine voltage signal of amplitude 150 V_{pp} at an arbitrary frequency of 40 kHz.

The spectrum of the resulting out-of-plane velocity component at the defect is shown in Figure 8.5 (a). The blue curve corresponds to the spectrum at the Shallow Side of the delamination whereas the orange curve corresponds to the spectrum measured at the Deep Side. The two highest maxima in the spectrum are found at the two excitation frequencies: f_{act1} = 27 kHz and f_{act2} = 40 kHz. The corresponding ODSs are shown in Figure 8.5 (b-c) and (d-e). At 27 kHz, the LDR_Z is observed at the Shallow Side of the delamination. Also at 40 kHz, an increase in vibrational activity observed at the delamination attributed to the locally reduced flexural rigidity. The ODSs of the Deep Side (Figure 8.5 (c,e)) do not reveal a pronounced amplitude increase at the defect's location.

A large number of additional peaks are present in the defect's Shallow Side and Deep Side spectra (see Figure 8.5 (a)). These peaks are attributed to defect nonlinearity (and partially due to source nonlinearity). They corresponds to: (i) HHs of the sine signal excited by the first actuator with frequencies: $i.f_{act1}$ (i = 1,2,3,…), (ii) HHs of the sine signal excited by the second actuator with frequencies: $i.f_{act2}$ (i = 1,2,3,…) and (iii) Modulation sidebands (SB) at $i.f_{act1} + j.f_{act2}$ (i,j = …,-2,-1,1,2,…). Vertical lines are added to the spectrum in Figure 8.5 (a) to indicate the HHs and a selection of the SBs (i.e. those with i = 1 or j = 1).

The amplitude of $\tilde{V}_Z$ at SB frequencies $f_{act1} + f_{act2}$ = 67 kHz and $2f_{act1} + f_{act2}$ = 94 kHz is shown in Figure 8.5 (f-g) and (h-i), respectively. Once again, the nonlinear source behavior of the delamination is revealed. The source behavior is evident when inspecting the test specimen from the Shallow Side of the delamination (Figure 8.5 (f,h)) but also when inspecting it from the side where the delamination is located deep into the component (Figure 8.5 (g,i)).

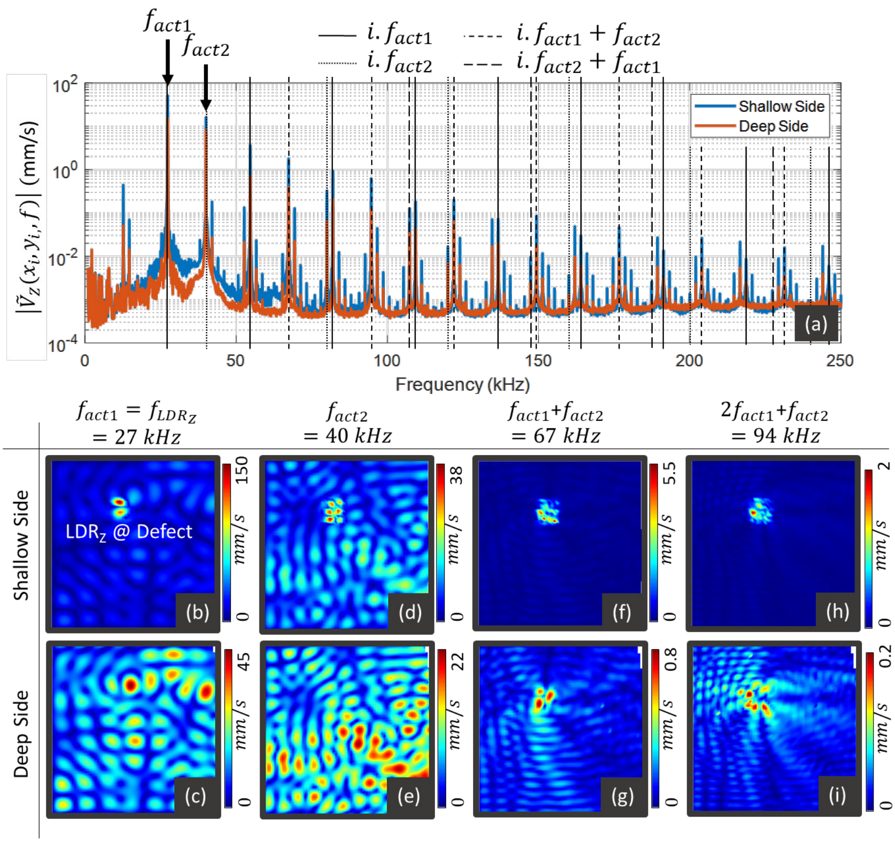

Figure 8.5: (a) Out-of-plane velocity spectrum at the defect, and ODSs at (b-e) excitation frequencies and at (f-i) sideband frequencies for dual sine excitation – Experimental observations.

5. Opportunities for NDT

In previous sections, it was observed that HH and SB frequency components are created at the location of a defect when the defect is resonating. These nonlinear vibrational components can radiate away from the defect into the damage-free material. This is clearly visible in the ODSs of the HH and SB components shown in Figure 8.1 (c-f), Figure 8.3 (d-g) and Figure 8.5 (f-i). The intensity of the nonlinear components decreases with the distance to the delamination because of geometrical wave spreading and wave attenuation (which is relatively high in this frequency range).

This nonlinear radiation of defects opens opportunities for out-of-sight defect detection (see [6, 12]) and defect detection based on nonlinear resonant air-coupled emission monitoring [13-16].

5.1. Out-Of-Sight Damage Detection

The nonlinear source behavior of defects is exploited in order to detect out-of-sight defects. Such defects are typically encountered if certain parts of the component are hidden and cannot be reached by the SLDV's laser beams, or simply if one wants to reduce the inspection time. As an example, the inspection area of the test specimen is reduced to a small square area of around 40 × 40 mm^2 at the surface of the test specimen where the delamination is deep (indicated in orange on Figure 8.6 (a)). The same dual harmonic excitation as was used in the previous section is applied. The resulting out-of-plane velocity response measured at this small scan area is used to not only detect, but also to localize the delamination. The procedure is illustrated for the velocity response at the SB frequency $f_{act1} + f_{act2}$ = 67 kHz, although note that similar results can be obtained for other nonlinear components (e.g. HHs).

To start, the out-of-plane velocity signal is transformed from the spatial-time domain to the wavenumber-frequency domain using three-dimensional FFT according to:

$$V_z(x, y, t) \xrightarrow{3D\ FFT} \tilde{V}_Z(k_x, k_y, f)$$

where k_x and k_y are the wavenumbers in horizontal and vertical direction, respectively. The wavenumber map corresponding to the SB response at $f_{act1} + f_{act2}$ = 67 kHz is shown in Figure 8.6 (b). Distinctive spots of high intensity are found in this wavenumber map. These spots correspond to the nonlinear SB component which radiates away from the delamination.

The direction of the nonlinear source can be found as: $\theta = \mathrm{atan}(\mathrm{k_y}/\mathrm{k_x})$ if $\mathrm{k_x} < 0$, or $\theta = \mathrm{atan}(\mathrm{k_y}/\mathrm{k_x}) + \pi$ if $\mathrm{k_x} > 0$. In Figure 8.6, arrows are drawn in these directions. The arrows correctly point towards the source of the nonlinear component, namely the artificial delamination. Note that for one of the observed directions, the wavefield originates at the delamination but is reflected at the bottom edge. The edge is perceived as a virtual source, and as such can be employed to further improve the localization of the actual defect. Hence, the observed nonlinear source behavior of the defect proves highly promising for out-of-sight damage detection and localization without the need for a baseline measurement.

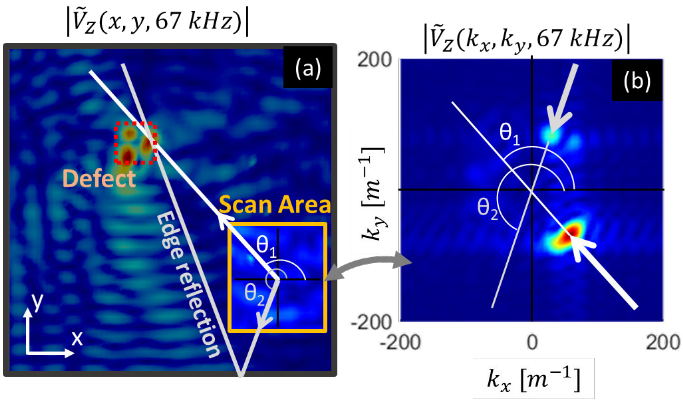

Figure 8.6: Detection of out-of-sight damage by using the sideband component at 67 kHz measured at a small area: (a) Sideband amplitude map with indication of the scan area in orange, (b) Sideband wavenumber map with indication of the direction of the incoming waves.

5.2. Nonlinear Resonant Air-Coupled Emission

The nonlinear source behavior of the defect opens the opportunity for defect detection through nonlinear resonant air-coupled emission monitoring [17]. As a proof-of-concept, the same experiment (with dual harmonic excitation) is repeated but with the test setup configured as shown in Figure 8.7 (a). The test specimen is positioned horizontally in front of a big plate covered in retroreflective tape, i.e. the reflector. Only one SLDV laser head is used and it is positioned perpendicular to the reflector. The measurement laser beam propagates through the air above and below the test specimen. Pressure waves in the air shift the frequency of the measurement beam due to the photoelastic effect [13]. As a result, acoustic emissions of the test specimen to the surrounding air can be observed by the SLDV (as a change in the velocity).

The velocity fields induced by the air-coupled emissions at the excitation frequency of the first actuator are shown in Figure 8.7 (b-c). Both the real part and the magnitude of the velocity field are plotted. Note that part of the area could not be scanned due to the presence of the cables that are attached to the piezoelectric actuators. Air-coupled emissions are detected all around the test specimen. These emissions originate from the excited elastic waves which gradually leak part of their energy into the surrounding air. Note that, Solodov et al. showed that these linear air-coupled emission maps may reveal shallow defects as concentration points of air-coupled emissions [16]. In our experiment however, this is not observed.

At the HH_2 frequency (see Figure 8.7 (d-e)) and at the SB frequency (see Figure 8.7 (f-g)), air-coupled emissions are detected that originate at the location of the delamination. The air-coupled emissions are dominantly present at the Shallow Side of the delamination as this is the plate's location where the nonlinear component's amplitude is maximal. Note however, that there are also indications of air-coupled emissions originating from the Deep Side. Hence, the nonlinear source behavior of the defect under LDR_Z excitation proves promising for damage detection through the monitoring of the air field around the test specimen.

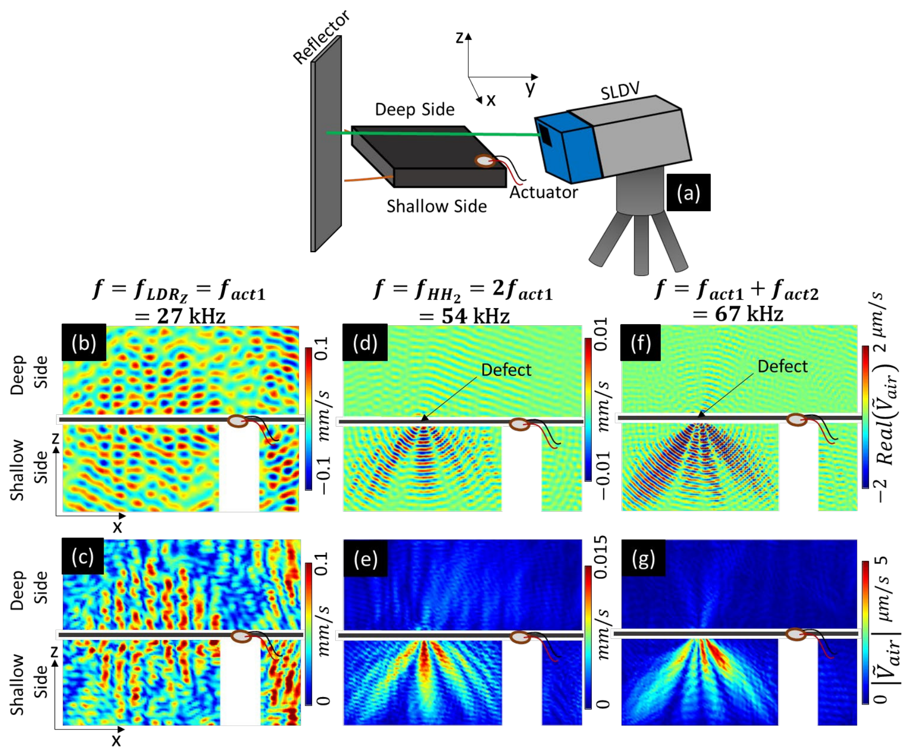

Figure 8.7: (a) Resonant air-coupled emission measurement setup and emission field at (b-c) LDR_Z excitation frequency, (d-e) Second higher harmonic and (f-g) Sideband frequency. (top row) Real part of velocity field and (bottom row) Magnitude of velocity field.

6. Conclusion

In this chapter, the nonlinear response of a vibrating delamination defect in a CFRP plate under sine excitation at the out-of-plane local defect resonance (LDR_Z) frequency is investigated both experimentally and numerically.

It is shown that the defect under LDR_Z excitation behaves as a radiating source of higher harmonic components, which are visible from the shallow side of the delamination as well as from the deep side. In case of a dual sine excitation, with one of the sine frequencies equal to an LDR_Z frequency of the defect, modulation sidebands are formed at the defect in addition to the higher harmonics. Also the generated sideband components are visible from the shallow side of the delamination as well as from the deep side.

These observations are of significant importance for the field of vibrometric non-destructive testing as well as structural health monitoring. It evidences that deep (backside) delaminations can be detected and localized by evaluating the local amplitude of the nonlinear higher harmonics and/or sidebands over the test specimen's surface using SLDV measurements. Furthermore, it is illustrated how the observed source nature of the induced defect nonlinearity allows (i) the localization of out-of-sight defects using source localization algorithms and (ii) the detection of defects by measuring the energy leakage of the nonlinear components into the air surrounding the test specimen (i.e. nonlinear resonant air-coupled emissions).

Based on these findings, advanced NDT methods are developed in Part 3 of this PhD thesis:

- The high intensity of the nonlinear components at the defects makes them appear in the damage maps constructed based on energy mapping of nonlinear components – See Chapter 12.
- The nonlinear source behavior of the defect is used for in-sight as well as out-of-sight damage detection through nonlinear local wave-direction estimation – See Chapter 14.

References

1. Segers, J., et al., *Backside delamination detection in composites through local defect resonance induced nonlinear source behaviour.* Journal of Sound and Vibration, 2020. **479**.

2. Segers, J., et al., *Probing the limits of full-field linear Local Defect Resonance identification for deep defect detection.* Ultrasonics, 2020. **105**.
3. Pieczonka, L., et al., *Damage imaging in composites using nonlinear vibro-acoustic wave modulations.* Structural Control and Health Monitoring, 2017.
4. Fierro, G.P.M. and M. Meo, *A combined linear and nonlinear ultrasound time-domain approach for impact damage detection in composite structures using a constructive nonlinear array technique.* Ultrasonics, 2018. **93**: p. 43-62.
5. Zhang, S., et al., *Far-sided defect recognition of FRP sandwich structures based on local defect resonance.* Journal of Sandwich Structures & Materials, 2019: p. 1-12.
6. Roy, S., T. Bose, and K. Debnath, *Detection of local defect resonance frequencies using bicoherence analysis.* Journal of Sound and Vibration, 2019. **443**: p. 703-716.
7. Solodov, I., *Resonant Acoustic Nonlinearity of Defects for Highly-Efficient Nonlinear NDE.* Journal of Nondestructive Evaluation, 2014. **33**(2): p. 252-262.
8. Ciampa, F., G. Scarselli, and M. Meo, *On the generation of nonlinear damage resonance intermodulation for elastic wave spectroscopy.* The Journal of the Acoustical Society of America, 2017. **141**(4): p. 2364.
9. Fierro, G.P.M., et al., *Nonlinear ultrasonic stimulated thermography for damage assessment in isotropic fatigued structures.* Journal of Sound and Vibration, 2017. **404**: p. 102-115.
10. Ooijevaar, T.H., et al., *Nonlinear dynamic behavior of an impact damaged composite skin–stiffener structure.* Journal of Sound and Vibration, 2015. **353**: p. 243-258.
11. Segers, J., et al., *In-plane local defect resonances for efficient vibrothermography of impacted carbon fiber-reinforced polymers (CFRP).* NDT & E International, 2019. **102**: p. 218-225.
12. Segers, J., et al., *Nonlinear Local Wave-Direction Estimation for In-sight and Out-of-sight Damage Localization in Composite Plates* NDT & E International, 2021. **119**.
13. Solodov, I., D. Döring, and G. Busse, *Air-coupled laser vibrometry: analysis and applications.* Applied Optics, 2008. **48**.
14. Derusova, D., et al., *Ultrasonic spectroscopic analysis of impact damage in composites by using laser vibrometry.* Composite Structures, 2019. **211**: p. 221-228.
15. Solodov, I. and M. Kreutzbruck, *Single-sided access remote imaging via resonant airborne activation of damage.* NDT & E International, 2019. **107**.
16. Solodov, I., A. Dillenz, and M. Kreutzbruck, *A new mode of acoustic NDT via resonant air-coupled emission.* Journal of Applied Physics, 2017. **121**(24).

17. Delrue, S. and K. Van Den Abeele, *Detection of defect parameters using nonlinear air-coupled emission by ultrasonic guided waves at contact acoustic nonlinearities.* Ultrasonics, 2015. **63**: p. 147-54.

Chapter 9

Local Defect Resonance based Vibrothermography

Summary:

This chapter further couples the concept of LDR_Z's and LDR_{XY}'s to vibrothermography, on the basis of the promising potential of especially the LDR_{XY}'s to enhance the rubbing (tangential) interaction and viscoelastic damping of defects. CFRPs with BVID are inspected and the significant contribution of LDR_{XY}'s in vibrational heating is demonstrated. Moreover, it is shown that the thermal contrast at the defect, induced by LDR_{XY}'s, is so high that it allows for detection of BVID by live monitoring of infrared thermal images during a single broadband sweep excitation. Thermal and vibrational spectra of the inspected surfaces are studied and the dominant contribution of LDR_{XY}'s in vibration-induced heating is demonstrated. At last, it is illustrated that the sweep thermographic response of the test specimen can be used for identification of unknown LDR frequencies.

The chapter is in close correspondence with journal publications:

[1] Segers, J., Hedayatrasa, S., Verboven, E., Poelman, G., Van Paepegem, W. and Kersemans, M. *In-plane local defect resonances for efficient vibrothermography of impacted carbon fiber-reinforced polymers (CFRP).* Journal of NDT & E International, 2019. **102**

[2] Hedayatrasa, S., Segers, J., Poelman, G., Verboven, E., Van Paepegem, W. and Kersemans, M. *Vibrothermographic spectroscopy with thermal latency compensation for effective identification of local defect resonance frequencies of a CFRP with BVID.* Journal of NDT & E International, 2020. **109**

[3] Hedayatrasa, S., Segers, J., Poelman, G., Van Paepegem, W. and Kersemans, M. *Vibro-Thermal Wave Radar: Application of Barker coded amplitude modulation for enhanced low-power vibrothermographic inspection of composites.* Materials (Special Issue: Mechanical Characterization of FRP Composite Materials), 2021

1. Introduction

Vibrothermography (also referred to as thermosonics or sonic thermography) is a NDT technique that takes advantage of vibrational energy dissipation at defects that are subjected to a dynamic stimulation. As such, the defects behave like localized heat sources and are detected with a sensitive thermographic camera [4]. This makes vibrothermography a promising technique for detection of tightly closed cracks and kissing bonds in composites, especially if the defect interfaces are aligned normal to the inspection surface which is hard to detect using other NDT techniques [5].

High-power piezoelectric (ultrasonic) horns and transducers are often used in classical vibrothermography in order to properly activate the defects and to increase the vibrational heating to a detectable level [6, 7]. However, such high-power excitation is usually chaotic and non-reproducible. In addition, the power has to be limited in order to prevent component degradation by the excitation source itself. Recently, alternative low power vibrothermography techniques were introduced by taking advantage of the high amplitude vibrations at global or local resonances.
In so called self-heating vibrothermography [8, 9] the fundamental global resonance frequencies of the test piece are used as the excitation frequency. An electrodynamic shaker is used to stimulate global resonance of the test piece at one particular resonance frequency or at a combination of multiple resonance frequencies (typically below 1000 Hz). This approach is shown to boost the global heating of the specimen induced by vibrational damping and reveals the defected areas as distinct thermal gradients.
Another low power vibrothermography alternative is based on the concept of local defect resonance (LDR) for enhanced efficiency [10, 11]. The excitation at LDR frequencies allows for selective resonation of the defect's by using low power piezoelectric actuators [12]. Generally, the component is excited at an out-of-plane LDR frequency of the defect and the resulting vibration induced heat is diffused to the surface and detected using a high-sensitivity infrared camera [13-18]. The efficiency of LDR-based vibrothermography can be enhanced through nonlinear ultrasound spectroscopy and selecting those LDR frequencies that indicate highest amplitudes of defect induced second harmonics [19-21]. Furthermore, applying a combination of an LDR and a modulation frequency that shows highest sideband amplitudes (so called nonlinear wave modulation thermography) intensifies the defect's interaction with excited vibrations and raises the resultant heating [22].

Various vibrational heating mechanisms can be activated through LDR, depending on the orientation, asperities and the gap or tightness of the defect's interfaces [23-25]. LDR induced interactions of the defect's interfaces dissipate heat by rubbing, friction and adhesion hysteresis at closures [23, 24]. Moreover, LDR induced deformation of the defect's features dissipates heat through viscoelastic damping, thermoelastic damping and plastic deformation [23-25]. The latter source may come to effect at a too large excitation power and must be avoided due to its destructive nature. Consequently, the polarization of LDR oscillations with respect to the defect's orientation has considerable impact on its detectability and the relative contribution of the heating mechanisms.

Traditionally, LDR was evidenced by out-of-plane local defect resonance (LDR_Z) behavior. LDR_Z is triggered by flexural waves and dominantly stimulates normal interaction of the defect's interfaces and dissipates heat through adhesion and partial rubbing of touching asperities [24]. In-plane local defect resonances (LDR_{XY}) were introduced in this PhD work (Chapter 5 Section 4.2.4 or [26]). It was shown that a CFRP coupon with barely visible impact damage (BVID) shows a clear LDR_{XY} response that reveals distinct damage features which are not present in the LDR_Z. LDR_{XY} is induced by axial waves and leads to dominant tangential interaction (full rubbing) of in-plane interfaces e.g. delamination as well as through-the-thickness interfaces e.g. matrix cracks and fiber breakages. Therefore, it is expected that LDR_{XY} is more effective than LDR_Z in terms of frictional heating at closures, as schematically shown in Figure 9.1. Moreover, LDR_{XY} frequencies are generally higher than LDR_Z frequencies which naturally leads to an increased viscoelastic and frictional dissipation [27].

In this chapter, the contribution of LDR_Z and LDR_{XY} in vibrational heating of BVID in CFRP specimens is experimentally investigated. The 3D SLDV is used to record the specimens' vibrational response and to identify the LDR frequencies. A cooled infrared camera is used to measure the vibrational heating dissipated at the BVID when subjected to the identified LDR frequencies.

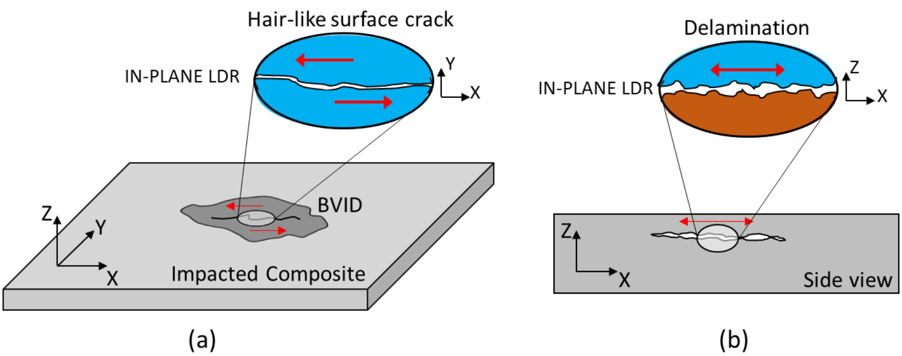

Figure 9.1. Schematic representation of dominant tangential interaction at in-plane LDR for (a) out-of-plane surface crack interfaces and (b) in-plane delamination interfaces of a typical impact damage in a composite component.

2. Material and Method

The vibrational and corresponding thermal responses are evaluated for two 100x150x5.45 mm^3 CFRP coupons. The samples are manufactured out of 24 layers of unidirectional carbon fiber according to a cross-ply $[(0/90)_6]_s$ and a quasi-isotropic $[(45/0/-45/90)_3]_s$ lay-up. Both samples were impacted with a 7.7 kg drop-weight from a height of 0.1 m according to the ASTM D7136 standard [28]. The impact energy was measured at 6.3 J, which introduced the BVID. Both samples are shown in Figure 9.2 together with the corresponding C-scan amplitude and time-of-flight (TOF) maps. The C-scan results are obtained in reflection mode using dynamic time gating and reveal the complex damage distribution at the impact location [29]. A focused transducer at 5 MHz (H5M, General Electric) is employed. Both samples display a hair-like surface crack at the backside resulting from the low velocity impact. A microscopic view of this crack is shown in the inset of Figure 9.2 (b) for the cross-ply coupon. Note that this cross-ply test specimen was also used to illustrate the LDR_Z and LDR_{XY} phenomena in Chapter 5 Section 4.2.4.

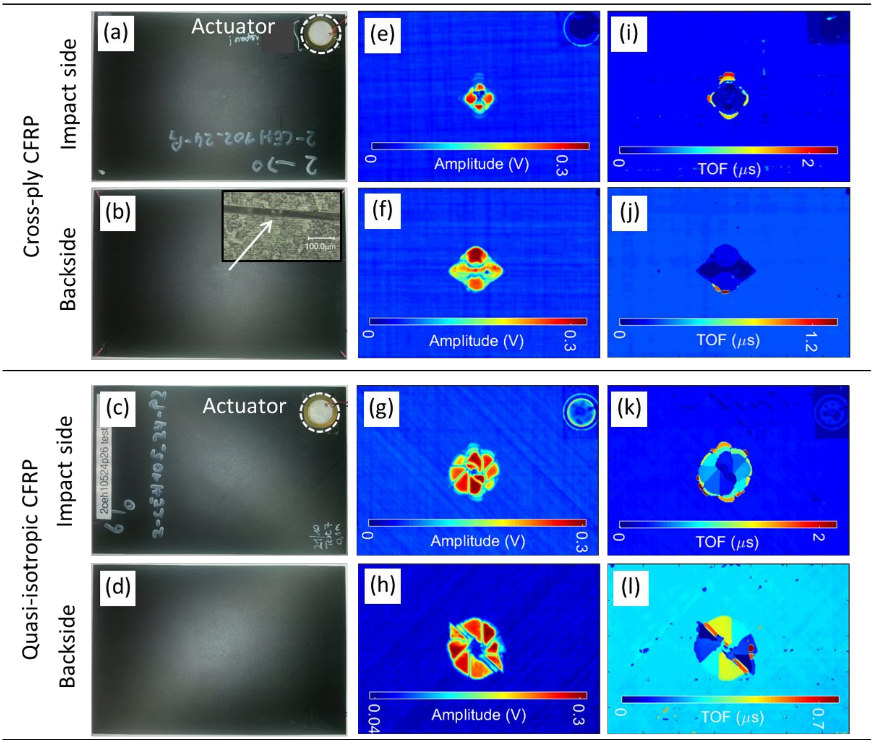

Figure 9.2. CFRP test specimens with BVID and corresponding C-scan amplitude and TOF images.

For the vibrational studies, each sample is excited using a low power piezoelectric bending disk (Ekulit EPZ-20MS64W) bonded to its impact side using phenyl salicylate. A sweep excitation from 1 to 250 kHz is used together with the Falco System WMA-300 voltage amplifier to increase the excitation voltage to 150 V_{pp}. The resulting electrical power supplied to the actuator is in the order of a few Watt (see Chapter 4 Section 2.3). The broadband in-plane (V_X, V_Y) and out-of-plane (V_Z) vibrational response is measured with the 3D SLDV (with sampling frequency 625 kS/s, number of samples 25 000 and scan point resolution 1 mm at defect and 2 mm at damage-free material).

BVID is a complex type of damage [30] and during this PhD work it was already observed that different parts of the damaged area show LDR_Z and LDR_{XY} behavior at distinct frequencies (see Chapter 5 Section 4.2.4 or [26]). In this chapter, the LDR_Z and LDR_{XY} frequencies are extracted manually from the acquired frequency spectra by analysis of the velocity amplitude maps for the most prominent LDR behavior. Alternatively, the automated LDR detection algorithm proposed in Chapter 6 (or in [2]) can be used.

Several extracted LDR frequencies are examined by lock-in vibrothermography (LVT) with a modulation frequency of 0.05 Hz for two cycles (i.e. 40 s) in order to enhance the signal-to-noise ratio [31]. Alternatively, a sweep vibrothermography (SVT) experiment is performed with a linear sine sweep excitation from 1 to 250 kHz for 50 s. The vibrational heating is measured with a FLIR A6750sc infrared camera (controlled by Edevis GmbH hardware-software), which has a cryo-cooled InSb detector with a pixel density of 640 x 512 pixels, a noise equivalent differential temperature (NEDT) of < 20 mK and a bit depth of 14 bit. For the excitation of the piezoelectric actuators, a function generator is used together with the voltage amplifier to apply the excitation voltage to 150 V_{pp} for all experiments. The thermograms are measured at a frame rate of 25 Hz and post-processed by FFT to extract corresponding amplitude and phase images in case of LVT. For SVT, live thermal images corresponding to the LDR frequencies and thermal spectra corresponding to the entire sweep frequency range are studied.

3. Results and Discussion

3.1. LVT of Impacted Cross-ply CFRP

The experimental results at LDR frequencies corresponding to the impact side and backside of the cross-ply $[(0/90)_6]_s$ CFRP sample (see Figure 5.7 (a)) are respectively summarized in Figure 9.3 and Figure 9.4. The left column corresponds to the SLDV measurements, the middle column to the amplitude of the LVT measurements, and the right column to the phase images of the LVT measurements. The SLDV images show the combined in- and out-of-plane velocity amplitude for an arbitrary frequency of 95 kHz, the out-of-plane velocity component for the LDR_Z and the in-plane velocity component for the LDR_{XY}. The LVT amplitude images are presented in digital level (DL) scale, which is the raw output measured by the infrared camera, and thus corresponds to the intensity of emitted infrared radiation. The limits of the color maps of the LVT images are set to the extreme values at the defected area. In this way the colormap scale defines the defect induced thermal contrast (DTC) regardless of the heating induced by the piezoelectric actuator itself.

The manually selected LDR frequencies are indicated in the figure. In addition, an arbitrary frequency of 95 kHz is also examined to emphasize the dominant contribution of LDR in vibrational heating. Note that the LDR frequencies used here are not identical to the LDR frequencies discussed in Chapter 5. The small discrepancies are related to variations in boundary conditions and the different position of the piezoelectric actuator.

3.1.1. Impact Side

According to Figure 9.3 (a-g), the impact side of the cross-ply sample shows three LDR_Z‘s in the lower frequency range 23.5-54.5 kHz and three LDR_{XY}‘s in the higher frequency range 133-174 kHz. The arbitrary frequency of 95 kHz indicates a very small DTC of 0.6 DL in the amplitude image (Figure 9.3 (h)) corresponding to the relatively small increased vibrational activity at the defect as shown in its combined in- and out-of-plane velocity map (Figure 9.3 (a)).

Regarding LDRs, except for the fundamental LDR_Z at 23.5 kHz, all others are detected by LVT in both amplitude and phase images. The agreement of the velocity maps and the thermal signature of the LDRs is excellent and there are minor blurring effects induced by the 3D anisotropic heat diffusion. Moreover, the increased global damping induced at relatively high frequencies of LDR_{XY} leads to thermal traces of the global resonance shapes in corresponding amplitude and phase images. This can be seen in the amplitude image of LDR_{XY} at 133 kHz (Figure 9.3 (l)) which is strongly affected by the global heating due to the in-plane plate resonance. The global heating and the in-plane heat flow induced by the actuator are more pronounced in the phase images, because they indicate the phase delay of the thermal evolution at each individual pixel regardless of the absolute temperature. Therefore, phase images are generally more noisy than amplitude images.

The fundamental LDR_Z at 23.5 kHz is not detected through LVT (Figure 9.3 (i,p)) while the other two LDR_Z's at 35.2 and 54.5 kHz are revealed with a DTC of 1.9 and 1.2 DL, respectively. This indicates that the normal interaction of relevant defect interfaces cannot heat the defect to a detectable limit at the relatively low out-of-plane velocity of 22 mm/s corresponding to this fundamental LDR_Z. However, the LDR_{XY} at 133, 151 and 174 kHz are all detected with higher DTC compared to the LDR_Z, equal to 3.2, 7.1 and 3.5 DL respectively (see also Table 9.1).

Although a higher LDR velocity implies increased viscoelastic and frictional energy dissipation, other factors e.g. depth, orientation, gap and morphology of asperities of the relevant interfaces also affect the vibrational heating and therefore the measured DTC. This argument can explain why the DTC of LDR_Z at 35.2 kHz is higher compared to the DTC of LDR_Z at 54.5 kHz, despite its lower out-of-plane velocity and smaller size. Likewise, the DTC of LDR_{XY} at 174 kHz with in-plane velocity of 56 mm/s is higher than the one at 133 kHz with in-plane velocity of 121 mm/s.

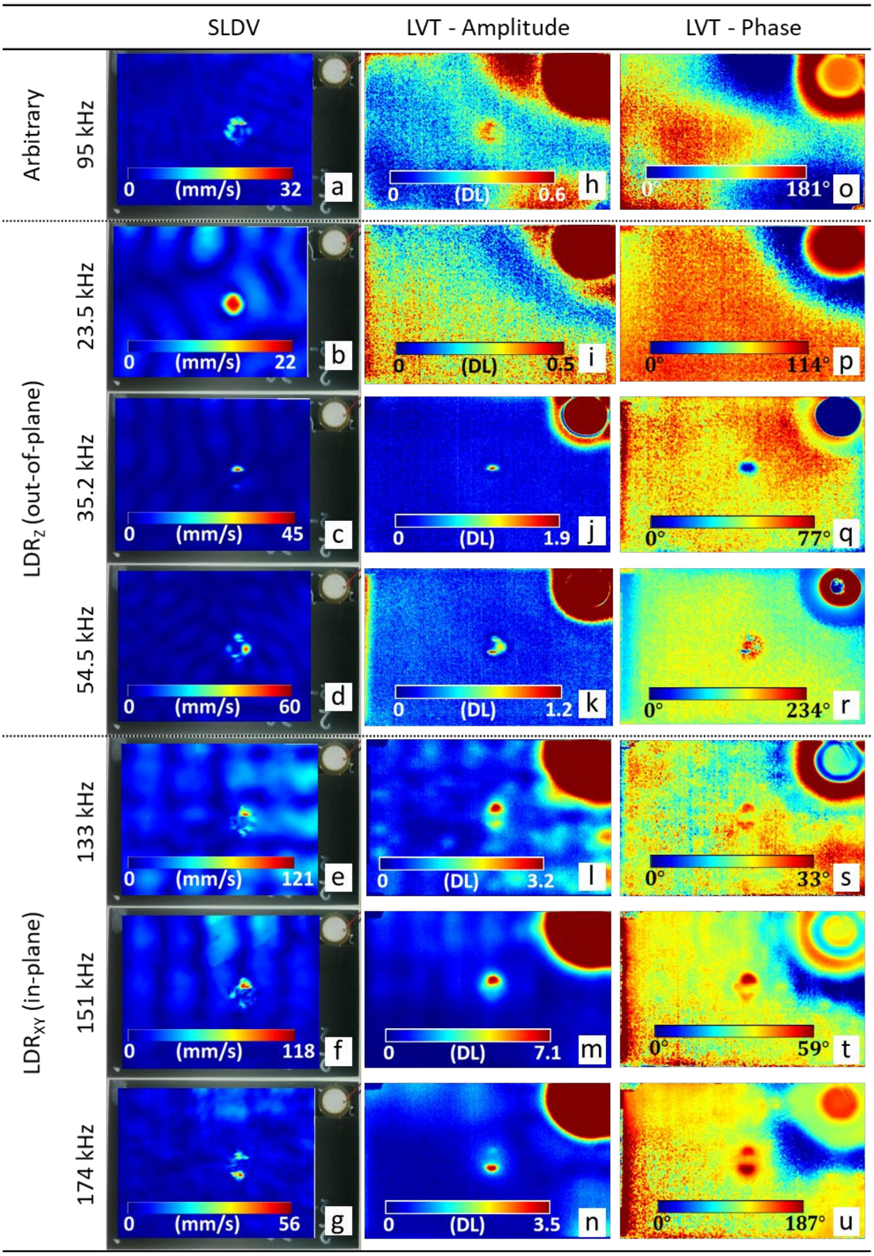

Figure 9.3. Measurements corresponding to the impact side of the cross-ply $[(0/90)_6]_s$ CFRP sample: (a-g) Amplitude of vibration, (h-n) Amplitude of LVT and (o-u) Phase of LVT.

3.1.2. Backside of BVID

The measurements corresponding to the backside of the cross-ply sample (see Figure 9.4) also show three LDR_Z's in the frequency range 17.2-109 kHz and three LDR_{XY}'s in the frequency range 82.9-142 kHz. There is a hair-like surface crack (see inset of Figure 9.2 (b)) at the center of the defect in the backside of this sample which affects its LDR behavior. The arbitrary frequency of 95 kHz barely shows a trace of the defect in the corresponding LVT images, while stimulation at the various LDR frequencies show clear signals in both amplitude and phase LVT images.

Among the LDR_Z's, the one at 17.2 kHz with an out-of-plane velocity of 40 mm/s leads to the highest DTC of 1.3 DL. According to the corresponding velocity map (see Figure 9.4 (b)), this is the fundamental LDR_Z of the defect leading to tangential interaction of the interfaces along the hair-like surface crack. The other two LDR_Z's at higher frequencies 49.6 and 109 kHz lead to lower DTC's of 0.5 and 0.9 DL despite their higher vibrational velocities. The corresponding velocity maps (see Figure 9.4 (c,d)) indicate that these LDR_Z's (particularly the one at 109 kHz) are comprised of a cluster of relatively smaller subsurface features spread over the BVID. These are dominantly in-plane interfaces with normal interaction and/or deeper defect features, leading to lower vibrational heating compared to the fundamental LDR_Z at 17.2 kHz. Moreover, the amplitude image of the LDR_Z at 109 kHz is influenced by a global in-plane resonance of the plate (see Figure 9.4 (k)).

Furthermore, the LDR_{XY}'s at 98.9 and 142 kHz, with maximum in-plane velocities of 126 and 165 mm/s (Figure 9.4 (f,g)), indicate defect features with very high DTC's of 14.6 and 12.9 DL (Figure 9.4 (m,n)), respectively. The DTC of the lowest LDR_{XY} at 82.9 kHz is 0.6 DL (Figure 9.4 (l)), which is relatively low caused by the corresponding low in-plane velocity of 41 mm/s (Figure 9.4 (e)). As mentioned earlier, other factors may also contribute to the low DTC of this LDR_{XY} like a too loose gap of relevant interfaces which reduces their tangential interaction and/or a deeper depth of relevant features that diffuses the defect's thermal signature.

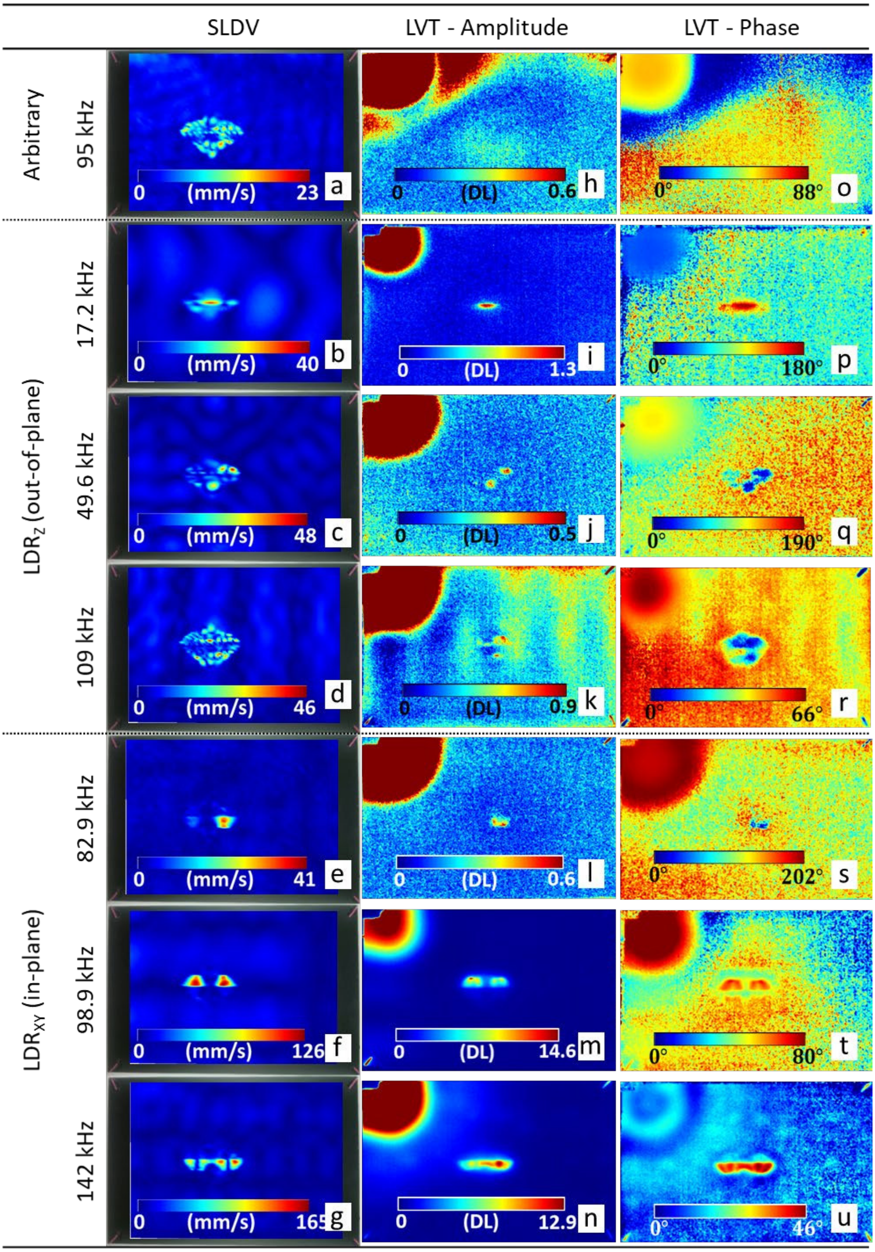

Figure 9.4. Measurements corresponding to the backside of the cross-ply $[(0/90)_6]_s$ CFRP sample: (a-g) Amplitude of vibration, (h-n) Amplitude of LVT and (o-u) Phase of LVT.

3.1.3. Overview of the Results

All measured DTC's of the impacted cross-ply CFRP are summarized in Table 9.1. Comparing the DTC's of the examined LDR frequencies evidently confirms the higher DTC (i.e. better detectability) of LDR_{XY} when inspecting BVID, either from the impact side or from the backside. It is noteworthy that the DTC of 0.5 at the fundamental LDR_Z at 23.5 kHz (Figure 9.3 (i)) is just an indication of the noise level and provides no defect contrast.

The defect features detected by LVT at different LDR frequencies are in good agreement with those areas having relatively low TOFs in the ultrasonic C-scan images (i.e. shallow features): the left and right inner lobes at the impact side (Figure 9.2 (i)) and the two left and right lobes at the backside (Figure 9.2 (j)). Deeper damage features including the outer peripheral features of the impact side (Figure 9.2 (e,i)) and the left and right lobes of the backside (Figure 9.2 (f,j)) are missing in the corresponding SLDV and LVT results.

Recently, the use of vibrothermal wave radar with barker coded amplitude modulation was proposed for better detection of these deep defect features. The reader is referred to Ref. [3] for a detailed discussion of this vibrothermal wave radar procedure.

Table 9.1. Summary of DTCs measured for the impact side (Figure 9.3 (h-n)) and the backside (Figure 9.4 (h-n)) of the cross-ply $[(0/90)_6]_s$ CFRP.

$[(0/90)_6]_S$ CFRP	Parameter	Arbitrary	LDR_Z			LDR_{XY}		
Impact side	f (kHz)	95	23.5	35.2	54.5	133	151	174
	DTC (DL)	0.6	0.5	1.9	1.2	3.2	7.1	3.5
Backside	f (kHz)	95	17.2	49.6	109	82.9	98.9	142
	DTC (DL)	0.35	1.3	0.5	0.9	0.6	14.6	12.9

3.2. SVT of Impacted Quasi-isotropic CFRP

To further evaluate the potential of LDR_{XY} in vibrothermography, the CFRP sample with quasi-isotropic layup $[(45/0/\text{-}45/90)_3]_s$ is inspected from the backside (Figure 9.2 (d)). First, the thermal and vibrational FFT results are presented at distinct LDR frequencies (see Figure 9.5). Subsequently, the spectra corresponding to the entire sweep frequency range are studied (see Figure 9.6 and Figure 9.7).

3.2.1. LDR Frequency Response

From the SLDV measurements, the following frequencies have been selected for further investigation: the arbitrary frequency of 95 kHz, the fundamental LDR_Z at 15.6 kHz and four LDR_{XY}'s in the frequency range 91.3-137 kHz. The left column of Figure 9.5 shows the SLDV measurements, the middle column the SVT measurements and the right column the LVT measurements (to validate the SVT measurements) at these frequencies. Similar to Figure 9.3 and Figure 9.4, the SLDV images (Figure 9.5 (a-f)) show the combined in- and out-of-plane velocity amplitude for the arbitrary frequency, the out-of-plane velocity component for the LDR_Z and the in-plane velocity component for the LDR_{XY}. Moreover, the combined in- and out-of-plane velocity amplitude is averaged over the whole sweep excitation and shown in Figure 9.5 (g). From the results it is clear that the vibrometric behavior of this impact damage is significantly influenced by the hair-like surface crack along the 45° fiber direction and the two adjacent triangle-like delaminations closest to the surface (see also Figure 9.2 (l)).

In order to examine the detectability of LDRs by vibrothermography, their instantaneous thermal signature during the sweep excitation is inspected. SVT is performed using the same sweep signal used for the SLDV experiment (f = 1 to 250 kHz, and amplitude 150 V_{pp}). The linear sweep rate is lowered, leading to a total sweep duration of 50 s. The instantaneous thermal images corresponding to the selected LDR frequencies are presented in Figure 9.5 (h-m) after cold image subtraction. Furthermore, the whole history of sweep excitation is post-processed by FFT in order to obtain an overall amplitude image for the sweep as shown in Figure 9.5 (n). The amplitude images corresponding to LVT at the same frequencies are shown in Figure 9.5 (o-t) for comparison.

The instantaneous SVT images explicitly show the presence of the BVID at the arbitrary frequency of 95 kHz and at the various LDR_{XY}'s. There is no indication of the BVID at the LDR_Z. The observed thermal signature at the arbitrary frequency of 95 kHz is found to be related to the neighboring LDR_{XY} at frequency 91.3 kHz through thermal inertia effects induced by the relative fast rate of the applied sweep. This is also clearly evidenced by the LVT at 95 kHz, in which not a single indication of the BVID is hinted. These results demonstrate the promising detectability of defects through LDR_{XY} in live monitoring of SVT.

By comparing the instantaneous SVT amplitudes of LDRs (Figure 9.5 (i-m)) with the corresponding LVT amplitudes (Figure 9.5 (p-t)), it is obvious that LVT leads to an increased signal-to-noise ratio. The fundamental LDR_Z is detected with a DTC of 1 DL and the LDR_{XY} are detected with a significantly higher DTC of 18, 5.8, 26.8 and 9.5 DL at 91.3, 116, 129 and 137 kHz, respectively. Although the signal-to-noise ratio of the SVT is lower compared to LVT, it has a clear benefit in experimental approach. Indeed, the LVT results have been obtained in a total time frame of ~4 hours for each inspected sample. This time frame includes (i) performing the SLDV measurement, (ii) selecting the different LDR frequencies, and (iii) finally performing the LVT measurements. In contrast, the SVT results have been obtained in only 50 s, free from any SLDV measurement.

The average sweep velocity map of SLDV (Figure 9.5 (g)) and overall amplitude of SVT (Figure 9.5 (n)) provide a comprehensive representation of all activated defect features during sweep excitation. However, the overall SVT image is affected by the 3D anisotropic heat diffusion, leading to some blurring effects. The activated areas correspond to the two diagonal lobes identified in the relevant C-scan images (Figure 9.2 (h,l)) as shallow delaminations (with the lowest TOF). As mentioned in earlier in Section 3.1.3, Barker coded vibrothermal wave radar can be used to improve the detection of deep defect features [3].

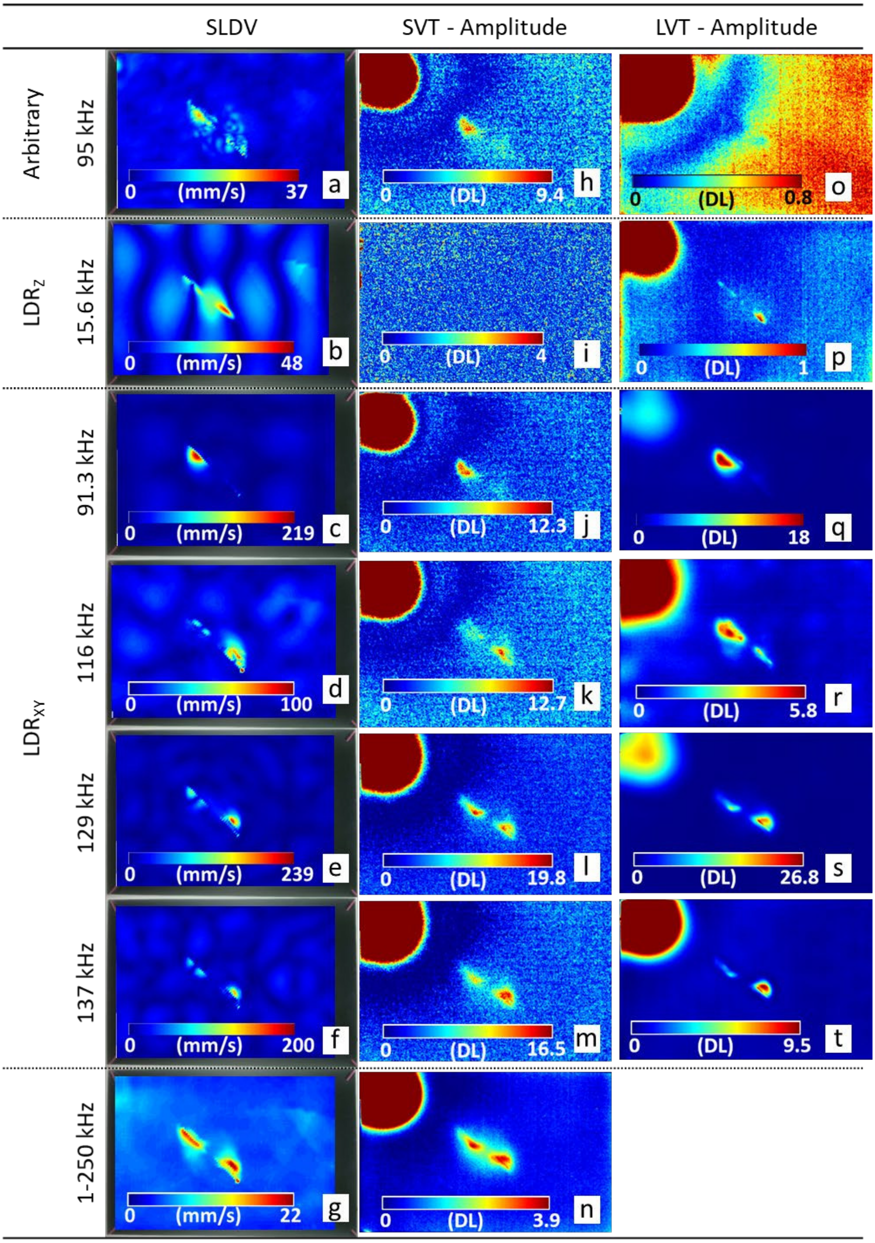

Figure 9.5. Measurements corresponding to the backside of the quasi-isotropic $[(+45/0/-45/90)_3]_s$ CFRP sample: (a-f) Amplitude of vibration, (g) Vibrational overall amplitude, (h-m) SVT instantaneous amplitude, (n) SVT overall amplitude, and (o-t) LVT amplitude.

3.2.2. Sweep Frequency Spectrum

In order to validate the dominant contribution of LDR_{XY} in the vibration induced heating, it is essential to have an accurate measure of the actual out-of-plane and in-plane energy deposited into the sample, and the resultant defect resonances, over the entire excitation frequency range. For this purpose, the thermal and vibrational spectra of the sweep excitation are studied as presented in Figure 9.6. The figure comprises three columns that show temperature T (DL) (a-c), in-plane velocity amplitude $|\tilde{V}_{xy}| = \sqrt{|\tilde{V}_x|^2 + |\tilde{V}_y|^2}$ (d-f) and out-of-plane velocity amplitude $|\tilde{V}_z|$ (g-i) data, respectively. The top row represents the average of T, $\tilde{V}_{xy}$ and $\tilde{V}_z$ over the sweep period. The path AB along the defected area is used as region of interest. The middle row shows a curve plot of T, $\tilde{V}_{xy}$ and $\tilde{V}_z$ versus frequency at the two most activated areas of the defect (D_1, D_2) and at a non-defected reference point (B). The bottom row represents a contour map of T, $\tilde{V}_{xy}$ and $\tilde{V}_z$ as a function of frequency along the path AB. The measured temperature data are smoothened by a Savitzky-Golay filter for improved presentation and interpretation of the thermal spectrum.

Figure 9.6 (b) shows the almost steady temperature rise at the non-defected point B and the intensified fluctuating temperature rise at the defected areas D_1 and D_2 attributed to LDR phenomena. This is further confirmed by the thermal response of the entire path AB as shown in Figure 9.6 (c). In the low frequency range 30-80 kHz, the LDR_Z contributes to a slightly higher vibration induced heating at the defected area. However, in the higher frequency range 80-150 kHz, a significantly higher temperature rise is observed including distinct spikes at LDR_{XY} frequencies as indicated with the dotted vertical lines.

The figures of the in-plane vibrational data (Figure 9.6 (e-f)) show that the in-plane velocity amplitude $\tilde{V}_{xy}$ reaches distinct local maxima at the same frequencies for which the elevated local heating takes place (see dotted vertical lines). This confirms again that elevated local heating takes place at LDR_{XY} frequencies. The frequencies corresponding to the local maxima in the thermal and in-plane velocity plots are identical to the four LDR_{XY} frequencies that were manually selected out of the vibrational frequency spectra and used in Figure 9.5.

Compared to the in-plane velocity amplitude $\tilde{V}_{xy}$, the defected area shows a quite steady elevation of out-of-plane velocity amplitude $\tilde{V}_z$ (Figure 9.6 (h,i)) over the total sweep frequency range (due to the relatively small wavelength of the A_0 mode guided wave modes effective at this low frequency) which is naturally intensified at LDR_Z frequencies. Nonetheless, the heating stages are observed at distinct local maxima of $\tilde{V}_{xy}$ and show minor sensitivity to $\tilde{V}_z$. Moreover, the elevated amplitude of $\tilde{V}_z$ at LDR_{XY} frequencies is significantly lower than the amplitude of corresponding $\tilde{V}_{xy}$ and has minor effect in vibration induced heating. This is the transversal effect of LDRXY which could be due to the Poisson's effect, possible buckling and rubbing interaction at the in-plane defect interfaces and also projected out-of-plane component of resonation at dominantly in-plane (i.e. slightly oblique) interfaces.

The in-plane velocity $\tilde{V}_{xy}$ and the out-of-plane velocity $\tilde{V}_z$ amplitude curves at the reference point B (see Figure 9.6 (e) and (h)) indicate the ability of the low power piezoelectric actuator to excite the coupon over this broadband frequency range. Desirably, the in-plane excitation is more efficient at the higher frequency range (evidenced by $\tilde{V}_{xy}$ at the reference point B) and the out-of-plane excitation is slightly more efficient at the lower frequency range (evidenced by $\tilde{V}_z$ at the reference point B). This is due to the known behavior of a piezoelectric actuator in stimulation of plate waves, which has better interaction with the wave mode having a wavelength comparable to its size (see Chapter 4 Section 2 or [32]). Therefore, the low frequency LDRZ and the high frequency LDRXY are adequately stimulated by the attached piezoelectric actuator.

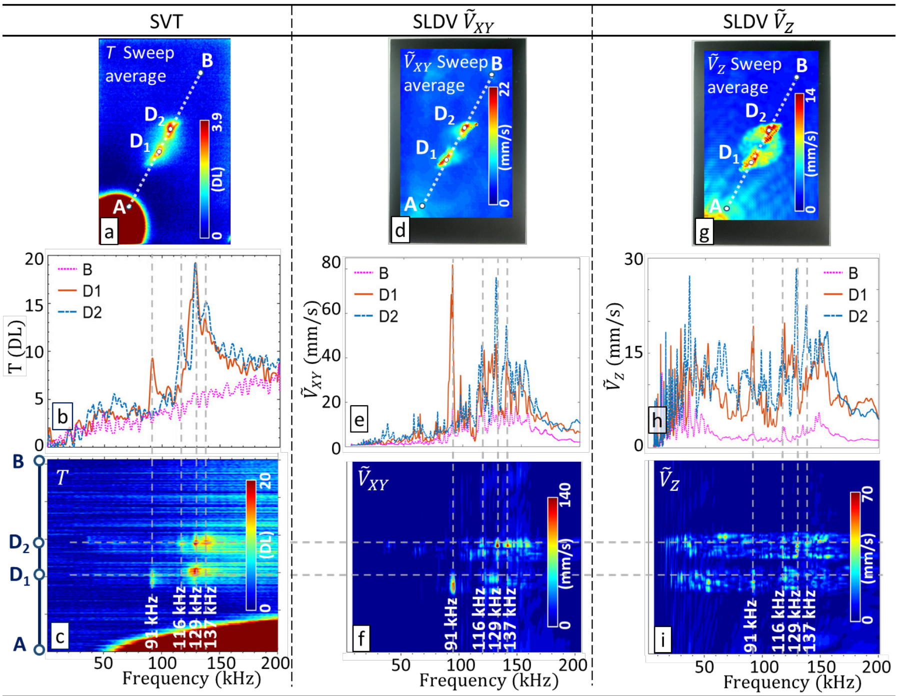

Figure 9.6. Measurements corresponding to the backside of the quasi-isotropic $[(+45/0/-45/90)_3]_s$ CFRP sample subjected to sweep excitation: (a-c) Thermal response, (d-f) In-plane vibration amplitude $\tilde{V}_{XY}$, (g-i) Out-of-plane vibration amplitude $\tilde{V}_Z$.

3.2.3. SVT for LDR Frequency Identification

Calculation of the second time (or frequency) derivative of the temperature T over the sweep duration, as shown in Figure 9.7, further quantifies the instantaneous gradient of heating intensity. This provides an exclusive signature of the defect's induced heating in the absence of the undesirable effects of heating induced by the piezoelectric actuator as well as the thermal traces of LDRs due to thermal inertia.

The second time derivative increases in the vicinity of LDR frequencies and has a local minimum value at the LDR frequencies as evidenced in Figure 9.7 (a) by red and blue fringes, respectively. This is further clarified by the curves shown in Figure 9.7 (b) corresponding to the defected points D_1 and D_2 and the non-defected point B where the dips correspond to the four LDR_{XY} frequencies (indicted with vertical dotted lines). As such, the SVT allows for fast identification of LDR_{XY} frequencies. Further improvement of the accuracy of LDR frequency identification is achieved through thermal latency compensation as explained by the current authors in Ref. [2].

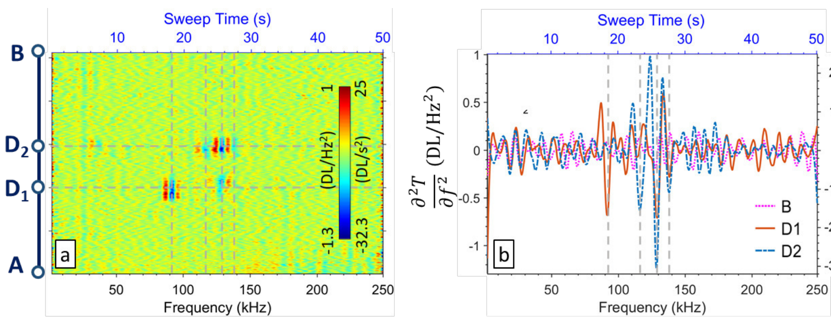

Figure 9.7. The second time (or frequency) derivative of the thermal response corresponding to SVT of the backside of the quasi-isotropic $[(+45/0/-45/90)_3]_s$ CFRP sample: (a) At the path AB along the defected area (see Figure 9.6 (a)), (b) At the defected points D_1 and D_2 and the non-defected point B.

4. Conclusions

Following the recent extension of the classical out-of-plane local defect resonance (LDR_Z) towards in-plane local defect resonance (LDR_{XY}) (see Chapter 5), its performance in vibrothermographic NDT is investigated. The combination of LDR_{XY} with vibrothermography for efficient inspection of BVID in CFRPs has been confirmed. Two CFRP coupons with different lay-up are stimulated with low power piezoelectric excitation, and are inspected using the 3D SLDV and a high sensitivity thermographic camera.

By lock-in vibrothermography, it is shown that the excitation at a LDR_{XY} frequency generally results in an increased thermal contrast at the BVID, compared to the excitation at LDR_Z. This can be explained by the increased in-plane friction of defect interfaces in combination with the higher viscoelastic damping induced at the elevated LDR_{XY} frequencies. The increased heat generation allows to perform the vibrothermal inspection using cheap and safe low power excitation sources.

Moreover, it is shown that due to the highly efficient heat generation at LDR_{XY}'s, fast sweep vibrothermographic inspection can be performed. In this case, the BVID heating is clearly visible in the live IR amplitude images at each time instance that the excitation frequency corresponds to a LDR_{XY} frequency. Thermal and vibrational spectra of the inspection surface are studied and the dominant contribution of LDR_{XY} in vibration induced heating is demonstrated. Time-frequency correlation of the thermal spectra obtained from SVT can be further post-processed for fast identification of LDR frequencies.

References

1. Segers, J., et al., *In-plane local defect resonances for efficient vibrothermography of impacted carbon fiber-reinforced polymers (CFRP).* NDT & E International, 2019. **102**: p. 218-225.
2. Hedayatrasa, S., et al., *Vibrothermographic spectroscopy with thermal latency compensation for effective identification of local defect resonance frequencies of a CFRP with BVID.* NDT & E International, 2020. **109**.
3. Hedayatrasa, S., et al., *Vibro-Thermal Wave Radar: Application of Barker Coded Amplitude Modulation for Enhanced Low-Power Vibrothermographic Inspection of Composites.* Materials, 2021(Special Issue Mechanical Characterization of FRP Composite Materials).
4. Reifsnider, K., E.G. Henneke, and W. Stinchcomb, *The mechanics of vibrothermography*, in *Mechanics of nondestructive testing*. 1980, Springer. p. 249-276.
5. Mendioroz, A., R. Celorrio, and A. Salazar, *Ultrasound excited thermography: An efficient tool for the characterization of vertical cracks.* Measurement Science and Technology, 2017. **28**(11): p. 112001.
6. Tsoi, K.A. and N. Rajic, *Non-destructive evaluation of aircraft structural components and composite materials at DSTO using sonic thermography*. 2011, DEFENCE SCIENCE AND TECHNOLOGY ORGANISATION VICTORIA (AUSTRALIA) AIR VEHICLES DIV.
7. Umar, M.Z., et al., *Detecting low-energy impact damages in carbon-carbon composites by ultrasonic infrared thermography.* Russian Journal of Nondestructive Testing, 2017. **53**(7): p. 530-538.

8. Katunin, A., *A Concept of Thermographic Method for Non-Destructive Testing of Polymeric Composite Structures Using Self-Heating Effect.* Sensors, 2018. **18**(1): p. 74.
9. Katunin, A. and D. Wachla, *Analysis of defect detectability in polymeric composites using self-heating based vibrothermography.* Composite Structures, 2018. **201**: p. 760-765.
10. Solodov, I. and G. Busse, *Resonance ultrasonic thermography: Highly efficient contact and air-coupled remote modes.* Applied Physics Letters, 2013. **102**(6).
11. Solodov, I., et al., *Highly-efficient and noncontact vibro-thermography via local defect resonance.* Quantitative InfraRed Thermography Journal, 2015. **12**(1): p. 98-111.
12. Solodov, I., D. Derusova, and M. Rahammer, *Thermosonic Chladni figures for defect-selective imaging.* Ultrasonics, 2015. **60**: p. 1-5.
13. Rahammer, M., et al., *Thermosonic Testing with Phase Matched Guided Wave Excitation.* Journal of Nondestructive Evaluation, 2016. **35**(3).
14. Fierro, G.P.M., et al., *Imaging of Barely Visible Impact Damage on a Complex Composite Stiffened Panel Using a Nonlinear Ultrasound Stimulated Thermography Approach.* Journal of Nondestructive Evaluation, 2017. **36**(4).
15. Rahammer, M. and M. Kreutzbruck, *Fourier-transform vibrothermography with frequency sweep excitation utilizing local defect resonances.* NDT and E International, 2017. **86**: p. 83-88.
16. Dionysopoulos, D., et al., *Imaging of barely visible impact damage on a composite panel using nonlinear wave modulation thermography.* NDT & E International, 2018. **95**: p. 9-16.
17. Derusova, D., V. Vavilov, and N. Druzhinin. *Evaluating impact damage in graphite epoxy composite by using low-power vibrothermography*. in *Thermosense: Thermal Infrared Applications XXXVIII*. 2016. International Society for Optics and Photonics.
18. Derusova, D., et al. *Highly efficient ultrasonic vibrothermography for detecting impact damage in hybrid composites*. in *Thermosense: Thermal Infrared Applications XXXIX*. 2017. International Society for Optics and Photonics.
19. Fierro, G.P.M., et al., *Nonlinear ultrasonic stimulated thermography for damage assessment in isotropic fatigued structures.* Journal of Sound and Vibration, 2017. **404**: p. 102-115.
20. Dyrwal, A., M. Meo, and F. Ciampa, *Nonlinear air-coupled thermosonics for fatigue micro-damage detection and localisation.* NDT & E International, 2018. **97**: p. 59-67.
21. Fierro, G.P.M., et al., *Imaging of Barely Visible Impact Damage on a Complex Composite Stiffened Panel Using a Nonlinear Ultrasound Stimulated Thermography Approach.* Journal of Nondestructive Evaluation, 2017. **36**(4): p. 69.
22. Dionysopoulos, D., et al., *Imaging of barely visible impact damage on a composite panel using nonlinear wave modulation thermography.* NDT & E International.

23. Renshaw, J.B., *The mechanics of defect detection in vibrothermography*. 2009: Iowa State University.
24. Renshaw, J., et al., *The sources of heat generation in vibrothermography.* NDT & E International, 2011. **44**(8): p. 736-739.
25. Rizi, A.S., et al., *FEM modeling of ultrasonic vibrothermography of a damaged plate and qualitative study of heating mechanisms.* Infrared Physics & Technology, 2013. **61**: p. 101-110.
26. Segers, J., et al., *Towards in-plane local defect resonance for non-destructive testing of polymers and composites.* NDT & E International, 2018. **98**: p. 130-133.
27. Zhang, W., S.D. Holland, and J. Renshaw. *Frequency dependence of vibrothermography*. in *AIP Conference Proceedings*. 2010. AIP.
28. ASTM, D., *7136/D 7136M-05.* Standard Test Method for Measuring the Damage Resistance of a Fiber-Reinforced Polymer Matrix Composite to a Drop-Weight Impact Event. ASTM International. West Conshohocken PA, USA, 2005.
29. Spronk, S., et al., *Comparing damage from low-velocity impact and quasi-static indentation in automotive carbon/epoxy and glass/polyamide-6 laminates.* Polymer Testing, 2018. **65**: p. 231-241.
30. Spronk, S.W.F., et al., *Comparing damage from low-velocity impact and quasi-static indentation in automotive carbon/epoxy and glass/polyamide-6 laminates.* Polymer Testing, 2018. **65**: p. 231-241.
31. Rantala, J., D. Wu, and G. Busse, *Amplitude-modulated lock-in vibrothermography for NDE of polymers and composites.* Research in Nondestructive Evaluation, 1996. **7**(4): p. 215-228.
32. Giurgiutiu, V. *Lamb wave generation with piezoelectric wafer active sensors for structural health monitoring*. in *Smart Structures and Materials 2003: Smart Structures and Integrated Systems*. 2003. International Society for Optics and Photonics.

Part 3:

Guided Wave Based Damage Detection

Chapter 10

Wavefield Manipulation

Summary:

Wavefield manipulation plays an important role in the derivation of a damage map from the full wavefield velocity response of an inspected component. It is often used to extract specific defect-wave interactions. In this chapter, the process of wavefield manipulation is illustrated for experimental data obtained from three damaged CFRP components: (i) a quasi-isotropic plate with a flat bottom hole defect, (ii) a cross-ply plate with low velocity impact damage and (iii) an impacted industrial aircraft panel with backside stiffeners. Different wavefield manipulation strategies are outlined, operated in either the frequency domain, the wavenumber domain, the combined wavenumber-frequency domain or the combined time-frequency domain.

This chapter introduces the wavefield manipulation strategies that are used in following journal publications:
[1] Segers, J. Hedayatrasa, S., Poelman, G., Van Paepegem, W. and Kersemans, M., *Robust and baseline-free full-field defect detection in complex composite parts through weighted broadband energy mapping of mode-removed guided waves.* Mechanical Systems and Signal Processing, 2021. **151**.
[2] Segers, J. Hedayatrasa, S., Poelman, G., Van Paepegem, W. and Kersemans, M., *Nonlinear Elastic Wave Energy Imaging for the Detection and Localization of In-Sight and Out-of-Sight Defects in Composites.* Applied Sciences, 2020. **10**(3924).
[3] Segers, J. Hedayatrasa, S., Poelman, G., Van Paepegem, W. and Kersemans, M., *Nonlinear Local Wave-Direction Estimation for In-sight and Out-of-sight Damage Localization in Composite Plates* NDT & E International, 2020. **109**.
[4] Segers, J. Hedayatrasa, S., Poelman, G., Van Paepegem, W. and Kersemans, M., *Broadband nonlinear elastic wave modulation spectroscopy for damage detection in composites.* Structural Health Monitoring, 2021.
[5] Segers, J. Hedayatrasa, S., Poelman, G., Van Paepegem, W. and Kersemans, M., *Self-Reference Broadband Local Wavenumber Estimation (SRB-LWE) for defect assessment in composites.* Mechanical Systems and Signal Processing, 163, 2021.

1. Introduction

Damage detection in thin-walled composite structures can be done by analyzing the guided elastic wave (or simply guided wave) propagation measured on the surface. Accurate and baseline-free defect detection is achieved through full wavefield monitoring of the excited waves. Such a full wavefield dataset can be obtained in multiple ways. In this PhD work, the 3D dataset of the vibrational velocity of the surface of the component in function of time is obtained through piezoelectric actuation and scanning laser Doppler vibrometer measurements (see Chapter 4).

Depending on (i) the excitation frequency, (ii) the component's thickness and (iii) the material's stiffness tensor, specific guided wave modes will propagate in the component (see Chapter 2). In correspondence with the displacement distribution through the thickness, the modes are classified as 'symmetric (S)' or 'anti-symmetric (A)' and are assigned a specific order. Each mode has a unique dispersion behavior that is characterized by the wavenumber k (i.e. the spatial frequency defined as the inverse of the spatial wavelength, expressed in m^{-1}) in function of the temporal frequency f.

The full-field monitoring of the guided waves allows to detect defects in the material because the characteristics of the guided wave modes depend on the characteristics of the material (i.e. the composite component). Multiple processing strategies can be employed to construct a damage map. These strategies may exploit one or more of the typical interactions of a guided wave and a defect: wave scattering, wave amplification or attenuation, wave trapping, wavenumber shift, etc. [6, 7]. In general, the damage map construction procedure comprises two major steps.
First, the defect-wave interaction is isolated from the measured wavefield response using specific filters in the time-, frequency- and/or wavenumber domain. This wavefield manipulation process is the subject of the current chapter. Secondly, the filtered wavefield response is converted into a single damage map where the potential damage can be distinguished from the surrounding damage-free material. Well-known damage map construction methods, as well as novel approaches developed in this PhD thesis, are discussed in Chapter 11 to Chapter 14.

In this chapter, multiple wavefield manipulation strategies are outlined using the experimentally obtained full wavefield response of a quasi-isotropic CFRP plate with a flat bottom hole (FBH) defect and a cross-ply CFRP plate with a barely visible impact damage (BVID). First, a description of the material and the test setup is given (see Section 2.1). Next, several wavefield manipulation strategies are explained:

- Wavefield manipulation in the frequency domain for conversion of a broadband (e.g. sine sweep) response to a narrowband (e.g. toneburst) response [8]. See Section 2.2.
- Wavefield manipulation in the wavenumber domain for extraction or removal of guided waves travelling in specific directions θ [3, 9, 10] or for extraction or removal of guided waves with specific wavenumbers k [11]. See Section 2.3.
- Wavefield manipulation in the wavenumber-frequency domain for extraction or removal of specific guided wave modes [1, 5, 9]. See Section 2.4.
- Wavefield manipulation in the time-frequency domain for extraction or removal of specific linear or nonlinear components [2-4]. See Section 2.5.

Finally, each wavefield manipulation method is applied on the measurement results of an industrial stiffened CFRP aircraft panel which has three areas of BVID.

The different wavefield manipulations that are applied to a velocity response are indicated with subscripts as illustrated with an example in Figure 10.1.

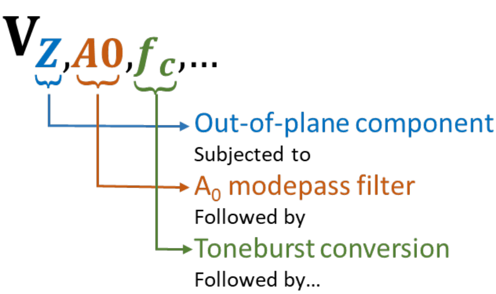

Figure 10.1: Notation convention for wavefield manipulated velocity signals, illustrated for $V_{Z,A0,f_c}$.

2. Wavefield Manipulation in Simple Components

2.1. Materials and Experiment

Wavefield manipulation is performed on the experimental results of the same two CFRP components as were already used in the explanation of elastic wave dynamics (see Chapter 2 Section 4.3). Figure 10.2 (a-b) shows the backside of both test specimens. The first test specimen (denoted $\mathrm{CFRP}_{\mathrm{FBH,1}}^{\mathrm{Plate}}$ and shown in Figure 10.2 (a)) is a square CFRP plate of size 330x330x5.45 mm^3 and quasi-isotropic material layup $[(+45/0/-45/90)_3]_s$. The FBH defect with diameter 15 mm and remaining material thickness 1.5 mm is visible from the backside. The second test specimen (denoted $\mathrm{CFRP}_{\mathrm{BVID}}^{\mathrm{Plate}}$ and shown in Figure 10.2 (b)) is again a square CFRP plate of size 330x330x5.45 mm^3 but now with a cross-ply layup $[(0/90)_6]_s$. The plate has been impacted with a 7.7 kg drop weight from a height of 0.09 m (i.e. theoretical impact energy 6.8 J). The low velocity impact resulted in BVID. To reveal the extent of the damage, an immersion ultrasonic C-scan inspection is performed at the impact side using a 5 MHz focused transducer (H5M, General Electric) in reflection mode. The C-scan's relative amplitude image reveals the complex distribution of delaminations and cracks, which is typical for low velocity impact damage in layered composite materials [39].

For both test specimens, the vibrations are excited with a piezoelectric actuator (type EPZ-20MS64W from Ekulit), bonded to the backside with phenyl salicylate. The actuator is supplied with a broadband linear sine sweep signal from 5 kHz to 300 kHz. The excitation voltage signal is amplified to 150 V_{pp} by a Falco System WMA-300 voltage amplifier to increase the vibrational energy input. This sine sweep excitation signal (U_{exc}) is shown in Figure 10.2 (c).

The SLDV (Polytec type PSV-500 3D Xtra) records the full wavefield velocity response of the frontside of the test specimens. The vibrations are measured at a grid of scan points with uniform spacing of 2.2 mm, resulting in a total of ±19 500 scan points for each test specimen. At every scan point, 10 000 time samples are recorded with sampling frequency 625 kS/s, resulting in a signal length of 16 ms. No retroreflective tape is used, instead 9 averages are taken in order to improve the signal-to-noise ratio. Figure 10.2 (d) shows the direction of the in-plane (V_X, V_Y) and the out-of-plane (V_Z) velocity components with respect to the plate's geometry.

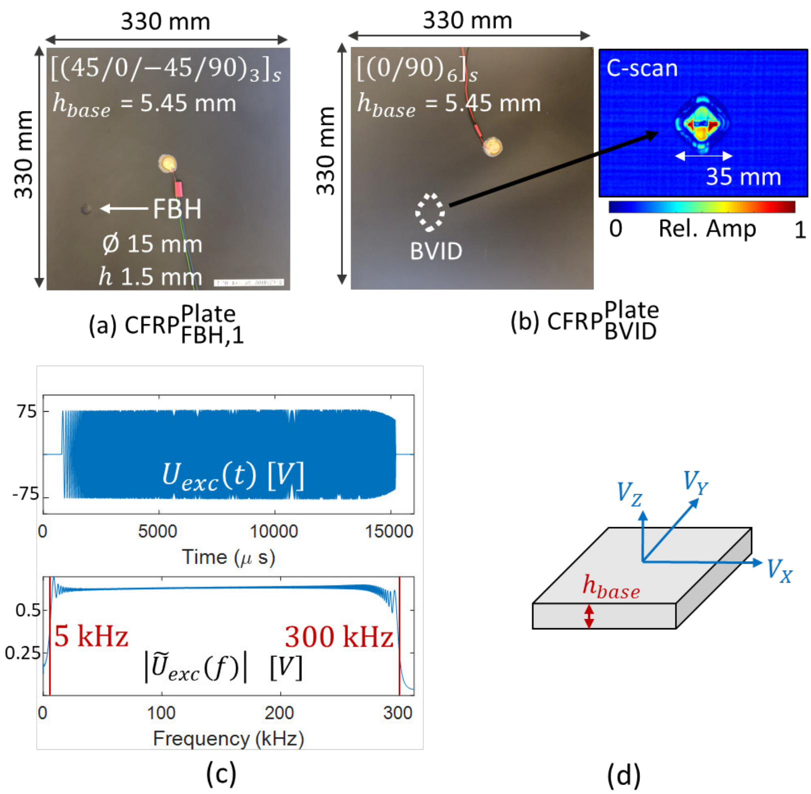

Figure 10.2: (a) Backside of quasi-isotropic CFRP plate with FBH defect (i.e. $\mathrm{CFRP}^{\mathrm{Plate}}_{\mathrm{FBH,1}}$), (b) Backside of cross-ply CFRP plate with BVID (i.e. $\mathrm{CFRP}^{\mathrm{Plate}}_{\mathrm{BVID}}$), (c) Sine sweep excitation signal in time and frequency domain and (d) Coordinate system for the velocity components.

For both test specimens, snapshots of the out-of-plane and in-plane horizontal velocity responses (V_Z and V_X, respectively) are shown in Figure 10.3. The snapshots reveal a typical wavefield that looks rather chaotic because it consists of multiple broadband modes which propagate in all directions. It is impossible to pinpoint the damage in these snapshots, illustrating the need for wavefield manipulation.

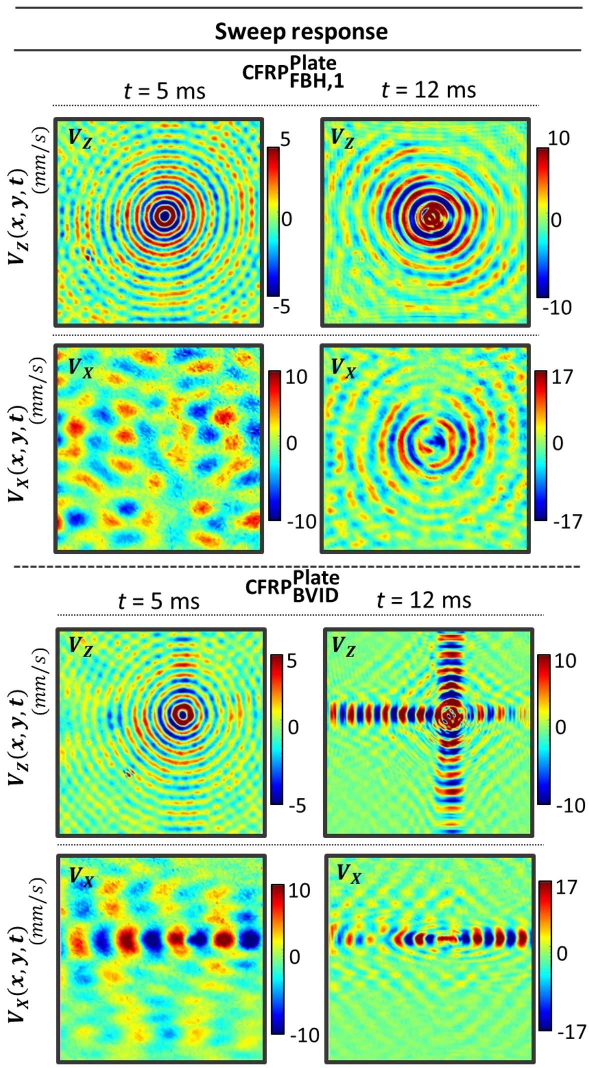

Figure 10.3: Snapshots of the sweep response at 5 ms and at 12 ms for the out-of-plane velocity V_Z and for the in-plane horizontal velocity V_X in $\text{CFRP}^{\text{Plate}}_{\text{FBH,1}}$ and in $\text{CFRP}^{\text{Plate}}_{\text{BVID}}$.

2.2. Frequency Spectrum Manipulation

Most damage map construction methods require the measurement of the full wavefield response of the test specimen when excited with a narrowband toneburst voltage signal [6]. As an example, a toneburst response allows for the construction of weighted-root-mean-square energy maps in which defects are pinpointed as locations of increased intensity (see Chapter 11 Section 3.2 or [1, 12-14]). A typical toneburst voltage signal is shown in Figure 10.4 (a). It is a Hanning windowed seven-cycle sine signal with center frequency f_c = 100 kHz.

The narrowband nature of this toneburst signal is clearly seen in its frequency spectrum representation (see Figure 10.4 (b)).

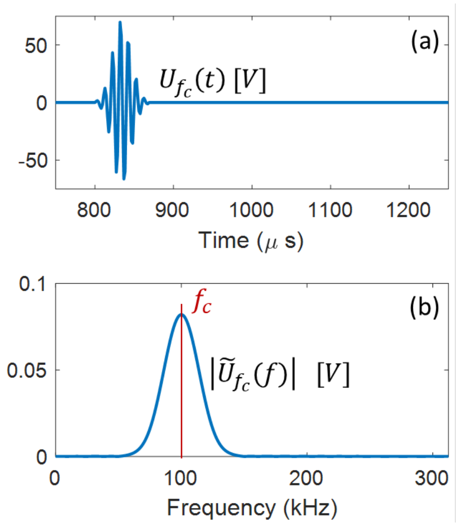

Figure 10.4: Example of a narrowband toneburst excitation signal with center frequency 100 kHz.

When inspecting an unknown material, it is desirable to obtain the toneburst response for a multitude of toneburst center frequencies. This is because the intensity of the sought-after defect-wave interaction is often highly frequency-dependent. However, repeating the same SLDV experiment for a multitude of toneburst excitation signals is highly cumbersome. As an alternative, under the assumption of a linear time-invariant (LTI) system, a broadband sweep experiment may be manipulated in the frequency domain to the desired toneburst response. Here, the transfer function method described by Michaels et al. [8] is used, which results in the conversion of a measured broadband (sweep) response to a desired narrowband toneburst response.

First, the broadband excitation signal $U_{exc}(t)$, the resulting vibrational response recorded by the SLDV $V_i(x,y,t)$ (with $i = X, Y, Z$), and the desired (virtual) toneburst excitation signal $U_{f_c}(t)$ are converted to the frequency domain:

$$U_{exc}(t) \xrightarrow{FFT} \tilde{U}_{exc}(f)$$
$$V_i(x,y,t) \xrightarrow{FFT} \tilde{V}_i(x,y,f)$$
$$U_{f_c}(t) \xrightarrow{FFT} \tilde{U}_{f_c}(f)$$

An example of $\tilde{U}_{f_c}(f)$ was already shown in Figure 10.4 (b) for f_c = 100 kHz.

Next, the desired toneburst velocity response $\tilde{V}_{i,f_c}(x,y,f)$ is calculated using the ratio of $\tilde{U}_{f_c}(f)$ over $\tilde{U}_{exc}(f)$ as the transfer function:

$$\tilde{V}_{i,f_c}(x,y,f) = \frac{\tilde{U}_{f_c}(f)}{\tilde{U}_{exc}(f)} \, . \tilde{V}_i(x,y,f) \tag{10.1}$$

At last, the virtual toneburst response in time domain $V_{i,f_c}(x,y,t)$ is obtained after inverse FFT:

$$\tilde{V}_{i,f_c}(x,y,f) \xrightarrow{IFFT} V_{i,f_c}(x,y,t)$$

Apart from the requirement to deal with a LTI system, the frequency spectrum of the desired toneburst signal $\tilde{U}_{f_c}(f)$ must lie within the bandwidth of the applied excitation signal. Therefore, a broadband sweep with low starting frequency (in this case 5 kHz) and high end frequency (here 300 kHz) is typically chosen for $\tilde{U}_{exc}(f)$ (see also Figure 10.2 (c)).

As an example, the out-of-plane sweep velocity response of both test specimens is converted to a seven-cycle Hanning windowed toneburst response with center frequency f_c = 100 kHz (see Figure 10.4). Figure 10.5 shows the obtained snapshots at t = 868 µs and at t = 944 µs. The snapshots reveal the wavefronts of the A_0 and S_0 guided waves (see indications on Figure 10.4 (a)). In case of the cross-ply $\mathrm{CFRP}^{\mathrm{Plate}}_{\mathrm{BVID}}$ plate, the wavefront of the S_0 mode is strongly affected by the orthotropic material properties as was already explained in Chapter 2. Also visible in Figure 10.5 (d) is the reflection of the A_0 wavefront at the top and right edge of the plate.

At the location of the FBH defect and the BVID, distortions of the propagating waves are noticeable (see enlarged views in Figure 10.5). As an example, the mode conversion of the S_0 mode to the A_0 mode is observed at the FBH in Figure 10.5 (a). Figure 10.5 (d) on the other hand, reveals the increase in local wavenumber (and amplitude) at the location of the BVID. Note again that these defect-wave interactions were not distinguished in the 'chaotic' snapshots of the sweep response (Figure 10.3).

Still, even in these snapshots of the toneburst response it is not straightforward to pinpoint the defect-wave interactions. It would be even more difficult in the case of a more complex test specimen, such as an aircraft panel with backside stiffeners, where the wavefronts are already distorted by the complex geometry of the component. This will be illustrated on Section 3. The wavefield manipulation methods discussed in the next sections aim to further isolate the defect-wave interactions.

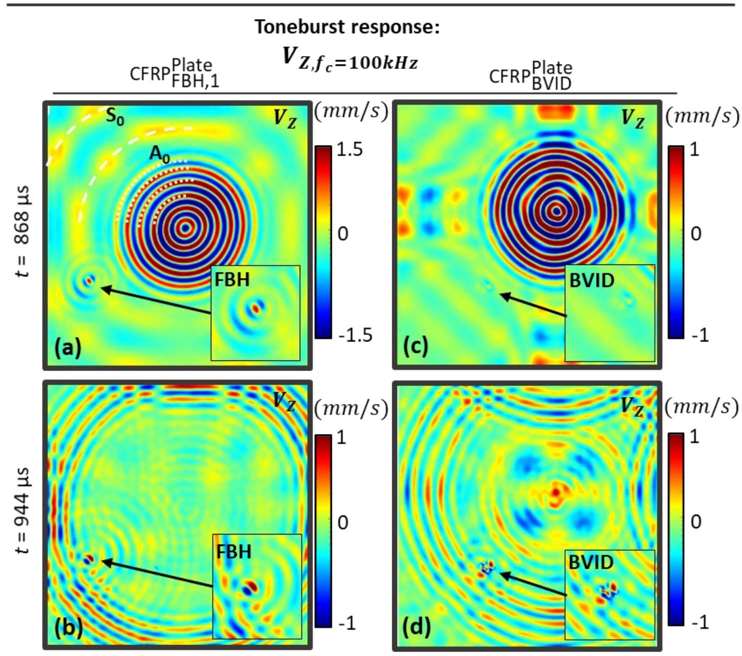

Figure 10.5: Snapshots at t = 868 µs and at t = 944 µs of the toneburst response $V_{Z,f_c=100kHz}$ for (a-b) $\mathrm{CFRP}^{\mathrm{Plate}}_{\mathrm{FBH,1}}$ and for (c-d) $\mathrm{CFRP}^{\mathrm{Plate}}_{\mathrm{BVID}}$.

The toneburst reconstruction accuracy is verified using an additional measurement performed for $\mathrm{CFRP}^{\mathrm{Plate}}_{\mathrm{FBH,1}}$. The test specimen is directly excited with the Hanning windowed seven-cycle sine signal with center frequency f_c = 100 kHz (i.e. $U_{f_c}(t)$) and the response is obtained with the SLDV. The SLDV settings are identical to those used for acquisition of the sweep response. Figure 10.6 shows a snapshot in time of the out-of-plane velocity, and the out-of-plane velocity in function of time at an arbitrary scan point. Figure 10.6 (a) and (b) correspond to the toneburst response derived from the measured sweep response through frequency filtering. Figure 10.6 (c) and (d) correspond to the new measurement where the piezoelectric actuator is directly supplied with the desired toneburst waveform. Comparing the snapshots in time and the signals at the arbitrary scan point reveals that the toneburst reconstruction accuracy is excellent. Moreover, the noise level in the reconstructed toneburst (Figure 10.6 (a) and (b)) is lower because the low and high frequency noise is removed by the frequency filter.

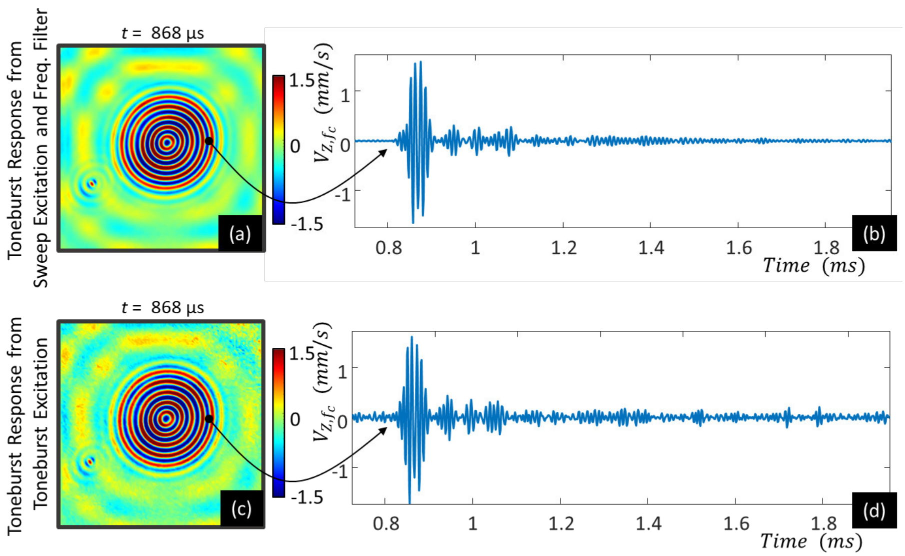

Figure 10.6: Out-of-plane toneburst response in $\mathrm{CFRP}_{\mathrm{FBH},1}^{\mathrm{Plate}}$ obtained from (a,b) Sweep excitation followed by frequency filtering and (c,d) Toneburst excitation.

2.3. Wavenumber Spectrum Manipulation

The wavenumber spectrum manipulation is applied here on the narrowband toneburst response (f_c = 100 kHz) of the out-of-plane velocity component V_{Z,f_c} which was calculated in previous section. Note however, that it can equally be applied for manipulation of the broadband sweep response or in-plane velocity components.

As the name indicates, the wavenumber spectrum manipulation is applied in the wavenumber domain. A 3D FFT is used to transform the velocity response from the space-time (x,y,t) domain to the wavenumber-frequency domain (k_x,k_y,f):

$$V_{i,f_c}(x,y,t) \xrightarrow{3D\ FFT} \tilde{V}_{i,f_c}(k_x,k_y,f)$$

Two different wavenumber spectrum manipulation methods are discussed in the next two section: (i) Wave-direction filters and (ii) Wavenumber filters.

2.3.1. Wave-direction Filter

Wave-direction filtering in the wavenumber frequency domain is a popular method for isolation of the reflected waves at defects. Ruzenne et al. introduced this techniques and showed its effectiveness in revealing the reflection of guided waves at a delamination in a composite plate and at a crack in a metallic plate [10, 15].

A schematic illustration of wave-direction filtering is provided in Figure 10.7 for the toneburst's out-of-plane velocity response V_{Z,f_c} in $\mathrm{CFRP}^{\mathrm{Plate}}_{\mathrm{FBH,1}}$. Figure 10.7 (a) shows the wavenumber map at $f = f_c = 100$ kHz. The small and large quasi-circular rings of increased intensity correspond to the slowness curves of the S_0 and A_0 modes, respectively (see also Chapter 2 Section 4.1.2). Figure 10.7 (b) shows the direction filter mask DF that passes only the waves with $k_x > 0$ and $k_y > 0$. This corresponds to waves propagating in the upward ($k_y > 0$) and right ($k_x > 0$) direction. Note that the mask is identical at every frequency bin *f*. Specific masks can be easily constructed to pass waves travelling in specific directions. Element-wise multiplication of the velocity response and the direction filter mask results in the wavenumber map $\tilde{V}_{Z,f_c,DF}$ shown in Figure 10.7 (c):

$$\tilde{V}_{Z,f_c,DF}\left(k_x, k_y, f\right) = \tilde{V}_{Z,f_c}\left(k_x, k_y, f\right) \odot DF_{k_x>0,k_y>0}\left(k_x, k_y, f\right)$$

Here, the operator $\odot$ refers to the element-wise multiplication (also known as the Hadamard product).

The wave-direction filtered toneburst response is finally obtained after inverse 3D FFT:

$$\tilde{V}_{Z,f_c,DF}(k_x, k_y, f) \xrightarrow{3D\ IFFT} V_{Z,f_c,DF}(x, y, t)$$

The subscript DF is added to the signal's name to indicate that it is obtained after wave-direction filtering.

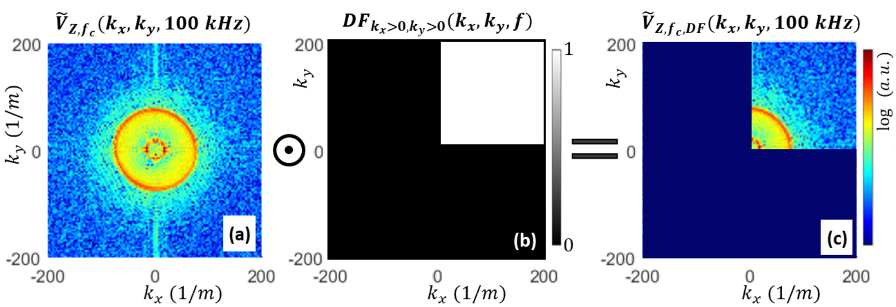

Figure 10.7: Schematic illustration of the wave-direction filter.

Snapshots of the wave-direction filtered toneburst response $V_{Z,f_c,DF}$ are provided in Figure 10.8. The effective isolation of the waves propagating in the upward-right direction is evident when comparing Figure 10.8 with the toneburst response snapshots given in Figure 10.5. The A_0 waves reflected at the FBH and at the BVID are distinguished in the enlarged views of Figure 10.8 (b) and (d), respectively.

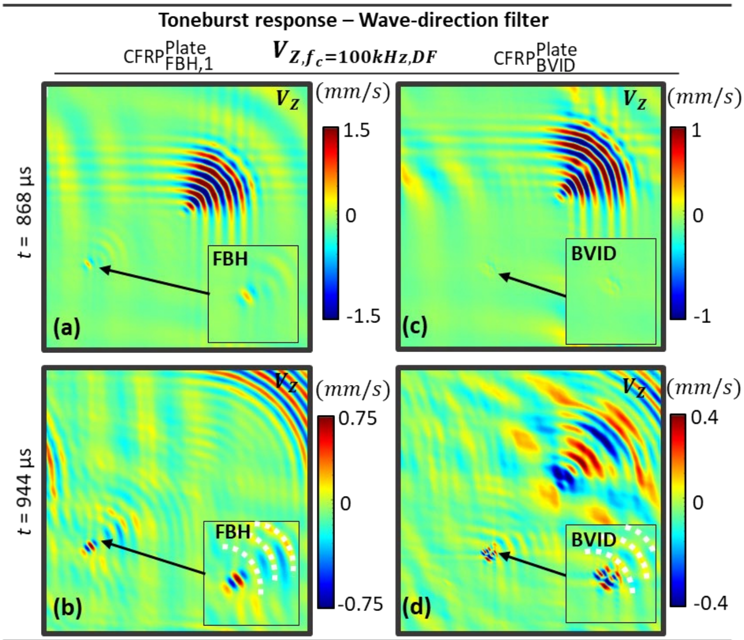

Figure 10.8: Snapshots at t = 868 µs and at t = 944 µs of the wave-direction filtered toneburst response $V_{Z,f_c=100kHz,DF}$ for (a-b) CFRP$^{\text{Plate}}_{\text{FBH},1}$ and (c-d) CFRP$^{\text{Plate}}_{\text{BVID}}$.

2.3.2. Wavenumber bandpass/bandstop Filter

A distinction is made between wavenumber band<u>pass</u> and wavenumber band<u>stop</u> filters. The former aims at retaining only the vibrations corresponding to guided waves with a specific wavenumber whereas the latter aims to remove the vibrations corresponding to guided waves with a specific wavenumber.

Wavenumber bandpass filter

A schematic illustration of the wavenumber bandpass filter algorithm is provided in Figure 10.9 for V_{Z,f_c} in CFRP$^{\text{Plate}}_{\text{FBH},1}$. Figure 10.9 (a) shows a 3D representation of the toneburst response in the wavenumber-frequency domain. The 3D representation consists of three slice planes at $k_x = 0$, $k_y = 0$ and $f = f_c = 100$ kHz. The dispersion curves $k(f)$, corresponding to the A_0 and S_0 modes, are visible as lines of increased intensity.

A wavenumber bandpass filter is constructed in the wavenumber domain. For instance, a circular cosine-shaped wavenumber bandpass filter with center wavenumber k_c = 65 m^{-1} and bandwidth BW = 75 m^{-1} is obtained as:

$$KF_{k_c}(k_x,k_y,f) = \begin{cases} 0 & \text{if } D(k_x,k_y) \geq \dfrac{BW}{2} \\ \dfrac{1}{2}+\dfrac{1}{2}\cos\left(\dfrac{2\pi D(k_x,k_y)}{BW}\right) & \text{if } D(k_x,k_y) < \dfrac{BW}{2} \end{cases}$$

$$\text{with} \quad D(k_x,k_y) = \left|\sqrt{k_x^2+k_y^2}-k_c\right|$$

Note that the filter is identical at every frequency bin. Figure 10.9 (b) gives a 3D representation of this wavenumber bandpass filter.

The wavenumber bandpass filtered response is obtained after element-wise multiplication:

$$\tilde{V}_{Z,f_c,k_c}(k_x,k_y,f) = \tilde{V}_{Z,f_c}(k_x,k_y,f) \odot KF_{k_c=65m^{-1}}(k_x,k_y,f)$$

The result is shown in Figure 10.9 (c). At last, the inverse 3D FFT is applied:

$$\tilde{V}_{Z,f_c,k_c}(k_x,k_y,f) \xrightarrow{3D\ IFFT} V_{Z,f_c,k_c}(x,y,t)$$

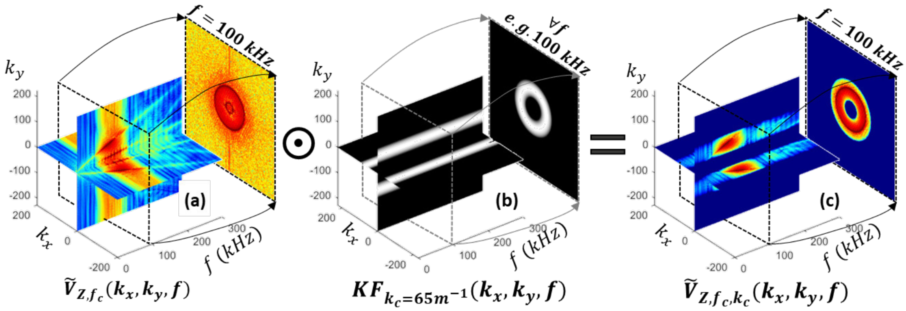

Figure 10.9: Schematic illustration of the wavenumber bandpass filter.

For both test specimens, Figure 10.10 shows two snapshots of V_{Z,f_c,k_c} at the same time instances as were used in Figure 10.5. The center wavenumber of the wavenumber bandpass filter (i.e. k_c = 65 m^{-1}) equals the wavenumber of the A_0 mode in the damage-free material. As a result, the vibrations of the A_0 mode are not affected by the wavenumber bandpass filter, whereas the vibrations corresponding to other modes (and noise) are removed. Indeed, the vibrations corresponding to the S_0 waves are successfully removed as seen by the snapshots in Figure 10.10 (a) and (c). At the location of the FBH (see inset on Figure 10.10 (a)), A_0 vibrations emerge caused by the conversion of the S_0 to the A_0 mode. This is not the case at the BVID as the S_0 waves that are propagating from the actuator in the direction of the BVID, are of relatively low amplitude. When comparing Figure 10.10 (b,d) with Figure 10.5 (b,d), it is noticed that the amplitude of vibration at the location of the FBH and the BVID is significantly reduced by the wavenumber bandpass filtering procedure. This is because the wavenumber of the A_0 mode at the (thin) defected material is different from the wavenumber of the A_0 mode at the damage-free base material. This observation is further exploited in Chapter 13 for the construction of a damage map based on local wavenumber estimation.

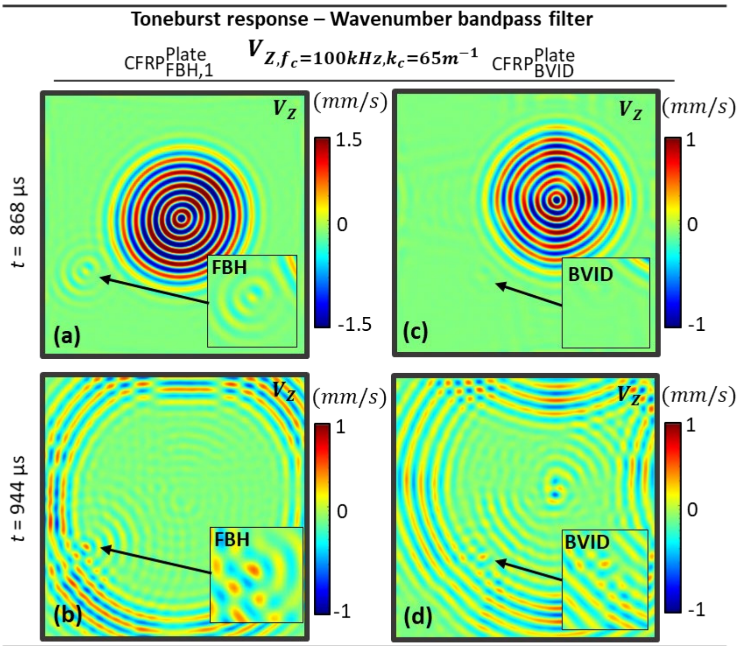

Figure 10.10: Snapshots at t = 868 µs and at t = 944 µs of the wavenumber bandpass filtered toneburst response $V_{Z,f_c=100kHz,k_c=65m^{-1}}$ for (a-b) $\mathrm{CFRP}^{\mathrm{Plate}}_{\mathrm{FBH,1}}$ and (c-d) $\mathrm{CFRP}^{\mathrm{Plate}}_{\mathrm{BVID}}$.

Wavenumber bandstop filter

Wavenumber bandstop filters are used to remove waves that have a specific wavenumber. The filter can be implemented in an identical manner as the wavenumber bandpass filter, with the exception that the filter is now constructed as:

$$KF_{\overline{k_c}}(k_x,k_y,f) = \begin{cases} 1 & \text{if } D(k_x,k_y) \geq \dfrac{BW}{2} \\ \dfrac{1}{2}-\dfrac{1}{2}\cos\left(\dfrac{2\pi D(k_x,k_y)}{BW}\right) & \text{if } D(k_x,k_y) < \dfrac{BW}{2} \end{cases}$$

Kudela et al. [11, 16] proposed an alternative wavenumber bandstop filter method that aims to remove all the vibrations that are characteristic to the damage-free material and thereby keep only the vibrations attributed to the defects. It exploits the difference in the wavenumber at the defected (e.g. reduced thickness) material compared to the damage-free base material for narrowband vibrations.

A schematic illustration of this wavenumber bandstop filter algorithm is provided in Figure 10.11 for V_{Z,f_c} in $\mathrm{CFRP}_{\mathrm{FBH},1}^{\mathrm{Plate}}$. Figure 10.11 (a) again shows a 3D representation of the toneburst response in the wavenumber-frequency domain. In order to construct the wavenumber bandstop filter, the average wavenumber intensity map $I(k_x, k_y)$ is calculated as:

$$I(k_x, k_y) = \sum_f \left|\tilde{V}_{Z,f_c}(k_x, k_y, f)\right|$$

The result is shown in Figure 10.11 (b). Assuming that the area encompassed by the damaged material is significantly smaller compared to the area encompassed by the damage-free material, the two quasi-circular rings in Figure 10.11 (b) correspond to the vibrations of the A_0 and S_0 modes in the damage-free material. The wavenumber bandstop filter is obtained by thresholding this global wavenumber map. As advised by Kudela et al. [11], the threshold is set in such a way that only 5% of the values in the global wavenumber map are passed by the filter. This threshold selection criterion can be written as:

$$TH = \mathrm{ArgMin}\left[\mathrm{cdf}\left(\sum_f \left|\tilde{V}_{Z,f_c}(k_x, k_y, f)\right|\right) - 0.05\right]$$

with cdf the cumulative distribution function. The resulting filter is calculated as:

$$KF_{5\%}(k_x, k_y, f) = \begin{cases} 1 & \text{if } \left|\tilde{V}_{Z,f_c}(k_x, k_y, f)\right| < TH \\ 0 & \text{if } \left|\tilde{V}_{Z,f_c}(k_x, k_y, f)\right| \geq TH \end{cases}$$

and shown in Figure 10.11 (c). Note again that this mask is identical at every frequency bin.

The wavenumber bandstop filtered velocity response in the wavenumber-frequency domain $\tilde{V}_{Z,f_c,\overline{KF}}(k_x, k_y, f)$ is obtained as:

$$\tilde{V}_{Z,f_c,\overline{KF}}(k_x, k_y, f) = \tilde{V}_{Z,f_c}(k_x, k_y, f) \odot KF_{5\%}(k_x, k_y, f)$$

The 3D representation of $\tilde{V}_{Z,f_c,\overline{KF}}(k_x, k_y, f)$ is shown in Figure 10.11 (d). At last, the wavenumber filtered velocity response in spatial-time domain $V_{Z,f_c,\overline{KF}}(x, y, t)$ is obtained as:

$$\tilde{V}_{Z,f_c,\overline{KF}}(k_x, k_y, f) \xrightarrow{3D\ IFFT} V_{Z,f_c,\overline{KF}}(x, y, t)$$

The subscript $\overline{KF}$ indicates that the signal was derived after application of a wavenumber bandstop filter.

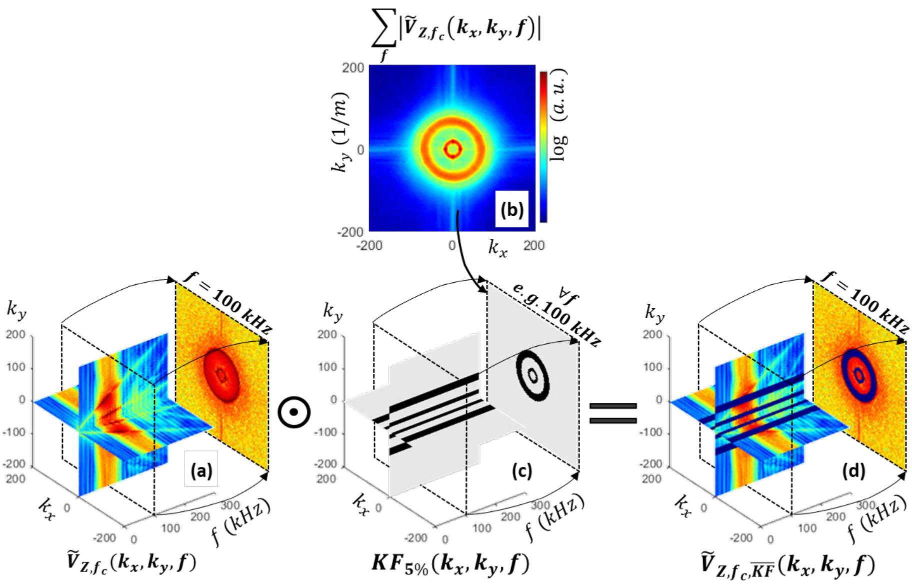

Figure 10.11: Schematic illustration of the wavenumber bandstop filter.

Snapshots of the wavenumber bandstop filtered toneburst response $V_{Z,f_c,\overline{KF}}$ are provided in Figure 10.12. Comparing this figure with Figure 10.5 indicates the effectiveness of the wavenumber bandstop filter in (partially) removing the vibrations in the damage-free material while retaining the vibrations at the FBH defect and at the BVID. In Figure 10.12 (a) and (c), the wavefronts of the A_0 and S_0 modes in the damage-free material are still visible but the corresponding amplitude is significantly reduced. At the defects (see insets in Figure 10.12 (b) and (d)), the high amplitude vibrations are successfully retained. As a result, the use of the wavenumber bandstop filter facilitates the detection of the defects.

Note that one could opt to slightly increase the threshold value used in the calculation of $KF_{5\%}(k_x, k_y, f)$ for further reduction of the vibrational amplitude in the damage-free material. Note however, that this has the consequence that also the vibrational amplitude at the defects may decrease.

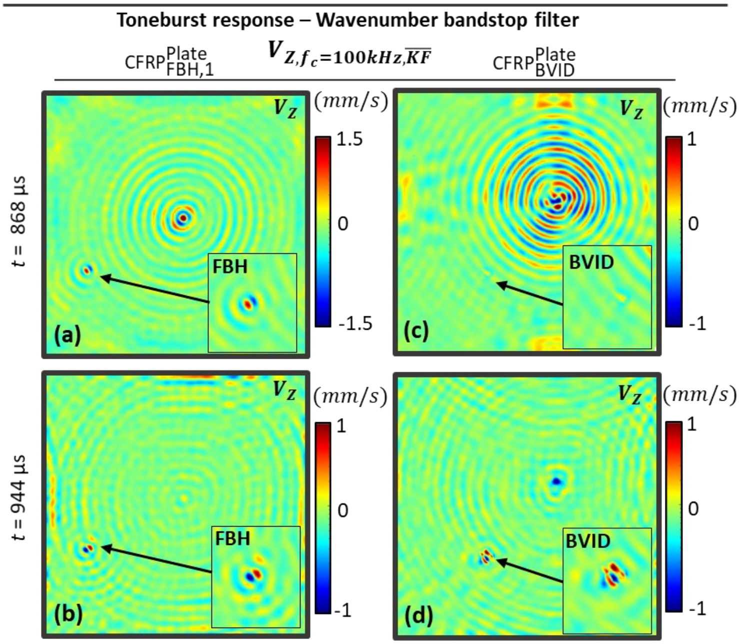

Figure 10.12: Snapshots at t = 868 µs and at t = 944 µs of the wavenumber bandstop filtered toneburst response $V_{Z,f_c=100kHz,KF}$ for (a-b) $\mathrm{CFRP}^{\mathrm{Plate}}_{\mathrm{FBH,1}}$ and for (c-d) $\mathrm{CFRP}^{\mathrm{Plate}}_{\mathrm{BVID}}$.

2.4. Mode Manipulation

Mode manipulation corresponds to the broadband extension of the wavenumber filter. Hence, a mode filter depends on the wavenumber as well as the frequency. A distinction is made between mode<u>pass</u> and mode<u>stop</u> filters. The former aims at retaining only the vibrations corresponding to a specific guided wave mode of interest whereas the latter aims to remove the vibrations corresponding to the specific guided wave mode. In order to be able to perform mode manipulation, first the dispersion curve(s) of the mode(s) of interest must be identified.

2.4.1. Dispersion Curve Identification

Considering unknown material properties, the dispersion curves must be somehow identified from the broadband sweep measurement. The broadband dataset $V_Z(x,y,t)$ is transformed from the spatial-time domain to the wavenumber-frequency domain:

$$V_i(x,y,t) \xrightarrow{3D\ FFT} \tilde{V}_i(k_x,k_y,f)$$

Figure 10.13 (a) shows the resulting 3D representation for $\mathrm{CFRP}^{\mathrm{Plate}}_{\mathrm{FBH,1}}$. A 2D representation along $k_x = 0$ is given in Figure 10.13 (b). As was the case for the wavenumber filter, it is assumed that the defected area is relatively small compared to the total scan area. As a result, the high intensity lines correspond in good approximation to the dispersion curves of the guided waves travelling in the damage-free base material.

Multiple methods can be used to identify the dispersion curves in a (semi-)automated manner e.g. the matrix-pencil algorithm [17], inhomogeneous wave correlation (IWC) [18] or an iterative curve detection procedure in the wavenumber-frequency domain [19]. Here, an updated version of the iterative curve detection procedure introduced by Flynn et al. [19] is used. The algorithm aims to identify the dispersion curves $k(f)$ along a specific wave propagation direction. It is advised to use a slice along a main axis of orthotropy. Here, the slice along $k_x = 0$, i.e. waves propagating in the 90° direction, is selected (see Figure 10.13 (b)).

First, the wavenumber-frequency point with the highest intensity is identified. The wavenumber and frequency values corresponding to this point are saved as: $k(1)$ and $f(1)$. The point is indicated with a star and denoted '1st maximum' in Figure 10.13 (c). Next, we move to the right and locate the maximum in the wavenumber-frequency range: $k \in \,]k(1), k(1) + \Delta k]$ and $f \in [f(1) - \Delta f, f(1) + \Delta f]$ (see '2nd maximum' in Figure 10.13 (c)). The coordinates of this second point are saved as $k(2)$ and $f(2)$. Next the maximum is located in the range $k \in \,]k(2), k(2) + \Delta k]$ and $f \in [f(2) - \Delta f, f(2) + \Delta f]$ and the coordinates are saves as $k(3)$ and $f(3)$ (see '3rd maximum' in Figure 10.13 (c)). This step is repeated until the maximum frequency of interest is reached. The same procedure is performed starting from the initially identified maximum, moving to the left side (i.e. range $k \in [k(1) - \Delta k, k(1)[$ and $f \in [f(1) - \Delta f, f(1) + \Delta f]$) and again repeated until the minimum frequency of interest is reached.
Following this iterative procedure, a vector of frequency values and a vector of wavenumber values is obtained. The mode dispersion curve is finally obtained by fitting a smoothing spline (e.g. using cubic smoothing spline fit function *csaps* in Matlab) or a low-order polynomial through these points. Best results are found when using the intensity values at the points as weights for the spline or polynomial fit.

As an example, Figure 10.13 (d) shows the wavenumber-frequency slice on which the identified local maxima are indicates with black markers. These local maxima were identified using following search settings Δf = 5000 kHz and Δk = 10 m^{-1}. The dispersion curve of the A_0 mode is found as the cubic smoothing spline fitted (with smoothing factor 10^{-15}) to all these points. In order to find the dispersion curves of other modes, the intensity is set to zero at all points in the wavenumber-frequency map which are located close to the dispersion curve identified in the previous step. The same algorithm can then be repeated. Figure 10.13 (e) shows the extracted dispersion curves of the A_0, S_0 and A_1 modes.

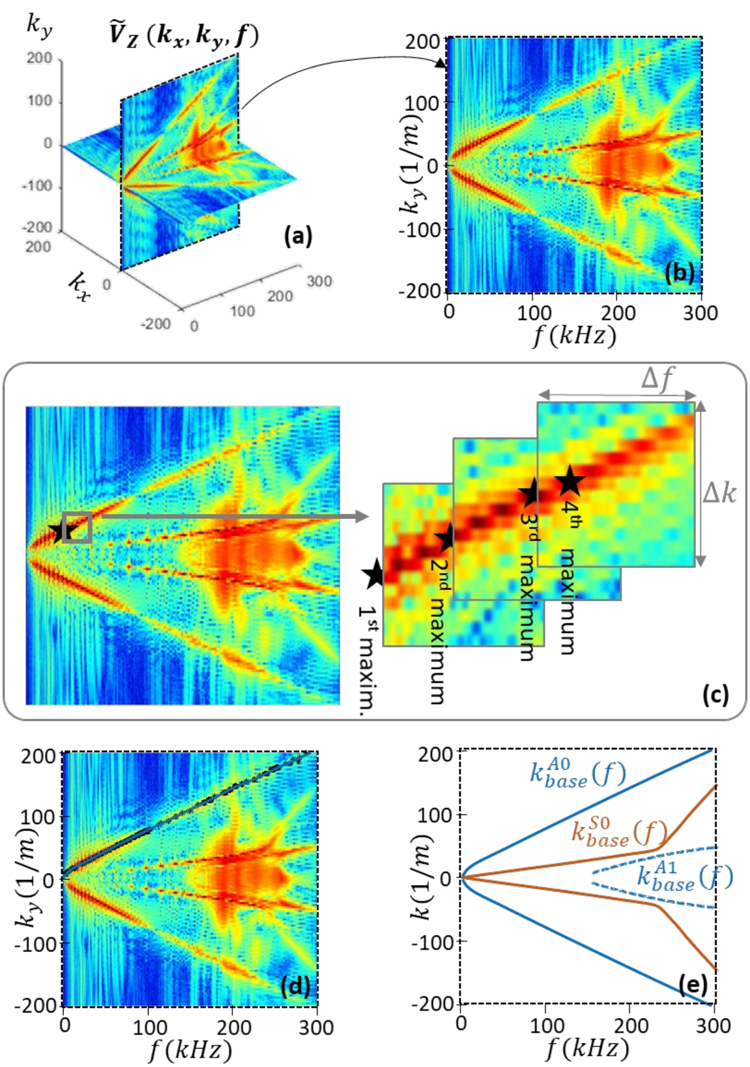

Figure 10.13: Sweep out-of-plane velocity response in $\mathrm{CFRP}_{\mathrm{FBH,1}}^{\mathrm{Plate}}$ (a) 3D wavenumber-frequency map, (b) Wavenumber-frequency map along k_x = 0, (c) Automated dispersion curve detection algorithm, (d) Identified points corresponding to the A0 mode dispersion curve and (d) All identified dispersion curves.

The dispersion curve identification procedure explained here is simple and fast but comes with some drawbacks. First, the search settings (Δk and Δf) and the spline fit smoothing factor may need to be adapted when trying to identify the dispersion curves in a different experimental dataset. This reduces the practicallity of the curve identification method. In some cases, it can be even faster or more robust to manually identify the curves in the wavenumber-frequency map (Figure 10.13 (b)) instead of using the proposed (semi-)automated approach. Next, the dispersion curves are identified for waves propagating in one specific direction (in this example along k_x = 0, i.e. vertical waves). However, as discussed in Chapter 2, dispersion curves are directional-dependent when dealing with anisotropic materials. In the following two sections, it is illustrated that the error introduced by not taking into account the anisotropic nature of the composite material is relatively small. This error can be avoided by identifying the dispersion curve along multiple wave propagation directions.

2.4.2. Modepass Filter

A modepass filter aims to keep only the vibrations that are characteristics to one (or more) mode(s) of interest. As an example, a modepass filter is used here to isolate the A_0 mode vibrations in the out-of-plane toneburst response of the two CFRP plates. The schematic representation of the modepass algorithm is shown in Figure 10.14. Figure 10.14 (b) follows from the dispersion curve identification step that was discussed in the previous section.

The vibrations corresponding to the A_0 mode are first isolated from the out-of-plane sweep velocity response V_Z using a frequency-dependent bandpass filter in the wavenumber-frequency domain. This frequency-dependent bandpass filter, denoted <u>m</u>odepass <u>f</u>ilter MF_{A0}, is cosine-shaped and constructed around the A_0 dispersion curve $k_{base}^{A0}(f)$:

$$MF_{A0}(k_x, k_y, f) = \begin{cases} 0 & \text{if } D(k_r, f) \geq \dfrac{BW}{2} \\ \dfrac{1}{2} + \dfrac{1}{2}\cos\left(\dfrac{2\pi|D(k_r, f)|}{BW}\right) & \text{if } D(k_r, f) < \dfrac{BW}{2} \end{cases}$$

$$\text{with} \qquad k_r = \sqrt{k_x^2 + k_y^2}$$

$$D(k_r, f) = \quad k_r - k_{base}^{A0}(f)$$

where BW is the full bandwidth of the cosine lobe. The bandwidth is set at BW = 75 m^{-1} and the filter is shown in Figure 10.14 (c). Note that this filter is frequency-dependent in contrast to the wave-direction filter (Figure 10.7 (b)) and the wavenumber filter (Figure 10.11 (c)).

The required A_0 mode response is obtained after element-wise multiplication of the modepass filter MF_{A0} with the out-of-plane sweep velocity response $\tilde{V}_z$ in the wavenumber-frequency domain (see Figure 10.14 (d)):

$$\tilde{V}_{Z,A0}(k_x, k_y, f) = MF_{A0}(k_x, k_y, f) \odot \tilde{V}_Z(k_x, k_y, f)$$

Inverse 3D FFT takes the result back to the spatial-time domain:

$$\tilde{V}_{Z,A0}(k_x, k_y, f) \xrightarrow{3D\ IFFT} V_{Z,A0}(x, y, t)$$

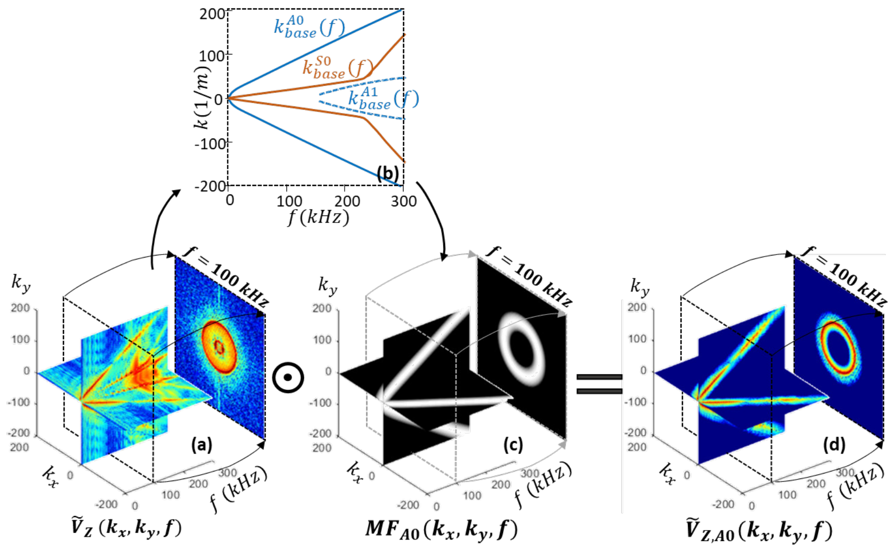

Figure 10.14: Schematic illustration of the A0 modepass filter.

The A0 mode-filtered sweep response $V_{Z,A0}(x, y, t)$ is finally transformed to the seven-cycle Hanning windowed toneburst response with f_c = 100 kHz using the algorithm explained in Section 2.2. The result is denoted as $V_{Z,A0,f_c}$ in which the subscripts indicate that it is the out-of-plane velocity component, after A0 modepass filtering and after sweep to toneburst conversion. Note that it is equally possible to perform the sweep to toneburst conversion before the application of the modepass filter.

For both test specimens, Figure 10.15 shows two snapshots of $V_{Z,A0,f_c}$. As expected, the snapshots are highly similar to those corresponding to the wavenumber bandpass filtered toneburst with center wavenumber equal to the wavenumber of the A0 mode in the damage-free material (see Figure 10.10). The S0 mode vibrations are successfully removed. In addition, the local amplitude at the defects is reduced because the dispersion curve of the A0 mode at the (thin) defected material is different from the dispersion curve of the A0 mode at the damage-free base material. The modepass filter was constructed around the latter dispersion curve, thus only the vibrations showing a dispersion behavior similar to the damage-free base material were retained. This modepass filter is further exploited in Chapter 13 for the construction of a local thickness map based on self-reference broadband local wavenumber estimation.

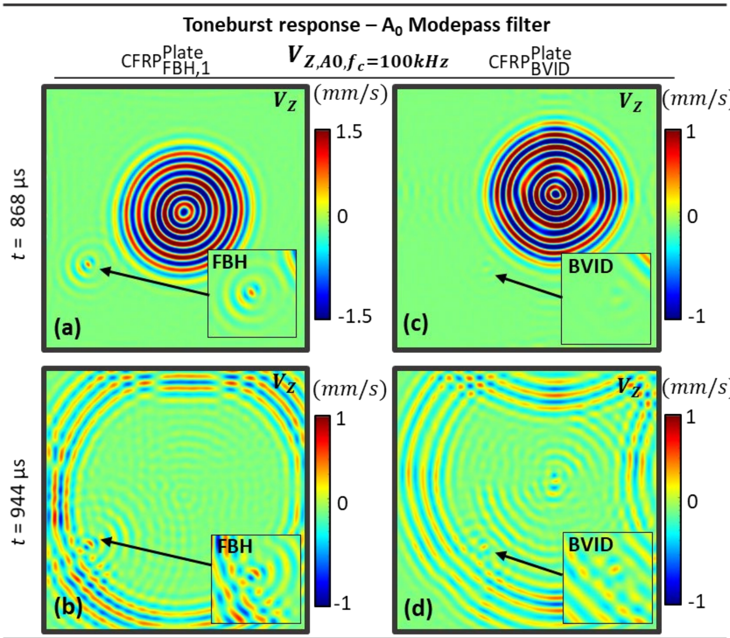

Figure 10.15: Snapshots at t = 868 µs and at t = 944 µs of the A0 modepass filtered toneburst response $V_{Z,A0,f_c=100kHz}$ for (a-b) $\mathrm{CFRP}^{\mathrm{Plate}}_{\mathrm{FBH,1}}$ and for (c-d) $\mathrm{CFRP}^{\mathrm{Plate}}_{\mathrm{BVID}}$.

2.4.3. Modestop Filter

The modestop filter operates in an opposite way compared to the modepass filter. The modestop filter aims at removing all vibrations that correspond to modes in the damage-free material. As a result, only the vibrations that are caused by the presence of damage (or anomalies) should remain.

In this explanatory example, a modestop filter $MF_{\overline{A0S0A1}}$ is used to remove the vibrations corresponding to the pre-identified A0, S0 and A1 dispersion curves. A cosine shaped modestop filter with full bandwidth BW is constructed as:

$$MF_{\overline{A0S0A1}}(k_x, k_y, f) = \begin{cases} 1 & \text{if } D(k_r, f) \geq \dfrac{BW}{2} \\ \dfrac{1}{2} - \dfrac{1}{2}\cos\left(\dfrac{2\pi|D(k_r, f)|}{BW}\right) & \text{if } D(k_r, f) < \dfrac{BW}{2} \end{cases}$$

$$k_r = \sqrt{k_x^2 + k_y^2} \tag{10.2}$$

with

$$D(k_r, f) = \min\begin{pmatrix} |k_r - k_{base}^{A0}(f)| \\ |k_r - k_{base}^{S0}(f)| \\ |k_r - k_{base}^{A1}(f)| \end{pmatrix}$$

Note that the bandstop filter may take other shapes, such as the Tukey-shaped modestop filter used in Chapter 11 Section 3.4 [1].

Figure 10.16 (a) shows the 3D representation of $\tilde{V}_Z\,(k_x, k_y, f)$ for the $\mathrm{CFRP}^{\mathrm{Plate}}_{\mathrm{FBH,1}}$ sample. A visualization of the modestop filter $MF_{\overline{A0S0A1}}$ is presented in Figure 10.16 (b). Then, the filtered dataset $\tilde{V}_{Z,\overline{A0S0A1}}(k_x, k_y, f)$ is obtained after element-wise multiplication of $\tilde{V}_Z\,(k_x, k_y, f)$ with $MF_{\overline{A0S0A1}}(k_x, k_y, f)$ (see Figure 10.16 (c)):

$$\tilde{V}_{Z,\overline{A0S0A1}}(k_x, k_y, f) = MF_{\overline{A0S0A1}}(k_x, k_y, f) \odot \tilde{V}_Z(k_x, k_y, f)$$

At last, inverse 3D FFT is applied to transform the result back to the spatial-time domain according to

$$\tilde{V}_{Z,\overline{A0S0A1}}(k_x, k_y, f) \xrightarrow{3D\ IFFT} V_{Z,\overline{A0S0A1}}(x, y, t)$$

The obtained mode filtered sweep response is transformed to the seven-cycle Hanning windowed toneburst response with f_c = 100 kHz using the algorithm explained in Section 2.2. The obtained signal is denoted as $V_{Z,,\overline{A0S0A1},f_c}$. The bar above the mode names that are listed in the subscript indicates that a modestop filtered was used (rather than a modepass filter).

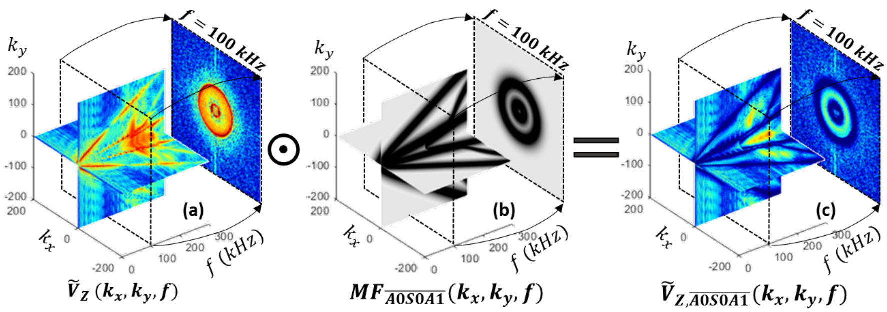

Figure 10.16: Schematic illustration of the A_0 , S_0 and A_1 modestop filter.

Snapshots of the modestop filtered toneburst velocity response $V_{Z,,\overline{A0S0A1},f_c}$ are provided in Figure 10.17. Comparing Figure 10.17 with the unfiltered toneburst response (Figure 10.5) indicates the successful removal of the vibrations in the damage-free material while keeping the high amplitude vibrations attributed to the FBH defect and to the BVID.

In Figure 10.17 (c), low amplitude artifacts of the S_0 wavefront are observed. This is caused by the anisotropic nature of the cross-ply CFRP material. From Chapter 2 (and also deduced here in Figure 10.3), it is known that the S_0 mode is strongly affected by anisotropy which causes the S_0 mode dispersion curve to become directional-dependent. However, the modestop filter constructed using Eq. (10.2) is based on one single S_0 mode dispersion curve identified along a primary propagation direction (see Section 2.4.1). As a result, the modestop filter is circular-shaped in the wavenumber domain (see Figure 10.16 (b)) and may be unsuccessful at removing all the S_0 mode vibrations. In case of very strong anisotropy (e.g. a pure unidirectional CFRP plate), one could opt to construct a directional-dependent modestop filter (i.e. elliptical cone / pyramid like functions in (k_x, k_y, f) space). This is possible using the proposed equations if the dispersion curves are determined along multiple propagation directions: $k^i_{mode}(f) \rightarrow k^i_{mode}(f, \theta)$ and $\theta = \text{angle}(k_x, k_y)$. Note however that the observed S_0 mode artefacts in Figure 10.17 (c), and especially in Figure 10.17 (d), are of considerably low amplitude compared to the vibrations at the defect. As such, the cumbersome directional-dependent modestop filter construction approach is not used in this PhD study.

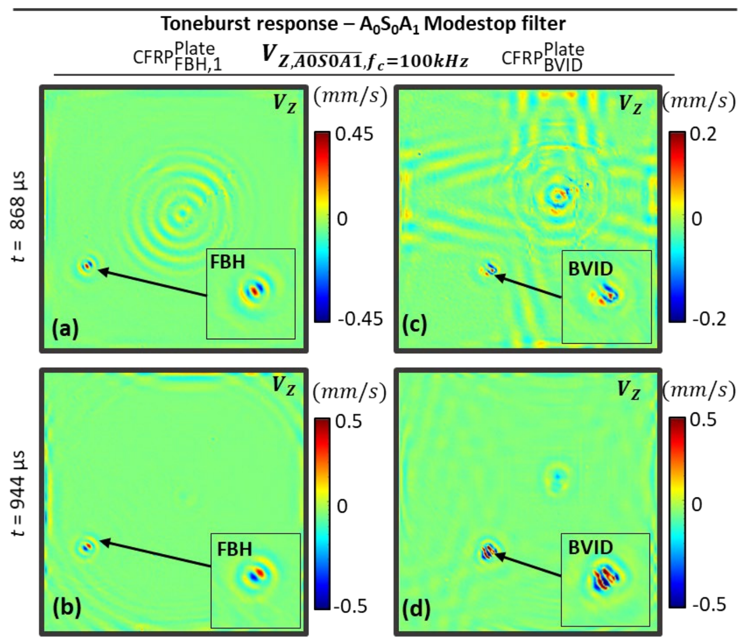

Figure 10.17: Snapshots at t = 868 μs and at t = 944 μs of the A_0, S_0 and A_1 modestop filtered toneburst response $V_{Z,,\overline{A0S0A1},f_c=100kHz}$ for (a-b) $\text{CFRP}^{\text{Plate}}_{\text{FBH},1}$ and (c-d) $\text{CFRP}^{\text{Plate}}_{\text{BVID}}$.

2.5. Time-Frequency Spectrum Manipulation

In Chapter 3 and in Chapter 8, it was explained and experimentally proven that nonlinear vibrational components are formed at clapping and/or rubbing defects. In order to exploit this observation for damage detection, the nonlinear components have to be extracted from the output response of the sample.

2.5.1. Adaptation to Measurement Protocol

The sample $\mathrm{CFRP}_{\mathrm{BVID}}^{\mathrm{Plate}}$ (see Figure 10.2 (b)) is used to illustrate the approach to extract the nonlinear defect response. The search for the nonlinear response of a defect requires an adaptation to the measurement protocol described in Section 2.1. The cross-ply CFRP plate is presented again in Figure 10.18, now with a different piezoelectric actuator and surface condition.

First, the nonlinear response is only triggered when the vibrational amplitude of the defect is sufficiently high. High vibrational amplitudes at the defect are achieved when the excitation frequency matches with one of the defect's LDR frequencies. From the parametric study on the LDR of typical defects in CFRP (Chapter 7), it is known that the LDR frequencies range typically from 10 to 125 kHz. As a result, a sweep excitation from 10 kHz to 125 kHz is used to make sure that the LDR frequencies are within the excitation bandwidth.

Next, the small piezoelectric bending disc is replaced by an ultrasonic cleaning transducer (with nominal power 70 W and resonance frequency 120 kHz) as it can deliver more vibrational power. A M10 bolt is screwed into the transducer and serves as a stinger, leading to a relative small contact area between the source and the plate. Again, phenyl salicylate is used to temporarily bond the actuator to the plate (see inset on Figure 10.18). The Falco WMA-300 voltage amplifier is used to increase the excitation voltage signal to 300 V_{pp}.

At last, the surface of the plate that is measured by the SLDV is covered with removable retroreflective tape (3M™ Scotchlite™ 680CRE10). This is required to be able to detect the nonlinear vibrational components which are of low amplitude [2, 20, 21]. A total of 25 000 time samples are taken (at 625 kS/s) corresponding to a signal length of 40 ms.

The updated measurement procedure is only used for inspection of $\mathrm{CFRP}_{\mathrm{BVID}}^{\mathrm{Plate}}$. Test specimen $\mathrm{CFRP}_{\mathrm{FBH,1}}^{\mathrm{Plate}}$ is not considered here. The FBH defect has no contact interfaces, resulting in the absence of defect induced nonlinear components.

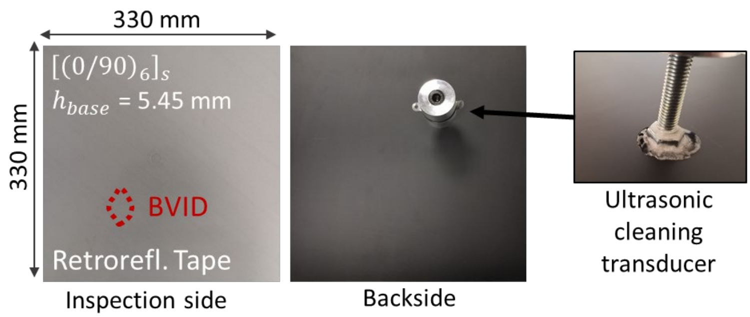

Figure 10.18: Cross-ply CFRP plate with BVID ($\mathrm{CFRP}_{\mathrm{BVID}}^{\mathrm{Plate}}$) inspected for nonlinear vibrational response analysis.

2.5.2. Time-Frequency Filter Algorithm

A broadband excitation signal is used to make sure that potential LDRs are excited. The broadband nature of the excitation signal makes higher harmonics extraction using the classical FFT impossible. This is graphically illustrated in Figure 10.19. For example, at the time instance t = 6 ms, the instantaneous frequency of the sweep signal is 15 kHz. This results in a linear response of the sample at f_{lin} = 15 kHz combined with the potential presence of nonlinear higher harmonic components: second harmonic at f_{HH2} = 30 kHz, third harmonic at f_{HH3} = 45 kHz, etc. (see Figure 10.19 (b) and (c), indicated in red). These higher harmonic components are of low amplitude and as such they are overshadowed by the linear part of the output response at 16 ms (i.e. f_{lin} = 30 kHz, indicated in green) and 28 ms (i.e. f_{lin} = 45 kHz), respectively. This is further indicated as 'overlap' on Figure 10.19 (c). Lowering the frequency bandwidth of excitation will reduce the overlap, but it will also reduce the likelihood of exciting LDRs (which mainly induce the nonlinear response). Hence, to extract nonlinear components from a broadband response signal, more involved processing tools are required. One possible solution is to use a combination of inverse filtering and phase symmetry analysis for extraction of the second and third higher harmonic components [22, 23]. Here, a more simple, yet effective, method is proposed using the short-time-Fourier-transformation (STFT) and subsequent bandpass filtering in the time-frequency domain. The proposed method allows to extract harmonic components as well as modulation sidebands of any specified order.

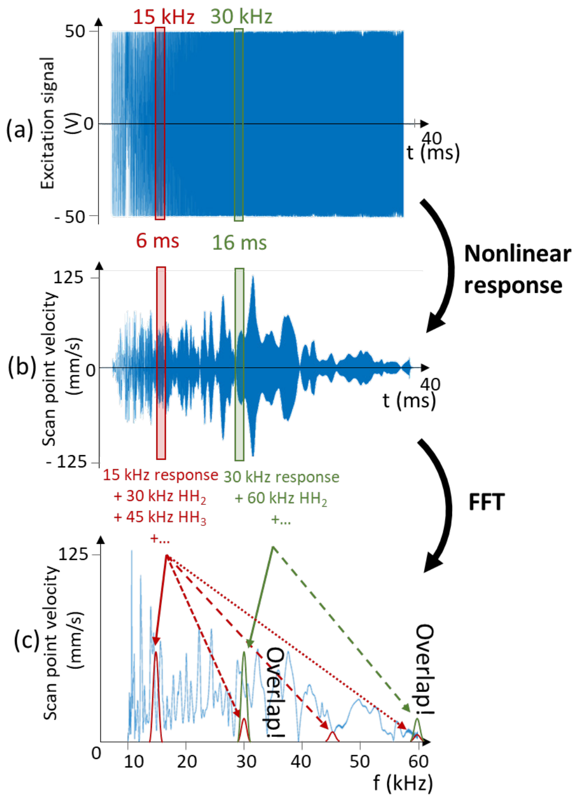

Figure 10.19: (a) (Burst) sweep excitation signal in time domain, Velocity response in (b) time domain and (c) frequency domain (using FFT).

The decomposition of the broadband out-of-plane velocity response $V_Z(x, y, t)$ into its linear and nonlinear components using bandpass filtering in the time-frequency domain is graphically illustrated in Figure 10.20.

First, the measured out-of-plane velocity response $V_Z(x, y, t)$ is transformed from the time domain to the time-frequency domain using the STFT (see Chapter 4 Section 4.3):

$$V_Z(x, y, t) \xrightarrow{STFT} \tilde{V}_Z(x, y, t, f)$$

The STFT is performed in Matlab following the implementation proposed in reference [24], with hop size H = 66, window length M = 512, number of time divisions $L = 1 + \left\lfloor \frac{N-M}{H} \right\rfloor$ = 372 and total number of time samples N = 25 000 (see Chapter 4 Section 4.3 for more information).

The absolute value of $\tilde{V}_Z(x,y,t,f)$, averaged over all scan points is shown in Figure 10.20 (a). The linear response of the component is visible as a line of increased amplitude from f_{start} = 10 kHz to f_{end} = 125 kHz. Next to this linear response, multiple lines are found corresponding to the higher harmonic components. The second and third higher harmonic components are marked *HH*2 and *HH*3.

In the next step, a time-frequency bandpass filter $TFF^*(t,f)$ is constructed around one of the components of interest. The asterisk * refers to the filtered component: lin., HH_2 or HH_3. The filter is constructed as:

$$TFF^*(t,f) = TFF_1^*(t,f).TFF_2(t) \tag{10.3}$$

with:

$$TFF_1^*(t,f) = \begin{cases} 1 & \text{if } |f^* - f_{lin}(t)| < \dfrac{FT(t)}{2} \\ 0 & \text{if } |f^* - f_{lin}(t)| > \dfrac{FT(t)}{2} + \dfrac{\pi\, BW(t)}{4} \\ \dfrac{1}{2} + \dfrac{1}{2}\cos\left(\dfrac{4\left(|f^* - f_{lin}(t)| - \dfrac{FT(t)}{2}\right)}{BW(t)}\right) & \text{elsewhere} \end{cases}$$

$$TFF_2(t) = \begin{cases} 0 & \text{if } t < 0.06\, t_{meas} \text{ or } t > 0.94\, t_{meas} \\ 1 & \text{elsewhere} \end{cases}$$

and

$$\begin{aligned} f_{lin}(t) &= f_{start} + t_r(t)\left(f_{end} - f_{start}\right) \\ FT(t) &= FT_1 + t_r(t)\,(FT_2 - FT_1) \\ BW(t) &= BW_1 + t_r(t)\,(BW_2 - BW_1) \\ t_r(t) &= \frac{t - 0.05\, t_{meas}}{0.90\, t_{meas}} \\ f^* &= \begin{cases} f & \text{for linear component extraction} \\ \dfrac{f}{2} & \text{for HH}_2 \text{ extraction} \\ \dfrac{f}{3} & \text{for HH}_3 \text{ extraction} \end{cases} \end{aligned}$$

where f_{start}= 10 kHz and f_{end} = 125 kHz are the start and end frequency of the sweep signal, respectively. t_{meas} = 40 ms is the measurement time, $t_r(t)$ represents the relative sweep advance and $f_{lin}(t)$ is the instantaneous sweep excitation frequency at time *t*. The filter is Tukey-shaped with time-dependent flat top length $FT(t)$ and taper bandwidth $BW(t)$. The term $TFF_2(t)$ limits the filter in time domain such that the response is only retained when the excitation signal is active.

As an example, Figure 10.20 (b) shows the filter for extracting the second higher harmonic component TFF^{HH2}. The filter settings are: flat top length FT_1 = 3 kHz (at start), FT_2 = 7 kHz (at end) and taper bandwidth BW_1 = 3 kHz (at start), BW_2

= 7 kHz (at end). These filter settings make sure that the window fully envelops the HH2 component. The HH2 velocity signal $\tilde{V}_{Z,HH2}(x, y, t, f)$ (see Figure 10.20 (c)) is obtained after element-wise multiplication of the sweep velocity signal $\tilde{V}_Z(x, y, t, f)$ and the time-frequency bandpass filter $TFF^{HH2}(x, y, t, f)$:

$$\tilde{V}_{Z,HH2}(x, y, t, f) = TFF^{HH2}(x, y, t, f) \odot \tilde{V}_Z(x, y, t, f)$$

As a final step, inverse STFT (ISTFT) is performed to transform the extracted velocity signal from the time-frequency domain back to the time domain (see Chapter 4 Section 4.3):

$$\tilde{V}_{Z,*}(x, y, t, f) \xrightarrow{ISTFT} V_{Z,*}(x, y, t)$$

Again, the asterisk * refers to the filtered component, e.g. $V_{Z,*} = V_{Z,HH2}$.

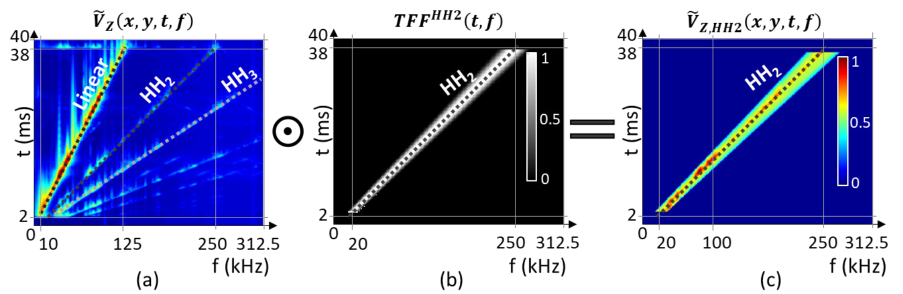

Figure 10.20: Extraction of the second higher harmonic component HH2 for $\mathrm{CFRP}^{\mathrm{Plate}}_{\mathrm{BVID}}$: (a) Average STFT of the measured out-of-plane velocity response, (b) Bandpass filter around the HH2 curve, (c) Extracted HH2 component in time-frequency domain.

2.5.3. Sweep to Toneburst Conversion for Nonlinear Components

In previous section, the HH2 signal was extracted from the broadband out-of-plane velocity response. In order to convert this broadband HH2 signal to a narrowband toneburst response, the frequency filtering procedure explained in Section 2.2 is followed.

One has to be careful when constructing the required transfer function: $\frac{\tilde{U}_{fc}(f)}{\tilde{U}_{exc}(f)}$ (see Eq. (10.1)). In general, the signal $\tilde{U}_{exc}(f)$ corresponds to the FFT transform of the sweep excitation signal. However, when dealing with nonlinear components, the reference sweep excitation signal must be adapted taking into account the frequency range of the nonlinear component of interest. As an example, the extracted HH2 signal starts at 2 x 10 kHz = 20 kHz and ends at 2 x 125 kHz = 250 kHz (see also Figure 10.20 (c)). As such, an artificial reference sweep excitation signal $U_{exc,HH2}(t)$ is used starting at f_{start} = 20 kHz and ending at f_{end} = 250 kHz with constant unity amplitude:

$$U_{exc,HH2}(t) = \cos\left(2\pi t\left(f_{start} + \frac{f_{end} - f_{start}}{t_{meas}}t\right)\right)$$

The toneburst response corresponding to the out-of-plane HH_2 component is then found as:

$$\tilde{V}_{Z,HH2,f_c}(x,y,f) = \frac{\tilde{U}_{f_c}(f)}{\tilde{U}_{exc,HH2}(f)} \cdot \tilde{V}_{Z,HH2}(x,y,f)$$

$$\text{and } \tilde{V}_{Z,HH2,f_c}(x,y,f) \xrightarrow{\text{IFFT}} V_{Z,HH2,f_c}(x,y,t)$$

2.5.4. Results

The out-of-plane sweep velocity response measured by the SLDV is converted to a toneburst response with center frequency f_c = 50 kHz. Two snapshots are shown in Figure 10.21 (a,b). The snapshots reveal the wavefront of the A_0 guided waves that interacts with the BVID (see insets). The extracted HH_2 signal is converted to a toneburst signal with center frequency f_c = 2 x 50 kHz = 100 kHz. This HH_2 toneburst signal is the second higher harmonic component triggered by the former out-of-plane toneburst velocity response with f_c = 50 kHz. The snapshots of this HH_2 toneburst are shown in Figure 10.21 (c,d).

At t = 2186 µs, the A_0 wave excited by the actuator reaches the BVID (see Figure 10.21 (a)). At this moment, HH_2 vibrational components are generated at the BVID (see Figure 10.21 (c)). At the later time instance t = 2246 µs, the excited wavefront completely overlaps with the BVID (see Figure 10.21 (b)), resulting in a further increase in HH_2 vibrations formed at the BVID (see Figure 10.21 (d)). This observation proves once more that nonlinear components are created at clapping/rubbing defects. The HH_2 vibrations at the damage spread to the damage-free material as revealed in Figure 10.21 (d). In addition, some HH_2 vibrations radiate away from the excitation position. These vibrations are attributed to source nonlinearity. The origin of the source nonlinearity is difficult to predict. It can be attributed to amplifier nonlinearity, a nonlinearity response of piezoelectric material and/or a potential bonding defect between the actuator and the test specimen. Note the relatively low amplitudes of the nonlinear components which necessitated the use of retroreflective tape.

The observation that nonlinear components are present at the location of the damage is exploited in Chapter 12 for construction of damage maps based on nonlinear vibrational energy mapping. In addition, the observation that the nonlinear defect response radiates away from the damage allows for out-of-sight damage detection (see Chapter 14).

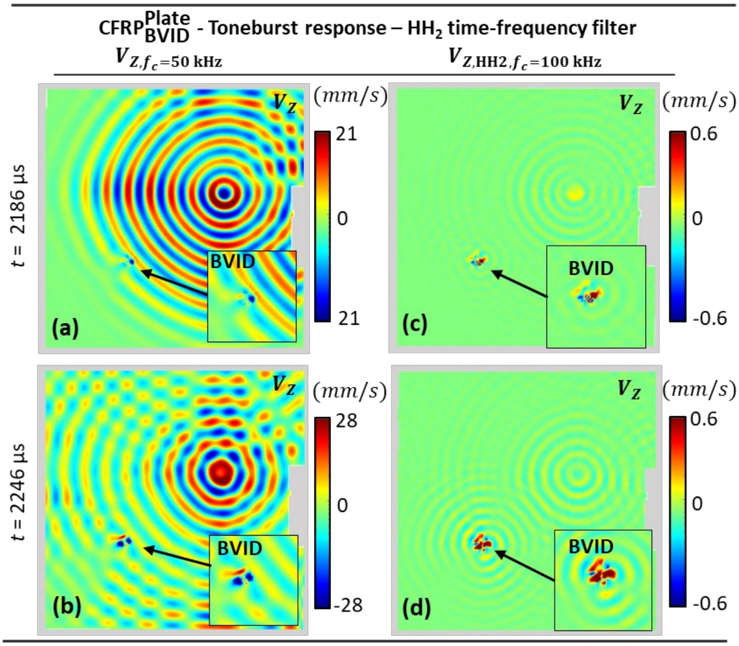

Figure 10.21: Snapshots at t = 2186 µs and at t = 2246 µs of the toneburst response for the out-of-plane velocity in $CFRP^{Plate}_{BVID}$: (a,b) Unfiltered velocity response and (c,d) Extracted second higher harmonic response.

3. Wavefield Manipulation in Complex Aircraft Panel

3.1. Material and Method

In order to demonstrate the introduced wavefield manipulation methods on a more challenging inspection case, the methods are applied on the measurement results of a CFRP aircraft panel. The panel is part of the vertical stabilizer of an Airbus A320 aircraft and it is shown in Figure 10.22. On the backside, stiffeners are visible which are bonded to a base plate. The layup and material properties are unknown. The component suffered impacts at three locations with a 7.7 kg weight from a height of 20 cm, 35 cm and 30 cm. These three impact events resulted in three areas of BVID marked as BVID-A, BVID-B and BVID-C, respectively. Also shown in Figure 10.22 are the time-of-flight (TOF) and relative amplitude images obtained from in-house immersion ultrasonic C-scan inspection of BVID-B using a 5 MHz focused transducer in reflection mode. The C-scan results reveal the complex distribution of delaminations and cracks at this

BVID. Two piezoelectric actuators (Ekulit EPZ-20MS64W) are temporarily bonded to the backside of the CFRP panel with phenyl salicylate.

Two separate SLDV measurements are performed.
For the first measurement, both actuators are supplied with a linear sweep voltage signal with start frequency 5 kHz, end frequency 300 kHz, peak-to-peak amplitude 50 V_{pp} and duration 16 ms. No retroreflective tape was used but 15 averages were taken to increase the signal-to-noise ratio.
The second measurement is tailored for detection of nonlinear vibrational components. The piezoelectric actuators are supplied with a 150 V_{pp} sweep velocity signal with start frequency 10 kHz, end frequency 125 kHz and duration 40 ms. This excitation setup aims at triggering the potential LDR frequencies of the damage in order to obtain the required high vibrational amplitude at the defects. Furthermore, the scan surface is covered in retroreflective tape and three averages were taken to reduce the noise level.
For both experiments, the vibrations are recorded with the SLDV at a grid of scan points with uniform spacing of 3 mm, using a sampling frequency of 625 kS/s.

Similar to the previous section, two snapshots of the out-of-plane velocity component are derived for each wavefield manipulation strategy. As a start, two snapshots of the unfiltered sweep response are shown in Figure 10.23. The observed wavefields are rather chaotic and the interactions of the waves with the areas of BVID are difficult to identify.

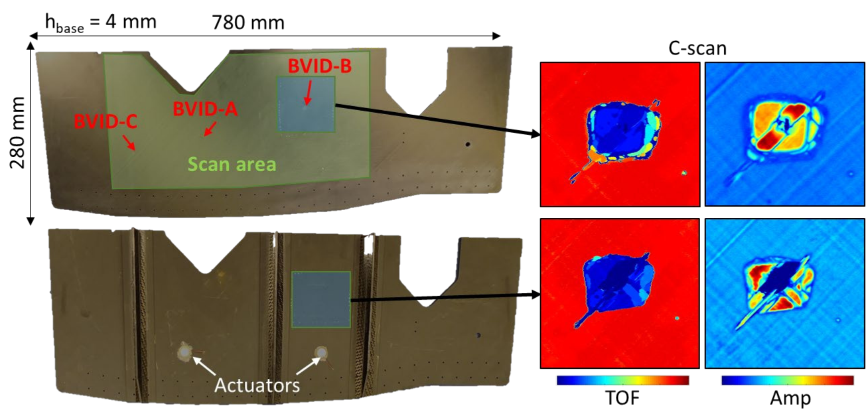

Figure 10.22: Inspected CFRP aircraft panel with three areas of BVID, including ultrasonic C-scan results (Time-Of-Flight and Amplitude) of BVID area B.

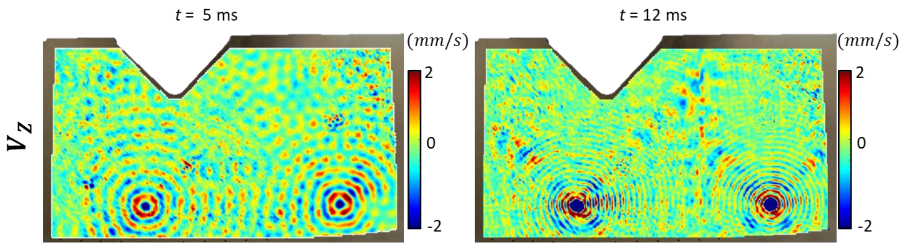

Figure 10.23: Out-of-plane velocity component in a CFRP aircraft panel excited with a broadband sweep signal.

3.2. Wavefield Manipulation Results

All wavefield manipulations strategies introduced in Section 2 are applied to the out-of-plane velocity response. For each specific strategy, two time snapshots of the resulting filtered out-of-plane velocity response are shown in Figure 10.24. The results are in good agreement with the observations made for the simple CFRP plates. A short summary is provided below.

Figure 10.24 (a) shows the snapshots corresponding to a seven-cycle Hanning windowed toneburst response with center frequency f_c = 100 kHz. This toneburst response is obtained from the sweep response using the frequency filtering procedure discussed in Section 2.2. The A_0 wavefront is observed as it travels away from the location of the two piezoelectric actuators. The wavefront interacts with the backside stiffeners and with the BVID's. In the background, large wavelength vibrations, corresponding to the S_0 guided waves, are visible.

The wave-direction filtered toneburst response is shown in Figure 10.24 (b). Only the waves travelling in a downward direction, i.e. $k_y < 0$, are retained. The wave-direction filter works but it does not noticeable facilitate the identification of the defects.

Wavenumber filtering is applied to remove the vibrations in the damage-free material and thereby reveal the defect as areas of high amplitude. The resulting snapshots are shown in Figure 10.24 (c). Indeed, the vibrational amplitude in the damage-free material is low compared to the vibrational amplitude at the three areas of BVID. BVID-B is not visible in the snapshot at t = 868 µs because the A_0 wavefront has not yet reached BVID-B.

The results after applying an A_0 modepass filter are shown in Figure 10.24 (d). The A_0 mode dispersion curve at the location of the BVID is different compared to the A_0 mode dispersion curve at the damage-free material. The latter dispersion curve is used for construction of the A_0 modepass filter. As a result, the amplitude of vibration at the location of the BVID is reduced by the modepass filter.

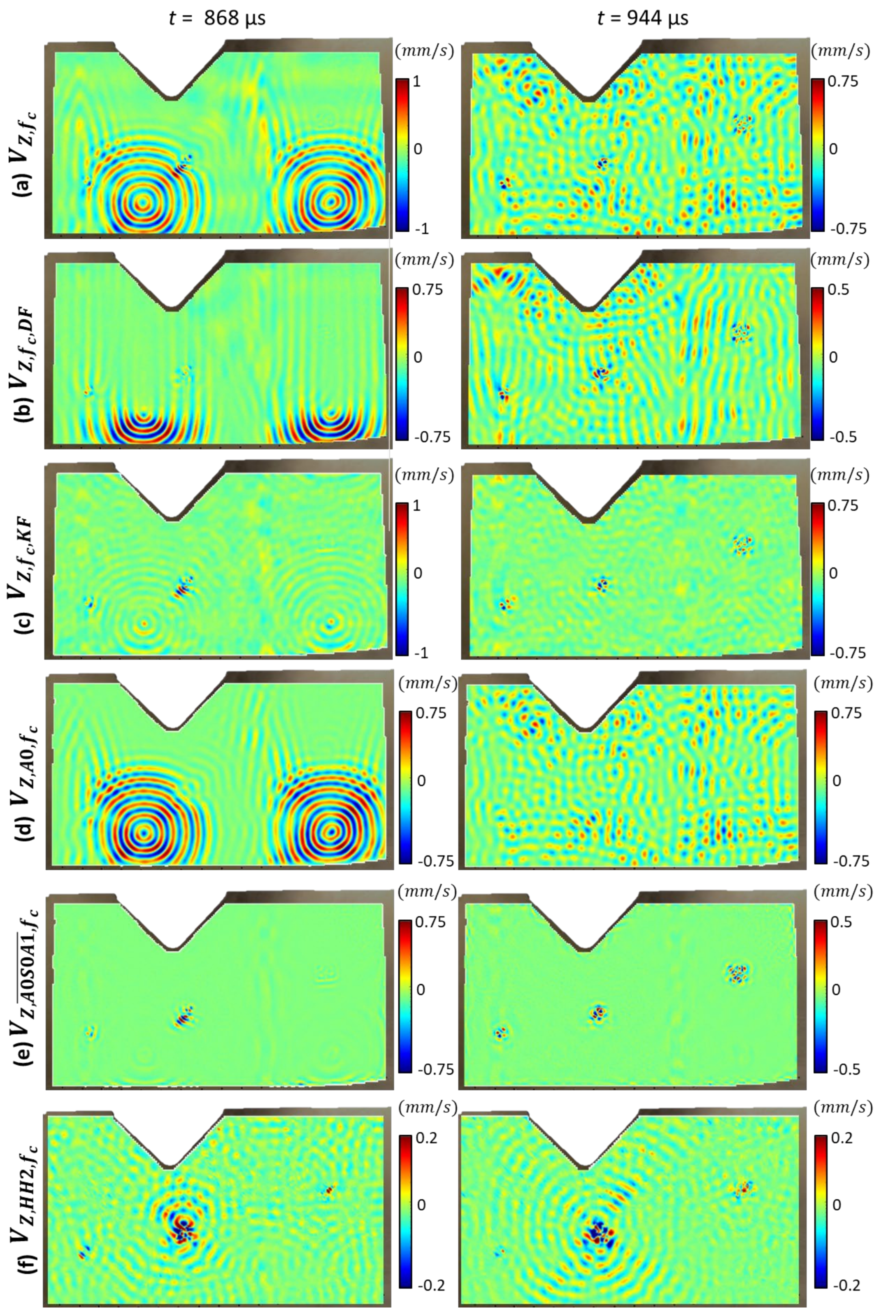

Figure 10.24: Wavefield manipulation for the out-of-plane velocity response in a CFRP aircraft panel (a) Toneburst response with f_c = 100 kHz, (b) Wave-direction filtered toneburst response and (c) Wavenumber filtered toneburst response, (d) A_0 modepassed toneburst response, (e) A_0 and S_0 modestopped toneburst response and (f) HH_2 toneburst response.

The opposite effect is observed in the wavefield obtained after A_0 and S_0 modestop filtering (see Figure 10.24 (e)). In this case, the vibrations are concentrated exclusively at the three locations of BVID. The absence of vibrations at BVID-B for t = 868 μs is again attributed to the A_0 wavefront which has not reached BVID-B yet (see also Figure 10.24 (a) at t = 868 μs).

At last, the second higher harmonic component is extracted and the corresponding toneburst response at f_c = 100 kHz is shown in Figure 10.24 (f). From these snapshots, it is confirmed once more that impact damages behave as secondary vibrational sources of HH components. The radiation of the HH_2 vibrations from the defect to the damage-free component is most pronounced for BVID-A.

4. Conclusion

The wavefield observed in a composite component excited with a broadband sweep excitation is complex and chaotic. The wavefield consists of multiple wave modes in a wide range of frequencies (and wavenumbers), travelling in all directions. Identification of defects in such a complex wavefield is extremely difficult. In order to facilitate the defect identification process, wavefield manipulation algorithms are proposed that allow to reveal specific defect-wave interactions. These wavefield manipulations are explained and illustrated for two academic test specimens, i.e. a CFRP plate with one FBH defect and a cross-ply CFRP plate with one area of BVID. In addition, wavefield manipulation is performed for an industrial CFRP aircraft panel with backside stiffeners and three areas of BVID.

The establishment of this wavefield manipulation framework opens opportunities for the construction of sensitive and robust damage maps. Different damage map construction methods are described and evaluated in the following chapters.

References

1. Segers, J., et al., *Robust and baseline-free full-field defect detection in complex composite parts through weighted broadband energy mapping of mode-removed guided waves.* Mechanical Systems and Signal Processing, 2021. **151**.
2. Segers, J., et al., *Nonlinear Elastic Wave Energy Imaging for the Detection and Localization of In-Sight and Out-of-Sight Defects in Composites.* Applied Sciences, 2020. **10**(3924).

3. Segers, J., et al., *Nonlinear Local Wave-Direction Estimation for In-sight and Out-of-sight Damage Localization in Composite Plates* NDT & E International, 2021. **119**.
4. Segers, J., et al., *Broadband nonlinear elastic wave modulation spectroscopy for damage detection in composites.* Structural Health Monitoring, 2021.
5. Segers, J., et al., *Self-Reference Broadband Local Wavenumber Estimation (SRB-LWE) for defect assessment in composites* Mechanical Systems and Signal Processing, 2021. **163**.
6. Ostachowicz, W., M. Radzieński, and P. Kudela, *50th Anniversary Article: Comparison Studies of Full Wavefield Signal Processing for Crack Detection.* Strain, 2014. **50**(4): p. 275-291.
7. Dawson, A.J., J.E. Michaels, and T.E. Michaels, *Isolation of ultrasonic scattering by wavefield baseline subtraction.* Mechanical Systems and Signal Processing, 2016. **70-71**: p. 891-903.
8. Michaels, J.E., et al., *Chirp excitation of ultrasonic guided waves.* Ultrasonics, 2013. **53**(1): p. 265-70.
9. Michaels, T.E., J.E. Michaels, and M. Ruzzene, *Frequency-wavenumber domain analysis of guided wavefields.* Ultrasonics, 2011. **51**(4): p. 452-66.
10. Ruzzene, M., *Frequency–wavenumber domain filtering for improved damage visualization.* Smart Materials and Structures, 2007. **16**(6): p. 2116-2129.
11. Kudela, P., M. Radzieński, and W. Ostachowicz, *Identification of cracks in thin-walled structures by means of wavenumber filtering.* Mechanical Systems and Signal Processing, 2015. **50-51**: p. 456-466.
12. Wojtczak, E. and M. Rucka, *Wave Frequency Effects on Damage Imaging in Adhesive Joints Using Lamb Waves and RMS.* Materials (Basel, Switzerland), 2019. **12**(11).
13. Radzieński, M., et al., *Application of RMS for damage detection by guided elastic waves.* Journal of Physics: Conference Series, 2011. **305**.
14. Żak, A., et al., *Damage detection strategies based on propagation of guided elastic waves.* Smart Materials and Structures, 2012. **21**(3).
15. Michaels, T.E., M. Ruzzene, and J.E. Michaels, *Frequency-wavenumber domain methods for analysis of incident and scattered guided wave fields*, in *Health Monitoring of Structural and Biological Systems 2009*. 2009.
16. Gyekenyesi, A.L., et al., *Damage visualization enhancement by the wave field filtering and processing*, in *Nondestructive Characterization for Composite Materials, Aerospace Engineering, Civil Infrastructure, and Homeland Security 2012*. 2012.
17. Chang, C.Y. and F.G. Yuan, *Extraction of guided wave dispersion curve in isotropic and anisotropic materials by Matrix Pencil method.* Ultrasonics, 2018. **89**: p. 143-154.
18. Berthaut, J., M.N. Ichchou, and L. Jezequel, *K-space identification of apparent structural behaviour.* Journal of Sound and Vibration, 2005. **280**(3-5): p. 1125-1131.

19. Flynn, E.B., et al., *Structural imaging through local wavenumber estimation of guided waves.* NDT & E International, 2013. **59**: p. 1-10.
20. Segers, J., et al., *Backside delamination detection in composites through local defect resonance induced nonlinear source behaviour.* Journal of Sound and Vibration, 2020. **479**.
21. Jhang, K.-Y., et al., *Measurement of Nonlinear Ultrasonic Characteristics*. Measurement Science and Technology, ed. M.G. Cain, et al. 2020: Springer.
22. Ciampa, F. and M. Meo, *Nonlinear elastic imaging using reciprocal time reversal and third order symmetry analysis.* The Journal of the Acoustical Society of America, 2012. **131**(6): p. 4316-23.
23. Ciampa, F., G. Scarselli, and M. Meo, *Nonlinear Imaging Method Using Second Order Phase Symmetry Analysis and Inverse Filtering.* Journal of Nondestructive Evaluation, 2015. **34**(2).
24. Zhivomirov, H., *On the Development of STFT-analysis and ISTFT-synthesis Routines and their Practical Implementation.* TEM, 2019. **8**(1): p. 56-64.

Chapter 11

Damage Map based on Local Linear Energy Estimation

Summary:

In this chapter, linear energy-based damage maps are constructed. Two methods are investigated for the mapping of the energy in the wavefield: (i) bandpower and (ii) weighed-root-mean-square WRMS energy calculation. The WRMS calculation procedure allows for automated compensation of the wave attenuation.
A broadband modestop filter in the wavenumber-frequency domain is proposed, in order to calculate a mode-removed WRMS energy map of the guided waves. Because this energy map relates exclusively to the abnormalities in the wavefield, it shows high sensitivity to all kinds of internal defects. The proposed damage map construction method does not require any a priori information on the inspected parts or measurement conditions.
The methods are tested on an academic case of a CFRP plate with flat bottom holes and on an industrial case of a large stiffened CFRP aircraft panel with distributed manufacturing defects. It is shown that the broadband mode-removed WRMS energy map is highly sensitive to various kinds of defects, even if they are small and located deep inside the material.

Sections 3.2 and 3.3 are in close correspondence with journal publication:
[1] Segers, J., Hedayatrasa, S., Poelman, G., Van Paepegem, W., Kersemans, M., *Robust and baseline-free full-field defect detection in complex composite parts through weighted broadband energy mapping of mode-removed guided waves.* Mechanical Systems and Signal Processing, 2021. **151**.

1. Introduction

Multiple damage map construction strategies are possible, exploiting one or more of the typical interactions of a guided wave and a defect: wave scattering, wave amplification or attenuation, wave energy trapping, wavenumber shift, nonlinear response, etc. [2, 3]. This chapter focusses on damage maps based on the energy distribution observed in the linear vibrational response of the test specimen.

A popular energy-based damage map construction method is weighted-root-mean-square (WRMS) energy calculation [4-6]. WRMS energy calculation allows to reveal defects as local areas of increased vibrational energy. The increased vibrational energy is associated to the typical reduction in rigidity at the defect's location. Compared to bandpower calculation, the weighting factors used in WRMS allow to compensate for wave attenuation effects. The sensitivity of the WRMS damage map can be improved by exploiting the shift in the local wavenumber at the defects [7-10]. For this, the measured wavefield is first manipulated in the wavenumber domain through a wavenumber filter in order to remove those waves that are characteristic to the damage-free material (see Chapter 10 Section 2.3.2 or [11-14]). The obtained filtered wavefield is then converted in a damage map using WRMS calculation.

The damage map construction techniques listed above use input data in the form of a full wavefield response to a narrowband toneburst excitation centered on a specific frequency. Proper selection of this center frequency is of utmost importance. In terms of the shift in energy, a high WRMS value at the defect is obtained at the local defect resonance (LDR) frequencies. At these frequencies, the wave energy is trapped [15] at the defect resulting in high amplitude standing waves. However, these LDR frequencies are not known a priori and their estimation requires prior knowledge of the material properties and the characteristics of the defect (see Part 2).

In this chapter, an NDT approach is proposed for which the damage map construction algorithm does not require any manual input or prior knowledge of the material properties and the defect parameters. The algorithm uses the concept of WRMS energy calculation combined with both modestop- and frequency filtering. Instead of a narrowband toneburst excitation at a specific center frequency, a broadband sweep excitation is used. The concepts are first introduced using data from a CFRP coupon with flat bottom holes (FBHs) ranging in size and depth.

As a first step, bandpower damage map construction, as introduced in Chapter 7, is reviewed. The problem of wave attenuation captured in the bandpower maps is illustrated.

Next, WRMS maps are constructed for specific toneburst center frequencies. For this, frequency filtering is performed to convert the measured broadband sweep response to multiple narrowband toneburst responses at different center frequencies. The effect of the center frequency on the damage map obtained using WRMS energy calculation is investigated. While the weighting factor used in the calculation of the WRMS damage maps is typically set by the user [8], an automated weighting factor selection method is presented here. It is further illustrated that all individual WRMS maps can be combined in one enhanced broadband damage map.

In the next step, the sensitivity of the proposed broadband WRMS method is further enhanced using modestop filtering. The modestop wavefield manipulation is performed directly on the broadband sweep response in order to remove all guided waves that travel in the damage-free material. This modestop filter leads to an improved damage map compared to the traditional used wavenumber filter. Again, WRMS maps at various center frequencies are constructed and it is shown that the combination of all individual WRMS maps leads to a damage map that reveals all defects, including small and deep defects. In the end, the proposed broadband, mode-removed WRMS method is applied for detection of production defects in a complex CFRP aircraft panel with backside stiffeners.

2. Materials and Measurements

Experiments are performed for two CFRP components with different defects. Figure 10.2 shows the inspection side as well as the backside of both components with indication of the damage.

The first component (see Figure 10.2 (a)) is a square CFRP plate of size 330 x 330 x 5.45 mm^3 and quasi-isotropic material layup $[(45/0/-45/90)_3]_s$. Multiple flat bottom holes (FBHs) are visible from the backside. The diameter d and relative thickness h of each FBH is indicated on the figure. Note that this test specimen was also used in the parametric study towards the LDR behavior of defects, i.e. Chapter 7. The relative thickness h is defined as the ratio of the remaining material thickness at the defect (h_{defect}, as seen from the flat inspection side) over the base material thickness (h_{base}): $h\ (\%) = 100 * \frac{h_{defect}}{h_{base}}$. Thus, the deeper the damage with respect to the inspection side, the higher the h value.

The second component is part of a flap skin manufactured for an Airbus A400M (see Figure 10.2 (b)). The part of the surface marked as ‘scan area’ is inspected for defects. The component was scrapped by the manufacturer after defects were detected using their ultrasonic C-scan inspection (not shown). These defects originated from the curing process. The area containing the defects is marked on the component. At the location of the defects, the skin thickness is 2.55 mm and the defects are estimated to be at a depth of 1.68 mm relative to the inspection side (i.e. h = 1.68/2.55 = 66 %). Flash thermographic inspection is performed by using a 6 kJ Hensel linear flash lamp. The surface temperature regime was recorded with a FLIR A6750sc infrared camera after which the recorded signals were decomposed into their harmonic components using pulsed phase thermography [16]. The phase of the thermal wave at 0.07 Hz was analyzed and revealed a complex cluster of multiple small defects (see indication on Figure 10.2 (b)). The flash thermography results also clearly provide a view of the backside stiffeners (as horizontal black lines).

Vibrations are excited using a piezoelectric actuator (Ekulit EPZ-20MS64W) that is temporarily bonded to the surface with phenyl salicylate (see Figure 10.2). The actuator is supplied with a broadband linear sweep signal from 5 kHz to 300 kHz. The excitation voltage signal is amplified to 50 V_{pp} by the Falco System WMA-300 voltage amplifier to increase the input vibrational energy.

The SLDV (Polytec PSV-500 3D Xtra) is used to record the velocity response at the inspection surface. In this chapter, only the out-of-plane component is used because the energy trapping is most pronounced for the A_0 mode which has a dominant out-of-plane surface displacement. The vibrations are measured for a grid of scan points with a uniform grid point distance of 2.5 mm, resulting in a total number of scan point of 13 624 and 17 627 for the flat coupon and for the stiffened aircraft panel, respectively. For each of the scan points, 10 000 time samples are recorded at 625 kS/s, resulting in a sweep length of 16 ms. No retroreflective tapes were used, however, 15 averages were taken in order to improve the signal-to-noise ratio. The SLDV scan duration was 56 min and 70 min for the flat coupon and for the stiffened aircraft panel, respectively, with a resulting data file size of around 2.2 GB and 2.7 GB. Future research will focus on methods to drastically decrease the measurement time (see Chapter 16).

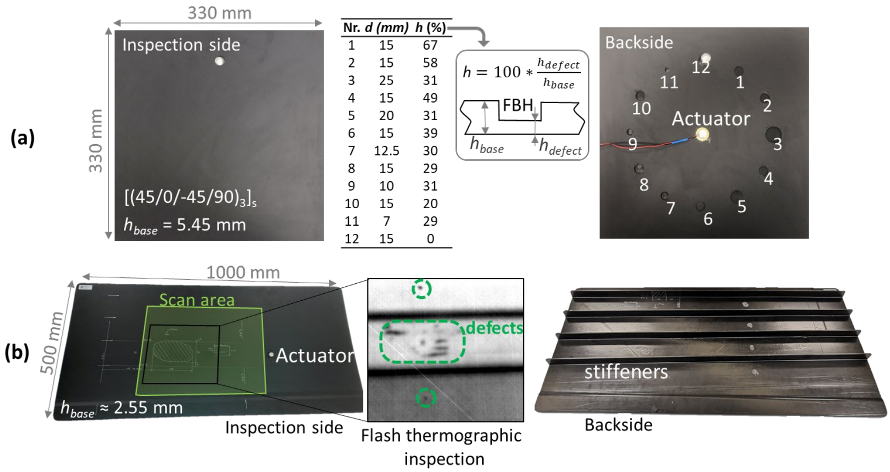

Figure 11.1: Inspected CFRP components. (a) Flat quasi-isotropic coupon with multiple flat bottom holes. (b) Stiffened aircraft panel with production defects.

3. Energy Mapping Approaches

The bandpower calculation method, which was already introduced in Chapter 7 Section 6, is reviewed first. Next (in Section 3.2), it is shown how the broadband sweep response allows constructing multiple WRMS maps at different center frequencies. The effect of the selected center frequency is investigated. Section 3.3 handles the construction of a broadband WRMS map. In Section 3.4, it is shown how the use a modestop filter, prior to the calculation of the WRMS maps, significantly increases the damage detectability. A comparison between the modestop filter and the wavenumber filter is included.

3.1. Bandpower Calculation

Bandpower calculation offers a fast and efficient means for construction of energy-based damage maps. The concept of bandpower was already outlined in Chapter 7 Section 6. A brief recapitalization is provided here. The bandpower gives the vibrational energy at every point with location (x, y) related to the out-of-plane velocity component $\tilde{V}_Z$ (i.e. FFT transform of V_Z) for a frequency band from f_1 up to f_2 (with $f_1 < f_2$):

$$BP_Z(x, y, f_1, f_2) = \frac{\Delta f}{f_2 - f_1} \sum_{f=f_1}^{f_2} \left(\frac{|\tilde{V}_Z(x, y, f)|}{|\tilde{U}_{Excitation}(f)\,|} \right)^2$$

$\tilde{U}_{Excitation}(f)$ represents the voltage amplitude of the excitation signal supplied to the piezoelectric actuator at the specified frequency f. The frequency limits f_1, f_2 must lie within the sweep excitation's bandwidth (i.e. 5 to 300 kHz) and Δf is the frequency axis' resolution.

As an example, Figure 11.2 (a) and (b) show the BP_Z map with f_1 = 5 kHz and f_2 = 200 kHz for the CFRP plate with FBHs and for the aircraft panel, respectively. An increase in the BP_Z intensity is observed at most FBH defects. However, the BP_Z is also elevated around the excitation location which obscures the effect of the defects. The elevated BP_Z at the actuator is attributed to the attenuation of the elastic waves due to geometric wave spreading ($\sim 1/\sqrt{r}$) and wave damping. The bandpower map corresponding to the aircraft panel (Figure 11.2 (b)) shows that the excited waves are partially trapped in between the two horizontal stiffeners. The map shows no indication of damage. This could have been expected as the damage is located relatively deep inside the specimen ($h \approx 66$ %). Application of a modestop filter is required to improve the sensitivity of the damage maps (see Section 3.4).

In Chapter 7, it was illustrated that frequency-dependent weighting windows can be used to compensate for the effect of wave attenuation. However, a major drawback of weighted bandpower calculation is that the weighting method assumes that the waves are attenuated in an equal manner in all directions starting at the actuator's location. This is only the case for (quasi-)isotropic materials of uniform thickness and infinite spatial dimensions (or with fully damped edges). As a result, weighted bandpower calculation cannot be used for robust damage detection in most composite components such as the aircraft panel considered here. WRMS energy calculation is proposed as an alternative for construction of attenuation-compensated energy-based damage maps.

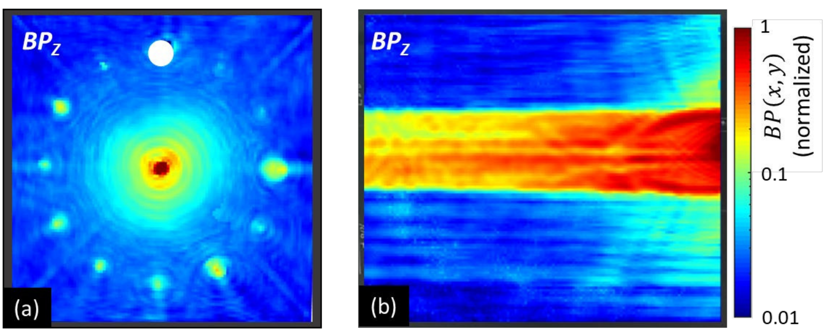

Figure 11.2: Bandpower damage maps with f_1 = 5 kHz, f_2 = 200 kHz for (a) Quasi-isotropic CFRP plate with FBHs and (b) CFRP aircraft panel with production defects.

3.2. Weighted-Root-Mean-Square WRMS Energy

WRMS energy calculation was proposed earlier by Radzieński et al. [5, 6]. The energy of a propagating wave is calculated at each position of the specimen as:

$$WRMS_{f_c}(\mathrm{x}, \mathrm{y}, \mathrm{WF}) = \sqrt{\frac{1}{n} \sum_{i=n_a}^{n_b} V_{z,f_c}(x, y, t_i)^2 \, . \, (i - n_a + 1)^{WF}} \qquad (11.1)$$

where $V_{z,f_c}(x, y, t_i)$ is the out-of-plane velocity at location (x,y) and time t_i for a propagating wave corresponding to a toneburst excitation with center frequency f_c. The time span of interest starts at t_{n_a} and ends at t_{n_b}. The term $(i - n_a + 1)^{WF}$ with weighting factor $WF \geq 0$ is added to give more weight to frames corresponding to later time instances. This compensates for the wave attenuation caused by both geometrical spreading ($\sim 1/\sqrt{r}$) and viscoelastic damping of the propagating waves.

It is important to emphasize that the required wavefield data $V_{z,f_c}(x, y, t_i)$ must correspond to a propagating wave excited using a narrowband toneburst excitation (e.g. a five-cycle Hanning windowed sine signal) with center frequency f_c. When the propagating wave hits the defect, one or more of the following interactions could happen: wave trapping, wave scattering, wave amplification and wave attenuation [13, 15, 17]. These defect-wave interactions must result in a change in the local vibrational energy to make the defect visible in the $WRMS_{f_c}$ damage map. However, which of these defect-wave interactions will happen, and to what extent, depends on (i) the characteristics of the incident guided wave (frequency), (ii) the properties of the material (dispersion characteristics) and (iii) the properties of the defect (depth, size, magnitude of stiffness reduction, contact conditions, etc.).

3.2.1. Calculation of V_{z,f_c} using Frequency Filtering

The transfer function method proposed by Michaels et al. [18] is used to convert the broadband sweep response V_z to the desired narrowband toneburst responses V_{z,f_c} (see Chapter 10 Section 2.2):

$$V_z(x, y, t) \xrightarrow{Freq.Filt.f_c} V_{z,f_c}(x, y, t)$$

In this chapter, a five-cycle Hanning windowed sine signal is chosen for the virtual toneburst excitation.

In the calculation of the $WRMS_{f_c}$ map using Eq. (11.1), it is important to limit the timespan of interest to the period where the toneburst response is of significant amplitude. As proposed by Radzienski et al. [10], the start and end times for WRMS calculation (t_{n_a}, t_{n_b}) are defined using the energy curve:

$$E_{f_c}(t_i) = \sum_x \sum_y V_{z,f_c}(x, y, t_i)^2 \qquad (11.2)$$

which represents the energy in the observed wavefield in function of the sampling time t. The energy curve is normalized as $E_{f_c}(t_i)/E_{f_c}^{max}$ with $E_{f_c}^{max} = \max\left[E_{f_c}(t_i)\right]$. As an example, Figure 11.3 shows the normalized energy curve for the toneburst with f_c = 90 kHz in the CFRP plate with FBHs. Time instance t_{n_a} is found as the moment where the energy is maximal and time instance t_{n_b} equals the time upon which the energy is dropped to a specified percentage. Here, the threshold is set at 1 % (see inset in Figure 11.3).

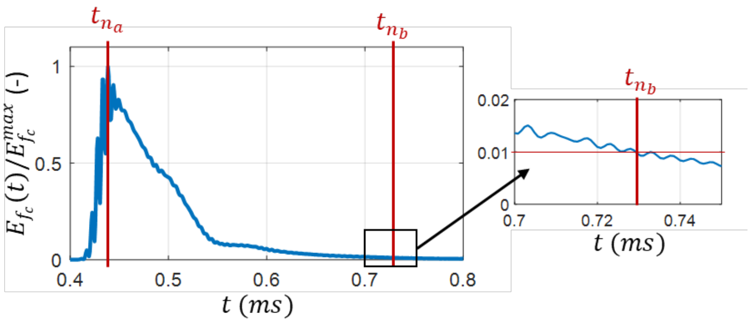

Figure 11.3: Identification of start and end times of interest using the normalized energy curve.

3.2.2. WRMS Energy Results

As an example, the sine sweep response of both test specimens is converted into a five-cycle Hanning windowed toneburst response with center frequency f_c = 100 kHz. The resulting $WRMS_{f_c=100kHz}$ map, calculated using weighting factor WF = 2, are shown in Figure 11.4. An increase in vibrational energy is observed at most FBH defects in Figure 11.4 (a). The $WRMS_{f_c=100kHz}$ map of the aircraft panel (Figure 11.4 (b)) provides no information on potential damage.

In this case, the values for f_c and WF were manually selected. In the next section, the influence of both parameters is further investigated and an automated procedure is proposed for identification of the optimal WF.

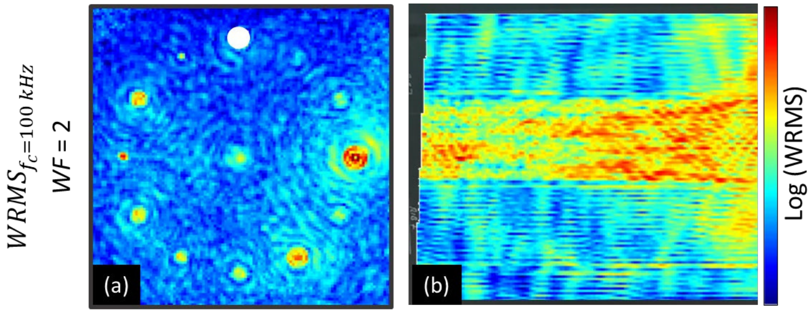

Figure 11.4: $WRMS_{f_c=100kHz}$ maps calculated with WF = 2 for (a) Quasi-isotropic CFRP plate with FBHs and (b) CFRP aircraft panel with production defects.

3.3. Broadband Weighted-Root-Mean-Square WRMS$_b$ Energy

From a NDT point of view, all material and defect properties are a priori unknown. As such, it is difficult to make a substantiated selection of the proper toneburst center frequency f_c and weighting factor WF, which thus limits the effectiveness of the WRMS approach. To cope with this, the present study proposes the use of a broadband sine sweep response to calculate the $WRMS_{f_c}$ maps for a multitude of toneburst responses with varying center frequencies. For each toneburst, the optimal weighting factor is automatically identified. All individual WRMS maps are then fused into one single damage map. This procedure requires the use of appropriate frequency filtering and automated weighting factor selection. The effect of the center frequency f_c on the obtained $WRMS_{f_c}$ map is analyzed.

3.3.1. Automated Weighting Factor Selection

A good weighting factor WF should compensate the decrease in wave amplitude over time and should result in a nearly uniform $WRMS_{f_c}$ value over the damage-free region. The value for the optimal WF depends on the material properties, the geometry of the specimen and the toneburst center frequency f_c. Typical values of WF range between 1 and 4, and are often selected manually [6]. If the dispersion relations are known (i.e. group velocity in function of frequency and in function of ply orientation), it is possible to use the energy-based root-mean-square index as proposed in Ref. [9]. Recently, an alternative method for compensation of wave attenuation in toneburst responses was proposed by Radzienski et al. [10]. The method is based on the energy curve (see Eq. (11.2)) and the equation for $WRMS_{f_c}$ calculation (i.e. Eq. (11.1)) is adapted to:

$$WRMS_{f_c}(\mathrm{x},\mathrm{y}) = \sqrt{\frac{1}{n}\sum_{i=n_a}^{n_b}\left(V_{z,f_c}(x,y,t_i)^2\ \frac{\max\limits_{i} E_{f_c}(t_i)}{E_{f_c}(t_i)}\right)} \tag{11.3}$$

Here, an alternative method is proposed to determine a suited WF in an automated manner. This allows to efficiently calculate the $WRMS_{f_c}$ maps for different f_c*'s*. The weighting factor suited for the $WRMS_{f_c}$ map (see Eq. (11.1)) is found as:

$$WF_{f_c}^{suited} = \underset{WF=0\ldots6}{\operatorname{argmin}}\left[\underset{(x,y)^*}{\operatorname{std}}\left(\frac{WRMS_{f_c}(x,y,WF) - \min\limits_{(x,y)^*} WRMS_{f_c}(x,y,WF)}{\max\limits_{(x,y)^*} WRMS_{f_c}(x,y,WF) - \min\limits_{(x,y)^*} WRMS_{f_c}(x,y,WF)}\right)\right]$$

First, the $WRMS_{f_c}$ map is calculated 25 times, corresponding to a WF ranging from 0 to 6 (in steps of 0.25). Next, each of these 25 maps is normalized and the uniformity of the map is estimated by calculation of the standard deviation (std) over the whole map, excluding outliers $(x,y)^*$. The outliers are defined as points with a WRMS value bigger (or smaller) than the average WRMS value plus, or minus, three times the std. These outliers are excluded as they are typically related to bad measurement points or defects. As a result, the whole map, excluding the outliers, is representative for the sound area. Finally, the WF that results in the minimal std (i.e. highest energy uniformity) is selected to be the optimal one for that f_c, i.e. $WF_{f_c}^{suited}$.

As an example, Figure 11.5 shows the std in function of the WF for the case of a toneburst with f_c = 90 kHz in the CFRP plate with FBHs. It took around 25 s to determine the optimal WF, $WF_{f_c=90kHz}^{suited}$ = 2.75, using the proposed approach. The figure illustrates the importance of selecting a suited WF that indeed corresponds to the best uniformity of the WRMS energy in the damage-free material.

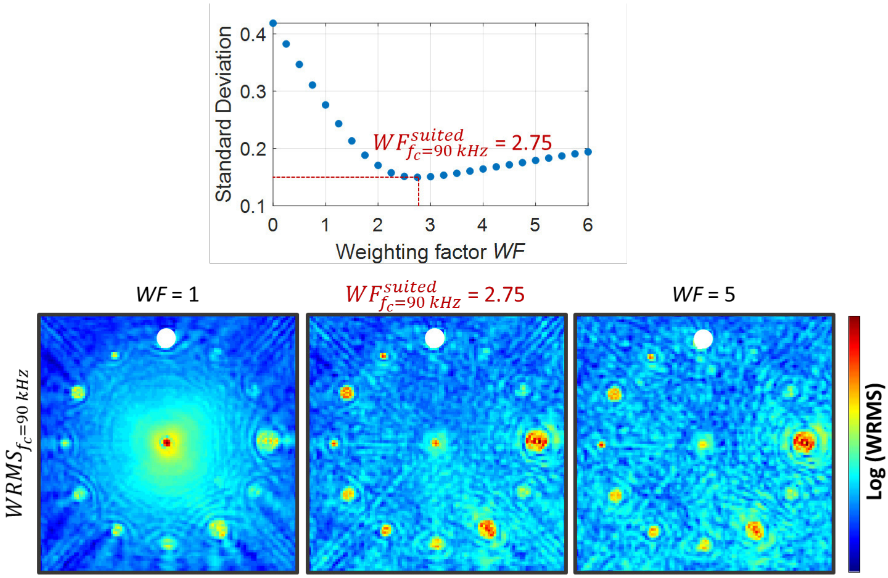

Figure 11.5: Selection of suited weighting factor ($WF^{suited}_{f_c}$) using analysis of the standard deviation illustrated for the $WRMS_{f_c=90kHz}$ damage map corresponding to the quasi-isotropic CFRP plate with FBHs.

3.3.2. Effect of Toneburst Center Frequency

The $WRMS_{f_c}$ damage maps are calculated for a propagating wave corresponding to a five-cycle Hanning-windowed toneburst excitation with center frequency f_c ranging from 30 kHz to 210 kHz in steps of 20 kHz. A selection of these $WRMS_{f_c}$ maps is shown in Figure 11.6. A logarithmically scaled colorbar is used to improve the readability of the damage maps. Note that the suited *WF* increases with the center frequency, which could have been expected as the viscoelastic damping is proportional to the frequency [4].

The results for the quasi-isotropic CFRP plate with FBHs are shown in the top row of Figure 11.6. At low center frequencies (e.g. f_c = 30 kHz), only the relatively large and shallow FBHs show an increased $WRMS_{f_c}$ value while the small and deep FBHs are not detected. This increased $WRMS_{f_c}$ value for large and shallow defects is attributed to the efficient wave trapping [15, 17], resulting in out-of-plane LDR [19], at these defects. Better sensitivity to deeper and smaller defects is obtained for center frequencies around 100 kHz. In this case, impressions of all FBHs are present although the two deepest defects are hardly distinguishable from the background. In case of f_c ≥ 150 kHz, the damping becomes excessive [4], resulting in a decreased defect sensitivity.
The $WRMS_{f_c}$ maps corresponding to the aircraft panel (Figure 11.6 (e-h)) show that the excited waves are partially trapped in between the two horizontal

stiffeners, especially at low frequencies. The maps show no indication of the production defects because the defects are located relatively deep inside the specimen ($h \approx 66$ %). Modestop filtering is required to improve the contrast at these deep defects (see Section 3.4).

From Figure 11.6 (a-d) it is clear that the proper selection of the toneburst center frequency f_c is of utmost importance, but even more important, it is evidenced that this optimal f_c is defect specific. For the smallest FBH (diameter 7 mm, relative thickness h of 29 %), Figure 11.7 shows the contrast at the defect in terms of the defect-to-background ratio DBR. The DBR is defined as the average $WRMS_{f_c}$ value at the FBH (i.e. Ω_{defect} with n_{defect} measurement points) divided by the average value at the surrounding material (circular area of diameter 50 mm around the defect with $n_{healthy}$ measurement points):

$$DBR(f_c) = \frac{n_{healthy}}{n_{defect}} \frac{\sum_{(x_i,y_i)\in\Omega_{defect}} \left|WRMS_{f_c}(x_i, y_{i,}, WF^{suited})\right|}{\sum_{(x_i,y_i)\notin\Omega_{defect}} \left|WRMS_{f_c}(x_i, y_{i,}, WF^{suited})\right|}$$

This DBR is calculated for each center frequency f_c. The results further illustrate that the defect can only be detected if a suited toneburst center frequency is used. As such, performing one single toneburst experiment resulting in one $WRMS_{f_c}$ damage map is insufficient to be used as an accurate NDT technique.

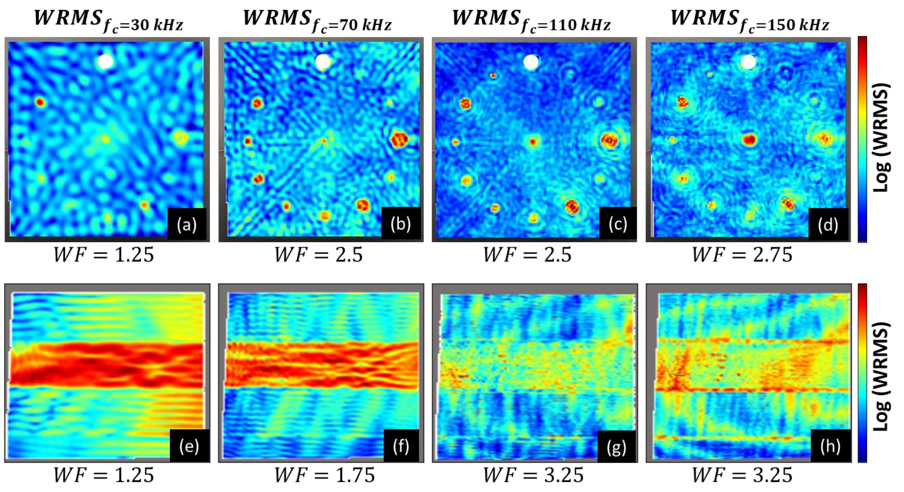

Figure 11.6: $WRMS_{f_c}$ maps calculated for the out-of-plane velocity response to a toneburst excitation centered at f_c = 30, 70, 110 and 150 kHz for (a-d) CFRP plate with FBHs and (e-h) CFRP aircraft panel with production defects.

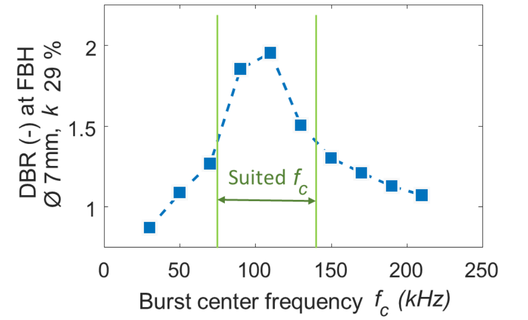

Figure 11.7: Defect-to-background ratio (DBR) in the $WRMS_{f_c}$ map at the FBH of diameter 7 mm with relative thickness 29 % in function of the toneburst center frequency.

3.3.3. Broadband Damage Map

In order to obtain one single damage map that shows good contrast at all defects, all calculated $WRMS_{f_c}$ maps are scaled by their mean value and summed:

$$WRMS_b(x,y) = \sum_{f_c} \frac{WRMS_{f_c}(x,y,WF^{suited})}{\underset{(x,y)}{\text{mean}}\, WRMS_{f_c}(x,y,WF^{suited})} \quad (11.4)$$

$$\text{with } f_c = 30, 50, \ldots, 210\ kHz$$

The resulting broadband $WRMS_b$ damage map is shown in Figure 11.8 (a) and (b) for the CFRP plate with FBHs and for the aircraft panel with production defects, respectively. Note that this figure is obtained without the need of user input. Looking back at the results of bandpower calculation (Figure 11.2), it is clear that the effect of wave attenuation is successfully removed from the damage maps thanks to the optimized weighting factors. The contrast between the defects and the sound material is good for all shallow FBH defects (h < 50 %). However, the contrast at the deep FBHs (h > 50%), and at the production defects in the aircraft panel (h ≈ 66 %), is too low for accurate localization of these defects.

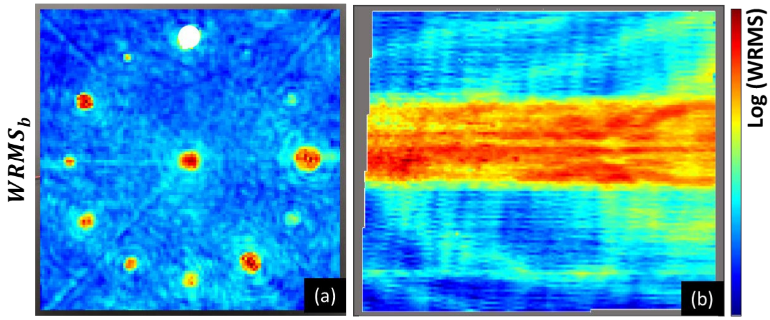

Figure 11.8: Broadband weighted root mean square ($WRMS_b$) damage map for (a) CFRP plate with FBH and (b) CFRP aircraft panel.

3.4. Mode-Removed (Broadband) Weighted-Root-Mean-Square Energy

In order to improve the sensitivity to deep defects, the out-of-plane velocity signal $V_z(x, y, t)$ is modestop filtered prior to the frequency filtering and to the calculation of the $\mathrm{WRMS_b}$ damage map. The modestop filtering procedure aims at removing all vibrations that are characteristic to the damage-free material. As a result, only the vibrations that are related to the presence of damage (or anomalies) should remain.

A detailed explanation of the modestop filtering method was provided in Chapter 10 Section 2.4.3. The vibrations that comply with the dispersion curves of the A_0, S_0 and A_1 modes are removed using a frequency-dependent bandstop filter in the wavenumber-frequency domain. For the CFRP plate with FBHs, the wavenumber-frequency map (along $k_y = 0$), with indication of the dispersion curves, is shown in Figure 11.9 (a). The wavenumber-frequency map (along $k_y = 0$) after application of the modestop filter is shown in Figure 11.9 (b).

This idea of removing the vibrations characteristic to damage-free material is similar to the wavenumber filtering procedure often used prior to WRMS calculation [7-10]. However, the here proposed implementation of modestop filtering is different. Both filtering approaches are graphically illustrated in Figure 11.10 (a,c). The figure shows the dispersion curves (A_0, S_0 and A_1 mode) of the base material of the CFRP plate with FBHs. At the A_0 mode, the wavenumber filter and the modestop filter are shown for the case of a toneburst excitation signal with f_c = 110 kHz in Figure 11.10 (a) and Figure 11.10 (c), respectively.

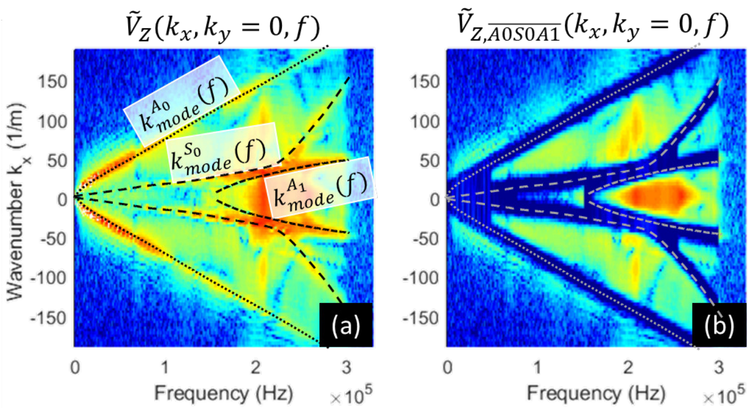

Figure 11.9: Out-of-plane velocity as seen in the wavenumber-frequency (k_x,k_y,f) domain for the CFRP plate with FBHs. (a) Out-of-plane velocity $\tilde{V}_Z$ along $k_y = 0$. (b) Mode-removed out-of-plane velocity $\tilde{V}_{Z,\overline{A0S0A1}}$ along $k_y = 0$.

In the case of wavenumber filtering (see Figure 11.10 (a) and Chapter 10 Section 2.3.2), the filter is applied in the wavenumber domain resulting in the bandstop window being independent of the frequency. Wavenumber filtering has the advantage that it automatically takes strong anisotropy (if present) into account. On the downside, the frequency-independent wavenumber filter removes part of the vibrations that are related to defects, while it retains part of the vibrations related to the damage-free material (see indication on Figure 11.10 (a)). Note that this becomes even more troublesome when multiple modes could propagate at the considered center frequency.

On the other hand, the modestop filter (see Figure 11.10 (b) and Chapter 10 Section 2.4.3) follows the dispersion curves and efficiently removes the vibrations related to damage-free materials, while it retains all information of the defected wavefield data. As a result, the use of a modestop filter leads to an enhanced defect detectability performance. The enhanced performance is evident when examining the $WRMS^{KF}_{fc=110kHz}$ map constructed using the wavenumber filter KF and the $WRMS^{MF}_{fc=110kHz}$ map constructed using the modestop filter MF (see Figure 11.10 (b) and (d), respectively). The intensity along a line through two defects further reveals the superior contrast achieved when using the modestop filter instead of the wavenumber filter (see Figure 11.10 (e)).

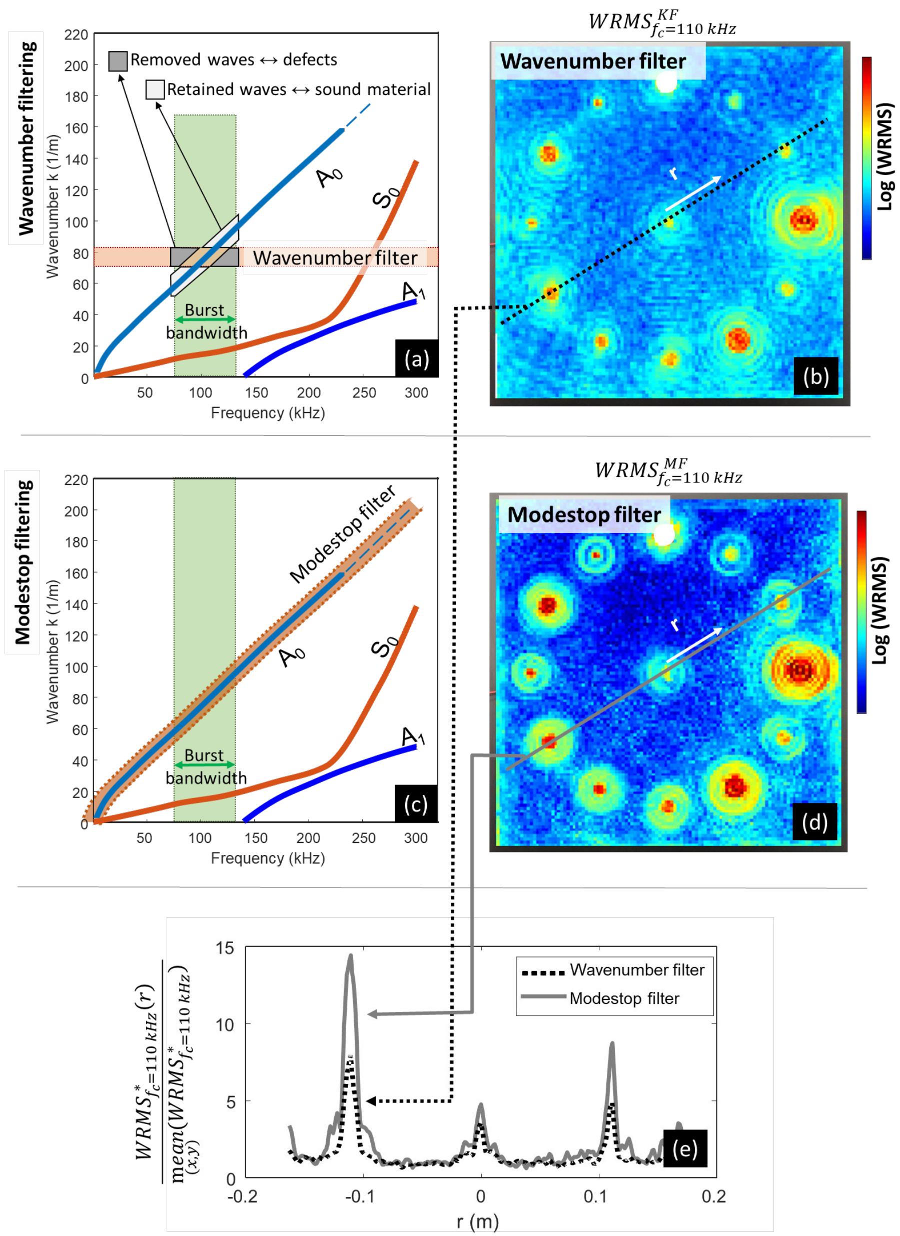

Figure 11.10: Difference between wavenumber filtering and modestop filtering. (a,b) Schematic representation of wavenumber filtering and resulting $WRMS^{KF}_{f_c=110kHz}$ damage map, (c,d) Schematic representation of modestop filtering and resulting $WRMS^{MF}_{f_c=110kHz}$ damage map, (e) $WRMS$ intensity along a line passing through a shallow defect, the actuator and a deep defect.

The mode-removed out-of-plane velocity response $V_{Z,\overline{A0S0A1}}$ is used for the calculation of the mode-removed weighted-root-mean-square damage maps $WRMS_{fc}^{MF}$. The same center frequency specific weighting factors *WFs,* as were used in the calculation of the $WRMS_{f_c}$ maps, are employed for the $WRMS_{fc}^{MF}$ maps.

Figure 11.11 shows a selection of the obtained narrowband $WRMS_{fc}^{MF}$ maps. When comparing these with the $WRMS_{f_c}$ maps shown in Figure 11.6, it is clear that the removal of the guided wave modes, characteristic to the damage-free material, successfully improves the contrast at all defects.

At the FBH defects (see Figure 11.11 (a-d)), the vibrations are not removed by the modestop filter due to the local shift in wavenumber attributed to the changed material thickness [20]. Also, the vibrations at the FBHs might become trapped showing a high amplitude for a long duration [15]. As a result, the FBHs are easily distinguished as zones of high intensity.

The $WRMS_{fc}^{MF}$ maps corresponding to the aircraft panel (Figure 11.11 (e-h)) again reveal the presence of the horizontal stiffeners. At the location of the stiffeners, the total material thickness is different, resulting in locally different dispersion characteristics compared to the base material. As a result, the vibrations at the stiffeners are not affected by the modestop filter, thus leading to the clear imprint of the backside stiffeners in the $WRMS_{fc}^{MF}$ maps. Apart from the increased intensity at the stiffeners, multiple $WRMS_{fc}^{MF}$ maps show additional small areas of increased vibrational intensity in between the two middle stiffeners, which correspond to a cluster of production defects. There is again a large influence of the toneburst center frequency f_c. For instance, the $WRMS_{fc=70\,kHz}^{MR}$ and $WRMS_{fc=110\,kHz}^{MR}$ maps provide a clear indication of the relatively large defects while the small defects are only shown for $f_c \geq 150$ kHz.

Apart from the high intensity at the defects, an increased intensity is visible at (i) the excitation location (i.e. the center of the plate in Figure 11.11 (a-d)), (ii) the edges of the scan area and (iii) the defects' boundaries. This increased intensity is attributed to (converted) guided wave build-up (at the excitation and defect locations), non-propagating modes (at the free edges and defect edges) [21], leakage of the trapped modes from the defects to the surrounding material (at the defect edges) [15] and non-periodicity in spatial dimensions when performing 3D FFT and 3D IFFT (at the scan area edges) [22].

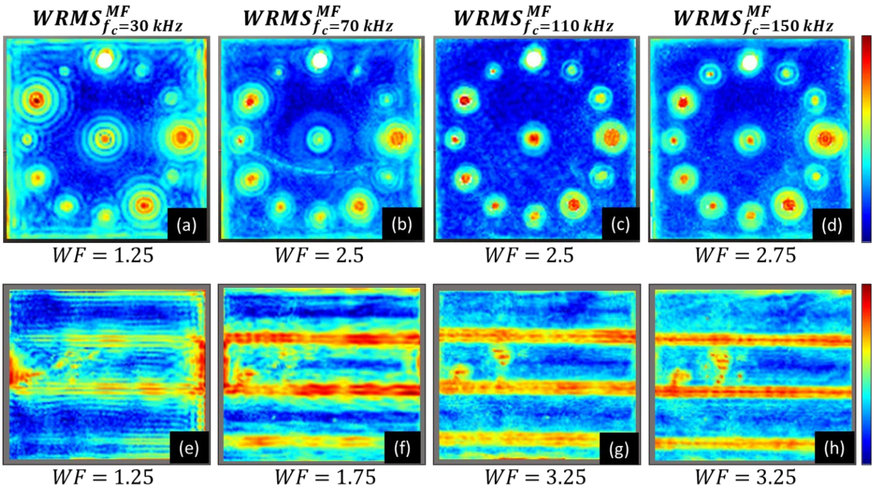

Figure 11.11: $WRMS^{MF}_{f_c}$ maps calculated for the mode-removed out-of-plane velocity response to a toneburst excitation centered at f_c = 30, 70, 110 and 150 kHz for (a-d) CFRP plate with FBHs and (e-h) CFRP aircraft panel with production defects.

The combination of all $WRMS^{MF}_{f_c}$ maps (according to Eq. (11.4)) results in a single broadband, mode-removed damage map $WRMS^{MF}_{\mathrm{b}}$ that successfully reveals all defects with satisfying contrast (see Figure 11.12). Note again that this map was obtained without user input or material property knowledge. For better interpretation of the results, the damage maps are provided in logarithmic colorscale as well as in linear colorscale.

A reference view of the production defect distribution in the aircraft panel, which was obtained through pulsed phase thermographic inspection at 0.07 Hz, is shown in Figure 11.12 (e). The locations of the defects (and the stiffeners) in the $WRMS^{MF}_{\mathrm{b}}$ map closely match with the thermographic inspection results.

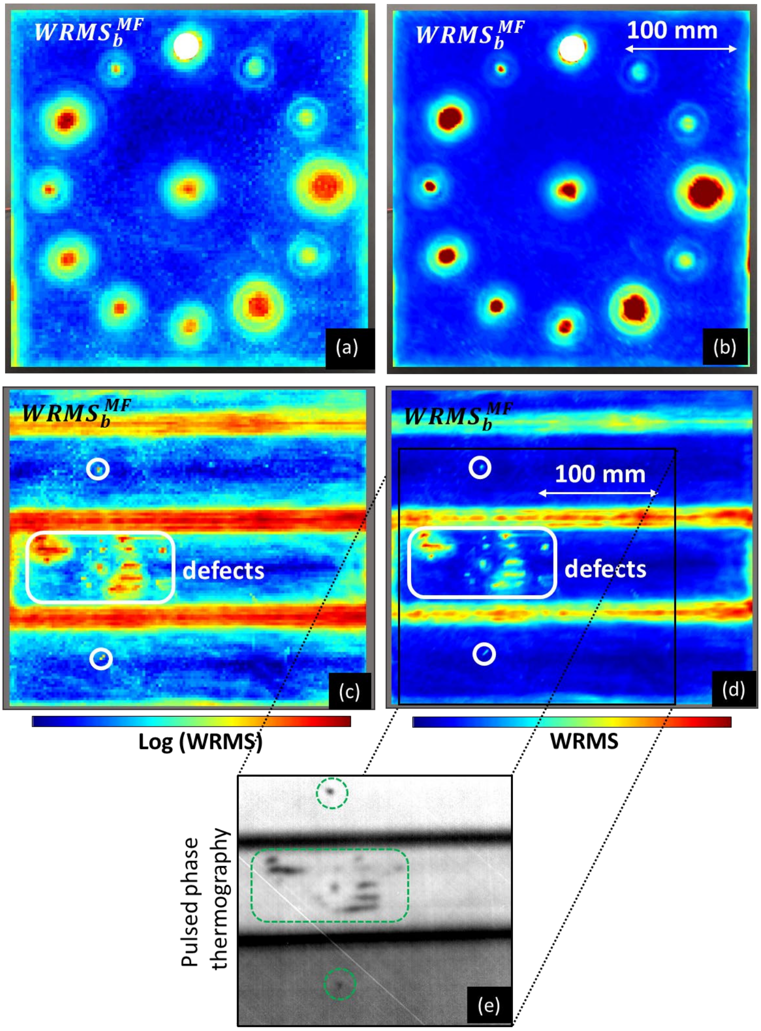

Figure 11.12: Broadband, mode-removed, weighted root mean square ($WRMS_{\mathrm{b}}^{MR}$) damage maps in (a-b) CFRP plate with FBHs and in (c-d) CFRP aircraft panel with production defects. (a,c) logarithmic colorscale and (b,d) linear colorscale. (e) Pulsed phase thermographic inspection phase image at 0.07 Hz.

4. Conclusion

First, well-known energy-based damage map construction techniques, like bandpower and WRMS are reviewed. In the obtained damage maps, defects are visible as local areas of increased intensity due to the typical wave amplification and trapping at the defects. However, it is challenging to pinpoint small and deep defects. Moreover, the methods require the manual selection of suited process parameters, e.g. toneburst center frequency and weighting factor.

Next, a novel method is introduced which decomposes the broadband velocity response into multiple narrowband toneburst responses. An automated and optimal WF selection method is proposed. The WRMS maps (corresponding to the multitude of toneburst responses) are then fused to a broadband WRMS map. To further increase the sensitivity to challenging defects, a modestop filtering procedure is applied to exclude all vibrations characteristic to the sound materials, and to retain only the vibrations at the material's anomalies (incl. defects).

This novel linear energy-based damage map construction method exploits various defect-wave interactions, such as energy trapping (incl. LDR) and local wavenumber (or dispersion) changes. The method does not require any a priori information on the material properties, or defect parameters. The effectiveness of the developed procedure has been demonstrated for a CFRP coupon with FBHs and for a complex stiffened CFRP aircraft panel with real production defects. Defects as small as 25 mm^2 and located deeper than the mid-thickness of the component are readily identified.

References

1. Segers, J., et al., *Robust and baseline-free full-field defect detection in complex composite parts through weighted broadband energy mapping of mode-removed guided waves.* Mechanical Systems and Signal Processing, 2021. **151**.
2. Ostachowicz, W., M. Radzieński, and P. Kudela, *50th Anniversary Article: Comparison Studies of Full Wavefield Signal Processing for Crack Detection.* Strain, 2014. **50**(4): p. 275-291.
3. Dawson, A.J., J.E. Michaels, and T.E. Michaels, *Isolation of ultrasonic scattering by wavefield baseline subtraction.* Mechanical Systems and Signal Processing, 2016. **70-71**: p. 891-903.
4. Wojtczak, E. and M. Rucka, *Wave Frequency Effects on Damage Imaging in Adhesive Joints Using Lamb Waves and RMS.* Materials (Basel, Switzerland), 2019. **12**(11).
5. Radzieński, M., et al., *Application of RMS for damage detection by guided elastic waves.* Journal of Physics: Conference Series, 2011. **305**.
6. Żak, A., et al., *Damage detection strategies based on propagation of guided elastic waves.* Smart Materials and Structures, 2012. **21**(3).
7. Kudela, P., M. Radzienski, and W. Ostachowicz, *Impact induced damage assessment by means of Lamb wave image processing.* Mechanical Systems and Signal Processing, 2018. **102**: p. 23-36.

8. Kudela, P., et al., *Application of scanning laser Doppler vibrometry for delamination detection in composite structures.* Optics and Lasers in Engineering, 2017. **99**: p. 46-57.
9. Kudela, P., M. Radzieński, and W. Ostachowicz, *Identification of cracks in thin-walled structures by means of wavenumber filtering.* Mechanical Systems and Signal Processing, 2015. **50-51**: p. 456-466.
10. Radzienski, M., et al., *Damage Identification in Various Types of Composite Plates Using Guided Waves Excited by a Piezoelectric Transducer and Measured by a Laser Vibrometer.* Sensors (Basel, Switzerland), 2019. **19**(9).
11. Michaels, T.E., M. Ruzzene, and J.E. Michaels, *Frequency-wavenumber domain methods for analysis of incident and scattered guided wave fields*, in *Health Monitoring of Structural and Biological Systems 2009*. 2009.
12. Ruzzene, M., *Frequency–wavenumber domain filtering for improved damage visualization.* Smart Materials and Structures, 2007. **16**(6): p. 2116-2129.
13. Tian, Z., L. Yu, and C. Leckey, *Guided Wave Propagation Study on Laminated Composites by Frequency-Wavenumber Technique*, NASA, Editor. 2014: Langley Research Center.
14. Dafydd, I. and Z. Sharif Khodaei, *Analysis of barely visible impact damage severity with ultrasonic guided Lamb waves.* Structural Health Monitoring, 2019.
15. Glushkov, E., et al., *Wave energy trapping and localization in a plate with a delamination.* Smart Materials and Structures, 2012. **21**(12).
16. Poelman, G., et al., *An Experimental Study on the Defect Detectability of Time- and Frequency-Domain Analyses for Flash Thermography.* Applied Sciences, 2020. **10**(22).
17. Munian, R.K., D.R. Mahapatra, and S. Gopalakrishnan, *Lamb wave interaction with composite delamination.* Composite Structures, 2018. **206**: p. 484-498.
18. Michaels, J.E., et al., *Chirp excitation of ultrasonic guided waves.* Ultrasonics, 2013. **53**(1): p. 265-70.
19. Segers, J., et al., *Probing the limits of full-field linear Local Defect Resonance identification for deep defect detection.* Ultrasonics, 2020. **105**.
20. Flynn, E.B., et al., *Structural imaging through local wavenumber estimation of guided waves.* NDT & E International, 2013. **59**: p. 1-10.
21. Lowe, M.J.S., *Reflection of the fundamental Lamb modes from the ends of plates*, in *AIP Conference Proceedings*. 2001. p. 89-96.
22. Richardson, M.H., *Fundamentals of the Discrete Fourier Transform.* Sound & Vibration Magazine, 1978.

Chapter 12

Damage Map based on Local Nonlinear Energy Estimation

Summary:

A novel damage map construction method is proposed by exploiting the energy present in the nonlinear vibrational components. Vibrations are excited using two low-power piezoelectric actuators. One actuator is supplied with a broadband sine sweep signal and the other is supplied with a single-frequency sine signal. A time-frequency wavefield manipulation method is used to extract specific nonlinear components of interest, i.e. second higher harmonics and first modulation sidebands. Next, energy-based damage maps are constructed using broadband bandpower calculation of the extracted nonlinear components. It is demonstrated that the modulation sidebands provide an exclusive imaging of defect nonlinearity, and are not affected by potential source nonlinearity coming from the actuators.
The proposed damage map construction procedure is applied for various CFRP test specimens with different damage features: (i) Coupon with quasi-static indentation damage, (ii) Coupon with artificial delaminations, (iii) CFRP/Nomex sandwich panel with a disbond between the core and the skin, (iv) Bicycle frame with impact damage and (v) Stiffened aircraft panel with partially disbonded stiffener. The obtained results indicate the high performance of the developed procedure for detection of various defect types, including backside delaminations, in curved and/or stiffened CFRP components.

The chapter is in close correspondence with journal publications:

[1] Segers, J., Hedayatrasa, S., Poelman, G., Van Paepegem, W., Kersemans, M., *Nonlinear Elastic Wave Energy Imaging for the Detection and Localization of In-Sight and Out-of-Sight Defects in Composites.* Applied Sciences, 2020. **10**(3924).
[2] Segers, J., Hedayatrasa, S., Poelman, G., Van Paepegem, W., Kersemans, M., *Broadband nonlinear elastic wave modulation spectroscopy for damage detection in composites.* Structural Health Monitoring, 2021.

1. Introduction

In Chapter 3, the clapping and rubbing of defect interfaces was investigated using phenomenological models. These models predicted that nonlinear vibrational components are formed at a delamination defect when the vibrational amplitude is sufficiently high. The predictions were confirmed in Chapter 8. When a defected test specimen is excited with a sine excitation with frequency equal to a LDR frequency of the defect, higher harmonic vibrational components are observed at the defect (see Chapter 8 Section 3 or [3-10]). The study of the nonlinear vibrational component arising from the excitation using one source is referred to as: Nonlinear Elastic Wave Spectroscopy (NEWS). A second excitation source can be added to further increase the vibrational amplitude at the defect. In this case, modulation sideband (i.e. mixed frequency) components are formed at the defect next to the higher harmonics (see Chapter 8 Section 4 or [11-17]). The study of this frequency modulation is referred to as: Nonlinear elastic Wave Modulation Spectroscopy (NWMS).

These observations are of great interest for NDT as it was observed that the nonlinear components are detected in the case of shallow delaminations, but more important, also in the case of deep (backside) delaminations. Detection of these deep delaminations using linear energy-based damage detection methods is possible but far from straight forward (see Chapter 11).

The NEWS and NWMS methods are promising for NDT but there are still some critical hurdles to be overcome:

- The nonlinear response is only triggered in case of a sufficiently high vibrational amplitude at the defect. When low power actuators are used, this high vibrational amplitude is typically only reached at specific excitation frequencies (e.g. a LDR frequency) [18].
- The nonlinear components of interest have to be extracted out of the measurement dataset. In case of a broadband excitation (e.g. a broadband sine sweep), the FFT cannot be used as the nonlinear components overlap with the linear response in the frequency domain (see Chapter 10 Section 2.5.2). As a work around, narrowband excitations are often used. However, the chance that the unknown LDR frequencies are located within the bandwidth of the applied narrowband excitation becomes small. Alternatively, multiple broadband excitation sequences are used and the corresponding measurements are combined with the aim to cancel out the linear response and to retain only specific nonlinear components. As an example, the modulation sidebands can be extracted by combination of the results of three individual excitation sequences: (i) only sweep

source activated, (ii) only sine source activated and (iii) both sources activated [19] or by combination of the results of two phase shifted excitations (i.e. phase symmetry analysis) [20]. However, the use of multiple excitation sequences increases the measurement time and complexity. In addition, this procedure requires that the employed actuators have a fully reproducible response which is not always the case.

- The excitation sources can introduce nonlinear vibrational components on their own (i.e. source nonlinearity [18]), which may dominate over the nonlinear vibrations created at the defect.

In this chapter, we aim to overcome these remaining hurdles or limitations using well-chosen excitation signals and advanced wavefield manipulation strategies:

- Two excitation sources are used and respectively supplied with a broadband sine sweep voltage signal and a single frequency sine voltage signal. The broadband nature of the excitation makes sure that efficient energy trapping at the defects occurs, e.g. at the LDR frequency. This results in a strong vibrational activity of the defect, and as such, triggers the defect's nonlinear behavior.
- Automated wavefield manipulation in time-frequency domain is applied for the extraction of specific nonlinear components, such as higher harmonics and modulation sidebands, from the single broadband measurement dataset. This time-frequency filtering method was already introduced in Chapter 10 Section 2.5.2.
- The origin of the extracted nonlinear components is investigated with the aim to exclude source nonlinearity, and to retain only defect nonlinearity.
- Broadband bandpower calculation is proposed for robust damage map construction. Compared to previous chapter, no compensation of wave attenuation is required here because the nonlinear components are formed at the damage and not (or in lower extend) at the piezoelectric excitation sources.

The performance of the obtained nonlinear energy-based damage maps is evaluated first for an academic CFRP coupon with quasi-static indentation damage (QSID) and for an academic CFRP coupon with artificial delaminations. Afterwards, the effectiveness of the proposed methods is verified using measurement results of a CFRP-Nomex sandwich panel and of two complex industrial CRFP components, i.e. a bicycle frame down tube with barely visible impact damage (BVID) and a stiffened aircraft panel with a partially disbonded stiffener.

In Section 2, the measurement procedure and the used test specimens are described. Section 3 outlines the proposed damage map construction methodology using the measurement results of the CFRP coupon with QSID. In Section 4, the damage detection capability is investigated the four other CFRP test specimens. At last, the conclusions are summarized.

2. Materials and Measurements

Measurements are performed on five different CFRP test specimens (see Figure 12.1).

The first test specimen ($CFRP_{QSID}^{Coupon}$, see Figure 12.1 (a)) is a 150x100x5.45 mm^3 coupon manufactured out of 24 layers of unidirectional carbon fiber according to a quasi-isotropic stacking sequence $[(45/0/-45/90)_3]_s$. A quasi-static indentation is applied according to ASTM D6264 standard with 2.2 mm indentation displacement. The resulting quasi-static indentation damage (QSID) is highly similar to the damage resulting from low velocity impact, i.e. BVID [21], as shown by the ultrasonic C-scan's time-of-flight (TOF) image. The C-scan is performed in reflection mode using dynamic time gating. A focused transducer at 5 MHz (H5M, General Electric) is employed. The backside of the specimen is inspected for damage (see Figure 12.1 (a)). Two identical piezoelectric actuators (Ekulit EPZ-20MS64W) are bonded to the indented side using epoxy (*Araldite rapid*). One of these actuators is supplied with a linear sine sweep voltage signal from 1 to 200 kHz at 100 V_{pp} whereas the other actuator is supplied with a 100 V_{pp} sine voltage signal. Three separate measurements are performed where the sine frequency is set at 50 kHz, 63 kHz and 70 kHz. This allows to investigate the effect of the sine frequency on the nonlinear response of the defect.

The second component ($CFRP_{Delam}^{Coupon}$, see Figure 12.1 (b)) is a 290x140x2.5 mm^3 CFRP coupon manufactured out of eight layers of unidirectional carbon fiber according to a cross-ply stacking sequence $[(0/90)_2]_s$. Two artificial delaminations were introduced during the layup process using 20×20 mm^2 inserts made out of a double layer of 25 μm thin brass foil sealed with flashbreaker tape. The inserts were placed between the 1st and 2nd layer, and between the 7th and 8th layer, resulting in a shallow (frontside) and a deep (backside) delamination, respectively. The same sample was already used in Chapter 8 for the proof-of-concept of the formation of nonlinear frequency components at a delamination under LDR conditions. Again, two small piezoelectric actuators (Ekulit EPZ-20MS64W) are bonded to the backside, this time using removable phenyl salicylate. One actuator is supplied with a linear sine sweep voltage from 10 to 125 kHz at 100 V_{pp} whereas the other actuator is supplied with a 30 kHz sine voltage at 100 V_{pp}.

The third component ($\mathrm{Sandwich}^{\mathrm{Plate}}_{\mathrm{Disb/BVID}}$, see Figure 12.1 (c)) is a sandwich panel. The panel is symmetric in the thickness direction and manufactured in-house out of the following layers (bought from EasyComposites®): (i) a 1 mm thick pre-cured woven CFRP plate with layup [22 twill/ +-45 biax / 22 twill] (type CFS-RI-1-0056), (ii) a 163 g/m^2 epoxy adhesive film (type XPREG® XA120), (iii) a Nomex® aramid honeycomb core with cell size 4.8 mm and thickness 5 mm (NHC-48-10-039), (iv) an additional layer of epoxy adhesive film and (v) another pre-cured woven CFRP plate. Before the five layers were stacked, vacuum bagged and oven-cured, two artificial defects were introduced: (i) a small area of BVID in the top (frontside) CFRP plate introduced by hammer hitting and (ii) a 30 x 30 mm^2 cutout in the first layer of epoxy adhesive film. The cutout resulted in a disbond between the core and the skin plate after oven-curing. Three piezoelectric actuators are attached to the backside of the plate. Two circular bending discs, type EPZ-27MS44W from Ekulit, are glued to the left bottom corner and are supplied with the sine sweep signal (2.5 to 100 kHz, 150 V_{pp}). One larger rectangular bending actuator, type DuraAct P-876 A15 from PiCeramics, is glued to right bottom corner and supplied with the sine excitation signal (30 kHz, 100 V_{pp}). The wave attenuation is relatively high in this sandwich panel. As a result, the excitation power is increased by using the increased sweep excitation voltage, two larger sweep actuators (instead of one) and the large DuraAct P-876 A15 type actuator for actuation of the sine signal. This last actuator is the one that shows the highest excitation power at this sine frequency (see Chapter 4 Section 2.2).

Next to these three academic test specimens, two industrial CFRP components are inspected. The first one is a CFRP bicycle frame ($\mathrm{CFRP}^{\mathrm{Tube}}_{\mathrm{BVID}}$, see Figure 12.1 (d)). There is no information on the layup or thickness of the tubular CFRP sections. The down tube suffered an impact that introduced BVID. From a previous experiment, three small actuators (Ekulit EPZ-20MS64W) were already bonded to the topside of the down tube using epoxy. The two actuators at the right are supplied with the sine sweep voltage signal (10 to 125 kHz, 100 V_{pp}) whereas the third actuator at the left is used for the sine excitation (30 kHz and 50 kHz, 100 V_{pp}).

The last test specimen is an Airbus A320 vertical fin rib panel ($\mathrm{CFRP}^{\mathrm{Air}}_{\mathrm{Disb}}$, see Figure 12.1 (d)). The component's base plate measures 600x200x1.1 mm^3 and contains three vertical stiffeners at the backside. The material layup is unknown. This component was scrapped by the manufacturer after damage was detected at the middle stiffener. The cause of the damage is unknown. The damage pattern is revealed using an in-house ultrasonic C-scan (reflection mode with dynamic time gating and 5 MHz focused transducer) and consists of a shallow delamination at the left side of the stiffener's fin and a larger disbond between the stiffener and the base plate at the right side of the fin (see inset on figure).

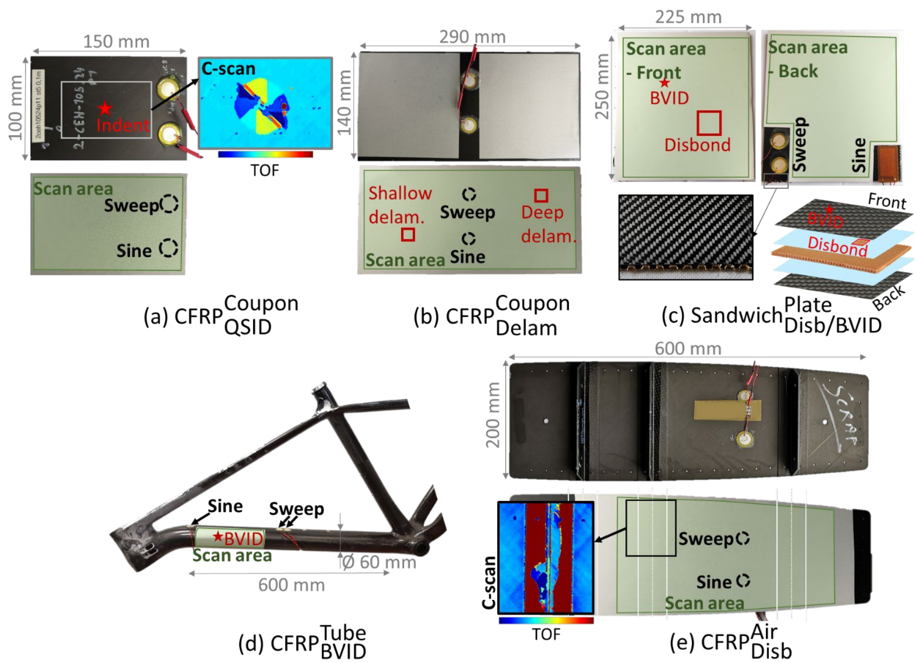

Figure 12.1: CFRP test specimens: (a) Quasi-isotropic coupon with QSID, (b) Cross-ply coupon with shallow and deep artificial delamination, (c) CFRP/Nomex sandwich panel with disbond and BVID, (d) Bicycle frame with impacted down tube, (e) Stiffened aircraft panel with damage at stiffener.

The piezoelectric actuators are temporarily bonded to the backside using phenyl salicylate. The smallest one (Ekulit EPZ-20MS64W) is supplied with the sine sweep voltage signal (10 to 125 kHz, 100 V_{pp}) and the other (Ekulit type EPZ-27MS44W) is supplied with the sine voltage signal (30 kHz, 100 V_{pp}).
In all cases, the sweep excitation signal is provided by the SLDV's built-in function generator and amplified through the Falco WMA-300 high voltage amplifier. The sine excitation signal is supplied by an external function generator (Tektronix AFG3021B) through an AR 150A100D power amplifier. The excitation characteristics are summarized in Table 12.1.

The selected excitation voltage amplitudes for the low power piezoelectric actuators result in a reliable and safe operation of these actuators. Using these voltages, the out-of-plane velocity amplitude at the defects goes up to 150 mm/s at the LDR frequencies, which is sufficient to trigger contact acoustic nonlinearity. Higher voltage amplitudes result in higher vibrational amplitudes (at all frequencies) and can further enhance the nonlinear response of the defect. However, the employed small actuators may quickly degrade when an excessive voltage amplitude is applied. The selected start f_{start} and end f_{end} frequencies of the sweep signal cover the broad frequency range where multiple LDR's and energy trapping phenomena are expected (see Chapter 7 or [22-24]). The CFRP coupon with QSID is considerably thicker compared to the other test specimens, resulting in the higher sweep end frequency.

The full wavefield velocity response is measured using the Polytec PSV-500-3D Xtra SLDV. For each component, the scanned area is indicated on Figure 12.1. The scan point spacing, sample frequency and signal duration are included in Table 12.1. In order to detect the nonlinear components, which are of very low amplitude (see Chapter 8 or [1, 18, 25]), removable retroreflective tape (3M type 680CRE-10) is attached to each scan area. In addition, averages are taken to further increase the signal-to-noise ratio of the measurements (see Table 12.1). Note that a more detailed description of these noise reducing measures was provided in Chapter 4 Section 3.3.

Table 12.1: Characteristics of excitation signals and SLDV data acquisition.

Component	Sweep Actuator			Sine Actuator		SLDV			
	f_{start} (kHz)	f_{end} (kHz)	V_{pp}	f_{sine} (kHz)	V_{pp}	$f_{sampling}$ (kS/s)	# time samples	# averages	point spacing (mm)
$\text{CFRP}_{\text{QSID}}^{\text{Coupon}}$	1	200	100	50 63 70	100	1250	10000	10	1.3
$\text{CFRP}_{\text{Delam}}^{\text{Coupon}}$	10	125	100	30	100	625	10000	7	1.5
$\text{Sandwich}_{\text{Disb/BVID}}^{\text{Plate}}$	2.5	100	150	30	100	625	15000	3	2
$\text{CFRP}_{\text{BVID}}^{\text{Tube}}$	10	125	100	30 50	100	625	10000	10	≈ 1
$\text{CFRP}_{\text{Disb}}^{\text{Air}}$	10	125	100	30	100	625	10000	10	2.5

3. Nonlinear Energy Damage Map Construction

The construction of the nonlinear energy-based damage map consists of multiple steps. A schematic illustration of the workflow is provided in Figure 12.2 using the results of $\text{CFRP}_{\text{QSID}}^{\text{Coupon}}$. Two major parts are differentiated, i.e. (i) Nonlinear component extraction using time-frequency filtering and (ii) Damage map construction using bandpower calculation. These two parts are discussed in detail after a short explanation of the working principle of the method where the benefits of using the modulation sidebands compared to the higher harmonics are emphasized.

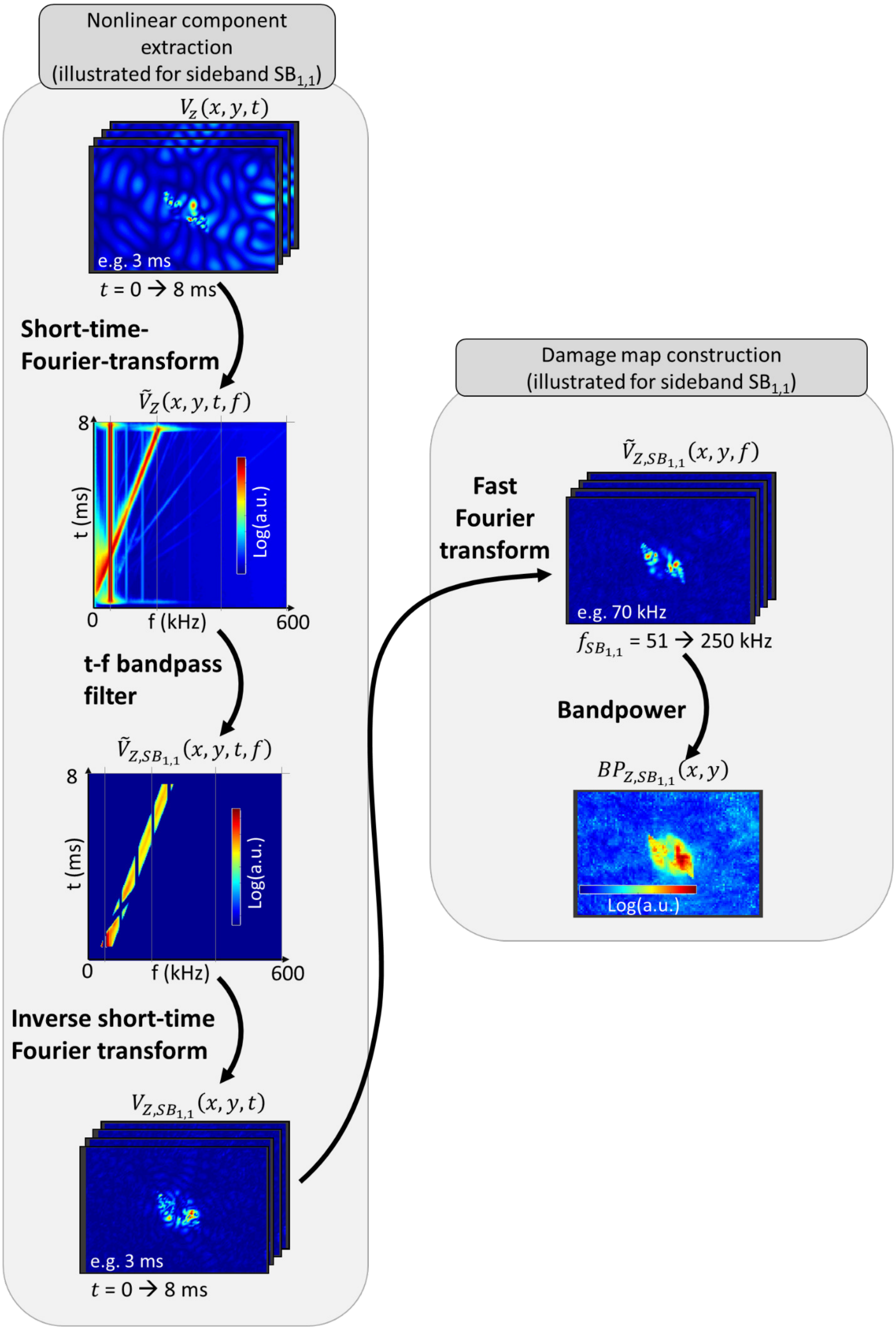

Figure 12.2: Workflow of the nonlinear broadband damage map construction algorithm, illustrated for $CFRP_{QSID}^{Coupon}$.

3.1. Working Principle

The interaction of elastic waves with a defect results in a non-classical nonlinear response of the defect due to contact and friction mechanisms [26]. Multiple models were developed to describe this nonlinear response [18, 27, 28] as explained in Chapter 3. Below, a short background is given assuming a clapping contact model (e.g. for delamination). This background illustrates the challenges in nonlinear inspection, and how to overcome them.

We consider the piezoelectric excitation of elastic waves in a delaminated composite component. When a sine voltage signal with frequency f_{in} is supplied to the actuator, elastic waves are excited with frequency f_{in}. In addition, higher harmonic (HH) components can be created due to source nonlinearity. This is schematically illustrated in Figure 12.3 (a) where $f_{HH_i} = i \, . \, f_{in}$ (with i an integer) represent the HH frequency components with amplitudes $a^s_{HH_i}$. The superscript ^{s} indicates that these components are excited by the source. The source nonlinearity is a combination of nonlinearity present in the signal generator, the amplifier, the piezoelectric material and the bonding layer [29, 30].
The propagating waves interact with the nonlinear defect and again HH components can be created (see proof-of-concept in Chapter 8). Thus, the resulting higher harmonics (with frequency f_{HH_i}) are a combination of both source nonlinearity (with amplitude factor $a^s_{HH_i}$) as well as defect nonlinearity (with amplitude factor $a^d_{HH_i}$). Note that the HH components that are present due to a nonlinear defect response to nonlinear components formed by the source are not included in the figure as they would be of an undetectable low amplitude ($a^s_{HH_i} \, . \, a^d_{HH_i}$). As a result, when HH components are detected, they could have been triggered by a nonlinear source, a nonlinear defect, or a combination of both.

In order to solve this problem, a second excitation source is added (see Figure 12.3 (b)). Each source is supplied with a different sine voltage signal (frequencies f_{in^1} , f_{in^2}) . Again, HHs of f_{in^1} and f_{in^2} are expected in the output signal that are partly attributed to source nonlinearity ($a^s_{HH^1_i}$ and $a^s_{HH^2_i}$) and partially to defect nonlinearity $\left(a^d_{HH^1_i} \text{ and } a^d_{HH^2_i}\right)$. In addition to the HHs, modulation sidebands (SB) are formed exclusively due to defect nonlinearity (see proof-of-concept in Chapter 8). Only in case of a poorly bonded actuator, resulting in a partial disbond between actuator and component, SBs can form at the location of the actuator. These SBs have frequency: $f_{SB_{i,j}} = i \, . \, f_{in^1} + j \, . \, f_{in^2}$ (with i and j integers) and amplitude $a^d_{SB_{i,j}}$. As such, the use of these SBs instead of HHs overcomes the source nonlinearity problem and should lead to an improved damage map. This statement is experimentally verified throughout this chapter for the first modulation sideband $SB_{1,1}$ (written in bold in Figure 12.3 (b)).

In order to activate contact acoustic nonlinearity, the vibrations at the defect must be of sufficient amplitude. Best is to match the excitation frequency with a LDR frequency. This was done in Chapter 8 to prove the generation of HHs and SBs at a delamination under LDR frequency excitation. However, in an actual non-destructive inspection, the LDR frequency is not known a priori (depends on defect structure). This necessitates the use of a broadband excitation. As a result, one piezoelectric source is supplied with a broadband sweep voltage signal which triggers the nonlinear response of the defect at specific (LDR) frequencies. A second piezoelectric source is supplied with a sine voltage signal which results in the formation of the SBs used for the creation of the damage map.

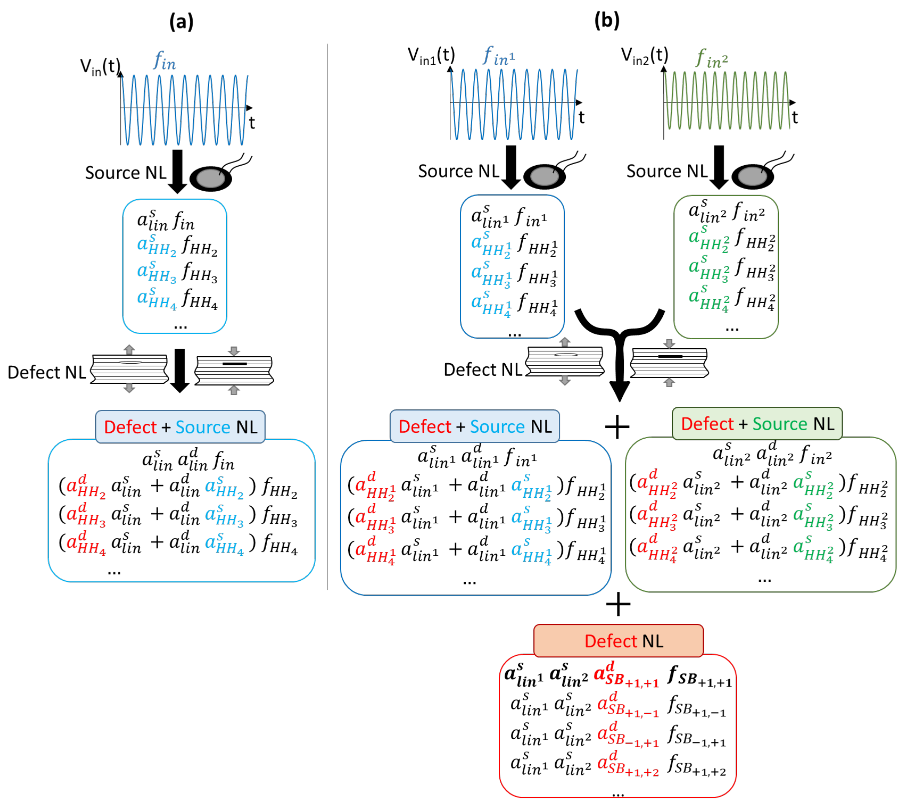

Figure 12.3: Schematic overview of the expected nonlinear components when using (a) a single piezoelectric actuator and (b) two actuators with different excitation frequencies.

3.2. Nonlinear Component Extraction

In Chapter 10 Section 2.5, it was illustrated how the short-time-Fourier-transform (STFT) and specific bandpass windows in the time-frequency domain can be used to extract HHs from the broadband measurement data. Here, the same technique is used with the difference that there is a second sine excitation source present. As a result, the construction of the time-frequency filter mask is adapted. The reader is referred to Chapter 10 (or [1]) for the details of the time-frequency domain wavefield manipulation and the associated equations.

First, STFT is performed to transform the broadband response signal at each scan point from the time domain to the time-frequency domain:

$$V_Z(x,y,t) \xrightarrow{STFT} \tilde{V}_Z(x,y,t,f)$$

Figure 12.4 (a) shows the average of the resulting spectrograms $\tilde{V}_Z(x,y,t,f)$ for $\mathrm{CFRP}_{\mathrm{QSID}}^{\mathrm{Coupon}}$ and Figure 12.4 (d) shows the derived frequency spectrum corresponding to time instance 6.5 ms. High intensity lines are visible in the spectrogram corresponding to: (i) the linear sine response f_{sine}^{lin} at 50 kHz, (ii) HHs of the sine response e.g. $f_{sine}^{HH_2}$ at 100 kHz, (iii) the linear sweep response f_{sweep}^{lin} from 1 to 200 kHz, (iv) SBs e.g. first sideband $f_{SB_{1,1}}$ from 1 + 50 = 51 kHz to 200 + 50 = 250 kHz, and (v) HHs of the sweep response e.g. $f_{sweep}^{HH_2}$ from 2 to 400 kHz. These components are also indicated on the spectrum in Figure 12.4 (d).

In order to extract one of these components, a bandpass window TFF is constructed around the component of interest. As an example, the window $TFF_{SB_{1,1}}$ shown in Figure 12.4 (b) is used to extract the $SB_{1,1}$ component. The bandpass window is constructed using Eq. (10.3) in Chapter 10. However, additional bandstop regions are added corresponding to the sine excitation frequency and its HHs, as well as the sweep excitation frequency and its HHs. As a result, all $SB_{1,1}$ components are retained with the exception of the components that overlap in time-frequency domain with the HHs of the sine and sweep excitation. This makes sure that no source nonlinearity is included in the filtered signal. For each scan point, the filter is multiplied with the local spectrogram:

$$\tilde{V}_{Z,SB_{1,1}}(x,y,t,f) = \tilde{V}_Z(x,y,t,f) \odot TFF_{SB_{1,1}}(t,f)$$

The average of all the filtered spectrograms $\tilde{V}_{Z,SB_{1,1}}(x,y,t,f)$ is shown in Figure 12.4 (c). Finally, the filtered nonlinear component is obtained in time domain after inverse STFT:

$$\tilde{V}_{Z,SB_{1,1}}(x,y,t,f) \xrightarrow{ISTFT} V_{Z,SB_{1,1}}(x,y,t)$$

The same filtering procedure (with adapted time-frequency bandpass windows) is used for the extraction of the linear part of the sweep response $\tilde{V}_{Z,lin}$ (see Figure 12.4 (e)) and for the extraction of the second order HH of the sweep response $\tilde{V}_{Z,HH_2}$ (see Figure 12.4 (f)).

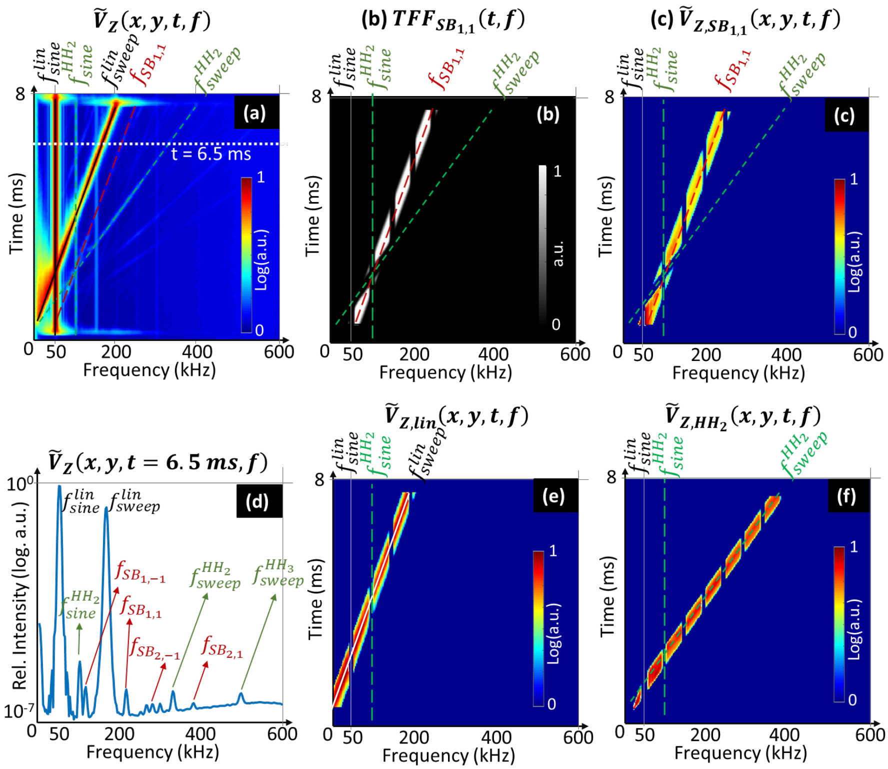

Figure 12.4: Extraction of velocity components for $\mathrm{CFRP}_{\mathrm{QSID}}^{\mathrm{Coupon}}$: (a) Average spectrogram, (b) Bandpass filter for first sideband $SB_{1,1}$ extraction, (c) Average spectrogram after $SB_{1,1}$ extraction, (d) Average frequency spectrum at time instance 6.5 ms, (e) Average spectrogram after linear component extraction and (f) Average spectrogram after second order higher harmonic (HH_2) extraction.

3.3. (Non)Linear Bandpower Damage Maps

Figure 12.5 shows the amplitude of vibration averaged over the area of the sweep actuator (blue curve), the damage-free material (black curve) and the defect (red curve) for: (a) the linear sweep response $\tilde{V}_{Z,lin}$, (b) the second higher harmonic response $\tilde{V}_{Z,HH_2}$ and (c) the first modulation sideband $\tilde{V}_{Z,SB_{1,1}}$ in $\mathrm{CFRP}_{\mathrm{QSID}}^{\mathrm{Coupon}}$. The amplitude axis is normalized and shown in logarithmic scale.

The low amplitude at 50, 100, 150 ... kHz is attributed to the bandstop filter at the sine excitation frequency and at its HHs (see previous section).

The linear response (see Figure 12.5 (a)) shows a lower intensity at the damage-free material than at the location of the sweep actuator. This is the result of wave damping, especially in the higher frequency range, and geometric wave spreading. The linear response at the defect is higher than at the background for the majority of frequencies which is caused by the reduced flexural rigidity at the defect. Such a pronounced increased intensity of the linear component would not be present in case of deeper defects (see Chapter 7 or [24]).

The curves of the HH_2 response (see Figure 12.5 (b)) show that HH_2 components are created both at the defect and at the actuator. The defect nonlinearity is dominant between 50 and 150 kHz whereas the source nonlinearity dominates in the higher frequency regime. The damage-free material shows only minor indications of HH_2 vibrations.

The $SB_{1,1}$ amplitude (see Figure 12.5 (c)) at the sweep actuator is low and similar to the amplitude measured in the damage-free material. This confirms that this SB component is not formed at the actuator. The $SB_{1,1}$ amplitude is considerably higher at the location of the defect over the entire frequency range. As such, it is confirmed that the use of $SB_{1,1}$ (compared to HH_2) is advantageous as it exists only due to the presence of a defect (and not due to source nonlinearity).

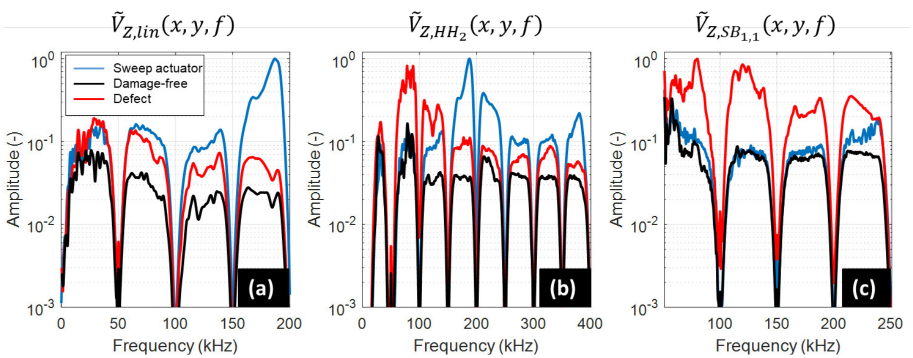

Figure 12.5: Vibrational intensity in $CFRP_{QSID}^{Coupon}$ at the sweep actuator (blue curve), at the damage-free material (black curve) and at the defect (red curve): (a) linear response, (b) second order higher harmonic response and (c) first modulation sideband response.

An energy-based damage map is derived from each of the extracted velocity components using broadband bandpower (BP) calculation:

$$BP_{Z,*}(x,y,f_1,f_2) = \frac{\Delta f}{f_2 - f_1}\sum_{f=f_1}^{f_2}\left|\tilde{V}_{Z,*}(x,y,f)\right|^2$$

The bandpower $BP_{Z,*}$ gives the vibrational energy at the point with location (x,y) related to velocity component $\tilde{V}_{Z,*}$ for a frequency band from f_1 up to f_2. Δf is the resolution in the frequency domain. The velocity component $\tilde{V}_{Z,*}$ is the FFT transform of any of the filtered signals: $V_{Z,lin}, V_{Z,HH_2}, V_{Z,SB_{1,1}}$ (as indicated by the *). Note that it is also possible to use the in-plane vibrational components $(\tilde{V}_{x,*}, \tilde{V}_{y,*})$ as input which can be beneficial to detect defects with out-of-plane interfaces such as cracks [31].

The resulting bandpower maps (for $\mathrm{CFRP}_{\mathrm{QSID}}^{\mathrm{Coupon}}$) are scaled according to their maximum and are shown in Figure 12.6 using a logarithmic colorscale. For each velocity component, the total relevant frequency range is used for the calculation of the damage map (see indication on figure). Similar as in Chapter 7, a defect-to-background ratio (DBR) is calculated as the ratio between the average intensity at the defect and the average intensity at the damage-free material (i.e. the total scan area excluding the defect area, but including the actuator area). As such, a DBR of 1 corresponds to an absence of the defect in the damage map while the defect detection improves for higher DBRs.

The $BP_{Z,*}$ is related to the integral of the curves shown in Figure 12.5. As a result, the damage maps reflect the same observations made in the analysis of Figure 12.5. The $BP_{Z,lin}$ map (see Figure 12.6 (a)) shows the presence of the QSID with a limited contrast compared to the damage-free material (DBR = 2). Wave attenuation results in a large amplitude at the sources of the linear vibrations, i.e. the piezoelectric sweep actuator. Note that this undesired effect of wave attenuation can be removed using the (broadband) WRMS damage map construction approach as discussed in previous chapter. However, the DBR at the defect would remain relatively small. The DBR is largely improved when using nonlinear components. For the BP_{Z,HH_2} map (see Figure 12.6 (b)), a pronounced amplitude increase at the QSID is observed leading to a DBR of 18. However, also the source nonlinearity is captured in this map. The $BP_Z^{SB_{1,1}}$ map (see Figure 12.6 (c)) shows the best damage map performance with a DBR of 47 and no influence of the source nonlinearity. In this case, the wave attenuation works in our advantage because the damage itself is the only source of the SB components.

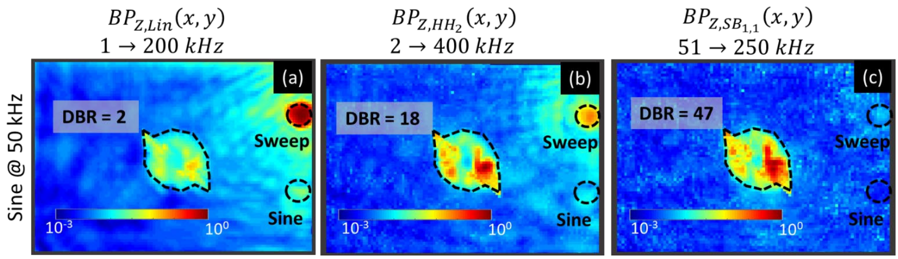

Figure 12.6: Broadband bandpower maps of $\mathrm{CFRP}_{\mathrm{QSID}}^{\mathrm{Coupon}}$ with indication of defect-to-background ratio (DBR): (a) Linear response, (b) Second order higher harmonic response and (c) First order modulation sideband.

3.4. Effect of the Sine Frequency

It is well known that the nonlinear response of a defect is highly dependent on the amplitude of vibrations at the defect. Sweeping the excitation signal of one source over a large frequency band ensures that several LDR frequencies are excited, resulting in the required high amplitude of vibration at the defect. The second actuator is then used to generate SB components in order to exclude the effect of source nonlinearity. A second important benefit of adding the secondary sine excitation is the additional increase of the amplitude of vibration at the defect. In order to investigate this further, the experiment for $\mathrm{CFRP}_{\mathrm{QSID}}^{\mathrm{Coupon}}$ is repeated twice using different sine excitation frequencies than the previously used 50 kHz: (i) another arbitrary frequency of 70 kHz and (ii) a LDR frequency of 63 kHz. The operational deflection shapes at these sine frequencies (50 kHz, 63 kHz and 70 kHz) are shown in Figure 12.7 (a-c). For all three cases, there is energy trapping at the defect leading to an increased vibrational amplitude. For the frequency of 63 kHz, the amplitude increase is the largest and occurs at a small area of the QSID that is indicated with LDR on Figure 12.7 (b).

Figure 12.7 (d-e) show the resulting $BP_{Z,SB_{1,1}}$ maps (with identical logarithmic colorscale). The highest DBR ratio (and thus the best damage map) is obtained for the case that the sine excitation frequency matches a LDR frequency (see Figure 12.7 (b,e)). The maximum in the bandpower map also matches well with the fraction of the defect showing the LDR behavior. The SB vibrations radiate away from the defect into the damage-free material. This nonlinear source behavior is seen by the wave-like increased intensity of the $BP_{Z,SB_{1,1}}$ in the damage-free material close to the defect. In Chapter 14, it is shown that this source behavior allows to detect defects even when they are not within the area measured by the SDLV.

In a real NDT experiment, there is no information on the defects (if any) and it is impossible to match the sine excitation frequency with a LDR. As a result, an arbitrary sine frequency is used in the remainder of the study. It is advised to use a frequency which results in elastic waves that have a spatial wavelength smaller than the size of the defects to be found. In this way, multiple wavelengths fit inside the defect resulting in an increased local amplitude (due to wave energy trapping) and potentially a LDR [22, 23]. For instance for this 5.45 mm thick CFRP coupon, the sine excitation frequencies 50 kHz, 63 kHz and 70 kHz are associated with a damage-free A_0 mode wavelength of 23 mm, 19 mm and 18 mm, respectively. At the defect, the wavelength is even smaller due to the local reduced thickness. As a result, the wavelengths at the defect are indeed smaller than the defect's width of ± 34 mm. The resulting energy trapping at the QSID was already confirmed in Figure 12.7 (a-c).

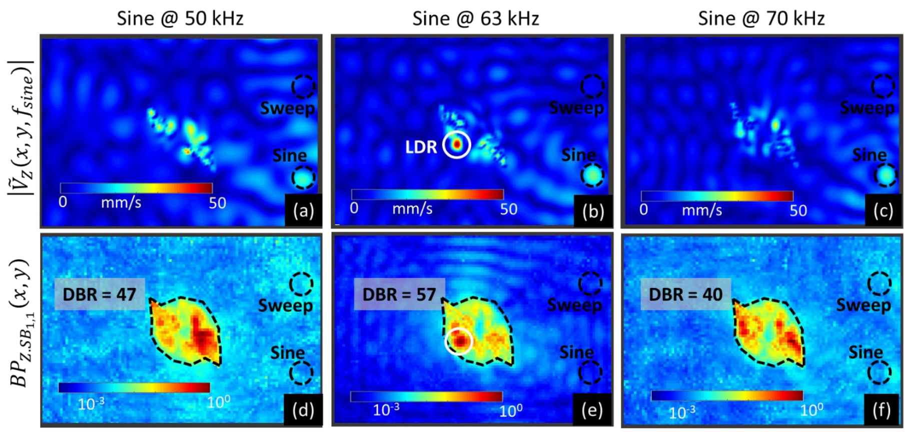

Figure 12.7: Effect of sine frequency on broadband nonlinear bandpower damage map for $\mathrm{CFRP}_{\mathrm{QSID}}^{\mathrm{Coupon}}$: (a-c) Operational deflection shape at the frequency of the sine excitation, (d-f) Bandpower maps of the first modulation sideband.

4. Damage Map Performance

4.1. CFRP Coupon with Delaminations

The processing steps discussed in the previous section are repeated for the measurement results of the CFRP coupon with one shallow and one deep artificial delamination ($\mathrm{CFRP}_{\mathrm{Delam}}^{\mathrm{Coupon}}$). Three potential energy-based damage maps are constructed using bandpower calculation: for the linear part of the out-of-plane velocity response, for the second higher harmonic and for the first spectral sideband. These maps are shown in Figure 12.8 (using an identical logarithmic colorscale) together with the operational deflection shape at the arbitrarily selected sine excitation frequency of 30 kHz.

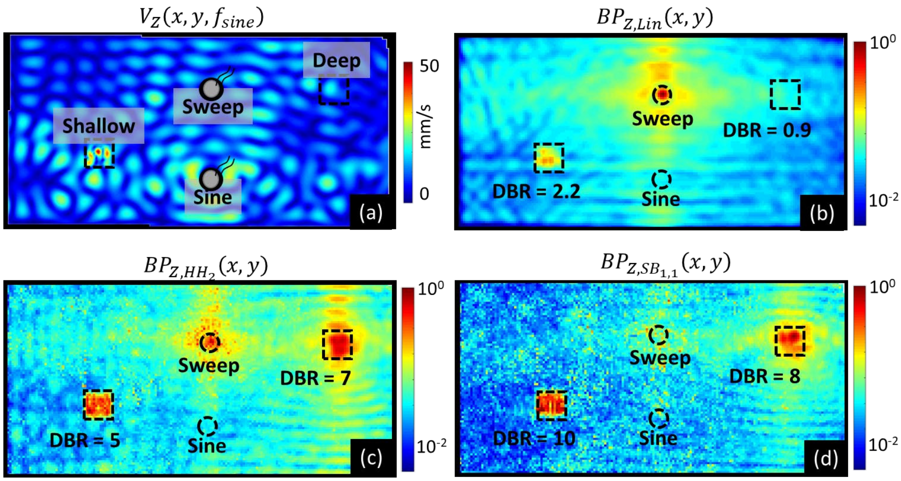

Figure 12.8: Results for $\text{CFRP}^{\text{Coupon}}_{\text{Delam}}$: (a) Operational deflection shape at sine excitation frequency f_{sine} = 30 kHz, and Bandpower of (b) Linear response 10 to 125 kHz, (c) Second order higher harmonic response 20 to 250 kHz and (d) First order modulation sideband 40 to 155 kHz.

The arbitrary selected sine frequency of 30 kHz does not match with a LDR. However, there is still an increased amplitude of vibration observed at the shallow delamination thanks to wave energy trapping (see Figure 12.8 (a)). The pronounced flexural rigidity reduction at the shallow delaminations makes it visible (DBR = 2.2) in the $BP_{Z,Lin}$ map (see Figure 12.8 (b)). The deep (backside) delamination is associated with a limited reduction in the flexural rigidity (when looking from the inspection side) which makes it invisible (DBR = 0.9) in the linear response.

The nonlinear bandpower maps reveal the shallow as well as the deep delamination. The $SB_{1,1}$ bandpower map (Figure 12.8 (d)) is superior compared to the HH_2 bandpower map (Figure 12.8 (c)). This is seen by the increase in DBR at both defect locations. In addition, the $SB_{1,1}$ bandpower map is not affected by source nonlinearity.

4.2. CFRP/Nomex Sandwich Plate with Disbond and Impact Damage

Test specimen $\text{Sandwich}^{\text{Plate}}_{\text{Disb/BVID}}$ is inspected from both sides. The disbond and the BVID are located at the skin plate of the frontside. Again, the linear response, the second higher harmonic and the first modulation sideband components are extracted from the total out-of-plane velocity response using the appropriate bandpass filters in the time-frequency domain.

The linear response of the front and backside at 17.5 kHz is shown in Figure 12.9 (a) and (d), respectively. The Nomex honeycomb core is relatively compliant resulting in a minor decrease in flexural rigidity at the location of the disbond. As a result, the increase in linear vibrational amplitude is small, even for the frontside of the component. The induced HH_2 and $SB_{1,1}$ vibrations corresponding to the instantaneous sweep frequency of 17.5 kHz are shown in Figure 12.9 (b,e) and (c,f), respectively. Both nonlinear components are observed at the location of the disbond. The nonlinear components are visible from the frontside (where the disbond is close to the surface) as well as from the backside, see Figure 12.9 (b-c) and (e-f), respectively. While the effect of source nonlinearity is visible in the HH_2 response, it is not present in the $SB_{1,1}$ component.

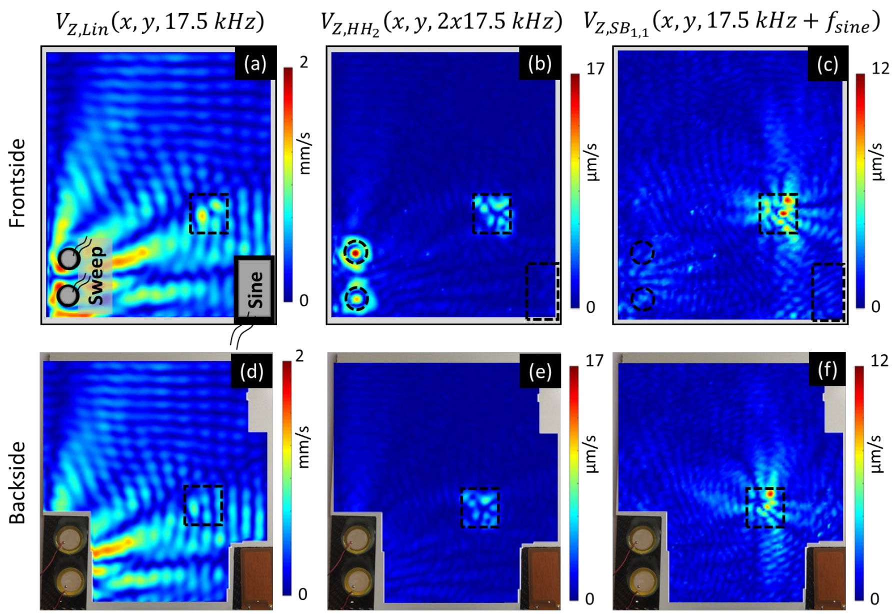

Figure 12.9: Results for $\text{Sandwich}^{\text{Plate}}_{\text{Disb/BVID}}$: (a,d) Linear response at 17.5 kHz, (b,e) Second higher harmonic at 2 x 17.5 = 35 kHz and (c,f) First modulation sideband at 17.5 + 30 = 47.5 kHz as seen from (top row) the frontside and (bottom row) the backside of the sandwich plate.

The instantaneous sweep excitation frequency that was selected for Figure 12.9, i.e. 17.5 kHz, was chosen manually as one of the frequencies that shows a good response for the nonlinear components. In order to get a robust indication of the damage, without the need of user input, the bandpower maps are constructed. The bandpower maps of the linear part of the response, the second higher harmonic and the first modulation sideband are shown in Figure 12.10 and in

Figure 12.11 for the frontside and backside of the test specimen, respectively. Also included are the operational deflection shapes at the sine excitation frequency f_{sine} = 30 kHz.

The relatively low flexural rigidity of the Nomex Honeycomb core results in a small increase in local vibrational activity at the sine excitation frequency of 30 kHz seen from the frontside of the component (see Figure 12.10 (a)). Also at the BVID, limited energy trapping is observed. None of the defects cause an increase in the velocity amplitude at f_{sine} = 30 kHz seen from the deep side (see Figure 12.11 (a)).

The bandpower maps of the linear response $BP_{Z,lin}$ (see Figure 12.10 (b) and Figure 12.11 (b)) cannot be used for detection of the damage. A DBR ratio smaller than or equal to one is observed at both defects.

The bandpower maps corresponding to the HH_2 vibrations BP_{Z,HH_2} reveal the disbond with a DBR of 0.8 and 1.8 as seen from the frontside and backside, respectively (see Figure 12.10 (c) and Figure 12.11 (c)). The small area of BVID is only marginally visible in the frontside's BP_{Z,HH_2} map with a DBR of 0.6. The relatively low DBR values for the frontside inspection are attributed to the high amount of source nonlinearity captured in the frontside's BP_{Z,HH_2} damage map.

The bandpower maps of the first modulation sideband $BP_{Z,SB_{1,1}}$ successfully reveal the disbond from both sides of the component (see Figure 12.10 (d) and Figure 12.11 (d)). The DBR value at the disbond is high (i.e. 5.5 and 5.7 for the frontside and backside, respectively) due to the absence of source nonlinear artifacts.

Unfortunately, the nonlinear response of the BVID is only visible in the frontside's damage maps. Taking into account the relatively high damping of the Nomex core, it is believed that a more powerful excitation is required in order to magnify the nonlinear response of this BVID. However, it was not possible to increase the voltage supplied to these small piezoelectric actuators as it would cause the actuators to generate excessive heat, resulting in the degradation of the piezoelectric material. The development of novel designated piezoelectric actuators is part of the future work of the current authors (see Chapter 16).

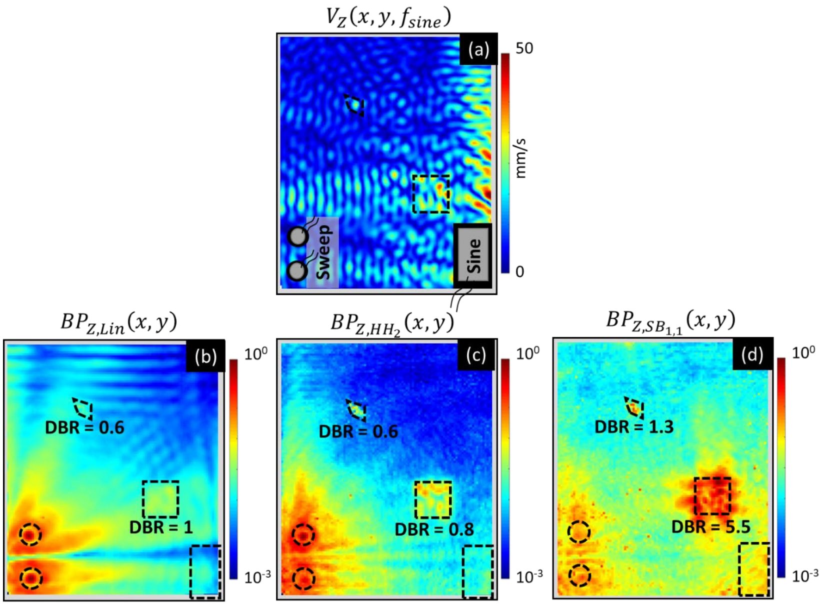

Figure 12.10: Frontside of $\text{Sandwich}^{\text{Plate}}_{\text{Disb/BVID}}$: (a) Operational deflection shape at sine excitation frequency, and bandpower of (b) Linear response 2.5 to 100 kHz, (c) Second order higher harmonic response 5 to 200 kHz and (d) First order modulation sideband 32.5 to 130 kHz, in logarithmic colorscale.

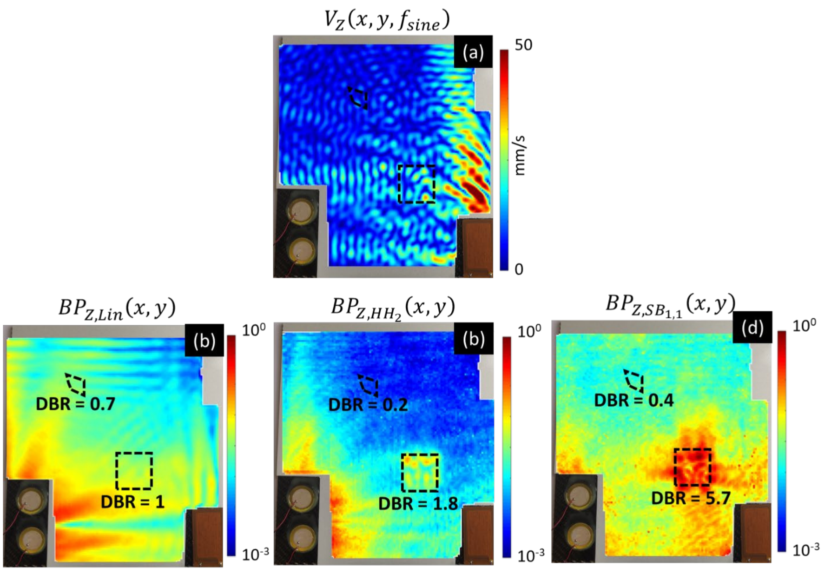

Figure 12.11: Backside of $\text{Sandwich}^{\text{Plate}}_{\text{Disb/BVID}}$: (a) Operational deflection shape at sine excitation frequency, and bandpower of (b) Linear response 2.5 to 100 kHz, (c) Second order higher harmonic response 5 to 200 kHz and (d) First order modulation sideband 32.5 to 130 kHz, in logarithmic colorscale.

4.3. Structural CFRP specimens

Structural CFRP components are often curved, have anisotropic material properties and may include add-ons such as stiffeners. Here, the robustness of the proposed nonlinear damage map construction method is verified using the measurement results of $\mathrm{CFRP}_{\mathrm{BVID}}^{\mathrm{Tube}}$ and $\mathrm{CFRP}_{\mathrm{Disb}}^{\mathrm{Air}}$.

4.3.1 Bicycle Frame with impact damage

Two measurements are performed for $\mathrm{CFRP}_{\mathrm{BVID}}^{\mathrm{Tube}}$ with sine excitation frequencies 30 kHz and 50 kHz. The overview of the results is shown in Figure 12.12. The curvature of the test specimen made it impossible to quantify the extent of the damage using our available ultrasonic C-scan setup. As a result, the estimate of the extent of the damage (as indicated by the black ellipse) is based on the outcome of the sideband bandpower (i.e. Figure 12.12 (i,j), see further).

The operational deflection shapes at the sine excitation frequencies are shown in Figure 12.12 (a,b). A limited increase in wave amplitude is observed at the location of the defect due to energy trapping. However, it is clear that these operational deflection shapes cannot be used for damage detection.
The bandpower maps of the linear response $BP_{Z,lin}$ (Figure 12.12 (c,d)) and the bandpower maps of the second higher harmonic component BP_{Z,HH_2} (Figure 12.12 (e,f)) cannot be used for damage identification either as the sweep actuators introduce a large amount of linear and nonlinear vibrations which cover almost the whole measurement domain. The relatively high amount of source nonlinearity captured in the BP_{Z,HH_2} maps is presumably caused by the geometric mismatch between the flat piezoelectric actuators and the tubular frame.
In contrast, the location of the BVID is successfully revealed using the bandpower maps calculated for the first modulation sideband $BP_{Z,SB_{1,1}}$ (see Figure 12.12 (g-j)). Note that the use of a linearly scaled colorbar further highlights this high intensity difference between BVID and damage-free material (see Figure 12.12 (i,j)).

A higher DBR is obtained when using a 50 kHz sine excitation (i.e. DBR = 23) compared to a 30 kHz sine excitation (i.e. DBR = 9). This is related to the superior wave energy trapping at 50 kHz than at 30 kHz as seen in the corresponding operational deflection shapes (Figure 12.12 (a,b)).

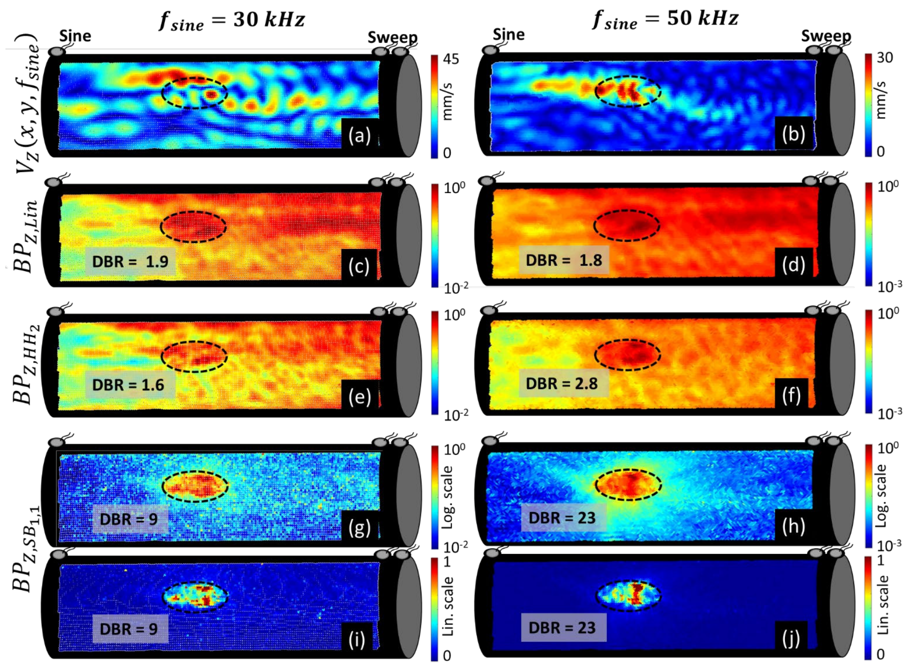

Figure 12.12: Impact damage detection in $CFRP^{Tube}_{BVID}$: (a,b) Operational deflection shape at sine excitation frequency, and Bandpower of (c,d) Linear response 10 to 125 kHz, (e,f) Second order higher harmonic response 20 to 250 kHz and (g-j) First order modulation sideband with logarithmic and linear colorscale. (Left column) 30 kHz sine excitation, (Right column) 50 kHz sine excitation.

4.3.2 Aircraft panel with disbond

The results for $CFRP^{Air}_{Disb}$ are shown in Figure 12.13 for a sine excitation frequency equal to 30 kHz. The operational deflection shape (Figure 12.13 (a)) has a chaotic appearance, and gives no indication of the damage.

The defect is marginally visible in the linear bandpower map $BP_{Z,lin}$ (Figure 12.13 (b)). Only at the location of the shallow delamination, the intensity is higher compared to the intensity at the virgin left-side of the stiffener.

The damage becomes visible as a zone of increased intensity in the second higher harmonic bandpower map BP_{Z,HH_2} (Figure 12.13 (c)). However, the BP_{Z,HH_2} map is again polluted by source nonlinearity resulting in the limited DBR of 2.

The bandpower map of the sideband vibrations $BP_{Z,SB_{1,1}}$ (Figure 12.13 (d)) is found to exclusively reveal the damage with a satisfying DBR of 11. The pronounced increase in intensity is further disclosed when using a linearly scaled colorbar (Figure 12.13 (e)).

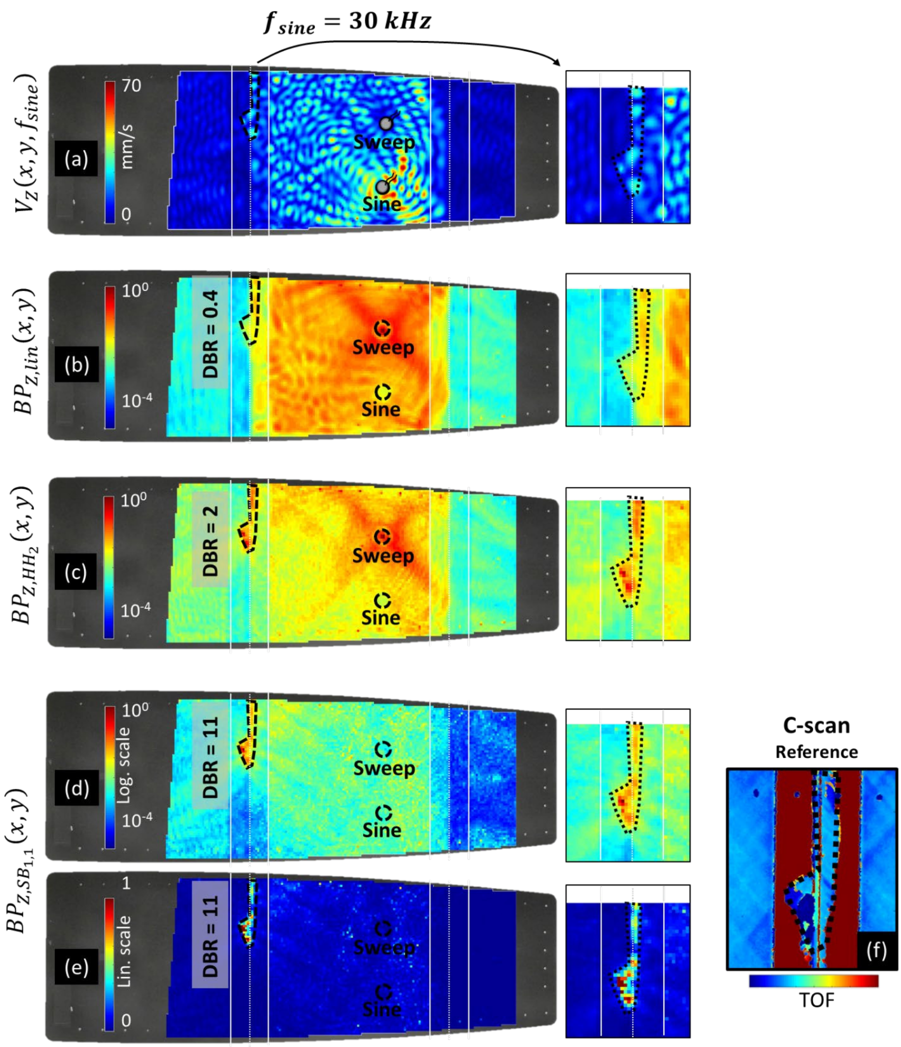

Figure 12.13: Damage detection in $\mathrm{CFRP}^{\mathrm{Air}}_{\mathrm{Disb}}$: (a) Operational deflection shape at sine excitation frequency of 30 kHz, and Bandpower of (b) Linear response 10 to 125 kHz, (c) Second order higher harmonic response 20 to 250 kHz and (d-e) First order modulation sideband 40 to 155 kHz with logarithmic and linear colorscale, respectively. (f) Time-of-flight map obtained from immersion ultrasonic C-scan inspection.

5. Conclusion

A full wavefield inspection method, based on the mapping of the energy related to nonlinear vibrational components, is proposed for damage detection in typical CFRP parts. The procedure results in a unique damage map which is baseline-free and user-independent. Further, the method only requires a single dual-excitation experiment, uses low power piezoelectric actuators, is not affected by source nonlinearity, and is applicable to complex structural CFRP components. Compared to other damage map construction methods (i.e. Chapter 11: *Broadband mode-removed WRMS* and Chapter 13: *Local wavenumber estimation*), no equidistant grid of scan point is required here. However, measurement noise reducing measures are required such as retroreflective tape, averaging and an increased piezoelectric excitation voltage.

The damage sensitivity of the broadband bandpower maps is verified using the measurement results of five test specimens: (i) a coupon with QSID, (ii) a coupon with one shallow and one deep delamination, (iv) a sandwich panel with a disbond and a small BVID, (iv) an impacted down tube of a bicycle frame and (v) an aircraft panel with damage at a backside stiffener. The nonlinear bandpower map of the first modulation sideband was highly effective in revealing all defects with satisfying contrast.

References

1. Segers, J., et al., *Nonlinear Elastic Wave Energy Imaging for the Detection and Localization of In-Sight and Out-of-Sight Defects in Composites.* Applied Sciences, 2020. **10**(3924).
2. Segers, J., et al., *Broadband nonlinear elastic wave modulation spectroscopy for damage detection in composites.* Structural Health Monitoring, 2021.
3. Van Den Abeele, K., et al., *Nonlinear Elastic Wave Spectroscopy (NEWS) Techniques to Discern Material Damage, Part II: Single-Mode Nonlinear Resonance Acoustic Spectroscopy.* Res Nondestr Eval 2000. **12**: p. 31–42.
4. Zhang, S., et al., *Far-sided defect recognition of FRP sandwich structures based on local defect resonance.* Journal of Sandwich Structures & Materials, 2019: p. 1-12.
5. Fierro, G.P.M. and M. Meo, *Nonlinear elastic imaging of barely visible impact damage in composite structures using a constructive nonlinear array sweep technique.* Ultrasonics, 2018. **90**: p. 125-143.
6. Fierro, G.P.M. and M. Meo, *A combined linear and nonlinear ultrasound time-domain approach for impact damage detection in composite structures using a constructive nonlinear array technique.* Ultrasonics, 2018. **93**: p. 43-62.

7. Ginzburg, D., *Damage Propagation and Detection using Nonlinear Elastic Wave Spectroscopy in Aerospace Structures*, in *Department of Mechanical Engineering*. 2016, University of Bath.
8. Ooijevaar, T.H., et al., *Nonlinear dynamic behavior of an impact damaged composite skin–stiffener structure.* Journal of Sound and Vibration, 2015. **353**: p. 243-258.
9. Broda, D., et al., *Modelling of nonlinear crack–wave interactions for damage detection based on ultrasound-A review.* Journal of Sound and Vibration, 2014. **333**(4): p. 1097-1118.
10. Su, Z., et al., *Acousto-ultrasonics-based fatigue damage characterization: Linear versus nonlinear signal features.* Mechanical Systems and Signal Processing, 2014. **45**(1): p. 225-239.
11. Van Den Abeele, K., P.A. Johnson, and A. Sutin, *Nonlinear Elastic Wave Spectroscopy (NEWS) Techniques to Discern Material Damage, Part I: Nonlinear Wave Modulation Spectroscopy (NWMS).* Res Nondestr Eval 2000. **12**: p. 17–30.
12. Pieczonka, L., et al., *Damage imaging in composites using nonlinear vibro-acoustic wave modulations.* Structural Control and Health Monitoring, 2017.
13. Dziedziech, K., et al., *Efficient swept sine chirp excitation in the non-linear vibro-acoustic wave modulation technique used for damage detection.* Structural Health Monitoring, 2017. **17**(3): p. 565-576.
14. Klepka, A., et al., *Impact damage detection in composite chiral sandwich panels using nonlinear vibro-acoustic modulations.* Smart Materials and Structures, 2013. **22**(8).
15. Mevissen, F. and M. Meo, *A Nonlinear Ultrasonic Modulation Method for Crack Detection in Turbine Blades.* Aerospace, 2020. **7**(6).
16. Fierro, G.P.M. and M. Meo, *IWSHM 2017: Structural health monitoring of the loosening in a multi-bolt structure using linear and modulated nonlinear ultrasound acoustic moments approach.* Structural Health Monitoring, 2018. **17**(6): p. 1349-1364.
17. Klepka, A., et al., *Nonlinear acoustics for fatigue crack detection – experimental investigations of vibro-acoustic wave modulations.* Structural Health Monitoring, 2011. **11**(2): p. 197-211.
18. Jhang, K.-Y., et al., *Measurement of Nonlinear Ultrasonic Characteristics*. Measurement Science and Technology, ed. M.G. Cain, et al. 2020: Springer.
19. Sohn, H., et al., *Nonlinear ultrasonic wave modulation for online fatigue crack detection.* Journal of Sound and Vibration, 2014. **333**(5): p. 1473-1484.
20. Malfense Fierro, G.P., F. Ciampa, and M. Meo, *Phase symmetry analysis for nonlinear ultrasonic modulated signals.* Structural Control and Health Monitoring, 2020. **27**(5).
21. Spronk, S.W.F., et al., *Comparing damage from low-velocity impact and quasi-static indentation in automotive carbon/epoxy and glass/polyamide-6 laminates.* Polymer Testing, 2018. **65**: p. 231-241.

22. Glushkov, E., et al., *Wave energy trapping and localization in a plate with a delamination.* Smart Materials and Structures, 2012. **21**(12).
23. Munian, R.K., D.R. Mahapatra, and S. Gopalakrishnan, *Lamb wave interaction with composite delamination.* Composite Structures, 2018. **206**: p. 484-498.
24. Segers, J., et al., *Probing the limits of full-field linear Local Defect Resonance identification for deep defect detection.* Ultrasonics, 2020. **105**.
25. Segers, J., et al., *Backside delamination detection in composites through local defect resonance induced nonlinear source behaviour.* Journal of Sound and Vibration, 2020. **479**.
26. Hirsekorn, S. and P.P. Delsanto, *On the universality of nonclassical nonlinear phenomena and their classification.* Applied Physics Letters, 2004. **84**(8): p. 1413-1415.
27. Ciampa, F., G. Scarselli, and M. Meo, *On the generation of nonlinear damage resonance intermodulation for elastic wave spectroscopy.* The Journal of the Acoustical Society of America, 2017. **141**(4): p. 2364.
28. Solodov, I., N. Krohn, and G. Busse, *CAN: an example of nonclassical acoustic nonlinearity in solids.* Ultrasonics, 2002. **40**(1): p. 621–625.
29. Sun, L., et al., *Technique to minimize couplant-effect in acoustic nonlinearity measurements.* The Journal of the Acoustical Society of America, 2006. **120**(5): p. 2500-2505.
30. Arafa, M. and A. Baz, *On the Nonlinear Behavior of Piezoelectric Actuators.* Journal of Vibration and Control, 2016. **10**(3): p. 387-398.
31. Segers, J., et al., *Towards in-plane local defect resonance for non-destructive testing of polymers and composites.* NDT & E International, 2018. **98**: p. 130-133.

Chapter 13

Damage Map based on Local Wavenumber Estimation

Summary:

Local wavenumber estimation (LWE) applied to a full wavefield response is a powerful approach for detecting and characterizing damage in composite structures. However, the narrowband nature of the traditional LWE techniques brings several challenges for application on actual test cases.

In this chapter, the traditional narrowband LWE implementations are reviewed. Further, a novel self-reference broadband version of the LWE technique is proposed by making use of modepass filters in the wavenumber-frequency domain.

The performance of the self-reference broadband LWE algorithm is demonstrated on aluminum plates with various flat bottom holes, as well as on cross-ply CFRP aircraft components with a stiffener disbond and with barely visible impact damage. Compared to the traditional narrowband LWE implementations, the proposed self-reference broadband LWE method allows a higher level of automation, removes the need for a priori knowledge on the material and/or defect properties, and results in an improved characterization of defects.

Section 5 of this chapter is in close correspondence with journal publication:

[1] Segers, J., Hedayatrasa, S., Poelman, G., Van Paepegem, W., Kersemans, M., *Self-Reference Broadband Local Wavenumber Estimation (SRB-LWE) for defect assessment in composites* Mechanical Systems and Signal Processing, 163, 2021.

1. Introduction

The elastic wave dynamics of composite plates were introduced in Chapter 2. It was shown that depending on (i) the excitation frequency f, (ii) the component's thickness h and (iii) the stiffness tensor C, specific guided elastic wave modes, are found to propagate in the thin-walled component [2]. In correspondence with the displacement distribution through the thickness, the modes were classified as 'symmetric (S)', 'anti-symmetric (A)', 'shear horizontal (SH)' and are assigned a specific order. Each mode has a unique dispersion behavior that is characterized by the wavenumber k (i.e. inverse of the spatial wavelength, expressed in m^{-1}) in function of the temporal frequency f.

Wavenumber-based damage map construction is most often referred to as local wavenumber estimation (LWE) [3-6] or as acoustic wavenumber spectroscopy/imaging (AWS/AWI) [7, 8]. As the name indicates, the wavenumber of a specific guided wave is estimated at each point of the component. For simplicity, the working principle of LWE is now explained for linear isotropic materials. For linear isotropic materials, the dispersion equation gives the relation between the local wavenumber k [1/m], the temporal frequency of the wave f [Hz] and the local material thickness h [m]. The dispersion equations for the A and S Lamb waves were derived in Chapter 2 (Eq. (2.31) and (2.32)):

$$\frac{\tanh\left(\frac{\alpha_1 h}{2}\right)}{\tanh\left(\frac{\alpha_2 h}{2}\right)} = \left[\frac{\left(\alpha_2^2+\kappa^2\right)^2}{4\kappa^2\alpha_1\alpha_2}\right]^S \quad \text{with} \quad \begin{aligned} \alpha_1^2 &= \kappa^2 - \frac{\omega^2}{V_L^2} \\ \alpha_2^2 &= \kappa^2 - \frac{\omega^2}{V_S^2} \\ \kappa &= 2\pi k \ ; \ \omega = 2\pi f \end{aligned} \tag{13.1}$$

where V_L and V_S are the material's bulk longitudinal and bulk shear (or transversal) wave velocity, respectively. The exponent s equals -1 or +1 for the A or S Lamb modes, respectively. The equation has to be solved numerically and the solutions are the dispersion curves of the material. In the case of anisotropic materials, for instance composites, no analytical expression such as Eq. (13.1) can be found (without approximations) and the dispersion curves need to be derived using semi-analytical or numerical tools (see Chapter 2 Section 4.2). The dispersion relation corresponding to the SH mode is not considered here. This is because the fundamental SH wave (i.e. SH_0) is non-dispersive (in isotropic materials) and not affected by the thickness of the component. As a result, it cannot be used for defect detection based on LWE.

As an example, the dispersion curves of the fundamental A and S Lamb waves in isotropic aluminum (V_L = 6420 m/s, V_S = 3040 m/s) are shown in Figure 13.1. In Figure 13.1 (a), the solution is given in terms of the wavenumber-thickness product versus the frequency-thickness product, resulting in a single dispersion curve that is valid for any material thickness h. In Figure 13.1 (b), the dispersion curves are shown for an aluminum plate of specified thicknesses. Note that for the A_0 mode, the wavenumber increases when the material thickness becomes smaller. As such, a horizontal crack (i.e. delamination) in the aluminum plate will result in the local increase of the A_0 mode wavenumber as graphically illustrated on Figure 13.1 (c). In the same way, a delamination defect in a composite plate results in an increased local wavenumber for the A_0 mode.

In most cases, LWE is performed for the A_0 mode because the A_0 mode dispersion curve varies in function of the material's thickness h over the complete frequency axis (see Figure 13.1 (b)). Only at very high frequencies, the A_0 mode dispersion curve converges with the non-disperse Rayleigh wave and becomes material thickness-independent (not shown in Figure 13.1 (b)). For the S_0 mode, the dispersion curve only starts to become thickness-dependent for frequencies higher than 400 kHz (in case of a 5 mm thick aluminum plate). Excitation and measurement of these high frequency vibrations is difficult, which favors the A_0 mode to be used for LWE instead of the S_0 mode. Note however that the depth sensitivity of the A_0 mode decreases considerably for higher material thicknesses, as evidenced by the reduced spacing between the A_0 dispersion curves for higher material thicknesses. As such, the use of the S_0 mode in combination with high frequency excitation can be required for detection of deep defects in very thick materials (see also [7]).

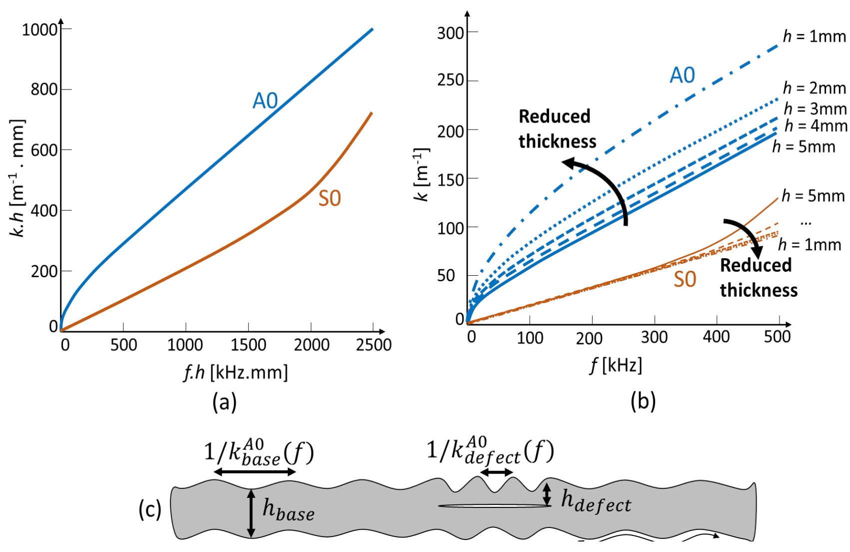

Figure 13.1: Dispersion characteristics of aluminum material: (a) Dispersion curves of A_0 and S_0 mode expressed as wavenumber-thickness *k.h* in function of frequency-thickness *f.h*, (b) Dispersion curves expressed as wavenumber k in function of frequency f for several material thicknesses h and (c) Schematic illustration of the local change in A_0 mode dispersion behavior at a horizontal crack or delamination.

Multiple LWE algorithms have been proposed in literature [3-14]. A first distinction can be made based on the type of input data. Originally, LWE was developed for finding the local wavenumber map corresponding to a narrowband toneburst response with specific center frequency f_c [3, 8, 9]. This toneburst response can be obtained using (i) piezoelectric excitation with a Hanning windowed sine voltage signal [9], (ii) piezoelectric excitation with a deterministic broadband voltage signal followed by a suitable frequency-filtering procedure (see Chapter 10 Section 2.2 or [15]) or (iii) pulsed laser excitation followed by a narrowband frequency bandpass filter [3].
In addition, LWE can be performed using standing wave excitation (i.e. steady-state regime) [11, 12] or using a single time or frequency frame (i.e. instantaneous LWE) [4, 14].
Next to the different types of input data, multiple LWE software implementations were proposed. Flynn et al. [3] proposed to run the wavefield dataset through a bank of narrowband wavenumber bandpass filters that are centered at specific wavenumbers. At the same moment, Rogge and Leckey [9] proposed the use of the short-space-Fourier-transform as an alternative to Flynn's method. Recently, it was shown by Jeon et al. [12] that the same wavenumber map can be obtained using 2D-wavelet transformations instead of the traditional spatial FFT approach.

All the mentioned LWE approaches have in common that the wavenumber map is obtained at a specific (center) frequency of excitation. From the estimated local wavenumber map, the local thickness of the material can then be derived if the dispersion relations, and thus the material's stiffness properties, are a priori known [4, 5, 7, 13]. Especially for composite materials with multiple plies and anisotropic stiffness parameters, this could become problematic.

Multiple researchers investigated the effect of the excitation (center) frequency on the obtained local wavenumber map [5, 7, 10, 16]. It was concluded that the optimal excitation frequency depends on:

i. the guided wave mode of interest.
ii. the dispersion characteristics (i.e. the material properties).
iii. the size and the depth of the defect.
iv. the frequency-dependent signal-to-noise ratio (SNR) of the experimental setup.

In addition to the optimal excitation frequency, also the optimal value of many LWE algorithm's parameters (e.g. the spatial window size used in the LWE approach based on the short-space-Fourier transform [9]) depends on the above listed characteristics. Hence, proper selection of these parameters is far from straightforward for a realistic test case with unknown material properties (e.g.

stiffness tensor, density, stacking sequence) and unknown defect characteristics (e.g. size, depth, shape).

As an alternative to the traditional LWE techniques, a novel LWE implementation is proposed in this chapter. The proposed method works on the broadband vibrational response of the test specimen, and uses a self-reference mode filter bank in the wavenumber-frequency domain. The novel technique is called self-reference broadband local wavenumber estimation (SRB-LWE) and aims to:

- Overcome the problem related to the selection of an optimal excitation frequency.
- Improve the obtained damage map by using an enhanced filtering procedure.
- Avoid the need for manual parameter optimization.
- Obtain an estimated local thickness map (rather than a local wavenumber map) without the need for the material's stiffness properties, layup and density.

The only parameter that needs to be known in advance is the base material's thickness (or the most prominent thickness) of the investigated test specimen. And even in case that also this thickness is unknown, the SRB-LWE will give the relative local thickness compared to the base material.

First, the measurement procedure and the used test specimens are described. Then, the traditional narrowband implementation of LWE are explained and reviewed. Next, the novel SRB-LWE algorithm is outlined and its outperformance is demonstrated for several test cases. At last, the conclusions are summarized.

2. Materials and Experiments

Five different test specimens (see Figure 13.2) are used in this study towards the performance of different LWE implementations.

The first three test specimens are 400x400x5 mm^3 aluminum plates. Ten FBHs with specified diameter (15 mm, 25 mm and 35 mm) are milled into the backside of each plate. Figure 13.2 (a) shows the plate with FBHs of diameter 25 mm together with a table wherein the remaining material thickness *h* and the diameter *d* of every FBH are specified. The plates are labeled as Al_{15mm}, Al_{25mm} and Al_{35mm}, according to the diameter of the FBH defects. Note that there are three FBHs with a remaining thickness of 0 mm that are thus through holes. The same test specimens were already used in the parametric study performed to investigate the detection limits of linear local defect resonance (see Chapter 7).

The fourth and fifth component are CFRP parts manufactured for use in the vertical stabilizer of an Airbus A320 aircraft (see Figure 13.2 (b) and (c), respectively). On the backside, stiffeners are visible which are bonded to the base plate. The thickness of the base plate h_{base}, on which the stiffeners are bonded, measures 1.5 mm and 4 mm, respectively for the fourth and fifth component. The components are manufactured in an autoclave curing cycle.
The CFRP components have a cross-ply layup, with unknown stiffness and density properties. The component shown in Figure 12.1 (b), and labeled $\mathrm{CFRP}_{\mathrm{Disb}}^{\mathrm{Air}}$, was scrapped by the manufacturer because an ultrasonic C-scan inspection revealed a defect at the central stiffener. The component shown in Figure 12.1 (c), and labeled $\mathrm{CFRP}_{\mathrm{BVID}}^{\mathrm{Air}}$, suffered low-velocity impacts at three locations by a 7.7 kg weight from a height of 20 cm, 35 cm and 30 cm. The corresponding theoretical impact energies equal 14 J, 24 J and 21 J, respectively. These three impact events resulted in three areas of BVID, marked as BVID-A, BVID-B and BVID-C respectively.
Also shown in Figure 13.2 (b-c) are the time-of-flight (TOF) and relative amplitude (Amp) images obtained from in-house immersion ultrasonic C-scan inspection with a 5 MHz focused transducer in reflection mode. The C-scan results in Figure 13.2 (b) reveal a relatively large disbond between the central stiffener and the base plate. The C-scans of BVID-B reveal a complex distribution of delaminations and cracks (see Figure 13.2 (c)).

In each component, vibrations are introduced through small, low power piezoelectric actuators (Ekulit EPZ-20MS64W). The actuators are temporarily attached to the backside using removable phenyl salicylate. A broadband sine sweep voltage signal is supplied to these actuators. The sweep's start and end frequencies (f_{start}, f_{end}) are listed in Table 13.1. The voltage signal is amplified through a Falco WMA-300 high voltage amplifier before it is supplied to the piezoelectric actuators. For $\mathrm{CFRP}_{\mathrm{BVID}}^{\mathrm{Air}}$, two piezoelectric actuators are used. Both actuators are simultaneously excited with the same excitation signal. The actuators are located at the backside of the component in between the stiffeners (see Figure 13.2 (c)). The use of multiple actuators makes sure that the guided waves, which are partially reflected at the stiffeners, are of sufficient amplitude throughout the scan area. The use of this deterministic broadband excitation signal, in combination with frequency-filtering, allows to test all the different LWE implementation using only one experimental recording.

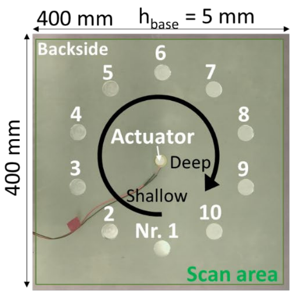

(a) Al_{15mm}, Al_{25mm} and Al_{35mm}

	d (mm)	FBH Nr. 1	2	3	4	5	6	7	8	9	10
		h (mm)									
Al_{15mm}	15	0	0	0.6	1.45	1.95	2.45	2.95	3.5	3.8	4.15
Al_{25mm}	25	0	0.3	0.9	1.35	1.9	2.7	2.95	3.3	3.9	4.35
Al_{35mm}	35	0.45	0.65	1	1.5	2.15	2.85	3.2	3.55	4.15	4.65

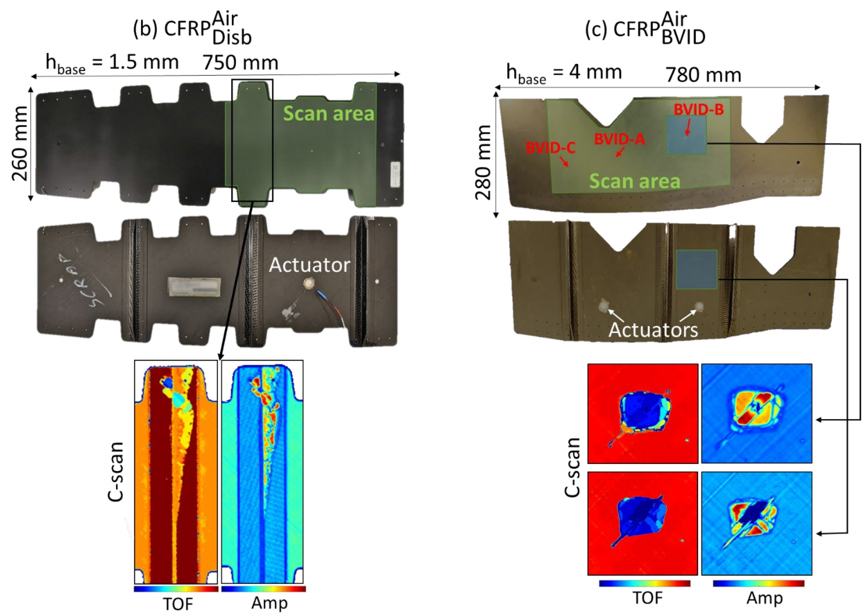

Figure 13.2: Test specimens: (a) Three aluminum plates with each 10 FBHs of specified diameter *d* (= 15, 25 and 35 mm, respectively) and remaining material thickness *h*, (b) CFRP aircraft panel with disbond at the central stiffener and (c) CFRP aircraft panel impacted at three locations.

As an alternative to the bonded piezoelectric actuator, the aluminum plate with FBHs of diameter 35 mm has also been excited by a pulsed laser. A compact diode pumped solid state laser (Quantel VIRON) with wavelength 1064 nm, pulse duration < 12 ns, beam diameter 3.8 mm, repetition rate 20 Hz and maximum pulse energy 50 mJ is positioned behind the component (distance ≈ 1.5 m, angle ≈ 30°). Laser pulses are fired at the center of the aluminum plate. Elastic waves are induced by the laser pulses due to the thermo-elastic effect [17] resulting in a non-contact excitation method. The optimal Q-switch delay was lowered (by trail and error) to reduced the pulse energy in order to prevent ablation of the test specimen's surface.

The full wavefield response is recorded with the 3D SLDV (Polytec PSV-500 3D Xtra). The area for which the wavefield is recorded (i.e. the scan area) is indicated on Figure 13.2 for each test specimen. For $\mathrm{CFRP}_{\mathrm{BVID}}^{\mathrm{Air}}$ (Figure 13.2 (c)), two additional measurements are performed focused at the BVID-B area. All relevant data acquisition settings, i.e. sampling frequency f_s, number of samples, number of averages and scan point spacing are included in Table 13.1. Only the out-of-plane velocity component $V_Z(x, y, t)$ is used because the LWE algorithms are operated on the A_0 mode, which has a dominant out-of-plane surface vibration. Retro-reflective tape is used only for the measurment with pulsed laser excitation.

Table 13.1: Characteristics of excitation signals and SLDV data acquisition.

Test Specimens	Excitation			SLDV			
	f_{start} (kHz)	f_{end} (kHz)	V_{pp}	$f_{sampling}$ (kS/s)	Samples (#)	Averages (#)	Point Spacing (mm)
Al_{15mm}	5	300	50	625	10 000	20	3
Al_{25mm}	5	300	50	1250	10 000	20	3
Al_{35mm}	5	300	50	625	10 000	10	3
Al_{35mm}	Pulsed laser			625	2 500	10	3
$\mathrm{CFRP}_{\mathrm{Disb}}^{\mathrm{Air}}$	20	250	100	1250	10 000	20	1.6
$\mathrm{CFRP}_{\mathrm{BVID}}^{\mathrm{Air}}$	5	300	50	625	10 000	15	2
$\mathrm{CFRP}_{\mathrm{BVID-B-front}}^{\mathrm{Air}}$	5	300	100	625	10 000	10	1
$\mathrm{CFRP}_{\mathrm{BVID-B-back}}^{\mathrm{Air}}$	5	300	100	625	10 000	10	1

Figure 13.3 shows three time snapshots of the measured out-of-plane velocity response for each of the three test specimens. The top row presents again a picture of each test specimen with indication of the damage. From these snapshots, it is impossible to clearly identify defects, illustrating the need for advanced signal processing. However, the increased wavenumber at some defects can already be observed in few of the snapshots, for instance in Figure 13.3 (g).

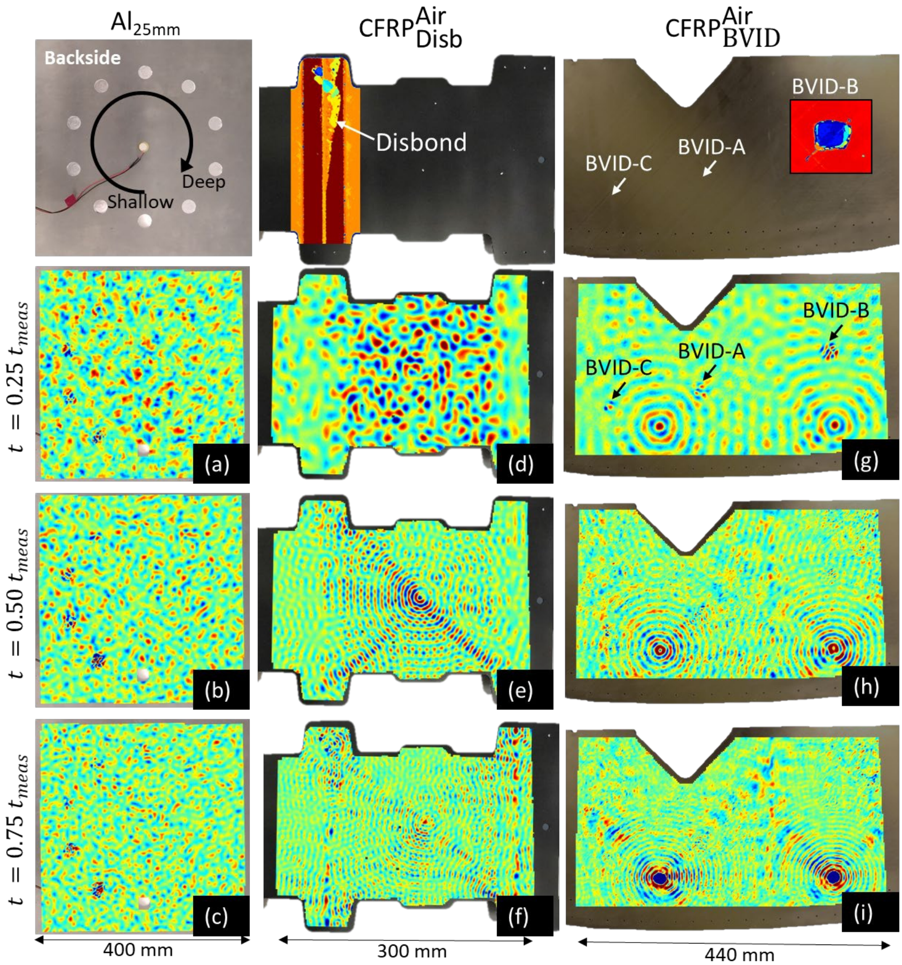

Figure 13.3: Time snapshots of the out-of-plane velocity of vibration in (a-c) Al_{25mm}, (d-f) $\mathrm{CFRP}^{\mathrm{Air}}_{\mathrm{Disb}}$ and (g-i) $\mathrm{CFRP}^{\mathrm{Air}}_{\mathrm{BVID}}$.

3. Local Wavenumber Estimation for Standing Wave Excitation

LWE using standing wave excitation is a well-known damage map construction technique [9-11, 18]. It is here illustrated for defect detection in the aluminum plate with FBHs of diameter 25 mm ($\mathrm{Al}_{25\mathrm{mm}}$) and for defect detection in the CFRP aircraft panel with the disbond at the stiffener (denoted $\mathrm{CFRP}^{\mathrm{Air}}_{\mathrm{Disb}}$).

The experimentally obtained sweep responses $V_Z(x, y, t)$ are converted to single-frequency standing wave responses $V_{Z,f_s}(x, y, t)$ using the frequency-filtering procedure explained in Chapter 10 Section 2.2:

$$V_Z(x, y, t) \xrightarrow{Freq.Filt.;\, U_{f_s}(t)} V_{Z,f_s}(x, y, t)$$

A sine excitation signal with frequency f_s is chosen for the desired waveform $U_{f_s}(t)$. For both $\mathrm{Al}_{25\mathrm{mm}}$ and $\mathrm{CFRP}^{\mathrm{Air}}_{\mathrm{Disb}}$, three standing wave responses are calculated corresponding to sine frequencies f_s = 50, 125 and 200 kHz. This allows to evaluate the effect of the standing wave excitation frequency on the resulting LWE map.

The working principle of the different standing wave LWE algorithms is explained using intermediate results corresponding to a f_s = 125 kHz sine response of $\mathrm{Al}_{25\mathrm{mm}}$.

3.1. Wavenumber Filtering for A_0 Mode Extraction

The LWE procedure is performed for the A_0 guided wave. As a result, if other modes of significant amplitude are present, they have to be removed from the dataset. When dealing with a single-frequency standing wave response, a wavenumber bandstop filter is used to remove the vibrations corresponding to the other mode(s). A detailed discussion on wavenumber bandstop filtering was already provided in Chapter 10 Section 2.3.2.

First, the $V_{Z,f_s}(x, y, t)$ wavefield is converted to the wavenumber-frequency domain:

$$V_{Z,f_s}(x, y, t) \xrightarrow{3D\ FFT} \tilde{V}_{Z,f_s}(k_x, k_y, f)$$

Figure 13.4 (a) shows the amplitude of $\tilde{V}_{Z,f_s}(k_x, k_y, f)$ at the sine excitation frequency f_s = 125 kHz for $\mathrm{Al}_{25\mathrm{mm}}$. In this wavenumber map, the slowness curves of the A_0 and S_0 modes are found as circles of high intensity. A wavenumber bandstop filter is constructed to remove the vibrations attributed to the S_0 mode:

$$KF_{\overline{S0}}(k_x, k_y, f) = \begin{cases} 1 & \text{if } \sqrt{k_x^2 + k_y^2} > k_{\overline{S0}} \\ 0 & \text{elsewhere} \end{cases} \tag{13.2}$$

This wavenumber bandstop filter with wavenumber cutoff $k_{\overline{S0}}$ = 30 m^{-1} is shown in Figure 13.4 (b). The filtered wavefield is obtained by element-wise multiplication of $\tilde{V}_{Z,f_s}(k_x, k_y, f)$ with the filter $KF_{\overline{S0}}(k_x, k_y, f)$:

$$\tilde{V}_{Z,f_s,\overline{S0}}(k_x, k_y, f) = \tilde{V}_{Z,f_s}(k_x, k_y, f) \odot KF_{\overline{S0}}(k_x, k_y, f)$$

The result is shown in Figure 13.4 (c). At last, inverse 3D FFT is used to transform the filtered result back to the spatial-time domain:

$$\tilde{V}_{Z,f_s,\overline{S0}}(k_x, k_y, f) \xrightarrow{3D\ IFFT} V_{Z,f_s,\overline{S0}}(x, y, t)$$

The optimal wavenumber cutoff $k_{\overline{S0}}$ value depends on the dispersion characteristics of the material and on the sine excitation frequency. As a result, the value is manually selected based on the wavenumber map plotted at the excitation frequency (see Figure 13.4 (a)).

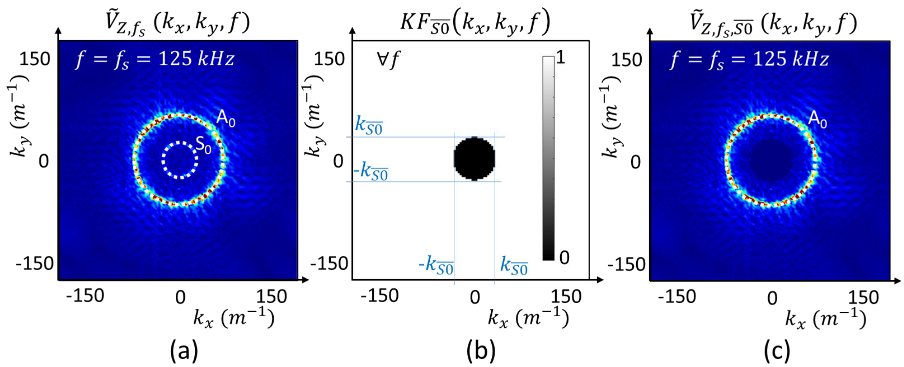

Figure 13.4: S_0 mode vibration removal in Al_{25mm}: (a) Wavenumber map at sine excitation frequency $f = f_s$ = 125 kHz, (b) Wavenumber bandstop filter and (c) Filtered wavenumber map at sine excitation frequency.

3.2. Construction of the Standing Wave Wavenumber Map

LWE is performed on the standing wave response of the A_0 mode, i.e. $V_{Z,f_s,\overline{S0}}(x, y, t)$, following two different implementations. First, LWE is performed based on the short-space-Fourier transform as proposed by Rogge, Leckey and Juarez [9, 10]. Next, LWE is performed using a wavenumber bandpass filter bank as proposed by Flynn et al. [3].

3.2.1. Method 1: LWE based on the Short-Space-Fourier-Transform

Rogge and Leckey proposed to use the short-space-Fourier-transform for LWE [9]. Strictly speaking, their method was developed for toneburst responses (see Section 4.2.1). However, it is also applicable for standing waves as is illustrated below (and by Juarez et al. in [10]). A graphical representation of this LWE implementation is shown in Figure 13.5.

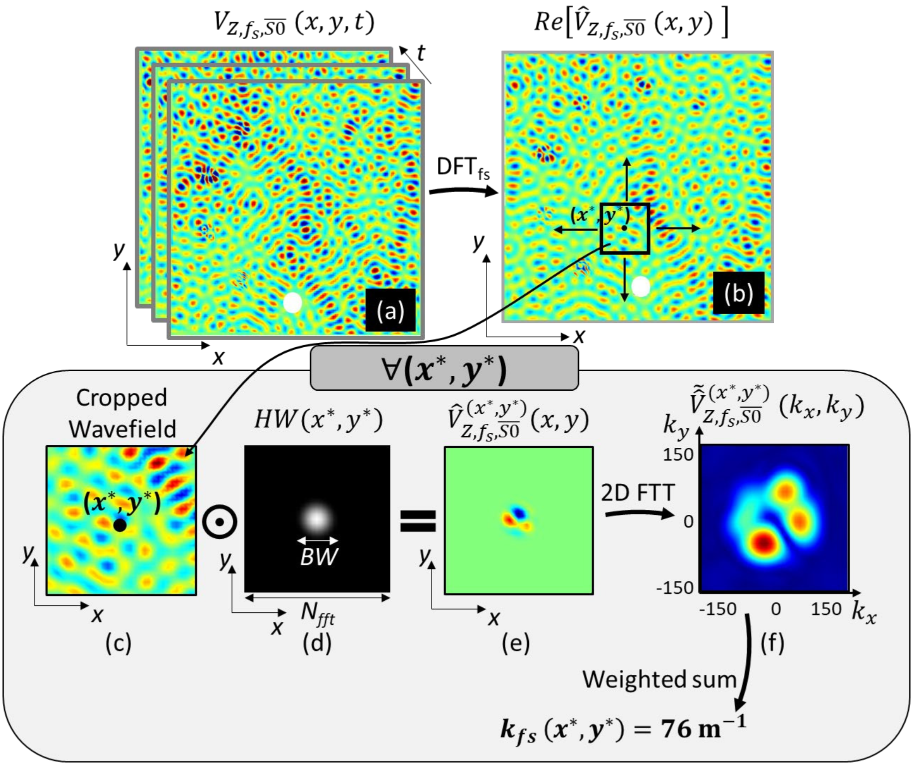

Figure 13.5: LWE for standing wave excitation in Al25mm based on the short-space-Fourier-transform: (a) Time snapshots of A0 mode wavefield, (b) Standing wavefield at f_s = 125 kHz, (c) Cropped wavefield at scan point of interest, (d) Spatial Hanning window, (e) Windowed cropped wavefield and (f) Wavenumber map at scan point of interest.

Discrete Fourier Transform at f_s

Figure 13.5 (a) shows time snapshots of the modestop filtered sine response in Al25mm, i.e. $V_{Z,f_s,\overline{S0}}(x,y,t)$. The discrete Fourier transform (DFT) at the sine excitation frequency f_s is used to efficiently convert the total time response into a single wavefield image [18]:

$$V_{Z,f_s,\overline{S0}}\,(x,y,t) \xrightarrow{DFT_{f_s}} \hat{V}_{Z,f_s,\overline{S0}}\,(x,y) \tag{13.3}$$

with N_t the number of time samples. The real part of $\hat{V}_{Z,f_s,\overline{S0}}\,(x,y)$ is shown in Figure 13.5 (b).

Short-Space-Fourier-Transform

The next processing steps are performed for every grid point.

First, the wavefield is cropped to a small square area centered at the grid point of interest. The cropped area has width and height N_{fft} (expressed in number of grid points). Figure 13.5 (c) shows the cropped wavefield for the grid point with coordinates (x^*,y^*), indicated by the black dot. Second, a spatial Hanning window $HW(x^*, y^*)$ with bandwidth BW is constructed (see Figure 13.5 (d)) and multiplied with the cropped wavefield:

$$\hat{V}_{Z,f_s,\overline{S0}}(x,y) \odot HW(x^*,y^*) = \hat{V}^{(x^*,y^*)}_{Z,f_s,\overline{S0}}(x,y)$$

The result is shown in Figure 13.5 (e). At last, the cropped and windowed wavefield is converted to the wavenumber domain using spatial (i.e. 2D) FFT transformation (see Figure 13.5 (f)):

$$\hat{V}^{(x^*,y^*)}_{Z,f_s,\overline{S0}}(x,y) \xrightarrow{2D\ FFT} \tilde{\hat{V}}^{(x^*,y^*)}_{Z,f_s,\overline{S0}}(k_x,k_y)$$

The superscript (x^*, y^*) indicates the local character of the wavenumber map. This wavefield transformation sequence is often referred to as the short-space-Fourier-transform.

It is of utmost importance to use appropriate values for the window size N_{fft} and bandwidth BW.

The selected crop size N_{fft} determines the wavenumber resolution: $\Delta k = \frac{1}{N_{fft}\,\Delta x}$, with $\Delta x = \Delta y$ the uniform distance between grid points in x- and y- direction. The smaller Δk, the more detailed the LWE will be. However, the calculation time of the spatial FFT scales with $\left(N_{fft}\ log\ N_{fft}\right)^2$ [19]. Taking into account that the spatial FFT must be performed for every grid point, the computational effort of this LWE algorithm increases significantly when using a high value for N_{fft}. For the results shown in Figure 13.5, N_{fft} is set at 33 samples (or 100 mm).

The bandwidth of the Hanning window BW must be large enough to allow for multiple wavelengths to propagate inside the window. On the other hand, it should be smaller than the smallest defect to allow for accurate wavenumber estimation at this defect. Rogge and Leckey advised to use a BW larger than two times the expected wavelength but smaller than the expected defect size [9]. In Al_{25mm}, the wavenumber in the 5 mm thick base material at f_s = 125 kHz is around 60 m^{-1}. This can be deduced from Figure 13.4 (a). As a result, the BW should be larger than $\frac{2}{60} = 33$ mm. As the FBH diameter is only 25 mm, the advice of Rogge and Leckey cannot be followed. As a trade-off, the BW is set at 30 mm. Only for higher sine excitation frequencies, their advice can be taken into account because the wavelength at higher frequencies becomes smaller.

Weighted Wavenumber

The dominant wavenumber in the wavenumber map corresponding to a specific grid point (Figure 13.4 (f)) is calculated using a weighted sum [10]:

$$k^{est}_{loc}(x^*,y^*) = \frac{\sum_{k_x,k_y}\left[\left|\tilde{\hat{V}}^{(x^*,y^*)}_{Z,f_s,\overline{S0}}(k_x,k_y)\right|\ \sqrt{k_x^2+k_y^2}\right]}{\sum_{k_x,k_y}\left|\tilde{\hat{V}}^{(x^*,y^*)}_{Z,f_s,\overline{S0}}(k_x,k_y)\right|}$$

Results of Standing Wave LWE based on Short-Space-Fourier-Transform
Following this standing wave LWE implementation, three LWE maps k_{loc}^{est} are constructed for both Al25mm and for $\mathrm{CFRP}_{\mathrm{Disb}}^{\mathrm{Air}}$. The maps correspond to sine excitation frequencies f_s = 50, 125 and 200 kHz. They are shown in Figure 13.6 (a-c) and in Figure 13.6 (d-f) for Al25mm and $\mathrm{CFRP}_{\mathrm{Disb}}^{\mathrm{Air}}$, respectively. The manually selected values for $k_{\overline{S0}}$, N_{fft} and BW, and the algorithm's calculation times, are listed in Table 13.2. Note that the S0 wave is not removed (i.e. $k_{\overline{S0}}$ = 0) in case of f_s = 50 kHz. At this low frequency, the piezoelectric actuator is not able to excite the S0 mode due to the high S0 mode wavelength. It took around 4.5 s and 24 s for the calculation of one k_{loc}^{est} map for Al25mm and $\mathrm{CFRP}_{\mathrm{Disb}}^{\mathrm{Air}}$, respectively. The higher calculation time for $\mathrm{CFRP}_{\mathrm{Disb}}^{\mathrm{Air}}$ is attributed to the higher number of grid points (see scan point spacing in Table 13.1).

There is a big effect of the sine excitation frequency f_s on the sensitivity of the obtained LWE maps for the various FBHs in Al25mm (see Figure 13.6 (a-c)). For f_s = 50 kHz, the three most shallow FBHs are distinguished and the size of these FBHs is significantly overestimated. A reference circle of diameter 25 mm is indicated on the figures. The overestimation of the defect's size is attributed to the chosen bandwidth of the Hanning window BW. At low sine frequencies, the BW needs to be relatively large to have at least two wavelengths inside the window. However, a large window size results in a blurring effect of the wavenumber map. For f_s = 125 kHz and for f_s = 200 kHz, some additional (deeper) FBH are detected and the size overestimation is less pronounced.
The local wavenumber at the most shallow defect is underestimated in case of f_s = 200 kHz (see Figure 13.6 (c)). This FBH has a local thickness of 0.3 mm which corresponds to a wavenumber of around 260 m^{-1} for the A0 mode at 200 kHz. The maximum observable wavenumber in this experiment is only $(1/2\Delta x)$ = 167 m^{-1}. As a result, the accurate detection of shallow defects is not possible when a high sine excitation frequency is used.
For all sine excitation frequencies, the wavenumber estimation in the damage-free base material is not accurate. For instance for f_s = 125 kHz, the estimated base material's wavenumber fluctuates in between 56 and 80 m^{-1} (k_{theory} = 60 m^{-1}).

The results for the $\mathrm{CFRP}_{\mathrm{Disb}}^{\mathrm{Air}}$ test specimen (see Figure 13.6 (d-f)) clearly reveal that none of the LWE maps can be used to identify the disbond at the stiffener. A strongly fluctuating wavenumber is also observed in the base material of the test specimen. The reduction in the wavenumber at the location of the stiffeners is only observed for the high sine excitation frequency (see Figure 13.6 (f)).

In addition to the poor quality of the LWE maps, the manual selection of N_{fft} and BW based on expected wavelengths and expected defect sizes is cumbersome and thereby further obstructs the use of this LWE implementation for NDT in an industrial environment.

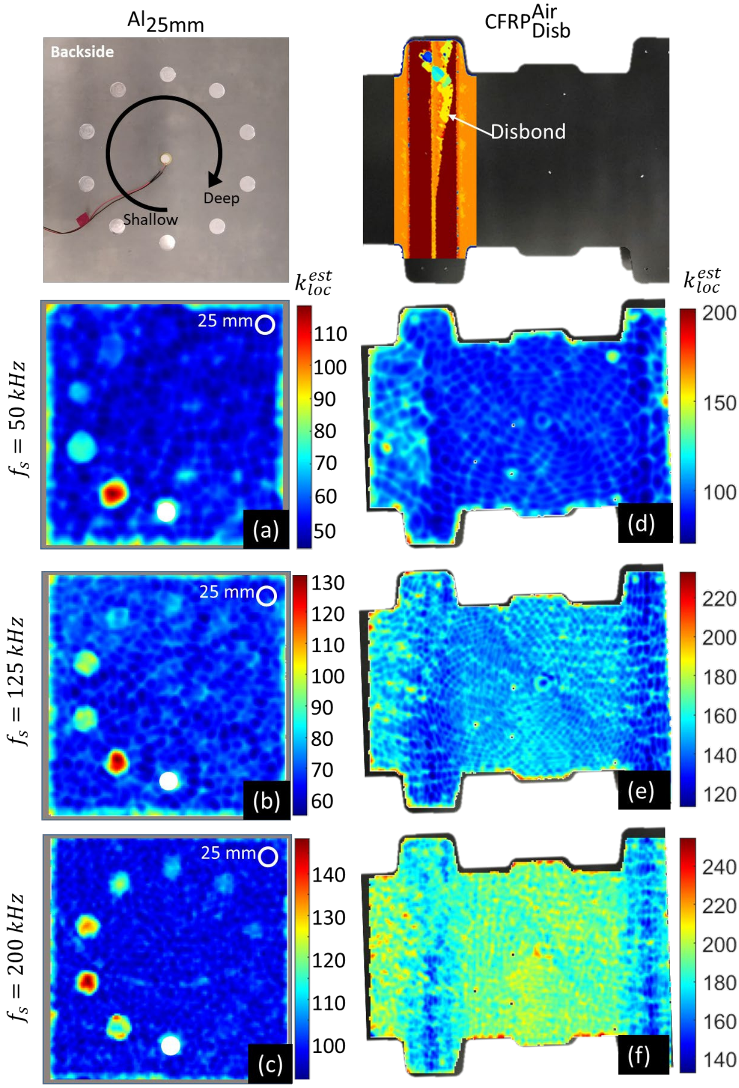

Figure 13.6: Standing wave LWE (in m^{-1}) based on short-space-Fourier-transform for (a-c) $\mathrm{Al}_{25\mathrm{mm}}$ and (d-f) $\mathrm{CFRP}_{\mathrm{Disb}}^{\mathrm{Air}}$. Sine excitation at frequency (top) 50 kHz, (middle) 125 kHz and (bottom) 200 kHz.

Table 13.2: Processing parameters corresponding to LWE based on short-space-Fourier-transform for the standing wave response in Al_{25mm} and $CFRP^{Air}_{Disb}$.

Al_{25mm}					$CFRP^{Air}_{Disb}$				
f_s	$k_{\overline{S0}}$	*BW*	N_{FFT}	*Calc. Time* (s)*	f_s	$k_{\overline{S0}}$	*BW*	N_{FFT}	*Calc. Time* (s)*
50	0	40	100	4.5	50	0	40	100	24
125	30	30	100	4.5	125	40	30	100	25
200	50	24	100	4.5	200	70	24	100	24

* Intel(R) Xeon(R) Gold 6146 CPU @ 3.20 GHz

3.2.2. Method 2: LWE based on the Wavenumber Bandpass Filter Bank

Flynn et al. proposed to use a wavenumber bandpass filter bank for LWE [11, 18]. A graphical representation of this LWE implementation is shown in Figure 13.7.

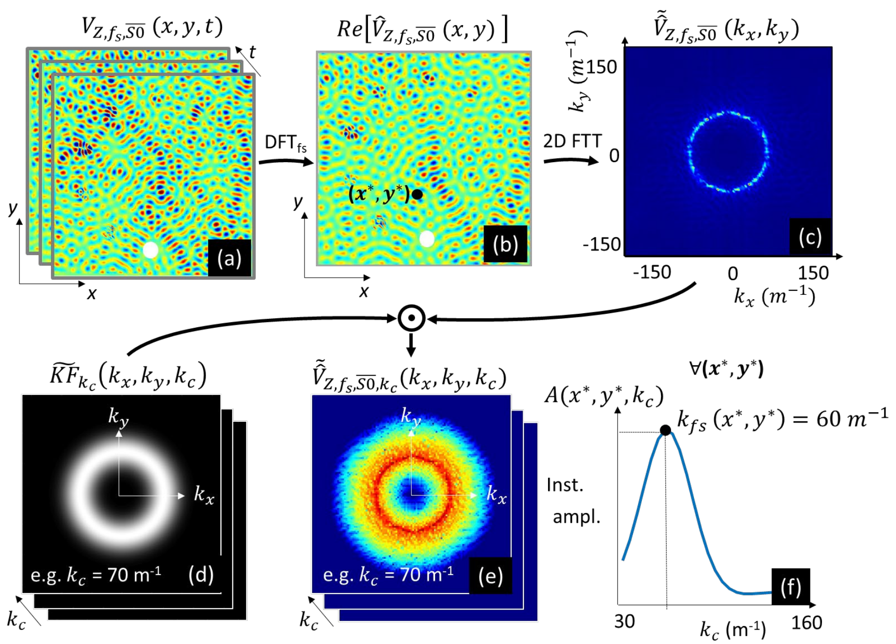

Figure 13.7: LWE for sine excitation in Al_{25mm} using a wavenumber bandpass filter bank (a) Time snapshot of the A_0 sine response, (b) Standing wavefield at f_s = 125 kHz, (c) Wavenumber map at f_s = 125 kHz, (d) Wavenumber filter bank, (e) Filtered wavenumber map and (f) Instantaneous amplitude at point (x*,y*) in function of center wavenumber.

Discrete Fourier Transform at f_s

Similar to the previously explained LWE method, the first step is to transform the A_0 mode sine response (see Figure 13.7 (a)) to one standing wavefield image. This is achieved using the discrete Fourier transformation at the sine excitation frequency f_s:

$$V_{Z,f_s,\overline{S0}}\,(x,y,t) \xrightarrow{DFT_{f_s}} \hat{V}_{Z,f_s,\overline{S0}}\,(x,y)$$

The real part of the obtained standing wavefield $\hat{V}_{Z,f_s,\overline{S0}}(x,y)$ is shown in Figure 13.7 (b) (for Al_{25mm} with f_s = 125 kHz).

The standing wavefield image $\hat{V}_{Z,f_s,\overline{S0}}(x,y)$ is converted from the spatial domain to the wavenumber domain using the spatial 2D FFT:

$$\hat{V}_{Z,f_s,\overline{S0}}\,(x,y) \xrightarrow{2D\ FFT} \tilde{\hat{V}}_{Z,f_s,\overline{S0}}(k_x,k_y)$$

The obtained wavenumber map $\tilde{\hat{V}}_{Z,f_s,\overline{S0}}(k_x,k_y)$ is shown in Figure 13.7 (c). The high intensity circle corresponds to the A_0 waves travelling in the damage-free material. Note that there is no sign of the S_0 mode because this mode was removed earlier through wavenumber filtering (see Section 3.1).

Wavenumber Bandpass Filter Bank

A bank of narrowband wavenumber bandpass filters (see also Chapter 10 Section 2.3.2) is constructed. Each filter $\widetilde{KF}_{k_c}$ is a circular Gaussian bandpass window centered at wavenumber k_c [18]:

$$\widetilde{KF}_{k_c}\big(k_x,k_y,k_c\big) = \exp\left[-\frac{\left(\sqrt{k_x^2+k_y^2}-k_c\right)}{0.72\,BW_k^2}\right] \qquad (13.4)$$

with BW_k the half-power bandwidth of the filter expressed in m^{-1}. The selection of an optimal value for bandwidth BW_k is ambiguous. Here, BW_k is set at 30 m^{-1} which is similar to the values used in [3, 18]. Filters are constructed for center wavenumbers $k_c = \left[k_{\overline{S0}} \ldots \max\,(k_x,k_y)\right]$ in steps of Δk_c = 5 m^{-1}. The selected minimum and maximum k_c values guarantee that no computational effort is wasted for the construction of filters with inappropriate center wavenumbers. The resolution of the wavenumber axis, i.e. Δk_c, can be further reduced on the expense of an increased computational effort ($O(1/\Delta k_c)$). As an example, Figure 13.7 (d) shows the wavenumber filter for k_c = 70 m^{-1}.

The wavenumber map $\tilde{\hat{V}}_{Z,f_s,\overline{S0}}(k_x,k_y)$ is ran through this filter bank:

$$\tilde{\hat{V}}_{Z,f_s,\overline{S0},k_c}\big(k_x,k_y,k_c\big) = \tilde{\hat{V}}_{Z,f_s,\overline{S0}}\big(k_x,k_y\big) \odot \widetilde{KF}_{k_c}\big(k_x,k_y,k_c\big)$$

As an example, the filtered wavenumber map for k_c = 70 m^{-1} is shown in Figure 13.7 (e) in logarithmic colorscale.

Monogenic Signal, Instantaneous Amplitude and Local Wavenumber
In order to estimate the most likely local wavenumber at every point of the specimen, the spatial distribution of the amplitude associated with specific center wavenumbers k_c has to be determined. The amplitude distribution is determined in a robust manner using the concept of the monogenic signal [18]. The monogenic signal was introduced by Felsberg and Sommer [20] as the multi-dimensional extension of the analytic signal.

The monogenic signal representation of the wavenumber map $\tilde{\tilde{V}}_{Z,f_s,\overline{S0},k_c}(k_x,k_y,k_c)$ at a specific center wavenumber k_c has three components:

$$\begin{cases} \widetilde{g_0}(k_x,k_y,k_c) = \tilde{V}_{Z,f_s,\overline{S0},k_c}(k_x,k_y,k_c) \\ \widetilde{g_1}(k_x,k_y,k_c) = \dfrac{-i\,k_x}{\sqrt{k_x^2+k_y^2}}\tilde{V}_{Z,f_s,\overline{S0},k_c}(k_x,k_y,k_c) \\ \widetilde{g_2}(k_x,k_y,k_c) = \dfrac{-i\,k_y}{\sqrt{k_x^2+k_y^2}}\tilde{V}_{Z,f_s,\overline{S0},k_c}(k_x,k_y,k_c) \end{cases} \quad \text{for every } k_c$$

The instantaneous amplitude $A(x,y,k_c)$ is found as:

$$A(x,y,k_c) = \sqrt{g_0^2(x,y,k_c) + g_1^2(x,y,k_c) + g_2^2(x,y,k_c)} \quad \text{for every } k_c$$

with g_0, g_1, g_2 the real parts of the inverse spatial FFT of $\widetilde{g_0}, \widetilde{g_1}, \widetilde{g_2}$.

At last, the local wavenumber is found as the center wavenumber for which the instantaneous amplitude is maximal:

$$k_{loc}^{est}(x,y) = \underset{k_c}{\mathrm{ArgMax}}[A(x,y,k_c)]$$

This last step is illustrated in Figure 13.7 (f) for the grid point (x^*,y^*) indicated with the black dot on Figure 13.7 (b).

Results of Standing Wave LWE using Wavenumber Bandpass Filter Bank
Again, three k_{loc}^{est} maps are constructed for $\mathrm{Al}_{25\mathrm{mm}}$ and for $\mathrm{CFRP}_{\mathrm{Disb}}^{\mathrm{Air}}$ corresponding to sine excitation frequencies f_s = 50, 125 and 200 kHz (see Figure 13.8). The selected values for $k_{\overline{S0}}$, Δk_c and BW_k, and the resulting calculation times, are listed in Table 13.3. It took only 1.3 s and 2.5 s for the calculation of each k_{loc}^{est} map for $\mathrm{Al}_{25\mathrm{mm}}$ and $\mathrm{CFRP}_{\mathrm{Disb}}^{\mathrm{Air}}$, respectively.

The obtained wavenumber maps are of improved quality compared to the LWE maps based on the short-space-Fourier-transform (see Figure 13.6). In addition, the calculation time is extremely short.
For $\mathrm{Al}_{25\mathrm{mm}}$, all FBHs can be identified as regions of increased wavenumbers when using a standing wave excitation of 125 kHz or 200 kHz. However, note again that the most shallow defect cannot be accurately detected at high excitation frequencies. The overestimation of the defect's size is limited, but the area of increased wavenumber is far from a perfect circle. For the damage-free base

material, the estimated wavenumber is correct except at the edges. In addition, an arc-shaped artifact resulting from the SLDV scanning procedure is observed in the k_{loc}^{est} map f_s = 200 kHz (see dashed white line in Figure 13.8 (c)).

Although the result for $\mathrm{Al_{25mm}}$ are promising, the detection of the disbond in $\mathrm{CFRP_{Disb}^{Air}}$ from Figure 13.8 (d-f) remains difficult. The wavenumber maps appear noisy which is attributed to the anisotropic material properties and to the lower signal-to-noise ratio of the $\mathrm{CFRP_{Disb}^{Air}}$ measurement (compared to the signal-to-noise ratio for $\mathrm{Al_{25mm}}$). A detailed explanation of the effect of anisotropy on LWE is provided in Section 5.3.2.

Table 13.3: Processing parameters corresponding to standing wave LWE using wavenumber bandpass filter bank for $\mathrm{Al_{25mm}}$ and $\mathrm{CFRP_{Disb}^{Air}}$.

$\mathrm{Al_{25mm}}$					$\mathrm{CFRP_{Disb}^{Air}}$				
f_s	$k_{\overline{S0}}$	Δk_c	BW_k	*Calc. Time* (s)*	f_s	$k_{\overline{S0}}$	Δk_c	BW_k	*Calc. Time* (s)*
50	0	5	30	1.4	50	0	5	30	2.5
125	30	5	30	1.3	125	40	5	30	2.6
200	50	5	30	1.3	200	70	5	30	2.3

* Intel(R) Xeon(R) Gold 6146 CPU @ 3.20 GHz

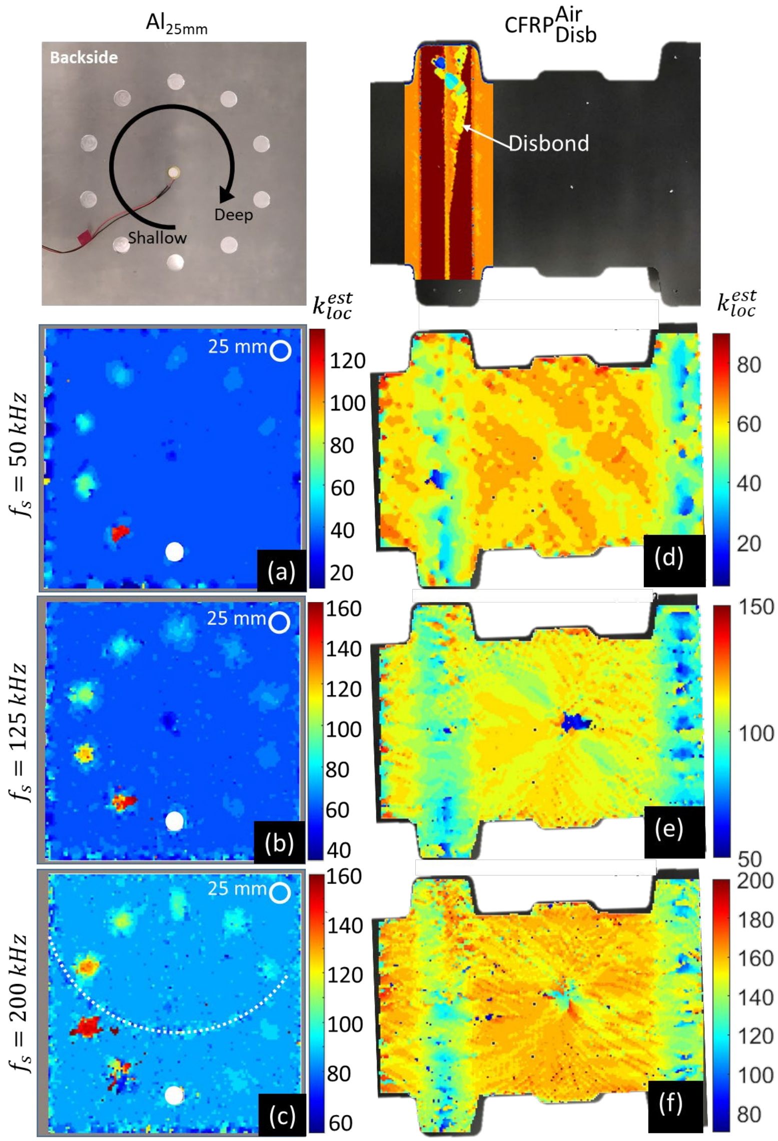

Figure 13.8: Standing wave LWE (in m^{-1}) based on a wavenumber bandpass filter bank for (a-c) Al_{25mm} and (d-f) for $CFRP_{Disb}^{Air}$. Sine excitation at frequency (top) 50 kHz, (middle) 125 kHz and (bottom) 200 kHz.

4. Local Wavenumber Estimation for Toneburst Excitation

Similar to previous section, two well-known LWE implementations from literature are considered, but this time for toneburst responses [3, 9]. The experimentally obtained sweep responses $V_Z(x,y,t)$ are converted to the required toneburst responses $V_{Z,f_c}(x,y,t)$ using the frequency-filtering procedure discussed in Chapter 10 Section 2.2:

$$V_Z(x,y,t) \xrightarrow{Freq.Filt.;\, U_{f_c}(t)} V_{Z,f_c}(x,y,t)$$

A five-cycle Hanning windowed sine signal is chosen for the desired toneburst waveform $U_{f_c}(t)$. For both Al_{25mm} and $CFRP_{Disb}^{Air}$, three toneburst responses are calculated with center frequencies f_c = 50, 125 and 200 kHz. This allows to evaluate the effect of the center frequency on the LWE map. The time and frequency spectrum of the 125 kHz toneburst is shown in Figure 13.9 (a) and (b), respectively.

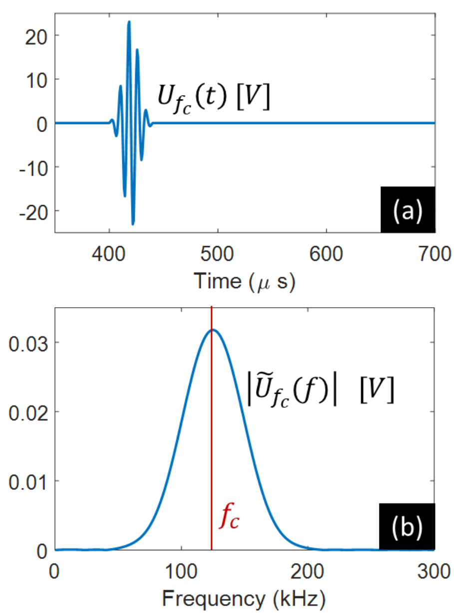

Figure 13.9: (a) Time and (b) frequency spectrum of a five-cycle Hanning windowed toneburst response with center frequency f_c = 125 kHz.

4.1. Wavenumber Filtering for A_0 Mode Extraction

The vibrations attributed to the S_0 mode are removed from the toneburst response in a similar way as done for the standing wave response (see Section 3.1). First, the toneburst response is transformed to the wavenumber-frequency domain using 3D FFT:

$$V_{Z,f_c}\,(x,y,t) \xrightarrow{3D\ FFT} \tilde{V}_{Z,f_c}\,(k_x,k_y,f)$$

Figure 13.10 (a) shows the resulting wavenumber map at the toneburst's center frequency f_c = 125 kHz in Al_{25mm}. The wavenumber map summed over all frequency bins is shown in Figure 13.10 (b). The slowness curves of the A_0 and S_0 modes are indicated. Based on these wavenumber maps, the cutoff wavenumber $k_{\overline{S0}}$ is selected and the wavenumber bandstop filter $KF_{\overline{S0}}$ is constructed using Eq. (13.2) (see Figure 13.10 (c)). The cutoff wavenumber $k_{\overline{S0}}$ is set at 30 m^{-1} for the toneburst response with f_c = 125 kHz in Al_{25mm}. The filtered toneburst response $\tilde{V}_{Z,f_c,\overline{S0}}(k_x,k_y,f)$ (see Figure 13.10 (d)) is obtained by element-wise multiplication of the wavenumber filter with the toneburst response in the wavenumber domain:

$$\tilde{V}_{Z,f_c,\overline{S0}}\big(k_x,k_y,f\big) = \tilde{V}_{Z,f_c}\,(k_x,k_y,f) \odot KF_{\overline{S0}}\big(k_x,k_y,f\big)$$

At last, inverse 3D FFT is used to transform the filtered result back to the spatial-time domain:

$$\tilde{V}_{Z,f_c,\overline{S0}}\big(k_x,k_y,f\big) \xrightarrow{3D\ IFFT} \tilde{V}_{Z,f_c,\overline{S0}}(x,y,t)$$

The effect of this wavenumber bandstop filtering procedure is illustrated in Figure 13.11. Figure 13.11 (a) shows a time snapshot at t = 0.45 ms of the unfiltered toneburst response with f_c = 125 kHz in Al_{25mm}. The wavefronts of the fast S_0 mode and slower A_0 modes are indicated. The snapshot obtained after applying the wavenumber bandstop filter is shown in Figure 13.11 (b). The S_0 mode is successfully removed without affecting the A_0 mode.

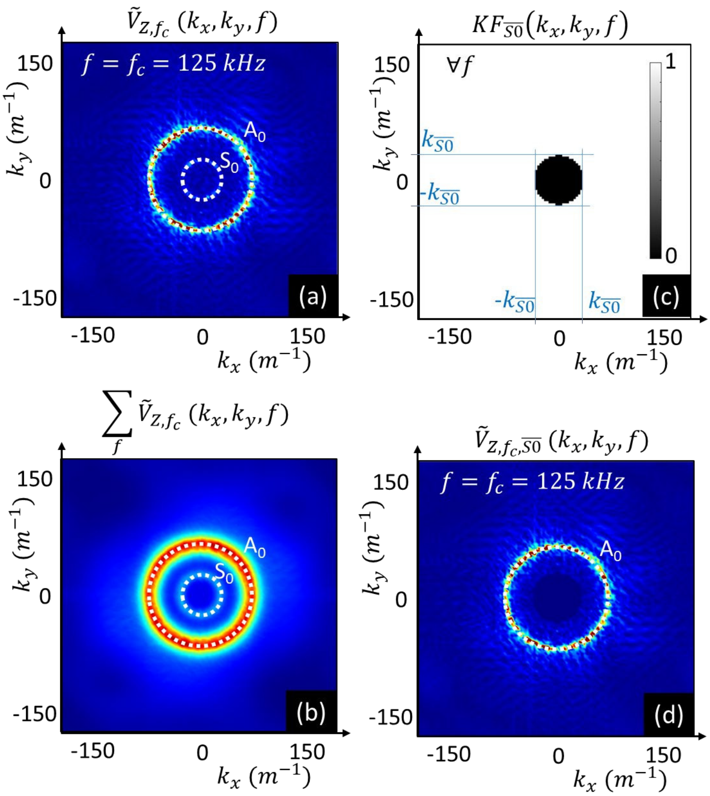

Figure 13.10: S_0 mode vibration removal in Al_{25mm}: (a) Wavenumber map at toneburst center frequency $f = f_c = 125$ kHz, (b) Summed wavenumber map, (c) Wavenumber bandstop filter and (d) Filtered wavenumber map at toneburst center frequency.

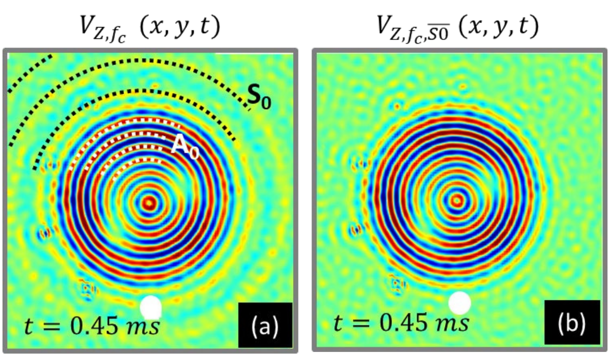

Figure 13.11: Snapshots of the toneburst response (f_c = 125 kHz) in Al_{25mm} (a) Unfiltered and (b) S_0 mode wavenumber bandstop filtered.

4.2. Construction of the Toneburst Wavenumber Map

4.2.1. Method 1: LWE based on the Short-Space-Fourier-Transform

Rogge and Leckey proposed to use the short-space-Fourier-transform for LWE in toneburst responses [9]. A graphical representation of this LWE implementation is shown in Figure 13.12. The implementation is highly similar to the LWE algorithm for standing wave responses that was discussed in Section 3.2.1.

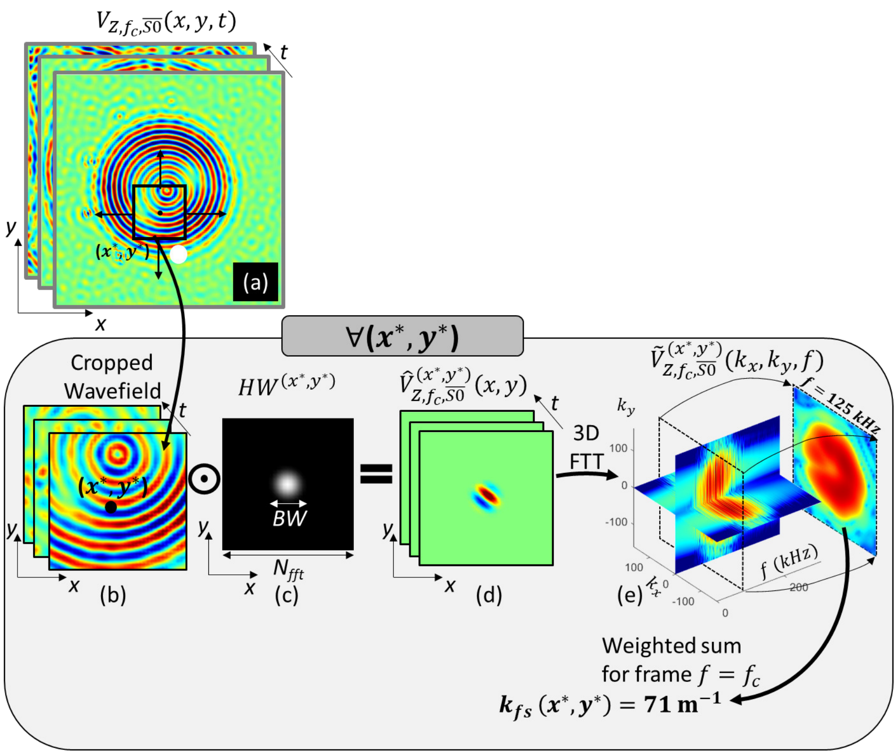

Figure 13.12: LWE for toneburst excitation in Al_{25mm} using short-space-Fourier-transform (a) Time snapshots of A_0 mode toneburst response, (b) Cropped toneburst response at scan point of interest, (c) Spatial Hanning window, (d) Cropped and windowed wavefield and (e) Wavenumber-frequency maps at scan point of interest.

Short-Space-Fourier-Transform

Figure 13.12 (a) shows a few snapshots of the A_0 mode's toneburst response $V_{Z,f_c,\overline{S0}}(x,y,t)$. First, a square area is cropped out of this toneburst response. The area is centered at the grid point for which the wavenumber is estimated and has width and height N_{fft} (expressed in number of grid points). Figure 13.5 (b) shows the cropped toneburst response for a grid point at (x^*,y^*) indicated with the black dot. Second, a spatial Hanning window with bandwidth BW is constructed (see Figure 13.5 (c)) and multiplied with the cropped out wavefield:

$$V_{Z,f_c,\overline{S0}}^{(x^*,y^*)}(x,y,t) = V_{Z,f_c,\overline{S0}}(x,y,t) \odot HW^{(x^*,y^*)}(x,y)$$

The result is shown in Figure 13.5 (d). At last, the local wavenumber-frequency map is obtained using 3D FFT transformation (see Figure 13.5 (e)):

$$V_{Z,f_c,\overline{S0}}^{(x^*,y^*)}(x,y,t) \xrightarrow{3D\ FFT} \tilde{V}_{Z,f_c,\overline{S0}}^{(x^*,y^*)}\left(k_x,k_y,f\right)$$

The superscript (x^*,y^*) indicates the local character of the wavenumber map.

Note again that a proper selection for the window size N_{fft} and bandwidth BW is of great importance. A detailed discussion and practical guidelines were already provided in Section 3.2.1.

Weighted Wavenumber

The wavenumber map at the toneburst center frequency $f = f_c$ is extracted from the dataset $\tilde{V}_{Z,f_c,\overline{S0}}^{(x^*,y^*)}\left(k_x,k_y,f\right)$. The dominant local wavenumber is calculated using the weighted sum [9]:

$$k_{loc}^{est}(x^*,y^*) = \frac{\sum_{k_x,k_y}\left[\left|\tilde{V}_{Z,f_c,\overline{S0}}^{(x^*,y^*)}\left(k_x,k_y,f_c\right)\right| \sqrt{k_x^2+k_y^2}\right]}{\sum_{k_x,k_y}\left|\tilde{V}_{Z,f_c,\overline{S0}}^{(x^*,y^*)}\left(k_x,k_y,f_c\right)\right|}$$

Results of Toneburst LWE using Short-Space-Fourier-Transform

Following this LWE implementation, three k_{loc}^{est} maps are constructed for $\mathrm{Al}_{25\mathrm{mm}}$ corresponding to toneburst center frequencies f_c = 50, 125 and 200 kHz. The LWE maps are shown in Figure 13.13. The selected values for $k_{\overline{S0}}$, N_{fft} and BW, and the resulting calculation times, are listed in Table 13.4.

The results are almost identical to those in Figure 13.6 (a-c). This could have been expected as the workflow for construction of the LWE maps for these toneburst responses (see Figure 13.12) is similar to the workflow proposed for construction of the standing wave LWE maps (see Figure 13.5). The only difference is that for the case of a standing wavefield response, the three-dimensional dataset is transformed to a two-dimensional wavefield (at the sine excitation frequency) at the start of the algorithm. Whereas for this toneburst response, the 3D to 2D conversion is only performed at the very end, upon calculation of the weighted wavenumber. As a result, calculation times for this toneburst LWE map are significantly higher, i.e. more than 5 minutes. The high computational effort in combination with the relatively poor quality of the obtained LWE maps are important drawbacks of this LWE implementation. As such, the maps for $\mathrm{CFRP}_{\mathrm{Disb}}^{\mathrm{Air}}$ were not derived.

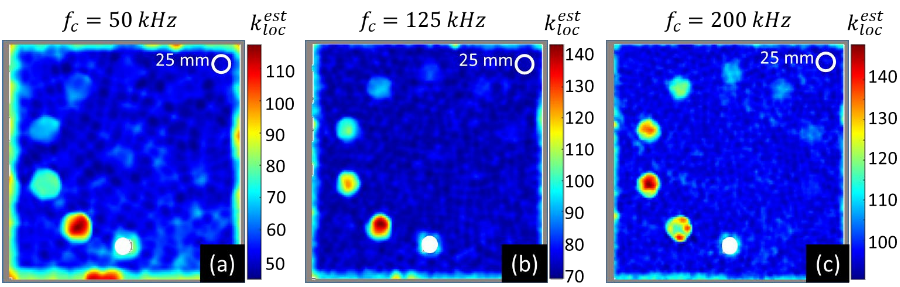

Figure 13.13: LWE (in m^{-1}) based on the short-space-Fourier-transform for Al_{25mm} excited with a toneburst with center frequency (a) 50 kHz, (b) 125 kHz and (c) 200 kHz.

Table 13.4: Processing parameters corresponding to toneburst LWE using short-space-Fourier-transform for Al_{25mm}.

		Al_{25mm}		
f_s	$k_{\overline{S0}}$	*BW*	N_{FFT}	*Calc. Time* (s)*
50	0	40	100	330
125	30	30	100	339
200	50	24	100	389

* Intel(R) Xeon(R) Gold 6146 CPU @ 3.20 GHz

4.2.2. Method 2: LWE based on Wavenumber Bandpass Filter Bank

Flynn et al. [3] proposed to use a wavenumber bandpass filter bank for LWE in toneburst responses. A graphical representation of this LWE implementation is provided in Figure 13.14. The algorithm is similar to the implementation used for standing wave responses (i.e. Figure 13.7) with the difference that it is now operated in the wavenumber-frequency domain instead of the wavenumber domain.

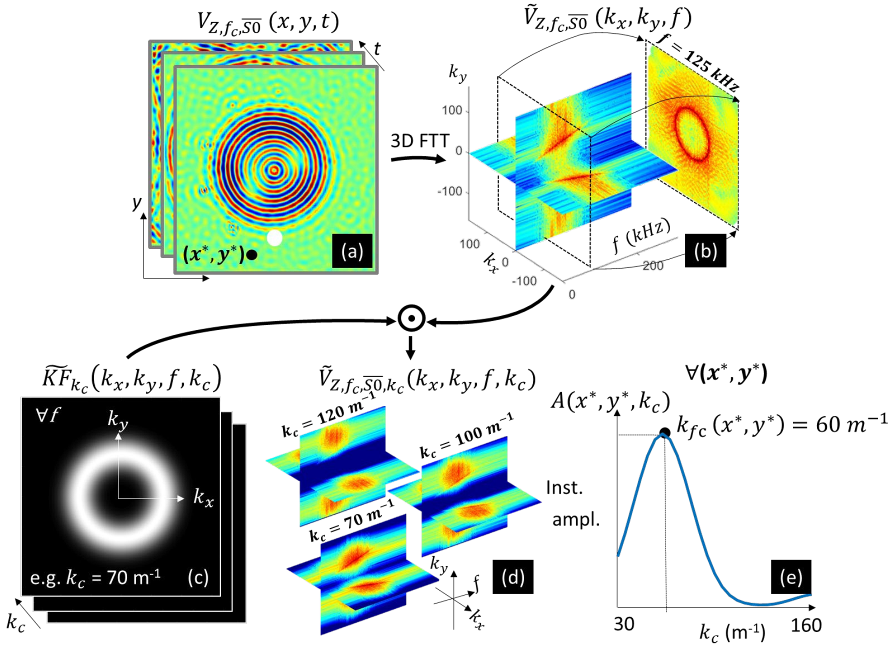

Figure 13.14: LWE for toneburst excitation in Al_{25mm} based on a wavenumber bandpass filter bank (a) Time snapshots of A_0 mode toneburst response with f_c = 125 kHz, (b) Wavenumber-frequency representation, (c) Wavenumber filter bank, (d) Filtered wavenumber-frequency maps and (e) Instantaneous amplitude at point (x^*,y^*) in function of center wavenumber.

Wavenumber Filter Bank

First, the A_0 mode's toneburst response (see Figure 13.14 (a)) is transformed to the wavenumber-frequency domain using 3D FFT:

$$V_{Z,f_c,\overline{S0}}(x,y,t) \xrightarrow{3D\ FFT} \tilde{V}_{Z,f_c,\overline{S0}}(k_x,k_y,f)$$

Figure 13.14 (b) shows a 3D representation of the resulting dataset in logarithmic colorscale.

Second, a narrowband wavenumber bandpass filter bank $\widetilde{KF}_{k_c}$ is constructed as done before using Eq. (13.4). The half-power bandwidth of the filter BW_k is set at 30 m^{-1} (similar to [3, 18]). Filters are constructed corresponding to center wavenumbers $k_c = [k_{\overline{S0}} \ldots \max(k_x,k_y)]$ in steps of Δk_c = 5 m^{-1}. The filter is repeated at every frequency bin resulting in a 4D filter bank $\widetilde{KF}_{k_c}(k_x,k_y,f,k_c)$. As an example, Figure 13.14 (c) shows the frequency-invariant wavenumber filter for k_c = 70 m^{-1}.

The A_0 mode's toneburst dataset $\tilde{V}_{Z,f_c,\overline{S0}}(k_x,k_y,f)$ is ran through this wavenumber bandpass filter bank:

$$\tilde{V}_{Z,f_c,\overline{S0},k_c}(k_x,k_y,f,k_c)=\tilde{V}_{Z,f_c,\overline{S0}}(k_x,k_y,f)\odot\widetilde{KF}_{k_c}(k_x,k_y,f,k_c)$$

As an example, a 3D representations of the filtered datasets $\tilde{V}_{Z,f_c,\overline{S0},k_c}(k_x,k_y,f,k_c)$ is given in Figure 13.14 (d) for k_c = 70, 100 and 120 m^{-1}.

Monogenic Signal, Instantaneous Amplitude and Local Wavenumber

As done before, the spatial distribution of the amplitude associated with specific center wavenumbers k_c is calculated using the monogenic signal representation. The monogenic signal representation of the dataset $\tilde{V}_{Z,f_c,\overline{S0},k_c}(k_x,k_y,f,k_c)$ at a specific center wavenumber k_c has four components:

$$\begin{cases}\widetilde{g_0}(k_x,k_y,f,k_c)=\tilde{V}_{Z,f_c,\overline{S0},k_c}(k_x,k_y,f,k_c)\\ \widetilde{g_1}(k_x,k_y,f,k_c)=\dfrac{-i\,k_x}{\sqrt{k_x^2+k_y^2+f^2}}\tilde{V}_{Z,f_c,\overline{S0},k_c}(k_x,k_y,f,k_c)\\ \widetilde{g_2}(k_x,k_y,f,k_c)=\dfrac{-i\,k_y}{\sqrt{k_x^2+k_y^2+f^2}}\tilde{V}_{Z,f_c,\overline{S0},k_c}(k_x,k_y,f,k_c)\\ \widetilde{g_3}(k_x,k_y,f,k_c)=\dfrac{-i\,f}{\sqrt{k_x^2+k_y^2+f^2}}\tilde{V}_{Z,f_c,\overline{S0},k_c}(k_x,k_y,f,k_c)\end{cases}\quad\text{for every } k_c$$

The instantaneous amplitude A is found as [3]:

$$A(x,y,k_c)=\sum_t\sqrt{g_0^2(x,y,t,k_c)+g_1^2(x,y,t,k_c)+g_2^2(x,y,t,k_c)+g_3^2(x,y,t,k_c)}$$

with g_0,g_1,g_2,g_3 the real parts of the inverse 3D FFT of $\widetilde{g_0},\widetilde{g_1},\widetilde{g_2},\widetilde{g_3}$.

At last, the local wavenumber is found as the center wavenumber for which the instantaneous amplitude is maximal:

$$k_{loc}^{est}(x,y)=\underset{k_c}{\mathrm{ArgMax}}[A(x,y,k_c)]$$

This last step is illustrated in Figure 13.14 (e) for the point (x^*,y^*) indicated with the black dot on Figure 13.14 (a).

Results of Toneburst LWE using Wavenumber Bandpass Filter Bank

The k_{loc}^{est} maps for Al_{25mm} and for $CFRP_{Disb}^{Air}$ excited with a toneburst of center frequencies f_c = 50, 125 and 200 kHz are shown in Figure 13.15. The algorithm's selected values for $k_{\overline{S0}}$, Δk_c and BW_k and the resulting calculation times are listed in Table 13.5.

The obtained k_{loc}^{est} maps are of improved quality compared to the k_{loc}^{est} maps derived for standing wave excitation using the wavenumber bandpass filter bank method (see Figure 13.8). The local areas of increased wavenumber at the FBHs in Al_{25mm} are more circular. In addition, the wavenumber estimation in the damage-free base material is more uniform. The improved sensitivity to damage comes at the expense of an increase in the computational effort (see Table 13.5).

There is still a significant effect of the selected toneburst center frequency on the obtained k_{loc}^{est} map. The deepest FBHs are not distinguished in the k_{loc}^{est} map for f_c = 50 kHz. They pop up when considering high center frequencies, such as f_c = 200 kHz. On the other hand, at these high frequencies the background non-uniformity increases and the wavenumber estimation at the most shallow defect becomes inaccurate.

The disbond in $\mathrm{CFRP}_{\mathrm{Disb}}^{\mathrm{Air}}$ is best revealed in the k_{loc}^{est} map corresponding to f_c = 125 kHz (i.e. Figure 13.15 (b)). The extent of the disbond (obtained from ultrasonic C-scan, see Figure 13.2 (b)) is indicated with a dashed line. Over the area of the disbond, the local wavenumber is estimated to be similar to the local wavenumber estimated for the damage-free material. This indicates that the backside stiffener is locally disbonded from the base plate.

Table 13.5: Processing parameters corresponding to LWE based on a wavenumber bandpass filter bank for toneburst excited $\mathrm{Al}_{25\mathrm{mm}}$ and $\mathrm{CFRP}_{\mathrm{Disb}}^{\mathrm{Air}}$.

$\mathrm{Al}_{25\mathrm{mm}}$					$\mathrm{CFRP}_{\mathrm{Disb}}^{\mathrm{Air}}$				
f_s	$k_{\overline{S0}}$	Δk_c	BW_k	*Calc. Time* (s)*	f_s	$k_{\overline{S0}}$	Δk_c	BW_k	*Calc. Time* (s)*
50	0	5	30	48	50	0	5	30	68
125	30	5	30	43	125	40	5	30	74
200	50	5	30	37	200	70	5	30	96

* Intel(R) Xeon(R) Gold 6146 CPU @ 3.20 GHz

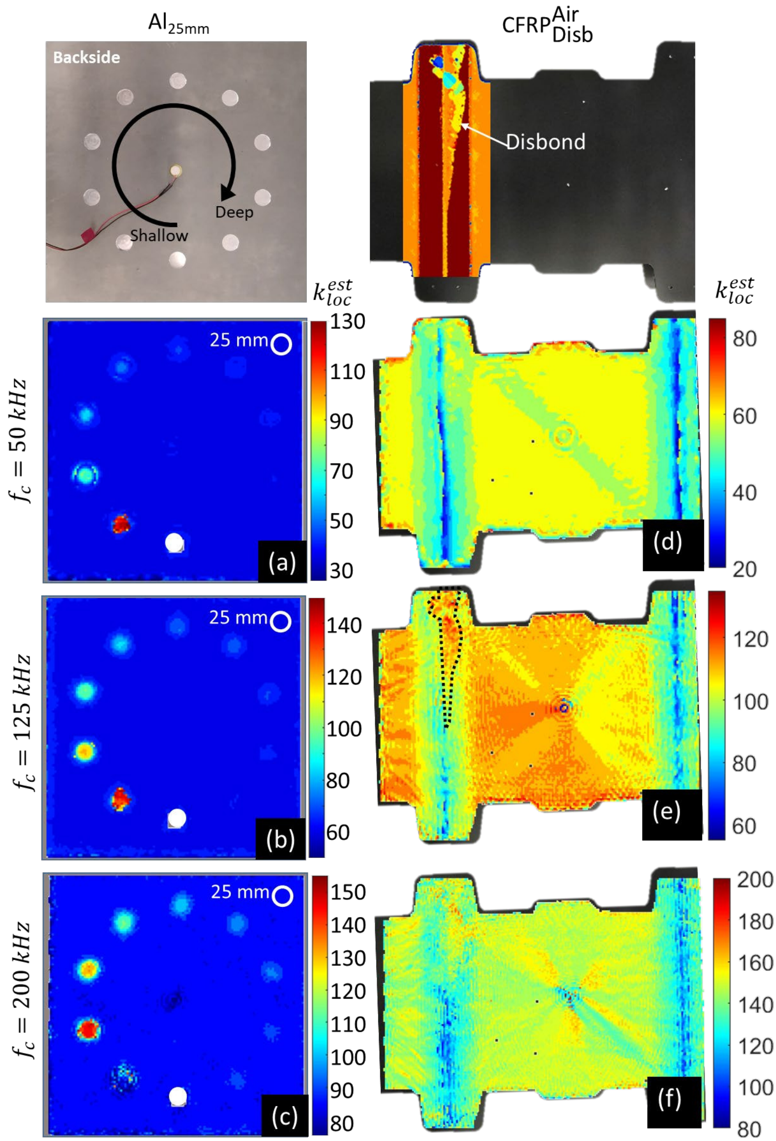

Figure 13.15: Toneburst LWE (in m^{-1}) based on wavenumber bandpass filter bank for (a-c) Al_{25mm} and (d-f) for $CFRP^{Air}_{Disb}$. Toneburst center frequency (top) 50 kHz, (middle) 125 kHz and (bottom) 200 kHz.

5. Self-reference Broadband Local Wavenumber Estimation SRB-LWE

The LWE maps obtained using the traditional LWE implementation suffer from some important disadvantages. First, there is the large effect of the selected excitation's center frequency on the obtained local wavenumber map. This necessitates the construction of multiple damage maps for different center frequencies. Next, processing parameters (such as filter bandwidths) have to be manually selected, and are often manually optimized, to achieve satisfying results. At last, the obtained LWE maps reveal the damage as areas of increased wavenumber, but do not by themselves provide information on the depth of these defects. As a solution, a self-reference broadband LWE (SRB-LWE) implementation is proposed [1]. This novel SRB-LWE implementation was developed during this PhD work and is therefore discussed in greater detail compared to the previously discussed traditional LWE implementations.

The SRB-LWE algorithm consists of multiple signal processing steps that are explained in separate subsections. As an additional aid in understanding the SRB-LWE procedure, a flow chart is provided in which all separate steps, and a selection of the intermediate results, are presented (see Figure 13.16). The intermediate results correspond to the measurement dataset of the aluminum plate with FBHs of diameter 25 mm (Al_{25mm}).

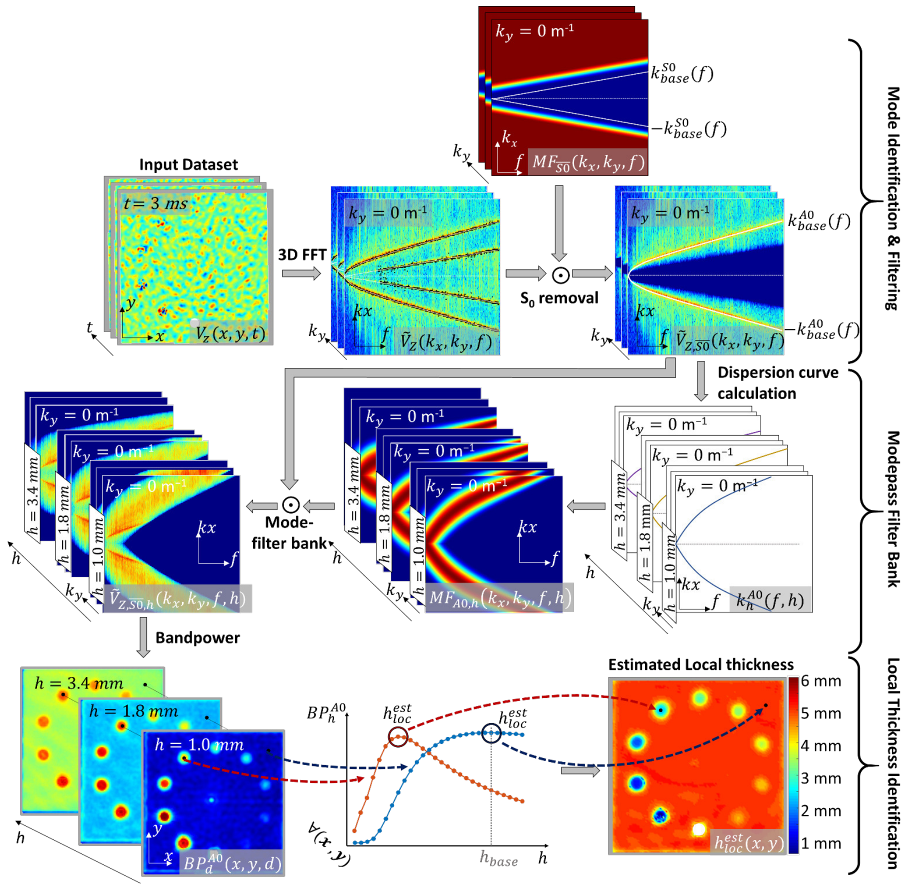

Figure 13.16: Flow chart of the proposed self-reference broadband local wavenumber estimation (SRB-LWE) algorithm.

5.1. Mode Identification and Filtering

Similar to the previously discussed LWE methods, the SRB-LWE procedure is performed for the A_0 mode. As a result of the broadband nature of the input dataset, i.e. the sweep response, a modestop filter is employed (instead of a wavenumber bandstop filter) in order to remove the vibrations attributed to the other mode(s). The idea behind modestop filtering was already discussed in Chapter 10 Section 2.4. This first step corresponds to the first row in the flow chart shown in Figure 13.16.

Note again that the A_0 mode is chosen as the mode of interest because of the high depth sensitivity of the A_0 mode in the excited frequency range (see also Figure 13.1 (b)). In addition, the A_0 mode is less affected by the potential anisotropic nature of the test specimen (compared to the S_0 mode), which simplifies the design of the filter bank in wavenumber-frequency domain. A discussion about the effect of anisotropy on the proposed SRB-LWE method is provided in Section 5.2.2.

5.1.1. Dispersion Curve Identification.

Assuming unknown material properties, the dispersion curves must first be identified from the broadband measurement result. The reader is referred back to Chapter 10 Section 2.4.1 for the detailed explanation of this dispersion curve identification procedure. A short summary is provided below.

Figure 13.17 (a) shows a 3D representation (in logarithmic colorscale) of the out-of-plane sweep response $\tilde{V}_Z(k_x, k_y, f)$ in the wavenumber-frequency domain (obtained through 3D FFT). The dispersion curves of the A_0 and S_0 modes pop-up as lines of increased intensity. It is assumed that the area of the defected material is significantly smaller compared to the area of the damage-free base material. Under this assumption, the dispersion curves seen in Figure 13.17 (a) correspond in good approximation to the damage-free base material. Automated identification of the dispersion curves is achieved through the iterative curve detection procedure outlined in Chapter 10 Section 2.4.1. Figure 13.17 (b) shows the identified curve points (black dots) as well as the resulting mode curves, $k_{base}^{A0}(f)$ and $k_{base}^{S0}(f)$ (along k_y = 0).

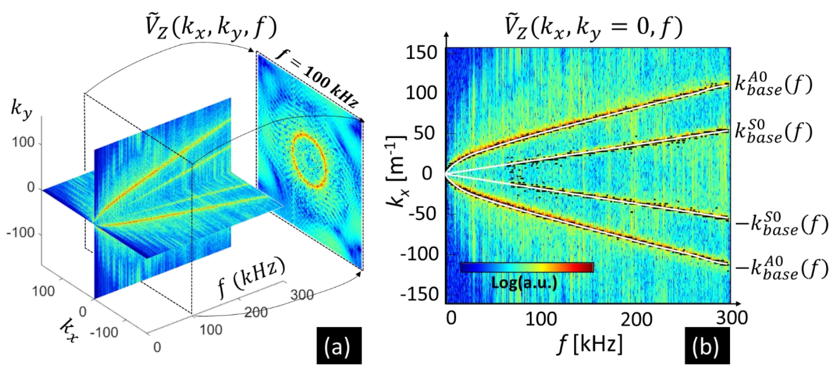

Figure 13.17: Out-of-plane velocity response in Al_{25mm} (a) 3D wavenumber-frequency map, (b) Wavenumber-frequency map along k_y = 0, together with the identified dispersion curves of the A_0 and S_0 Lamb modes.

5.1.2. Modestop Filtering for A_0 Mode Extraction

The vibrations corresponding to the S_0 mode are removed from the dataset using a frequency-dependent modestop filter in the wavenumber-frequency domain (see also Chapter 10 Section 2.4.3). The mode filter $MF_{\overline{S0}}$ is Tukey-shaped and constructed around the identified S_0 dispersion curve $k_{base}^{S0}(f)$:

$$MF_{\overline{S0}}(k_x, k_y, f) = \begin{cases} 0 & \text{if } D(k_r, f) \leq FT \\ \frac{1}{2} - \frac{1}{2}\cos\left(\frac{2\pi(D(k_r, f) - FT)}{BW_{S0}}\right) & \text{if } FT < D(k_r, f) < FT + \frac{BW_{S0}}{2} \\ 1 & \text{if } D(k_r, f) \geq FT + \frac{BW_{S0}}{2} \end{cases}$$

$$\text{with} \quad k_r = \sqrt{k_x^2 + k_y^2}, \quad D(k_r, f) = \left|k_r - k_{base}^{S0}(f)\right|$$

where FT is the flat top length and BW_{S0} is the half-power bandwidth of the cosine lobe. The following filter parameters are used FT = 5 m^{-1} and BW_{S0} = 10 m^{-1} which leads to the removal of the vibrations related to the S_0 mode, as well as the removal of the noise associated with very low wavenumbers. These filter parameter values are also applicable for other materials or other base material thicknesses. The filter is shown in Figure 13.18 (a).

The required A_0 mode response is obtained after element-wise multiplication of the modestop filter $MF_{\overline{S0}}$ with the out-of-plane velocity response $\tilde{V}_z$ in the wavenumber-frequency domain (see Figure 13.18 (b)):

$$\tilde{V}_{Z,\overline{S0}}(k_x, k_y, f) = MF_{\overline{S0}}(\mathrm{k_x}, \mathrm{k_y}, \mathrm{f}) \odot \tilde{V}_Z(k_x, k_y, f)$$

It is also possible to obtain the required A_0 mode response using a mode<u>pass</u> filter constructed around the A_0 mode curve (instead of a mode<u>stop</u> filter around the S_0 mode curve). However, the authors advise against this approach because the selection of the bandpass filter's bandwidth would become critical. If the A_0 bandpass filter's bandwidth is set too low, the filter would partially remove vibrations at the defects, resulting in an inferior damage map and potentially even missing the deep defects. On the other hand, if the bandwidth is set too high, the filter can allow vibrations of the S_0 mode to pass, which would also result in an inferior damage map.

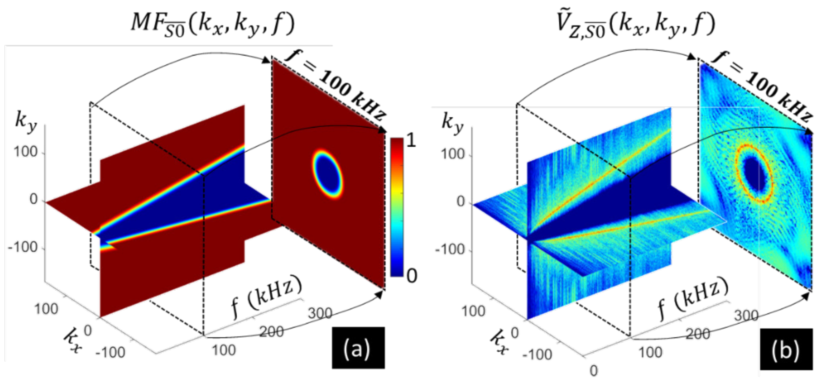

Figure 13.18: 3D view of (a) S_0 modestop filter and (b) Wavenumber-frequency map for the out-of-plane velocity response in Al_{25mm} after applying the S_0 modestop filter.

5.2. Construction of the Local Thickness Map

5.2.1. Modepass Filter Bank

The next big step in the SRB-LWE algorithm is the construction and application of a modepass filter bank (see second row in the flow chart of Figure 13.16).

The dispersion curve of the mode of interest (i.e. $[f, k_{base}^{A0}]$, as identified in previous section) corresponds to the dispersion behavior of the damage-free base material with material thickness $h = h_{base}$. The dispersion curves corresponding to the same material but with a different thickness h are derived from $[f, k_{base}^{A0}]$ using a scaling procedure along both the frequency and the wavenumber axis:

$$[f, k_{base}^{A0}] \overset{h}{\Rightarrow} \left[\frac{f\,.\,h_{base}}{h}, \frac{k_{base}^{A0}\,.\,h_{base}}{h}\right] \Rightarrow [f, k_h^{A0}] \tag{13.5}$$

This derivation is based on the thickness invariance of the dispersion curves when plotted on a $k.h$ versus $f.h$ coordinate system (see also Figure 13.1 (a)). The assumptions connected to the use of Eq. (13.5) are discussed in Section 5.2.2. For the aluminum plate with FBHs, the dispersion curves are calculated for assumed material thicknesses h = 0.2 mm, 0.4 mm … 6 mm. Figure 13.19 (a) shows the obtained dispersion curve for the A_0 mode in aluminum with thickness h = 3 mm, derived from $[f, k_{base}^{A0}]$ using Eq. (13.5). In addition, the theoretical dispersion curve is included that is calculated using Eq. (13.1) with material properties obtained from the manufacturer (i.e. Lamé constants: λ = 56.4 GPa, μ = 26.15 GPa and density ρ = 2693 kg/m3). Excellent agreement between both curves is observed, confirming the proposed self-reference approach. Figure 13.19 (b) shows a selection of dispersion curves for various thicknesses. Note again that the wavenumber increases when the thickness h is reduced and that the distance between the different dispersion curves becomes smaller for higher material thicknesses.

A cosine-shaped modepass filter is constructed around each thickness-specific dispersion curve k_h^{A0}:

$$MF_{A0,h}(k_x, k_y, f, h) = \begin{cases} \frac{1}{2} + \frac{1}{2}\cos\left(\frac{2\pi\, D(k_r, f, h)}{BW_{A0}(f)}\right) & \text{if } D(k_r, f, h) < \frac{BW_{A0}(f)}{2} \\ 0 & \text{elsewhere} \end{cases}$$
$$\text{with} \quad k_r = \sqrt{k_x^2 + k_y^2} \qquad D(k_r, f, h) = \left|k_r - k_{\mathrm{h}}^{A0}(f, h)\right| \tag{13.6}$$

The bandwidth $BW_{A0}(f)$ of the filter is function of the frequency and is defined as:

$$BW_{A0}(f) = k_{max} - k_{\mathrm{base}}^{A0}(f) \qquad \text{with} \qquad k_{max} = \frac{1}{2\,\Delta x}$$

where k_{max} is the maximal observable wavenumber for a measurement with equidistant scan point spacing $\Delta x = \Delta y$. This definition of $BW_{A0}(f)$ makes optimal use of the available information in the wavenumber domain, and does not require manual optimization. As an example, Figure 13.19 (c) and (d) show a 2D and 3D representation of the modepass filter corresponding to a material thickness h = 1.8 mm. Note that it should be avoided to vary the bandwidth BW_{A0} directly in function of the assumed material thickness h, because this would imply that every $MF_{A0,h}$ filter passes a different amount of energy (and noise).

The A$_0$ mode sweep response $\tilde{V}_{Z,\overline{S0}}(k_x, k_y, f)$ is passed through this modepass filter bank:

$$\tilde{V}_{Z,\overline{S0},h}(k_x, k_y, f, h) = MF_{A0,h}(k_x, k_y, f, h) \odot \tilde{V}_{Z,\overline{S0}}(k_x, k_y, f)$$

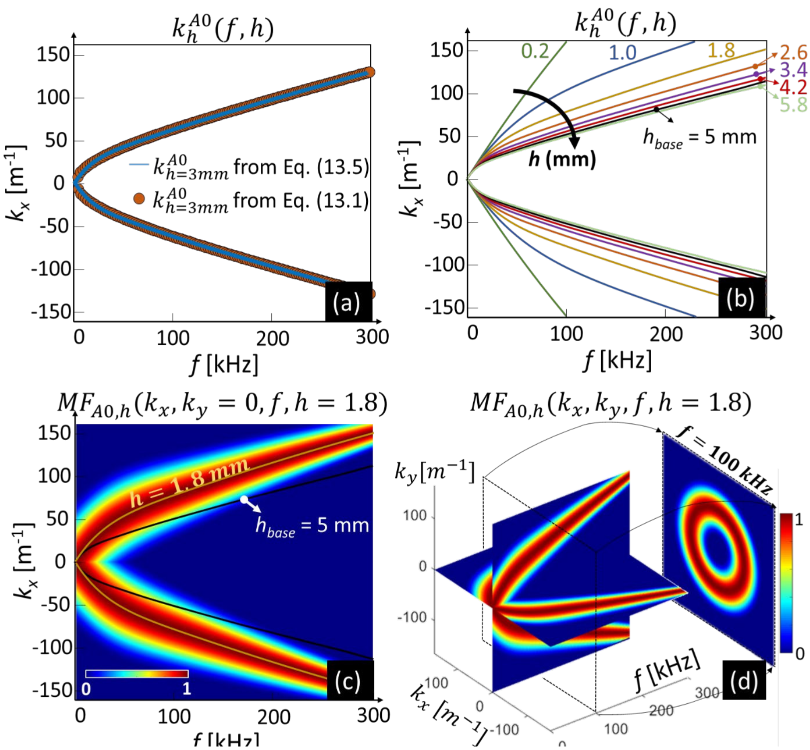

Figure 13.19: (a) A$_0$ mode curves for 3 mm thick aluminum calculated using Eq. (13.5) and using Eq. (13.1), (b) A$_0$ mode curves of different material thickness h for Al$_{25mm}$ and (c-d) 2D and 3D representation of the modepass filter constructed around the mode curve corresponding to material thickness h = 1.8 mm.

5.2.2. Assumptions

Two important assumptions are associated with the use of this modepass filter bank.

First, the derivation of the dispersion curves for different material thicknesses (Eq. (13.5)) is strictly speaking only valid for materials of which the stiffness tensor is constant throughout the thickness. However, layered composite components have ply-dependent elastic properties, resulting in locally different homogenized stiffness in the presence of a delamination.

Second, the mode bandpass filters (see Eq. (13.6)) are circular cone-shaped in the (k_x, k_y, f) domain (see Figure 13.19 (d)) and thus do not take into account potential strong anisotropy of the medium. Note that this assumption is also made in the traditional implementations of LWE (which use wavenumber filters). While the effect of anisotropy on the A_0 mode dispersion behavior is limited for quasi-isotropic and cross-ply composites (as considered in this study), it can result in a less accurate defect evaluation in the case of unidirectional composites.

In case all material properties (density, ply thickness, ply stiffness tensor, layup) are known, it is possible to relax both assumptions. In that case, the dispersion curves can be calculated for a delamination at every possible ply interface (instead of using Eq. (13.5)) and along every specific propagation direction $\theta = \text{atan}\left(\frac{k_y}{k_x}\right)$. Using these angular- and depth-dependent dispersion curves $k_h^{A0}(\theta, f)$, the mode bandpass filters derived using Eq. (13.6) become non-circular cone-shaped (e.g. elliptical cone-shaped). A recent study [10] investigated such a local wavenumber to local depth conversion for a quasi-isotropic CFRP.

In practice however, the ply thickness, ply stiffness and layup of the evaluated composites are often unknown. If one would consider the full wavenumber-frequency map of the measured velocity response, it will provide knowledge on the global dispersion behavior of the base material. However, it cannot provide information on the local dispersion behavior in the presence of a delamination. As a result, Eq. (13.5) and the associated assumptions cannot be relaxed without having complete knowledge on the ply parameters and layup of the composite.

The depth estimation in this study is obtained through the proposed SRB-LWE for CFRPs parts for which no prior knowledge on material properties was available. Hence, the above two assumptions might result in small discrepancies in the estimated local thickness maps derived for the layered cross-ply CFRP components. This is further discussed in Section 5.3.2 - *Inspection of two CRFP aircraft panels* where it is shown that although there are small discrepancies observed, they do not adversely affect the defect assessment.

5.2.3. Local Thickness Identification

As a last step, the local thickness map is constructed. The workflow can be found in the last row of Figure 13.16. In order to estimate the local thickness, the 4D dataset $\tilde{V}_{Z,\overline{S0},h}(k_x, k_y, f, h)$ is transformed back to the spatial domain using the inverse FFT along the (k_x, k_y) dimensions:

$$\tilde{V}_{Z,\overline{S0},h}(k_x, k_y, f, h) \xrightarrow{2D\ IFFT} V_{Z,\overline{S0},h}(x, y, f, h)$$

The obtained dataset $V_{Z,\overline{S0},h}(x, y, f, h)$ represents the out-of-plane velocity after S_0 mode removal and after mode bandpass filtering at location (x, y) and associated to a specific material thickness h and excitation frequency f.

The local material thickness is estimated as that thickness for which the bandpower of $\tilde{V}_{Z,\overline{S0},h}(k_x, k_y, f, h)$ becomes maximal. For the calculation of the bandpower, it is important to compensate for the fact that the excitation source does not excite all frequency bins with the same amount of energy [21]. The compensation is based on the introduction of a frequency-dependent weighting factor $WF(f)$ and a threshold mask $TH(f)$ related to the signal-to-noise ratio $SNR(f)$ of the measurement.

The dimensionless frequency-dependent weighting factors $WF(f)$ are defined as:

$$WF(f) = \frac{\sum_{(x,y)} \left| V_{Z,\overline{S0},h}(x, y, f, h_{base}) \right|^2}{\sum_{(x,y,f)} \left| V_{Z,\overline{S0},h}(x, y, f, h_{base}) \right|^2}$$

The numerator represents the energy of vibrations with frequency f in the base material, summed over all scan points. The denominator makes the weighting factors dimensionless.

The $SNR(f)$ is expressed in dB and can be derived as:

$$SNR(f) = \frac{Signal(f)}{Noise(f)} = 20 \log \frac{\sum_{(x,y)} |V_Z(x, y, f)|^2}{\sum_{(x,y)} \left| V_Z^{V_{pp}=0}(x, y, f) \right|^2}$$

where $V_Z^{V_{pp}=0}(x, y, f)$ is the response signal measured by the SLDV when the actuator is not activated. Based on observing the results for different experiments, a threshold value SNR_{Thres} is defined as the mean value of the SNR spectrum:

$$SNR_{Thres} = \frac{1}{f_{max}^{actuator} - f_{min}^{actuator}} \sum_{f=f_{min}^{actuator}}^{f_{max}^{actuator}} SNR(f)$$

with $f_{min}^{actuator}$ and $f_{max}^{actuator}$, the minimum and maximum frequency of excitation (see Table 13.1). The corresponding threshold mask $TH(f)$ is found as:

$$TH(f) = \begin{cases} 0 & \text{if } SNR(f) < SNR_{Thres} \\ 1 & \text{elsewhere} \end{cases} \tag{13.7}$$

Finally, the bandpower BP_h^{A0} is obtained as:

$$BP_h^{A0}(x,y,h) = \frac{1}{\sum_{f=0}^{f_{max}(h)}(TH(f))} \sum_{f=0}^{f_{max}(h)} \left(\frac{\left|V_{Z,\overline{S0},h}(x,y,f,h)\right|^2}{WF(f)} TH(f) \right) \qquad (13.8)$$

At some frequencies, the excited wavefield has limited amplitude resulting in a low SNR. This is often the case in the high frequency regime where the wave damping is high, the piezoelectric actuators are less effective and the intrinsic noise level of the SLDV increases (see Chapter 4). As an example, Figure 13.20 shows $SNR(f)$ for the $\mathrm{Al}_{25\mathrm{mm}}$ together with the threshold SNR_{Thres}. Illustrated on the figure are those frequency ranges that are automatically disregarded in the calculation of the bandpower (i.e. $TH(f) = 0$). Further, also frequencies lower than the minimum frequency of excitation and higher than the maximum frequency of excitation are automatically excluded.

Care has to be taken in the selection of the maximum frequency limit $f_{max}(h)$ used in Eq. (13.8). In order to avoid spatial aliasing, the maximum frequency $f_{max}(h)$ must be smaller than the frequency for which the thickness-specific dispersion curve reaches the maximum observable wavenumber: $k_{\mathrm{h}}^{A0}(f_{max}(h), h) = (2.GridSize)^{-1} = 167\, m^{-1}$. This criterion for $f_{max}(h)$ is illustrated in Figure 13.21 (see orange rectangle). Note that this criterion makes the maximum frequency of interest dependent on the evaluated thickness h i.e. it becomes lower for decreasing material thickness h.

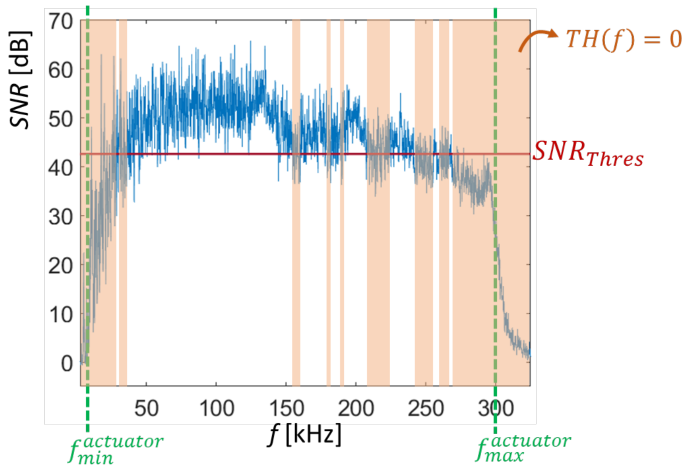

Figure 13.20: Signal-to-noise ratio for $\mathrm{Al}_{25\mathrm{mm}}$ with indication of the threshold used in the bandpower calculation.

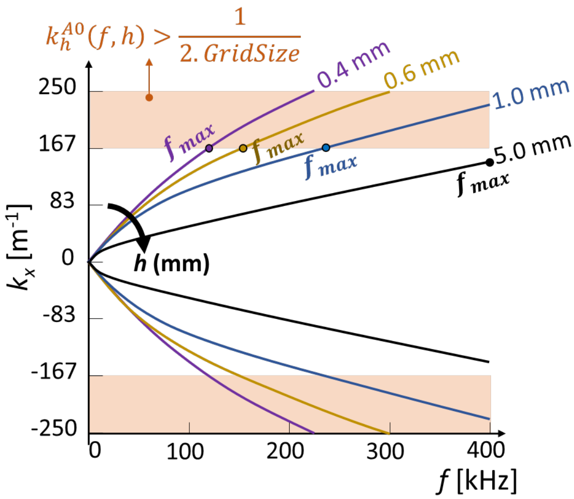

Figure 13.21: Illustration of the automated selection of the maximum frequency of interest for bandpower calculation in Al_{25mm}.

Figure 13.22 (a) shows the resulting $BP_h^{A0}(x,y,h)$ curve at three specific points corresponding to (i) a FBH with true remaining thickness 1.9 mm (p_1), (ii) a FBH with true remaining thickness 3.3 mm (p_2) and (iii) damage-free material with true thickness 5 mm (p_3). For each point, the local material thickness is estimated as the thickness for which BP_h^{A0} becomes maximal:

$$h_{loc}^{est}(x,y) = \underset{h}{\mathrm{ArgMax}}[BP_h^{A0}(x,y,h)]$$

As seen on Figure 13.22 (a), the estimated local thickness h_{loc}^{est} closely corresponds to the true local thickness h_{loc}^{true}. Further note that the peak in the BP_h^{A0} curve becomes less pronounced for higher local thicknesses. This is the result of the decreasing distance between the k_{h}^{A0} curves for higher material thicknesses (see discussions of Figure 13.1 (b) and Figure 13.19 (a)). The estimated local thickness map $h_{loc}^{est}(x,y)$ is shown in Figure 13.22 (b) with indication of the points p_1, p_2 and p_3. A more in-depth discussion of this map is provided in Section 5.3.1.

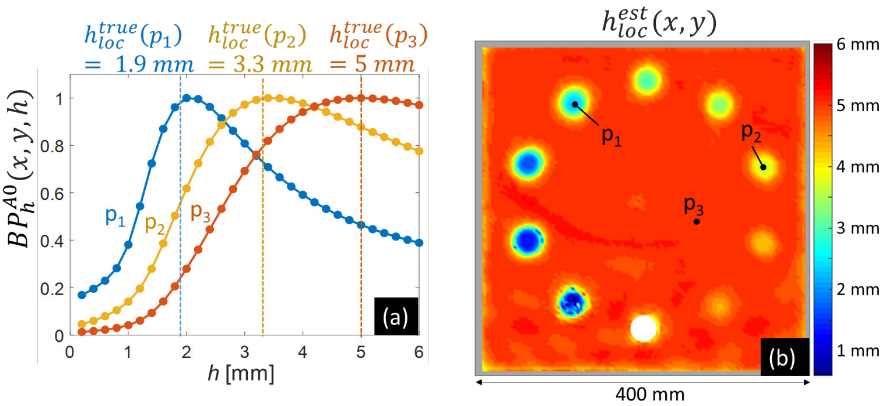

Figure 13.22: (a) Bandpower density in function of evaluated material thickness at three locations (p_1, p_2 and p_3) and (b) Estimated local thickness map for Al_{25mm}.

5.2.4. Advantages of Self-Reference Broadband Local Wavenumber Estimation

The proposed SRB-LWE algorithm has some specific advantages over the traditional narrowband LWE approaches. Figure 13.23 (a,b) gives a schematic representation of the wavenumber bandpass filter used in traditional (narrowband) LWE and the modepass filter proposed here. Also included in Figure 13.23 are the estimated local thickness maps obtained using the SRB-LWE method (Figure 13.23 (d)) and the estimated local thickness map obtained using the toneburst LWE algorithm based on the wavenumber filter bank explained in Section 4.2.2 (Figure 13.23 (c)). This traditional LWE algorithm is operated on a five-cycle Hanning windowed sine response with center frequency 200 kHz. The center frequency was selected by trial and error in order to improve the results. The resulting estimated local wavenumber map was already shown in Figure 13.15 (c). The estimated local wavenumber map is converted to an estimated local thickness map (see Figure 13.23 (d)) using the wavenumber-thickness relations (at f = 200 kHz) derived with Eq. (13.5).

A first advantage of SRB-LWE is related to the use of a modepass filter bank instead of the wavenumber bandpass filter bank. The effect of both filter types is graphically explained in Figure 13.23 (a,b). The modepass filter ($MF_{A0,h}$) follows the thickness-specific dispersion curve $k_h^{A0}(f)$. As a result, the central wavenumber of the modepass filter is frequency-dependent. This is in contrast to the traditional LWE algorithm based on wavenumber bandpass filters that are frequency-independent. Suppose that only the vibrations that correspond to a certain thickness of material must be extracted from the velocity response. The A_0 mode curve corresponding to this specific thickness is indicated in blue. In case a wavenumber bandpass filter (see Figure 13.23 (a)) is constructed around the central wavenumber, some vibrations are retained that correspond to a different material thickness (see dark gray color on inset). In addition, some of the vibrations that correspond to the desired thickness are removed (see light gray color on inset). On the other hand, when a modepass filter (see Figure 13.23 (b)) is constructed around the dispersion curve, the vibrations are correctly filtered. Only when the input dataset would correspond to a steady-state sine response (i.e. an infinitely small bandwidth), a wavenumber filter is as effective as a mode filter. The same mode filter concept was also exploited in Chapter 11 for the calculation of a broadband mode-removed energy-based damage map [22].

The second advantage of the proposed SRB-LWE is related to the estimation of the local thickness (or the local wavenumber) at a multitude of frequencies using a single experiment. This large number of evaluated frequencies results in an averaging effect which increases the robustness of LWE, especially when the SNR of the measurement is limited. This increase in robustness was also described by Juarez and Leckey [10] and Moon et al. [7] who performed traditional LWE on multiple input datasets with varying center frequencies.

The broadband nature of the proposed SRB-LWE also solves the problem of traditional LWE methods related to shallow defect detection. For traditional narrowband LWE, it proved challenging to detect shallow defects when using typical center frequencies of excitation (e.g. 150 kHz) in combination with moderate scan point resolutions (e.g. 2 mm). This is because the maximum observable wavenumber k_{max} is lower than the true wavenumber at the shallow damage. This problem is further revealed in Figure 13.23 (c). For SRB-LWE, low and high frequencies are taken into account, resulting in a correct thickness estimation for shallow as well as deep defects.

A minor disadvantage is that this broadband nature of the dataset is related to a bigger data size which increases the calculation time of SRB-LWE to around 144 s for $\mathrm{Al}_{25\mathrm{mm}}$ (and 220 s for $\mathrm{CFRP}_{\mathrm{Disb}}^{\mathrm{Air}}$).

The third benefit of the proposed algorithm is that the depth of the defect is readily obtained without the need to know material properties. Only the thickness of the base material h_{base} needs to be known for quantitative local thickness estimation. If h_{base} would be unknown, the procedure can still be used (by setting h_{base} = 1) and the estimated local thickness map will give the relative thickness compared to the base material.

At last, the parameters used in this SRB- LWE implementation are defined in such a way that they are independent of the test case. In addition, the use of the threshold function $TH(f)$, based on the measurement's SNR, further diminishes the required user input and increases the robustness. This is in contrast to the traditional LWE techniques, which have several parameters that require manual tweaking when applied on measurements obtained for components with different base and defect thicknesses, different signal-to-noise ratios, different scan point spacing or different expected defect types [3, 9, 10]. Thus, the proposed SRB-LWE largely improves the level of automation compared to the traditional LWE implementations.

The advantages of SRB-LWE reflects back in the obtained local thickness map. A line plot of the local thickness through two defects (Figure 13.23 (e)) is included to facilitate the comparison of the results. It is observed that the estimated local thickness using the SRB-LWE technique is very good for the 5 mm thick base material (expect for a small area at the actuator) as well as for the 1.9 mm and 4.35 mm deep FBHs. The local thickness estimate obtained using the traditional LWE technique is less accurate as seen by the irregular curve plot and by the less circular FBH areas in Figure 13.23 (c). The difference in the quality of the estimated local thickness maps becomes even more pronounced for measurements with a lower SNR. This will be illustrated for $\mathrm{CFRP}_{\mathrm{Disb}}^{\mathrm{Air}}$ in Section 5.3.2.

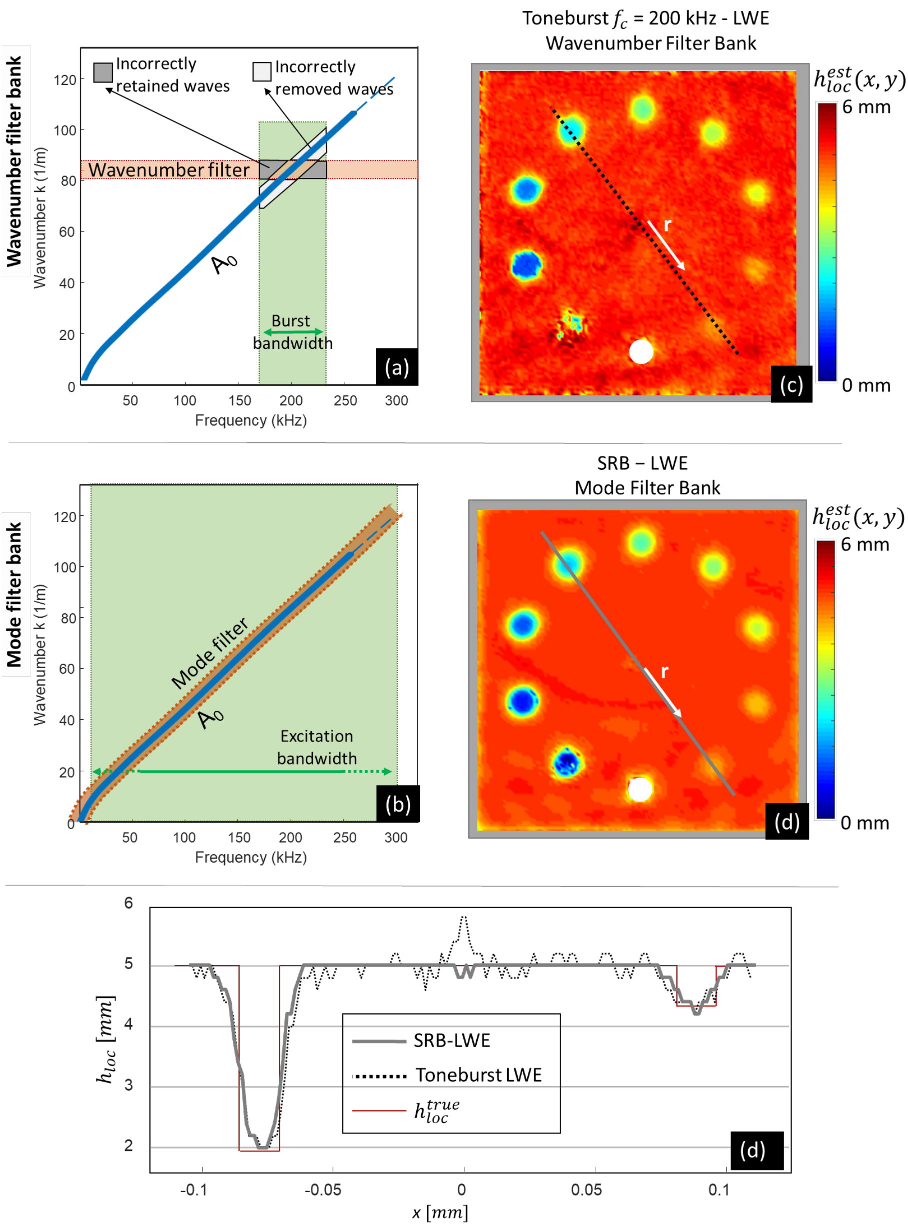

Figure 13.23: Comparison of the SRB-LWE technique using a modepass filter bank with the traditional toneburst LWE technique using a wavenumber bandpass filter bank applied for Al_{25mm}: (a,b) Schematic illustration of both filter types, (c,d) Estimated local thickness maps obtained using traditional LWE and using SRB-LWE, respectively and (e) Estimated and true local thickness along the lines indicated on figures (c,d).

5.3. Results of Self-Reference Broadband Local Wavenumber Estimation

5.3.1. Aluminum Plate with Flat Bottom Holes

Piezoelectric Excitation

SRB-LWE is performed for the measurement results of the three 5 mm thick aluminum plates that are excited using piezoelectric actuators, and that contain FBH defects of variable diameter and remaining material thickness (see also Figure 13.2 (a)). The resulting estimated local thickness maps are presented in Figure 13.24 (a-c). Figure 13.24 (d-f) show line plots of the estimated local thickness at the location of each FBH defect. The true defect diameter and the true remaining thicknesses are indicated on these graphs using dashed lines. In addition, the estimated and true local thickness at the center of each FBH are listed in Table 13.6.

In contrast to the LWE maps derived using the traditional narrowband LWE methods (see Sections 3 and 4), the deepest defects as well as the shallowest defects are detected in every SRB-LWE map. In general, the estimated thickness is in good agreement with the true remaining material thickness as seen in Figure 13.24 (d-f) and in Table 13.6. Note that the thickness is estimated with a resolution of 0.2 mm. For the smallest FBHs (d = 15 mm), the true local thickness is slightly underestimated. This is a known consequence of performing LWE using a limited maximum frequency of excitation and a limited scan point resolution (see also [7, 16]).

Figure 13.24 and Table 13.6 indicate that the SRB-LWE can be used successfully for the detection and evaluation of defects in isotropic materials in an automated manner. The estimated local thickness maps are of high quality and reveal all defects, including shallow defects as well as deep defects with a depth higher than 80% of the base material's thickness.

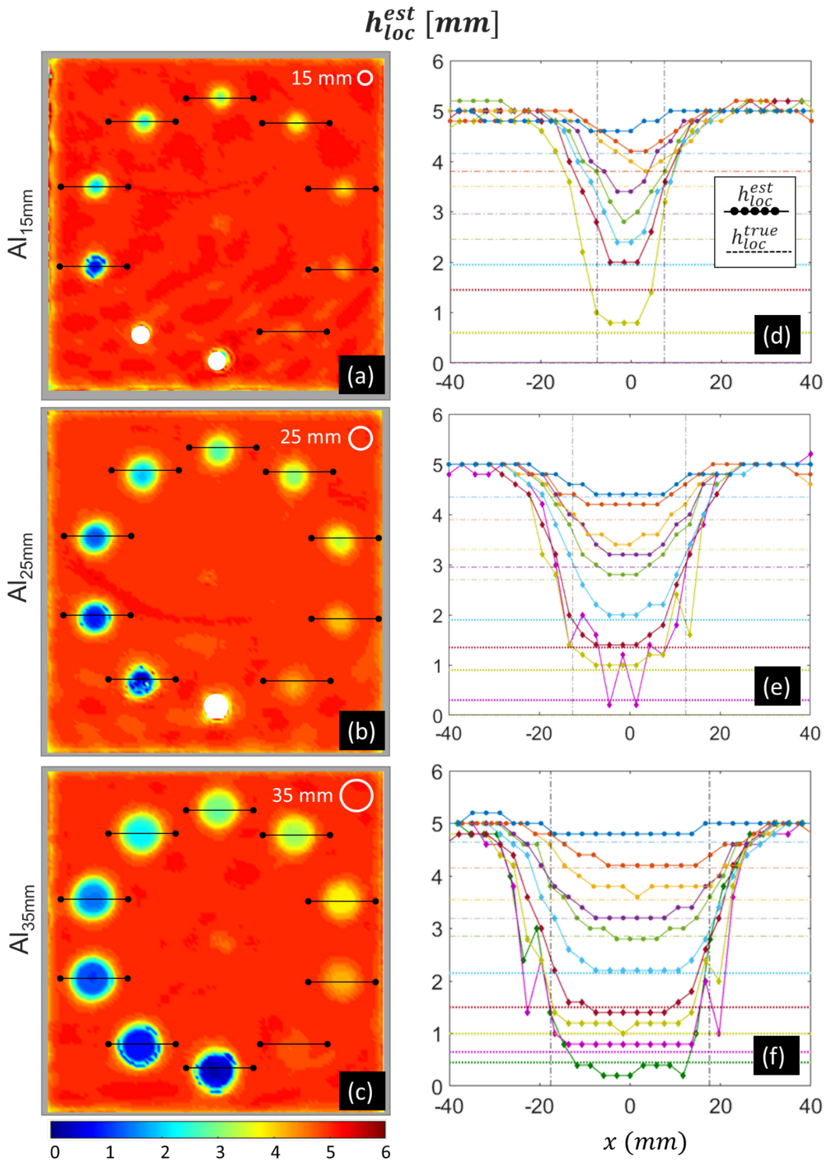

Figure 13.24: Results from the SRB-LWE, (a-c) Estimated local thickness maps and (d-f) estimated local thickness at the FBHs for the three piezoelectric excited aluminum plates with FBHs of diameter 15, 25 and 35 mm, respectively.

Pulsed Laser Excitation

The proposed SRB-LWE algorithm can equally be applied to measurement results obtained from pulsed laser excitation (see Section 2 for details) instead of piezoelectric excitation, resulting in a completely non-contact NDT approach. This is illustrated for Al_{35mm}. Figure 13.25 (a) shows one slice of the wavenumber-frequency map along k_y = 0 for the out-of-plane velocity component excited by the pulsed laser. The SNR and the associated threshold value (see Eq. (13.7)) are shown in Figure 13.25 (b). Comparing the wavenumber-frequency map and SNR curve with those corresponding to piezoelectric excitation (see Figure 13.17 and Figure 13.20, respectively) shows that (i) the pulsed laser excitation does not excite the S_0 mode efficiently and (ii) the amplitude of the laser excited A_0 mode decreases considerably for frequencies in excess of 100 kHz. Therefore, frequencies in excess of ≈ 125 kHz are automatically disregarded (i.e. $TH(f >\approx 125\ ) = 0$).

The resulting estimated local thickness map and the line plot of the estimated local thickness at each FBH defect are shown in Figure 13.25 (c-d), respectively. The estimated local thickness at each FBH has also been added to Table 13.6. It can be seen that also for this inspection using pulsed laser excitation, a good correspondence is found between the true local thickness and the output of the SRB-LWE algorithm.

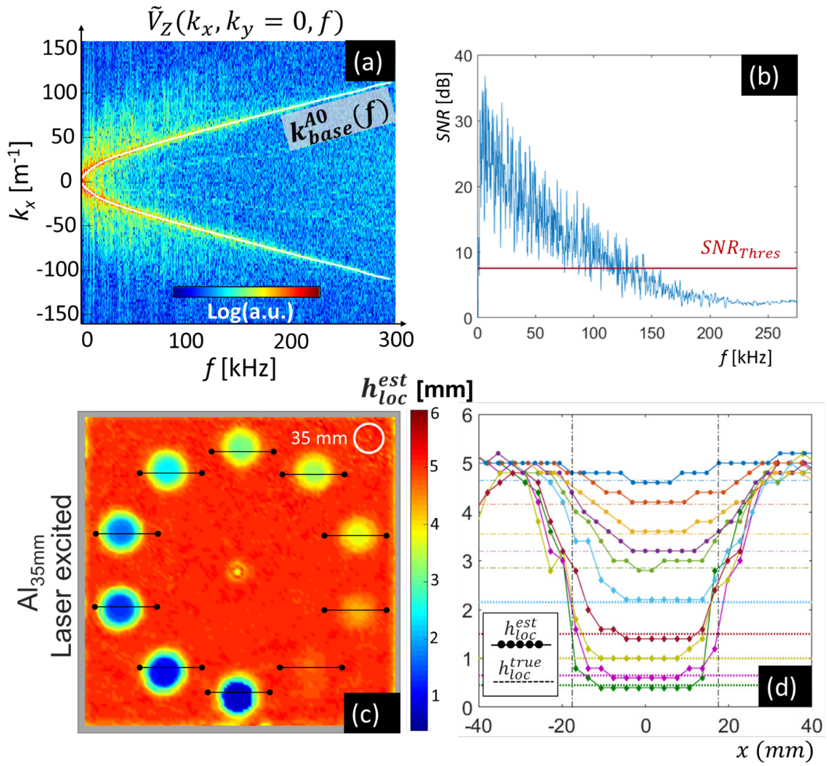

Figure 13.25: Laser excited Al_{35mm} (a) Wavenumber-frequency map for the out-of-plane velocity response along $k_y = 0$, (b) SNR with indication of the threshold used in Eq. (13.7), (c) SRB-LWE derived local thickness map and (d) Line plot of the estimated local thickness at all FBHs.

Table 13.6: Estimated local thickness h_{loc}^{est} (mm) and true local thickness h_{loc}^{true} (mm) for each FBH in the three aluminum plates.

Ø (mm)	Nr.	1	2	3	4	5	6	7	8	9	10
15	h_{loc}^{true}	\	\	0.6	1.45	1.95	2.45	2.95	3.5	3.8	4.15
	$h_{loc}^{est-piezo}$	\	\	0.8	2	2.4	2.8	3.4	3.8	4.2	4.6
25	d_{loc}^{true}	\	0.3	0.9	1.35	1.9	2.7	2.95	3.3	3.9	4.35
	$h_{loc}^{est-piezo}$	\	0.2	1	1.4	2	2.8	3.2	3.4	4.2	4.2
35	h_{loc}^{true}	0.45	0.65	1	1.5	2.15	2.85	3.2	3.55	4.15	4.65
	$h_{loc}^{est-piezo}$	0.2	0.8	1	1.4	2.2	2.8	3.2	3.8	4.2	4.6
	$h_{loc}^{est-laser}$	0.4	0.6	1	1.4	2.2	3	3.2	3.6	4.2	4.6

5.3.2. CFRP A320 Aircraft Panels

SRB-LWE is performed on the measurement results of two stiffened cross-ply CFRP aircraft components (see also Figure 13.2 (b-c)). The thickness of the damage-free base material is respectively 1.5 and 4 mm. Note that the previously defined SRB-LWE's characteristics, for instance the bandwidth BW_{A0} in Eq. (13.6), are defined in such a way that they require no manual tweaking for new inspection cases.

Aircraft panel with disbond

The results of the 1.5 mm thick aircraft panel with a disbond at a stiffener ($\mathrm{CFRP}_{\mathrm{Disb}}^{\mathrm{Air}}$) are discussed first. The panel was manufactured by an industrial partner, and the disbond was unintentionally generated during the manufacturing process. The global wavenumber-frequency map (along k_y = 0 m^{-1}) of the out-of-plane velocity is displayed in Figure 13.26 (a), and the identified dispersion curves are shown on top with white lines. The evaluated thicknesses h range from 0.1 mm up to 3.9 mm in steps of 0.2 mm. In that way, it is possible to also estimate the increased thickness at the location of the backside stiffeners.

Figure 13.26 (b) shows the time-of-flight (TOF) map (converted to depth estimate) derived from the ultrasonic C-scan inspection, in which the disbond at the left stiffener can be observed. Except for the disbonded area, the local thickness at the stiffener equals 2.58 mm. Note that the thickness of the stiffener's middle fin is not found using these TOF C-scan results.

Figure 13.26 (c) and (d) represent the estimated local thickness maps obtained from the proposed SRB-LWE algorithm and from the traditional LWE implementation based on a wavenumber bandpass filter bank (see Section 4.2.2), respectively. For the traditional LWE, a five-cycle Hanning windowed sine excitation with center frequency 175 kHz was employed, in which the algorithm's parameters were selected through trial and error. The obtained local wavenumber map (k_{loc}^{est}) is converted to an estimation local thickness map using the relations given by Eq. (13.5) for f = 175 kHz.

The estimated local thickness maps obtained through both the traditional LWE and the SRB-LWE correctly show the extent of the disbond, i.e. where a local thickness is found similar to the thickness of the base material. However, a significant improvement in estimated local thickness map quality is noticed in case of SRB-LWE. The improved quality is caused by the superior filter efficiency of using a modepass filter bank (instead of a wavenumber filter bank), by the averaging effect of employing a broadband approach and by the use of the SNR criterion for frequency frame selection (see also Section 5.2.4). Because of this high-quality output of SRB-LWE, it is even possible to estimate the local thickness at the non-defected stiffener's area. The estimated thickness h_{loc}^{est} = 2.50 mm matches well with the true local thickness h_{loc}^{true} = 2.58 mm at the stiffener's area. Note that a step size of 0.2 mm in thickness direction was used in the SRB-LWE algorithm.

One may notice small discrepancies in the estimated local thickness maps that are attributed to the non-isotropy of the composite material. In between the two stiffeners, the true local thickness is 1.5 mm. However, the estimated local thickness maps show a small increase in estimated thickness in the +45° and -45° directions around the piezoelectric actuator (see Figure 13.26 (c)). This local thickness increase should be linked to the layup of the laminate. As such, a cross-ply layup with ply angles +45° and -45° is expected. Further, Figure 13.26 (c) indicates that the thickness is highest in the -45° direction, and to a lesser extent in the +45° direction. Therefore, it may be expected that the outer plies, which contribute most to the flexural rigidity, have a -45° angle. This expected cross-ply layup is confirmed after consulting the manufacturer of the aircraft component, who specifies a $[(-45°/+45°)_3]_s$ layup for the studied component.

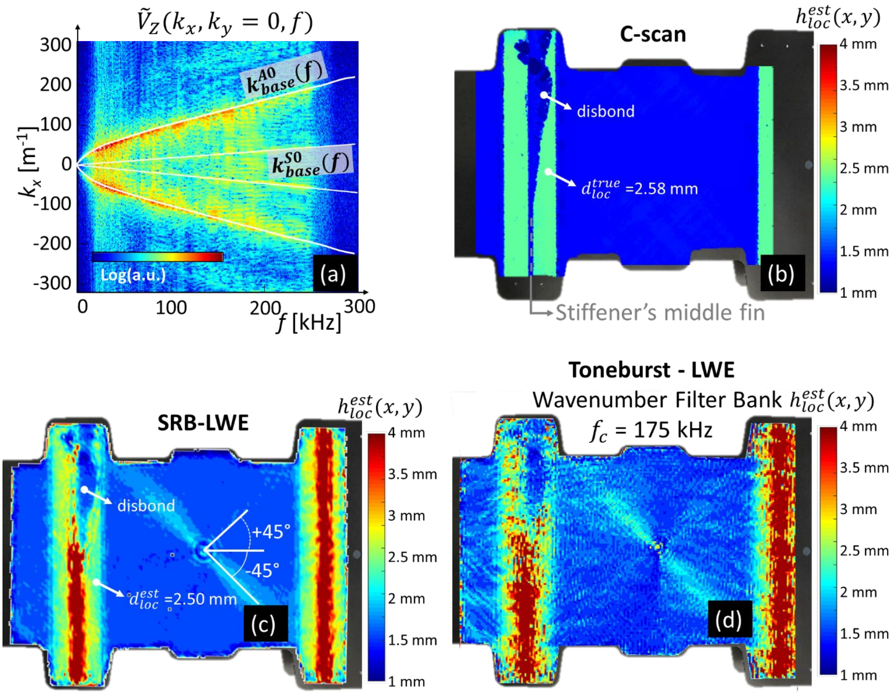

Figure 13.26: SRB-LWE for $\mathrm{CFRP}^{\mathrm{Air}}_{\mathrm{Disb}}$: (a) Wavenumber-frequency map for the out-of-plane velocity response along k_y = 0, with identified A_0 and S_0 mode curves and Local thickness maps derived from (b) Ultrasonic C-scan, (c) SRB-LWE and (d) Traditional toneburst (f_c = 175 kHz) LWE based on wavenumber bandpass filter bank.

Aircraft panel with BVID

The second aircraft panel ($\mathrm{CFRP}^{\mathrm{Air}}_{\mathrm{BVID}}$) has been intentionally impacted in order to induce BVID regions A, B and C. The inspection is performed in a 2-step way, in order to increase the inspection efficiency. First, a relatively rough SLDV scan, with scan point spacing of 2 mm, is performed to roughly locate possible defects. Second, a more detailed SLDV scan, with dense scan point spacing of 1 mm, is performed on one of the identified hotspots to get detailed information on the damage.

Figure 13.27 (a) shows the out-of-plane velocity response in the wavenumber-frequency domain (along k_y = 0). The identified dispersion curves, corresponding to the 4 mm thick base material, are indicated. SRB-LWE is performed for the A_0 mode using an evaluated thickness axis: 0.2 mm, 0.4 mm, 0.6 mm, ..., 7 mm. The resulting estimated local thickness map is shown in Figure 13.27 (b). The three locations of BVID are clearly distinguished as areas of significantly reduced local thickness. Again, the effect of the cross-ply layup is observed close to the excitation locations.

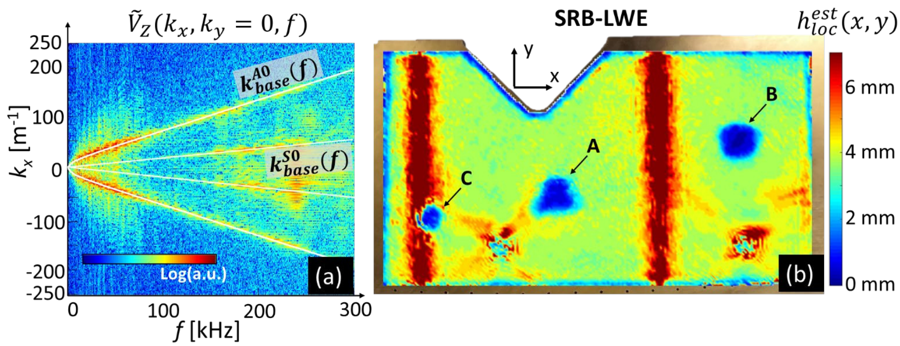

Figure 13.27: SRB-LWE for $\mathrm{CFRP}_{\mathrm{BVID}}^{\mathrm{Air}}$: (a) Wavenumber-frequency map for the out-of-plane velocity response along k_y = 0 with identified A_0 and S_0 mode curves and (b) SRB-LWE derived estimated local thickness map.

In order to accurately quantify the damage hotspot at BVID-B, two additional SLDV scans are performed. The new SLDV scans are focused on the BVID-B region, from the impact side as well as the backside, and have an increased scan point resolution of 1 mm (see also Table 13.1). Local thickness maps, obtained for ultrasonic C-scan TOF data of the impact- and the backside, are shown in Figure 13.28 (a) and (b), respectively. The SRB-LWE derived local thickness maps are shown in Figure 13.28 (c) and (d), respectively. A high contrast colormap is used to facilitate the comparison of these figures. Overall, a good correspondence is found between both inspection methodologies. The different delaminations that make up the BVID, and that are of significant size, can be distinguished in the estimated local thickness map obtained from SRB-LWE. Only the very small delamination fragments cannot be distinguished properly in the SRB-LWE result. In order to detect those with SRB-LWE, higher excitation frequencies and smaller scan point resolutions are required.

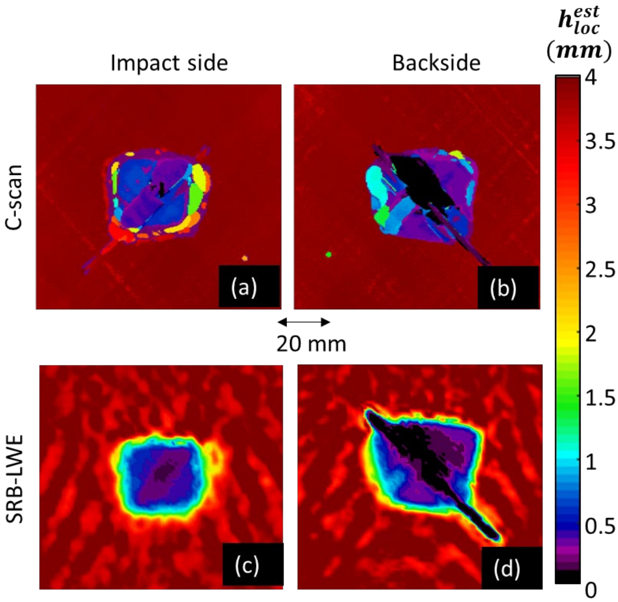

Figure 13.28: Enlarged view of the estimated local thickness at BVID-B derived from (a,b) Ultrasonic C-scan time-of-flight data and (c,d) SRB-LWE. Left column corresponds to the inspection from the impact side, right column to the inspection from the backside.

6. Conclusions

Broadband vibrations are introduced in the component using low-power piezoelectric actuators or a pulsed laser and the full wavefield response is measured with the SLDV. The full wavefield response is converted into a damage map based on local wavenumber estimation LWE. Different LWE strategies are outlined.

First, the traditional LWE strategies are reviewed. These traditional LWE strategies are operated on narrowband velocity responses corresponding to a standing wave (i.e. sine) excitation or to a toneburst excitation. Some of the traditional LWE methods prove successful for detection of FBHs in an aluminum plate as well as for detection of a disbond at a backside stiffener in an industrial CFRP aircraft panel. However, the LWE methods use multiple process parameters that require manually tweaking to obtain satisfying result. For instance, the center frequency of the narrowband excitation has a big effect on the obtained wavenumber-based damage map.

To remediate this, a novel damage map construction method is proposed: self-reference broadband local wavenumber estimation (SRB-LWE). The procedure results in an estimated local thickness map of the inspected area, in which defects are found as areas of reduced local thickness. The obtained local thickness map allows for more accurate defect detection and evaluation compared to the local wavenumber maps derived using traditional (narrowband) LWE methods (e.g. using a wavenumber bandpass filter bank). The proposed SRB-LWE algorithm is baseline-free, user-independent and does not require the elastic material properties to be known.

The high performance of the SRB-LWE algorithm is verified on three aluminum plates with FBHs defects, and on two defected cross-ply CFRP aircraft panels. The estimated local thickness maps are found to not only reveal the extent of the damage with high precision, but to also provide an accurate estimation of the defects' depth.

References

1. Segers, J., et al., *Self-Reference Broadband Local Wavenumber Estimation (SRB-LWE) for defect assessment in composites* Mechanical Systems and Signal Processing, 2021. **163**.
2. Rose, J.L., *Ultrasonic Guided Waves in Solid Media*. 2014: Cambridge University Press.
3. Flynn, E.B., et al., *Structural imaging through local wavenumber estimation of guided waves.* NDT & E International, 2013. **59**: p. 1-10.
4. Mesnil, O., C.A.C. Leckey, and M. Ruzzene, *Instantaneous and local wavenumber estimations for damage quantification in composites.* Structural Health Monitoring, 2014. **14**(3): p. 193-204.
5. Gao, T., et al., *Hidden Corrosion Detection Using Laser Ultrasonic Guided Waves with Multi-frequency Local Wavenumber Estimation.* Ultrasonics, 2020. **108**.
6. Gao, F., et al., *Local wavenumber method for delamination characterization in composites with sparse representation of Lamb waves.* IEEE transactions on ultrasonics, ferroelectrics, and frequency control, 2020. **PP**.
7. Moon, S., et al., *Optimization of excitation frequency and guided wave mode in acoustic wavenumber spectroscopy for shallow wall-thinning defect detection.* Journal of Mechanical Science and Technology, 2018. **32**(11): p. 5213-5221.
8. Michaels, T.E. and J.E. Michaels, *Application Of Acoustic Wavefield Imaging To Non-Contact Ultrasonic Inspection Of Bonded Components.* AIP Conference Proceedings, 2006. **820**.
9. Rogge, M.D. and C.A. Leckey, *Characterization of impact damage in composite laminates using guided wavefield imaging and local wavenumber domain analysis.* Ultrasonics, 2013. **53**(7): p. 1217-26.

10. Juarez, P.D. and C.A. Leckey, *Multi-frequency local wavenumber analysis and ply correlation of delamination damage.* Ultrasonics, 2015. **62**: p. 56-65.
11. Jeon, J.Y., et al., *Damage detection on composite structures with standing wave excitation and wavenumber analysis.* Advanced Composite Materials, 2017. **26**(sup1): p. 53-65.
12. Jeon, J.Y., et al., *2D-wavelet wavenumber filtering for structural damage detection using full steady-state wavefield laser scanning.* NDT & E International, 2020. **116**.
13. Tola, K.D., et al., *Determination of Plate Corrosion Dimension Using Nd:YAG Pulsed Laser-generated Wavefield and Experimental Dispersion Curves.* Materials (Basel, Switzerland), 2020. **13**(6).
14. Lugovtsova, Y., et al., *Damage Quantification in an Aluminium-CFRP Composite Structure using Guided Wave Wavenumber Mapping: Comparison of Instantaneous and Local Wavenumber Analyses.* NDT & E International, 2021.
15. Michaels, J.E., et al., *Chirp excitation of ultrasonic guided waves.* Ultrasonics, 2013. **53**(1): p. 265-70.
16. O'Dowd, N.M., et al., *Exploring the Performance Limits of Full-Field Acoustic Wavenumber Spectroscopy Techniques for Damage Detection through Numerical Simulation*, in *8th European Workshop on Structural Health Monitoring*. 2016, NDT.net: Bilbao Spain.
17. Davies, S.J., et al., *Laser-generated ultrasound: its properties, mechanisms and multifarious applications.* Journal of Physics D: Applied Physics, 1993. **26**(3): p. 329-348.
18. Flynn, E.B. and G.S. Jarmer, *High-Speed, Non-Contact, Baseline-Free Imaging of Hiddden Defects Using Scanning Laser Measurements of Steady-State Ultrasonic Vibration*, in *9th International Workshop on Structural Health Monitoring*. 2013.
19. Frigo, M. and S.G. Johnson. *FFTW: an adaptive software architecture for the FFT*. in *IEEE International Conference on Acoustics, Speech and Signal Processing, ICASSP '98* 1998. Seattle USA: IEEE.
20. Felsberg, M. and G. Sommer, *The Monogenic Signal.* IEEE TRANSACTIONS ON SIGNAL PROCESSING, 2001. **49**.
21. Kundu, T., M. Gresil, and V. Giurgiutiu, *Guided wave propagation in carbon composite laminate using piezoelectric wafer active sensors*, in *Health Monitoring of Structural and Biological Systems 2013*. 2013.
22. Segers, J., et al., *Robust and baseline-free full-field defect detection in complex composite parts through weighted broadband energy mapping of mode-removed guided waves.* Mechanical Systems and Signal Processing, 2021. **151**.

Chapter 14

Damage Map based on Local Wave-Direction Estimation

Summary:

A novel wavefield processing algorithm: "local wave-direction estimation (LWDE)", is proposed to localize sources of guided waves in full wavefield SLDV measurements. The LWDE algorithm uses angular bandpass filters in the wavenumber domain to determine the local propagation direction of the guided waves. The obtained estimated local wave-direction map is converted into an error map by the use of a virtual local wave-direction field. This error map reveals the sources of guided waves as local minima. The exploitation of local wave-direction information provides the opportunity to scan only a small part of the component for localization of out-of-sight sources of guided waves. The source localization performance of LWDE is illustrated by retrieving the position of multiple piezoelectric sources in a quasi-isotropic CFRP plate.
LWDE is further coupled to nonlinear vibrations (NL-LWDE) and used for (out-of-sight) damage detection. The nonlinear components are extracted from the SLDV measurement and the sources of these nonlinear components, i.e. the defects, are localized. This is demonstrated for a cross-ply CFRP plate with low velocity impact damage. In addition, NL-LWDE is applied to measurement results of a damaged CFRP bicycle frame's down tube. NL-LWDE proves successful for localization of the damage, also when the damage is located at the back of the down tube.

This chapter is in close correspondence with journal publication:

[1] Segers, J., Hedayatrasa, S., Poelman, G., Van Paepegem, W., Kersemans, M., *Nonlinear Local Wave-Direction Estimation for In-sight and Out-of-sight Damage Localization in Composite Plates.* NDT&E International, 2021. **119**.

1. Introduction

In the last three chapters, three different damage map construction approaches were proposed for damage detection in thin-walled composite components. The damage map construction approaches are applied on the component's full-field elastic wave response, obtained through piezoelectric excitation and SLDV sensing. Damage map construction was based on the defect induced change in (i) the linear vibrational energy, (ii) the nonlinear vibrational energy and (iii) the wavenumber. One last important guided elastic wave characteristic can be exploited for damage detection, i.e. the local direction of the propagating waves. Such a local wave-direction based damage detection approach is the subject of this chapter.

We built further on the nonlinear defect-wave interactions observed earlier in this PhD book. In Chapter 3, it was illustrated that, as a result of contact acoustic nonlinearity [2-4], new vibrational components are formed at the defect with a frequency different to the frequency of the incoming vibrations. In Chapter 12, damage maps were constructed based on the mapping of the energy present in these nonlinear vibrational components [5, 6]. The nonlinear vibrational components, formed at the defect, are (partly) transferred by the defect to the surrounding damage-free material (see Chapter 8 Section 5.1). Or in other words, the defect behaves as a source of nonlinear vibrational components.

Based on this observation, a novel source localization algorithm, named "(Nonlinear) Local wave-direction estimation (NL-)LWDE", is proposed to localize the defects as sources of nonlinear vibrations. Over the entire scan area, the local direction of the propagating waves is determined based on an angular bandpass filter bank in the wavenumber domain. The observed local wave-direction map is then converted into an error map where the sources (i.e. actuators or defects) are identified as local minima. The proposed NL-LWDE method proves successful for the detection of in-sight and out-of-sight barely visible impact damage (BVID) in flat and tubular CFRP components.

The chapter is split up into two major parts. In the first part, the process of source localization using the LWDE algorithm is outlined and all processing steps are discussed in detail. For this, the measurement results of a damage-free quasi-isotropic CFRP plate are used. The plate is excited with piezoelectric actuators and the LWDE is used to find the location of the in-sight and out-of-sight sources. In the second part, the LWDE algorithm is used in the nonlinear regime (i.e. NL-LWDE) for the detection of BVID in a cross-ply CFRP plate and for the detection of BVID in a CFRP bicycle frame's down tube. It is shown that the proposed NDT method can equally be used in case that the damage is located outside of the measurement area (i.e. out-of-sight damage), for instance at the back of the bicycle frame's down tube.

2. Materials and Experiments

Three CFRP test specimens are used in this chapter (see Figure 14.1). They are referred to as '$\mathrm{CFRP}^{\mathrm{Plate}}_{\mathrm{Virgin}}$','$\mathrm{CFRP}^{\mathrm{Plate}}_{\mathrm{BVID}}$' and '$\mathrm{CFRP}^{\mathrm{Tube}}_{\mathrm{BVID}}$'.

The first test specimen (i.e. $\mathrm{CFRP}^{\mathrm{Plate}}_{\mathrm{Virgin}}$, Figure 14.1 (a)) is a damage-free 330x330x5.45 mm^3 plate manufactured out of 24 layers of unidirectional carbon fiber prepreg according to quasi-isotropic $[(+45/0/-45/90)_3]_s$ lay-up.

The second plate (i.e. '$\mathrm{CFRP}^{\mathrm{Plate}}_{\mathrm{BVID}}$, Figure 14.1 (b)) also measures 330x330x5.45 mm^3 and is manufactured according to cross-ply layup $[(0/90)_6]_s$. It has been impacted with a 7.7 kg drop weight from a height of 0.09 m (i.e. theoretical impact energy 6.8 J) according to ASTM D7136. The low velocity impact resulted in BVID. To reveal the extent of the damage, an immersion ultrasonic C-scan inspection is performed using a 5 MHz focused transducer (H5M, General Electric) in reflection mode. The C-scan's relative amplitude image reveals the complex distribution of delaminations and cracks, which is typical for low velocity impact damage in layered composite materials [7]. The plate is inspected from the side where the low velocity impact took place.

The third test specimen (i.e. $\mathrm{CFRP}^{\mathrm{Tube}}_{\mathrm{BVID}}$, Figure 14.1 (c)) is a CFRP bicycle frame. The layup or thickness of the tubular CFRP sections is unknown. The down tube suffered an impact that introduced BVID. In Chapter 12, a nonlinear energy-based damage map was constructed that revealed this BVID.

Vibrations are introduced using piezoelectric actuators. Table 14.1 summarizes the characteristics of the excitation signals.

For $\mathrm{CFRP}^{\mathrm{Plate}}_{\mathrm{Virgin}}$ (see Figure 14.1 (a)), two different actuators are used: a small (Ø 20 mm) piezoelectric bending disc (Ekulit EPZ-20MS64W) and a larger (Ø 50 mm) piezoshaker (Isi-Sys PS-X-03-6/1000). The bending disc is bonded to the plate using phenyl salicylate while the piezoshaker is attached by vacuum. The use of vacuum and phenyl salicylate allows to easily remove the actuators after the measurements are finished without damaging the component's surface. A five-cycle Hanning-windowed toneburst signal with center frequency 100 kHz is used for exciting the propagating waves. Two separate measurements are performed. First, only the bending disc actuator is attached and used for excitation. Next, the piezoshaker is added and both actuators are supplied with the same excitation signal. This allows to explain the LWDE algorithm first for the simple case of a single source and afterwards for the case of multiple sources. The Falco WMA-300 voltage amplifier is used to increase the excitation signal's voltage to 250 V_{pp}.

For $\mathrm{CFRP}^{\mathrm{Plate}}_{\mathrm{BVID}}$ (see Figure 14.1 (b)), an ultrasonic cleaning transducer (with nominal cleaning power 70 W and resonance frequency 120 kHz) is used as it can deliver more vibrational power. A M10 bolt is screwed into the transducer and serves as a stinger, leading to a relative small contact area between the source and the plate. Again, phenyl salicylate is used to temporarily bond the actuator to the plate (see inset on Figure 14.1 (b)). The actuator is supplied with a linear sine sweep voltage signal from 10 kHz to 125 kHz with amplified voltage 300 V_{pp}.

$CFRP^{Tube}_{BVID}$ is excited with three small piezoelectric actuators (Ekulit EPZ-20MS64W) bonded to the topside of the tube using epoxy. The two actuators at the right are supplied with a sine sweep voltage signal (10 to 125 kHz, 100 V_{pp}) whereas the third actuator at the left is used for a sine excitation at frequency 50 kHz and amplitude 100 V_{pp}.

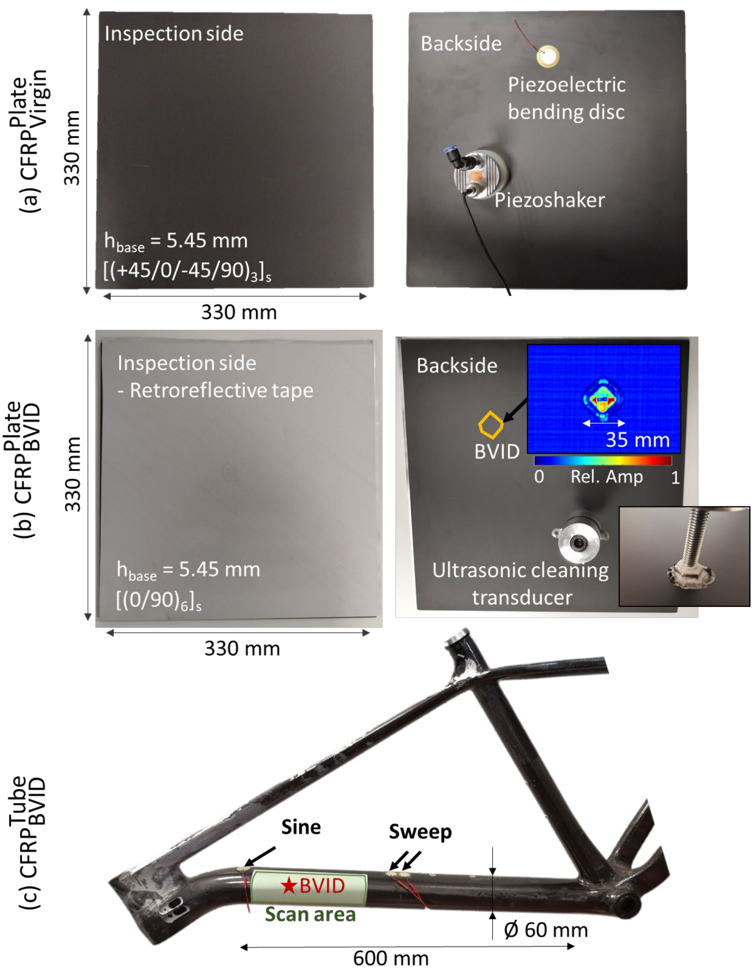

Figure 14.1: CFRP components: (a) Damage-free quasi-isotropic plate ($CFRP^{Plate}_{Virgin}$), (b) Cross-ply plate with BVID ($CFRP^{Plate}_{BVID}$) and (c) Bicycle frame with BVID ($CFRP^{Tube}_{BVID}$).

The full wavefield velocity response of the components is measured using the 3D SLDV (Polytec PSV-500-3D Xtra). The measurement settings are listed in Table 14.1. Both $\mathrm{CFRP}_{\mathrm{BVID}}^{\mathrm{Plate}}$ and $\mathrm{CFRP}_{\mathrm{BVID}}^{\mathrm{Tube}}$ are covered in removable retroreflective tape (3M™ Scotchlite™ 680CRE10). This was required to be able to detect the nonlinear vibrational components which are of low amplitude [3, 5, 6]. The bicycle frame is inspected from both sides. In all cases, the propagation of the fundamental anti-symmetric Lamb mode (A_0), which has a dominant out-of-plane surface velocity response, is investigated. As a result, only the out-of-plane velocity component (V_Z) is considered.

Table 14.1: Excitation and measurement settings.

Sample	Excitation signal					SLDV			
	Type	f_{start} (kHz)	f_c (kHz)	f_{end} (kHz)	Vpp	$f_{sampling}$ (kS/s)	Samples #	Averages #	Scan grid (mm)
$\mathrm{CFRP}_{\mathrm{Virgin}}^{\mathrm{Plate}}$	Toneburst		100		250	1250	1000	10	2.5
$\mathrm{CFRP}_{\mathrm{BVID}}^{\mathrm{Plate}}$	Sweep	10		125	350	625	25000	3	2.5
$\mathrm{CFRP}_{\mathrm{BVID}}^{\mathrm{Tube}}$	Sweep + Sine	10	 50	125	100 100	625	10000	10	≈ 1

3. Source Localization using Local Wave-Direction Estimation

The local wave-direction estimation (LWDE) method is introduced for the measurement results of the damage-free quasi-isotropic CFRP plate ($\mathrm{CFRP}_{\mathrm{Virgin}}^{\mathrm{Plate}}$). First, the LWDE is used for the detection of a single in-sight source of A_0 mode guided waves. Next, the algorithm is extended to detect multiple sources. At last, it is shown that LWDE can equally be used for the detection of multiple out-of-sight sources.

The different steps of the algorithm are schematically illustrated in Figure 14.2. The procedure is inspired by the local wavenumber estimation algorithms based on wavenumber- or modepass filter banks (see Chapter 13) and uses extensive filtering in the wavenumber-frequency domain [8].

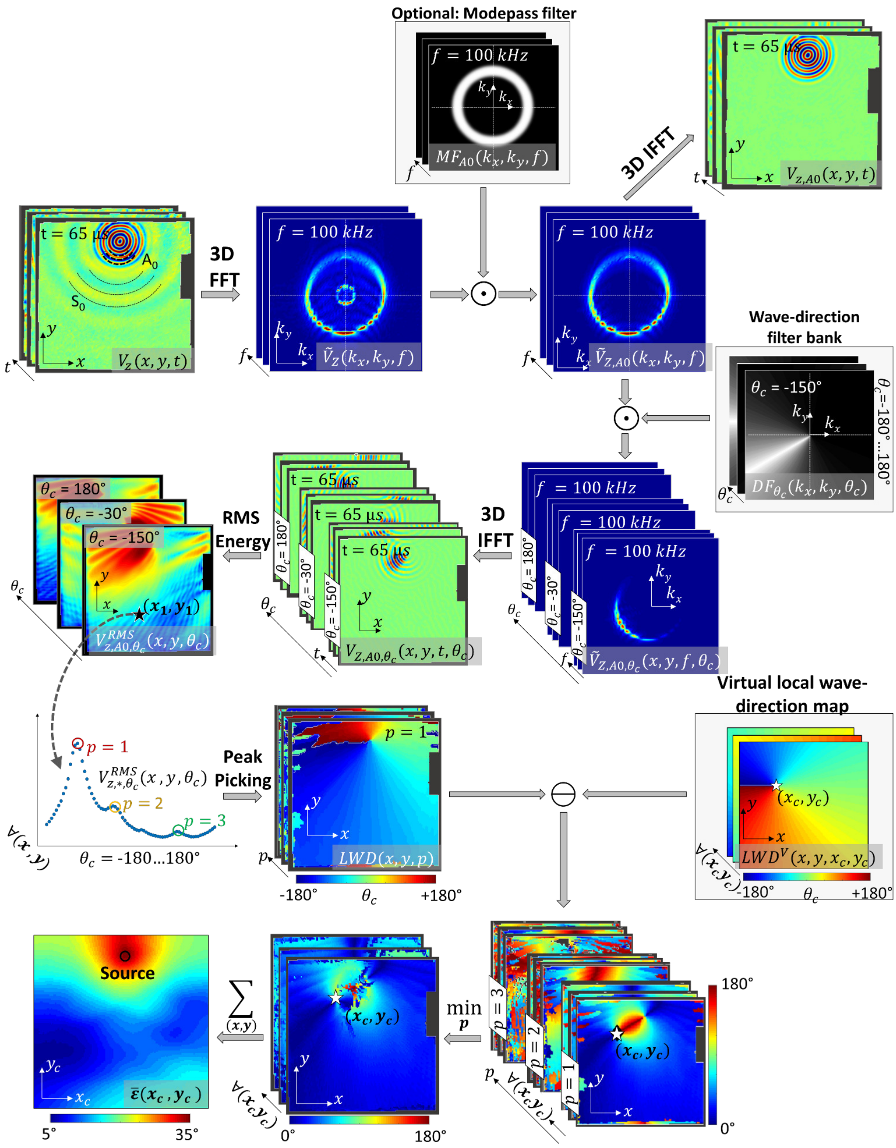

Figure 14.2: Flow chart of source localization using local wave-direction estimation.

3.1. Local Wave-Direction Estimation – Single Source, In-sight

In the first experiment, only the piezoelectric bending disc is used to excite the plate with propagating waves. Figure 14.3 (a) shows a snapshot in time at t = 0.065 ms. From this figure, it is seen that there are two propagating modes: A_0 and S_0.

3.1.1. Wavefield Manipulation – A_0 Modepass Filtering

In order to improve the source localization using LWDE, the toneburst response is first filtered and only the A_0 mode's vibrations are retained. The application of the modepass filter was already discussed in Chapter 10 Section 2.4 and is also used Chapter 13 Section 5.1. A brief summary is provided here.

The modepass filter is applied in the wavenumber-frequency (k_x, k_y, f) domain [8]. First, the toneburst response $V_z(x, y, t)$ is transformed to $\tilde{V}_z(k_x, k_y, f)$ using the 3D FFT:

$$V_z(x, y, t) \xrightarrow{3D\ FFT} \tilde{V}_z(k_x, k_y, f)$$

The wavenumber-frequency map of $\tilde{V}_z(k_x, k_y = 0, f)$ is shown in Figure 14.3 (b) and reveals the dispersion curves of both the A_0 and the S_0 mode. In order to extract only the vibrations corresponding to the A_0 mode, a cosine-shaped bandpass filter $MF_{A0}(k_x, k_y, f)$ is constructed around the dispersion curve of the A_0 mode. The bandpass filter is multiplied with $\tilde{V}_z(k_x, k_y, f)$ in the wavenumber-frequency domain:

$$\tilde{V}_{Z,A0}(k_x, k_y, f) = \tilde{V}_Z(k_x, k_y, f) \odot MF_{A0}(k_x, k_y, f)$$

The resulting wavenumber-frequency map (again for k_y = 0) is shown in Figure 14.3 (c). At last, the inverse 3D FFT is performed to obtain the desired A_0 toneburst response in spatial-time domain:

$$\tilde{V}_{Z,A0}(k_x, k_y, f) \xrightarrow{3D\ IFFT} V_{z,A0}(x, y, t)$$

Figure 14.3 (d) shows the snapshot in time of the filtered signal where it is observed that the S_0 mode is successfully removed. In addition, the application of the A_0 modepass filter results in a reduction of the measurement noise. The snapshots, as well as the A_0 modepass filter (at 100 kHz), are also included in the schematic overview of Figure 14.2.

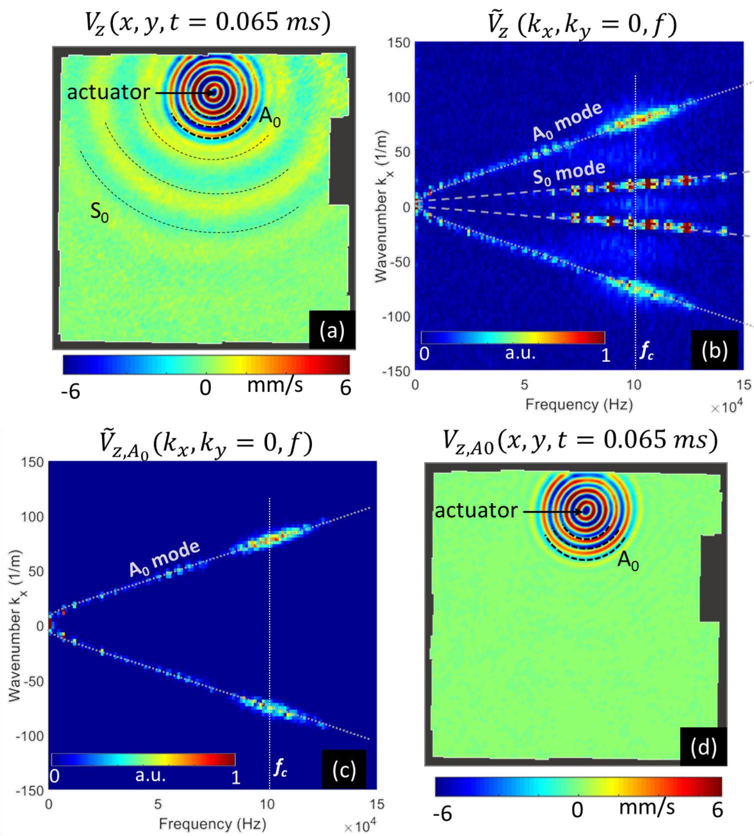

Figure 14.3: Modepass filtering of the A0 mode in the toneburst response of $\mathrm{CFRP}_{\mathrm{Virgin}}^{\mathrm{Plate}}$: (a,b) Snapshot and wavenumber-frequency map (at k_y = 0) for the unfiltered velocity response, (c,d) Wavenumber-frequency map (at k_y = 0) and snapshot for the A0 mode-filtered velocity response.

3.1.2. Local Wave-Direction Estimation - Wave-direction Filter Bank

The wavenumber map corresponding to $\tilde{V}_{z,A0}(k_x, k_y, f)$ at $f = f_c$ = 100 kHz is shown in Figure 14.4 (a). The A0 mode is visible as a quasi-circular ring of increased intensity. Figure 14.4 (b) presents a snapshot in time of the A0 mode toneburst response. A bank of Gaussian-shaped angular bandpass filters DF_{θ_c} is constructed as:

$$DF_{\theta_c}(k_x, k_y, \theta_c) = \exp\left(\frac{\angle(k_x,k_y) - \theta_c}{0.72\ BW_\theta}\right)$$
$$\text{with} \quad \angle(k_x, k_y) = \begin{cases} \operatorname{atan}(k_y/k_x) & \text{if } \mathrm{k_x} < 0 \\ \operatorname{atan}(k_y/k_x) + \pi & \text{if } \mathrm{k_x} \geq 0 \end{cases} \tag{14.1}$$

where $\angle(k_x, k_y)$ denotes the angle of the $[k_x, k_y]$ vector, BW_θ is the filter's angular bandwidth and $\theta_c = [-180 \ldots -5, 0, 5 \ldots 180]$ is the bandpass filter's center angle. As an example, the bandpass filter for θ_c = -30° and BW_θ = 7° is shown in Figure 14.4 (c). The response after applying this filter:

$$\tilde{V}_{z,A0,\theta_c}(k_x, k_y, f, \theta_c) = DF_{\theta_c}(k_x, k_y, \theta_c) \odot \tilde{V}_{z,A0}(k_x, k_y, f)$$

is shown in Figure 14.4 (d). This specific bandpass filter results in the extraction of all the vibrations for which the propagation direction $\angle(k_x, k_y)$ is close to θ_c = -30°, i.e. waves travelling in the downward-right direction [8]. Inverse 3D FFT takes the signal back to the spatial-time domain:

$$\tilde{V}_{z,A0,\theta_c}(k_x, k_y, f, \theta_c) \xrightarrow{\text{3D IFFT}} V_{z,A0,\theta_c}(x, y, t, \theta_c)$$

Figure 14.4 (e) shows the snapshot in time of the directional filtered response $V_{z,A0,\theta_c}$ with center angle θ_c = -30°. Additionally, Figure 14.4 (f-h) presents the wave-directional filter procedure illustrated for center angle θ_c = -110°. Please note again, that the different processing steps are also included in Figure 14.2 as an aid in understanding the algorithm.

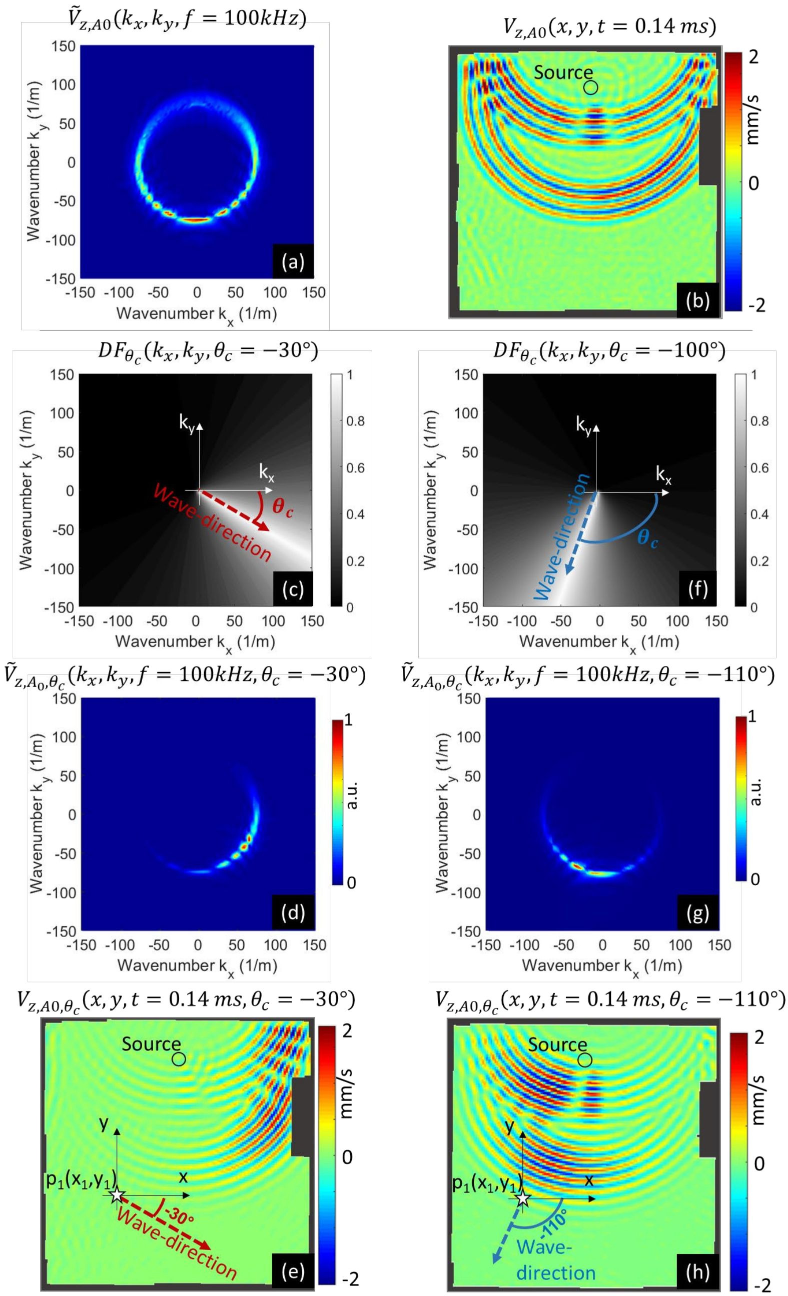

Figure 14.4: Illustration of the wave-direction bandpass filtering procedure for the A0 toneburst response in $\mathrm{CFRP}^{\mathrm{Plate}}_{\mathrm{Virgin}}$. (a) Wavenumber map at f = 100 kHz. (b) Snapshot of unfiltered response, (c-e) Wave-direction filter, wavenumber map and snapshot for wave-direction filter with θ_c = -30° and (f-h) Wave-direction filter, wavenumber map and snapshot for wave-direction filter with θ_c = -110°.

3.1.3. Local Wave-Direction Estimation – Direction Detection

After applying the wave-direction (or angular) bandpass filter bank, a 4D dataset $V_{z,A0,\theta_c}(x,y,t,\theta_c)$ is obtained where the last dimension corresponds to the propagation direction of the guided waves. As an example, the $V_{z,A0,\theta_c}(x,y,t,\theta_c)$ signal is shown in Figure 14.5 (a) for the scan point $p_1(x_1,y_1)$ and two propagation directions θ_c = -30° and -110°. The location of this point is indicated with a star on Figure 14.4 (e,h). From Figure 14.5 (a) it is observed that the vibrations with direction θ_c = -110° have more energy compared to the vibrations with direction θ_c = -30°. In order to find the dominant wave propagation direction at each scan point, the energy of the waves travelling in each direction θ_c is determined as the root-mean-square (RMS) of $V_{z,A0,\theta_c}(x,y,t,\theta_c)$ over time:

$$V_{z,A0,\theta_c}^{\mathrm{RMS}}(x,y,\theta_c) = \frac{1}{N}\sqrt{\sum_{i=1}^{N}\left(V_z{}^{\mathrm{A_0}}(x,y,t_i,\theta_c)\right)^2} \tag{14.2}$$

Figure 14.5 (b) shows the obtained energy curve $V_{z,A0,\theta_c}^{\mathrm{RMS}}(x,y,\theta_c)$ for the point $p_1(x_1,y_1)$. The direction corresponding to the maxima in the curve is identified:

$$LWD(x,y) = \underset{\theta_c}{\mathrm{ArgMax}}\left(V_{z,A0,\theta_c}^{\mathrm{RMS}}(x,y,\theta_c)\right)$$

For point $p_1(x_1,y_1)$, a dominant local wave-direction LWD is found at θ_c = -110°. This direction is indicated with a blue arrow on Figure 14.5 (c) and correctly points towards the source of vibrations. Other local maxima of lower intensity are visible in the energy curve at around -30°, +100° and 22°. These small maxima are attributed to edge reflections of the excited wave packet. This is illustrated on Figure 14.5 (c) for the wave with propagation direction -30°.

The direction detection procedure is repeated for every scan point, resulting in a local wave-direction map $LWD(x,y)$. The $LWD(x,y)$ map is shown in Figure 14.6 (a). From this figure, the location of the actuator is clear because for the majority of the scan points, a dominant wave propagation direction is found that points to the source's location.

The flowchart shown in Figure 14.2 shows a stack of LWD maps corresponding to the order p of the detected peaks in the $V_{z,A0,\theta_c}^{\mathrm{RMS}}(x,y,\theta_c)$ curve. For the detection of a single source, only the first LWD map is required corresponding to $p = 1$. In case of multiple sources, or when dealing with strong edge reflections, all LWD maps must be taken into account as will be explained in Section 3.2.

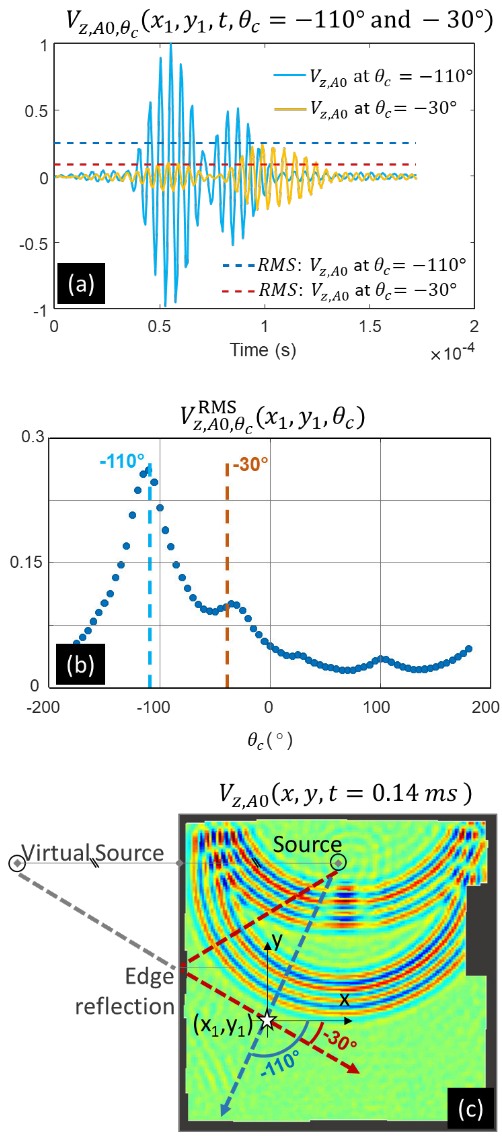

Figure 14.5: (a) Velocity signal in $\text{CFRP}^{\text{Plate}}_{\text{Virgin}}$ corresponding to the A0 mode at scan point $p_1(x_1, y_1)$ for waves travelling in the 30° and -110° directions. (b) RMS energy of A0 mode in function of the propagation direction. (c) Snapshot of A0 mode toneburst response at t = 0.14 ms with indication of wave propagation directions.

3.1.4. Local Wave-Direction Estimation - Error Map

While the location of the source could already be distinguished in the $LWD(x, y)$ map (see Figure 14.6 (a)), this might not be the case anymore for more challenging test cases (see further). Therefore, it is proposed to use a virtual local wave-direction field $LWD^V(x,y,x_c,y_c)$ for the construction of an error map. The virtual local wave-direction field LWD^V is constructed by assuming that the point with coordinates (x_c,y_c) is the only source of propagating waves:

$$LWD^V(x,y,x_c,y_c) = \angle(x - x_c, y - y_c) \tag{14.3}$$

As an example, the LWD^V field is plotted in Figure 14.6 (b) for the scan point $p_1(x_1,y_1)$ indicated with the white star. Important to note is that this definition of the LWD^V field assumes a circular wave energy flow. As explained in Chapter 2, this assumption is valid only for isotropic materials. In case of anisotropic materials, such as composites, it is important to use the A_0 mode as this mode is less affected by the anisotropy compared to for instance the S_0 mode.

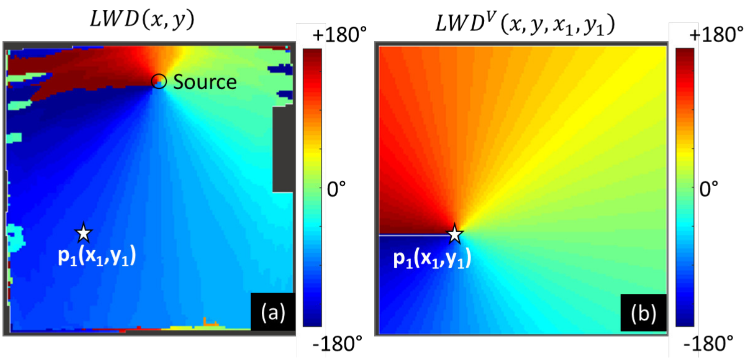

Figure 14.6: $\text{CFRP}_{\text{Virgin}}^{\text{Plate}}$ with 1 source activated (a) Observed local wave-direction map (b) Virtual local wave-direction field in case point $p_1(x_1,y_1)$ is a source.

Next, for each point (x_c,y_c) the difference (in degrees) between the observed LWD map and the virtual LWD^V field is calculated (see also flow chart in Figure 14.2). The local error $\bar{\epsilon}$ is then obtained as the average of this difference over all points:

$$\bar{\epsilon}(x_c,y_c) = \frac{1}{N_x\,N_y}\sum_{(x,y)} |LWD(x,y) - LWD^V(x,y,x_c,y_c)| \tag{14.4}$$

The resulting error map $\bar{\epsilon}(x_c,y_c)$ is shown in Figure 14.7. A low error value at a point indicates that the virtual LWD^V field for this point is similar to the observed LWD map. As such, the source is found as a local minimum in $\bar{\epsilon}(x_c,y_c)$ (note the inverted colorbar).

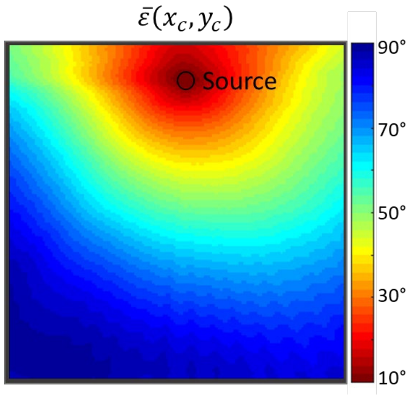

Figure 14.7: $\text{CFRP}_{\text{Virgin}}^{\text{Plate}}$ with 1 source activated: Local wave-direction error map.

3.2. Local Wave-Direction Estimation – Multiple Sources, Insight

In the previous section, there was only one source of propagating waves. Now, the experiment is repeated using both the actuators (see Figure 14.1 (a)). Figure 14.8 (a) shows a snapshot in time of the A_0 modepass filtered toneburst response $V_{z,\text{A0}}(x, y, t)$ at t = 0.1 ms. An exemplary point $p_2(x_2, y_2)$ is marked with a white star.

All processing steps are identical to the previous case up to the direction detection (see Figure 14.2 – *Peaks Picking*). In this case, the *Peak Picking* algorithm is used to identify all local maxima in the RMS energy curve:

$$V_{z,A0,\theta_c}^{\text{RMS}}(x, y, \theta_c) \xrightarrow{Peak\ Picking\ \theta_c} LWD(x, y, p)$$

The detected peaks in the RMS curve are sorted according to their maximum value and denoted with integer p. As such, the global maximum (i.e. the highest peak) corresponds to p = 1. For the marked point $p_2(x_2, y_2)$, the RMS energy in function of the propagation direction is shown in Figure 14.8 (b) and two local maxima (or peaks) are found at θ_c = -70° and θ_c = 15°. These directions correspond to the direction of the piezoelectric bending disc (i.e. Source 1) and the piezoshaker (i.e. Source 2), respectively (see arrows on Figure 14.8 (a)).

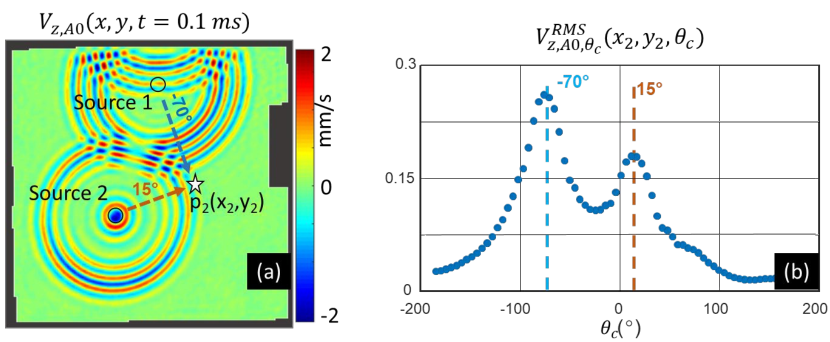

Figure 14.8: $\text{CFRP}_{\text{Virgin}}^{\text{Plate}}$ with 2 sources activated: (a) Snapshot at t = 0.1 ms and (b) RMS energy in function of wave propagation direction at point $p_2(x_2, y_2)$.

The multi-direction detection is performed at each scan point leading to a three-dimensional local wave-direction dataset: $LWD(x, y, p)$. As an example, the $LWD(x, y, p = 1)$ and $LWD(x, y, p = 2)$ maps are shown in Figure 14.9 (a) and (b), respectively. The detected wave propagation directions θ_c are indicated for the exemplary point $p_2(x_2, y_2)$. Point $p_2(x_2, y_2)$ is located at nearly equal distances from both sources. However, Source 1 (i.e. the bending disc) has a higher vibrational power output. As a result, the primary (p = 1) wave propagation direction at point $p_2(x_2, y_2)$ corresponds to Source 1 (see Figure 14.9 (a)) while the secondary (p = 2) wave propagation direction at point $p_2(x_2, y_2)$ corresponds to Source 2 (see Figure 14.9 (b)).

The edges of the component are not damped leading to the edge reflection of the propagating waves (see also previously in Figure 14.5 (c)). The resulting edge reflections are visible in the $LWD(x, y, p = 2)$ map (see Figure 14.9 (b)). For instance, above Source 1 a local wave-direction is found corresponding to downward travelling waves (i.e. $\theta_c < 0°$). This direction is attributed to the waves excited by Source 1 that are reflected at the top edge of the component.

The equation for the calculation of the error map (Eq. (14.4)) is adapted to allow for multiple source identification and to deal with the presence of the edge reflections (see also flowchart in Figure 14.2):

$$\bar{\epsilon}(x_c, y_c) = \frac{1}{N_x\, N_y} \sum_{(x,y)} \min_{p} |LWD(x, y, p) - LWD^V(x, y, x_c, y_c)| \quad (14.5)$$

The resulting error map $\bar{\epsilon}(x_c, y_c)$ is shown in Figure 14.9 (c). The two sources are correctly found as local minima. The observed edge reflections in Figure 14.9 (b) correspond to virtual sources that are located outside of the structure (see also Figure 14.5 (c)). As a result, they have only a minor effect on the obtained error map and don't increase the error value at the actual sources. Also for the case of a single source, the error map $\bar{\epsilon}(x_c, y_c)$ is improved when using Eq. (14.5) instead of Eq. (14.4). This is seen by comparing the error map $\bar{\epsilon}(x_c, y_c)$ calculated using Eq. (14.5) (see last step in Figure 14.2) with the error map $\bar{\epsilon}(x_c, y_c)$ in Figure 14.7.

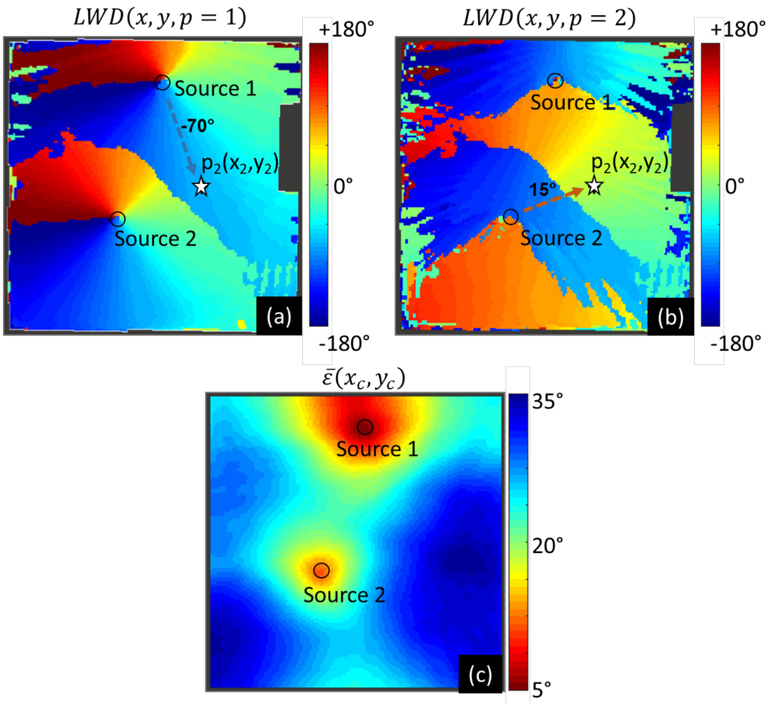

Figure 14.9: $\mathrm{CFRP}_{\mathrm{Virgin}}^{\mathrm{Plate}}$ with 2 sources activated: Local wave-direction maps for (a) $p = 1$ and (b) $p = 2$ and (c) Local wave-direction error map.

3.3. Local Wave-Direction Estimation – Multiple Sources, Out-of-sight

As a last step, it is illustrated that the LWDE algorithm equally works for the detection of sources that are not part of the measurement area (i.e. out-of-sight sources). This allows to find sources (and later damage) that are hidden behind other structures. It could also be exploited to reduce the measurement time as the SLDV would only need to scan part of the component.

Here, the out-of-sight source localization is illustrated for two cases where the incomplete scan areas are indicated with green rectangles on Figure 14.10 (a) and (b). All processing steps are identical to the previous section with the exception that only part of the measurement dataset is utilized. In order to increase the resolution in the wavenumber domain, the incomplete scan area is zero-padded in spatial domain so that the amount of points is identical to the case where the total area was scanned.

First, the local wave-direction maps $LWD(x, y, p)$ are determined. The obtained $LWD(x, y, p = 1)$ maps are superimposed on Figure 14.10 (a,b). Next, the damage maps are constructed using Eq. (14.5). The coordinates (x_c, y_c) span the entire component, whereas the points (x, y) are limited to the incomplete scan area. The resulting error maps $\bar{\epsilon}(x_c, y_c)$ are shown in Figure 14.10 (c,d). For each of these maps, a reduced error value is found at the location of both sources. The use of only a small part of the component's surface response led to a correct but less accurate source localization. In order to improve the accuracy, the results of multiple individual incomplete scan areas can be combined by taking the sum of the error values, see Figure 14.10 (e).

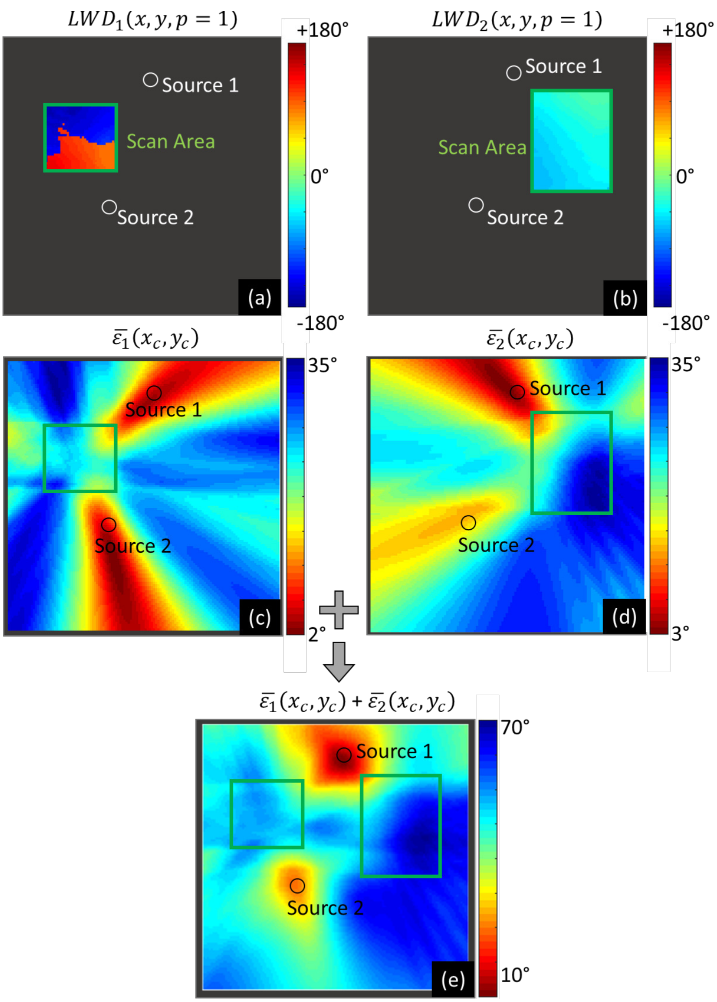

Figure 14.10: $\text{CFRP}^{\text{Plate}}_{\text{Virgin}}$ with two out-of-sight sources: (a-b) Local wave-direction maps for small scan areas (c-d) Local wave-direction error maps for small scan areas and (e) Combined error map.

4. Nonlinear Defect Localization using Local Wave-Direction Estimation

In the previous section, it was explained how LWDE can be used for localization of piezoelectric sources of guided waves. From previous studies of the current authors (see Chapter 8 Section 5.1 and [5, 6]), it is known that defects behave as secondary sources of nonlinear vibrational components. As such, a damage detection procedure is proposed where LWDE is used for defect detection by localization of all sources of nonlinear vibrational components. This nonlinear version of LWDE is indicated as NL-LWDE. Results are shown for in-sight as well as out-of-sight damage detection in the impacted cross-ply CFRP plate ($\mathrm{CFRP}_{\mathrm{BVID}}^{\mathrm{Plate}}$) and the bicycle frame's down tube ($\mathrm{CFRP}_{\mathrm{BVID}}^{\mathrm{Tube}}$).

The same workflow is followed as was schematically illustrated in Figure 14.2. The only difference is in the first wavefield manipulation step. In previous example, an A_0 modepass filter was used to extract the linear A_0 mode response from the toneburst measurement, resulting in $V_{z,A0}(x,y,t)$. In this case, the wavefield manipulation handles the extraction of a nonlinear component of interest from a sweep measurement in combination with a sweep to toneburst conversion, resulting in $V_{z,HH_2,f_c}(x,y,t)$ and in $V_{z,SB_{1,1},f_c}(x,y,t)$.

4.1. Wavefield Manipulation

The contact acoustic nonlinearity at the BVID results in the generation of nonlinear vibrational components. Here, the second higher harmonic component (HH_2) is used for the sweep response of $\mathrm{CFRP}_{\mathrm{BVID}}^{\mathrm{Plate}}$ and the first modulation sideband ($SB_{1,1}$) is used for the combined sweep and sine response of $\mathrm{CFRP}_{\mathrm{BVID}}^{\mathrm{Tube}}$. As such, the measured sweep responses $V_z(x,y,t)$ need to be converted to the HH_2 toneburst response $V_{z,HH_2,f_c}(x,y,t)$ and to the $SB_{1,1}$ toneburst response $V_{z,SB_{1,1},f_c}(x,y,t)$, respectively. These nonlinear toneburst responses are then used as input for the NL-LWDE algorithm. The construction of $V_{z,HH_2,f_c}(x,y,t)$ and $V_{z,SB_{1,1},f_c}(x,y,t)$ requires: (a) the extraction of the specified nonlinear components and (b) the sweep to toneburst conversion. In this case, it is not necessary to perform an additional A_0 modepass filtering step because the nonlinear components are already dominated by the A_0 mode.

4.1.1. Extraction of Nonlinear Component

The HH_2 and $SB_{1,1}$ components are extracted from the total response of $\mathrm{CFRP}_{\mathrm{BVID}}^{\mathrm{Plate}}$ and $\mathrm{CFRP}_{\mathrm{BVID}}^{\mathrm{Tube}}$, respectively, using a bandpass filter in the time-frequency domain. The filtering procedure was explained in detail in Chapter 10 Section 2.5 (or in [6]). In addition, this wavefield manipulation was already applied to the measurement result of $\mathrm{CFRP}^{\mathrm{Tube}}_{\mathrm{BVID}}$ in Chapter 12. A short recapitulation is given here.

The nonlinear component extraction procedure has three steps. First, short-time-Fourier-transformation (STFT) is used to go from the time domain to the time-frequency domain:

$$V_z(x,y,t) \xrightarrow{STFT} \tilde{V}_z(x,y,t,f)$$

The resulting average spectrogram of $\mathrm{CFRP}^{\mathrm{Plate}}_{\mathrm{BVID}}$ is shown in Figure 14.11 (a). Straights lines of increased intensity are visible corresponding to the linear sweep response and to the HH components (e.g. HH_2 and HH_3). Secondly, the nonlinear component of interest is extracted from the spectrogram using a bandpass filter in time-frequency domain TFF:

$$\tilde{V}_{Z,HH_2}(x,y,t,f) = \tilde{V}_z(x,y,t,f) \odot TFF^{HH_2} \qquad \text{for } \mathrm{CFRP}^{\mathrm{Plate}}_{\mathrm{BVID}}$$
$$\tilde{V}_{Z,SB_{1,1}}(x,y,t,f) = \tilde{V}_z(x,y,t,f) \odot TFF^{SB_{1,1}} \qquad \text{for } \mathrm{CFRP}^{\mathrm{Tube}}_{\mathrm{BVID}}$$

Figure 14.11 (b) shows the bandpass filter used for extracting the HH_2 component in $\mathrm{CFRP}^{\mathrm{Plate}}_{\mathrm{BVID}}$. The resulting filtered spectrogram is shown in Figure 14.11 (c). At last, the nonlinear sweep response is obtained in spatial-time domain after inverse STFT:

$$\tilde{V}_{Z,HH_2}(x,y,t,f) \xrightarrow{ISTFT} V_{Z,HH_2}(x,y,t) \qquad \text{for } \mathrm{CFRP}^{\mathrm{Plate}}_{\mathrm{BVID}}$$
$$\tilde{V}_{Z,SB_{1,1}}(x,y,t,f) \xrightarrow{ISTFT} V_{Z,SB_{1,1}}(x,y,t) \qquad \text{for } \mathrm{CFRP}^{\mathrm{Tube}}_{\mathrm{BVID}}$$

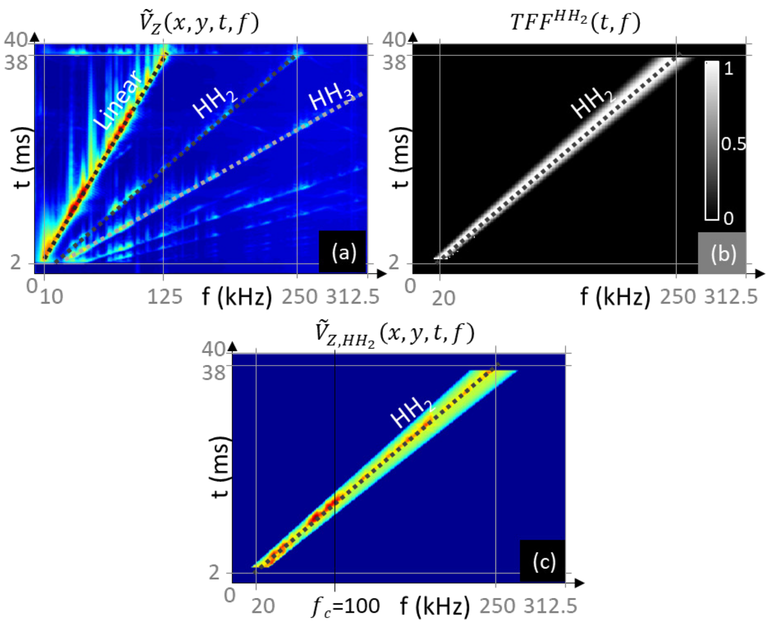

Figure 14.11: HH_2 extraction in $\mathrm{CFRP}^{\mathrm{Plate}}_{\mathrm{BVID}}$: (a) Total sweep response, (b) HH_2 bandpass filter and (c) Extracted HH_2 component response.

4.1.2. Sweep to Toneburst Conversion

As the NL-LWDE relies on propagating waves, the nonlinear sweep responses, i.e. $V_{Z,HH_2}(x,y,t)$ for $\mathrm{CFRP}_{\mathrm{BVID}}^{\mathrm{Plate}}$ and $V_{Z,SB_{1,1}}(x,y,t)$ for $\mathrm{CFRP}_{\mathrm{BVID}}^{\mathrm{Tube}}$, are transformed to toneburst responses, i.e. $V_{Z,HH_2,f_c}(x,y,t)$ and $V_{Z,SB_{1,1},f_c}(x,y,t)$, using frequency-filtering:

$$V_{Z,HH_2}(x,y,t) \xrightarrow{Freq.Filt.f_c} V_{Z,HH_2,f_c}(x,y,t) \qquad \text{for } \mathrm{CFRP}_{\mathrm{BVID}}^{\mathrm{Plate}}$$

$$V_{Z,SB_{1,1}}(x,y,t) \xrightarrow{Freq.Filt.f_c} V_{Z,SB_{1,1},f_c}(x,y,t) \qquad \text{for } \mathrm{CFRP}_{\mathrm{BVID}}^{\mathrm{Tube}}$$

This wavefield manipulation method is explained in Chapter 10 Sections 2.2 and 2.5.3.

For $\mathrm{CFRP}_{\mathrm{BVID}}^{\mathrm{Plate}}$, the broadband (20 to 250 kHz) HH_2 response is converted to a narrowband ten-cycle Hanning-windowed toneburst response at center frequency f_c = 100 kHz. This frequency was selected because at 100 kHz a high intensity of the HH_2 component is observed in the spectrogram (see Figure 14.11 (c)). The same methodology is repeated for $\mathrm{CFRP}_{\mathrm{BVID}}^{\mathrm{Tube}}$ where the broadband (40 to 155 kHz) $SB_{1,1}$ response is also converted to a ten-cycle toneburst response at f_c = 100 kHz. Similar results are obtained for other numbers of cycles.

Figure 14.12 shows time snapshots of the linear as well as the nonlinear toneburst responses in $\mathrm{CFRP}_{\mathrm{BVID}}^{\mathrm{Plate}}$ and in $\mathrm{CFRP}_{\mathrm{BVID}}^{\mathrm{Tube}}$. There are two figures for each toneburst in $\mathrm{CFRP}_{\mathrm{BVID}}^{\mathrm{Tube}}$ corresponding to the two sides of the bicycle frame. The linear response was obtained after extracting the linear part using time-frequency filtering (see Chapter 10 Section 2.5) followed by a toneburst conversion with f_c = 100/2 kHz = 50 kHz for $\mathrm{CFRP}_{\mathrm{BVID}}^{\mathrm{Plate}}$ and f_c = 100-30 kHz = 70 kHz for $\mathrm{CFRP}_{\mathrm{BVID}}^{\mathrm{Tube}}$. These linear signals are not used in the NDT procedure but were constructed solely to make the snapshots in Figure 14.12 (a,c,e).

At the moment that the piezoelectric excited wave packet meets the defect (see Figure 14.12 (a,c)), contact acoustic nonlinearity takes place and the defect acts as a secondary source of the nonlinear vibrations (see Figure 14.12 (b,d)). For $\mathrm{CFRP}_{\mathrm{BVID}}^{\mathrm{Tube}}$, the nonlinear vibrations, which are created at the BVID, propagate to the other side of the tube. This is visible in Figure 14.12 (f) where the waves are emerging from the top side of the scan area (as indicated with gray dotted lines). Note the low amplitude of the nonlinear components which necessitated the use of retroreflective tape for these SLDV measurements.

Apart from the nonlinear components generated at the defect, nonlinear waves can also be excited at the actuator (i.e. source nonlinearity). This is observed in Figure 14.12 (d) for the HH_2 component in $\mathrm{CFRP}_{\mathrm{BVID}}^{\mathrm{Plate}}$. Although these waves are of relatively low amplitude compared to the defect nonlinearity, they affect the NL-LWDE procedure (see further). The nonlinear response of $\mathrm{CFRP}_{\mathrm{BVID}}^{\mathrm{Tube}}$ is not affected by source nonlinearity because modulations sidebands are exclusively created at defects (as explained in Section 3.1 of Chapter 12).

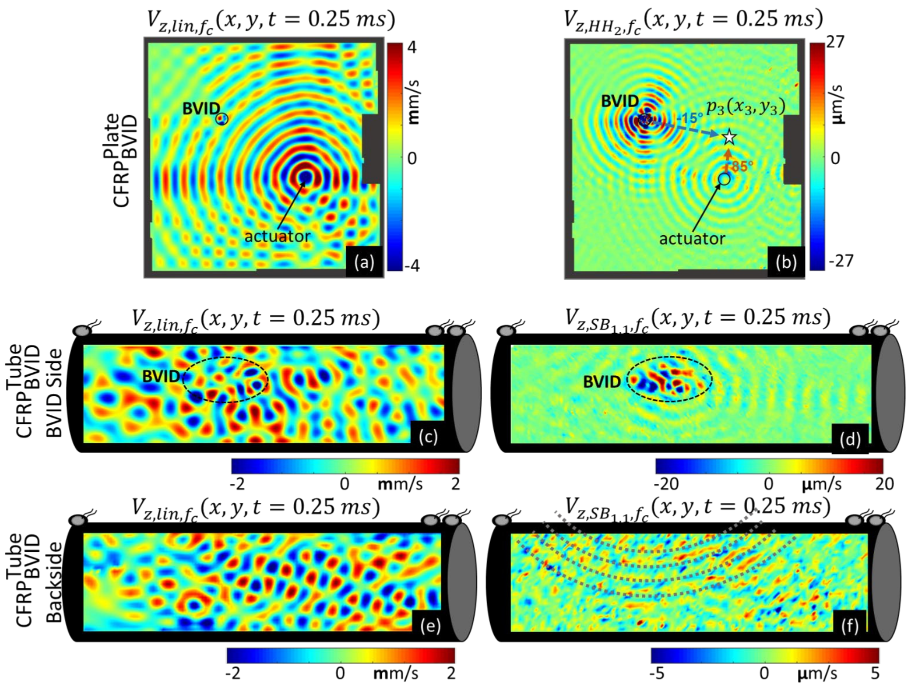

Figure 14.12: Snapshots of the (left) linear component and (right) nonlinear component for the toneburst responses in (a-b) $\mathrm{CFRP}_{\mathrm{BVID}}^{\mathrm{Plate}}$ and in (c-f) $\mathrm{CFRP}_{\mathrm{BVID}}^{\mathrm{Tube}}$.

4.2. Nonlinear Local Wave-Direction Estimation NL-LWDE for In-sight Damage Detection

The NL-LWDE damage maps are constructed first for the cases where the BVID is part of the measurement area, thus for $\mathrm{CFRP}_{\mathrm{BVID}}^{\mathrm{Plate}}$ and for $\mathrm{CFRP}_{\mathrm{BVID}}^{\mathrm{Tube}}$ when inspected from the side where the impact damage is located. In order to construct the observed LWD maps, the flowchart shown in Figure 14.2 and explained in Section 3.1 is followed.

For $\mathrm{CFRP}_{\mathrm{BVID}}^{\mathrm{Plate}}$, there are two sources of HH_2 vibrations: the defect and the actuator (see Figure 14.12 (b)). As a result, two peaks are found in the $V_{Z,HH_2,f_c,\theta_c}^{RMS}(x_3, y_3, \theta_c)$ curve as shown in Figure 14.13 (a) for the exemplary point $p_3(x_3, y_3)$ marked on Figure 14.12 (d) with a white star. For this particular point, the dominant peak (p = 1) corresponds to a propagation direction θ_c = -15° which points to the BVID, whereas the second peak (p = 2) is around θ_c = 85° and points to the actuator. This observation is reflected in the $LWD(x, y, p)$ maps shown in

Figure 14.13 (b,c) for p = 1 and p = 2, respectively. The exemplary point $p_3(x_3, y_3)$ is again marked with a white star and the dominant wave propagation directions are indicated.

The error map is obtained using Eq. (14.5) where the virtual LWD^V is constructed assuming a circular wave front (see Eq. (14.3)). Although these materials are not isotropic, the use of the A_0 mode allows to make this assumption. The quasi-circular waveform in $\mathrm{CFRP}_{\mathrm{BVID}}^{\mathrm{Plate}}$ is also visible in Figure 14.12 (a,d). For illustration purposes, the error map is first constructed for $\mathrm{CFRP}_{\mathrm{BVID}}^{\mathrm{Plate}}$ by only looking at the dominant propagation direction observed at each point (p_{max} = 1). The result is shown in Figure 14.13 (d) and reveals only the dominant source of HH_2 vibrations, which is the BVID. For the error map of Figure 14.13 (e), all detected peaks in the $V_{z,HH_2,f_c,\theta_c}^{\mathrm{RMS}}(x, y, \theta_c)$ are taken into account (incl. potential edge reflections). It can be seen that by using also the information of the other peaks, both sources of the HH_2 waves are found and the BVID is more accurately localized.

The LWD map (p = 1) for $\mathrm{CFRP}_{\mathrm{BVID}}^{\mathrm{Tube}}$ is shown in Figure 14.14 (a) and reveals the direction of the $SB_{1,1}$ waves that are created at the BVID. The resulting error map (with p_{max} unlimited) is shown in Figure 14.14 (b) and correctly reveals the BVID as the only source of the $SB_{1,1}$ vibrations.

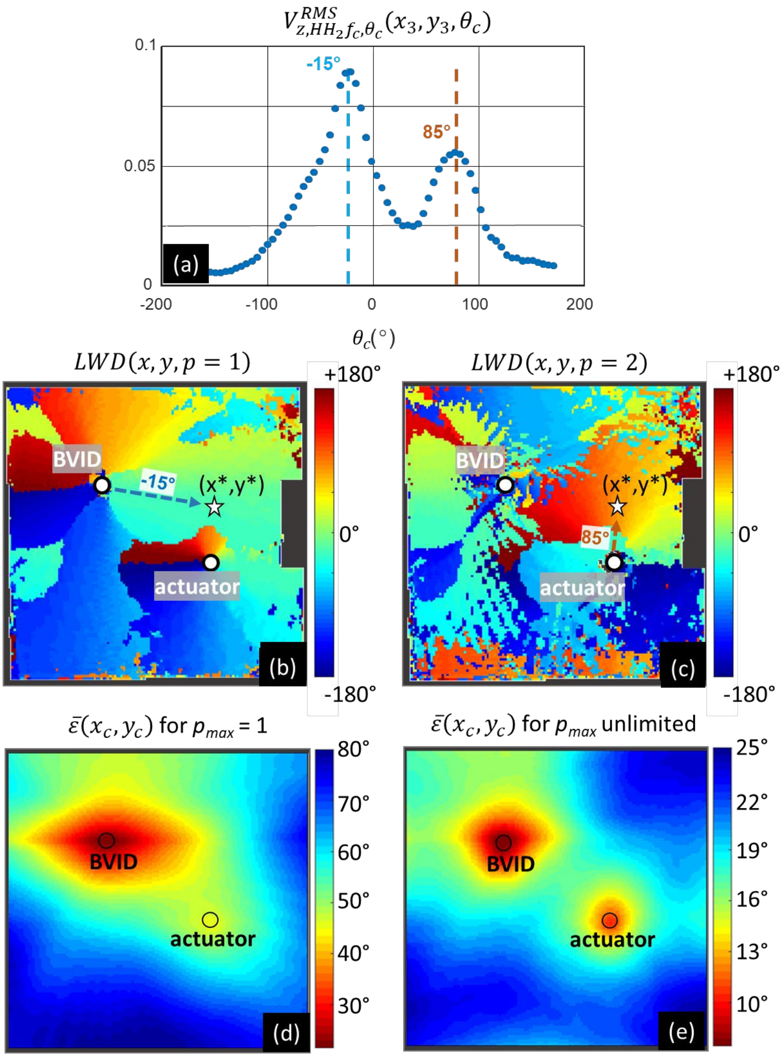

Figure 14.13: NL-LWDE for $\text{CFRP}^{\text{Plate}}_{\text{BVID}}$ (a) RMS energy of the HH_2 signal at point $p_3(x_3, y_3)$ in function of the propagation direction θ_c, Observed local wave-direction map for (b) p = 1 and for (c) p = 2 and Error map under (d) single source assumption and (e) multiple source assumption.

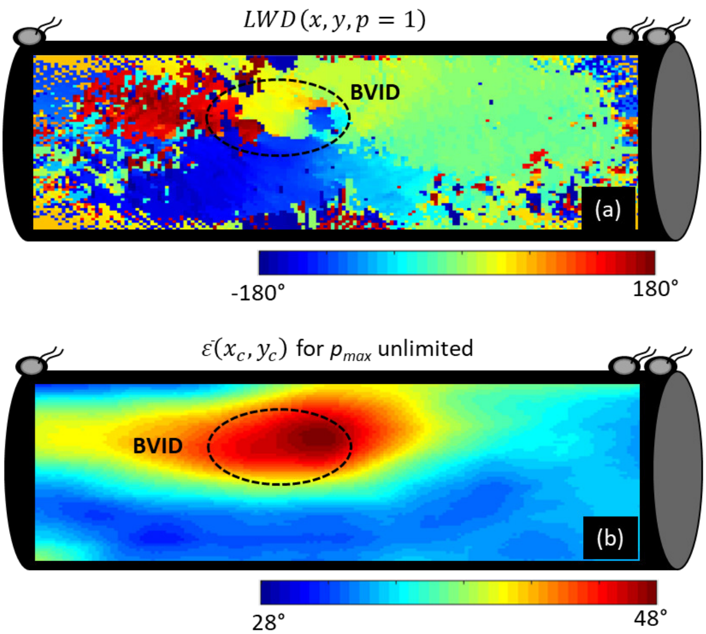

Figure 14.14: (a) Observed local wave-direction map in $\mathrm{CFRP}_{\mathrm{BVID}}^{\mathrm{Tube}}$ for p = 1 and (b) Error map for $\mathrm{CFRP}_{\mathrm{BVID}}^{\mathrm{Tube}}$ under multiple source assumption.

4.3. Nonlinear Local Wave-Direction Estimation NL-LWDE for Out-of-sight Damage Detection

In the previous section, it was illustrated how NL-LWDE can be used to detect damage without the need for a baseline measurement and with limited user input. While this is certainly promising for NDT in an industrial environment, there are other damage map construction methods that can do the same e.g. mode-removed weighted-root-mean-square energy mapping (see Chapter 11 or [9-11]), nonlinear broadband energy mapping (see Chapter 12 or [6]) or local wavenumber estimation (see Chapter 13 or [12-17]). The main advantages of using NL-LWDE for NDT is that the method is promising for detection of out-of-sight damage.

First, out-of-sight damage detection is illustrated for $\mathrm{CFRP}_{\mathrm{BVID}}^{\mathrm{Plate}}$. In order to show the robustness of the NL-LWDE method, four damage maps are constructed where in each case a different incomplete scan area is considered. Moreover, each of these four incomplete scan areas differ in location and shape. The areas are indicated with green rectangles on Figure 14.15 (a-d).
The local wave-direction maps are determined and superimposed on Figure 14.15 (a-d) for p = 1. The corresponding error maps $\bar{\epsilon}(x_c, y_c)$ are constructed using Eq. (14.5). Note again that the coordinates (x_c, y_c) cover the entire

component while the points (x, y) are limited to the incomplete scan area. The resulting error maps $\bar{\varepsilon}(x_c, y_c)$ are shown in Figure 14.15 (e-h). For each of these maps, a low error is found at the location of the BVID, even when the incomplete scan area is located relatively close to the sample's edge and close to the excitation position (i.e. case (d,h)). This indicates the robustness of the proposed method.

For improved accuracy, multiple distributed small areas can be considered and the obtained error maps can be combined as shown in Figure 14.15 (i,j).

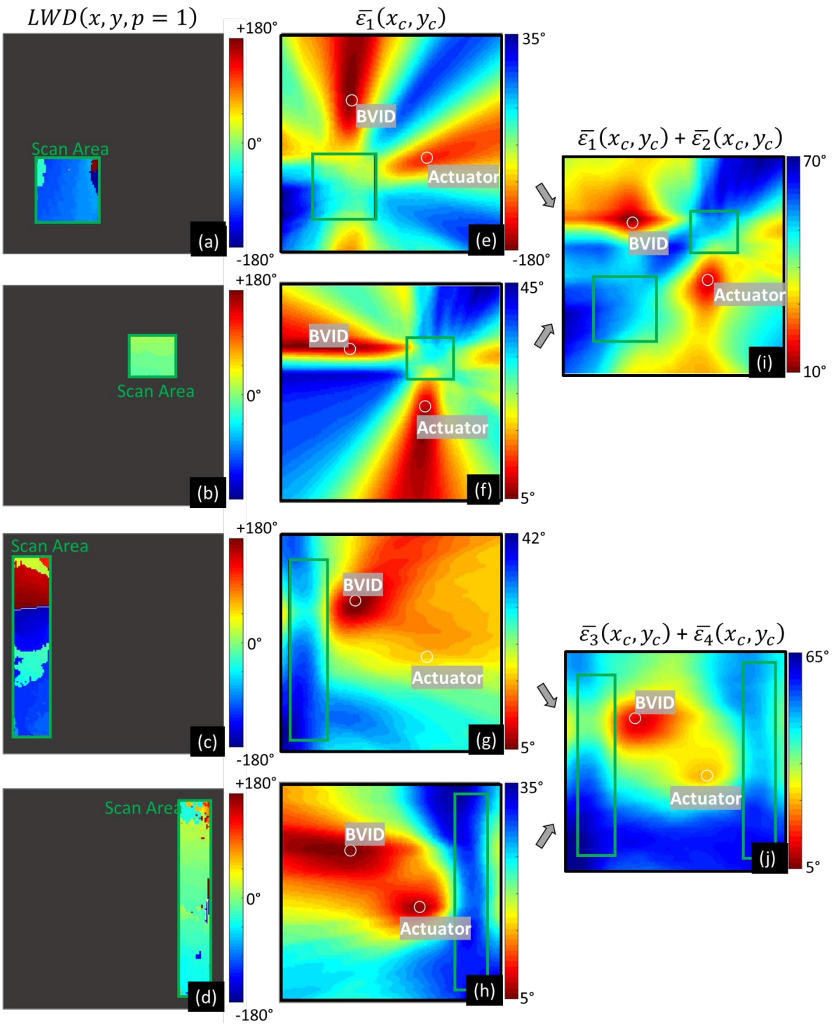

Figure 14.15: Damage detection in $\mathrm{CFRP}_{\mathrm{BVID}}^{\mathrm{Plate}}$ using NL-LWDE for four cases of an incomplete scan area. (a-d) Local wave-direction maps for $p = 1$ with indication of the scan area, (e-h) Error maps with indication of the incomplete scan area and (i,j) Combined error maps.

Next, the measurement of the backside of $\mathrm{CFRP}_{\mathrm{BVID}}^{\mathrm{Tube}}$ is considered. The local wave-direction map for p = 1 is shown in Figure 14.16 (a). The dotted rectangle that is superimposed on the figure corresponds to the unfolded cylinder's surface when it is virtually cut open at the backside. The location of the BVID is indicated. The LWD map is of less quality compared to the LWD maps in previous figures. This is because the observed nonlinear vibrations are of extremely low amplitude (see Figure 14.12 (f)). Nevertheless, the observed local wave-direction, at many locations in the LWD map, correctly points to the BVID (as indicated with gray arrows).
The resulting error map is shown in Figure 14.16 (b). All identified wave-directions were taken into account in the construction of this map (i.e. p_{max} unlimited). A local minimum is found close to the actual location of the BVID. As such, the NL-LWDE proves successful for detection and (to certain extent localization) of BVID in tubular structures, even when the structure is inspected from the side opposite to the BVID.

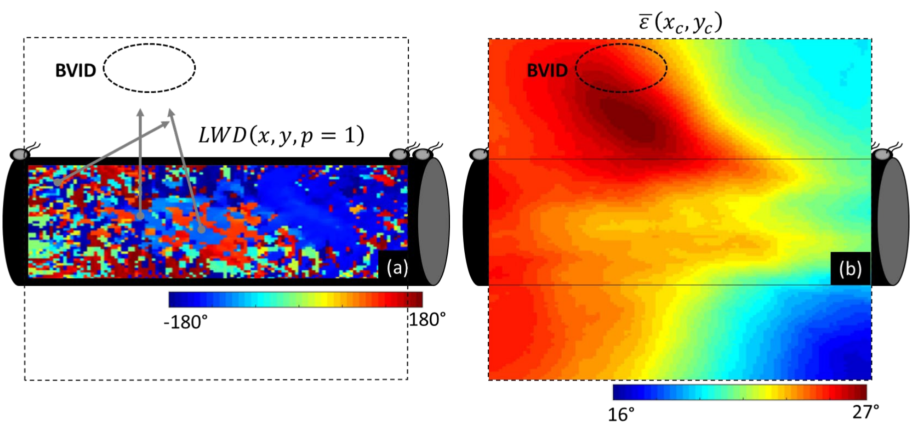

Figure 14.16: Damage detection using NL-LWDE in $\mathrm{CFRP}_{\mathrm{BVID}}^{\mathrm{Tube}}$ when inspected from the backside: (a) Local wave-direction map for p = 1, (b) Error map.

Very precise localization of the damage is not possible when only a single small incomplete scan area is used. For this it is proposed to use the obtained 'rough' NL-LWDE error map as a fast initial inspection tool. Afterwards, an additional measurement can be performed solely for the areas of increased damage likelihood using a more time-consuming but accurate NDT technique (e.g. an ultrasonic C-scan).

5. Conclusions

Local wave-direction estimation (LWDE) is proposed as a novel method for the localization of propagating wave sources in full wavefield measurements. The algorithm makes use of directional bandpass filters in the wavenumber domain in order to determine the dominant wave propagation directions at every scan point. While the location of the sources can already be distinguished in the obtained local wave-direction maps, an error map is constructed using a virtual local wave-direction field. The resulting error map reveals sources of vibrations as local minima. The proposed algorithm is baseline-free, user-independent and not compromised by possible edge reflections. Considering that the LDWE method exploits wave-direction features, it can be used to localize not only in-sight but also out-of-sight sources which may even be correlated.

Next, a nonlinear variant of the LWDE procedure is introduced. NL-LWDE proves successful in localizing the nonlinear response of a barely visible impact damage (as well as the nonlinear response of the piezoelectric actuator) in a cross-ply CFRP plate and in a CFRP bicycle frame's down tube. Moreover, the out-of-sight damage detection capability is shown, proving the potential of the proposed method for baseline-free detection of hidden damage in a fast manner.

References

1. Segers, J., et al., *Nonlinear Local Wave-Direction Estimation for In-sight and Out-of-sight Damage Localization in Composite Plates* NDT & E International, 2021. **119**.
2. Solodov, I., N. Krohn, and G. Busse, *CAN: an example of nonclassical acoustic nonlinearity in solids.* Ultrasonics, 2002. **40**(1): p. 621–625.
3. Jhang, K.-Y., et al., *Measurement of Nonlinear Ultrasonic Characteristics*. Measurement Science and Technology, ed. M.G. Cain, et al. 2020: Springer.
4. Hirsekorn, S. and P.P. Delsanto, *On the universality of nonclassical nonlinear phenomena and their classification.* Applied Physics Letters, 2004. **84**(8): p. 1413-1415.
5. Segers, J., et al., *Backside delamination detection in composites through local defect resonance induced nonlinear source behaviour.* Journal of Sound and Vibration, 2020. **479**.
6. Segers, J., et al., *Nonlinear Elastic Wave Energy Imaging for the Detection and Localization of In-Sight and Out-of-Sight Defects in Composites.* Applied Sciences, 2020. **10**(3924).
7. Spronk, S.W.F., et al., *Comparing damage from low-velocity impact and quasi-static indentation in automotive carbon/epoxy and glass/polyamide-6 laminates.* Polymer Testing, 2018. **65**: p. 231-241.

8. Michaels, T.E., J.E. Michaels, and M. Ruzzene, *Frequency-wavenumber domain analysis of guided wavefields.* Ultrasonics, 2011. **51**(4): p. 452-66.
9. Kudela, P., M. Radzienski, and W. Ostachowicz, *Impact induced damage assessment by means of Lamb wave image processing.* Mechanical Systems and Signal Processing, 2018. **102**: p. 23-36.
10. Radzienski, M., et al., *Damage Identification in Various Types of Composite Plates Using Guided Waves Excited by a Piezoelectric Transducer and Measured by a Laser Vibrometer.* Sensors (Basel, Switzerland), 2019. **19**(9).
11. Segers, J., et al., *Robust and baseline-free full-field defect detection in complex composite parts through weighted broadband energy mapping of mode-removed guided waves.* Mechanical Systems and Signal Processing, 2021. **151**.
12. Flynn, E.B., et al., *Structural imaging through local wavenumber estimation of guided waves.* NDT & E International, 2013. **59**: p. 1-10.
13. Rogge, M.D. and C.A. Leckey, *Characterization of impact damage in composite laminates using guided wavefield imaging and local wavenumber domain analysis.* Ultrasonics, 2013. **53**(7): p. 1217-26.
14. Jeon, J.Y., et al., *Damage detection on composite structures with standing wave excitation and wavenumber analysis.* Advanced Composite Materials, 2017. **26**(sup1): p. 53-65.
15. Gao, T., et al., *Hidden Corrosion Detection Using Laser Ultrasonic Guided Waves with Multi-frequency Local Wavenumber Estimation.* Ultrasonics, 2020. **108**.
16. Moon, S., et al., *Optimization of excitation frequency and guided wave mode in acoustic wavenumber spectroscopy for shallow wall-thinning defect detection.* Journal of Mechanical Science and Technology, 2018. **32**(11): p. 5213-5221.
17. Segers, J., et al., *Self-Reference Broadband Local Wavenumber Estimation (SRB-LWE) for defect assessment in composites* Mechanical Systems and Signal Processing, 2021. **163**.

Part 4:

Damage Detection Performance and Conclusions

Chapter 15
Comparison of Damage Map Construction Approaches

Summary:

Multiple novel damage detection approaches were introduced in Part 2 and in Part 3 of this PhD thesis. In this chapter, the most promising approaches are applied to the measurement results of three CFRP test specimens with a variety of defect types, sizes, shapes and depths. The performance of all methods is critically evaluated and compared.

1. Introduction

In Part 2 and in Part 3 of this PhD dissertation, multiple approaches were outlined for damage identification, and in some cases damage evaluation, from the full-field elastic wave response of composite components. The elastic waves are excited using low power piezoelectric actuators and sensed by means of a 3D scanning laser Doppler vibrometer (SLDV). Each of the proposed approaches was based on a specific interaction of the propagating elastic waves with the damage.

Novel damage map construction methods were proposed, and compared with similar methods known in literature. The novel approaches use the broadband velocity response of the test specimen to insure the robustness and maximize the defect detectability. The following list gives these novel damage detection approaches:

- Automated local defect resonance detection
  Part 2 – Chapter 6 or [1]
- Mode-removed broadband weighted-root-mean-square (linear) energy mapping
  Part 3 – Chapter 11 Section 3.3 or [2]
- Nonlinear bandpower mapping for the modulation sideband
  Part 3 – Chapter 12 or [3, 4]
- Self-reference broadband local wavenumber estimation
  Part 3 – Chapter 13 Section 5 or [5]
- Nonlinear local wave-direction estimation
  Part 3 – Chapter 14 Section 4 or [6]

A total of 24 test specimens were used in Part 2 and Part 3 to illustrate the work flow and show the performance of these methods. What is still missing is a thorough comparison of the performance between these novel methods. This comparison is provided in this chapter. Each of the five methods listed above is operated on the measurement results of the same CFRP test specimens. The performance of each method is evaluated based on: defect detection capability, defect evaluation capability, computational effort, experimental procedure, etc.

The chapter starts with an explanation of the three composite test specimens under consideration and the measurement procedure. Afterwards, a short recapitulation is provided for each of the evaluated damage detection approaches. Next, the obtained damage maps (for all three test specimens) are compared and the performance of each damage map construction method is evaluated. In the end, a final comparison is provided and the conclusions are summarized.

2. Materials and Measurements

Three CFRP test specimens are inspected for defects (see Figure 15.1). Note that each of these samples was already used in one or more of the previous chapters. The first component ($\mathrm{CFRP}^{\mathrm{Plate}}_{\mathrm{FBH,12}}$, see Figure 15.1 (a)) is a 330x330x5.45 mm^3 coupon manufactured out of 24 layers of unidirectional carbon fiber according to a quasi-isotropic stacking sequence $[(45/0/\text{-}45/90)_3]_s$. Twelve FBH defects (with one through hole) are milled into the backside. The diameter d and relative remaining material thickness $h\ [\%] = 100.\, h_{defect}/h_{base}$ are listed in the figure. The second component ($\mathrm{CFRP}^{\mathrm{Air}}_{\mathrm{Disb}}$, see Figure 15.1 (b)) is a 600x200 mm^2 fin rib panel from the tail piece of an Airbus A320. Three vertical stiffeners are visible from the backside. The base plate, on which the stiffeners are bonded, has a thickness of 1.1 mm. The material's layup and stiffness properties are considered unknown. The panel was scrapped by the manufactured after damage was detected at one of the stiffeners.

The third and last component ($\mathrm{CFRP}^{\mathrm{Air}}_{\mathrm{BVID}}$, see Figure 15.1 (c)) is again part of an A320 aircraft. The panel measures around 780x280 mm^2, has a base material thickness of 4 mm, and contains three vertical stiffeners that are visible from the backside. Damage was introduced by impacting the panel at three different location with a 7.1 kg weight from a height of 20 cm, 35 cm and 30 cm. The resulting areas of BVID are marked as BVID-A, BVID-B and BVID-C, respectively.

Ultrasonic pulse-echo inspection of both aircraft panels reveals the presence of the damage. The time-of-flight (TOF) C-scan maps, obtained from ultrasonic pulse-echo inspection at 5 MHz, are shown in Figure 15.1 (b.1) and (c.1). These maps reveal the disbond at the topside of the middle stiffener in $\mathrm{CFRP}^{\mathrm{Air}}_{\mathrm{Disb}}$, and the complex distribution of delaminations and cracks that make up the BVID-B in $\mathrm{CFRP}^{\mathrm{Air}}_{\mathrm{BVID}}$.

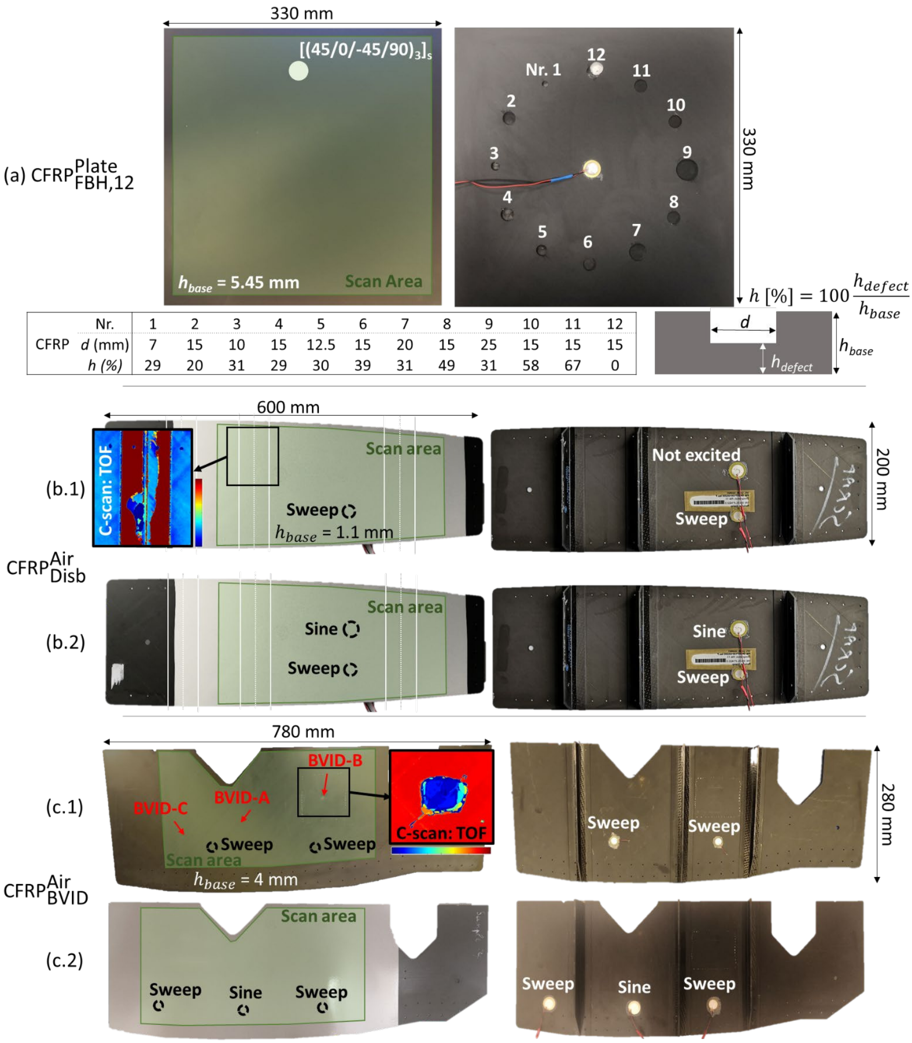

CFRP	Nr.	1	2	3	4	5	6	7	8	9	10	11	12
	d (mm)	7	15	10	15	12.5	15	20	15	25	15	15	15
	h (%)	29	20	31	29	30	39	31	49	31	58	67	0

Figure 15.1: CFRP test specimens: (a) Quasi-isotropic coupon with FBHs of specified diameter d and relative thickness h, (b) Aircraft panel with disbond at stiffener and (c) Aircraft panel with three areas of BVID. Measurements performed for (1) linear wave analysis and (2) nonlinear wave analysis.

A total of five different SLDV measurements are performed. All piezoelectric actuators are bonded to the structures with removable phenyl salicylate.

Component $\mathrm{CFRP}^{\mathrm{Plate}}_{\mathrm{FBH,12}}$ is measured once. One piezoelectric actuator (Ekulit EPZ-20MS64W) is attached and excited with a broadband sine sweep signal. The SLDV measures the velocity response of the surface that is indicated with 'scan area'. The measurement characteristics (sweep start frequency f_{start}, sweep end frequency f_{end}, sweep voltage amplitude V_{pp}, sampling frequency f_{sample}, number of samples, number of averages, scan point spacing and number of points) are listed in Table 15.1. The measurement result is used to construct damage maps that are based on the linear velocity response of the structure. As a result, the use of retroreflective tape is not required. Note however that a relative high amount of averages is used. This is because the noise level of the SLDV is relatively high at the employed high sampling frequency (See Chapter 4 Section 3.3) and the test specimen is relatively thick resulting in low vibrational amplitudes.

Component $\mathrm{CFRP}_{\mathrm{Disb}}^{\mathrm{Air}}$ is measured twice. The first measurement (see Figure 15.1 (b.1)) is used for the construction of damage maps based on the linear response of the component. For this first measurement, the component is excited with a broadband sine sweep signal using one piezoelectric actuator (Ekulit EPZ-20MS64W). The SLDV measures the full wavefield response of the frontside (see 'scan area'). All measurement characteristics are listed in Table 15.1. Although not required for this measurement, the scan area is covered with retroreflective tape.

The second measurement (see Figure 15.1 (b.2)) is tailored for nonlinear vibrational analysis. The scan area is again covered in removable retroreflective tape to enhance the signal-to-noise ratio (SNR) of measurement. This is required to detect the nonlinear vibrational components which are of extremely low amplitude (order of μm/s). Vibrations are introduced using two piezoelectric actuators. The first one (Ekulit EPZ-20MS64W) is supplied with a linear sine sweep signal and the second one (Ekulit EPZ-27MS44W) is supplied with a sine signal, see Table 15.1 for characteristics. The SLDV records the velocity response of the scan area.

Also for $\mathrm{CFRP}_{\mathrm{BVID}}^{\mathrm{Air}}$, two separate measurements are performed. For the first one (see Figure 15.1 (c.1)), no retroreflective tape is used and the vibrations are excited using two piezoelectric actuators (Ekulit EPZ-20MS64W). Each actuator is supplied with an identical sweep signal. Two actuators are used to make sure that vibrations of detectable amplitude are present in every part of the scan area.

The second measurement (see Figure 15.1 (c.2)) is again tailored for the construction of nonlinear (i.e. first modulation sideband) damage maps. Three actuators (Ekulit EPZ-20MS64W) are used. Two of them are excited with a sine sweep signal and the third one is excited with a sine. The scan area is covered in removable retroreflective tape to enhance the SNR of the measurement. All the excitation and measurement characteristics are summarized in Table 15.1.

Also included in Table 15.1 is the minimum duration of each experiment. It is calculated as:

$$\text{Scan Time} = \frac{\#\text{Averages} \,.\, \#\text{ScanPoints} \,.\, \#\text{Samples}}{f_{sampling}}$$

The actual measurement time is typical around 20 % higher because the SLDV needs time to adjust the angles of the mirrors and to perform the averaging. These measurement times are long. Current and future research focusses on methods to reduce these measurement times considerably (see Chapter 16). As an example, the measurement time can be reduced by an order of magnitude by performing out-of-sight damage detection using nonlinear local wave-direction estimation (see further in this chapter).

Table 15.1: Excitation and measurement characteristics.

Sample		Excitation					SLDV					Time (min)
		Sine Sweep			Sine		f_{samp} (kS/s)	# samples	# averages	Point spacing (mm)	# points	
		f_{start} (kHz)	f_{end} (kHz)	V_{pp}	f_s (kS/s)	V_{pp}						
$CFRP^{Plate}_{FBH,12}$	Lin.	5	300	100	/	/	1250	10000	40	2.5	13786	73
$CFRP^{Air}_{Disb}$	Lin.	10	300	100	/	/	625	10000	7	1.75	24178	45
	Nonlin.	10	125	100	30	100	625	10000	10	2.5	12512	33
$CFRP^{Air}_{BVID}$	Lin.	5	300	50	/	/	625	10000	15	2	22425	89
	Nonlin.	10	125	200	30	100	625	25000	3	2.5	16466	33

3. Damage Map Construction Methods

A short recapitulation is provided for each of the five novel damage detection approaches.

Automated local defect resonance detection

Local defect resonance (LDR) is the local resonance phenomenon that takes place at defects caused by the local reduction in flexural and/or axial rigidity. In Chapter 6, the automated LDR detection algorithm is proposed for fast detection of defects through an automated search for LDR phenomena in the full wavefield response of the structure. Most optimal defect detection performance was obtained for LDR_Z detection using bandpower data conditioning (with bandwidth 1 kHz). For all test specimens, the LDR_Z search is performed 10 times because there may be multiple defects in the scan area.

Mode-removed broadband WRMS (linear) energy mapping

Stiffness-reducing defects pop up as areas of increased vibrational activity in the energy map corresponding to the linear velocity response of the component. In order to improve the quality of the linear energy-based damage map, three measures were taken: (i) the wave attenuation is compensated for by means of weighted-root-mean-square (WRMS) energy calculation, (ii) the amplitude of the vibrations in the damage-free material is reduced using modestop filtering and (iii) broadband vibrations are considered (instead of a single narrowband toneburst) to increase the damage map's robustness. The full details can be found in Chapter 11.

Bandpower map of the nonlinear modulation sideband

Defect's that have contact interfaces, such as delaminations, can show a nonlinear response to vibrations. As a result, nonlinear vibrational components may be created at the locations of the defects. The observed nonlinear components include: (i) higher harmonics (HHs) and (ii) modulations sidebands (SBs). The SBs are formed when the component is excited with two different excitation signals.

In Chapter 12, it was illustrated that the mapping of the nonlinear energy, by means of bandpower calculation, reveals the nonlinear defects with high contrast. The best damage map was obtained by mapping the energy in the first modulation sideband because this modulation sideband is created exclusively at defects and not at the actuators.

Self-reference broadband local wavenumber estimation (SRB-LWE)

Defects in composites, e.g. delaminations, often lead to a local reduction in thickness. As such, also the dispersion behavior of a propagating wave changes at the location of a defect. The proposed SRB-LWE exploits this change in local dispersion behavior for broadband signals in view of detecting, localizing and evaluating defects. The SRB-LWE is implemented such that it is automated, user-independent and requires no knowledge of the material properties. The full details on the SRB-LWE method can be found in Chapter 13.

Nonlinear local wave-direction estimation (NL-LWDE)

As explained earlier, nonlinear vibrational components (HHs and SBs) are created at defects. These nonlinear components radiate away from the defect, into the damage-free material. As a result, defects can be localized by looking at the local direction of the propagating nonlinear components.

The detection of defects by means of local wave-direction estimation of nonlinear waves was the subject of Chapter 14. Similar to the nonlinear energy-based damage maps, best performance is obtained for the SBs because they are exclusively formed at the defects (and not at the nonlinear actuators).

First, the nonlinear component of interest, i.e. the first SB, is extracted from the broadband sine sweep response using time-frequency filtering. Next, the broadband SB response is converted to a narrowband toneburst response corresponding to a five-cycle Hanning windowed sine excitation with center frequency f_c = 70 kHz. Afterwards, the local direction of the propagating waves (in the toneburst response) is estimated at every measurement point. A damage map is created where all sources of the SB components, i.e. the defects, pop up as local minima.

Out-of-sight damage detection is illustrated here by removing part of the original measurement data.

4. Damage Map Construction Results

4.1. CFRP Coupon with FBHs

Figure 15.2 shows the results of the three linear damage detection methods when applied to the measurement result of the CFPR coupon with FBH defects ($\mathrm{CFRP}^{\mathrm{Plate}}_{\mathrm{FBH,12}}$). The backside of the test specimen, with indication of all FBHs, is shown in Figure 15.2 (a). Figure 15.2 (b) shows a typical snapshot of the unprocessed out-of-plane velocity response at t = 2 ms. The calculation times are listed in Table 15.2.

The artificial FBH defects do not have a contact interface and are therefore not associated to contact acoustic nonlinearity. As a result, the damage detection approaches that exploit nonlinear elastic waves, are not considered here.

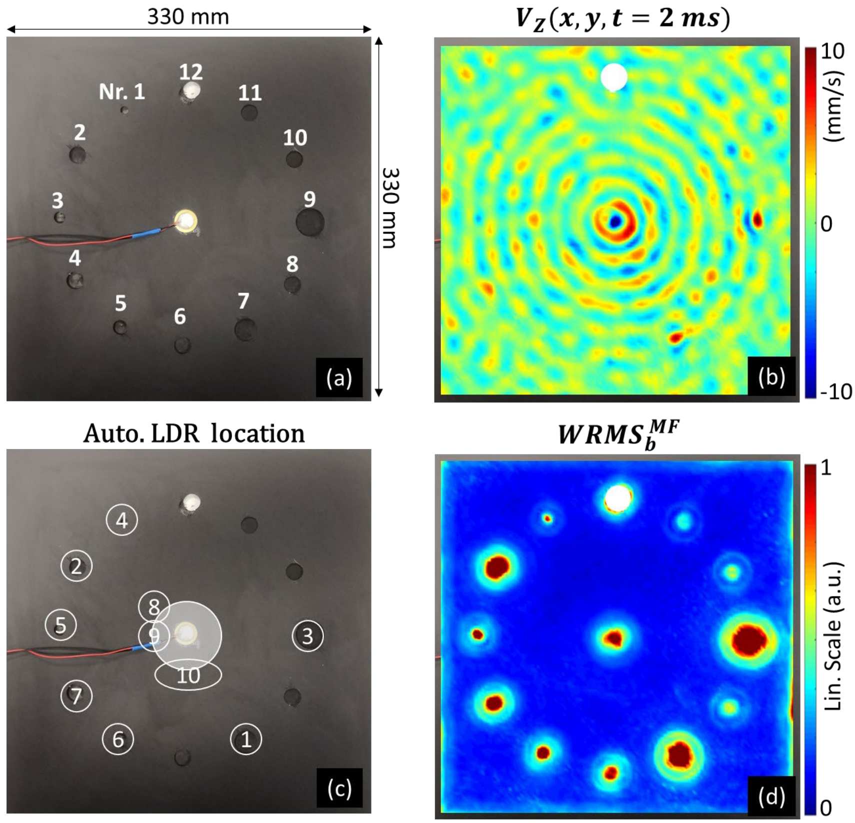

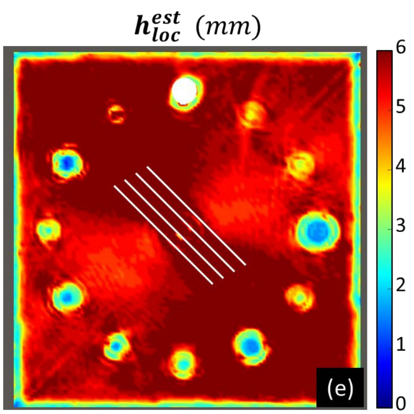

FBH Nr.	d (mm)	h_{loc}^{true} (mm)	LDR_Z	h_{loc}^{est} (mm)
1	7	1.58	✓	3.25
2	15	1.09	✓	1
3	10	1.69	✓	2
4	15	1.58	✓	1.75
5	12.5	1.64	✓	1.75
6	15	2.13		2.25
7	20	1.69	✓	1.75
8	15	2.67		3
9	25	1.69	✓	1.75
10	15	3.16		3.25
11	15	3.65		3.75

(f)

Figure 15.2: Damage detection in $\mathrm{CFRP}_{\mathrm{FBH},12}^{\mathrm{Plate}}$: (a) Backside of test specimen, (b) Snapshot of unprocessed out-of-plane velocity at t = 2 ms, (c) Location of detected LDR_Z's, (d) Broadband mode-removed WRMS map, (e) SRB-LWE local thickness map, (f) List of FBHs with indication of LDR_Z detection and true and estimated local thickness.

Automated LDRz

Figure 15.2 (c) shows the first 10 locations that are identified as an LDRz. The locations are numbered in chronological order, thus number '1' represents the first LDRz that is detected. The area around the actuator was cropped out before the automated LDRz detection algorithm was executed. The first seven LDRz's are correctly identified at the location of FBHs. As an example, the velocity maps corresponding to the second and the seventh identified LDRz are shown in Figure 15.3 (a) and (b), respectively. Next, the algorithm identifies high amplitude regions close to the actuator as LDRz.

The algorithm is fast (12.9 s) and fully automated, but only successful for identification of the rather shallow defects with remaining material thickness < 2 mm in the 5.45 mm thick plate (see Figure 15.2 (f)). This comes as no surprise knowing that deep defects do not show pronounced LDR behavior (see Chapter 7).

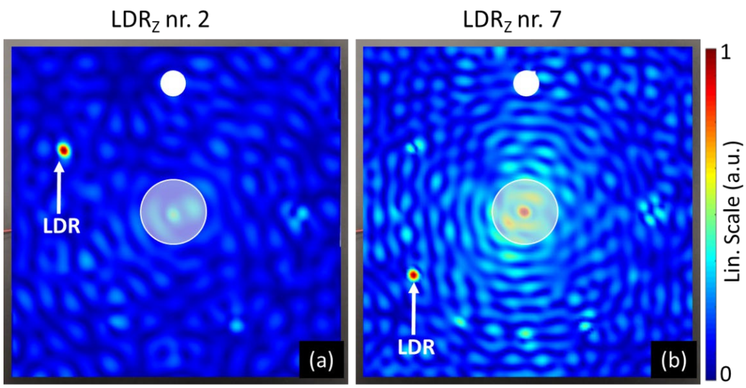

Figure 15.3: (a) Second and (b) Seventh identified LDRz in $CFRP^{Plate}_{FBH,12}$.

$WRMS_b^{MR}$

The damage map obtained from mode-removed broadband WRMS energy calculation is shown in Figure 15.2 (d). All defects can be distinguished in this linear energy-based damage map with satisfying contrast. The calculation time is around 244 s. The relative long calculation time is attributed to the conversion of the broadband sine sweep response into multiple narrowband toneburst responses. In addition, the automated selection of the optimal weighting factor (for WRMS calculation) for each toneburst is computationally intensive.

SRB-LWE

The estimated local thickness map h_{loc}^{est}, obtained through SRB-LWE, is shown in Figure 15.2 (e). The true and estimated local thickness at each FBH are listed in Figure 15.2 (f). All FBH defects are detected. The estimation of the local thickness is close to the real local thickness (see Figure 15.2 (f)). Only for the smallest FBH

(d = 7 mm), the thickness is largely overestimated. A smaller scan point resolution is required to accurately detect such small defects using SRB-LWE. The estimated local thickness of the damage-free material fluctuates between 5 mm and 6 mm. This is the result of the non-isotropic material properties (see also explanation in Chapter 13 Section 5.2.2). The fiber direction of the outer plies is indicated on Figure 15.2 (e). These plies contribute most to the flexural rigidity and, as a result, the estimated local thickness is highest along this ply direction. It took 162 s to calculate this local thickness map.

Table 15.2: Calculation times for damage detection in $\mathrm{CFRP}_{\mathrm{FBH},12}^{\mathrm{Plate}}$.

Method	**Calculation Time* (s)**
Auto. LDR	12.9
$WRMS_b^{MF}$	244
SRB-LWE: h_{loc}^{est}	162

* Intel(R) Xeon(R) Gold 6146 CPU @ 3.20 GHz

4.2. CFRP Aircraft Panel with Disbond at Stiffener

All damage detection methods are applied to the measurement result of the $\mathrm{CFRP}_{\mathrm{Disb}}^{\mathrm{Air}}$. The results are discussed separately for the linear and the nonlinear methods.

4.2.1. Linear Approaches

The damage maps constructed with the linear approaches are shown in Figure 15.4. Also included in Figure 15.4 (a) and (b) are a photograph of the inspection side of the test specimen with ultrasonic C-scan's TOF map of the damage and a typical snapshot of the unprocessed out-of-plane sweep response at t = 2 ms. The calculation times are listed in Table 15.3. From the TOF data, it is found that part of the backside stiffener is disbonded from the skin plate. Furthermore, there are small areas with relatively low TOF value (dark blue color). This indicates the presence of shallow delaminations. From the time snapshot of the acquired vibrational response (see Figure 15.4 (b)), it is observed that the stiffened regions are characterized by lower vibrational amplitudes. This is due to the locally increased material thickness (skin plate + stiffener). In addition, part of the piezoelectric excited waves become trapped in between the two vertical stiffeners. There is no sign of the damage in this unprocessed velocity response.

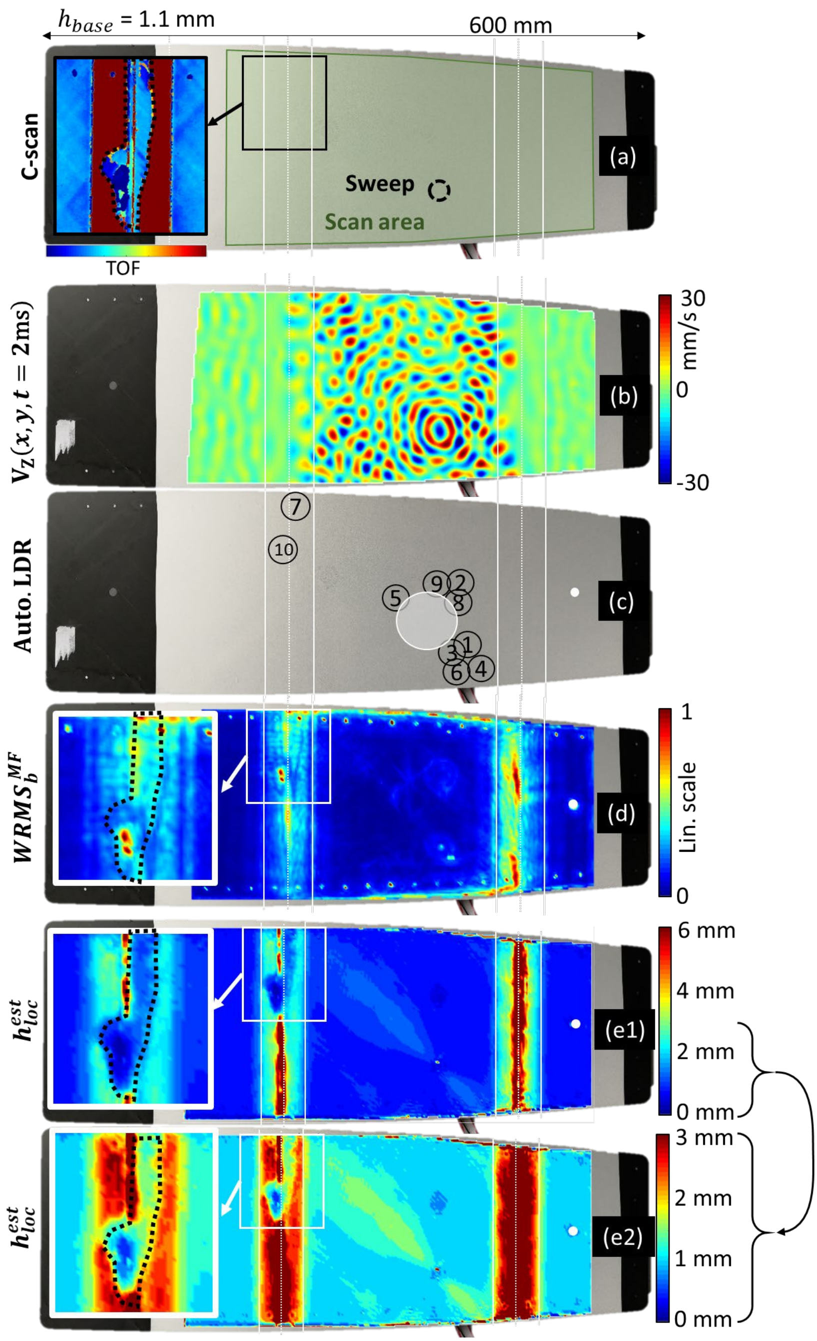

Figure 15.4: Damage detection in $\text{CFRP}_{\text{Disb}}^{\text{Air}}$: (a) Inspection side of test specimen for the first measurement with ultrasonic C-scan of defect, (b) Snapshot of out-of-plane velocity at t = 2 ms, (c) Location of automated detected LDR_Z's, (d) Broadband mode-removed WRMS map, (e) SRB-LWE local thickness map with two different colorscales.

Automated LDR

The automated LDRz detection algorithm is not successful in finding LDRz at the damage (see Figure 15.4 (c)). High amplitude regions close to the excitation location are erroneously identified as LDRz. Figure 15.5 shows identified LDRz number 2 which is indeed an area of increased vibrational amplitude close to the actuator. Only the 7th and 10th identified LDRz correspond to the disbond. The 7th LDR is presented in Figure 15.5 (b). The automated LDR search took around 30 s.

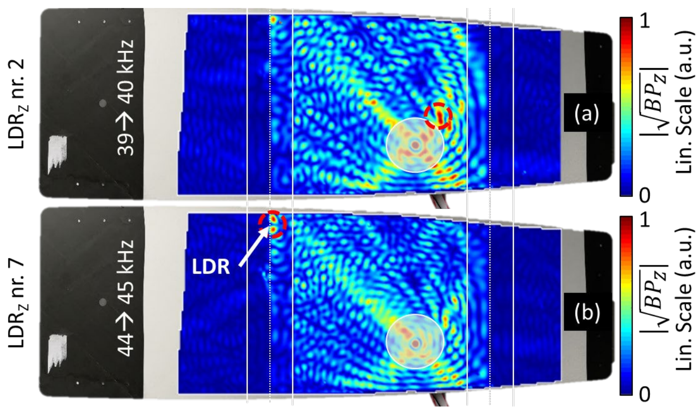

Figure 15.5: (a) Second and (b) Seventh identified LDRz in $\mathrm{CFRP}_{\mathrm{Disb}}^{\mathrm{Air}}$.

$\mathbf{WRMS}_{\mathbf{b}}^{\mathbf{MR}}$

The fact that the damage is located at the interface between the backside stiffener and the base material is also problematic for the broadband mode-removed WRMS approach. At the disbond, the dispersion behavior is identical to the damage-free material. As a result, the modestop filter, which aims at removing the vibrations in the damage-free material, also removes the vibrations at the disbond. Moreover, the vibrations are retained at the intact areas of both stiffeners. The resulting damage map (see Figure 15.4 (d)) cannot be used for damage detection. It only reveals the two small shallow delaminations within the disbond area. It took 429 s to obtain the $\mathrm{WRMS}_{\mathrm{b}}^{\mathrm{MR}}$ map.

SRB-LWE

The local thickness map obtained via SRB-LWE is shown with two different colorscales in Figure 15.4 (e1) and (e2). The high amount of scan points resulted in a calculation time of 325 s. The thickness map correctly reveals both stiffeners as areas with a thickness bigger than h_{base} = 1.1 mm. The local thickness reduction at the top side of the left stiffener matches well with the TOF map obtained from the ultrasonic C-scan. The main part of the damage has a local thickness similar to the base material thickness. As such, the presence of the disbond is confirmed. In addition, a small part of the damage is located close to the inspection surface.

4.2.2. Nonlinear Approaches

The damage maps constructed with the nonlinear approaches are shown in Figure 15.6. Again, a picture of the inspection side (with TOF map) and a snapshot of the unprocessed out-of-plane velocity response are included in Figure 15.6 (a) and (b). The calculation times are included in Table 15.3. The damage detection approaches that are based on nonlinear elastic waves successfully reveal the presence of the disbond.

$\mathbf{BP_Z^{SB_{1,1}}}$

The bandpower map for the first modulation sideband is shown in Figure 15.6 (c) and provides an exclusive, high contrast, view of the damage. It took around 120 s to obtain this damage map. Further reduction of the calculation time could be achieved by optimizing the code for time-frequency filtering.

NL-LWDE

The nonlinear local wave-direction estimation procedure is executed twice. First, the full measurement dataset is considered and the resulting damage map is given in Figure 15.6 (d). The calculation time was 155 s and the damage map correctly reveals the disbond as a source of modulation sideband vibrations.
Next, the NL-LWDE is applied to a limited portion of the measurement dataset. The part of the wavefield that is used is indicated with a green square on Figure 15.6 (e). Measuring the vibrational response exclusively at this small area takes only 4 min. Also the calculation time for damage map construction reduces to 39 s. Although less accurate, the obtained damage map still predicts the presence of an out-of-sight defect near the top side of the left stiffener.

Table 15.3: Calculation times for damage detection in $\mathrm{CFRP}_{\mathrm{Disb}}^{\mathrm{Air}}$.

Method	**Calculation Time* (s)**
Auto. LDR	29.9
$WRMS_b^{MF}$	429
SRB-LWE: h_{loc}^{est}	325
$BP_Z^{SB_{1,1}}$	117
NL-LWDE	155
NL-LWDE: Out-of-Sight	39

* Intel(R) Xeon(R) Gold 6146 CPU @ 3.20 GHz

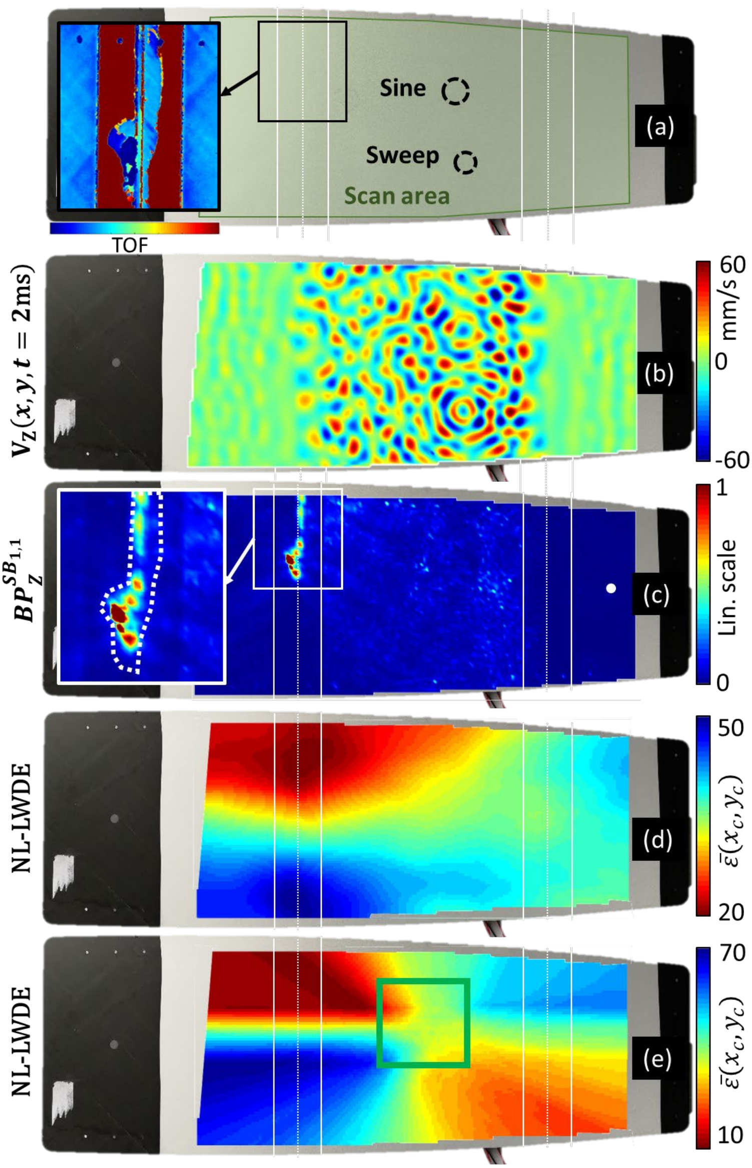

Figure 15.6: Damage detection in $\text{CFRP}^{\text{Air}}_{\text{Disb}}$: (a) Inspection side of test specimen for the modulation sideband measurement, (b) Snapshot of out-of-plane velocity at t = 2 ms, (c) Bandpower map of the first modulation sideband, (d) Damage map obtained from NL-LWDE using all the measurement data, (e) Damage map obtained from NL-LWDE using only the measurement data located in the green square.

4.3. CFRP Aircraft Panel with BVID

4.3.1. Linear Approaches

The damage maps for $CFRP_{BVID}^{Air}$, constructed with the linear approaches, are shown in Figure 15.8. Figure 15.8 (a) and (b) present the inspection side of the test specimen with ultrasonic C-scan TOF map of BVID region B and a snapshot of the unprocessed out-of-plane sweep response at t = 2 ms, respectively. The C-scan results reveal the distribution of delaminations and cracks that make up the BVID. The delaminations are distributed through the thickness. The calculation times are listed in Table 15.4.

Automated LDR

The delaminations that are closest to the inspection surface show pronounced LDR_Z behavior. As a result, all three areas of BVID are successfully detected using the automated LDR_Z search. Figure 15.8 (b) shows the first 10 locations that are identified as LDR_Z. The first and second location correspond to the two actuators. The next 6 identified LDR_Z's coincide with the locations of BVID. For instance, the 3rd, 4th and 7th LDR_Z take place at BVID-A, BVID-B and BVID-C, respectively, as revealed in Figure 15.7. The 9th and 10th locations are again in the vicinity of the actuators because there are no other defects present. The automated LDR_Z search was performed in only 26 s.

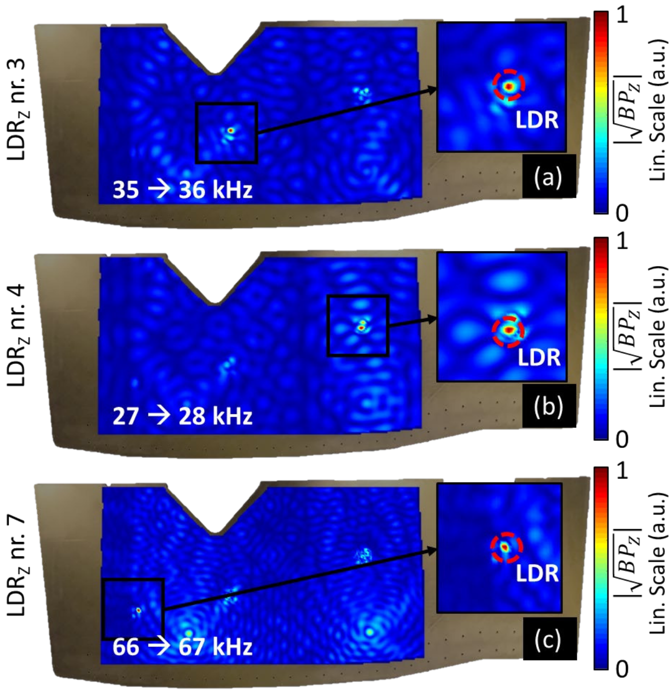

Figure 15.7: (a) Third, (b) Fourth and (c) Seventh identified LDR_Z in $CFRP_{BVID}^{Air}$.

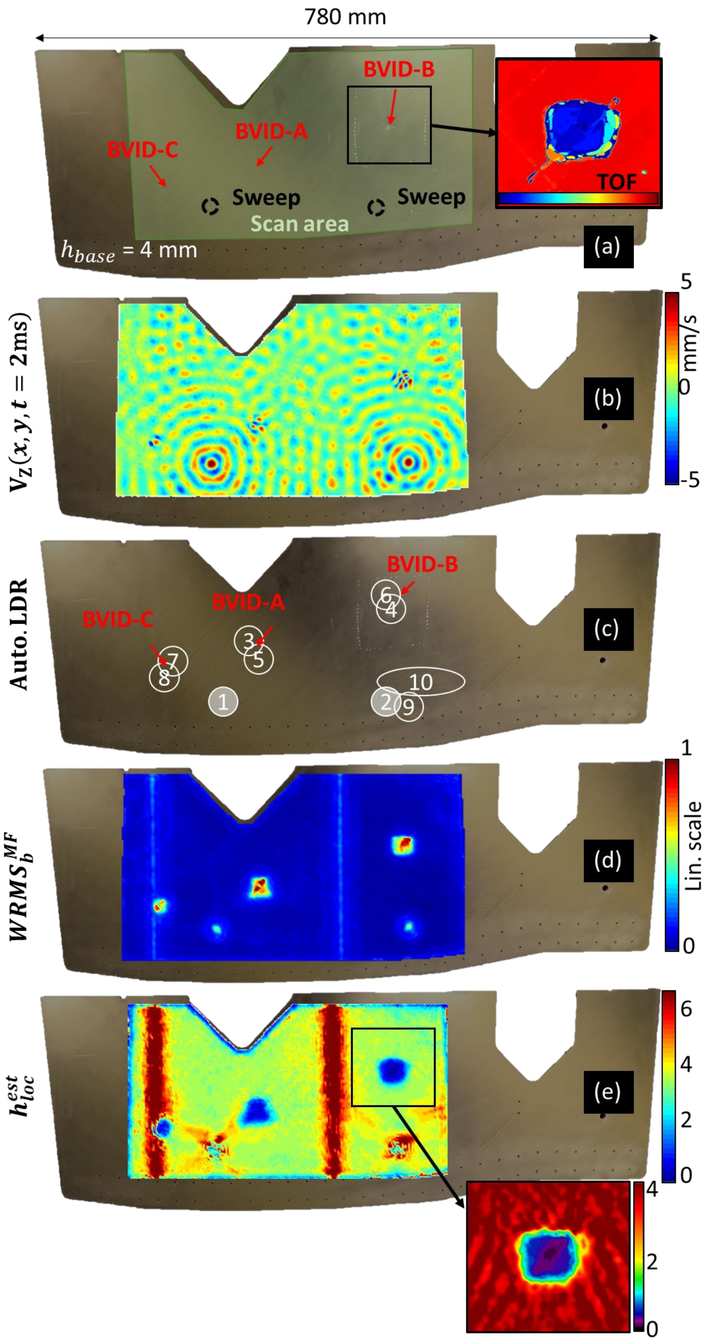

Figure 15.8: Damage detection in CFRP$^{\text{Air}}_{\text{BVID}}$: (a) Inspection side of test specimen for the first measurement, (b) Snapshot of raw out-of-plane velocity signal at t = 2 ms, (c) Location of automated detected LDR$_Z$, (d) Broadband mode-removed WRMS map, (e) SRB-LWE local thickness map,

$\mathbf{WRMS_b^{MR}}$

The three areas of BVID are also distinguished in the mode-removed WRMS energy map (see Figure 15.8 (d)). The vibrations in the damage-free material are successfully removed by the modestop filter. Also the vibrations at the stiffeners are significantly reduced. This is because there is a small difference in the dispersion behavior between the A_0 mode in the 4 mm thick CFRP base material and the A_0 mode in the ± 6 mm thick CFRP stiffened regions. The multiple sweep to toneburst conversions and automated weighting factor selections resulted in the relatively long calculation time of 377 s.

SRB-LWE

The local thickness map (from SRB-LWE) reveals the backside stiffeners as vertical bands of increased thickness (see Figure 15.8 (e)). The three areas of BVID are distinguished as local areas of relatively low material thickness. The calculation of this damage map took 212 s. It is possible to gain more insight into the structure of the BVID by performing SRB-LWE on a more detailed measurement dataset (see inset on figure). This was already illustrated in Chapter 13 Figure 13.28.

4.3.2. Nonlinear Approaches

The damage maps constructed with the nonlinear approaches are shown in Figure 15.9. Again, a picture of the inspection side (with TOF map) and a snapshot of the unprocessed out-of-plane velocity response are included in Figure 15.9 (a) and (b). The calculation times are added to Table 15.4.

$\mathbf{BP_Z^{SB_{1,1}}}$

The local formation of nonlinear components makes all three BVIDs pop up in the bandpower map calculated for the first modulation sideband (see Figure 15.9 (c)). The bandpower map is shown in logarithmic colorscale. Insets are provided in linear colorscale for each BVID region. The high contrast at the damage is evident. Calculation of this damage map took around 235 s.

NL-LWDE

The nonlinear source behavior of BVID-A and BVIB-B is already visible in the $BP_Z^{SB_{1,1}}$ map (i.e. Figure 15.9 (c)). The bandpower at BVIB-C is relatively low which tempers the source behavior of this BVID. These observations reflect back in the damage map obtained through NL-LWDE (see Figure 15.9 (d)). Only BVID-A and BVIB-B are detected. In order to detect BVID-C using NL-LWDE, a higher excitation amplitude is required to enhance the defect nonlinearity. The high number of time samples resulted in a calculation time of 255 s.

The calculation time, and more important also the SLDV measurement time, can be drastically reduced by exploiting the out-of-sight defect detection capability of NL-LWDE. The SLDV measurement takes less than 6 min when only the surface within the indicated green squares (see Figure 15.9 (e)) is scanned. The subsequent NL-LWDE takes around 60 s to perform and the corresponding damage map is shown in Figure 15.9 (e). The damage map correctly indicates BVID-B and BVID-A as local minima. As a result, the out-of-sight NL-LWDE approach proves promising for fast initial inspection of CFRP structures.

Table 15.4: Calculation times for damage detection in $\mathrm{CFRP}_{\mathrm{BVID}}^{\mathrm{Air}}$.

Method	**Calculation Time* (s)**
Auto. LDR	26.1
$WRMS_b^{MF}$	377
SRB-LWE: h_{loc}^{est}	212
$BP_Z^{SB_{1,1}}$	235
NL-LWDE	255
NL-LWDE: Out-of-Sight	60

* Intel(R) Xeon(R) Gold 6146 CPU @ 3.20 GHz

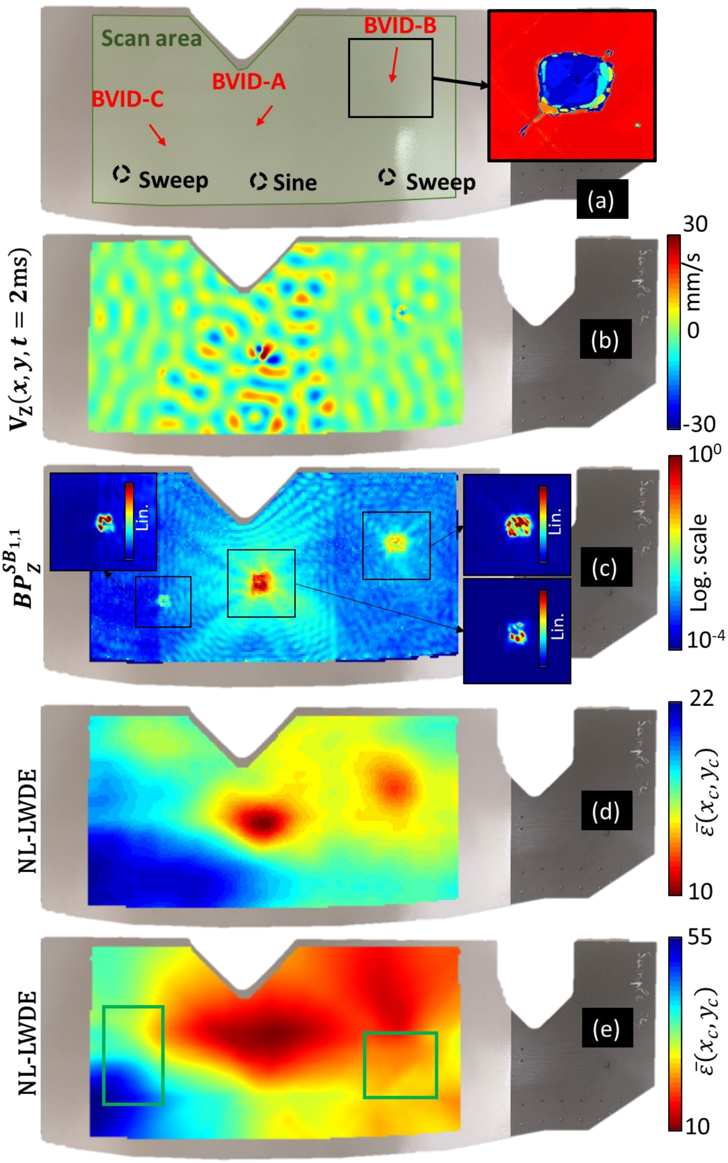

Figure 15.9: Damage detection in $\mathrm{CFRP}^{\mathrm{Air}}_{\mathrm{BVID}}$: (a) Inspection side of test specimen for the modulation sideband measurement, (b) Snapshot of unprocessed out-of-plane velocity signal at t = 2 ms, (c) Bandpower map of the first modulation sideband, (d) Damage map obtained from NL-LWDE using all the measurement data, (e) Damage map obtained from NL-LWDE using only the measurement data located in the green square.

5. Discussion and Conclusions

The five novel damage detection methods that are proposed in this PhD works are applied to three different CFRP structures. The novel damage detection methods are: (i) Automated detection of LDR_Z, (ii) Calculation of the WRMS energy map for broadband mode-removed guided waves, (iii) Self-reference broadband local wavenumber estimation (SRB-LWE) for calculation of a local thickness map, (iv) Calculation of the bandpower map for the nonlinear first modulation sideband vibrations and (V) Nonlinear local wave-direction estimation for localizing the defects as in-sight or out-of-sight sources of nonlinear vibrations. The inspected CFRP components are: (a) a square coupon with FBHs, (b) an aircraft panel with a disbond at a backside stiffener and (c) an aircraft panel with BVID.

The performance characteristics of each of the damage detection methods is summarized in Table 15.5. The information within this table is derived from the experimental results discussed in this chapter as well as from the previous chapters in which the methods were introduced. A qualitative comparison is given for: (i) the calculation time, (ii) whether the method is affected by anisotropy, curvature and the piezoelectric sources and (iii) the kind of defects that can be found. The methods that are based on filtering procedures in the wavenumber domain or in the wavenumber-frequency domain require an equidistant grid of data points for performing the spatial (2D) FFT. When dealing with curved structures, this necessitates that the 3D measurement surface is unwrapped. While this is easily done for single curved structures based on the 3D scan point coordinates obtained from the 3D SLDV (e.g. the bicycle tube in Chapter 12), it can be cumbersome when dealing with a higher degree of curvature. As an alternative to the surface unwrapping, a non-uniform FFT algorithm can be used. As a result, the criterion 'affected by curvature' is included in Table 15.5.

The automated LDR detection method is fast and is not affected by potential anisotropy of the material or curvature of the structure. On the other hand, the locations of the piezoelectric sources are often identified as LDRs. More important, only shallow damage can be detected. As such, the component needs to be inspected from both sides when using automated LDR damage detection.

Broadband mode-removed WRMS energy calculation is an effective method for revealing defects, which may be small and located deep into the component. The effect of anisotropy is limited and is easily compensated for by increasing the bandwidth of the modestop filter. On the other hand, the calculation time is high and an equidistant grid of data points is required. Also the location of the sources are typically associated with high intensity values in the damage map. Disbonds between stiffeners and base material are hard to detect using this method.

SRB-LWE is a highly promising method for detection of all the typical damage types. The calculation times are moderate. The method is affected by anisotropy but not to the extent that damage detection is compromised. It also requires an equidistant grid of data points for calculation of the spatial FFTs. The main advantage of SRB-LWE is that it provides quantitative information on the local thickness of the material, thus on the depth of the damage.

The bandpower map calculated for nonlinear vibrational components can reveal defects that are located extremely deep in the component. For instance in Chapter 12 Section 4.2, it was illustrated how this method allows for the detection of a disbond at the backside of a CFRP/Nomex honeycomb. The method cannot detect FBHs because a contact interface is required for the generation of the nonlinear waves. The method does not require spatial FFTs and is therefore not affected by curvature or anisotropy. When using the modulation sidebands, the bandpower map provides an exclusive view of the damage, even when using nonlinear sources. The main drawback of this method is that it requires a tailored measurement approach with sufficient excitation power and high signal-to-noise ratio (SNR). This necessitates the use of retroreflective tape and averaging. Without retroreflective tape, the measurement time would be extremely long. Note however that in this PhD work, simple low power piezoelectric bending discs were mostly used. Future research focusses on the development and testing of more performant excitation devices.

The NL-LWDE approach is not very effective for damage detection in a SLDV scan of the total component. In such a case, it is better to calculate the bandpower map for the first modulation sideband. However, the out-of-sight damage detection capability of NL-LWDE allows to construct a damage map of the total component using only the measurement of the vibrational response at a small part of the surface. As a result, inspection times are reduced. The method is based on nonlinear vibrations. As such, it can be used for the detection of very deep defects but it requires a tailored measurement approach. Curvature and anisotropy affect the propagation direction of the guided elastic waves, and therefore decrease the accuracy of the damage localization.

Overall, all defects in the test specimens are successfully detected by most of the proposed approaches. Finding a solution for the remaining drawbacks is the topic of current and future research (see next chapter).

Table 15.5: Overview of the characteristics of the proposed damage map construction methods.

Method		Calc. Time	Not affected by...			Detectable defects	Additional remarks
			Anisotropy	Curvature	Sources		
Linear	**Automated LDR**	+	+	+	-	Shallow delaminations Shallow FBHs BVID	
	Broadband Mode-removed WRMS	-	0	-	-	Delaminations FBHs BVID	
	SRB-LWE	0	-	-	-	Delaminations FBHs BVID Disbonds	Provides depth information
Nonlinear	**Sideband Bandpower**	-	+	+	+	Delaminations BVID Disbonds Extremely deep defects (e.g. backside disbond in sandwich panel)	High excitation amplitude required
	LWDE	-	-	-	+		
	Out-of-sight LWDE	+ Reduced inspection time!	-	-	+		High SNR required

References

1. Segers, J., et al., *Efficient automated extraction of local defect resonance parameters in fiber reinforced polymers using data compression and iterative amplitude thresholding.* Journal of Sound and Vibration, 2019. **463**.
2. Segers, J., et al., *Robust and baseline-free full-field defect detection in complex composite parts through weighted broadband energy mapping of mode-removed guided waves.* Mechanical Systems and Signal Processing, 2021. **151**.
3. Segers, J., et al., *Broadband nonlinear elastic wave modulation spectroscopy for damage detection in composites.* Structural Health Monitoring, 2021.
4. Segers, J., et al., *Nonlinear Elastic Wave Energy Imaging for the Detection and Localization of In-Sight and Out-of-Sight Defects in Composites.* Applied Sciences, 2020. **10**(3924).
5. Segers, J., et al., *Self-Reference Broadband Local Wavenumber Estimation (SRB-LWE) for defect assessment in composites* Mechanical Systems and Signal Processing, 2021. **163**.
6. Segers, J., et al., *Nonlinear Local Wave-Direction Estimation for In-sight and Out-of-sight Damage Localization in Composite Plates* NDT & E International, 2021. **119**.

Chapter 16

Summary, Conclusions and Future Prospects

Summary:

The conclusions for the different parts of this thesis are summarized. In addition, research lines are presented, which in the author's opinion, show great potential for further improvement of the proposed full-field elastic wave NDT methods with the aim to use these methods in industrial NDT environments.

1. Summary and Conclusions

Composite materials (e.g. carbon fiber reinforced polymers CFRP) are increasingly used for critical components in several industrial sectors (for example aerospace and automotive). A major challenge is the detection of internal defects in these composites that may have formed during manufacturing or damages introduced during its operational life.

One promising approach for damage detection in thin-walled composite structures is to analyze the vibrational response measured on the surface. Elastic waves are stimulated and guided by the surfaces, which then travel over large distances with relatively low loss, and interact with several damage features. One of the remaining challenges in this NDT technique concerns the analysis of the vibrational response signals in order to gain in-depth insight on a range of defects in composite parts.

In this PhD thesis, the full-field elastic wave based inspection of composite structures has been investigated using state-of-the-art experiments. Novel wavefield processing algorithms are proposed to convert the complex measurement data into effective damage maps. The presented research consists of four major parts.

Part 1: Vibrations in Composite Components
The foundations for NDT methods based on elastic waves were laid in Part I of the thesis. First, the theoretical framework for linear elastic wave dynamics in bulk solids and plates was outlined. Next, it was illustrated how defects may respond in a nonlinear manner to vibrations. At last, the experimental procedure for proper excitation and recording of the full-field elastic wave response of composites was detailed. A range of basic signal processing tools were introduced and used in the remainder of the PhD thesis.

Part 2: Local Defect Resonance based Damage Detection
The proof-of-concept of local defect resonance was provided in an analytical, numerical and experimental manner. Next, the concept of LDR was exploited for automated defect detection. The limits of LDR for defect detection were discussed based on a parametric (finite element simulation and experiment) study. At last, it was illustrated how LDR gives rise to the local generation of nonlinear vibrational components as well as thermal energy.

- Chapter 5 demonstrated the presence of LDR for a range of defects, e.g. FBH, delaminations and BVID. The concept of LDR has been extended towards the in-plane polarization direction, resulting in in-plane LDR_{XY}. Compared to the classical out-of-plane LDR_Z, the in-plane LDR_{XY} showed higher sensitivity to defects with vertical interfaces, and typically appeared at higher frequencies. A simplified analytical framework has been setup resulting in following observations:

- The LDR_Z frequency scales with h/r^2
  h: local material thickness = defect depth
  r: defect's spatial size).
- The LDR_{XY} frequency scales with $1/a^2$
  a: defect's spatial size

- An automated LDR detection procedure was proposed in Chapter 6 and proved successful for shallow defect detection.

- Chapter 7 handled a parametric study based on FE simulations and experiments. It was found that the (linear) LDR is mainly sensitive to shallow defects. Deep defects do not show distinct LDR behavior due to their limited reduction of the local rigidity. As an alternative, bandpower was proposed to get access to deeper defects.

- In Chapter 8 the nonlinear source behavior of a defect under LDR excitation was revealed. Higher harmonics and modulation sidebands were observed. Proof-of-concepts were provided for nonlinear defect detection (i) using wavefield source localization algorithms and (ii) by measuring the nonlinear air-coupled emissions surrounding the test specimen.

- In Chapter 9, it was illustrated that the thermal contrast at the defect, induced by LDR_{XY}'s, is so high that it allows for easy detection of BVID by live monitoring of infrared thermal images during a single broadband sine sweep excitation.

Part 3: Guided Wave Based Damage Detection

Damage detection in thin-walled composite structures was performed by analyzing the guided elastic wave propagation measured on the surface. The full wavefield monitoring of these guided waves allowed to detect defects in the material because the characteristics of the guided waves depend on the characteristics of the material (i.e. the composite component).

Multiple damage map construction strategies were developed, exploiting one or more of the typical interactions of a guided wave and a defect: (i) local change in linear vibrational energy, (ii) local change in nonlinear vibrational energy, (iii) local change in wavenumber and (iv) local change in wave propagation direction. Wavefield manipulations are required to isolate specific defect-wavefield interaction.

- Following wavefield manipulations have been proposed in Chapter 10:
    - Conversion of a broadband (e.g. sine sweep) response to a narrowband (e.g. toneburst) response using wavefield manipulation in the frequency domain.
    - Extraction or removal of guided waves travelling in specific directions or guided waves with specific wavenumbers using wavefield manipulation in the wavenumber domain.
    - Extraction or removal of specific guided wave modes using wavefield manipulation in the wavenumber-frequency domain.
    - Extraction or removal of specific nonlinear vibrational components using wavefield manipulation in the time-frequency domain.

- Mode-removed broadband weighted-root-mean-square energy mapping was proposed in Chapter 11. The resulting energy map related exclusively to abnormalities in the wavefield and showed high sensitivity to all kinds of internal damage features.

- The nonlinear response of the defects was exploited in nonlinear energy-based damage map construction (see Chapter 12). Broadband bandpower calculation of higher harmonic and modulation sidebands was proposed. The modulation sidebands provided an exclusive imaging of defect nonlinearity, and were not affected by potential source nonlinearity. The damage maps revealed all nonlinear defects, even when they were located at the backside of the structure. A proof-of-concept for detection of a backside disbond in a CFRP-Nomex sandwich panel was provided.

- A novel self-reference broadband version of the well-known local wavenumber estimation technique was proposed in Chapter 13 and was denoted as SRB-LWE. The novel SRB-LWE method allowed a high level of automation, removed the need for a priori knowledge on the material and/or defect properties, and resulted in an effective depth characterization of the damage.

- A novel local wave-direction estimation algorithm was introduced in Chapter 14 and proved successful for localization of nonlinear defects. This damage detection approach also allowed for detection of defects that were not part of the area scanned by the SLDV. As a result, it allowed for a strong reduction in measurement time. In addition, it could be used to detect hidden defects. The latter was illustrated for detection of impact damage at the invisible backside of a bicycle frame tube.

Part 4: Damage Detection Performance and Conclusions

Chapter 15 provided a comparison of the performance of the novel and most promising damage detection approaches. The methods were all applied to the measurement results of three CFRP test specimens with a large variety of defect types, sizes, shapes and depths. Each approach was evaluated in terms of inspection time, defect detection capability and the effect of anisotropy, curvature and bonded piezoelectric actuators.

In addition, a recapitulation of the PhD thesis was provided (see Chapter 16), conclusion were summarized and future prospects were revealed.

2. Future Prospects and Recommendations

Throughout this PhD dissertation, it was extensively illustrated that full-field elastic wave based inspection of thin-walled composite components is possible. The thesis focused on the development of novel wavefield manipulation strategies and damage map construction methods, which improved the robustness and effectiveness of the damage detection to a point where it is competitive with the current state-of-the-art in industrial NDT methods (e.g. the ultrasonic C-scan).

Now, a short overview is provided of future works and recommendations, which in the author's opinion, are promising for the further development of the proposed NDT methods. These prospects and recommendations predominately aim at increasing the practicality of the methods and reducing the inspection times. Thereby opening the way for an effective and efficient industrial implementation of full-field elastic wave based damage detection in composite materials.

All proposed works have already been partially tackled during this PhD work.

<u>Increase the amplitude of excitation</u>

Throughout this PhD work, low power piezoelectric actuators (most often type EPZ-20MS64W from Ekulit) were used for exciting the propagating elastic waves. The actuators were chosen for their ability to excite waves in a broad frequency range. In addition, the actuators cost less than 1 euro. The drawback of using these small actuators is that they cannot introduce waves of considerable power. When the voltage supplied to the actuator is increased, the actuator heats up and the piezoelectric material degrades.

It makes sense to search for a replacement of these low power actuators that can deliver more vibrational power. An increase in vibrational power would result in an increase in signal-to-noise ratio of the measurement and an increase in the nonlinear response at the defects. As a result, the amount of averages, and the associated inspection times, will reduce and the addition of retroreflective tape (for measuring the nonlinear components) may no longer be necessary. Off course, care has to be taken that the excitation remains noninvasive.

Therefore, an aluminum casing was designed which can hold different piezoelectric actuators (including stack actuators), and which can be easily attached to the test specimen using vacuum. Figure 16.1 shows a picture of the first prototype. Note that a similar concept can already be found in industry, e.g. Isi-Sys Piezoshaker [1].

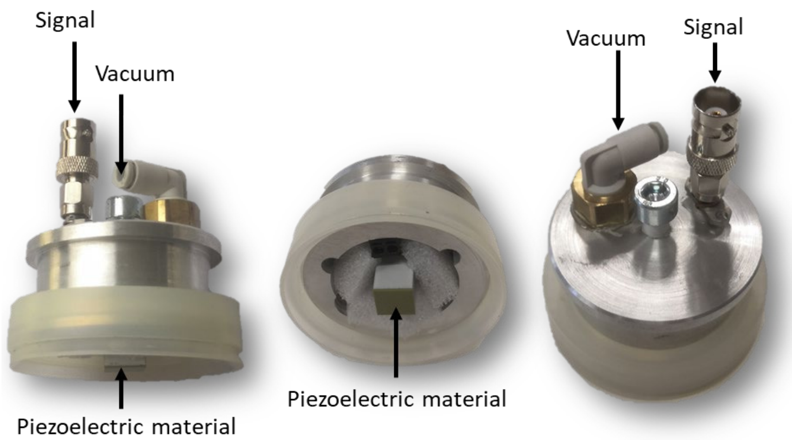

Figure 16.1: Vacuum attachable aluminum case for piezoelectric actuators.

Improve the understanding of defect nonlinearity
This PhD showed promising performance in detection and localization of defects using damage maps based on nonlinear vibrational components. Further work is needed to even extend it to defect characterization. Therefore, it is of added value to gain a better understanding in the formation of nonlinear vibrations in realistic damage, such as barely visible impact damage. A better understanding can help us to improve the robustness of the damage maps that are based on nonlinear energy calculation and on nonlinear local wave-direction estimation. In addition, the type of nonlinear components that are observed can give insight into the structure of the damage. For instance, the detection of only odd harmonics should relate to a perfect rubbing contact interface (see Chapter 3).

Use scanning pulsed laser excitation instead of bonded piezoelectric actuators
The replacement of the bonded piezoelectric wave excitation by a scanning pulsed laser excitation (operating in the thermoelastic regime) would, in the author's opinion, significantly improve the practicality, applicability and effectiveness of the proposed NDT methods. A scanning pulsed laser excitation:

- is non-contact and thus more practical.
- results in a roving excitation. As a result, a single point laser Doppler vibrometer (LDV) can be used and only a tiny patch of retroreflective tape is required (at the location where the LDV is aimed at) to achieve a good SNR.
- can be used for laser ultrasonic C-scan inspection when combined with a scanning laser Doppler vibrometer.

In Chapter 13 Section 5.3.1, a proof-of-concept of laser-excited (thermo-)elastic wave propagation was already provided.

<u>Exploit other means for reducing the inspection time</u>
Current inspection times are too long (see Chapter 15). Reduction of inspection time can be achieved by:

- skipping a certain percentage of measurement points and using wavefield reconstruction method such as compressed sensing [2-4].
- combination of multiple damage map construction methods.
  As an example, a fast initial inspection of the total structure can be achieved by performing a low-resolution SLDV scan followed by (linear or nonlinear) energy-based damage map construction. Next, the regions that show anomalies in the low resolution damage map, can be inspected again with a high-resolution SLDV scan. Within these small regions, accurate localization and evaluation of the damage is than achieved through self-reference broadband local wavenumber estimation.
- further investigation and improvement of out-of-sight damage detection using nonlinear local wave-direction estimation (e.g. through the use of a simulation-based expected local wave-direction map).
- Changing the experimental setup to:
  - a single point LDV combined with scanning pulsed laser excitation with high pulse repetition rate and high scan speed,
  - a continuous SLDV [5],
  - or a low-cost on-chip multi-point LDV [6].

References

1. Mäckel, P. *Piezoshaker Systems*. cited 2021; Available from: http://www.isi-sys.com/piezoshaker-systems-2/.
2. Mesnil, O. and M. Ruzzene, *Sparse wavefield reconstruction and source detection using Compressed Sensing.* Ultrasonics, 2016. **67**: p. 94-104.
3. Esfandabadi, Y.K., et al. *Accelerated guided waves inspection using Compressive sensing and Local wavenumber domain analysis*. in *IEEE International Ultrasonics Symposium (IUS)*. 2017. Washington, DC.

4. Sabeti, S. and J.B. Harley, *Spatio-temporal undersampling: Recovering ultrasonic guided wavefields from incomplete data with compressive sensing.* Mechanical Systems and Signal Processing, 2020. **140**.
5. Di Maio, D., et al., *Continuous Scanning Laser Vibrometry: A raison d'être and applications to vibration measurements.* Mechanical Systems and Signal Processing, 2021. **156**.
6. Li, Y., et al., *Six-beam homodyne laser Doppler vibrometry based on silicon photonics technology.* Opt Express, 2018. **26**(3): p. 3638-3645.

Scientific Output

Publications in journals of the Science Citation Index – A1 Papers –

[2018- 1] **J. Segers**, M. Kersemans, S. Hedayatrasa, J. Calderon, and W. Van Paepegem, '*Towards in-plane local defect resonance for non-destructive testing of polymers and composites*', NDT & E International, 98, pp 130-133, 2018.

SCI-IF(2018) = 2.934 ; Q1 (6/33)

[2019- 2] **J. Segers**, S. Hedayatrasa, E. Verboven, G. Poelman, W. Van Paepegem, and M. Kersemans, '*In-plane local defect resonances for efficient vibrothermography of impacted carbon fiber-reinforced polymers (CFRP)*', NDT & E International, 102, pp 218-225, 2019.

SCI-IF(2019) = 3.461 ; Q1 (5/33)

[2019- 3] S. Hedayatrasa, G. Poelman, **J. Segers**, W. Van Paepegem, and M. Kersemans, '*Performance of frequency and/or phase modulated excitation waveforms for optical infrared thermography of CFRPs through thermal wave radar: A simulation study*', Composite Structures, 225, 2019.

SCI-IF(2019) = 5.138 ; Q1 (6/26)

[2019- 4] S. Hedayatrasa, G. Poelman, **J. Segers**, W. Van Paepegem, and M. Kersemans, '*Novel discrete frequency-phase modulated excitation waveform for enhanced depth resolvability of thermal wave radar*', Mechanical Systems and Signal Processing, 132, pp 512-522, 2019.

SCI-IF(2019) = 6.471 ; Q1 (5/130)

[2019- 5] **J. Segers**, S. Hedayatrasa, E. Verboven, G. Poelman, W. Van Paepegem, and M. Kersemans, '*Efficient automated extraction of local defect resonance parameters in fiber reinforced polymers using data compression and iterative amplitude thresholding*', Journal of Sound and Vibration, 463, 2019.

SCI-IF(2019) = 3.429 ; Q1 (4/32)

[2020- 6] S. Hedayatrasa, **J. Segers**, G. Poelman, E. Verboven, W. Van Paepegem, and M. Kersemans, '*Vibrothermographic spectroscopy with thermal latency compensation for effective identification of local defect resonance frequencies of a CFRP with BVID*', NDT & E International, 109, 2020.

SCI-IF(2020) = 3.739 ; Q1 (8/32)

[2020- 7] **J. Segers**, S. Hedayatrasa, G. Poelman, W. Van Paepegem, and M. Kersemans, '*Probing the limits of full-field linear Local Defect Resonance identification for deep defect detection*', Ultrasonics, 105, 2020.

SCI-IF(2020) = 2.890 ; Q1 (8/32)

[2020- 8] **J. Segers**, S. Hedayatrasa, G. Poelman, W. Van Paepegem, and M. Kersemans, '*Backside delamination detection in composites through local defect resonance induced nonlinear source behaviour*', Journal of Sound and Vibration, 479, 2020.

SCI-IF(2020) = 3.655 ; Q1 (5/32)

[2020- 9] G. Poelman, S. Hedayatrasa, **J. Segers**, W. Van Paepegem, and M. Kersemans, '*Multi-scale gapped smoothing algorithm for robust baseline-free damage detection in optical infrared thermography*', NDT & E International, 112, 2020.

SCI-IF(2020) = 3.739 ; Q1 (8/32)

[2020- 10] **J. Segers**, S. Hedayatrasa, G. Poelman, W. Van Paepegem, and M. Kersemans, '*Nonlinear Elastic Wave Energy Imaging for the Detection and Localization of In-Sight and Out-of-Sight Defects in Composites*', Applied Sciences, 10, No 3924, 2020.
Invited contribution to the Special issue 'Guided Wave-Based Damage Identification for Composite Structures'

SCI-IF(2020) = 2.679 ; Q2 (38/91)

[2020- 11] G. Poelman, S. Hedayatrasa, **J. Segers**, W. Van Paepegem, and M. Kersemans, '*Adaptive spectral band integration in flash thermography: Enhanced defect detectability and quantification in composites*', Composites Part B: Engineering, 202, 2020.

SCI-IF(2020) = 9.078 ; Q1 (1/91)

[2020- 12] G. Poelman, S. Hedayatrasa, **J. Segers**, W. Van Paepegem, and M. Kersemans, '*An Experimental Study on the Defect Detectability of Time- and Frequency-Domain Analyses for Flash Thermography*', Applied Sciences, 10, No 22, 2020.
Invited contribution to the Special issue 'Infrared Imaging and NDT'

SCI-IF(2020) = 2.679 ; Q2 (38/91)

[2021- 13] S. Hedayatrasa, G. Poelman, **J. Segers**, W. Van Paepegem, and M. Kersemans, '*On the application of an optimized Frequency-Phase Modulated waveform for enhanced infrared thermal wave radar imaging of composites*', Optics and Lasers in Engineering, 138, 2021.

SCI-IF(2020) = 4.836 ; Q1 (13/99)

[2021- 14] **J. Segers**, S. Hedayatrasa, G. Poelman, W. Van Paepegem, and M. Kersemans, '*Robust and baseline-free full-field defect detection in complex composite parts through weighted broadband energy mapping of mode-removed guided waves*', Mechanical Systems and Signal Processing, 151, 2021.

SCI-IF(2020) = 6.823 ; Q1 (7/135)

[2021- 15] F. Marchetti, N.B. Roozen, **J. Segers**, K. Ege, M. Kersemans, and Q. Leclère, '*Experimental methodology to assess the dynamic equivalent stiffness properties of elliptical orthotropic plates*', Journal of Sound and Vibration, 495, 2021.

SCI-IF(2020) = 3.655; Q1 (5/32)

[2021- 16] T.D. Dinh, S. Han, V. Yaghoubi, H. Xiang, H. Erdelyi, T. Craeghs, **J. Segers**, and W. Van Paepegem, '*Modeling detrimental effects of high surface roughness on the fatigue behavior of additively manufactured Ti-6Al-4V alloys*', International Journal of Fatigue, 144, 2021.

SCI-IF(2020) = 5.186 ; Q1 (15/135)

[2021- 17] **J. Segers**, S. Hedayatrasa, G. Poelman, W. Van Paepegem, and M. Kersemans, '*Nonlinear Local Wave-Direction Estimation for In-sight and Out-of-sight Damage Localization in Composite Plates* ', NDT & E International, 119, 2021.

SCI-IF(2020) = 3.739 ; Q1 (8/32)

[2021- 18] T. Duerinck, **J. Segers**, E. Skrodzka, G. Verberkmoes, M. Leman, W. Van Paepegem, and M. Kersemans, '*Experimental comparison of various excitation and acquisition techniques for modal analysis of violins*', Applied Acoustics, 177, 2021.

SCI-IF(2020) = 2.639 ; Q2 (11/32)

[2021- 19] **J. Segers**, S. Hedayatrasa, G. Poelman, W. Van Paepegem, and M. Kersemans, '*Broadband nonlinear elastic wave modulation spectroscopy for damage detection in composites*', Structural Health Monitoring, First published online, 2021.

SCI-IF(2020) = 5.929 ; Q1 (8/91)

[2021- 20] S. Hedayatrasa, **J. Segers**, G. Poelman, W. Van Paepegem, and M. Kersemans, '*Vibro-Thermal Wave Radar: Application of Barker Coded Amplitude Modulation for Enhanced Low-Power Vibrothermographic Inspection of Composites*', Materials, 2021.
Invited contribution to the Special issue 'Mechanical Characterization of FRP Composite Materials'

SCI-IF(2020) = 3.623; Q1 (17/80)

[2021- 21] **J. Segers**, S. Hedayatrasa, G. Poelman, W. Van Paepegem, and M. Kersemans, '*Self-Reference Broadband Local Wavenumber Estimation (SRB-LWE) for defect assessment in composites* ', Mechanical Systems and Signal Processing, 163, 2021.

SCI-IF(2020) = 6.823 ; Q1 (7/135)

Conference papers available in ISI Proceedings – P1 Papers –

[2018- 1] S. Hedayatrasa, **J. Segers**, J. Calderon, W. Van Paepegem, and M. Kersemans, '*On Efficient FE Simulation of Pulse Infrared Thermography for Inspection of CFRPs*', in 14th Quantitative InfraRed Thermography Conference, Berlin, 2018.

Conference papers not available in ISI Proceedings – C1 Papers –

[2018- 1] M. Kersemans, E. Verboven, **J. Segers**, S. Hedayatrasa, and W.V. Paepegem, '*Non-Destructive Testing of Composites by Ultrasound, Local Defect Resonance and Thermography*', in 18th International Conference of Experimental Mechanics, Brussels: MDPI, 2018.

[2018- 2] G. Poelman, S. Hedayatrasa, **J. Segers**, J.A.C. Tellez, W.V. Paepegem, and M. Kersemans, '*Optical Infrared Thermography of CFRP with Artificial Defects: Performance of Various Post-Processing Techniques*', in 18th International Conference of Experimental Mechanics, Brussels: MDPI, 2018.

[2018- 3] **J. Segers**, M. Kersemans, E. Verboven, S. Hedayatrasa, J. Calderon, and W. Van Paepegem, *Investigation to Local Defect Resonance for Non-Destructive Testing of Composites*, in 18th International Conference of Experimental Mechanics, Brussels: MDPI, 2018.

[2018- 4] **J. Segers**, E. Verboven, S. Hedayatrasa, G. Poelman, J. Calderon, W. Van Paepegem, and M. Kersemans, '*Automated extraction of local defect resonance for efficient non-destructive testing of composites*', in 9th European Workshop on Structural Health Monitoring, Manchester, 2018.

[2019- 5] S. Hedayatrasa, **J. Segers**, G. Poelman, W. Van Paepegem, and M. Kersemans, *Sweep vibrothermography and thermal response derivative spectroscopy for identification of local defect resonance frequencies of impacted CFRP*, in International Conference on Ultrasonic, Brugge: Proceedings of Meetings on Acoustics, 2019.

[2019- 6] **J. Segers**, S. Hedayatrasa, G. Poelman, W. Van Paepegem, and M. Kersemans, '*Full wave field signal processing techniques for NDT of composites: a case study*', in International Conference on Ultrasonic, Brugge: Proceedings of Meetings on Acoustics, 2019.

[2019- 7] **J. Segers**, S. Hedayatrasa, G. Poelman, W. Van Paepegem, and M. Kersemans, *Enhanced low power vibrothermography of impacted CFRP through in-plane local defect resonances*, in International Conference on Ultrasonic, Brugge: Proceedings of Meetings on Acoustics, 2019.

[2019- 8] G. Poelman, S. Hedayatrasa, **J. Segers**, W. Van Paepegem, and M. Kersemans, '*Application of Flash Thermography and Advanced Post-Processing Techniques for Rapid NDT of CFRP Aircraft Component: A Case Study*', in 11th Symposium on NDT in Aerospace, Paris-Saclay, 2019.

[2019- 9] **J. Segers**, S. Hedayatrasa, E. Verboven, G. Poelman, W. Van Paepegem, and M. Kersemans, '*Full wave field signal processing techniques for NDT of CFRP aircraft panel: A case study*', in 11th International Symposium NDT in Aerospace, Paris-Saclay, 2019.

[2019- 10] G. Poelman, **J. Segers**, S. Hedayatrasa, E. Verboven, W. Van Paepegem, and M. Kersemans, '*The state-of-the-art and beyond in non-destructive testing of a complex CFRP component*', in 11th International Symposium NDT in Aerospace, Paris-Saclay, 2019.

[2020- 11] G. Poelman, S. Hedayatrasa, **J. Segers**, W. Van Paepegem, and M. Kersemans, '*A robust multi-scale gapped smoothing algorithm for baseline-free damage mapping from raw thermal images in flash thermography*', in 15th Quantitative InfraRed Thermography Conference, Porto, 2020.

[2020- 12] G. Poelman, S. Hedayatrasa, **J. Segers**, W. Van Paepegem, and M. Kersemans, '*Efficient Detection Of Production Defects In A CFRP Aircraft Component By Means Of Flash Infrared Thermography*', in SAMPE Europe 2020 Conference, 2020.

[2020- 13] **J. Segers**, S. Hedayatrasa, E. Verboven, G. Poelman, W. Van Paepegem, and M. Kersemans, '*Robust and Baseline-free defect detection in aircraft CFRP components using full-field guided wave analysis*', in SAMPE Europe 2020 Conference, Amsterdam, 2020.

[2020- 14] A.H. Orta, **J. Segers**, J. Vandendriessche, N.B. Roozen, W.V. Paepegem, M. Kersemans, and K.V.D. Abeele, '*Characterization of orthotropic elastic tensor using lamb waves*', in Forum Acusticum, Lyon, France, 2020.

Conference abstracts and posters – C3 Papers –

[2018- 1] G. Poelman, S. Hedayatrasa, **J. Segers**, J. Calderon, W. Van Paepegem, and M. Kersemans, '*Thermographic Inspection of Composites: Shining light on a hot topic*', in FEARS Gent, 2018.

[2019- 2] S. Hedayatrasa, G. Poelman, **J. Segers**, W. Van Paepegem, and M. Kersemans, '*Frequency-Phase Modulated Thermal Wave Radar: Stepping beyond State-of-the-art Infrared Thermography*', in SIM User Forum, Gent, 2019.

[2019- 3] G. Poelman, S. Hedayatrasa, **J. Segers**, W. Van Paepegem, and M. Kersemans, '*Flash Thermographic Inspection of Composites Shining Light on a Hot Topic*', in SIM User Forum, Gent, 2019.

[2019- 4] **J. Segers**, S. Hedayatrasa, G. Poelman, W. Van Paepegem, and M. Kersemans, '*Local Defect Resonance for NDT of Composites*', in SIM User Forum, Gent, 2019.

[2019- 5] S. Hedayatrasa, G. Poelman, **J. Segers**, W. Van Paepegem, and M. Kersemans, '*Enhanced detectability of barely visible impact damage in CFRPs: Vibrothermography of in-plane local defect resonances*', in

Measuring by Light meets OPTIMESS 2019, International Meeting on Optical Measurement Techniques and Industrial Applications, Antwerp, 2019.

[2019- 6] M. Kersemans, S. Hedayatrasa, G. Poelman, **J. Segers**, and W. Van Paepegem, '*Inspection of Impacted Composites: Evaluation of state-of-the-art NDT Approaches*', in Measuring by Light meets OPTIMESS 2019, International Meeting on Optical Measurement Techniques and Industrial Applications, Antwerp, 2019.

[2019- 7] G. Poelman, S. Hedayatrasa, **J. Segers**, W. Van Paepegem, and M. Kersemans, '*Flash Thermography of Composites: Evaluation of Advanced PostProcessing Approaches*', in Measuring by Light meets OPTIMESS 2019, International Meeting on Optical Measurement Techniques and Industrial Applications, Antwerp, 2019.

[2019- 8] **J. Segers**, S. Hedayatrasa, E. Verboven, G. Poelman, W. Van Paepegem, and M. Kersemans, '*Efficient automated extraction of local defect resonance parameters for non-destructive testing of fiber reinforced polymers*', in Measuring by Light meets OPTIMESS 2019, International Meeting on Optical Measurement Techniques and Industrial Applications, Antwerp, 2019.

[2019- 9] M. Kersemans, S. Hedayatrasa, **J. Segers**, E. Verboven, and W. Van Paepegem, '*Imaging of BVID in Composites: Comparison of Advanced NDT Methodologies*', in International Congress on Ultrasonics, Brugges, 2019.

[2019- 10] F. Marchetti, K. Ege, Q. Leclère, N.B. Roozen, M. Kersemans, and **J. Segers**, '*Caractérisation dynamique large bande d'un sandwich en nids d'abeille*', in JJCAB 2019 : Journées Jeunes Chercheurs en vibrations, Acoustique et Bruit, Abstracts, Besancon, 2019.

[2019- 11] G. Poelman, S. Hedayatrasa, **J. Segers**, W. Van Paepegem, and M. Kersemans, '*Thermographic NDT of Composite Aerospace Components*', in Aviation@KU Leuven, Leuvem, 2019.

[2019- 12] **J. Segers**, S. Hedayatrasa, G. Poelman, W. Van Paepegem, and M. Kersemans, '*Vibrometric NDT of Composite Aerospace Components*', in Aviation@KU Leuven, Leuven, 2019.

[2021- 13] G. Poelman, S. Hedayatrasa, **J. Segers**, W. Van Paepegem, and M. Kersemans, '*Adaptive spectral band integration in thermographic inspection of composites*', in Sampe Benelux Spring Meeting, Virtual, 2021.

Scientific Guide for Master Theses

[2020- 1] Van Heesvelde, Sebastiaan. *New materials for soundboards of the violin: modal analysis,* 2020

[2020- 2] Vancoillie, Tijs. *Investigation on Local Defect Resonance in Delaminated Composites: Optimized Excitation and Controlled Defect Introduction,* 2020

[2020- 3] Cardinaels, Alessandro. *Acoustical analysis of string instruments with composite soundboards*, 2020

Awards

Winner with team UGent-MMS (Joost Segers, Gaétan Poelman, Saeid Hedayatrasa, Erik Verboven, Wim Van Paepegem and Mathias Kersemans) of 'NDT in Aerospace Student Challenge, 2019', Paris-Saclay

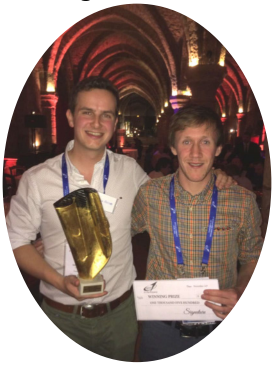

Selected 'Feature paper' of the special issue *Guided Wave-Based Damage Identification for Composite Structures*:

Segers, J., et al., *Nonlinear Elastic Wave Energy Imaging for the Detection and Localization of In-Sight and Out-of-Sight Defects in Composites.* Applied Sciences, 10, 2020.

Selected 'Editor's choice' of the journal of Ultrasonics:

Segers, J., et al., *Probing the limits of full-field linear local defect resonance identification for deep defect detection.* Ultrasonics, 105, 2020.

NDT of aerospace component: Elastic wavefield measurement before and after post-processing.